Developing a Method to Evaluate Interventions for Osteochondral Defects of the Talus

Ahranee Canden

Submitted in accordance with the requirements for the degree of
Tissue Engineering and Regenerative Medicine-
Innovations in Medical and Biological Engineering

The University of Leeds

Institute of Mechanical and Biological Engineering

School of Mechanical Engineering

May 2023

The candidate confirms that the work submitted is his/her own and that appropriate credit has been given where reference has been made to the work of others.

Acknowledgements

I would like to thank all the important people who supported me to the end. This was one of the hardest challenges I have ever had to face and I am grateful for every person who helped me get here.

Firstly, thank you to my family for their support throughout the whole PhD process. I would like to dedicate this thesis to my grandmother, Dr Meena Jeyapalina. The first female doctor in the family and an amazing women who continuously inspired me to push my boundaries and supported me throughout every endeavour. You were my biggest cheerleader and I am sad that you could not be with me until the end. I know that you had complete faith in my ability to get here and I would not have made it here with out you. I hope I continue to make you proud. To my parents, Malini and Sananda, for never letting me know that I had limits and allowing me to believe I could achieve anything. To my Aunt, Sujee, for guiding me in life and pushing me to do more and to Elachumee and Haraen, for keeping me grounded and being there for every phone call, triumph and failure.

Alex, my best friend, rock and partner, thank you for everything. I would not survived the whole process without you. Your perspective, unwavering support and the 2 am pizzas during late night working session were always appreciated. I would not have been able to get to the end without you.

I would like to thank all my supervisors, support staff, friends and members of iMBE and Oral Biology whose input, guidance and friendship were always appreciated in the long days in the lab. I have made some amazing life long friends at the University of Leeds and in the CDT. Thank you to Professor Claire Brockett for everything. I would not have made it through the whole process with you. With your support, I managed to reach the finish line, with a PhD I can be proud of, a friend and mentor. You continue to inspire me and remind me how exiting academia and research can be.

Finally, I would like to thank the collaborative efforts of my clinical advisor Mr Mark Farndon and the extremely generous people at Joint Operations Ltd. who have provided so much clinical insight and support throughout my PhD. I am so proud of the range and depth of outputs we have been able to produce in such a short period of time.

Abstract

Osteochondral lesions of the talus (OLTs) are commonly caused by an acute traumatic ankle injury. Multiple treatment modalities are available for OLTs, with the size and location of the lesion informing treatment choice. Hydrogels provide an exciting possibility for future therapies for OLTs due to their tunable properties and similarities to native cartilage. However, there is a lack of understanding relating to the differences in clinical success seen with different lesions and a notable paucity in long term studies or appropriate *ex vivo* methods to assess the biomechanical changes within the tibiotalar joint.

A functionalised hydrogel was developed as an injectable therapy for OLTs. Reproducible synthesis using sequential functionalisation of 4-vinylbenzyl chloride (4VBC) and methacrylamide (MA) on type I rat tail collagen was performed to create an injectable precursor material. Successful photocrosslinking of 4VBC-MA precursor was performed using vis-light photoinitiation in physiological conditions. Encapsulation of ATDC-5 immortalised chondrocytes and MSCs showed viability within the scaffolds for up to 7 days and maintenance of chondrogenic morphology.

The subsequent studies aimed to develop a greater understanding by characterising the biomechanical changes associated with OLTs through changes in contact area, contact pressure, and frictional properties. Presence of a 10 mm defect within the human talar dome caused a significant increase to the coefficient of friction compared with that of native tibiotalar joint but did not significantly change the contact mechanics. Repair of the defect with the 4VBC-MA hydrogel was able to reduce the friction coefficient in the tibiotalar joint to a similar level as that seen using autologous matrix induced chondrogenesis (AMIC) and osteochondral allograft treatments ($p < 0.05$). None of the treatments were able to return the friction coefficient to the value seen in healthy tissue, with only the osteochondral allograft treatment allowing for loading to occur through the defect site. The outcomes of AMIC treatments varied depending on size, shape and lesion location. Stability of AMIC repair was dependent on shape, with square repairs performing poorer compared to circular repairs. AMIC treatment of kissing lesions is subject to material-material interactions which negatively impacts the tissue frictional properties, reducing the stability of the repair.

Contents

List of Tables

List of Figures

List of Abbreviations

4VBC	4-vinylbenzyl chloride
AC	Atelocollagen
ACI	Autologous chondrocyte implantation
ADAMTS	A disintegrin and metalloproteinase with thrombospondin
AMIC	Autologous matrix-induced chondrogenesis
AOFAS	American orthopaedic foot and ankle score
AOT	Osteochondral allo/autograft transplants
AP	Anterior and posterior
BMS	Bone marrow stimulation
BMDCT	Bone marrow derived cells transplantation
BSE	Back scatter electrons
CLAI	Chronic Lateral Ankle Instability
CT	Computer tomography
DMEM	Dulbecco's modified Eagle Media
ECM	Extra cellular matrix
ESED	Environmental secondary electron detector
FCS	Foetal calf serum
F/E	Flexion / Extension
FFI	Foot function index
GAG	Glycosaminoglycans
HA	Hyaluronan or Hyaluronic acid
HIF	Hypoxia inducible factor
IHC	Immunohistochemistry
IL	Interleukin

LAP	Lithium phenyl-2,4,6-trimethylbenzoylphosphinate
MA	Methacrylic anhydride
MACI	Matrix associated chondrocyte implantation
MAST	Matrix associated stem cell therapy
MMP	Metallomatrix proteases
MMP-I	Metallomatrix proteases inhibitors
MOCART	Magnetic resonance observation of cartilage repair tissue
MRI	Magnetic resonance imaging
MSC	Mesenchymal stem cells
MSS	Musculoskeletal syndrome
NFKB	Nuclear Factor Kappa B
NH_2	Amine group
NICE	National Institute for Health and Care Excellence
NSAID	Nonsteroidal anti-inflammatory drugs
OA	Osteoarthritis
OAT	Osteochondral allo/autograft treatment
OCL	Osteochondral lesions
OLT	Osteochondral lesions of the talus
OLTP	Osteochondral lesions of the tibial plafond
O/N	Over night
PBS	Phosphate buffered saline
PCL	Poly-ε-caprolactone
PGA	Poly glycolic acid
PLA	Poly lactic acid
PLGA	Poly lactic-co-glycolic acid
PMMA	Polymethylmethacrylate
PRP	Platelet-rich plasma therapy
PTOA	Post traumatic osteoarthritis
PTFE	Poly tetrafluoroethylene
ROM	Range of motion
RPM	Revolutions per minute

RT	Room temperature
RTC	Rat tail collagen
SEM	Scanning Electron Microscopy
STTA	Sagittal tibio-talar angle
TEA	Triethylamine
TGF-β	Transforming growth factor beta
TIMPS	Tissue inhibitors of metalloproteases
TNBS	2,4,6-Trinitrobenzene Sulfonic Acid
VAS	Visual Analogue Scale

Chapter 1

Literature review

1.1 Clinical rationale

Osteochondral lesions of the talus (OLTs) are the most common injury occurring within the ankle joint and are found in over 50% of patients with ankle sprains and two thirds of patients presenting with lateral ankle instability (Saxena and Eakin, 2007, Veronesi et al., 2023). They are increasingly identified in young, active patients as a results of acute trauma to the ankle joint (Peters et al., 1991, Vannini et al., 2016). Damage caused to the cartilage surface of the talar dome may impair the biomechanical function of the joint; thus reducing the structural integrity of the tissue and propagating development to osteoarthritis (OA) within the tissue. OLTs can have a severe impact on a patients quality of life, especially in active individuals as it is associated with deep pain in the ankle during weight bearing. Furthermore, it results in elevated risks of in the development of end-stage OA in the ankle, with 78% of cases of ankle OA having post-traumatic origins compared to the 9% attributed to primary OA (Valderrabano et al., 2009). 15% of the worlds population is affected by OA, however, ankle OA attributed to only 1% of cases (Peyron, 1984). This results in the sparsity of literature attribute to ankle OA compared to knee and hip OA.

In this literature review, the general structure and function of the tibiotalar joint, structure and function of cartilage, changes to the joint environment and properties due to presence OLTs will be discussed.

The size and type of lesion affects the intervention strategy adopted to manage OLTs. These include conservative treatments, such as partial loading of the joint, insoles to correct alignment and a reduction in physical activity. These also include surgical intervention such as osteochondral fragment repairs, bone marrow stimulation techniques, autologous osteochondral transplantation, or matrix based techniques. However, there is a gap in the comparative literature, in particular a noticeable paucity of long term randomised clinical trials comparing techniques for the identification of a superior approach (Migliorini et al., 2022b). Furthermore, there is a lack of understanding relating to the biomechanical and biochemical changes that occur within the true tibiotalar joint and relating to the insult and OLTs. Many of the studies discussed within this thesis will highlight the absence of prospective studies, retrospective nature of the studies and the low samples sizes present in most studies. All of this concatenates into a paucity of information and a lack of understanding of the range of treatments in approaches being taken.

1.2 The Ankle Joint and Osteoarthritis

Ankle OA is a chronic debilitating disorder that affects the young and active population, with 1% of the global OA population affected by ankle OA (Valderrabano et al., 2009). It is considered to be a disease that affects the whole joint and unlike hip and knee OA, the exact aetiology of ankle OA is unknown, with a lack of clinical and basic research focused on the ankle present currently. It is believed that the main cause of OA in the ankle is the result of traumatic insult to the joint and not primary OA, as is seen commonly in the hip and knee. Only 7% of ankle OA cases are thought to be caused by idiopathic OA compared to the 75% attributed to a traumatic event (Herrera-Pérez et al., 2021). While the clinical implications of early ankle OA are not frequently discussed, it is known that more advanced stages are highly debilitating with a severe reduction in quality of life often seen, including increased risk of cardiovascular disease (Glazebrook et al., 2008, Rahman et al., 2013).

Within this section the anatomy of the ankle and the pathological changes associated with ankle OA will be discussed.

1.2.1 Anatomy of the ankle joint

The ankle joint complex is one of the most complex joints within the human body. It comprises of seven bones- tibia, fibula, talus, calcaneous, navicular, cuboid and cuneiform, and has three main articulating surfaces- talocalcaneal, tibiotalar and talocalcaneonavicular (fig. 1.1) (Brockett and Chapman, 2016). The joint complex compromises of both bony and ligamentous structures which play a crucial role in maintenance of stability and function of the joint. This allows the joint to endure high compressive loads and shear forces during normal gait cycle (Anderson et al., 2010, Brockett and Chapman, 2016).

A combination of motions including plantar- and dorsiflexion, inversion-eversion and ab- and adduction occurs within the joint in the sagittal, frontal and transverse planes, respectively, contributing to the normal action of the ankle known as supination and pronation (fig. 1.2) (Brockett and Chapman, 2016). The range of motion (ROM) within the complex is controlled by multiple joints, with each joint required to ensure that a full ROM is achieved and provides stability to the joint complex.

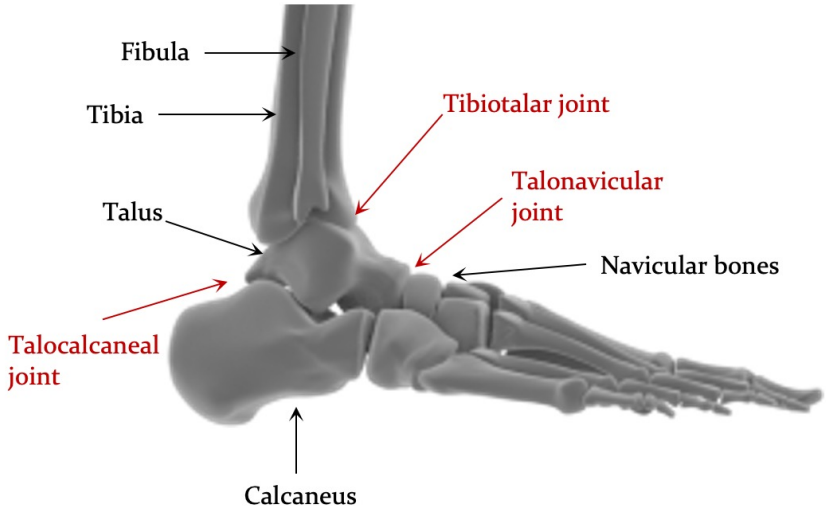

Figure 1.1: Foot and ankle anatomy
Anatomy of the foot and ankle showing the key bones and joints within the complex.

1.2.2 Talus: Role and function

The talus is located within the ankle joint complex (fig. 1.1). It acts as a link between the foot and leg; connecting the tibia and fibula with the calcaneous, navicular and cuboid bones, displaying

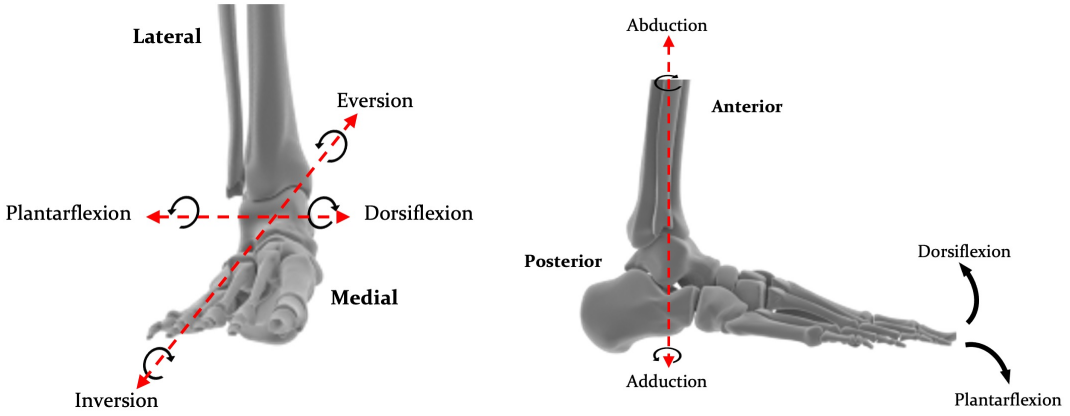

Figure 1.2: Axes of the foot and ankle
A shows the joint motion within the ankle joint. Highlighting inversion and eversion motions as well as the dorsiflexion and plantarflexion. **B** shows lateral views of the foot highlighting abduction and adduction and dorsiflexion and plantarflexion movement of the natural joint.

congruency with these surrounding bones and allowing it to transfer forces from the body to the foot during loading or impact (fig. 1.3) (Bidmos et al., 2018, Standring, 2015).

The talus has no muscular attachments and its stability is dependent on the presence of attached ligaments and its bony geometry. Although 70% of the surface of the talus is covered in articular cartilage, contact areas in the ankle are lower than that seen in the knee and the hip even though the forces experienced by the joint are higher (Egloff et al., 2012, Standring, 2015).

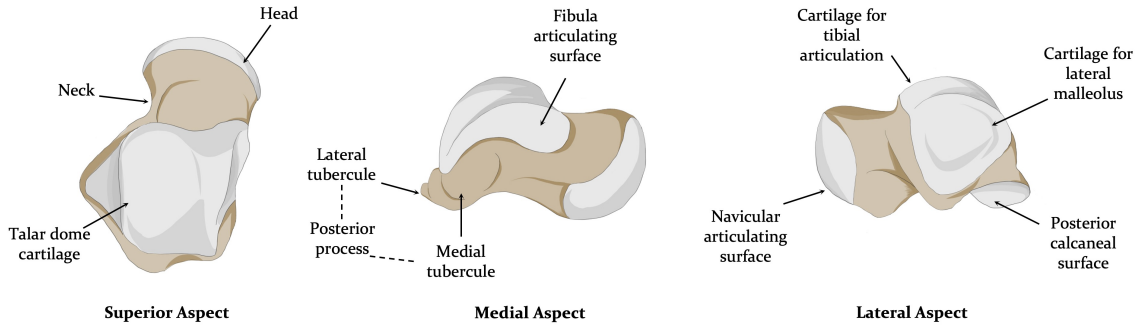

Figure 1.3: Talus morphology
Schematic showing the key morphological features of the talus and areas in which articular cartilage is located from the superior, medial and lateral aspects.

1.2.3 The Talocrural Joint

The talocrural joint is a uniaxial, hinge joint that allows for the ankle to shift between dorsi- and plantarflexion during normal walking gait (fig: 1.2) (Standring, 2015). It consists of the tibia, fibula and talus contained within a joint capsule. This creates the main synovial joint seen within the ankle complex (Standring, 2015). The talocrural joint has the greatest range of motion during the gait cycle and helps to maintain stability during load bearing (Brockett and Chapman, 2016).

As previously mentioned, the shape of the talus is congruent to the surrounding bones. Fig: 1.3 highlights the areas in which congruency of the talus can be seen in its morphology. The talus follows a convex-concave-convex shape as you move from the medial to lateral side (Riegger, 1988). The articular surfaces, too, show high levels of congruency to the underlying bone and are thickest on the convex osseous surfaces. The proximity of the ankle joint to the ground results in the joint supporting nearly all of the ground force load. High levels of congruency has been associated with thinner cartilage and this can be seen in the talus where cartilage thickness is extremely uniform, unlike that seen in either the hip or knee (Shepherd and Seedhom, 1999).

Generally, talar cartilage is thinner and has lower elasticity compared to cartilage seen within other joints, making it more susceptible to acute or traumatic damage (McGoldrick et al., 2017). The thickness however, does not impede its function but it still allows for the ankle joint to transmit large forces throughout normal gait cycle- for example during the heel rise, the ankle is loaded with 3.9 - 5 times body weight (McGoldrick et al., 2017, O'loughlin et al., 2010). This high level of force passing through the joint during normal gait cycle is greater than that seen in other joints. Histological analysis of talocrural cartilage has shown that it differs to that of like-tissues, such as the knee, in depth (Egloff et al., 2012).

1.2.4 Biomechanical loading of the tibiotalar joint

The ankle joint complex receives some of the highest loads during normal gait function, with up to thirteen times body weight thought to go through the joint during running (Brockett and Chapman, 2016, Burdett, 1982). The normal ankle gait cycle can be broken into two distinct phases, the stance phase and the swing phase.

The stance phase can be divided into three distinct loading patterns: heel strike, midstance and

toe-off. At heel strike, the ankle joint displays dorsiflexion, in midstance the joint is in a more neutral position and in the final phase, a plantarflexion motion occurs (Brockett and Chapman, 2016). It is believed that up to 83% of load is transmitted through the tibiotalar joint and 90% of this acts through the talar dome (Calhoun et al., 1994, Michael et al., 2008). Excessive motion within the joint is limited by the presence of ligaments located on the lateral side of the ankle joint such as the anterior and posterior talofibular ligaments and the calcaneofibular ligament (Anderson et al., 2010). During the normal gait function the dorsiflexion range of the joint can vary from 10 - 30° and plantarflexion angle range between 40 - 50° in the sagittal plane (Brockett and Chapman, 2016, Nordin and Frankel, 2001, Riegger, 1988, Standring, 2015). Computational modelling of the gait cycles of nine normal ankles suggests that less than 50% of the contact areas of the cartilage are involved during the stance phase of walking with the contact areas seen to be located more within the lateral and central surfaces found within the talocrural joint. In addition, lower contact was seen in the posterior location of the talocrural joint (Wan et al., 2006).

1.3 Articular Cartilage in the Tibiotalar Joint

Articular cartilage is present on all articulating surfaces found in synovial joints within the body. It is a load-bearing connective tissue that provides a smooth, resistant surface which permits nearly frictionless movement within the joint for optimal movement (Standring, 2015). Native, healthy articular cartilage is white and glossy in appearance, however its appearance and properties change depending on age and location. The function of this unique tissue is dependent on its structure, composition and organisation, as the issue is highly specialised to ensure correct joint function and provide longevity to the joint. It does this by maintaining a low coefficient of friction between the two surfaces, high resistance to tension, compression and shearing, as well as providing a high capacity for load bearing (Athanasiou et al., 1994). Damage to this tissue on either side of the joint causes pain and reduction of mobility (Van Dijk et al., 2010).

1.3.1 Structure of articular cartilage

Hyaline articular cartilage is a specialised tissue that comprises of cells, or chondrocytes, interacting with a highly regulated extracellular matrix (ECM). The composition and organisation of matrix macromolecules within the ECM of cartilage is closely related to its function. The nutrients and

lubrication for the tissue are provided by secreted synovial fluid as it is an avascular and aneural tissue. The thickness of articular cartilage varies throughout joints (Table 1.1), with the average thickness seen on the talar dome being reported to be between 1 and 3 mm, with this differing between men and woman on average at 1.35 mm and 1.11 mm, respectively (McGoldrick et al., 2017, Shepherd and Seedhom, 1999, Standring, 2015, Wodicka et al., 2016). Ankle joints are known to have the highest congruency ratio (length of congruent surface : length of total articular surface) compared to other joints in the lower body (Simon et al., 1973). It has been hypothesised that this high level of congruency is inversely correlated to joint thickness, as the compressive load is distributed over a wider area therefore decreasing local joint stresses (Shepherd and Seedhom, 1999). Thus, positional changes to the ankle joint, such as malalignment, will affect load distribution across the joint and cause an increase in shear forces and damage to the cartilage. A 2021 study looking at differences between cartilage thickness across the talar dome saw that the average thickness was 1.00 mm ± 0. 1 mm (Nott et al., 2021),

Table 1.1: Average thickness of articular cartilage within lower limb joints
Comparison of average cartilage thickness across the same cadaveric samples of cartilage thickness taken from the joints of the leg. For each specimen three measures were made in the posterior, superior and anterior regions of the ankle, hip and knee joint. Thickness was measured using load displacement between contact of cartilage and contact with subchondral bone (Shepherd and Seedhom, 1999).

Mean cartilage thickness (mm)			
	Hip	Knee	Ankle
Male	1.68	2.1	1.23
Female	1.61	2.17	1.25

1.3.2 Composition of articular cartilage

The primary component of hyaline cartilage is water, which makes up to 80% of the total weight of the tissue. The solid component of cartilage is predominantly made of collagen (roughly 50%), followed by proteoglycans which can make up to 15-30% of the dry mass. The rest of the matrix is made of smaller protein molecules and also chondrocytes. It is the composition of the protein, collagen and proteoglycan network that allows for cartilage to exhibit unique mechanical properties (Athanasiou et al., 2009, Standring, 2015).

Biochemical composition of articular cartilage

There are two main groups of extracellular macromolecules that make up the solid components of cartilage: fibrous proteins (collagen, elastin, fibronectin and laminin) and proteoglycans (fig. 1.4) (Athanasiou et al., 2009). Articular cartilage is predominantly made of collagen type II, which is rich in proline and glycine residues allowing it to form a triple helix structure (Athanasiou et al., 2009). These are then further packed into a three helical chain complex called a super helix. Collagen fibres seen within cartilage can vary in diameter between 10 -20 nm. The size and orientation of the collagen fibres vary within different types of cartilage. Within the superficial zone of cartilage, located closest to the articulating edge, the collagen fibres are smaller with an average diameter of between 4 and 6 nm (Standring, 2015). There are other fibrillar and globular collagen proteins present to varying degrees within the cartilage tissue such as type IV, V,VI, IX and XI (Athanasiou et al., 2009).

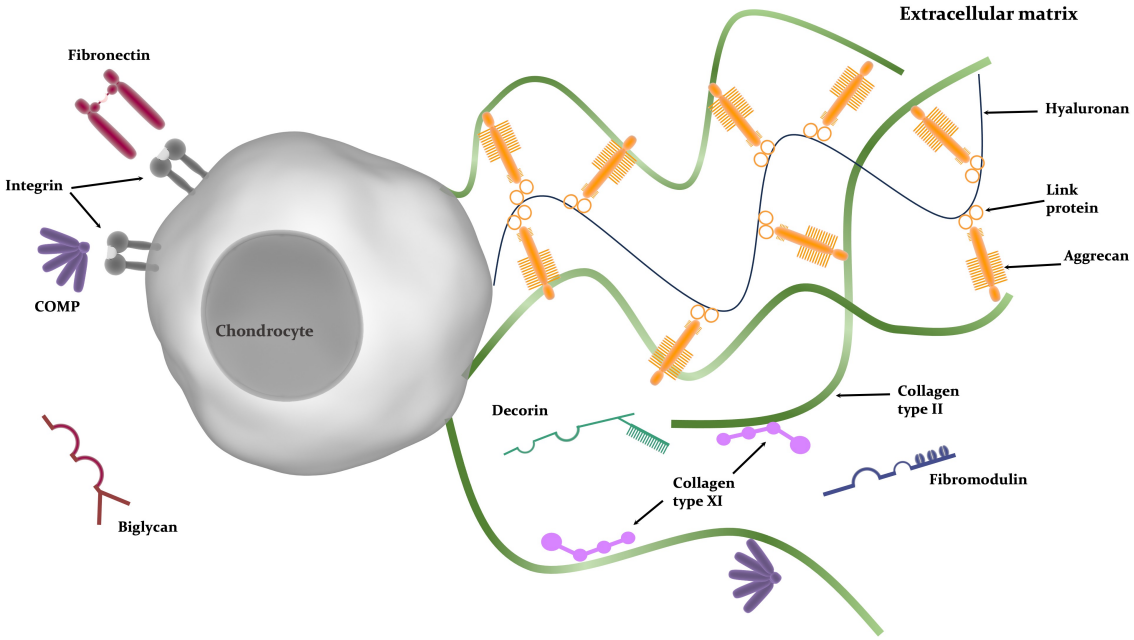

Figure 1.4: Extracellular matrix of articular cartilage
Schematic of the ECM of articular cartilage showing the interactions between the chondrocytes and proteinaceous matrix. Adapted from (Sophia Fox et al., 2009).

The primary proteoglycan found within articular cartilage is aggrecan. Aggrecan comprises of a hyaluronan core with multiple glycosaminoglycan (GAG) side chains- such as chondroitin and keratan sulphates (Athanasiou et al., 2009). The proteoglycan network acts as a mesh within the cartilage tissue and organised collagen network to ensure correct function. The role of this

hyaluronan core is to ensure that the joint surface is able to resist compressive forces (Mankin and Lippiello, 1969). The carboxyl and sulphate groups seen within the proteoglycans provide the ECM with a negative charge. This allows for a fixed charge density permitting the matrix to absorb fluids and maintain the fluid equilibrium (Maroudas et al., 1969). A reduction in the proteoglycan content within the cartilage, commonly seen in OA, results in a reduction in function of the cartilage (Standring, 2015).

A smaller portion of proteoglycans found within cartilage are biglycan, decorin and fibromodulin. These too contain GAG side chains and are thought to play a role in matrix assembly by interacting with the collagen matrix during development and repair of the tissue (Roughley and Lee, 1994).

The ankle has been shown to have a higher level of proteoglycan content compared to other articulating joints like the knee which provides it with greater compressive rigidity. This results in the ankle having a reduced susceptibility to developing primary OA, unless a traumatic or chronic injury has occurred (Treppo et al., 2000).

Hyaline cartilage is constantly in a state of remodelling and is a metabolically active tissue. The degeneration and regeneration of extracellular matrix components of cartilage occurs in areas in direct proximity to chondrocytes. The rate of turnover of different composites of the cartilage ECM varies, for example, collagen has a estimated turn over rate of over 100 years, whereas, aggrecan has been shown to have a half life of roughly one year (Mankin and Lippiello, 1969). Thus adding to the limited regenerative capacity seen in cartilage tissue.

Cellular composition

Articular cartilage is a sparsely populated tissue and the majority cells present are chondrocytes and chondroblasts (Athanasiou et al., 2009). Chondrocytes are the major cellular component of cartilage, representing only 1% of the total volume of the tissue (Mankin and Lippiello, 1969, Temenoff and Mikos, 2000). They are located within small lacunae found within the main body of the ECM of the cartilage. Chondrocytes are able to receive mechanical cues from the surrounding ECM through interactions with the local pericellular matrix (fig. 1.4). The mechanical stimuli provided by the ECM helps maintain their differentiated state and allows for chondrocyte to sense changes in their environment and alter their metabolism accordingly as chondrocytes have been shown to lose their phenotypes when in 2D culture *in vitro* (Kean et al., 2019).

Chondrocytes originate from mesenchymal stem cells (MSCs) which are present in bone marrow (Temenoff and Mikos, 2000). MSCs are a multlineage stem cells that are able differentiate into chondrocytes, ostoecytes and apidocytes. They differentiate and begin to secrete cartilaginous matrix during embryogenesis.

Hypertrophic chondrocytes are located close to the bone surface and produce proteins that cause calcification of the matrix. Whereas, chondrocytes located closer to the periphery secrete matrix molecules (Temenoff and Mikos, 2000). As they begin to secrete matrix proteins and components they lose their intercellular contacts and gap junctions. The loss of these result in a reduction in metabolic activity and signal a senescence in the cell. Mature chondrocytes are constantly regenerating the pericellular matrix- or the surrounding ECM in response to stimuli (Guilak et al., 1999, Pap and Korb-Pap, 2015).

1.3.3 Zones and topography of articular cartilage

Articular cartilage has a unique appearance and the tissue can be characterised as having specific zones in which the composition and structure varies based on function. In mature articular cartilage it can be seen that there are 4 specific zones (fig. 1.5). These four successive regions are known as the: superficial or tangential region located at the surface of the cartilage, the transitional zone, the radial or deep zone and the calcified zone located closest to the bone. Variations between the zonal regions can be identified by changes to the cell morphology, collagen alignment and biochemical composition (Hunziker et al., 1997).

The superficial layer is found at the articulating surface of the tissue. This cell free layer can be up to 3 µm thick and contains mainly fine fibres of collagen type II densely packed together. These fibres run parallel to the articulating surface, and the organisation of the collagen fibres permits reduced friction during articulation (Athanasiou et al., 2009). A low content of proteoglycans are present within this zone, resulting in it have a low permeability (Athanasiou et al., 2009, Muir et al., 1970).

This is followed by a layer in which there are small oval or elongated, relatively inactive cells that lay parallel to the surface (Athanasiou et al., 2009). These cells secrete specialised proteins that are believed to provide the frictional properties seen in the tissue (Flannery et al., 1999). Within the talus, the superficial zone makes up a larger proportion of the full thickness cartilage. This may

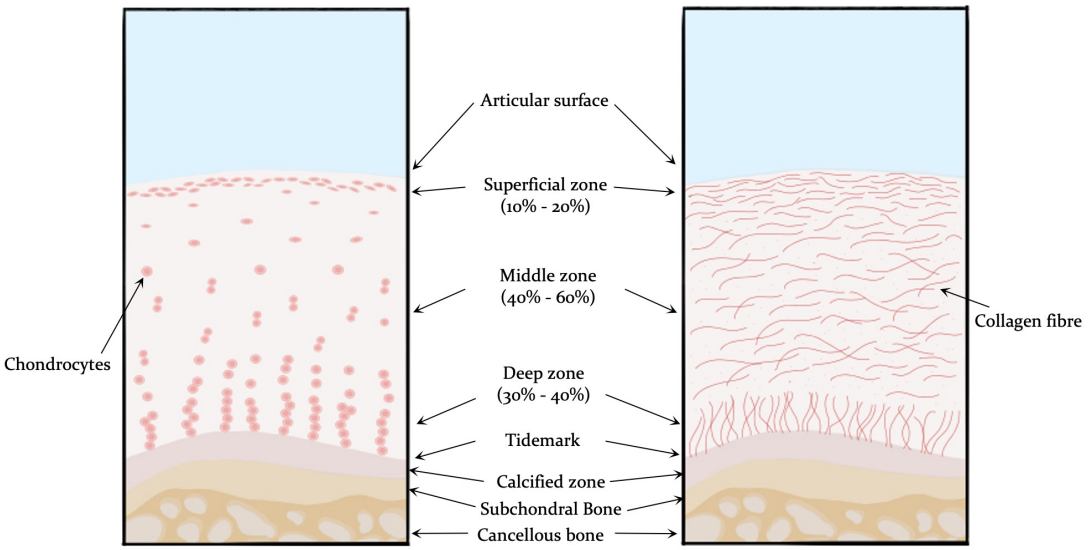

Figure 1.5: Schematic of the cross section of articular cartilage
Schematic shows the tissue architecture and the orientation of collagen fibres within the different zones. Adapted from (Sophia Fox et al., 2009).

provide talar cartilage with a higher degree of resistance to damage (Treppo et al., 2000).

The second zone is the translational or intermediate zone. Cells within the translational zone are larger, have a rounder morphology and are found as either single cells or doublets. These cells are actively remodelling the ECM (Standring, 2015). In comparison, cells within the radiate layer are aligned with the collagen fibres, in a striated nature and lie perpendicular to the surface of the articular cartilage (Athanasiou et al., 2009).

The final layer of cartilage is the zone that lies adjacent to the subchondral bone and is known as the deep zone. This layer lies in confluence with the adjacent surface and acts to resist shear stresses produced by muscle action and joint motion. The junction between the calcified layer and the radial zone is known as the tidemark (Standring, 2015).

The tidemark serves as a tethering mechanism for the perpendicular collagen fibrils seen in the deep layer and prevents these fibrils from shearing off at the point of integration with the bone. The undulating morphology of the tidemark increases its ability to resist shear forces caused by articulation of the joint (Redler et al., 1975). Below the tidemark is the calcified zone and subchondral bone (Athanasiou et al., 2009).

The calcified zone is a region of transition between the 'pliable' articular cartilage and the stiffer subchondral bone. In this region, a gradient of stiffness can be seen (Athanasiou et al., 2009). The

subchondral bone acts as the final anchorage point for the cartilage tissue within the joint.

1.3.4 Role of subchondral bone

Within the ankle, the subchondral bone seems to be less responsive to changes in mechanical loading as introduction of damage does not increase bone density, unlike within the knee (Treppo et al., 2000). As subchondral bone and cartilage are dynamic tissues that work synergistically to support distribution of mechanical load within the joint. It is expected that damage to one would cause changes in the other, especially as they are known to be metabolically active tissue that remodels as a results in changes in loading.

Localised bone changes are often associated with early degeneration of cartilage and for many patients an increase in subchondral bone density is seen during this stage (Muehleman et al., 2002). Damage and prolonged exposure of the subchondral bone can result in osteolysis, sclerosis or increase in defect and cyst size. This weakens the bone making the resultant tissue unable to support the cartilage causing an increase in joint damage (Wodicka et al., 2016).

1.3.5 Role and function of articular cartilage

As a tissue, cartilage displays unique biological and mechanical properties that influence the behaviour and function of the tissue (Buckwalter and Mankin, 1998). Articular cartilage is a biphasic material. The intrinsic material properties associated with each zone and their interactions produce the interesting rheological properties exhibited by the tissue (Mow et al., 1980). The unique properties of articular cartilage allow it to successfully support the compressive forces and distribute the mechanical load during normal loading and minimise friction during joint surface articulation.

There are four primary mechanical properties that create the normal loading and unloading properties seen in articular cartilage. These can be characterised as compression, shear, tension and friction (fig. 1.6). During a normal gait cycle the mechanical behaviours of the tissue varies depending on the stage of and duration of loading. During the initial stages of loading, the interstitial fluid present within the cartilage is bound to GAGs in the ECM. This allows for pressurisation of the fluid within the tissue, permitting it to dissipate the load applied to the tissue. As the duration of loading increases, the tissue depressurises as the interstitial fluid is able to move through the

ECM. It is at this time that the compressive forces experienced by the tissue are applied to the solid extracellular matrix of the tissue (Ateshian, 2009).

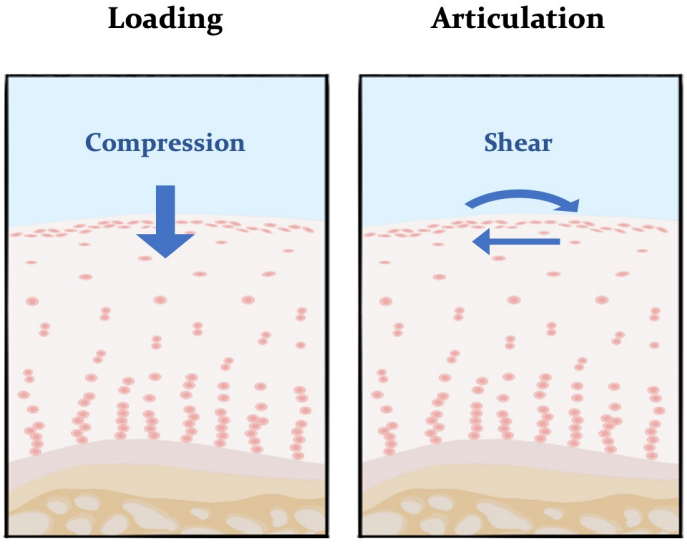

Figure 1.6: Compression and shear forces on cartilage
Schematic showing the direction of forces experienced by articular cartilage during normal joint motion.

Compression and the role of interstitial fluid

As previously stated, water is the main component of cartilage and it is stored in the molecular pore space found in the ECM of the tissue. This interstitial fluid not only acts as the primary carrier of nutrients and waste, it also plays an important role in providing the biomechanical function of cartilage. The compressive behaviour of cartilage is governed by the movement of interstitial fluid through the pore structure of the solid matrix. Compressive loading is the primary mechanical stress that is experienced by articular cartilage (Athanasiou et al., 2009). Compression of the tissue ensures load distribution within the joint. It has been seen that continuous pressure applied throughout the day decreases the total water content of the tissue (Athanasiou et al., 2009). The compressive modulus (the ratio of compressive stresses applied vs actual material compression) of cartilage can vary between 0.08 - 2 MPa and this can be dictated by the thickness of tissue, movement of interstitial fluid throughout the ECM, pore size and structure (Athanasiou et al., 1991, 1994, Hayes and Mockros, 1971, Mak, 1986, Mansour and Mow, 1976, Maroudas et al., 1968, Mow et al., 1984).

Interstitial fluid is able to flow throughout the pore network of cartilage and it is the movement of fluid that allows it to resist load when compressed. Thus, tissue permeability impacts its ability to

resist load. Cartilage has a low degree of permeability and is resistant to fluid flow. This resistance to compression allows for the interstitial fluid to dissipate a large compressive load across the tissue (Athanasiou et al., 2009).

The biphasic theory of cartilage is attributed to flow and pressurisation of interstitial fluid. These characteristics have contributed to the understanding of compression creep, stress-relaxation and dynamic loading properties of cartilage (Ateshian, 2009). During compression as the interstitial fluid is confined within the cartilage matrix, the matrix maintains its volume immediately after a load is applied, and does this by interstitial fluid pressurisation. The interstitial fluid pressurisation allows for the tissue to continue resisting axial compression through the high tensile modulus. This stops the tissue expanding in the transverse direction to the load (Ateshian, 2009).

However, when the period for loading is longer, the viscoelastic properties of the cartilage matrix allows for the fluid to move out of the cartilage and for the solid matrix to absorb the compressive load. This can be seen in the creep and stress experiments done on healthy cartilage (Mow et al., 1980). It is this viscoelastic nature which allows for cartilage tissue to undergo multiple cycles of load bearing through a day, whilst recovering to its initial state after the compressive load is removed (Athanasiou et al., 2009).

Mechanical properties of chondrocytes

The ECM of cartilage not only provides the structural and functional components allowing the tissues to slide across one and another and help dissipate impact, it also provides mechanical cues to the chondrocytes embedded within the tissue. Thus allowing them to modulate their metabolic activity and remodel the environment (Redler et al., 1975). Chondrocytes exhibit different mechanical properties based on their location within the superficial zone or the mid/deep zone.

The Young's modulus of superficial chondrocytes is twice that seen of chondrocytes found in the middle zone with a Young's modulus of 460 and 260 Pa, respectively (Athanasiou et al., 2009).The elastic and viscoelastic properties follow a similar trend. These trends may be associated with variations in the levels of strain experienced by the cells in each zone; as tissue near the surface undergoes more compression and needs to be stiffer to exist in an environment that experiences higher stiffness (Athanasiou et al., 2009).

Moreover, the matrix is able to provide signals through mechanical cues modifying chondrocytes'

behaviour or by retaining soluble mediators such as transcription growth factor beta (TGF-β) (Pap and Korb-Pap, 2015).

Tension

Tension is seen within the joint complex when two articular surfaces move across one another and this in turn causes the collagen fibrils within the ECM to align and stretch along the axis in the applied direction. This force is counteracted by the frictional forces seen between the two surfaces (Athanasiou et al., 2009).

The overall tensile strength of cartilage is dependent on the diameter of fibres, fibre density, degree of cross-linking and degree of ionic bonding seen between the collagen fibres and charged proteoglycans within the ECM. It has been shown that articular cartilage presents with a range of tensile strengths throughout the human body of between 5 - 25 MPa (Akizuki et al., 1986, Kempson et al., 1968, Wu et al., 2008). Similar to compression, depth of tissue and location of the joint will affect the tensile modulus.

Cartilage displays non-linear tensile properties due to the collage fibres. Initially, small deformations cause cartilage tissue to realign in the direction of loading, however as the tension applied increases the collagen fibres themselves begin to stretch resulting in increased stiffness at greater strains. As the orientation of collagen fibres vary within the different zones of cartilage, the Young's modulus of the tissue varies throughout the matrix. The superficial zone of cartilage has been shown to have a highest Young's modulus compared with that of middle and deep zones (Athanasiou et al., 2009).

Shear

Shear occurs within the articulating joint when the two surfaces slide in opposing directions creating a higher magnitude of compressive strain near the articular surface compared to that seen in the deeper zones (fig. 1.6) (Wong et al., 2008). Rotational and translational movement have been attributed to shear forces and the resultant deformation of the cartilage (Athanasiou et al., 2009). At equilibrium the shear properties of the cartilage are characterised by the interactions of the solid components of cartilage and the shear equilibrium modulus can vary between 0.05 and 0.25 MPa in humans (Callaghan, 2003). As cartilage has both solid and liquid components, the dynamic shear

modulus of cartilage can vary from 0.1 and 4 MPa. Dynamic loading of chondrocytes, through the application of shear stresses, induces the release of soluble mediators and ECM macromolecules; maintaining cartilage homeostasis (Lane Smith et al., 2000, Wu et al., 2000).

Friction

Friction within the joint occurs when two articulating joint surfaces move laterally against each other. One of the most unique features of articular cartilage is its low coefficient of friction (Mow and Huiskes, 2005). The low friction and wear resistant properties of cartilage allow for lifelong joint function (Accardi et al., 2013). Cartilage displays a time-dependent coefficient of friction,with a constant load causing the coefficient of friction to increase over time until it reaches equilibrium as the tissue deformation equilibrates (Wang and Ateshian, 1997).

Several methods have been suggested to explain the low friction values seen in cartilage. These include: squeeze film lubrication, elasto-hydrodynamic lubrication, boundary lubrication and fluid pressurisation (Ateshian, 2009, Athanasiou et al., 2009). It is believed that the coefficient of friction of cartilage negatively correlates to the fluid load support or fluid pressurisation (Ateshian, 2009). Boundary lubrication occurs under high compressive loading and low articulation speeds where the higher coefficients of friction have been measured (Gleghorn et al., 2007). Maximising the potential to cause wear or high shear stress to the tissue. Whereas, the biochemical interactions at the surface involving glycoplroteins have been shown to be mediators of frictional properties and reduce the coefficient of friction under the boundary mode conditions Krishnan et al. (2004), Schmidt and Sah (2007). Therefore, boundary lubrication and pressurisation of the interstitial fluid are crucial in facilitating the low frictional properties seen in cartilage (Wong et al., 2008). In addition, fibre orientation strongly affects the shear properties of cartilage minimising damage to the tissue (Accardi et al., 2013).

Cartilage lubrication theory

Wear is commonly observed when two surfaces articulate against one another under load. This is particularly prominent in synovial joints, especially the ankle, in which high loads are seen in the joint during motion (Van Dijk et al., 2010). *In silico* modelling of ankle joints has suggested range of coefficients of friction from 0.0009 - 0.01 under different loading cycles (Medley et al., 1984).

Mechanical or biochemical degradation of the cartilage surfaces over time can compromise the ability of the two surfaces to successfully articulate over one another. Thus, damage to the cartilage surface, potentially due to the presence of an OLT, can cause a increase in the coefficient of friction leading to impaired function through changes in tissue properties and surface roughness.

To prevent degradation of the cartilage and minimise functional impairment, it is believed that the body has evolved to utilise multiple potential lubrication mechanisms, each employed during a different stage of the gait cycle (Ateshian, 2009). The mechanisms of cartilage lubrication have been studied for decades but the exact mechanisms remains unclear. Figure 1.7 represents the potential mechanisms of lubrication that articular cartilage in the tibiotalar joint experience during loading and articulation. It is thought that each of these plays a different role during different stages of the gait cycle or normal lading to prevent tissue damage, such as elastohydrodynamic lubrication occurring at heel-strike (Wright and Dowson, 1976). The principles of these theories are discussed below.

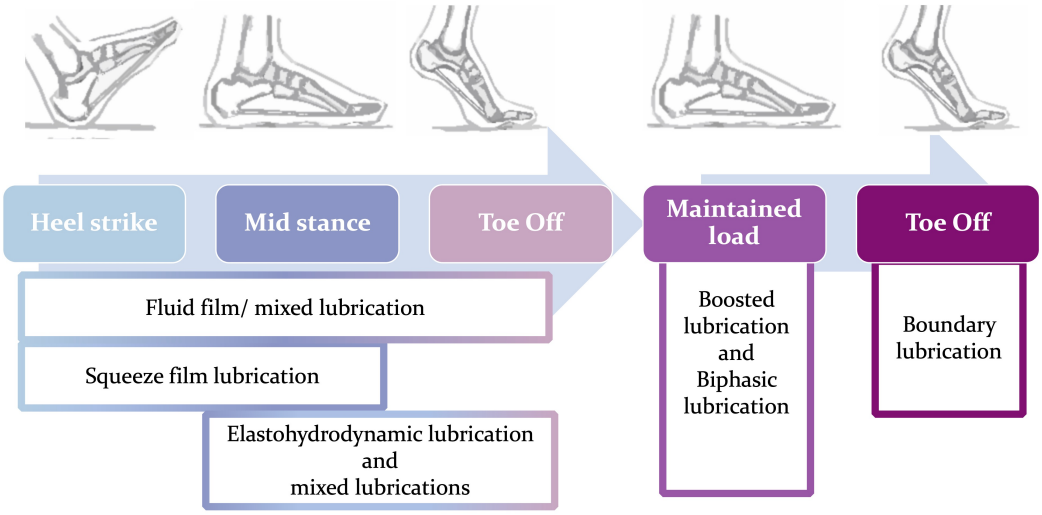

Figure 1.7: Hypothesised lubrication mechanisms utilised during the normal walking gait in the ankle joint.

During each stage of joint motion, different mechanisms of lubrication are theorised to occur and these may explain the mechanical properties observed in the tissue (fig. 1.7).

As load is applied to the joint, there is an increasing in pressurisation and entraining velocity of the synovial fluid within the joint. This allows for the formation of a fluid film. The fluid film acts as a lubricant and reduces the coefficient of friction using two strategies. The first is to create a boundary directly separating the two surfaces. The second is through ensuring that when loaded

the shearing forces occur within the lubricant as it has a lower shear strength compared with the articulating surfaces (Wright and Dowson, 1976). The synovial fluid acts as the lubricant within articulating joints.

An extension of fluid film lubrication is elastohydrodynamic lubrication which considers the articulating surface to be elastic.This model works well in articulating joints, where cartilage displays viscoelastic properties. During loading, hydrostatic pressures present in the fluid film induce cartilage deformation. As the tissue deforms it becomes more conforming, improving lubrication conditions. This causes a decrease in contact stress and promotes the movement of fluid into the articulating site by entraining or squeeze film action (Hlaváček, 2000, Medley et al., 1984, Wright and Dowson, 1976).

In areas of the joint where compression has resulted in direct contact between the opposing cartilage, boundary lubrication acts as a method to reduce the friction coefficient. This process is mediated by constituents of cartilage including glycolipids. During articulation these surface molecules slide over one another creating a boundary and protecting the articulating surfaces from sheer stresses (Morita et al., 2006, Wright and Dowson, 1976).

In addition, lubrication of the joint during articulation can be attributed to the synovial fluid present on the joint surface. This fluid creates a boundary of liquid between the two articulating surfaces and acts as a boundary lubricant. It is believed that this boundary lubricant may be central to the low coefficients of friction observed during articulation. These lubricating boundary layers are thought to be caused by interactions between the HA present in synovial fluid and constituents of the outer superficial zone including lubricin, aggrecans and other phospholipids (Jahn et al., 2016). During loading the synovial fluid is thought to move into the porous network of the cartilage ECM which is flattened as the load is applied. This creates a squeeze-action film which concentrates the macromoleules in the synovial fluid until it reaches a limit. After which the fluid film is depleted causing the formation of a film of synovial gel like material acting as a boundary lubricant . This prevents contact between the opposing articulating surfaces. It is the cyclic nature of walking that permits the movement of fluid through the cartilage allowing for the formation of the boundary lubrication.

During extreme loading, such as a constant load being applied to the cartilage for a prolonged period of time, biphasic lubrication theory is used to explain how articular cartilage is able to maintain lubrication. A biphasic medium is one which contains a solid porous matrix and a fluid

component. During compression, the initial load is supported by the fluid phase as interstitial fluid pressurises and supports a large amount of the contact load. Through extended loading, this fluid begins to exude from the cartilage matrix. As this occurs, load is then transferred to the solid matrix and this then undergoes deformation. As the frictional force on cartilage is dependent on load transmission between the directly contacting cartilage surface, during this shift to ECM support, an increase in the coefficient of friction is seen (Ateshian, 2009, Mow et al., 1980, 1984).

It is important to note that it is likely that during articulation multiple modes of the theorised lubrication models coexist at the boundary between the two tissues and that these modes must occur concurrently. Furthermore, current methods used to measure friction within the natural joints have either measured friction as independent of velocity (boundary lubrication model) or decreasing as velocity increases (fluid-film lubrication model).

Most studies which have informed cartilage lubrication have been performed using tissue form the hip or knee joint (Jahn et al., 2016). Although these mechanisms maybe present in all joints, the multimodal nature of cartilage lubrication during joint motion may differ between the tissues. If anything, the uniformity and thickness of articular cartilage on the talar dome and its resistance to primary OA changes suggests that the ankle may be more dependent on boundary lubrication, provided by interactions between the synovial fluid and the upper layer of the superficial zone, to minimise friction at the joint surface. In addition, there is less synovial fluid present in the ankle joint compared with the knee, which is reported to be in range from 0.5 - 4.0 mL, therefore there would be less fluid to move through matrix to allow for such boundary gels to form (Kraus et al., 2007). Further studies are required to characterise the composition of the tissue to see if there are higher proportions of these macromolecular constituents present on the surface of talar cartilage which could explain its wear resistive properties.

1.4 Osteochondral Lesions of the talus

Everyday 1 in 10,000 people suffer from an ankle injury (O'loughlin et al., 2010). Throughout daily living the ankle joint complex undergoes high compressive and shear forces and can experience forces up to 5 times body weight during a normal gait cycle. The joint, although undergoing high forces, is far less susceptible than others at experiencing degeneration of the cartilage unless first initiated by the occurrence of a traumatic injury (Brockett and Chapman, 2016).

One or multiple traumatic injuries to the articular cartilage and/or the subchondral bone can allow for the formation of a lesion on the talar dome. These lesions have been described as an osteochondral lesion of the talus, and are also known as: osteochondritis dissecans, transchondral fracture, osteochondral fracture or flake fracture (Ferkel et al., 2008). Each of these terms describes pathophysiological changes occurring within the articular cartilage, the subchondral bone plate and the sub-articular spongiosa of the talus (Gerards et al., 2015). The talus is thought to be the third most common location for osteochondral defects, only superseded by the knee and elbow, with the average age of patients being 20 – 30 years (Steinhagen et al., 2001).

Initially the defect may consist only of the damage to the cartilage surface and may sometimes, spontaneously heal and stabilize. However application of continuous compression, shear stresses or high-impact forces may lead to subchondral bone damage and the formations of cysts or bony damage (van Bergen et al., 2014, Van Dijk et al., 2010). During loading and compression of the cartilage, water moves in to the subchondral bone through the defect site This causes an increase intraosseous fluid pressure. Repetitive changes to fluid pressure during normal ankle use can cause joint pain as nerves within the subchondral bone are stimulated (Van Dijk et al., 2010). The presence of such cyst can cause deep ankle pain, swelling, reduction in motion and synovitis (van Bergen et al., 2014).

1.5 Occurrences of OLTs

The first OLT was described by Munro in 1737, in which they identified and removed a loose body of bone from the ankle thought to have originated through a traumatic injury (O'loughlin et al., 2010). Although the exact aetiology of OLTs has yet to be fully elucidated, it is believed that the formation of lesions within the talus may be due to a plethora of causes. Most commonly described within the literature is acute trauma. It has been reported that 20 – 50% of acute ankle trauma results in the formation of lesions (O'loughlin et al., 2010). More recent studies have reported that 78 - 80% of lesions have been attributed to patient reported trauma (Krause and Anwander, 2022, van Diepen et al., 2021). Lesions may also develop due to an individuals' predisposition to factors such as age, genetic factors, gender, infection, muscle weakness and limb alignment (Horisberger et al., 2009, Santos et al., 2014). Alternative causes further include vascular insult, soft tissue impingement due to Bassett's ligament, microtrauma, chronic ankle instability and systemic endocrine or metabolic

abnormalities, such as vitamin D deficiency or hypothyroidism (Looze et al., 2017).

The presence of OLTs can result in the progressive deterioration of the cartilage and thickening of the underlying subchondral bone resulting in pain, reduced quality of life, loss of function of the joint and progression to OA (El-Jawhari et al., 2018, Krause and Anwander, 2022, O'loughlin et al., 2010, Yang et al., 2017).

1.5.1 Lesion location

The talar dome can be separated into the lateral and medial sides through the sagittal plane, and similar to the knee, these two sections contain two raised surfaces (fig. 1.3). OLTs can occur anywhere on the surface of the talar dome; with lesions being described as being located on either the medial or lateral sides of the talus. The appearances of medial and lateral defects differ and it is believed that it is related to their cause. Medial defects tend to have a deeper, cup-shaped morphology, whereas, lateral lesions appear to have a shallower, more wafer-like morphology (Raikin et al., 2007, van Bergen et al., 2014). In addition, medial defects appear to have a greater area and deeper mean depth compared to their lateral counterparts (Raikin et al., 2007). A recent systematic review assessed the location distribution of 2087 OLTs using a 9 by 9 grid across the talar dome showed that most common locations for lesion were the centromedial (31%)and posteromedial (28%) regions(Raikin et al., 2007, van Diepen et al., 2021). In addition, the largest lesions were seen in the centrocentral zone of the talus (van Diepen et al., 2021).

The nature of OLTs and early asymptomatic stages often results in many patients being unable to identify if the lesion was caused by an acute or traumatic injury. This has resulted in much debate pertaining to the common causes of specific lesions and also the frequency of lesion occurrences.

A 2007 study showed that within a cohort of 424 patients, medial talar dome lesions were significantly more common than lateral lesions (Raikin et al., 2007). Choi *et al.,* showed that of the 120 ankles studied, 66.7% of injuries were associated with the abnormalities present on the medial talar dome and 29.1% of the ankles studied showed the presence of lesions on the lateral side of the dome (Choi et al., 2009). Similar results were seen by Verhagen *et al.,*, who showed that 58% of lesions were located on the medial aspect of the talar dome (Verhagen et al., 2003). Lesion occurrence within the literature may be biased based on cohort selection, with groups reporting varying frequencies of occurrences.

With regards to aetiology, Flick and Gold examined over 500 patients and identified that 90% of lateral lesions were caused by a traumatic injury where as only 70% of medial lesions were caused in such a way (Flick and Gould, 1985, Kawabata et al., 2022). Raikin *et al.,* hypothesised that the difference may be due to sheer stress or continual degradation associated with the shallower lateral lesions, compared with trauma induced injury which prompts the formation of medial lesions (Raikin et al., 2007). With the shallow, wafer shaped lateral lesions occurring after dorsiflexion and inversion injuries and the deep, cup like medial lesions being a result of a plantar flexion and inversion (Melenevsky et al., 2015).

1.6 Progression to OA

OA is a heterogeneous disease which can be caused due to a plethora of mechanisms which all result in joint failure: such as, malalignment and deformity in the joint, muscular weakness, ligament failure and weakness, damage to the surface hyaline cartilage and formation of subchondral cysts (Dunn et al., 2016). Although differences in the development of OA can be seen between different joints and the exact mechanism which initiates the early events in OA might not be clear, it is believed the presence of OLTs within the ankle joint show progression to OA, especially in younger patients; with over 70% of OA cases in the ankle being post traumatic of origin (Post traumatic osteoarthritis, PTOA)(Valderrabano et al., 2007). It is believed that presence of OLTs cause changes in behaviour and promote deviation to an osteoarthritic phenotype. It is through that the chronic alteration in the joint mechanics, malalignment, instability and incongruity are contributory factors that introduce abnormal loading in the joint (Delco et al., 2017). It is unclear whether chronic mechanisms or the acute trauma play the greatest role in the development of ankle OA.

Ankle OA is a progressive, degenerative cartilage disorder characterised by symptoms such as pain, reduced range of motion. PTOA develops secondary to joint trauma with symptoms displaying a lag phase post initial injury of over a decade in some cases (Delco et al., 2017). The presence of OLTs trigger biological and mechanical changes within the joint that cause progression to OA (fig. 1.8).

1.6.1 Biological changes associated with OLTs

Articular cartilage structure and composition is carefully defined in adults and this delicate balance is maintained by the behaviour of mechanically sensitive chondrocytes within the collagen matrix of cartilage. These residing "resting" or quiescent chondrocytes maintain a metabolically active state in which they assemble and degrade the matrix in response to changes in the physiological environment. Thus, carefully balancing the remodelling of cartilage (fig. 1.9) (Kim et al., 2015, Pap and Korb-Pap, 2015).

The expression patterns of chondrocytes change due the presence of osteochondral lesion (OCL) as they change to a more active phenotype (fig. 1.8 & fig. 1.9). They develop a reactive phenotype in response to the damage to cartilage and loss of inter-territorial proteoglycans (Vincent and Saklatvala, 2008). Deviation from the natural homeostatic state of chondrocytes promotes abnormal remodelling of the extracellular matrix (ECM) and the collagen network, resulting in joint failure and progression to OA (Vincent and Saklatvala, 2008, Yang et al., 2017).

This remodelling can be characterised by changes to the biochemical pathways that causes alteration to the biophysical properties of the chondrocyte micro-environment triggering changes to the cartilage matrix (fig. 1.8) (Kim et al., 2015). Dunn *et al.,* showed that GAG composition within the damaged cartilage was reduced within damaged sites on the chondyles compared with intact cartilage (Dunn et al., 2016).

Hypertrophic metabolic chondrocytes show increased metabolic activity and release transcription factors and growth factors: producing an injury response. This in turn activates the production of enzymes that degrade the collagen fibres found loose within the synovial fluid of the joint capsule, however these collagen fragments further upregulate the production of enzymes. Enzymes such as metalloproteases and serine proteases, secreted by chondrocytes, cooperate to degrade matrix proteins such as collagen, laminin, and fibronectin. The chondrocytes secrete these enzymes to degrade the cartilage to permit cell migration to the damage sites whilst maintaining integrity of the matrix (Pap and Korb-Pap, 2015).

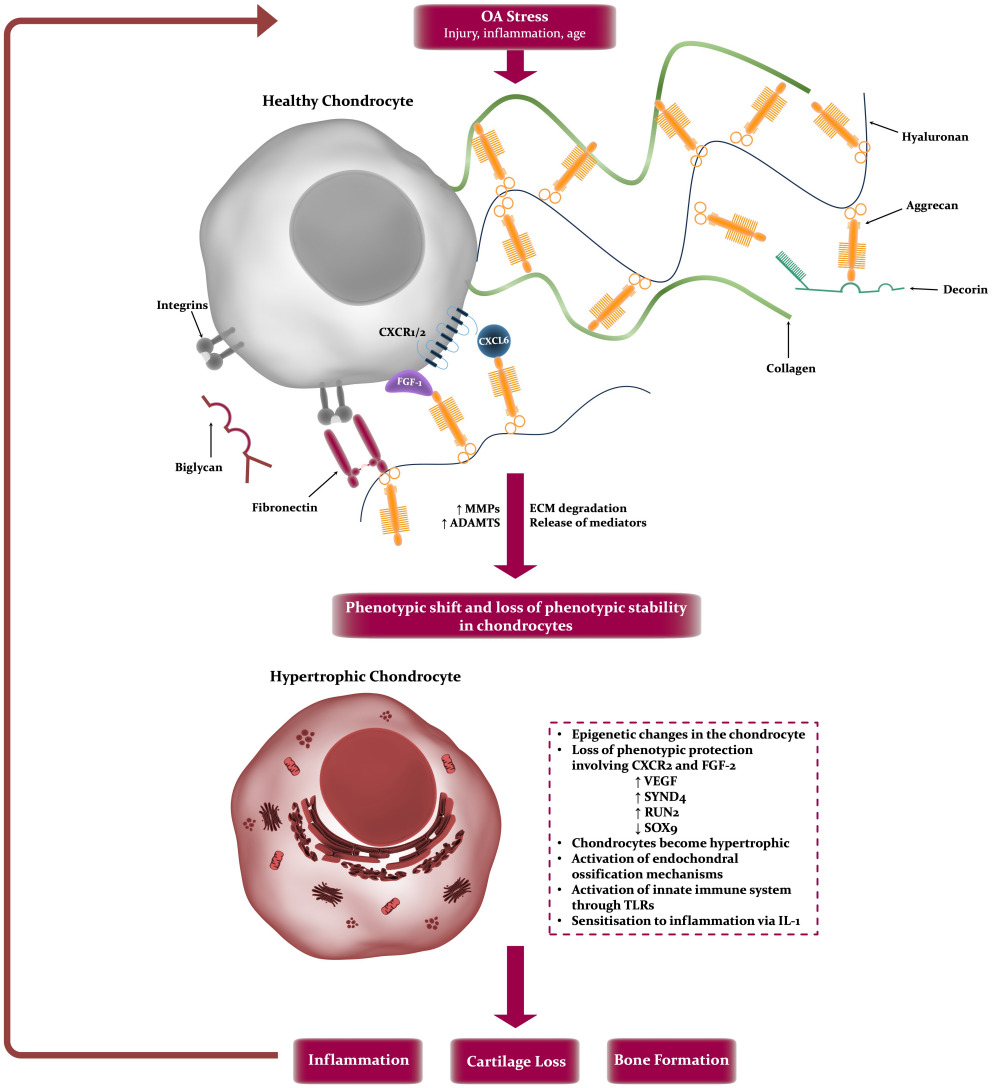

Figure 1.8: Chondrocyte matrix interaction
Interactions of chondrocytes and the matrix during OA. OA causes changes to the ECM and that alters the phenotypic behaviour of chondrocytes. Epigenetic factors include modification to expression patterns of cells within the cartilage. Adapted from (Pap and Korb-Pap, 2015).

Metalloproteases are key mediators for the development of OA and have been identified as being crucial in initiating and perpetuating the progression of OA and cartilage destructions with a joint- these include matrix metalloproteases (MMPs) and aggrecanases (ADAMTS 4 & 5).

MMP-13 has been shown to be expressed in higher levels in OA cartilage tissue (Davidson et al., 2009). It is able to degrade aggrecan and collage type II found in the cartilage ECM. An increase in its expression occurs within hypertrophic chondrocytes seen within the superficial zone of cartilage. This increase in expression triggers the degradation of the superficial zone of the tissue.

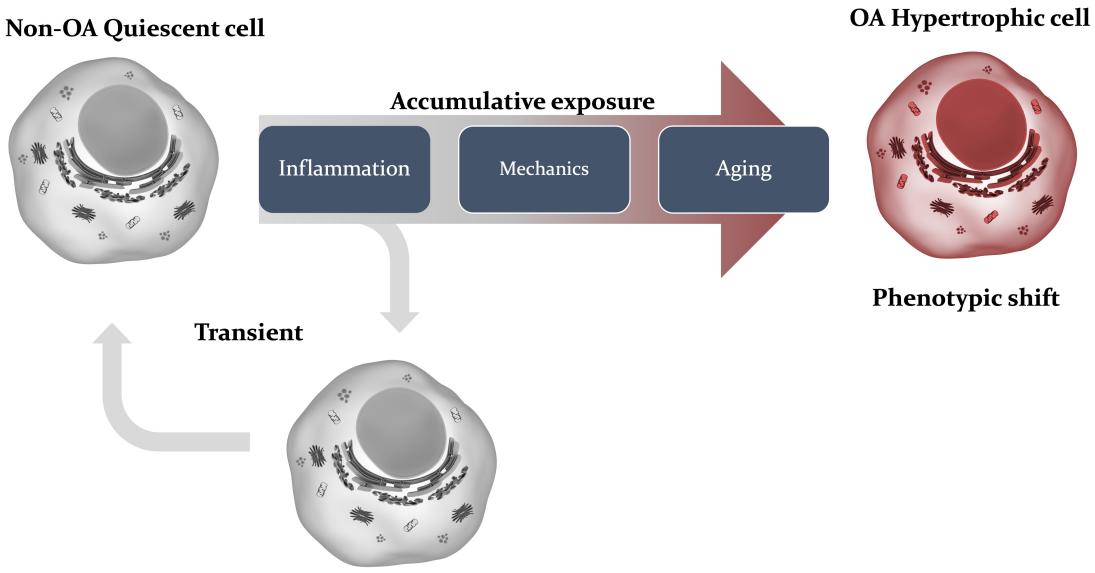

Figure 1.9: Phenotypic instability of chondrocytes
Phenotypic instability of chondrocytes is commonly seen in OA cells. Injury stimulates a phenotypic shift from a transient state to a hypertrophic state. Mechanisms that trigger this shift in phenotype are seen in grey. Adapted from (Singh et al., 2018).

Furthermore, MMP-13 is key in changing the regulation of inflammatory mediators such as hypoxia inducible factor 2 α (HIF-2 α) (Pap and Korb-Pap, 2015). ADAMTS-4 and ADAMTS-5 has also been closely related to OA changes, and this has been correlated with changes to cartilage and inherent damage to the structure of cartilage. Expression of these two proteases has been associated with upregulation of inflammatory catabolic cytokines like interleukin-1 (IL-1) (Pap and Korb-Pap, 2015). This further triggers the inflammatory changes seen within the OA joint space that causes progression of the disease.

Inflammatory mediators also play a key role in the progression of OA (fig. 1.9). These inflammatory factors may affect the metabolism of chondrocytes within the osteoarthritic tissue as well as amplifying the negative cascades seen within the tissue that result in the chondrocytes hypertrophic phenotypic shift. Triggering cartilage destruction and bone remodelling (Pap and Korb-Pap, 2015). It is also been seen that chondrocytes become more reactive to inflammatory signals such as IL-1 and IL-6 after losing their chondrogenic phenotype (Pap and Korb-Pap, 2015). However, chondrocytes found within talus are less responsive to catabolic factors such as IL-1 and fibronectin fragments compared to the knee (Treppo et al., 2000).

1.6.2 Inflammatory mediators of OA

Many biochemical markers are intrinsic to cartilage repair, matrix degradation or inflammation and different pathologies will exhibit different markers (Schmal et al., 2014, 2015). Inflammatory changes precede the biomechanical or pathological changes attributed to OA. During the initial steps of OA can cause an upregulation of proinflammatory cytokines and proteases; the main proteases involved in the early stages of OA are matrix proteases such as MMPs and ADAMTS (fig. 1.10 & 1.11) (Billinghurst et al., 1997, Schmal et al., 2009, 2014, Wang et al., 2004). In particular, MMP-1, 8 and 13 are of interest as potential therapeutic targets as they are one of the few proteases that are able to cleave the fibrils of collagen at the first molecule attached to the triple helix (Billinghurst et al., 1997).

MMP-13 or collagenase 3 is thought to be a potential candidate for therapeutic targeting as it plays a significant role in OA progression (Billinghurst et al., 1997). It is involved in initiating phenotypic changes associated with chondrocyte hypertrophy and MMP-13 is thought to be the main cartilage degrading collagenase (Singh et al., 2018). MMP-13 synthesis within chondrocytes is also stimulated/induced by inflammation and mechanical stress (Van der Kraan and Van den Berg, 2012). Within ankles other inflammatory markers including other MMPs have also been shown to be upregulated in tissue within 17 days of an interarticular fracture. These include MMP 1, 2, 3, 9 and 10, IL-6, 8, 10, 1-Band TNF-Aand these indicate that biochemical changes are occurring at the joint after insult (Adams et al., 2015, Adams Jr et al., 2014, Pham et al., 2021). Significant changes in their expression in the joint after injury, of up to 100 fold, maybe attributed to the traumatic nature of OA in the ankle joint. The increased expression of these markers may trigger the pathological changes attributed to OA and initiate the expression of MMP13 and ADAMTS through degradation of the ECM (Chang et al., 2016, Schmal et al., 2015).

MMPs are not expressed in healthy tissues but is expressed in the joints of OA patients and its expression varies at different stages of OA progression (fig. 1.11). In early stage OA in the ankle, stage I and II, MMP-13 has been seen to be unregulated in diseased tissues. Whereas, in later stages, grade III and above, downregulation of MMP-13 was seen within the tissue (Li et al., 2011, Schmal et al., 2015). This initial upregulation of MMP-13 is thought to be an key initiator of OA, as over expression of MMP-13 in transgenic mice has been shown to present OA-like symptoms (Wang et al., 2004).

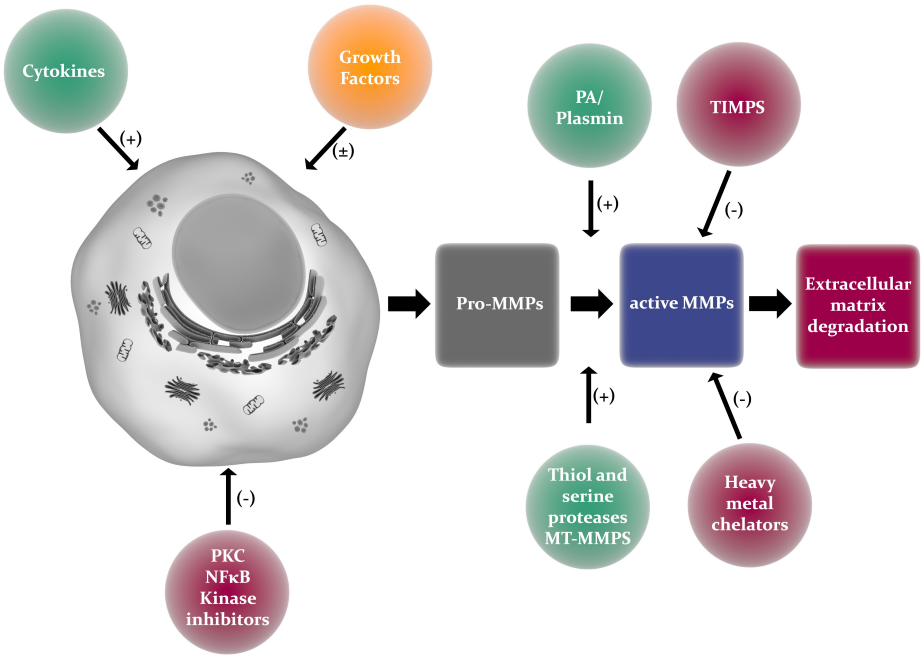

Figure 1.10: Activation and inhibition of MMP activity within chondrocytes
Diagram showing the activators (+) and inhibitors of MMP synthesis and activity. TIMPs = tissue inhibitors of MMPs, PKC & NFKB are transcription factors and MT-MMPs are membrane type MMPs. Modified from (Pelletier et al., 2001).

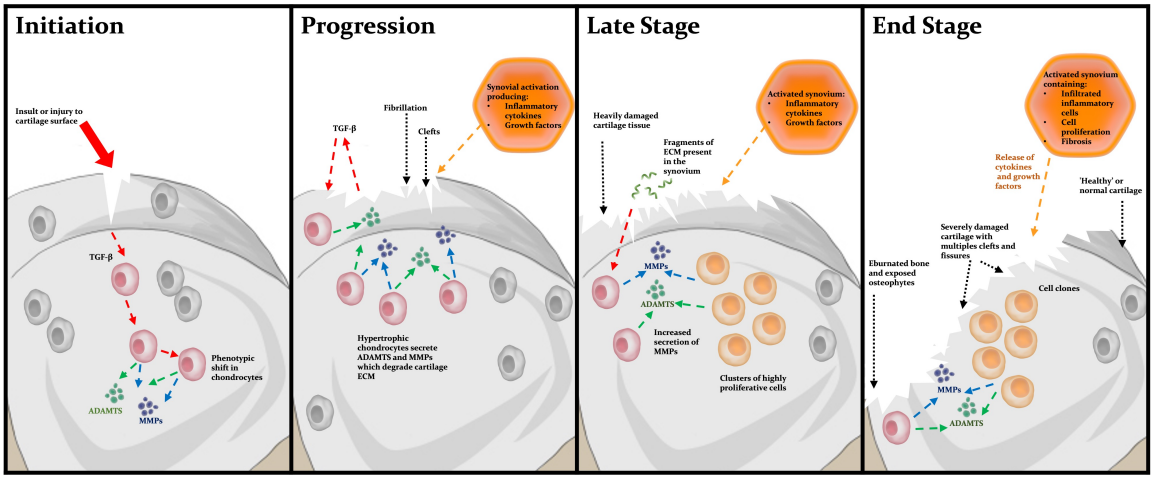

Figure 1.11: Diagram demonstrating changes in chondrocyte behaviour through the progression of OA. Activation and inhibition of MMP activity within chondrocytes.
Hypertrophic-like phenotypes are demonstrated as black cells. These play a crucial role in cartilage degeneration through the expression of MMPs and ADAMTS. TGF-B is a chondroprotective factor which is present in young cartilage. Ageing results in loss of this capability within the tissue. Cell clones seen in neighbouring cartilage unsuccessfully attempt to repair the damage but cause additional degradation through the secretion of proteolytic enzymes. Modified from (Van der Kraan and Van den Berg, 2012).

MMP-13 expression is not only initiated by cytokines like IL-1 but also as a response to mechanical stimuli or microtraumas (fig. 1.10 & 1.11). Increase in MMP-13 expression has been seen as early as 3 hours after cyclic tensile stress tests was applied *in vitro* to cartilage tissue (Li et al.,

2017). It role in initiation of OA was additionally supported by an *in vivo* evidence in mice that saw induction of MMP-13 expression after mechanical stress was applied to cartilage (Li et al., 2011). Thus implying that MMP-13 is a key mediator in early cartilage degradation.

1.6.3 Mechanical changes associated with OLTs

Cartilage degeneration also affects the mechanical properties of the tissue, in particular deformation and recovery of the tissue when compressed. Damaged or degenerated cartilage may become fibrillated or roughened and this will increase the interactions between the articulating surfaces (Wong et al., 2008). Over time, with continual loading, this can eventually cause changes to the matrix structure that will result in a decrease in the mechanical stiffness and elevated shear deformation (Wong et al., 2008). Concomitantly, other mechanical properties also deteriorate; including compression, tension and friction. In this way, the deformation and strain magnitudes of degraded cartilage increase compared to healthy cartilage in response to the same amplitude of applied load (Wong et al., 2008).

Frictional properties may be affected in two ways. Surface irregularities, such as OCLs or tears in the cartilage, may cause the surface roughness to increase which in turn would increase friction. This also results in elevated shear deformation with in the joint. Frictional response of cartilage is also dependent on interstitial fluid support. Loss of GAG content within damage cartilage reduces the ability for it to retain fluid within the tissue, thus not being able provide the require support. Furthermore, an increase in the coefficient of friction was reported to be caused by a decrease in peak interstitial fluid load support (Basalo et al., 2005). These changes may result in further degeneration of the cartilage and joint (Wong et al., 2008, Wu et al., 2000).

It is thought that shear forces are critical contributors to cartilage degradation. However, it is unclear as to whether increases in friction or deterioration of shear properties can be primarily attributed to the changes seen in cartilage biomechanics (Wu et al., 2000). The resultant mechanical change also affect chondrocyte metabolism, with moderate levels of dynamic compressive loads and shear strain stimulating chondrocytes to synthesis matrix but higher mechanical forces inhibiting matrix repair and therefore promoting degeneration of the tissue (Wong et al., 2008).

Within the knee, a less congruent joint, introduction of articular lesions to the lateral joint caused by increased loading has been shown to induce subchondral bone thickening (Poulet et al.,

2015). However, compared with the knee, the ankle shows increased levels of congruency which may result in load being evenly distributed across the articulating surface. This presence of lesions on the surface may not affect the stress and load distribution within the talus. Especially in talar bone where peak impact forces can easily be distributed over the small volume of the talar bone, compared to that of a long bone like the tibia (Van Dijk et al., 2010). Thus, the initial presence of an OLT will not trigger thickening of the subchondral bone below the OLTs.

Chronic lateral ankle instability (CLAI) is often seen to occur concurrently with OLTs, with the presence of both being attributed to development of OA. CLAI creates chronic overload of the ankle caused by instability. The increased duration of the abnormal loading due to instability could result in the formation of OLTs (Delco et al., 2017, Kawabata et al., 2022).

1.7 Diagnosis and Classification of OLTs

For many early stage OLTs, patients often present as asymptomatic, therefore making it difficult to diagnose unless it is serendipitously found whilst imaging for a concomitant pathology (Kraeutler et al., 2017). Symptomatic OLTs commonly present with chronic ankle pain, swelling, stiffness or weakness; often exacerbated by prolonged weight bearing or high impact activities (O'loughlin et al., 2010).

Methods commonly used to diagnose the presence of OLTs utilise detailed patient history, physical examination and/or imaging of the joint (Gerards et al., 2015). As most OLTs present in a similar manner during physical examination regardless of location and size, subsequent development of classification systems for OLTs are based on the imaging modalities used to visualise them.

The most common method used to image the ankle is radiographical imaging. Typical radiographs struggle to show early stage damage to the OLTs. However, later stage OLTs containing fractures or detached bone can be clearly visualised (Gerards et al., 2015). The limited sensitivity and difficulty in imaging damaged articular cartilage using X-ray imaging has resulted in a migration to more sensitive visualisation techniques such as computer tomography (CT) and magnetic resonance imaging (MRI). CT images have a high level of specificity and sensitivity when detecting the presence of OLTs, they also lack the capability to visualise cartilage. Thus is unable to detect grade I or II lesions (Verhagen et al., 2003).

MRI is an alternative method used to image OLTs. Cartilage sensitive pulse sequences are able to evaluate the surface of articular cartilage for the presence of chondral and subchondral bone damage, as well as providing superior detail of the surrounding soft tissue (Gerards et al., 2015). MRI has an increased sensitivity and specificity associated with identifying the presence of OLTs compared to CT imaging (Verhagen et al., 2003). However this method of imaging can often overestimate lesion size, especially in the presence of large bony oedemas (Gerards et al., 2015).

Further clinical assessments may be made of the postoperative outcomes may be made using MRI imaging techniques. This is known as the MR observations of cartilage repair tissue (MOCART) scoring system. One of the main benefits of MOCART is that it can study the long term success of treatments by comparing the types of cartilage formed (Marlovits et al., 2006). Thus, many studies use this system as a method to report successful outcomes over that of patient reported systems as it reduces reporting bias.

MOCART includes the assessment of cartilage integrity and the formation of repair tissue through a non-invasive manner known as T2- weighted assessment of the tissue. MRI images are used to measure relaxation time of cartilage to map collagen content and orientation by identifying changes to the diffusion coefficients associated with age, composition and alignment of fibres (Choi et al., 2008). Thus, T2 imaging provides valuable information pertaining to the biochemical and histological properties of the reparative tissues as the stratification of T2 relaxation times change- as less organised tissues are show to produce prolonged relaxation times due to higher water mobility within the tissue (Giannini et al., 2009a).

1.7.1 Classification of OLTs

Multiple classification methods have been generated based on the imaging technique used to study the ankle joint. These include the Berndt and Harty, Ferkel and Sgaglione, and Hepple classification systems (table. 1.2, 1.3 and 1.4). Each system builds upon the previous one and includes additional considerations relating to damage of the underlying bone including fragment separation, subchondral cysts and the level of osteonecrosis (Ferkel et al., 2008).

Table 1.2: Berndt and Harty classification system
Classification based on radiographical images of the ankle (Berndt and Harty, 1959).

Stage	**Berndt and Harty Classification**
I	Subchondral compression fracture
II a	Chondral fracture (partial avulsion)
IIb	Subchondral cyst
III	Chondral fracture with separated segment (non-displaced)
IV	Chondral fracture with separated segment displaced

Table 1.3: Ferkel and Sgaglione Classification System
Descriptions of Ferkel's modified classification system for OLTs based on CT imaging of site (Ferkel et al., 2008).

Stage	**Ferkel and Sgaglione Classification**
I	Subchondral compression fracture
II a	Chondral fracture (partial avulsion)
IIb	Subchondral cyst
III	Chondral fracture with separated segment (non-displaced)
IV	Chondral fracture with separated segment displaced

Table 1.4: Hepple's Classification System
Hepple *et al.*, modified OLT classification system based on MRI imaging of the talocrural joint (Hepple et al., 1999)

Stage	**Hepple *et al.*, Classification**
1	Articular cartilage damage only
2a	Cartilage damage and underlying fracture with bony oedema
2b	Cartilage damage and underlying fracture without bony oedema
3	Detached fragment
4	Detached and displaced fragment
5	Subchondral cyst present

1.8 Current Treatments

Diagnosis of OLTs can be challenging as they often present with non-specific and vague symptoms; such as low grade pain within the joint, joint instability and oedema (Polat et al., 2016). However, OLTs are becoming more frequently diagnosed due to improvements in diagnostic techniques and a

greater understanding of the symptoms. Currently there is no effective treatment that can successfully halt the progression of ankle degeneration and current replacement modalities do not have the same success rates as those seen in other joints, such as hip and knee (Hintermann and Valderrabano, 2003). A recent systematic review which looked at fifty two studies showed that for primary OLTs, none of the current treatment options showed superiority over one and another, with bone marrow stimulation yielding a success rate of 82% and osteochondral auto-/allo- graft transplantations or osteoperiosteal cylinder grafts showing a success rate of 77% (Dahmen et al., 2018). Furthermore, due to the poor regenerative native of cartilage therapeutic interventions are required to provide relief to the patient (Gottschalk et al., 2017).

OLTs continue to challenge clinicians with regards to the optimal treatment strategy. The two main types of treatment range from conservative, non-surgical approaches or through reparative or replacement-type surgical therapies.

1.8.1 Clinical outcomes measurements

Success in many of the studies discussed in this review are decided through American orthopaedic foot and ankle society ankle-hindfoot scale (AOFAS) or visual analogue foot and ankle (VAS) scores. The VAS-foot and ankle system is a subjective scoring system in which patients mark on straight line where they scored against questions; with the far left being a low score and the far right being a high score (Richter et al., 2006). Questionnaires are then evaluated to produce a numerical score based on the location of the answers on a line.

AOFAS is a clinical rating system that combines subjective scoring, like pain and function, with score based on physicians examination of joint; i.e, sagittal motion, hindfoot motion, ankle hindfoot stability and alignment. It is graded using these three subscales: pain, function and alignment, to produce a score out of 100. 100 points indicates an fully functioning ankle joint with no symptoms (de Boer et al., 2017). For most studies, clinical success is determined by an excellent AOFAS score (≥ 80). MOCART scoring maybe used in conjugation with these to assess the success of treatments, whilst removing bias or variation associated with patient reported outcomes. Occasionally patient reported outcomes will be measured using the functional foot index (FFI) and it measures foot function in terms of pain, disability and activity (Budiman-Mak et al., 1991).

1.9 Conservative interventions

The choice of treatment is often dependent on the duration of symptoms, the size, location and stability of the defect (Gerards et al., 2015). The National Institute for Health and Care Excellent (NICE) recommend the use of analgesics, corticosteroids and physiotherapy as conservative treatments for ankle OA (NICE, 2015). Asymptomatic, low grade lesions or in paediatric patients may be resolved through immobilisation or orthoses (O'loughlin et al., 2010). Juvenile OLTs have greater healing potential than that seen in adults as the growth plate is still active in the articulating surface and therefore allows for regeneration (Lam and Siow, 2012). Alternative treatments also include rest, ice and reduced weight bearing and for patients that are in pain non-steroidal anti-inflammatory drugs are provided (O'loughlin et al., 2010). C

The degree of success associated with conservative treatments vary within the literature (Zengerink et al., 2010). A study conducted by Shearer *et al.,* displayed good or excellent outcomes for 54% of patients that underwent non-operative treatments for chronic cystic talar lesions (Shearer et al., 2002). Tol *et al.,* reported lower figures of success with 45% of patients reporting successful outcomes (Tol et al., 2000). Higher success rates of up to 59% compared with 41% has been previously reported in patients with grade I-III lesions when patients were treated with rest rather than immobilisation of the joint (Tol et al., 2000).

A systematic review of studies form 1966 - 2006 saw that 50% of patients who received conservative treatments for primary OLTs found that the treatment failed to successfully resolve symptoms (Zengerink et al., 2010). For most patients, failure of conservative treatments results in the need for surgical interventions.

1.9.1 Biological interventions

Biological interventions, including intra-articular injections of platelet-rich plasma (PRP) and hyaluronic acid (HA), have been used as treatment in the knee and ankle OA. NICE consider both HA and PRP as an effective management strategy for OLTs (Engebretsen et al., 2010, NICE, 2019, Petrella and Petrella, 2006, Salk et al., 2006). Patients have reported short term reduction in symptoms such as pain and improved joint function after treatments.

HA has been suggested to reduce pain and inflammation within the joint, whereas PRP is thought

to improve the quality of the synovial fluid surrounding the joint and promote endogenous HA production (Anitua et al., 2007, Mei-Dan et al., 2012, Sánchez et al., 2008). A randomised non-blind study comparing leukocyte-poor PRP against HA showed that both groups of patients had improved joint functionality for at least 6 months compared to the baseline, with PRP injections appearing to provide a greater success for patients with OLTs graded I - III (Ferkel classification) (Mei-Dan et al., 2012). The results of this study were limited due to lack of control groups, small sample size and short follow up time. In addition, the study did not assess if there had been any changes to lesion size or grade of OLT, therefore not assessing the progression of the lesion. Although PRP is a safe procedure, the efficacy of the treatment is limited with the poor quality of data currently presented (Laver et al., 2017, NICE, 2019).

1.10 Surgical interventions

Surgical approaches attempt to either regenerate cartilage within the defect or repair/replace the tissue. As hyaline cartilage is avascular, it displays low healing rates, especially where there has been no damage to the subchondral bone and thus preventing stimulation of an inflammatory or healing response (O'loughlin et al., 2010). When a lesion is deep enough to penetrate the subchondral bone, it is able to stimulate marrow cells to produce new fibrocartilage to fill the defect.

Fibrocartilage is mechanically inferior to articular cartilage as it is a densely packed fibrous tissue predominantly made of collagen type I (Benjamin and Evans, 1990, Hannon et al., 2014, O'loughlin et al., 2010). It displays increased tensile strength of 10 MPa compared with the 4 MPa reported for hyaline cartilage (Benjamin and Evans, 1990). Fibrocartilage is sufficient to repair the defect caused by smaller lesions without impacting on the effectiveness of the joint or the articulating surface. However, it is known to be mechanically and biologically inferior to the native cartilage and will deteriorate over time (Ramponi et al., 2017). In the case of larger lesions, the inferiority of fibrocartilage reduces the longevity of the joint by increasing frictional forces and reducing its ability to react to compressive loads (Krause and Anwander, 2022, O'loughlin et al., 2010).

Surgical approaches can take many forms, depending on the size and location of lesion, with the choice of intervention being dependent on the length of symptoms, stability, size and location of defect, and whether it is a primary or secondary lesion (Gerards et al., 2015, Hurley et al., 2021).

1.10.1 Microfracture

Microfracture or bone marrow stimulation (BMS) treatments have been shown to have 85-88% success rates in short and mid-term studies post-treatment (McGoldrick et al., 2017, Ramponi et al., 2017, Zengerink et al., 2010).

The process of microfracture involves initially debriding of the site to remove the damaged bone, cyst or oedema, followed by drilling a series of holes into the subchondral plate at 3 - 4 mm intervals, which stimulates the release of MSCs and growth factors, and induces the formation of a fibrin clot. Early microfracture procedures were performed by entering the joint space through an anterior medial or anterior lateral portal and performing a limited synovectomy to visualise and access the lesion site (Robinson et al., 2003). However, modern adaptations to the procedure allow it to be performed arthroscopically (Choi et al., 2009, Chuckpaiwong et al., 2008, Ferkel et al., 2008, Lee et al., 2015, Murphy et al., 2018, Reilingh et al., 2016, Saxena and Eakin, 2007).

Microfracture is commonly used in lesions less than 15 mm in diameter (Choi et al., 2009, Chuckpaiwong et al., 2008). Choi *et al.,* identified a critical lesion size for which treatments such as microfracture had significantly reduced success rates (Choi et al., 2009). Where higher failure rates were seen in defects greater than 150 mm^2 or 15 mm in diameter. Failure rates of 5% and 18% was reported for lesions with areas <100 mm^2 and 100 - 150 mm^2, respectively (Choi et al., 2009, Chuckpaiwong et al., 2008). Clinical failure was defined as an AOFAS score of less than 80 and the authors did not look at images or histology of the reparative tissues. In contrast, Ramponi *et al.,* suggested that lesions > 107.4 mm^2 and 10.2 mm in diameter correlated with significantly poorer clinical outcomes when treated with microfracture.

Microfracture techniques assume that stem cell populations are stimulated to migrate into the lesion site to form fibrous tissues and fibrocartilage (Robinson et al., 2003). This may explain the poor long term results of microfracture and long-term studies suggests that 1-in-3 patients progress to later stage OA in the ankle and report an increase in pain within the joint post microfracture treatment (McGoldrick et al., 2017, Polat et al., 2016, Ramponi et al., 2017).

1.10.2 Autologous matrix-induced chondrogenesis

Autologous matrix-induced chondrogenesis (AMIC) is a treatment that was first reported in 2005 for the repair of full-thickness chondral defects within the knee (Benthien and Behrens, 2010). AMIC is a one-stage procedure that involves an acellular collagen type I/III matrix being placed above a microfracture site to promote cartilage regeneration (Wiewiorski et al., 2013). The technique has several benefits over other treatments because it does not require a donor site or tissues and shows improved healing due to the recruitment of MSCs in the defect site (Waltenspül et al., 2023). AMIC treatment has been proven as an effective surgery that has shown short- and mid-term clinical success as a treatment for OLTs (Budiman-Mak et al., 1991, Galla et al., 2018, Gottschalk et al., 2017, Valderrabano et al., 2014, Wiewiorski et al., 2016). A medium term study (5-year follow up) of 21 patients with average defect size of 1.4 cm^2, saw that there was significant decrease in FFI 1-year postoperatively, with a further non-significant decreases after 5-years (Gottschalk et al., 2017).

Valderrabano *et al.,* showed that for OLTs caused by acute trauma and chronic instability, AMIC treatment showed an increase in AOFAS score after at least two years (Valderrabano et al., 2014). Studies looking at changes in recreational activity post AMIC treatment showed that there was no change between pre-operative and post-operative activity. However improvement were seen in the VAS score from 6.9 to 2.3 at the lasts follow up (Wiewiorski et al., 2016). Reportedly for AMIC reoperation rates range from 5% to 58%. A recent study saw that 50% of patients who received AMIC treatment in the talus required revision surgery with complications attributed to AMIC procedures in the ankle including deep fissuring and thinning of the grafts (Waltenspül et al., 2023).

1.10.3 Autologous chondrocyte implantation

Autologous chondrocyte implantation (ACI) is a treatment modality that is offered as an alternative to osteochondral grafting techniques. ACI is performed through harvesting, *ex vivo* expansion and culturing of chondrocytes from the patient. Cartilage is obtained from the trochlea or the superlateral femoral ridge of the knee, which are known low-weight bearing regions (Whittaker et al., 2005). Chondrocytes are cultured for around 30 days before implanting into a debrided defect that has been filled with autologous cancellous bone taken from the ipsilateral distal tibia metaphysis or the iliac crest (Galla et al., 2018). It is then implanted within the defect and sutured under a periosteal patch to promote regrowth of the cartilage within the defect site (O'loughlin et al., 2010).

ACI has shown success in treating focal cartilage defects in other joints, such as the knee, and is now performed in the ankle (Bazaz and Ferkel, 2004, Brittberg et al., 1994, Koulalis et al., 2002, Kwak et al., 2014, Nam et al., 2009, Romeo et al., 2002). Short and medium-term studies report that patients displayed significant improvement in AOFAS scores (Chan et al., 2018a). Kwak *et al.,*'s study of 29 patients, 23 medial and 6 lateral lesions with an average lesion size of 198 mm^2, showed that an increase in AOFAS score was seen up to 10-years post operatively (Kwak et al., 2014). Although, only one patient in the study was considered a clinical failure as they reported a reduction in AOFAS score, MRI imaging of 6 patients showed that there was an increase in OA stage within the joint.

This is a major limitation with self reported scores, and with many of the studies presented in this review, as although patients may report improvement in the joint functionality, hypertrophy and softening of the tissue can occur within the ankle resulting in further progression to OA not being reported (Mankin and Lippiello, 1969).

A recent study by Chan *et al.,* looked at the correlation of clinical outcomes with AOFAS scores and MRI imaging. MRI imaging of ACI treatments showed that there was heterogeneous formation of cartilage filling up at least 75% of the defect site in 92% of cases which was considered as'good' (AOFAS Score: 80-89) within this study. However, they also saw irregularities in the surface appearance of the cartilage and the subchondral bone plate with presence of focal defects seen in 42% of cases, depression in 28% of cases and 2% both depression and focal defects were present (Chan et al., 2018a). Consequently, although the study had a small cohort and they did not assess degradation of the graft over time, they reported that abnormalities seen within MRI images did not result in poor clinical outcomes (Chan et al., 2018a).

Once again studies exist supporting the short- to mid- term success of ACI, there is a current lack of literature reporting long term outcomes in the ankle (Niemeyer et al., 2012, Vannini et al., 2013). Further limitations associated with ACI is the opportunity for donor site morbidity in the knee after bone tissue is harvested. Whittaker *et al.,* reported that after 23 months patients experienced donor site morbidity and a decrease in knee function. All patients reported their knee activity as excellent pre-operatively and post-operatively the score ranged from good to poor (Whittaker et al., 2005).

1.10.4 Matrix-induced autologous chondrocyte implantation

Matrix-induced autologous chondrocyte implantation (MACI) is a modified form of ACI where chondrocytes are embedded within a scaffold prior to implantation. Materials commonly used for this mode of treatment can vary from synthetic scaffolds such as HA, polyglycolic acid (PGA) or poly lactic acid (PLA) to natural scaffolds made of types I/III collagen (McGoldrick et al., 2017).

Similar to ACI treatments, short and mid-term success of arthroscopic MACI treatments have been reported (Chan et al., 2018b, Giannini et al., 2008, 2009b, 2013, 2014).

A 4-year study of collagen based MACI technique showed 90% of patients displayed complete or hypertrophic tissue filling the defect site, with 65% of implants completely integrated (Giannini et al., 2013). Although the postoperative AOFAS score increased from 63.73 to 91.76 after 24 months; at 48 month this decreased to 82.19 (Giannini et al., 2013). In addition, they saw that lesion size affected the clinical outcome at 12, 18 and 24 months- with patients with larger lesions reporting lower AOFAS scores. T2 mapping showed only 78% of the repaired lesion cartilage had a T2 value similar to healthy cartilage. Furthermore, 16.5% of the remaining defect area contained cartilage with a T2 value of $>$ 45 ms and 5.1% had values $<$ 35 ms, indicative of inflammation and degradation of the tissue suggesting incomplete repair of the defect site. Patients with a T2 value of less than 35 milliseconds, indicative of fibrocartilage, showed a greater decline in AOFAS score during follow up (Giannini et al., 2013).

A 7-year follow up study of MACI, utilising a HA scaffold, showed a significant increase in the average AOFAS score from preoperative values of 57.2 to 86.8, 89.5 and 92.0 at 12, 36 and 87.2 months (p =0.0005), respectively (Giannini et al., 2008, 2014). Histological analysis on three failed specimens showed that there was no integration of the scaffold and that the surrounding subchondral bone appeared malacic. In addition, fibrocartilage formed within the scaffold and altered cell organisation, with a duplication of the tidemark present (Giannini et al., 2014).

A long-term, 12-year follow up of MACI using a fibrin polymer variant in one patient showed promising results showing a reduction in VAS score suggesting functional improvement of the joint after treatment. T2 relaxation time was 42.2 ms and 42.6 ms in the sagittal and coronal planes respectively, implying the formation of articular cartilage (Kreuz et al., 2017). However, weighting of the success was limited by its sample size.

An alternative version of MACI has been developed for use in the ankle using stem cells. These are known as matrix associated stem cell transplantation (MAST) or bone-marrow derived cell transplantation (BMDCT). MAST treatment implants pluripotent stem cells harvested from the iliac crest into the defect site in a collagen type I/III scaffold (Richter and Zech, 2013).. It believed that this introduces higher quantity of MSCs into the scaffold facilitating improved regeneration and healing. MAST treatment have displayed an improved post operative VAS score of 49.2 to 94.5 after 2 years (Giannini et al., 2009b, Richter and Zech, 2013). Comparisons of MACI versus BMDCT using a HA membrane scaffold reported no difference in AOFAS scores after v48 months (Buda et al., 2015). Nonetheless, T2 mapping of the defect sites showed that there was a higher presence of hyaline-like tissue in the patients treated with BMDCT and fewer incidences of fibrocartilage. Suggesting that repair tissue augmented with stem cells is superior and produces more native-like tissue compared with that of traditional MACI procedures.

1.10.5 Auto- and allograft transplantation

Alternative treatments for larger lesions include the transplantation of tissue from a site of low weight bearing in a patient (autograft), or from a donor to the defect site (allograft). Autologous osteochondral transplantation (AOT) is a treatment commonly used for lesions greater than 150 mm^2 with mosaicplasty approaches used to repair larger defects with multiple cores (Valderrabano et al., 2009).

These grafting techniques tend to be used in cases where the defect is too large for microfracture or BMS treatment, or in cases where revision is required as prior drilling or curettage has failed (Looze et al., 2017). Osteochondral grafting appears to be one of the only methods that is able to repair the height and contouring of the cartilage lost by the presence of a defect (Choung and Christensen, 2002). Commonly, plugs used for AOT treatments are taken from ipsilateral femoral condyle. However femoral cartilage has a lower equilibrium modulus and is thicker than compared to talar cartilage, therefore its load bearing qualities differ (Fraser et al., 2016). This results in the graft cartilage having a lower structural stiffness thus being inferior at resisting load compared to the surrounding native cartilage (Fansa et al., 2011).

Although such treatments have shown initial success, the long-term sustainability of the repaired tissue is not guaranteed (McGoldrick et al., 2017).This may be due to a low degree of integration

between the tissue and the formation of fibrocartilage within the lesion site (Sermer et al., 2015). With the presence of this fibrocartilage promoting further degeneration of the joint (McGoldrick et al., 2017).

There are several further limitations associated with auto/allograft transplantation and mosaicplasty. For autografts, one of the major limitations is donor site morbidity, as healthy cartilage must be extracted from a non-load bearing region of the knee. Harvesting plugs from the knee can result in decreased function or increased pain in the donor site. In addition, for mosaicplasty, multiple donor sites are required to obtain enough plugs. Mean donor site morbidity has been reported in 19.5% of cases involving mosaicplasty in the ankle (Andrade et al., 2016). Conversely, allograft transplantation is limited by the lack of donor tissue availability. Furthermore, due to the high conformity of the ankle joint, the shape of the graft needs to be congruent with the surface of the cartilage and this limits the locations where grafts can be obtained from (Fansa et al., 2011). Finally, graft height mismatch has been shown to affect local contact mechanics of the talar dome. 1 mm of sinking or elevation of the graft has shown to increase contract pressure in the ankle, whereas sunken grafts show decrease in contact pressure and introduction of loading in the opposite facet of the talus. Only, flush grafts are able to show near normal joint mechanics (Latt et al., 2011).

1.10.6 *Ex vivo* testing of current treatments

Several studies have been used to assess changes in biomechanics of the tibiotalar joint attributed to the presence of lesions and their repairs (Anderson et al., 2010, Choung and Christensen, 2002, Fansa et al., 2011, Hunt et al., 2012, Latt et al., 2011)

Three of these studies assessed the restoration of contact mechanics within the ankle joint as a result of AOT treatment. Fansa *et al.,* and Latt *et al.,* looked at the changes to contact stress within the medial region of the talus due to the presence of an OLT and examined whether the surface congruency and height of an AOT would affect the success of therapy with regards to changes in contact stress. Changes in contact pressure Fansa *et al.,* created a medial OLT using a AOT coring tool to create defects to a depth of 8 mm, as they reported this to be the most common size used to create grafts in surgery. Latt *et al.,* created 10 mm defects and assessed how graft height affected the local contact mechanics seen on the talar dome. They both showed that AOT treatment was able to partially restore ankle contact mechanics (Fansa et al., 2011, Latt et al., 2011).

Choung *et al.,* studied the ability of mosaicplasty to restore the ankle joint mechanics after a defect was created (Choung and Christensen, 2002). Here, they created reproducible defects by using a 8 by 12 mm oval metallic cutting dye to cut into the central contact zone of cadaveric tissues to create a chondral defect alone (Choung and Christensen, 2002). They utilised a pressure sensitive film to study how contact mechanics is affected by the presence of 4 mm plugs or 6 mm plugs used to fill a defect during mosaicplasty. They showed that 4 x 4 mm plug placed within the defect nearly restored contact area and pressure to normal levels (Choung and Christensen, 2002).

Theses studies applied static, uniaxial loads to the ankle through the tibia and measured contact pressures using a pressure sensor place within the tibiotalar joint. Fansa *et al.,* tested their defects with an axial load of 300 N, which represents a load equal to half the normal load of a person standing in supine position (Anderson et al., 2010). Whereas, contact pressures were measured after a load of 560 N was applied for 10 seconds by Choung *et al.,*. Latt *et al.,* applied a maximum load of 800 N through the joint, ramping the load in 200 N intervals for 50 seconds. As the behavioural properties of cartilage changes during sustained loading it could be inferred that the duration of loading could affect the contact pressures seen. A major limitation with the Fansa *et al.,* study was that it created defects to the depth of an AOT plug, which is not physiologically relevant as throughout the literature the average defect depth roughly 5 mm, with an average depth of 5.77 $\pm$ 2.45 previously reported (Choi et al., 2009). Furthermore, the ankle undergoes higher compressive loads during normal gait cycle than that tested potentially reducing the observed contact (Choung and Christensen, 2002, Fansa et al., 2011).

Hunt *et al.,* assessed the impact of defect size on rim stress concentration, peak rim stress, contact area and load redistribution on the talus. To create a defect, an OATs coring device was used to remove cartilage from the mid medial talar dome to a depth of 6mm and using a range of diameters (6-12 mm). Uniaxial loading at a magnitude of 686 N was applied using a 10-second loading rate to test the effects of the defect on contact mechanics. For defects $>$ 10 mm contact stresses are seen closer to the defect rim and contact area decreased as defect size increased (Hunt et al., 2012). However, Fansa *et al.,* did not identify significant changes to the force of peak contact stress on the peripheral defect rim.

One of the major limitations of these studies is that they are statically loading the defect and therefore do not account for rotational or shear stresses associated with normal motion. A second limitation is that the defects which are modelled are made by a corer and therefore do not mimic the

pathological changes associated with an OLT fully; or indeed that defects vary in location, depth and shape depending on aetiology.

1.11 Current research in cartilage engineering in the ankle joint

There is currently a large amount of novel research into the development of biomaterial scaffolds to repair or replace the tissue that is lost due to the presence of a lesion. Materials commonly used are selected for their similarities to the native mechanical properties of the tissue or for their ability to promote regeneration.

1.11.1 Synthetic and natural scaffolds

A variety of scaffold materials have been tested both *in vitro*and *in vivo* as treatments for OCL. A range of natural materials have been reported for OCL treatments, this includes collagen, calcium alginate and silk based materials (Vega et al., 2017).

Natural collagen matrices are promising as they have been shown to promote chondrocytes to produce GAGs, and also as the tissue can be recognised by cellular enzymes found within the native environment, it can be remodelled and degraded according to biological cues. Collagen matrices have also been shown to contain many of the molecular cues that induce additional collagen expression in transplanted cells (Temenoff and Mikos, 2000). However, a limitation of natural polymers is the feasibility of a product with regards to source and limited supply of material.

Synthetic scaffolds are an attractive option as they are more readily available and can be tailored for specific applications (Temenoff and Mikos, 2000). In addition, the properties of such materials are more tunable compared to that natural polymers and can be easily functionalised. Recent research into polyglycolic acid (PGA), polylactic acid (PLA), poly-ε-caprolactone (PCL) and poly-lactic-coglycolic acid (PGLA) produced promising results (Casper et al., 2010, Temenoff and Mikos, 2000). PLA meshes have been shown to produce hyaline-like cartilage six weeks after implantation in femoral chondyles of rabbits. Non-woven PGA and nanofibrous PCL scaffolds have been shown to produce tissue with cartilage like morphologies, even displaying some of the zonal topography

seen in the native tissue (Casper et al., 2010, Temenoff and Mikos, 2000). A limitation of synthetic scaffolds is that they usually require open surgery to implant the scaffold.

Beyond material scaffolds, research has occurred into looking at modulating the biochemical factors involved in OA.

In a 2017 review, Correa *et al,.* highlighted the importance of utilising biomaterial approaches that mimic of are functionally similar to the composition of the native tissue (Correa and Lietman, 2017). Any materials that are used to repair or replace the tissue needs to be able to:

- resist radial and longitudinal deformation and absorb compressive loads applied to the tissue
- hydrate environment that allows for nutrient exchange and maintain and permits cell function and differentiation
- establish and allow for cell-matrix contact
- integrate with both cartilage tissue and subchondral bone

Hydrogels present a promising material scaffold due to its wide range of properties and ability to entrap and support cells within the scaffold. Furthermore, with advancements in crosslinking methodology, 3D printing and processing of the gel and the incorporation of biological signals and cues, the material may now be developed specifically to mimic the natural cartilage environment to enhance regeneration of the tissue (Correa and Lietman, 2017, Vega et al., 2017).

Cartilage formation is regulated by spatial and temporal presentation of a selection of biomolecules that interact with cells within the tissue to trigger protein production and cell differentiation (Vega et al., 2017). Biomaterials can target particular biomolecules to enhance tissue repair or regeneration.

1.11.2 Modulation of inflammatory molecules: MMP-13

As MMP-13 is thought to be a central node within cartilage degeneration, inhibition of it may prevent the cyclic nature degeneration and thus make it an ideal target for therapeutic treatment (Li et al., 2017, 2011). MMP inhibitors (MMP-I) have been shown to block OA changes in explanted human tissue and synthetic MMP-13 therapeutic agents have been shown to slow down OA progression (Li

et al., 2011). However, MMP-Is have been tried in previous clinical trials but produced poor clinical success (Burrage et al., 2007). Systemic delivery of MMP-I has had low success in clinical trials as it induces musculoskeletal syndrome (MSS) which is diagnosed by the presence of joint stiffness, pain, oedema, a decrease in mobility and discolouration of the joint (Li et al., 2017, 2011).

Li *et al.,* identified 4 key failures associated with MMP inhibitory therapeutics. Firstly, MMP-Is tend to be broadly specific and target the Zn^{2+} ion present within the enzyme subsites. Therefore systemic delivery of non-specific MMP-Is not only target MMPs that play a role in OA but also inhibit the activity of other enzymes that utilise Zn^{2+}, or other divalent cations. Secondly, the non-selectivity of MMP-Is results in many patients developing MSS. This has been postulated to be caused by inhibition of either MMP-1 or MMP-14. MMP-14 knockout mice have been shown to display similar symptoms to MSS. In addition, most MMP-I have only been screened against a limited range of available MMPs and therefore the full extent inhibition is not fully known (Li et al., 2011). The third failure highlighted was that of inaccurate dosage estimation which is required to prevent drug toxicity. For many clinical trials, clinical efficacy could not be determined due to dose limiting toxicity and the onset of MSS (Li et al., 2011). The final failure of current clinical testing of MMP-Is, and potentially the most challenging one to overcome with regards to systemic delivery of MMP-Is for OA, is that target MMPs for OA are expressed and located in the joint capsule, synovium, cartilage and at the bony interface. Many of the MMP-I compounds are unable to penetrate into these sites and if they are able to enter are not able to do so at an effective dose; therefore rendering them ineffective as a therapeutic (Li et al., 2011).

MMP modulatory hydrogels have been previously created by Park *et al.,* in 2004, where a MMP sensitive poly(ethylene glycol)(PEG) hydrogel was created to contain a MMP sensitive protein motif. Within this study, it was seen that bovine chondrocytes had increased proliferation in the presence of MMP sensitive PEG gel compared with PEG gel, also saw that the protease sensitive hydrogels showed increase expression of matrix proteins such as collagen type II, collagen type XI, and aggrecan based on RNA quantification after 1 month. Cells within the insensitive PEG gels also shows higher expression of collagenases. However, no statistical analysis was performed (Park et al., 2004). Thus, although visible difference were seen in chondrocyte behaviour and morphology, between the sensitive and insensitive gels as well as the size of the PEG arms, the effectiveness or impact of the gels needs to be further assessed. The overall results shows that a lower elastic modulus, and thus a stiffer gel, in addition to the presence of an MMP-sensitive peptide within the cross linking chains impacted the proliferative and expression profile of chondrocytes within the scaffold.

1.11.3 Translation of treatments in the ankle joint

One of the biggest challenges with ankle treatments in the sparsity of primary literature studying the treatments within the tibiotalar joint. Instead, successful treatments are translated from the hip or knee to the ankle joint. However there are many differences that can be seen in vascularisation, surrounding soft tissue and local biology. It has been suggested that the ankle joint has a different response to damage compared to the knee joint as it is a peripheral joint meaning it has reduced blood supply, lower temperature and is a much smaller tissue. Furthermore there is a lack of clinically relevant models for the development of novel treatment. Previous studies described mainly used cadaveric tissue to assess biomechanical changes within the talocrural joint (Anderson et al., 2007, Choung and Christensen, 2002, Fansa et al., 2011, Hunt et al., 2012, Latt et al., 2011). Although this is the more relevant ethical considerations and tissue availability makes these studies challenging.

Alternatively, there is a notable lack of a standardised large animal model used to study the natural ankle joint. Major challenges can be attributed to differences in tissue morphology, shape, size, vascularity (Delco et al., 2017). There are some key shortcomings that must be weighed against one and another when evaluating the success of an animal model as a surrogate for clinical human research. These include, but are not limited to, the postural, healing difference, anatomical characteristics (including morphology and histological comparisons) and *in vivo* biomechanical loads. For orthopaedic applications, bone composition and the micro and macroarchitecture of the bone also plays a large role in the translatability of research.

Small animal models have historically been the gold standard for the studying orthopaedic foot and ankle models (Delco et al., 2017). However they possess the challenges of that prevent the meaningful translation to a clinical setting as they have different healing rates, bone structure and morphology.

Common large animal models used in to study OA in ankles include pigs, sheep, dogs and goats. Sheep joints have been suggested to provide a clinically and anatomically relevant large animal model (Gadomski et al., 2022). Sheep present similar weight, bone morphology and structure make them promising. However the general morphology of the joint was not that similar to humans. However sheep did show a high tolerance to surgical procedure, similar healing response to that documented in human patients when being treated for a carpometacarpal joint vs the rate seen in syndesmosis ligament repair (Gadomski et al., 2022). Delco *et al.,* showed that morphologically the sheep and

caprine ankles are a similar size to human ankles but as OA appears to be non-extant in these species, they may be less susceptible to OA.

1.12 Conclusions, challenges with current interventions and future research

Overall, current treatment modalities still result in poor long term outcomes for most patients. In most cases, these treatment methods attempt to fix the defect with reparative fibrocartilage and do not successfully promote the regeneration of articular cartilage. Their limited success in treating OLTs could be attributed to their inability to successfully replicate the mechanical properties of native cartilage or provide the biochemical signal to promote the regeneration of hyaline cartilage. Very few studies also image the defect site during post-operative follow ups, therefore it is hard to assess the success of the treatment beyond the clinical values given through patient reported scores like AOFAS scores.

Thus, there is the potential for the development of a novel material that is able to rectify the mechanical, cellular and biological limitations associated with current treatment methods, to provide improved reparations of an OLT.

An ideal treatment strategy for OLTs would be one that:

- promotes the development of articular cartilage in the defect site
- develops tissue that displays the same topography as articular cartilage
- provides initial restoration of mechanical properties
- utilises stem cells to produce superior tissue
- can be delivered arthroscopically
- will not result in donor site morbidity

Currently, no current treatment is able to successfully meet these needs.

In most cases, when a new material is developed, studies focus on the biological mechanisms of repair, with very few studies assessing the biomechanical capabilities of materials. This could

be attributed to the lack of appropriate *ex vivo* testing methods. As ankle joint biomechanics and cartilage properties differ from the knee, understanding how a novel treatment behaves in this environment could improve its capabilities. But, this is limited by the lack of *ex vivo* defect testing methodologies for the ankle which could test the efficacy of different treatment modalities against lesions of various sizes and locations within the talar dome. The development of which could allow for the production or identification of superior treatments. Therefore, there is an opportunity to create a reproducible method to test biomechanical changes associated with OLTs and their treatments. This will provide the opportunity to develop more rationally designed treatments for OLTs and provide the potential to investigate these areas further and to develop novel therapeutics.

Chapter 2

Introduction

2.1 Rationale, Aims and Objectives

Osteochondral lesions of the talus (OLTs) are often a result of a traumatic injury or repetitive micro-trauma within the tibiotalar joint. The presence of OLTs can cause the progression to OA within the ankle joint. Although the exact aetiology eludes scientists and clinicians to this day, the diagnosis of OLTs faces additional difficulties. The aneural and avascular nature of the talus results in poor regeneration but also provides challenges in the diagnosis and detection of an OLT. After initial insult, OLTs often remain asymptomatic. However, the presence of a chondral defect compromises the articular surface of the talus, allowing synovial fluid to enter the damaged tissue and cause changes to the pressures within the joint promoting the formation of cysts. It is believed that the presence of these cysts results in the local pain, tenderness or swelling that is often attributed to an OLT.

Various treatment modalities are available for OLTs depending on their size, location and the severity of the defect. These range from conservative treatments, such as reducing physical activity, using insoles to correct alignment and reduced weight bearing, to surgical treatments with a focus on either regeneration or repair. Regenerative techniques include bone marrow stimulation (BMS), biomaterial approaches and cartilage implantation and reparative techniques include fixation of the fragment, total ankle replacement and ankle arthrodesis. There is a lack of evidence comparing the different techniques and their long-term outcomes are still yet to be fully reported within the

literature. Ankle OA, unlike OA seen in the knee or hip, is mainly attributed to a traumatic injury and is often seen in younger active patients. Thus, it requires longevity in the treatment options. Due to this notable paucity in literature, no gold standard of treatment has been identified but clinical approaches taken are often driven by the size and severity of the defect.

Furthering the understanding of the biomechanical and biochemical changes within the ankle joint attributed to an injury could help to elucidate the underlying causes of OLTs and their progression to OA to inform treatment strategies. It is believed that continuous changes in the loading on the talar dome can be attributed to the development of OLTs. Furthermore, failure of many of these treatments could also be attributed to the lack of understanding of how the presence of OLTs changes the biomechanics.

An ideal material to treat OLTs would be a natural hydrogel that is able to control the joint space environment to promote a regenerative phenotype. As discussed in Chapter 1, a natural scaffold provides many of the intrinsic signals required for the cells within the pericellular matrix. As the main solid component of cartilage ECM is collagen type II, it would be assumed that this material would the provide the most comprehensive scaffold to promote, induce and maintain cartilage tissue. However, the availability, abundance and cost of the material makes it challenging to work with. An appropriate alternative material is collagen type I. Not only is it more available commercially, it also is naturally found within the joint tissue, in reparative fibrocartilage, is easily tunable and also provides a biocompatible environment for cells. Furthermore, collagen type I is already found in current AMIC or MACI treatments including ChondroGide®.

A current biomaterial available for chronic wound treatment is a 4 vinyl-benzyl chloride (4VBC) functionalised collagen type I scaffold that is able to cross-link using ultraviolet (UV) light (Liang et al., 2022, Neffe et al., 2015). The 4VBC-collagen based scaffolds was initially developed within the lab to treat chronic wounds. It has been shown to inhibit the activity of MMPs to promote healing in chronic wounds due to its ability to inhibit inflammation (Liang et al., 2018b, 2022, Tronci et al., 2016). Previous discussions have occurred highlighting the similarities between OA and chronic wounds, with similar biochemical cascades, inflammatory reactions and most noticeably the stimulation of MMP expression. Similar to OA, chronic wounds see an increase in MMP expression *in situ* and also dysregulation of normal pathways attributed to healing mechanisms. 4VBC-collagen type I gels have been shown to previously improve chronic wound healing and also has been applied to MSK work for bone regeneration (Liang et al., 2022). In addition this material has been assessed

for its ability to promote bone regeneration so it has been successfully translated across to similar musculoskeletal systems (Liang et al., 2022, Neffe et al., 2015). Thus, this scaffold was selected to be modified for an injectable treatment for OLTs (Woodell-May and Sommerfeld, 2020). However, due to difference in the properties of bone and cartilage, the material must be adapted to generate a more mechanically competent material designed specifically for cartilage. As the mechanical properties of the material may be controlled through the degree functionalisation, this material is an ideal candidate for a potential novel treatment for cartilage regeneration.

In addition, discussions with clinicians identified that access to the natural joint space of the tibiotalar joint was challenging in patients, with difficulties being attributed to lesion location, size of defect and surrounding supporting tissue. Often joint distraction is required to access the defect site for scaffold based therapies. Therefore, the 4VBC system was required to be modified for injectable delivery.

The aim of this PhD was to develop a method to assess biomechanical changes within the natural tibiotalar joint and use this to evaluate the ability for a hydrogel based treatment to mechanically repair the defect site. The aims of this project were achieved through the following objectives.

2.1.1 Objectives

1. Modification and characterisation of 4VBC-collagen type I hydrogel scaffold for injection into OLTs using vis-light crosslinking (Chapter 3)

2. Development a natural tissue based model to assess biochemical and tribological changes in the natural tibiotalar joint caused by the presence of an OLT (Chapter 4). This was achieved by:

   (a) Perform compression and frictional testing on the a porcine ankle to measure changes in the coefficient of friction and contact mechanics caused by the presence of OLTs.

3. Investigate the biomechanical effects of a 4VBC collagen hydrogel used to repair a 10 mm chondral defect in the human tibiotalar joint (Chapter 5). This included:

   (a) Translation of the methodology developed in Chapter 4 to cadaveric tissue

   (b) Characterisation of contact mechanics and frictional properties of the healthy tibiotalar joint

(c) Creation of a 10 mm defect on the talar dome and characterisation biomechanical and tribological changes attributed to the presence of a defect

(d) *In situ* cross-linking of injected hydrogel with vis-light in a full thickness OLT and mechanical characterisation of contact mechanics and frictional properties of repaired tissue.

(e) Testing of AMIC and OAT treatments to compare 4VBC collagen hydrogel to currently available treatments

4. Utilise the developed biomechanical compression and friction testing models to assess the ability of AMIC treatments to repair different types of lesion commonly seen within the tibiotalar joint (Chapter 6). The following lesion types will be assessed:

(a) Large lesions (> 150 mm^2)

(b) Shoulder lesions

(c) Kissing lesions

2.1.2 Graphical Abstract

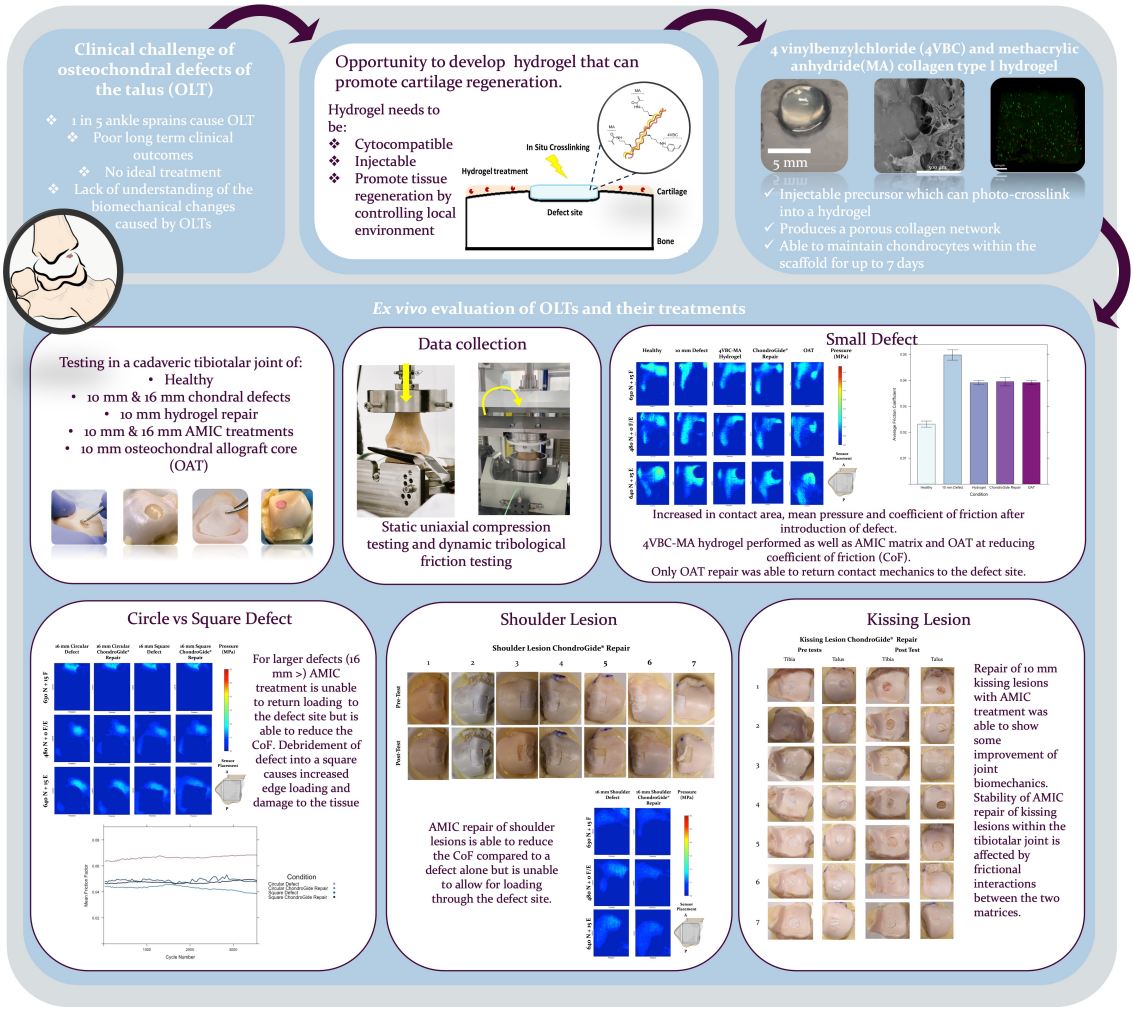

Chapter 3

Development of a Dual Functionalised Hydrogel for Osteochondral Lesion Repair

3.1 Introduction

The regenerative capability of cartilage is known to be limited, owing to its avascular and aneural properties and the lack of progenitor cells within the tissue. Due to the complex structure of articular cartilage, its specific functionality and its poor regenerative capabilities, interventions or therapies are required to promote the regeneration of the tissue, especially within the ankle joint. Two of the main strategies employed for larger defect repair currently are AMIC and MACI treatments. Figure 3.1 is a schematic showing the current AMIC procedure. Both of which use implantable 3D membranes to encourage repair of the tissue, however this has been reported to have a rate of failure between 1% and 10% (Migliorini et al., 2022a,b). This failure rate is similar to that reported in knees of 2- 13 % (Migliorini et al., 2022b, Waltenspül et al., 2021). Treatment of chondral defects can be improved using interventions to augment the healing process, improve regenerative potential and ideally reduce the risk of the formation of fibrocartilage. Tissue engineering has many promising strategies to develop therapies for treating cartilage and bone defects. Hydrogels are an emerging

potential therapy that can be harnessed for cartilage repair. This is because they mimic many of the native properties of cartilage ECM such as the high water content and can be tailored in an attempt to fulfil the deficiencies of other approaches.

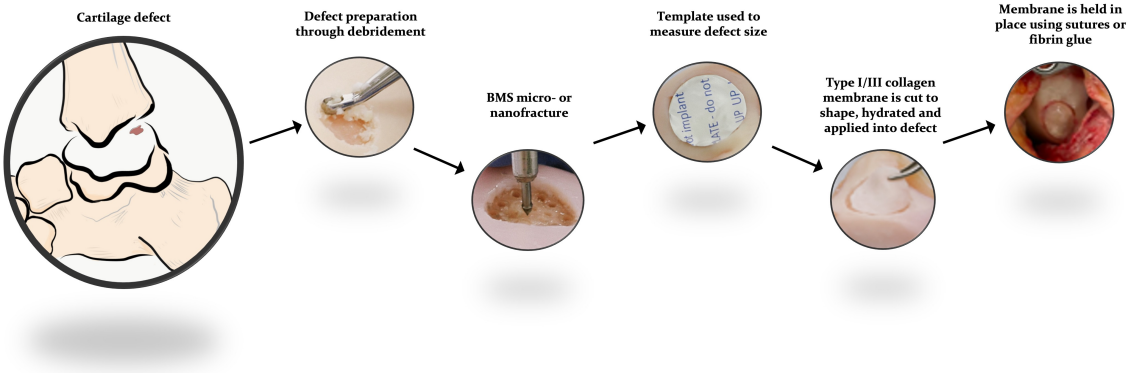

Figure 3.1: Schematic of current autologous matrix induced chondrogenesis (AMIC) procedure including bone marrow stimulation (BMS).

Hydrogels can be manufactured with controllable properties, such as the architecture, mechanical and biological properties. However, the ideal combination continues to remain elusive for cartilage tissue engineering. This is mainly due to the unique structure and function of the articular cartilage and the underlying osteochondral interfaces that produce a highly complex zonal architecture and composition. Therefore many biomaterial strategies have been adopted to focus on providing biological cues required to promote cell differentiation and proliferation within the defect site. Thus, resulting in the matrix material in question providing a temporary material that does not need to provide the same mechanical properties of cartilage but provides the 3D microenviroment to initiate the process of repair (Yang et al., 2017).

Many biomaterials have been developed to repair osteochondral lesions, these include calcium alginate, collagen type I and III and poly ethylene glycol using both physical and photopolymerisation techniques (Yang et al., 2017). Collagen is a naturally occurring protein and a major component of the ECM that has been used to study cell physiology and act in a tissue mimetic, three-dimensional environment. Furthermore, it is known that the mechanical properties of collagen can influence the behaviour of cells within the scaffold, as they can remodel their surrounding environment by secreting catabolic enzymes that are able to degrade the material. This make it an attractive material to be used for tissue engineering.

Although the majority of articular cartilage is made of collagen type II, the abundance and

availability of type I collagen makes it a more available material for tissue engineering approaches. Indeed, collagen type I hydrogels have been able to show improved *in vitro* chondrogenesis after 28-days, and support cell growth and adhesion (Marquass et al., 2010, Yuan et al., 2014). Native collagen has thus been shown to have excellent biological properties, however the mechanical and swelling properties of the material can be further enhanced through chemical modification of the collagen peptide. This modification can occur by utilising the amino groups present within the collagen peptide structure and chemically altering the backbone. These modification have been harnessed to allow for drug delivery and improved biocompatibility through the addition of GAGs or growth factors or by producing bioresponsive materials (Bahney et al., 2011, Liu et al., 2018, Zhou et al., 2022).

In situ polymerization of hydrogels allows for flexibility when repairing defects of irregular shapes (Zhou et al., 2022). Injectable hydrogels provide the ability to fill irregularly shaped defects, which is a challenge for traditional strategies such as OAT graft repair, and permitting increased shape fidelity and congruency between the hydrogel and the articulating tissue (Liu et al., 2017, Olov et al., 2022). Most injectable systems are injected as a hydrogel-forming solution that undergoes gelation post implantation following application of an external stimulus. Commonly, through the combination of two materials that react when they come into contact through a reaction (Jin et al., 2010). Alternative strategies that have been adopted include photogelation through a photoinitiated crosslinking method (Park et al., 2013, Rothrauff et al., 2018, Yang et al., 2016).

Bioresponsive materials are able to interact with the tissue to allow for improved regeneration. Whether that is by interacting with the tissue using tunable degradation or through interacting with constituents of the tissue or joint space such as enzymes (Bahney et al., 2011). A promising target enzyme for OA treatment is the matrix metalloprotease family. MMP activity is crucial for the remodelling of the ECM in cartilage and the maintenance of tissue homeostasis controlled by a careful balance of anabolic and catabolic activity. However an imbalance of these catabolic factors can cause enhanced degradation of the tissue seen within the diseased OA tissues. MMP-13 has been shown to play a pivotal role in the break down of cartilage in the osteoarthritic joint and is the primary MMP involved in cartilage degradation (Hu and Ecker, 2021, Rowan et al., 2008). In addition, its preferred substrate is collagen type II which degrades 5X faster than collagen type I (Howes et al., 2014). As MMP-13 is a key factor in the early pathology of OA, it provides an attractive target for therapeutics to improve the treatment of OA. Therefore, by creating materials that are able to reduce the activity of MMP enzymes it could promote the regeneration of cartilage.

Based on these requirements, developing a hydrogel system that is able to mediate the activity of MMPs, can be delivered directly into the defect site and crosslinked *in situ* and utilises a natural scaffold such as collagen would be an attractive treatment for OLTs. The aims of this chapter are to present preliminary data to produce Vis-light crosslinkable, dual-functionalised collagen type I hydrogel aimed for the treatment of OLTs.

3.1.1 Rationale for functionalised hydrogel scaffold

Targeting of MMP activity can be done in many ways (Hu and Ecker, 2021). A current collagen based system used for chronic wound healing utilises the functionalisation of 4VBC to the surface of atelocollagen was harnessed and modified for this body of work (Liang et al., 2018b, 2022, Tronci et al., 2016). These have been shown to reduce the activity of MMP proteins which are upregulated in chronic wounds and also directly after insult or injury ro the anjke joint (Adams et al., 2015, Tronci et al., 2016). The addition of 4 vinylbenzyl chloride (4VBC) moieties provide drug-free inhibition of MMPs and thus delays enzymatic degradation of the scaffold within the defect site. This may allow for a shift of phenotype to a less OA-like state. The presence of 4VBC within crosslinked scaffolds is able to accomplish a reduction in MMP activity through induced cation-π interaction between the aromatic structures of the 4VBC functional groups and the active zinc site present in the MMP enzyme (Liang et al., 2022).

Sequential functionalisation of methacrylic anhydride (MA) was selected for the scaffold to provide long lasting proteolytic stability, drug-free MMP deactivation and maintain mechanical competence *in situ*. MA is a highly reactive monomer and coupling of both MA and 4VBC to the scaffold was done to provide improved mechanically competency of the material, with a reduced swelling ratio and barrier functionality due to the increased functionalisation of the primary amino groups (Liang et al., 2022).

The degree of functionalisation selected for 4VBC was based on a study by Liang *et al.,* in which the degree of functionalisation was measured based on the molar concentration of free lysine residues present on the collagen backbone and the functional agent. The degree of reported functionalisation seen for 25 molar excess of 4VBC (25 4VBC) and 0.3 molar excess (0.3 MA) was similar when reacted with atelocollagen. In addition, a 1 MA molar excess (1 MA) produced a degree of functionalisation of about twice that of 25-4VBC (Liang et al., 2018b). Thus, a dual functionalised gel of 25 4VBC

and 0.3 MA would theoretically produce an equal degree of functionalisation for both groups onto the collagen peptide backbone. Thus these concentrations were chosen for the studies described within this chapter. Furthermore, it was predicted that 1 MA functionalisation would produce the same degree of functionalisation as that seen in the dual functionalised samples and this was selected as a control material.

Additional modifications were selected to adapt the hydrogel for the intended uses. Visible light (vis-light) curing at a wavelength of 405 nm was selected to minimise damage to the cells or tissues caused by UV exposure (Lee and Tae, 2007). In additional dental blue light at this wavelength can be delivered arthroscopically to the joint, providing improved application. Previously either acetic acid or hydrochloric acid was used to solubilise the hydrogel precursor solution for the gel system. To improve cell viability the hydrogel forming solution need to be soluble at more physiologically relevant conditions. The precursor material need to be solubilised at pH 7.4.

3.1.2 Study aims

The aim of the studies presented in this chapter was to develop an injectable collagen based hydrogel for OLT treatment and to investigate the cell viability and functionality within the scaffold. This was achieved by:

1. Modifying current 4VBC-MA scaffold fabrication methods so that it can be performed at a neutral/physiological pH using a vis-light crosslinking methodology through:
   (a) Synthesis of precursor materials with both 4VBC and MA moieties on the surface
   (b) Development a methodology to allow for crosslinking using Vis-light in neutral or physiological conditions
   (c) Characterisation of the mechanical properties of the gels
2. Developing a method to encapsulate cells within the 3D matrix of the hydrogel and to assess the viability of cells within the scaffold for up to 7 days. Assessing the viability of chondrocytes and mesenchymal stems cells within the scaffolds.

3.2 Materials and Methods

3.2.1 Materials

All reagents and chemicals used for these experiments were purchased from Sigma-Aldrich (Sigma Aldrich, UK).

3.2.2 Extraction of Collagen Type I from Rat Tail Collagen

Type I collagen was obtained from fresh frozen rat tails provided by the University of Leeds (UK). Rat tails were defrosted in deionised water for 30 minutes before the skin was removed and the four tendons excised from the tail. Tendons were then macerated and added to 50 mL of 17.4 mM glacial acetic acid per tail. Collagen was extracted from the tendons by incubating at 4°C for a minimum of 72 hours, stirring constantly. The resulting collagen solution was harvested through centrifugation at 30,000 *g*, 4°C for 1 hour with the supernatant was collected. Collagen solutions were then freeze-dried for a minimum of 7 days to extract the liquid resulting in purified rat tail collagen (RTC). This was then used for the subsequent experiments.

3.2.3 Synthesis of photoactive functionalised collagen

A two-step functionalisation system was developed to allow for the covalent coupling of both methacrylic anhydride (MA) and 4 vinylbenzyl chloride (4VBC). Currently, the methodology that was being adapted for this research utilised an acid based solvent for the functionalised 4VBC-collagen precursor using acetic acid of hydrochloric acid. To allow for direct delivery into the tissue, a more physiologically relevant pH was required. Previous work has shown that functionalisation of collagen with methacrylic anhydride (MA) allowed for solubility in phosphate buffered saline (Liang et al., 2018b). To promote solubility at physiological conditions and MMP inhibitory activity, dual functionalisation of the material with both 4VBC and MA was selected. Based on work previously performed within the research group, it was shown that when reacted with bovine atelocollagen, a 25 molar excess of 4VBC and 0.3 molar excess of MA, compared to free amines present on collagen type I, presented with similar degrees of functionalisation, of 18 ± 1 % and 19 ± 1 %. These concentrations were selected as they would produce equal degrees of functionalisation. In addition,

functionalisation with 1 molar excess of MA allowed for 44 ± 1 % of the free amines to be reacted and this would be used as a control group for the 4VBC activity as it is these functional groups that allow for cross-links to form during the gelation process. The processes used to synthesise the precursors material are described below. For the dual functionalised scaffolds, quantification of reactions was performed in between each step to assess success and degree of functionalisation using 2,4,6-Trinitrobenzene Sulfonic Acid (TNBS) assay.

Primary functionalisation with 4-vinylbenzyl chloride

Extracted RTC was dissolved at 0.25% w/v into a 10 mM HCl solution O/N at room temperature (RT). Solutions were neutralised to pH 7.4 and a 1:1 molar ratio triethlyamine (TEA) was added to the solution. 4VBC was added at 25 molar excess compared to the free amine content of the collagen solution identified by TNBS assay. 1% w/v Tween 20 was added and the reaction was performed for 24 h at RT. Functionalised collagen was then precipitated out by adding a 10-fold excess of 100% ethanol for 24 h at RT. Collagen was recovered and concentrated by centrifugation at 10,000 rpm, 10°C for 45 mins. Supernatant was removed and the collagen was left to bench dry allowing for excess ethanol was left to evaporate out. Functionalised collagen was then assessed using a TNBS assay to measure the remaining free amine groups present on the polymer.

Characterisation of reacted products using 2,4,6- Trinitobenzene sulfonic acid assay

Confirmation of RTC functionalisation was performed by assessing the number of free amine groups (-NH_2), primarily due to the presence of lysine residues, present on the collagen surface. TNBS assay (n=3) was used to measure the degree of functionalisation with either MA or 4VBC. 11 mg of dry sample was reacted with 1 mL of 4 wt % $NaHCO_3$, and 1 mL of 0.5 wt.% TNBS solution at 40°C for 4 h. 3 mL of 6N HCl was then added to each sample and incubated for a further 1 h at 60°C to ensure complete dissolution of the functionalised collagen. Solutions were then cooled to RT and diluted 1:2 with 5 mL of dH_2O. Three wash steps were performed using 15 mL of diethyl ether to remove any of the unreacted TNBS. A 5 mL aliquot was taken from each sample and diluted in 15 mL of dH_2O before being analysed using a UV-vis spectrophotometer. The molar content of free amine groups present in the collagen was calculated using equation 3.1:

$$\frac{mol(Lys)}{g(RTC)} = \frac{2 \times Abs(346nm) \times 0.02}{1.46 \times 10^4 \times b \times x} \tag{3.1}$$

In which, Abs (346 nm) was the UV absorbance recorded at 346 nm, 2 is the dilution factor used, 0.02 is the volume of sample in the solution in litres, 1.46 x10^4 is the molar absorption coefficient for modified 2,4,5-trinitrophenyl lysine groups, b is the cell path of a length of 1 cm and x is the dry weight of the sample.

To calculate the degree of functionalisation Equation 3.2 was used:

$$F = 1 - \frac{mol(Lys)_{\text{functionalised}}}{mol(Lys)_{\text{RTC}}} \times 100 \tag{3.2}$$

Here, $mol(Lys)_{functionalised}$ and $mol(Lys)_{RTC}$ relate to the total content of free amine groups present in the functionalised sample compared with the native RTC, respectively.

Primary or secondary functionalisation with methacrylic anhydride

After the free lysine content of the reacted 25 4VBC precursors collagen was assessed, secondary functionalisation was performed using the same method as described above. This was done at a varied molar ratio with respect to the molar lysine content seen in the RTC, with molar ratios selected at either 0.3 or 1 molar excess of [MA]: [Lys] for the single functionalisation samples and 0.3 molar excess of the remaining free lysine residues seen on the 4VBC- RTC for the dual functionalised precursors.

For the reaction step, the appropriate molar ratio of MA to free lysine residues was performed with equal monomer content of TEA added. The reaction was performed as described above and the collagen was collected through precipitation and centrifugation of the samples. The degree of secondary functionalisation was once again assessed through TNBS assay to identify remaining free lysine residues.

3.2.4 Preparation of functionalised collagen hydrogels

Solutions were created for each of the functionalised collagen precursors of 0.3 MA, 1 MA and 4VBC-MA. These were generated by solubilising the precursors material in 10 mM HCl at 1.6 wt.% for 24 h at room temperature, stirring continuously. A 1% w/v LAP solution was made in phosphate buffered saline (PBS). Precursor solution and LAP photoinitiator solutions were combined at a 1:1 ratio and vortexed to produce a final working solution of 0.8 wt.% functionalised collagen and 0.5% w/v LAP. Using a 16 g sterile hypodermic needle and a 1 mL syringe, the precursor solution was cast into 5 mm diameter and 1.5 mm height circular silicon moulds placed on a sterile tissue culture plate; generating scaffolds with a volume of 30 mm^3. Gels were left to be crosslinked for 7 minutes under a 405 nm light before being washed twice for 10 mins in PBS prior to testing.

3.2.5 Hydrogel swelling tests

Swelling tests of the hydrogels were performed in PBS. The scaffolds (n=3) were then incubated in PBS for 24 hours. Scaffolds were collected, paper-blotted and weighed (m_s). The dry weight of the scaffolds (m_d) was obtained by allowing the scaffolds to air dry for 72 hours before being weighed. the swelling ratio was calculated using equation 3.3:

$$SR = \frac{m_s - m_d}{m_d} \times 100 \tag{3.3}$$

3.2.6 Scanning Electron Microscopy

The surface morphology of the hydrogels were explored using variable pressure, and cool stage SEM. Back scatter electron (BSE) and environmental secondary electron detector (ESED) images were taken with hydrated gels at 80 MPa vacuum and 1000 Volts. Optimisation of cool-stage SEM was performed to minimise the development of ice crystals on the gel through sublimation under the chamber vacuum.

3.2.7 Cellular Encapsulation Studies

Cells and cell culture

ATDC-5 cells and Y201 cells were used for the following experiments. ATDC-5 is a murine teratocarcinoma cell line that are characterised as a chondrogenic cell line. Y201 cells are immortalised MSC cell line that has been shown to have adipogenic, chondrogenic and osteogenic potential with chemical induction (Galarza Torre et al., 2018).

ATDC-5 cells were cultured in Dulbecco's Modified Eagle Medium (DMEM) /Ham F12 50/50 with L-glutamine and 5 mM HEPES supplemented with 5% foetal calf serum (FCS), 100 U/mL penicillin and 100 µg/mL streptomycin. Y201 cells were cultured in high glucose DMEM with 10% FCRS, 10% L-glutamine, 100 U/mL penicillin and 100 µg/mL streptomycin. All cells were incubated at 37 °C and 5% CO_2.

Cell encapsulation in functionalised scaffolds

Cells were cultured to 70% confluency prior to testing. Hydrogel precursor material was prepared as described above.

Media was removed cells and cells were washed in 10 mL of PBS. PBS was removed and cells were trypsinised for 5 mins at 37°C. DMEM was added to the cell suspension and this was collected and centrifuged for 5 mins at 500 g. The supernatant was removed and cells were resuspended in 1 mL of PBS. Cell concentration was determined using a hemocytometer. 50,000 cells were encapsulated per 5 mm scaffold or 1.67 x10^6 cells per mL. 2D cell seeding density was predetermined dependent on the duration of incubation and can be seen in table 3.1.

Table 3.1: Cell seeding densities for encapsulation studies

Day	Seeding density per well
1	80,000
4	25,000
7	15,000

Cells were concentrated by centrifugation and resuspend to the working cell concentration of 3.34 $\times 10^6$ cells per mL in PBS supplemented with 1% LAP. Equal volumes of precursors collagen solution and cell-LAP suspension were combined and vortexed to mix. The mixture was syringed

into the silicon moulds and was crosslinked for 7 mins under the 405 nm vis-light.

Cell-laden hydrogels were extracted from the moulds and twice washed in PBS for 5 mins and then in cell culture medium for 5 mins. Scaffolds were cultured in a 24-well tissue culture plate containing 1 mL of media per well. Scaffolds and cell monolayers were incubated at 37 °C and 5% CO^2. Samples were incubated for up to 7 days with media changes after 24 hours and 96 hours. Scaffolds were harvested on days 1, 4 and 7, and imaged using confocal microscopy.

3.2.8 Live Dead imaging using Calcein AM and Ethidium Homodimer staining

A live-dead solution of 2 µM Calcein AM and a 4 µM of ethidium homodimer was made in 1 × PBS. Scaffolds were washed twice in PBS. 1 mL of live-dead staining solution was added to each well containing either empty scaffolds, cell-laden scaffolds or cell monolayer. Samples were incubated for 30 mins at 37 °C and 5% CO^2 before being imaged using a Leica SP8 confocal microscope (Leica microsystems, Germany).

3.2.9 Statistical Analysis

Statistical analysis was performed using R (Version 4.2.2). A complete list of packages used is presented in Appendix D. Shapiro-Wilk test was used to assess the normality of the data and Levene's test was used to asses variance. One-way ANOVA with post-hoc Tukeys test was used to determine statistical significance. A p-value of less than 0.05 was considered to be significantly different.

3.3 Results

3.3.1 Fabrication of Vis-light cured hydrogel precursors

Fabrication of the collagen precursors was achieved through sequential functionalisation of both 4VBC and MA moieties to free lysine residues on the RTC backbone (fig. 3.2). Control precursors containing different concentrations of MA, either 0.3 or 1 molar excess, were also synthesised through

a single step reaction. Quantification of free lysine residues present on the collagen was used to assess the success of the reaction.

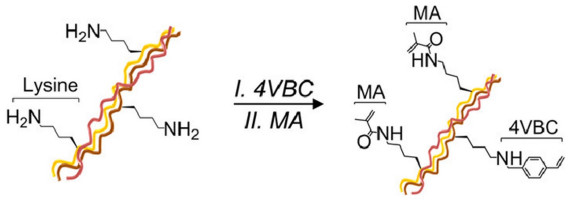

Figure 3.2: Design of functional RTC precursor through sequential functionalisation with both 4-vinylbenzyl chloride (4VBC, I) and then methacrylic anhydride (MA, II) (Modified from (Liang et al., 2022).

Chemical characterisation of functionalised hydrogels

Native, extracted RTC was measured to have a free lysine residue of 3.17 × 10^4. the degree of covalent functionalisation of 4VBC and/or MA to the free lysine residues on the RTC was measured through the use of a TNBS assay. The assay was able to confirm a decrease in the molar content of free amines in all three samples (table 3.2). Reaction with only 0.3 MA ([monomer].[Lysine]$^{-1}$ = 0.3) produced the lowest loss of free amine content. The degree of functionalisation of 4VBC to the RTC at a molar ratio of 25 [4VBC]:[Lys] was measured at 23%. Secondary functionalisation with 0.3 MA reduced the molar content of primary amino acids from 2.53 ± 0.012 mol.g^{-1} to 2.17 ± 0.014mol.g^{-1}. This reduction in free amines was smaller than that observed when 0.3 MA was reacted directly on to the RTC which resulted in a free amine content on the reacted product of 2.67 ± 0.008 mol.g^{-1}. The dual functionalisation of RTC with 4VBC-MA resulted in an average degree of functionalisation of 33 mol.% which is similar to that seen for the 1 MA reacted gels of 31 mol.%.

Table 3.2: TNBS assay data showing the degree of functionalisation (F) for the different sample synthesis conditions (n=3) showing the specific monomer-lysine molar ratios ([M].[Lys]$^{-1}$) used for each reaction. Quantification of the remaining lysine residues allowed for calculation of the degree of functionalisation seen (F/mol.%) ± Standard Deviation (SD)

Sample	**[M].[Lys]$^{-1}$**	**[Lys]/mol.g^{-1} (× 10^4)**	**F/ mol.%**
4VBC	25	2.53 ± 0.012	23 ± 3
4VBC-MA*	0.3	2.17 ± 0.014	33 ± 4
0.3 MA	1	2.67 ± 0.008	19 ± 2
1 MA	0.3	2.28 ± 0.009	31 ± 3

*Secondary functionalisation reaction of MA to 4VBC-RTC

Vis-light crosslinking of functionalised collagen scaffolds

Fabrication of hydrogels was performed using the synthesised precursors. Full gelation of the scaffolds was observed after exposure to 405 nm wavelength of light for 7 mins (fig. 3.3). Cool-stage SEM imaging of swollen hydrogels showed heterogeneity in the microarchitecture and pores size within the hydrogels (fig. 3.4). It can be seen that the 4VBC-MA gels appear to have the greatest degree of porosity within the scaffolds compared with the MA only containing gels. Interconnectivity between pores is seen to vary in size between the different samples. A more even surface was seen for 4VBC-MA hydrogel compared with the 1 MA and 0.3 MA scaffolds, whose morphology appears to contain more areas of visible peaks and troughs suggesting a rougher surface (fig 3.4c, 3.4f & 3.4i).

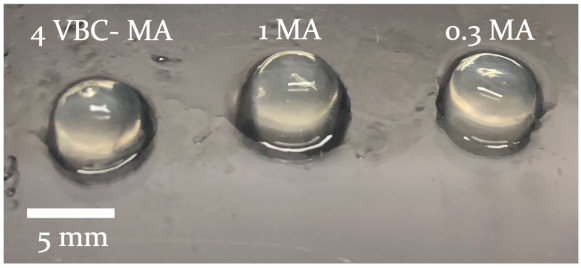

Figure 3.3: Exemplary images of 5 mm 4VBC-MA, 1 MA and 0.3 MA hydrogels.

Figure 3.5a shows images of the swollen and dry hydrogels. No differences were seen in the swelling ratio between the 4VBC-MA hydrogels and the 1 MA gels (fig 3.5b). A significant increase in swelling ratio was seen in 0.3 MA samples compared with the 4VBC-MA and the 1 MA gels with $p = 0.004$ and 0.006, respectively.

3.3.2 Cell morphology and distribution within the hydrogel scaffolds

The developed fabrication methodology was able to be successfully adapted to allow for the encapsulation and survival of both ATDC-5 and Y201s within the scaffolds after 7 days in the 4VBC-MA hydrogels (fig. 3.6 & 3.7). It can be seen that for all three hydrogel types, ATDC cells were able to be successfully encapsulated within the gels and that a relatively even distribution of cells can be seen across all three scaffolds (fig. 3.6b, 3.6f & 3.6j). The morphology of the cells in scaffolds differed from the morphology of the cells in the 2D monolayer. The cells appear to form a rounded morphology of chondrocytes within 3D culture after 1 day of incubation within the gels. Whereas,

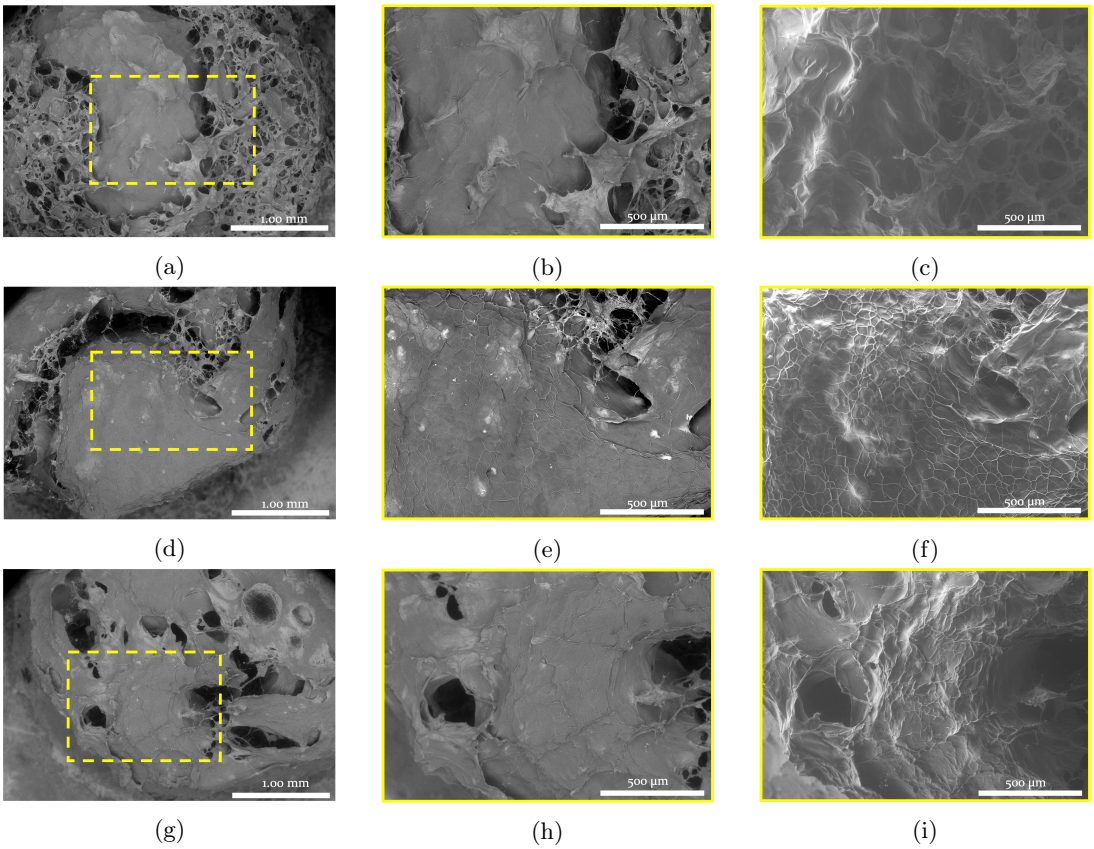

Figure 3.4: Cool-stage electron microscopy of the 4VBC-MA, 1 MA and 0.3 MA hydrogels prepared with LAP-supplemented PBS solutions at x37 magnification and X80 magnification using back scatter (BSE) imaging and x80 magnification side scatter defect (ESED). (A-C): 4VBC-MA hydrogel, (D-F): 1 MA hydrogel and (G-H): 0.3 MA hydrogel. (A,D,G) show scaffolds at x37 magnification using BSE. The scale bar represent 1 mm. The region highlighted in yellow is explored at x80 magnification. (B, E, H) shows scaffolds at x80 magnification using BSE. The scale bar represents 500 µm. (C,F,I) shows the same scaffold region at x80 magnification using ESED. The scale bar represents 500 µm.

the ATDC-5 in the 2D monolayer displayed a more fibroblast-like appearance (fig. 3.6m, 3.6n & 3.6o)

It can be seen that a greater proportion of dead cells were present within the MA only containing gels compared to the 4VBC-MA gels after 24 h of incubation. In addition, a greater proportion of dead cells were located at the bottom of the hydrogel. After 4 days of culture, the morphology of the cells within the scaffold remains relatively rounded, with greater proportions of dead cell seen in both the 1 MA and 0.3 MA hydrogels compared with the 4VBC-MA hydrogels. The 0.3 MA hydrogel on day 4 appears to have the highest proportion of live cells encapsulated within the scaffold. Confocal imaging showed some autofluorescence for all of the scaffolds however, clear differences can be seen between the background scaffolds and the cells within. After 7 days, viable cells can be seen in all three scaffolds. 0.3 MA gels appear to have the greatest number of dead cells located within the

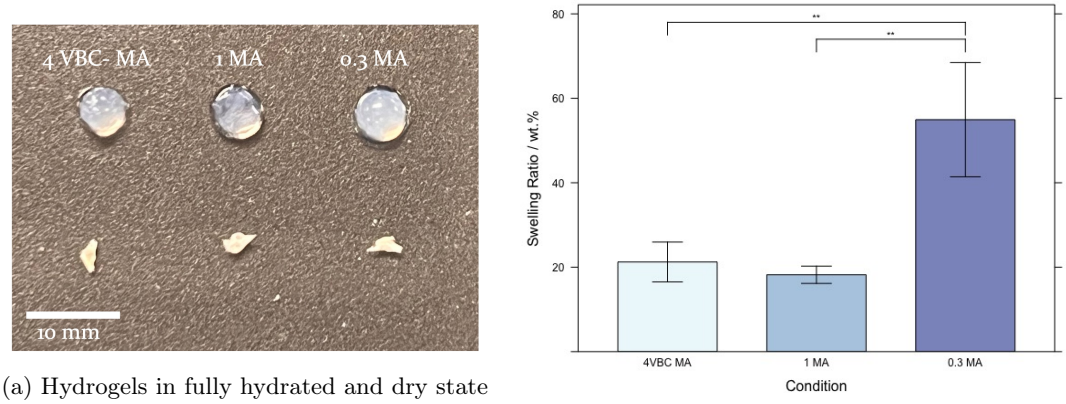

(a) Hydrogels in fully hydrated and dry state

(b) Graph of swelling ratios

Figure 3.5: Outcomes of swelling ratio studies. (A) Exemplary macrographs of the 4VBC-MA, 1 MA and 0.3 MA hydrogels in both the dry state and the fully hydrated state. The scale bar represents 10 mm. (B) Swelling ratio for 4VBC-MA, 1 MA and 0.3 MA Vis-light cured hydrogels in neutral conditions. Data presented is mean ± SD (n=3). *$p < 0.05$, **$p < 0.01$. p-values represent ANOVA with Tukey's post hoc.

.

scaffold compared with the 1 MA or 4VBC-MA gels. The dead cells appear to be evenly distributed throughout the 0.3MA scaffold (fig. 3.6l). Whereas, it appears like the dead cells are clustered at the same depth in the 4VBC scaffold (fig. 3.6d).

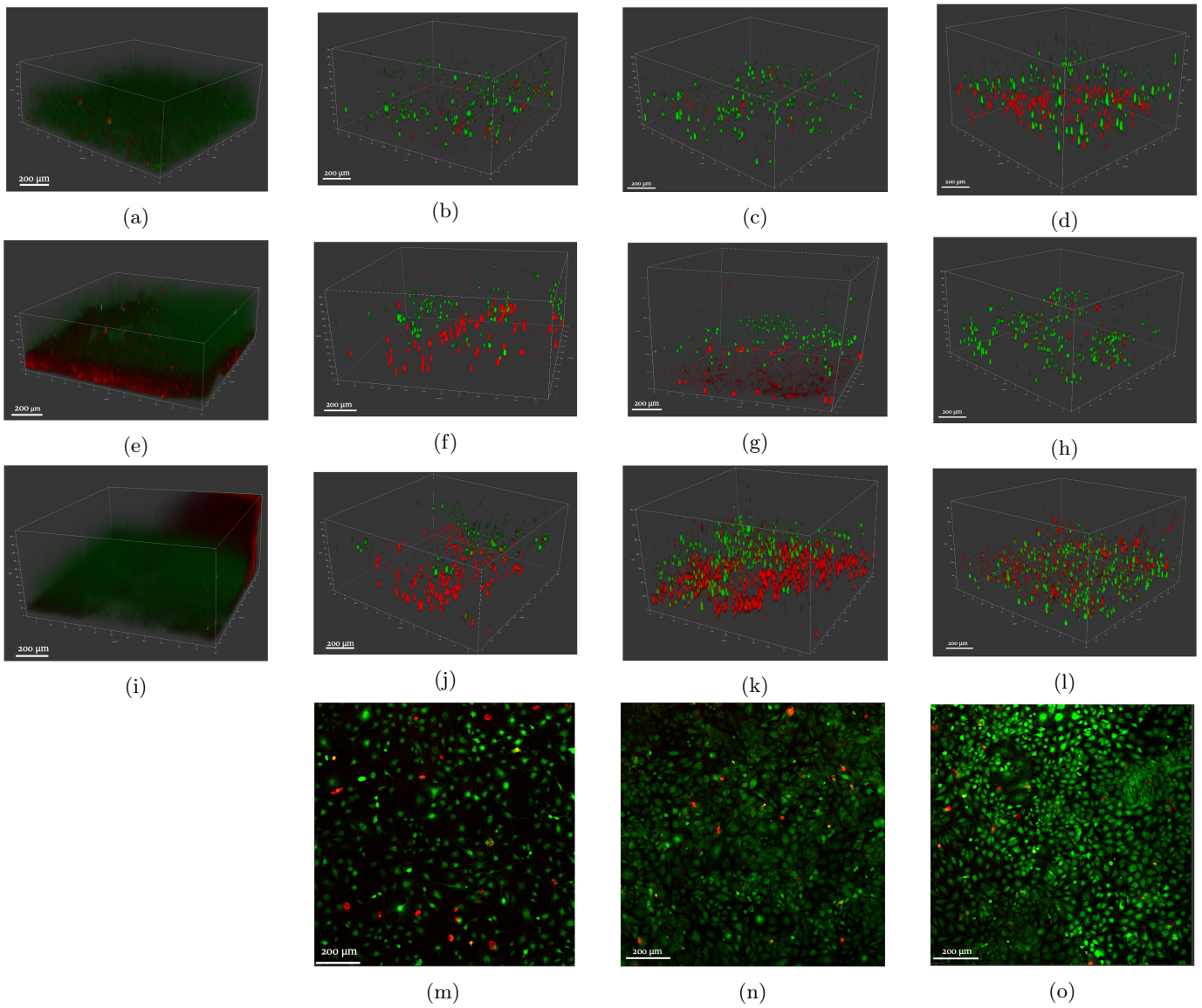

Figure 3.6: Confocal fluorescent microscopy images of a 7 day encapsulation study of ATDC-5 immortalised chondrocytes within the 4VBC- MA, 1 MA and 0.3 MA hydrogels, 2D cultured cell monolayers and empty scaffolds. Cells are strained with Calcein AM (Green) and Ethidium Homodimer (Red). Scale bar represents 200 µm. (A): empty 4VBC - MA hydrogel. (B-D): 4VBC-MA hydrogels containing ATDC-5 cells on Day 1, Day 4 and Day 7. (E): empty 1 MA hydrogel. (F-H): 1 MA hydrogel containing ATDC-5 cells on Day 1, Day 4 and Day 7. (I): empty 0.3 MA hydrogel. (J-L): 0.3 MA hydrogel containing ATDC-5 cells on Day 1, Day 4 and Day 7. (M-O) is ATDC-5 2D cultured cell monolayer on Day 1, Day 4 and Day 7.

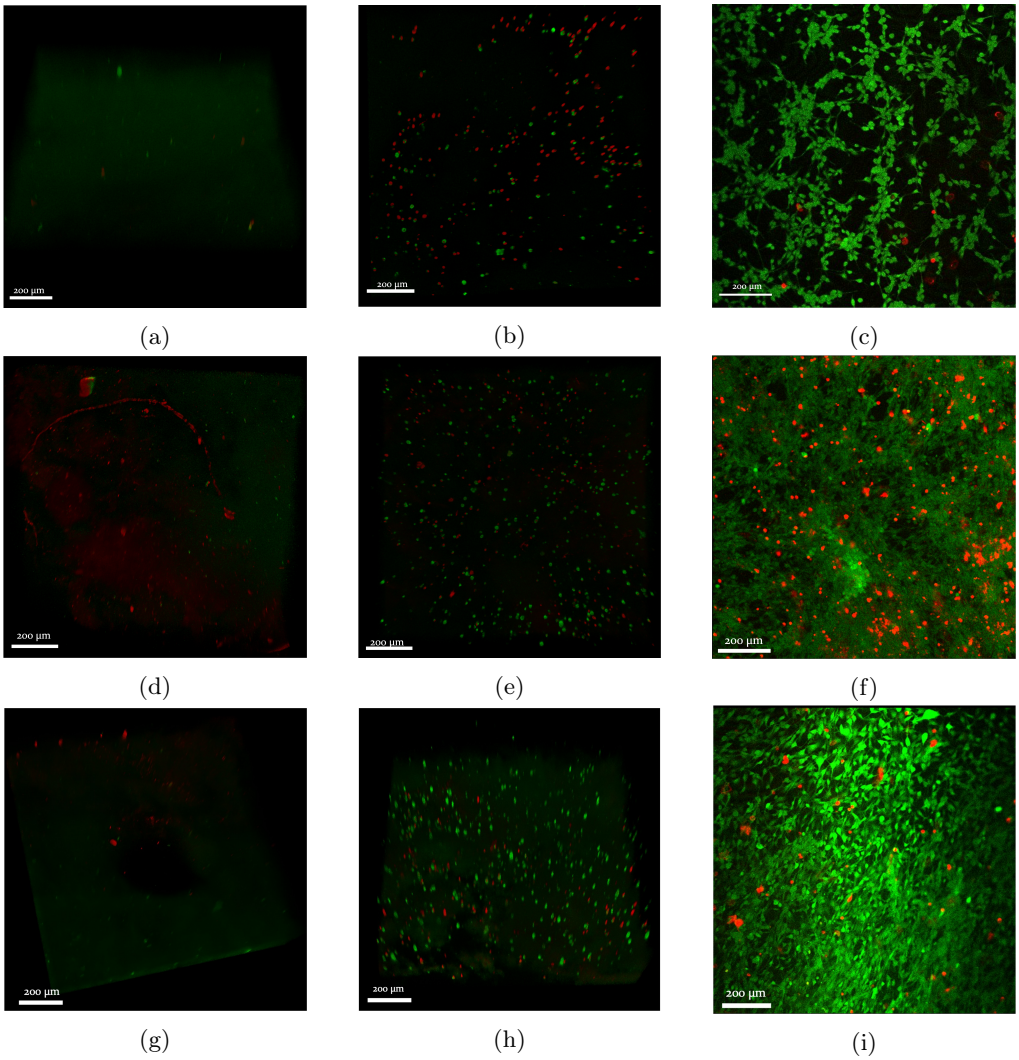

Figure 3.7: Confocal fluorescent microscopy images of the viability of Y201 mesenchymal stem cells encapsulated within the 4VBC-MA collagen type I hydrogel (b, e, h), 2D cultured cell monolayers (c, f, i) and empty scaffolds (a, d, g) after up to 7 days of cell culture. Cells were stained with Calcein AM (Green) and Ethidium Homodimer (Red). Scale bar represents 200 µm. Images show scaffolds and cells on Day 1 (A-C), Day 4 (D-F) and Day 7 (G-I) of incubation.

Y201 immortalised MSCs were able to be successfully encapsulated within the scaffolds and viable within the scaffold after 7 days (fig. 3.7h). Figure 3.7b shows cells within the scaffold 1 day post encapsulation. Where ia high proportion of dead cells can be seen present within the scaffold, however this proportion appears to decrease during the experiment with lower levels of dead cells seen on day 4 and day 7 of incubation (fig. 3.7e & Figure 3.7h). Furthermore, the morphology of the cells within the scaffolds was rounded compared to the Y201s cultured in a 2D monolayer where some cells showed a more elongated fibroblastic morphology (fig. 3.7c). Autofluorescence was seen within the empty scaffolds (fig. 3.7a, 3.7d & 3.7g).

3.4 Discussion

To ensure that the developed hydrogel would be able to be delivered directly to the defect site and crosslinked *in situ* using visible light photoinitiation, the precursor collagen needed to be able to remain in solution at neutral conditions. This would permit it to contain the LAP photoinitiator in the pre-mixed precursor solution that would be delivered by syringe directly in to the defect site but also reduce the risk of damaging the tissue further by exposing it to the low pH conditions previously used for manufacturing the hydrogel (Liang et al., 2018b, 2022). This method of fabrication would also permit the encapsulation of cells throughout the scaffold to further study their behaviour. Both these requirements resulted in adaptations to the current fabrication methodologies to fulfil the needs of the material. In addition, to allow for the material to stay in the solution once it was neutralised, the functionalised material needed to not contain only 4VBC as a moiety but also MA. As the presence of the 4VBC moieties allowed for the MMP inhibitory properties but also would reduced the solubility in aequeous solutions.

The outcomes of the studies presented in this chapter showed that successful synthesis of the precursor material and fabrication of the collagen hydrogels was able to occur. Some characterisation of the adapted vis-light cured gels was able to be performed, including the degree of functionalisation of precursors material and swelling ratio. A methodology to encapsulate cells with the scaffold was also developed, with both chondrocyte and MSC cell lines able to be supported within the 4VBC-MA hydrogel for up to 7 days. Potentially providing a platform for long-term studies to assess cell remodelling of the scaffolds.

3.4.1 Functionalisation of precursor material

Synthesis of the precursor material was able to be successfully performed with the primary functionalisation of 4VBC and MA moieties and secondary functionalisation of MA to the free amines present on the surface of the rat tail collagen. The reported outcomes of the TNBS assays showed that the degree of functionalisation of 4VBC functionalisation was similar to that reported for previous studies using atelocollagen (AC). Here they reported 18% functionalisation with 25 molar excess of 4VBC which is less than 23% presented in this study (Liang et al., 2022). 0.3 MA functionalisation was also the same as previously reported with AC of 19% functionalisation seen in both studies (Liang et al., 2018b). However, 1 MA showed a lower level of functionalisation than the

44% previously reported with atelocollagen. Secondary functionalisation of 0.3 molar excess MA compared to primary functionalisation resulted in a lower degree of reaction with the free amines. This reduction in the reaction is believed to be caused by steric hindrance caused by the primary reaction with 4VBC. This prevents MA binding by reducing the reactivity of the remaining groups in the material, resulting in a lower level of reaction seen for 0.3 MA when reacted secondarily to the 4VBC-MA samples. Nonetheless the overall degree of total functionalisation for the 4VBC-MA and the 1 MA precursors materials was similar, providing the potential for a comparable level of crosslinking in both precursor materials. The degree of methacrylation of collagen has been demonstrated to directly correlate to the gel content and as a method to assess the molecular crosslinking density (Liang et al., 2018b).

In addition, within this study batch to batch variation resulted in ± 4% variation in functionalisation of both 4VBC and MA and ± 2-3% in the single step reactions. This is greater than the ± 1 -2% reported previously (Liang et al., 2018b, 2022). This could be attributed to source of the collagen as previous work was performed on atelocollagen compared with the rat tails studied here. Rat tail collagen has been shown to be more reactive with 4VBC compared to atelocollagen and this could be attributed to the higher batch to batch variation reported in this study (Brooker and Tronci, 2022).

3.4.2 Vis-light crosslinking of collagen hydrogels

To ensure that the scaffold was able to be successfully crosslinked *in situ*, without damaging the surrounding tissue, modifications to the previously published crosslinking methodologies were required. As the hydrogel system proposed here is to be directly applied to the defect and utilise blue/ vis-light crosslinking, LAP was used as the photoinitiator. LAP is a water-soluble photoinitiator with improved cytocompatability compared to Igacure 2959. LAP showed reduced solubility at low pHs, however, the presence of more than 30% functionalisation of the free lysine residues within collagen precursor could be attributed to a reduction in the isoelectric point, which reduces the ability of collagen to solubilise in neutral or high pH solutions (Liang et al., 2022). Instead it favoured acidic conditions. To allow for the repeatable solubilisation of the 4VBC-MA collagen precursor into solution and the use of LAP as a photoinitiator, the precursor material was solubilised in 10 mM HCl and this solution was neutralised prior to the addition of the PBS-LAP solution. This allowed for the production of an injectable precursor material that would only crosslink when exposed to 405 nm

light. This methodology allowed for reproducible hydrogels to be generated for all three conditions with similar morphologies (fig 3.3).

Although visibly similar in macrostructure, the properties of the three gels varied. As the degree of functionalisation of the 4VBC-MA and 1 MA scaffolds were similar, 33% and 31% respectively. The number of available places for crosslinks to occur should be similar within the network. This is because three different potential crosslinks may occur within the vis-light cured networks. Two homo-crosslinks of either 4VBC-4VBC or MA-MA and one hetero-crosslink of 4VBC-MA. It is expected that for the dual-functionalised gel a combination of these covalent crosslinks would be seen throughout the network. The similarities in the swelling ratios observed for both the 4VBC-MA and 1 MA gels suggests that the degree of crosslinking between the two gels is similar so they exhibit similar mechanical properties. Whereas, the significantly higher swelling ratio seen in the 0.3 MA gels and lower degree of functionalisation is indicative of a reduction in the number of covalent crosslinks present in the network and a more porous network.

SEM imaging of the hydrogels saw varying microstructures present, with heterogeneity observed in pore distribution, number and size across the scaffold. Previous crosslinking and fabrication methods for this hydrogel included a dehydration step in which the gel was submerged in increasing concentrations of ethanol. This dehydration step was required to remove water from the sample (Liang et al., 2022). However, this step could not be included in the fabrication process as it would not be able to be performed when directly delivered into the defect. The loss of this step, potentially has resulted in heterogeneity of porosity seen in the SEM images of the gel systems. Previously, sequential functionalisation gel synthesis methods produced hydrogels with a repetitive porous scaffold, however, cold-stage SEM imaging of all three gels showed that the scaffolds had areas where porosity could be seen and areas where there were no pores (Liang et al., 2022). 4VBC-MA scaffolds appeared to show the greatest amount of porosity compared to the 0.3 MA and 1 MA samples. This lack of porosity may have also affected cell survival within the scaffolds during the early stages of the encapsulation study. In which a lack of nutrient transfer through the gel due to the lack or reduction in pores in the 0.3 MA would have caused the higher levels of cell death seen. Furthermore, the increase in cell viability after day 7 could be attributed to cells within the scaffold beginning to remodel the material in the pericellular environment or moving through the scaffold. This would allow for the creation of more pores and improved fluid flow (Iordan et al., 2010). It has been suggested that cells are able to reorder the initial collagen matrix resulting in changes in the collagen density and allowing fluid flow through the network. Thus, it could be why an increase

in cell viability was seen on day 7 compared to day 4 as there could be remodelling of the matrix occurring. To assess changes to the collagen fibres further within the scaffold to study remodelling, depolarisation of polarised light could allow for imaging of the 3D fibres.

3.4.3 4VBC-MA collagen hydrogel was able to support cell viability for up to 7 days

The adapted methodology used here was able to successfully encapsulate cells throughout the hydrogel network and the viability of both ATDC-5s and Y201s was seen after 7 days. Furthermore, Calcein AM staining of the cells after 7 days shows rounded morphologies with no fibroblast-like behaviour, as seen in the 2D monolayer cultured cells. Encapsulation helped to maintain the morphology and the chondrogenic phenotype of cells, creating an actively favourable 3D microenvironment locally for the cells. Low viability of cells on day 1 seen at the bottom of the gel could be attributed to poor diffusion of nutrients through the scaffold when in the culture dish.

The heterogeneity in the microstructure of the different hydrogels may also relate to the variation in cell distribution throughout the scaffolds. The cell death present on the bottom of the scaffolds could be due to the scaffold adhering to the bottom of the plate and not allowing those cells to receive adequate nutrient transfer and waste removal. However, as previously discussed, the lack of porosity seen in the 0.3 MA hydrogels may also have resulted in poorer nutrient transfer throughout the gel.

3.4.4 Injectable hydrogels for osteochondral repair

A variety of methods have been employed for injectable hydrogel systems including chemical or physical crosslinking of hydrogels through ionic interactions, self assembly or click reactions (Olov et al., 2022). Photopolymerisation by vis-light curing has several benefits. Firstly, compared to materials that use chemical crosslinking through the combination of two solutions, it only requires one precursor material. Secondly, the crosslinking can be spatially and temporally controlled. Finally, it has fast curing rates with crosslinking occurring within minutes of exposure and also minimal production of heat during the curing process (Olov et al., 2022). One of the main challenges associated with photopolymerisation is the requirement for the crosslinking to occur at a biologically applicable pH, and for the photoinitiator selected to be water-soluble and non toxic. The 4VBC-MA collagen

type I hydrogel is able to overcome these challenges as the hydrogel precursor material is neutralised to pH 7.4 prior to use and LAP is also water soluble photoinitiator. Both of these features allowed for the 4VBC-MA collagen hydrogel to be stable for biological application and support cells within the scaffolds.

The use of a natural biomaterials such as collagen or chitosan for repair of cartilage and bone is more advantageous compared to synthetic materials because they show improved biocompatibility, biodegradation and mimic the ECM more successfully (Liu et al., 2017). Collagen is an attractive material as it is the most abundant mammalian protein in connective tissues and has been shown to be weakly antigenic (Liu et al., 2017). Collagen based injectable systems have been previously developed for tissue engineering (Chen et al., 2018, Funayama et al., 2008, Gao et al., 2018, Kontturi et al., 2014, Yuan et al., 2016). Collagen based materials have been shown to maintain chondrocyte morphology and promote the secretion of cartilage specific ECM. A variety of collagen types have been used including collagen type I, II and combinations have been successfully used as an injectable system (Funayama et al., 2008, Yuan et al., 2016). Furthermore, Funayama *et al.,* saw that 8 weeks post injection formation of favourable hyaline cartilage was seen in damaged rabbit tissue. Integration of collagen with other biomaterials, such as HA, have also presented with excellent cell proliferation, viability and morphology when encapsulated within the scaffold (Chen et al., 2018, Kontturi et al., 2014).

A study previously looking at encapsulated chondrocytes within a collagen based scaffold using photopolymerisation showed a reduction in chondrocytes within the scaffold over 14 days of incubation from 41 000 $\pm$ 4000 cells/mg to 22000 $\pm$ 8000 cells/mg, however an increase in GAG production was seen (Elisseeff et al., 2000). Furthermore, increases in both the equilibrium modulus and dynamic modulus of the material was observed after to 6 weeks, however this was still orders of magnitude less than cartilage tissue. This suggests that the chondrocytes within the scaffold had begun to deposit and remodel the matrix surrounding them through the secretion of proteoglycans and GAGs, even though a reduction in cell number was seen over time. The rounded morphology of cells within the 4VBC-MA collagen hydrogels suggests that the cells are maintaining a chondrocytic phenotype. Additional work to assess changes in mechanical properties of the hydrogel over time and also the protein expression/secretion of cells encapsulated within the 4VBC-MA hydrogels is important to understand the capabilities of the scaffold for osteochondral repair.

3.4.5 Limitations and future work

Due to time limitations, further assessments of the mechanical properties of the hydrogels and cellular behaviours were not able to be assessed. The main aims of the studies presented here were to develop a hydrogel as a potential therapeutic for OLTs and to create a platform for further investigation of the capabilities of the hydrogel.

Mechanical Characterisation of Hydrogel

Future work should be performed to assess more of the mechanical properties of the hydrogel that have changed as a result of changes to the gel preparation and processing. This would include performing rheological studies and assessing if the material is sheer thinning, as previously reported and also as this thought improve hydrogel performance for articular cartilage tissue engineering (Tronci et al., 2016, Zhou et al., 2022). Furthermore, rheological studies should also be performed on the cell-encapsulated scaffolds, as studies have shown that an increase in collagen stiffness can be attributed to an increase in cell density within the collagen hydrogels (Iordan et al., 2010). Thus mechanical properties of both the empty hydrogel scaffolds and the cell encapsulated scaffold need to be performed. Further imaging of the scaffolds could be performed using polarised light microscopy to look at the orientation of collagen fibres within the scaffolds.

Cell encapsulation and enzymatic inhibition

One of the major limitations of the work presented is the absence of a viability assay. Cells were assessed based on Calcein AM and ethidium homodimer staining of the gels showing live/dead cells. However, the viability of the gels could be further assessed using an assay such as Alamar blue or an ATP-based assay to assess cellular activity within the scaffolds.

Further studies should also be performed to assess the effect of the 4VBC-MA hydrogel on MMP activity, especially MMP-13 which is commonly seen within arthritic tissue. This should be done by assessing the ability of the gel to inhibit the activity of upregulated MMPs seen in the synovium of arthritic tissue. This encapsulation model also provides a platform for future work to study the behaviour of cells within the scaffold. This could be used to investigate the differentiation capabilities of MSC within the collagen network, or study the behaviour of encapsulated cells harvested from OA

donors to assess whether the presence of the 4VBC groups is able to reduce the activity of MMPs and promote a regenerative phenotype.

3.4.6 Conclusion

Due to its non-invasive nature and ability to fill irregular defects, injectable hydrogel systems are an attractive opportunity for the development of therapeutics. Commercially, the translation of injectable scaffolds are limited due to the production of harmful radicals, stability of the gel, controlling the spatiotemporal gelation and the cytotoxicity of the scaffold. The dual functionalised 4VBC-MA collagen type-I hydrogel presented in this chapter has addressed many of challenges facing injectable hydrogels for osteochondral repair. The photoinitiated injectable system was able to produce reproducible hydrogels that were able to cure at pH 7.4 and were able to support both chondrocytes and MSCs for up to 7 days. In addition the proposed scaffold system presents a drug-free method to improve regeneration of the tissue. The 4VBC-MA collagen type I hydrogel presented in this chapter was translated for mechanical testing within OLTs to assess the mechanical repair capabilities of the material.

Chapter 4

Methods to Assess Biomechanical Changes in the Porcine Tibiotalar Joint

4.1 Introduction

One of the main challenges associated with assessing the outcomes of current clinical treatments for OLTs is the paucity of primary literature, laboratory based *ex vivo* or cadaveric testing of the ankle joint. Current literature shows that many of the assessments used to measure the success of treatments are based solely on retrospective clinical studies or extrapolated data from other joints (Choi et al., 2009). This challenge was described in a pivotal retrospective clinical study in 2009, subsequently little progress has been made especially in establishing laboratory based methods to study the tibiotalar joint. Thus the development of a testing methodology or model which can reproducibly assess the effect of an OLT or repair method on tibiotalar joint behaviour and biomechanics is key to counteracting the lack of primary literature.

Thus, the primary aim of this study was to develop *ex vivo* testing methods within a suitable animal model to assess the biomechanical changes within the tibiotalar joint due to the introduction of an osteochondral lesion. These methods are to be translated to cadaveric tissue to evaluate the

biomechanical changes associated with current and novel treatments for OLTs.

In this study, two different methods were proposed to assess biomechanical changes seen within the tibiotalar joint as a result of the introduction of a defect to the talar dome. The first method focused on assessing changes to the joint contact mechanics: differences in the contact area and pressure. The second methodology identified tribological changes to the joint as a result of the introduction of an osteochondral defect to the talar dome.

4.2 Study Rationale

One of the main challenges associated with the development of a preclinical model for ankle OA is choosing an appropriately scaled, alternative joint that is able to mimic the ankle joint size and geometry, bone properties/skeletal maturity and cartilage thickness seen in an adult human ankle (Delco et al., 2017). A review on animal joint morphology highlighted the diversity of *in vivo* animal models currently used to study OA within the ankle joint. These include small animal models such as rodents or rabbits, which have been previously used for OA models in knee, and larger animal models including dog, sheep, goat, pig and horse. Larger animals have increased joint sizes and as a result have more similar bone properties compared to human bone. Most *ex vivo* studies existing in the literature that looked at the biomechanics of the natural joint utilised cadaveric joints (Choung and Christensen, 2002, Fansa et al., 2011, Hunt et al., 2012). Due to the challenging nature of the human ankle joint and its difficulty to find an appropriate animal tissue alternative for the joint, thorough complexity and constraints associated with morphology and curvature of the ankle joint. there is a lack of a standardised animal model for studying OA in the ankle. As this body of work focused on the development of methods for later studies, a porcine tibiotalar joint was selected to provided the tissue for testing including the development of fixtures, cementing and alignment of samples.

In general a porcine talus can be considered a good alternative to human talus. It is a readily available, cheap tissue that is comparable in geometry and size to human tali, however the curvature of the joint is much greater; with the talar dome and tibia forming a highly conforming joint. In addition, porcine ankles have been suggested to be an alternative model to train clinicians in arthroscopic treatments for the ankle (Mattos e Dinato et al., 2010).

Previous studies that have looked directly at changes to contact pressures and contact area in the natural ankle utilised either a pressure film or sensor placed in the joint space between the tibia and talus (Anderson et al., 1997, Choung and Christensen, 2002, Fansa et al., 2011, Hunt et al., 2012). In this chapter a similar methodology was adapted to perform static uniaxial compression testing to include different loading profiles to study if variations caused by the changes in loading angle due to the joint moving through the gait cycle might affect the compression or loading profile.

The studies presented within this chapter were intended to replicate a simplified gait cycle and the range of motion (ROM) of the tibiotalar joint needed to be considered. The studies presented below dissected all bones and soft tissue from ankle joint complex, except the distal tibia and talus. The tibiotalar joint was then constrained so that movement only occurred within the sagittal plane. Ankle motion is mainly maintained in the sagittal plane, where dorsiflexion and plantarflexion occur through movement in the tibiotalar joint. ROM within the sagittal plane of the tibiotalar joint has been reported to vary between 40 - 50° and 10 - 20° for plantar- and dorsiflexion, respectively (Brockett and Chapman, 2016). It has further been reported that within the sagittal plane there is a reduction in the ROM to 30° whilst walking (Brockett and Chapman, 2016, Nordin and Frankel, 2001). Therefore within the studies reported below the ROM selected test the tibiotalar joints were a total of 30° in dorsi- and plantarflexion to replicate a natural human gait.

The primary goal of the presented porcine study was to develop a method to identify whether changes in contact mechanics and frictional outputs could be ascertained using two different testing methods; in which comparisons were made between initially a 'healthy' or normal sample and a specimen containing a simulated defect. These models must be able to detect biomechanical changes in response to the introduction of a defect in comparison to a healthy specimen. The biomechanical properties that were assessed within this study were changes to local joint contact mechanics looking at contact area and pressure across the talar dome and changes to whole joint friction.

This was tested using:

1. Uniaxial compression testing of a porcine talocrural joint to assess contact area and pressure.
2. Friction testing of porcine joint to measure the coefficient of friction between the two articulating surfaces within the talocrural joint.

Successful methods will then be translated to cadaveric samples to assess the impact of OLTs

and treatment modalities on the mechanical properties of the tibiotalar joint.

4.3 Materials and Methods

4.3.1 Methodology rationale and equipment selection

For the studies presented in this chapter two different pieces of equipment were selected to perform the joint biomechanics tests. For uniaxial compression testing an Instron 3365/3366 (Instron, MA, USA) was selected to perform this work. To study the impact of friction on a whole joint model a ProSim Pendulum Friction Simulator (Simulator Solutions, Manchester, UK) was chosen. This technique has previously been used to assess the behaviour of the natural hip joint and also hemi cap treatment in the knee and ankle joint (Groves et al., 2017, McCann et al., 2008).

Uniaxial compression experimental set up and calibration

An Instron 3360 series dual column tabletop testing system was used to perform the compression tests. All tests performed within the subsequent studies used a 5kN load cell and a linear displacement rate of 2 $mm.min^{-1}$.

A TekScan 5033 pressure sensor (TekScan, MA, USA) was selected to assess changes in contact mechanics on the joint surface. This is an off-the-shelf pressure mapping sensor that has been designed to be used within the ankle joint. The sensors' matrix is 38.4 mm x 26.7 mm and comprises of 1472 sensels. The density of which is set at 144.1 sensels/ cm^2 or spatial resolution of 0.694 mm^2 per sensel, a maximum pressure of 25511 kPa and a resolution of 14 kPa. This sensor has previously been used in studies assessing the ability of hemicaps and OCA to repair ankle contact mechanics (Anderson et al., 2010, Fansa et al., 2011, Hunt et al., 2012).

Methods of calibration vary and are dependent on whether the assessments made will occur using static or dynamic testing as this can dictate the appropriate calibration techniques. A study by Brimacombe *et al.,* in 2009 assessed the best method of calibration using the two methods suggested by the manufacturer and found that polynomial calibration introduced low levels of error, especially when the range of data points are low. For this study, the three static loads were applied to the ankle and were grouped closely around points representing 80%, 105% and 107% body weight of a 60 kg

person so thus the values of load are close together (Anderson et al., 2007, Brimacombe et al., 2009). As a small range of loads were applied for this study, the two-point static polynomial calibration method was selected for the pressure sensor using 128 N and 512 N, following the manufactures recommendation. This represented 20% and 80% of the peak load intended for testing and is equivalent to 125 kPa and 499 kPa, respectively. These loads were applied to the sensor using polyurethane rectangles, cut to the same dimensions as the sensor, to ensure even loading across the sensor (fig. 4.1). Load was applied at a rate of 2 mm.min^{-1} and the peak load was held for30 seconds.

Figure 4.1: Calibration of 5033 TekScan Pressure Sensor
Labelled diagram of the calibration method used for the TekScan Pressure Sensor. Polytetrafluoroethylene (PTFE) tape was used to reduce incidence of sensel drop out during testing and thus was included during calibration.

During calibration of the sensor, sensitivity settings were adjusted to alter the saturation pressure set to correspond with the maximum pressure measured for the range of loads applied and was calculated through a calibration scale factor that was automatically generated through the software calibration process.

Pendulum Friction Simulator Experimental Set Up and Calibration

To assess changes seen to the joint frictional properties as a result of the introduction of a defect and for future repair studies, the ProSim Friction Simulator (Simulation Solutions, Stockport, UK) was chosen. This simulator is a single station pneumatically loaded machine controlled by a personal

computer (fig. 4.2).

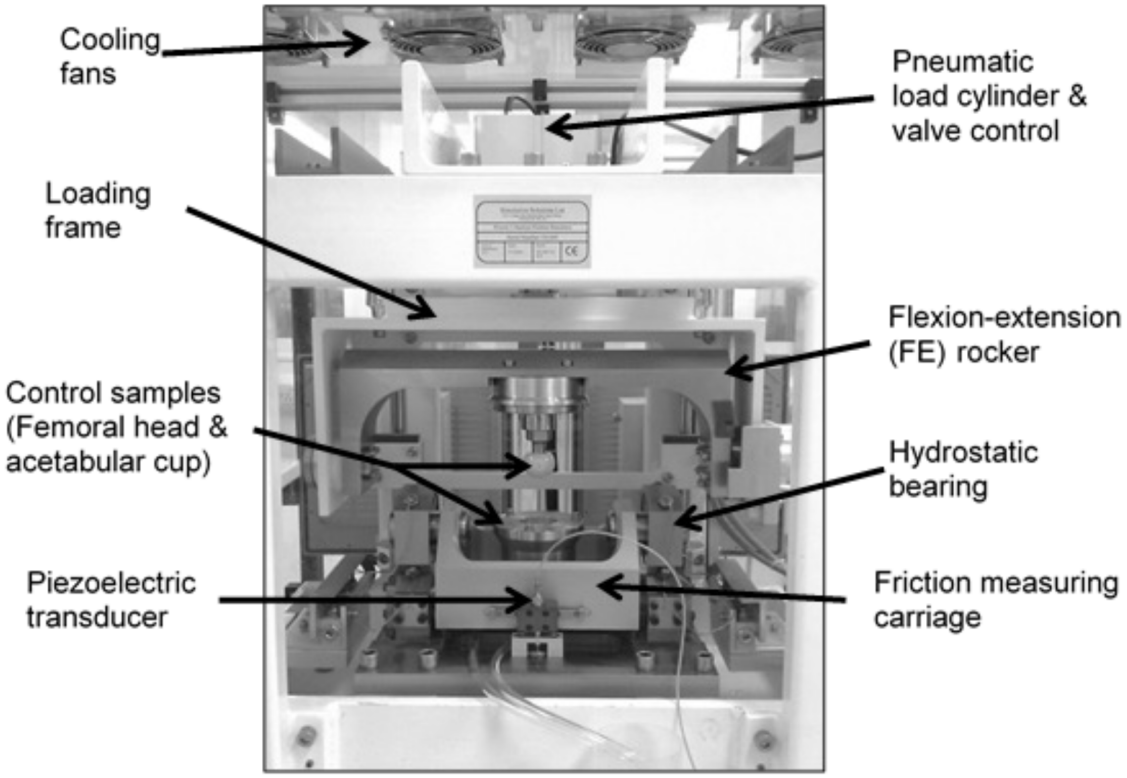

Figure 4.2: Pendulum Friction Simulator
Labelled diagram of the ProSim Pendulum Friction Simulator.

The simulator consists of a fixed frame with a motion arm housed in a loading frame. The motion arm provides flexion-extension through the rocker and also contains a self-aligning friction measuring carriage. This carriage is mounted on two externally pressurised hydrostatic oil bearings. The machine also contains a piezoelectric transducer at the front of the carriage. This acts as to determine the frictional torque in the system by measuring the changes between the forces transferred between the surrounding fixed frame and the carriage. Load and sweep/displacement is applied through the flexion-extension rocker arm. Custom designed fixtures were created to allow for an ankle to be tested within the pendulum friction simulator (Appendix A.1.1 and A.1.5). The tibial component was designed to be fixed to the motion arm. The talar fixture was designed to secure it self to the friction measuring carriage and is able to contain a lubricant bath for testing. The tibial and talar components were designed so that when the joint is in contact the centre of rotation of the joint is aligned with the centre of rotation of the simulator. These are shown in Appendix A-Pendulum Fricton Simulator Parts.

The simulator was calibrated, prior to the start of testing and repeated monthly, to ensure that the friciton measurements and outputs were reliable and that the load cell was calibrated.

Calibration of the frictional torque was performed using the automatic calibration feature present on the software. For calibration of the frictional torque, known weights were placed on to a loading arm which sits above the frictional carriage attached to a frictional torque calibration base (fig. 4.3). Frictional torque was measured for each weight and a calibration constant was calculated.

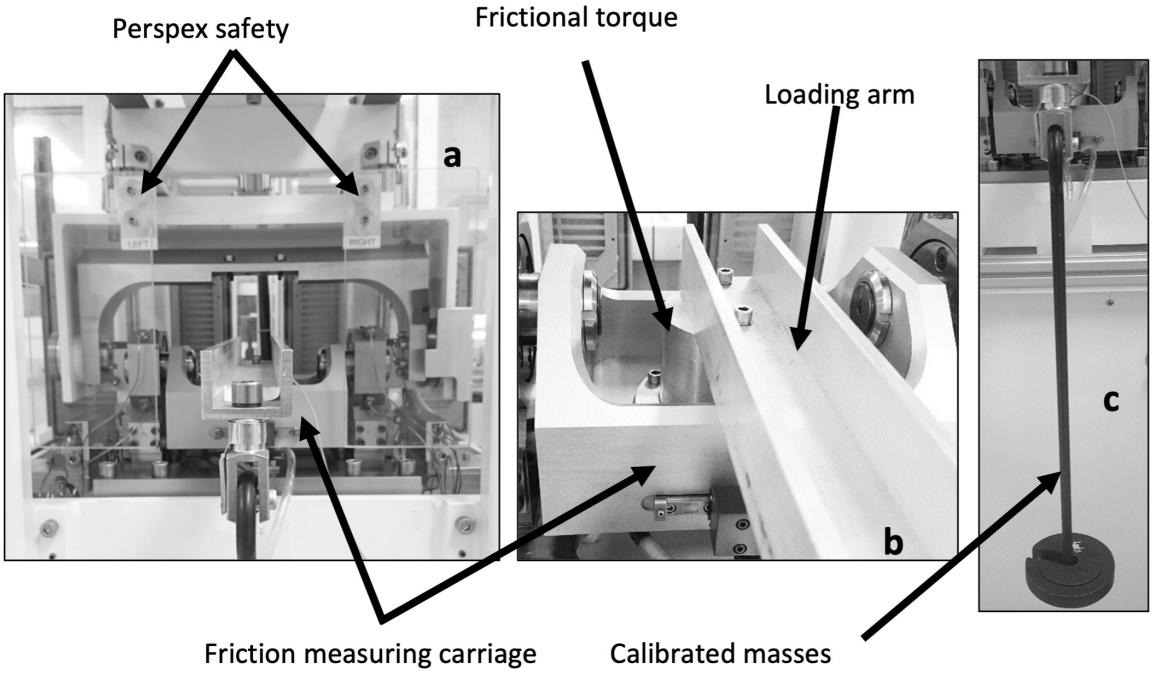

Figure 4.3: Friction calibration equipment and set up for the pendulum friction simulator

To ensure that the axial load recorded by the load cell in the simulator was correct, an external load cell was used along with the automatic calibration option present on the software. A secondary load cell was mounted to the flexion extension rocker arm and a delrin load calibration cylinder block was placed in the frictional measuring carriage (fig. 4.4). During the automated load cell calibration, the air pressure valve within the simulator opened to 5 different positions and pressure was applied through the load cell. The values between the two load cells, the simulator and external load cells, are compared within the program and a calibration constant is calculated to correct for difference between the simulator demand load and that seen on the external load cell.

Both these calibration values were inputted into the software and reproducibility of the simulator outputs was performed measuring the frictional coefficient and torque of a metal-on-poly and

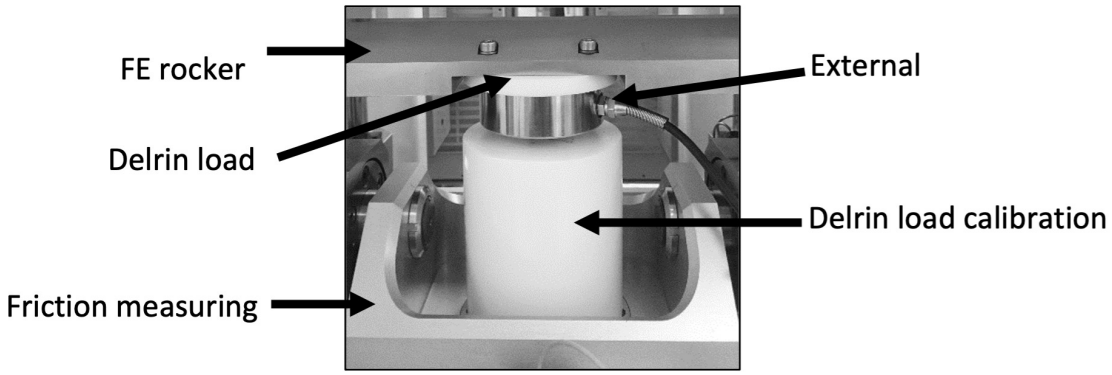

Figure 4.4: Pendulum Friction Simulator load cell calibration and equipment

ceramic-on-ceramic hip implant, acetabular cup and femoral head, based on local standard operating procedures (fig. 4.2). For each of these tests, the following conditions were used: water or 25% serum as lubricant, under 2 kN/300N loading conditions for 121 cycles at a frequency of 1 Hz.

4.3.2 Porcine tibiotalar joint

As outlines in section 5.2, there are differences in the geometry and morphology in human and porcine tissues. This difference was accounted for during the cementing process where the natural angle of the porcine ankle complex was taken into account to ensure that the articulating surface was fully exposed. For all testing presented in this chapter, fresh right hind legs from immature, six-month old pigs were procured from John Penny & Sons (Leeds, UK) within 48 hours of slaughter. During testing all samples underwent a maximum of 3 freeze thaw cycles and were thawed to room temperature prior to any testing. In addition, tissue was kept hydrated using phosphate buffered saline (PBS) during dissecting, cementing and testing.

4.3.3 Specimen Preparation

The ankle joint was harvested from the right hind leg of immature pigs. A scalpel was used to make an incision through the skin and surrounding musculature halfway between the knee and ankle joints. An oscillating bone saw was used to cut through the tibia and fibula separating the two joints. A secondary incision was made vertically along the dorsal region of the ankle to identify the joint capsule and a third incision was made mediolaterally to fully expose the capsule (fig. 4.5a & fig. 4.5b). All musculature, soft tissue and the fibula was then removed from around the tibia. A scalpel

was carefully inserted around the talus to separate the talaonavicular and the talocalcaneal joints. The joint capsule was pierced and all protecting tissue was removed to expose the tibiotalar joint (fig. 4.5c).

The talus was then further dissected with a mediolateral cut through the neck of the talus removing the head of the talus (fig. 4.6). This ensured correct alignment of the joint was obtained for cementing and that the articulating surface of the talar dome was fully exposed for testing.

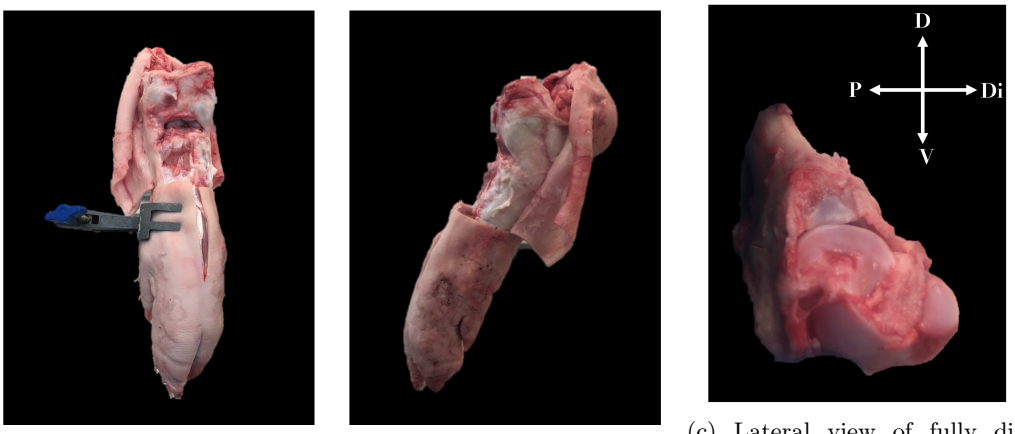

(a) Anterior view (b) Medial view (c) Lateral view of fully dissected tibiotalar joint

Figure 4.5: Dissection of porcine tibiotalar joint
Dissection and natural alignment of the porcine foot. (A) shows the anterior view of the foot with partial dissection exposing the tibiotalar joint. (B)Shows the medial view, removal of the skin from around the tibiotalar joint. (C) shows complete dissection of the tibiotalar joint with no soft tissue. D = Dorsal, Di = Distal, V = Ventral and P = Proximal.

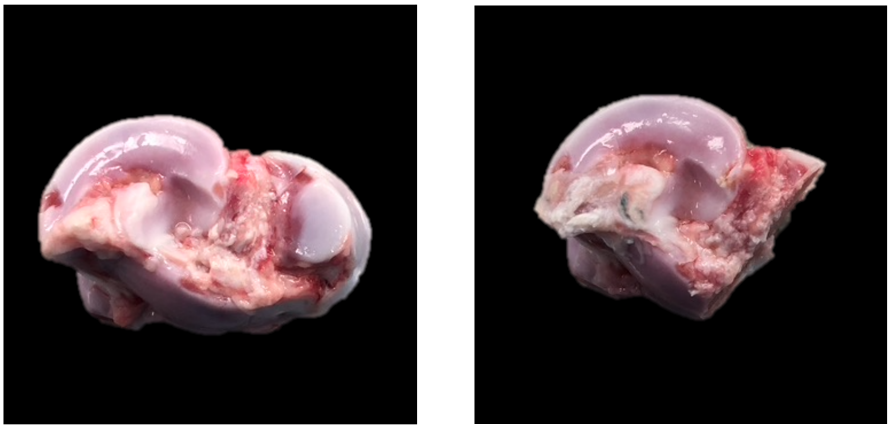

(a) Porcine talus (b) Dissected talus

Figure 4.6: Lateral view of dissected porcine talus
A) shows whole porcine talus. B) shows dissected porcine talus where the tissue has been resected across the neck

4.3.4 Cementing tissue samples

Custom designed fixtures were used for both testing methodologies discussed in this chapter to prepare and cement the tissue prior to testing.

Cementing for uniaxial compression testing

Figure 4.7 shows the fixtures used for uniaxial compression testing (Kwanyuang, 2016). These fixtures had been designed to be compatible with the Instron 3065a equipped using a 5 KN load cell (Instron, Buckinghamshire, UK).

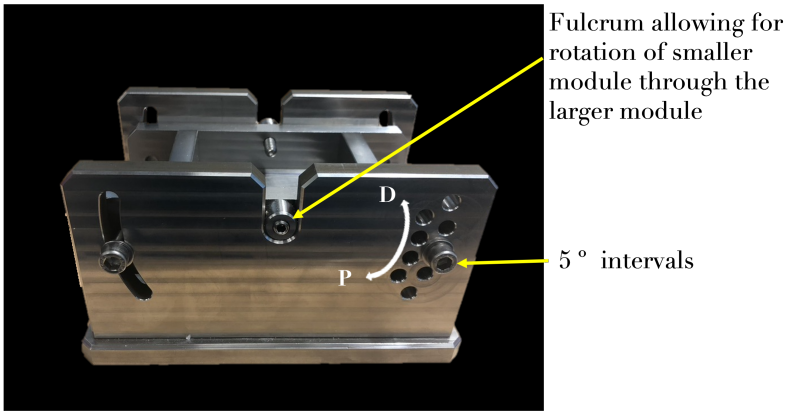

(a) Complete talar testing platform

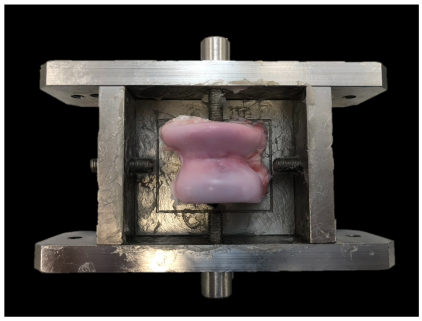

(b) Talar jig with dissected porcine talus

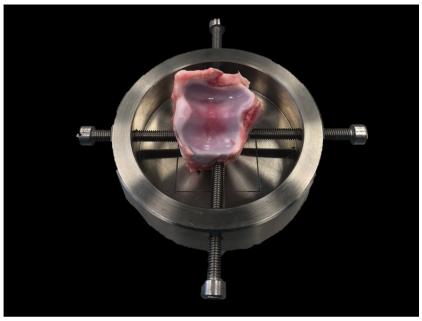

(c) Tibial jig with distal porcine tibia

Figure 4.7: Tibia and talar components for uniaxial compression testing
A) shows complete talar component including the larger module containing a fulcrum allowing for rotation of the central platform that contains the samples. B) Superior views of the central platform containing the dissected talus specimen. C) Superior view of the tibial jig containing the distal tibia. Both tissues were aligned in the centre of the fixtures using 4 screws located and cemented into the fixtures.

The dissected porcine tibia was placed into the tibial fixture and aligned as seen in fig. 4.7c. The tibial shaft was then held in place with screws before polymethylmethacrylate (PMMA) bone cement (Centri™ Base, WHW Plastics Lts, Hull, UK) was added at a 2:1 ratio to cement the sample.

The talus was placed into the talar fixture and aligned following the natural geometry of the joint against the tibia and held into place with four screws. Once aligned, as seen in fig. 4.7b, bone cement was added to the samples to hold it in place. This fixture allowed for the angle of the talus to be changed in 5° increments from 20° plantarflexion to 20° dorsiflexion. This angle was changed to adjust joint angle through dorsi- and plantarflexion to mimic the gait cycle during testing.

Further minor adjustments were made by eye to the fixture positioning of the samples once loaded onto the Instron to ensure the correct alignment for each sample was obtained. This was to account for any specimen variation seen within natural tissue.

Cementing for pendulum friction simulator testing

To ensure that the centre of rotation (COR) for the natural tibiotalar joint aligned with that of the simulator, a custom designed cementing jig and fixtures were created (Designed in collaboration with Dr Gregory Price; Appendix A). These fixtures allowed for the samples to be adjusted to the appropriate height and orientation for testing within the simulator and thus facilitated for natural tissue variation. Furthermore this reduced the risk of experimental artefacts caused by errors in potting and sample variations, such as size of the joint, as it ensured that the COR of tibiotalar joint was able to align correctly with the COR of the PFS. Alignment was checked using the simulator which had an alignment rod supplied by the manufacturers. The alignment rod is designed to slide into holes in the FE rocker base and the friction measuring carriage. When the COR of the sample and simulator are aligned the alignment rod is able to smoothly pass through the hole and smooth motion is observed through the FE motion arm.

The COR of the porcine ankle joint was identified by using a modified method previously used in the knee in which the condyles of the femur were matched to circular templates. (McCann et al., 2008). To identify the COR, an assumption was applied to the samples that the surface talar dome aligns within the circumference of a circle and that the COR lay in the centre of this circle. The diameter of each porcine talus was measured using vernier callipers across the widest part of the talar dome (fig. 4.8) and data for each sample is presented in table 4.1 and used to inform the cementing process.

A delrin cementing arc was set to the appropriate height the for identified centre of rotation and diameter of the talus. The tibial shaft was then cut so that the central ridge of the articulating

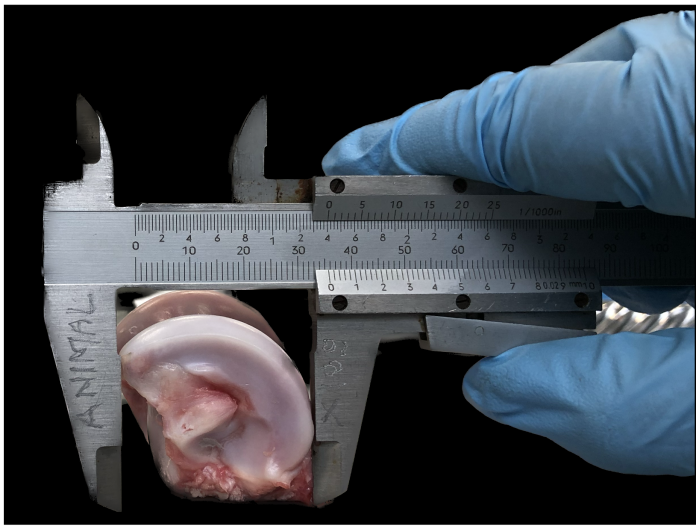

Figure 4.8: Methodology to measure talar diameter
Image shows method used to measure the diameter of a porcine talus.

Table 4.1: Porcine specimen talar dome diameter

Specimen	**Diameter of talus (mm)**
1	36
2	33
3	30
4	31
5	35

cartilage on the distal tibia was able to sit flush against the delrin pin (fig. 4.9). A 5mm hole was drilled into the base of the tibial shaft and a 15 mm delrin pin was placed into the side of the shaft. This was to provide the sample with extra stability during testing by providing added support and contact between the cement and tibial shaft. The tibia was then held by 3 screws within the custom pot. PMMA cement was added to the pot to secure the tibial shaft in place and this left to cure for at least 30 minutes.

The jig was then rearranged so that the cemented tibia was used to inform the positioning and cementing of the talus (fig.4.10). This ensured that alignment of the joint followed the natural geometry of the tissue. The talus was placed in a custom designed pot and screws were used to adjust the height and orientation of the talus so that it was sitting flush against the tibia and that the two articulating surfaces were in complete contact. PMMA cement was added to the talar pot to fix the talus specimen in place so the alignment could be maintained. PMMA bone cement was left to cure for at least 30 minutes to ensure that the sample was fixed.

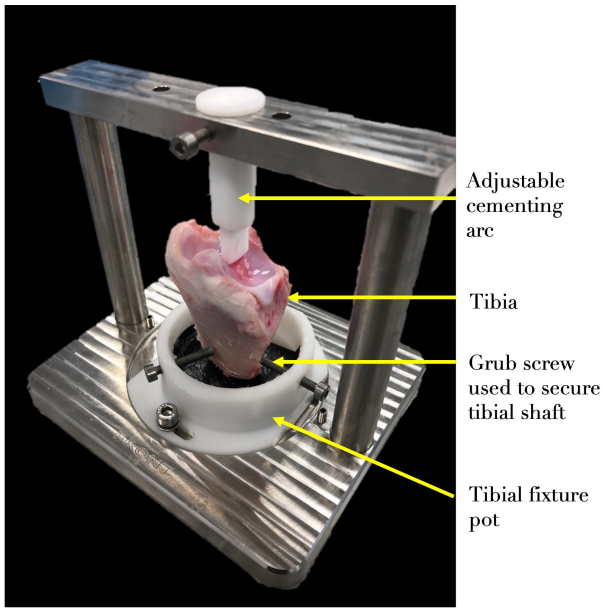

(a) Anterior view

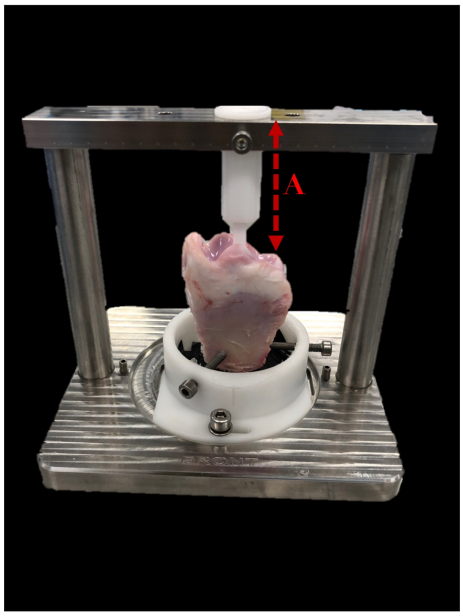

(b) Lateral view

Figure 4.9: Tibia cementing rig for the pendulum friction simulator
Anterior and lateral views of a portion of the distal porcine tibia showing the delrin pin placed flush against the central ridge of the articulating surface. Length A shows the identified height of the cementing arc referencing the height of the talar dome to ensure alignment of the centre of rotations.

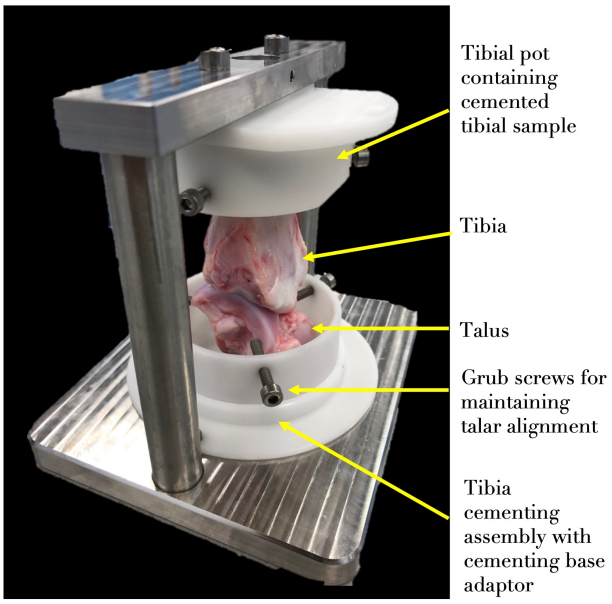

(a) Lateral view

(b) Posterior view

Figure 4.10: Talar cementing rig for the pendulum friction simulator
Lateral and posterior views of the cementing rig apparatus used to align and cement the talar dome with the tibia. Screws can be seen holding the talus flush against the tibia and that the two articulating surfaces are in contact.

4.3.5 Uniaxial Compression Testing

The potted samples were loaded into an Instron and set up as seen in figure 4.11. The cemented tibial specimen within the Instron fixture was attached to the 5kN load cell seen in figure 4.7. The talar testing platform containing the talar specimen was placed on the base plate of the Instron and was fixed with clamps.

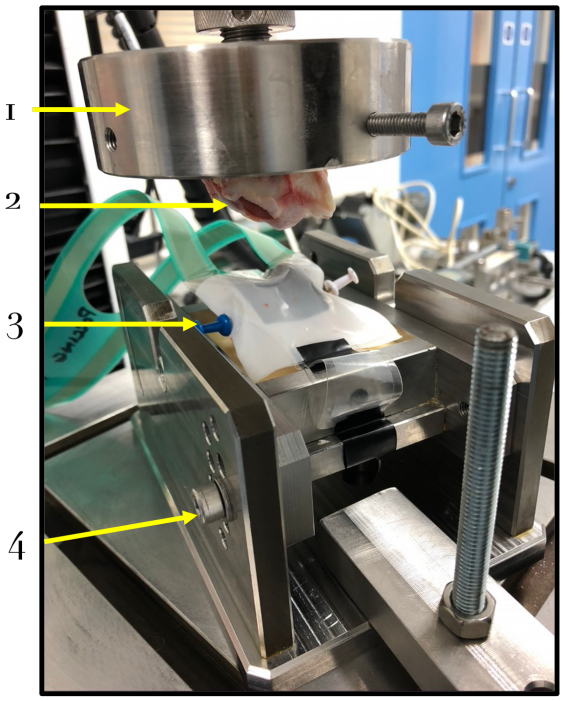

Figure 4.11: Set up for compression testing with natural joint samples
Labelled diagram of the set up for the natural joint within the Instron using the custom fixtures and the 5033 TekScan Pressure Sensor. 1 = Tibial component attached Instron arm to , 2 = Tibia, 3 = Sensor with PTFE tape, 4 = Talar component with adjustable platform angle.

The pressure sensor was wrapped in a poly tetrafluoroethylene (PTFE) film to minimise the risk and effects of sensel dropout caused by folding or damage to the sensor when load is applied. The taped sensor was place across the surface of the talar dome and was held in place with the additions of pins on to the medial and lateral faces of the talus and tape attaching it to the talar fixture. The calibrated sensor was then used to measure and record the contact area and pressure for each of the loading conditions as described below.

Loading conditions used to test the ankle mimicked that of a basic gait cycle, containing heel strike,midstance and toe off. Each ankle was initially loaded at 480 N and 0° flexion/extension (F/E), 630 N and - 15°/15° flexion (F) and 640 N and + 15 °/ 15° extension (E), simulating

midstance, heel strike and toe off, respectively. The change in the flexion and extension angles was achieved by titling the talar mount. Axial load applied for each stage was determined based on a previous study that calculated the vertical ground reaction force experienced by the ankle joint during gait cycle. They showed that this was equivalent to 107%, 80% and 105% of body weight during heel strike, midstance and toe off, respectively and using 600 N to represent the average body weight of a person (Anderson et al., 2010, Marasović et al., 2009). Compressive extension was applied at a rate of 2 $mm.min^{-1}$ until maximum load was applied. This was held for 2 minutes during which data was collected.

Data collection and analysis

Data was collected from the pressure mapping sensor using the I-scan ® Software. Pressure maps were collected during testing and recorded at a frame rate of 64 frames per second. Videos were collected as a movies and ASCII data files for further analysis. ASCII data frames were assessed using R Statistical Programme (Version 4.2.2), in which the final data frame was selected for further analysis to assess contact pressure and area at peak load. Contact area was measured by counting all sensels on the matrix that presented with a pressure greater than 0 and was converted to an area based on the known dimensions of the pressure sensor and number of sensels provided by the manufacturer of 1025 mm^2 and 1472 sensels. Contact areas and pressures were then compared between the different conditions using a paired t- test. Further regional analysis was performed by dividing the sensor into four areas representing the anterior-lateral (AL), anterior-medial (AM), posterior-lateral (PL) and posterior-medial (PM) regions of the talus (fig. 4.12). Each region was representative of 368 sensels and an area of 256 mm^2.

Statistical analysis was performed using R (Version 4.2.2). Normality of data was assessed using a Shapiro-Wilk test and either a paired T-test or Wilcoxon signed rank test was performed to compare differences in data. When p-value of less than 0.05 was considered to be significantly different.

4.3.6 Measurements of Friction

Ex vivo tests were performed on natural porcine tibiotalar joints (n=5). The pendulum friction simulator was used to apply a dynamic axial force during a cycle to simulate a simplified gait cycle and mimic the swing and stance phase through a single sinusoidal loading profile (fig. 4.13). The

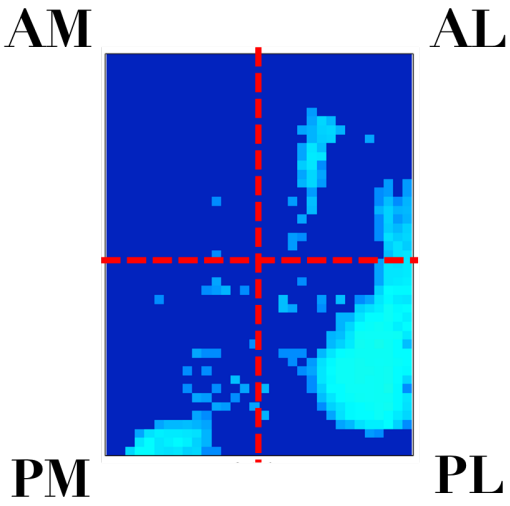

Figure 4.12: Tekscan data showing the division of the sensor map into 4 distinct regions representing different areas of the talar dome.
The four areas represent the anterior-lateral (AL), anterior-medial (AM), posterior-lateral (PL) and posterior-medial (PM) regions of the talus. .

stance phase was represented by a higher axial force and the swing phase was represented by the lower force present at the start and end of each cycle. This was performed by using a 50 N load during swing phase and a maximum peak load of 640 N during stance phase; the same as the peak load applied for the uniaxial compression testing (fig. 4.13a).Movement of the motor arm controlled the flexion-extension applied during a cycle and was limited to $\pm$ 15° (fig. 4.13b). This allowed for a physiological motion arc to be tested within reduced risk of bone impingement caused by anatomical differences.

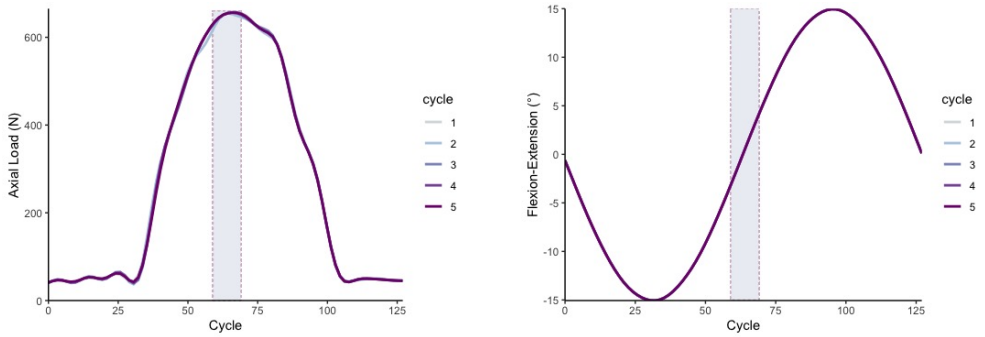

(a) Loading Profile (b) Motion Profile

Figure 4.13: Loading and motion profiles for 5 cycles used for porcine testing
Shaded areas represent the regions of high load and velocity used for obtaining frictional outputs including the coefficient of friction.

Samples were loaded in to the friction simulator as seen in figure 4.14. Tests ran for 3600 cycles at

1 Hz, equivalent to 1 hour of simulated walking. Friction was measured using a piezoelectric sensor which measured the frictional torque between the contacting articulating surfaces of the distal tibia and the talar dome.

Pre- and post-test, a 121 cycle or 2 minute test under constant load test was performed at 640 N and ± 15° FE. The outputs of this was used to calculate the frictional offset. This accounted for any additional frictional torque that had arisen during testing due to misalignment of the joint or incidental movement of the carriage (Lizhang et al., 2013). This maybe caused by the non-uniform shape or asymmetrical geometry of natural tissue resulting in movement of the carriage in the medial-lateral direction. The pre- and post tests allow for normalisation of the data to account for additional torque introduced into the system by off-centre loading of aspherical samples, as seen within the natural talar joint.

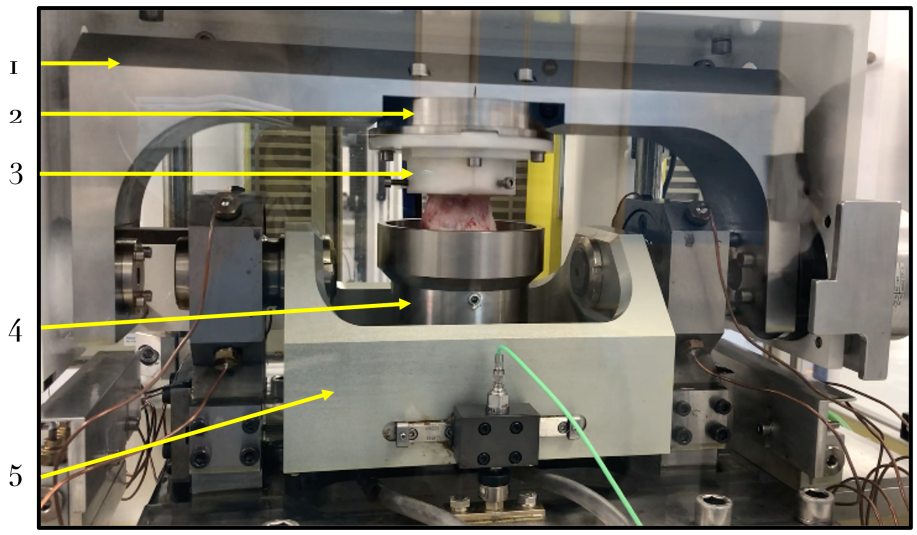

Figure 4.14: Porcine natural joint set up in the pendulum friction simulator
Labelled diagram of the ProSim Pendulum Friction Simulator with a porcine tibiotalar joint. 1 = Flexion-extension (FE) rocker arm, 2 = Tibia fixture attached to the FE rocker, 3 = Porcine tibia in test pot, 4 = Talar test pot containing cemented porcine talus and PBS bath, 5 = Friction measuring carriage containing the piezoelectric transducer.

Data Analysis

Frictional outputs were measured during the stance phase where maximum load and velocity was applied to the joint (fig. 4.13). These values were used to calculate the dynamic frictional factor (f) using the following equations:

$$f_{\mathrm{d}} = \frac{T}{r \times W} \tag{4.1}$$

In which, T represents the true torque magnitude detected by the transducer, and r is the radius of the articulating or bearing surface. For each cycle, the mean friction factor was calculated at the peak load and high velocity phase. The frictional offset was calculated using the data obtained from the 121 cycle pre- and post- tests using Eq.4.2. Where the mean frictional offset (f_o) was calculated by using the data obtained from the post test data (f_b) and the pretest data (f_a).

$$f_{\mathrm{o}} = \frac{f_{\mathrm{b}} + f_{\mathrm{a}}}{2} \tag{4.2}$$

For each sample, the data obtained was normalised against the frictional offset using Eq.4.3. This was done by subtracting the frictional offset from the dynamic friction factor providing a normalised dynamic profile for each condition.

$$f_{\mathrm{n}} = f_{\mathrm{d}} - f_{\mathrm{o}} \tag{4.3}$$

Mean friction factor values or coefficient of friction values, and standard deviation (SD) during the tests were calculated and Shapiro-Wilk test was used to assess normality of data and Wilcoxon signed rank test or paired T-test was used to compare the friction factor of the conditions against the cycle number using R-software. When p-value of less than 0.05 was considered to be significantly different.

4.3.7 Defect Modelling

After initial compression or friction tests were performed on the complete natural tibiotalar joint first to simulate a healthy condition, defects were created on the posterior-lateral region of the porcine talar dome. The lateral side of the talar dome was selected for the defect site as the curvature of the trochlea is shallower and thus there was increased surface area available to create a better and more uniform defect site. The osteochondral defect was introduced using a pillar drill with a 5 mm drill bit to create a defect to the depth of 5 mm (fig. 4.15). The tissue was then allowed recover in

PBS for one hour before repeating the compression or friction testing as described above.

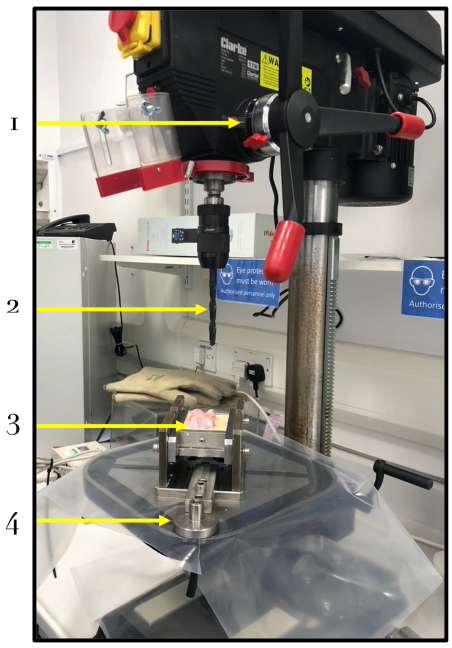

Figure 4.15: Pillar Drill Set Up for Defect Creation
Image shows set up for the pillar drill to create defects on the porcine talus. 1) Depth adjustment. 2) 5 mm drill bit. 3) Talar fixture containing cemented tissue. 4) Clamps holding talar fixture to the base plate of the drill.

.

4.3.8 Angular velocity sensitivity test

A sensitivity test was performed to assess if angular velocity and resultant outputs were able to be maintained when the flexion and extension or arc of movement on the friction simulator was reduced; mainly to assess if a reduction in arc length and an increase in frequency would result in the same frictional torque outputs.

This study was performed to allow for samples to be tested with a reduced flexion extension motion to prevent dislocation of the joint during testing due to the lack of constraints present; normally provided by the soft tissues and fibular found in the natural ankle joint.

When measuring the frictional torque to calculate the coefficient of friction during a single cycle of the simulator, values were taken from the point at which the velocity is the greatest. This was identified by the steepest part of the graph. This velocity, or the angular velocity, may be calculated using the following equations:

$$Angular\,velocity = \frac{\Delta\, radians}{\Delta\, s} \tag{4.4}$$

$$Angular\,velocity = \frac{\Delta\, degrees \times \pi}{180 \times \Delta\, s} \tag{4.5}$$

A 28 mm, metal-on-polyethylene hip implant (metal femoral head and polyethylene acetabular cup) (Depuy Synthes, UK) was used to assess the frictional output of the simulator whilst adjusting the frequency of the swing. A metal-on-polyethylene implant was selected as it is the control sample used to verify the calibration results as it has a well defined friction coefficient.

Tests were run using 25% serum solution as the lubricant with the following loading and motion conditions of 121 cycles. A single sinusoidal dynamic loading range of 300 N to 2000 N was applied through the femoral head. FE motion and the frequency of swing was varied for each test using the values seen in table 4.2.

Table 4.2: Flexion and extension and frequency conditions used for sensitivity test

± **Flexion Extension Angle (°)**	**Frequency (Hz)**
10	1
9	1.1
8	1.25
7	1 .43
6	1.67
5	2

Frictional torques was calculated for the forward and reverse conditions for 5 cycles for each set of 30 cycles. The friction coefficient was calculated from the mean of these torque values using equation 4.1.

4.4 Results

4.4.1 Uniaxial compression testing

Max pressure, mean pressure and contact area across the talar dome for both the healthy and defects samples is presented in figure 4.16 and figure 4.17. For the healthy sample, the maximum contact pressure observed ranged from 0.66 MPa to 4.28 MPa. The largest mean contact pressure was

observed at 630 N 15° F loading condition with a mean ± standard deviation (SD) of 3.01 ± 1.05 MPa, representing heel strike. This condition also corresponds with lowest average contact area of 255 ± 156 mm^2.

The lowest peak pressure was seen at 480 N 0° FE, representing midstance, where the average max contact pressure was 1.95 ± 0.97 MPa. The mean average pressure across the talus was 0.21 ± 0.14, 0.19 ± 0.09 and 0.22 ± 0.09 for 630 N 15° F, 480 N 0° F/E, and 640 N 15 ° E, respectively.

Compression maps showed changes in contact mechanics as a result of the introduction of a 5 mm circular osteochondral defect to the surface for all 5 porcine joints with all loading conditions (fig. 4.16). Introduction of a 5 mm lateral defect caused changes to the average contact pressure, contact area and max pressures experienced within the tibiotalar joint. These changes can be seen in the contact pressure maps where a general trend shows an increase in contact area as a result of the introduction of a defect (fig. 4.16 & fig. 4.17c). However, these changes were not significant (p = 0.81, 0.86 and 0.95 for 630 N 15° F, 480 N 0° F/E, and 640 N 15° E, respectively; paired t-test).

The increase in contact area across the tibiotalar joint after the introduction of a lateral defect also corresponded with a decrease in max pressure for all three conditions. A significant change in max pressure was measured at 630 N 15° F, where an average reduction was seen from 3.01 ± 1.05 MPa to 1.33 ± 0.12 MPa representing a 56 % reduction in max contact pressure (p = 0.013) (fig. 4.17a). Although a change in contact area was measured no significant changes could be seen in the overall contact area or pressure of the ankle joints ($p > 0.05$; paired t-test). A significant change could be seen in mean contact pressure between samples at 630 N 15 F ($p = 0.049$).

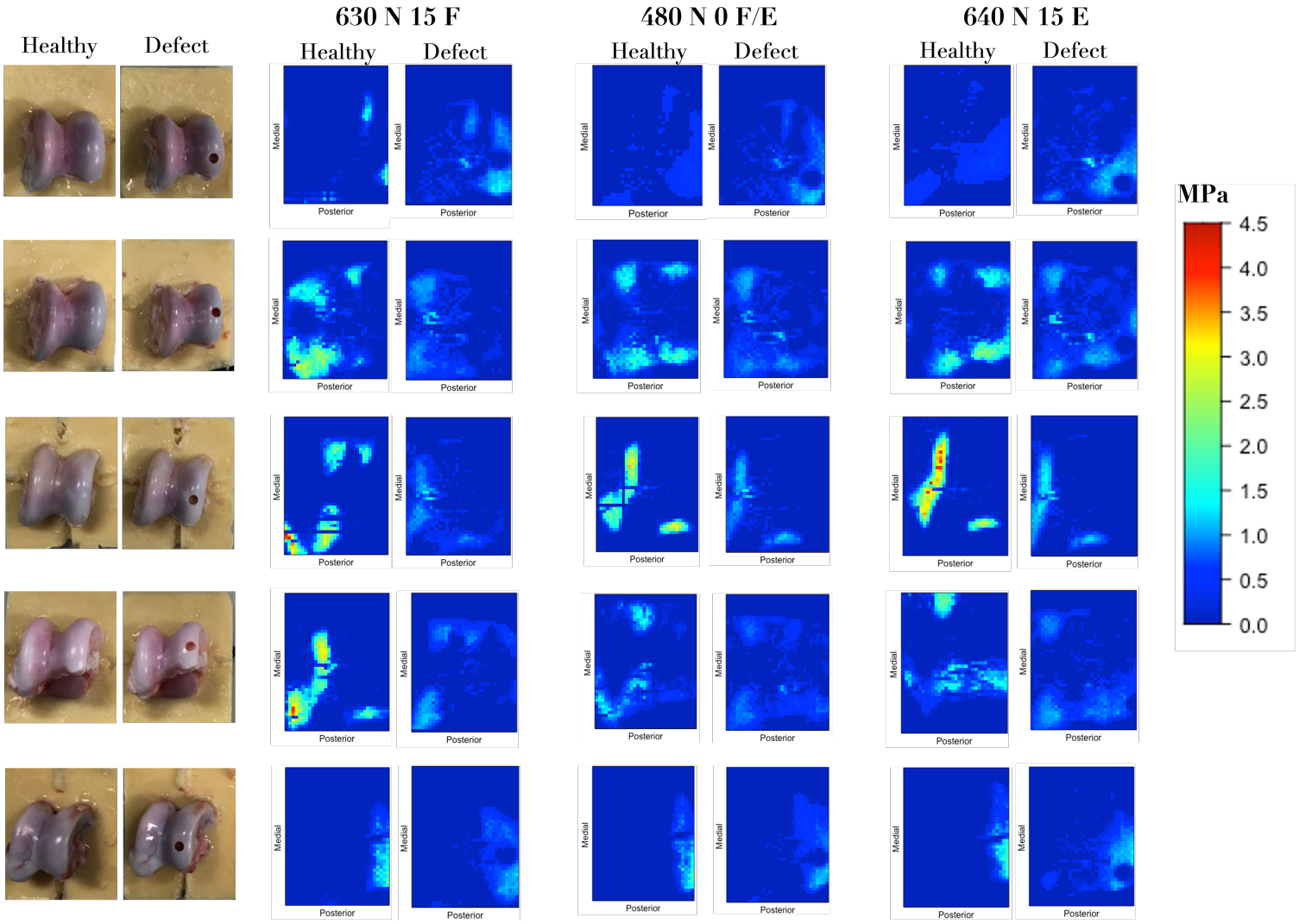

Figure 4.16: Compression maps showing contact area for each loading condition for healthy and simulated defects
Left images shows healthy and simulated osteochondral defect samples. Compression maps show loading across the TekScan pressure sensor for each condition with and without defect. Unresponsive sensels can be seen in some samples, where sensors were damaged or bent during testing.

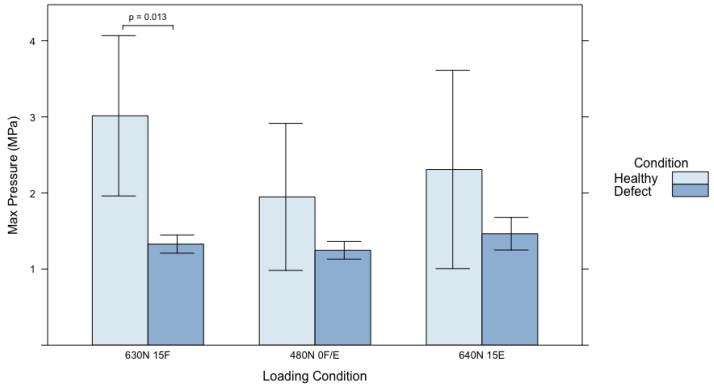

(a) Max contact pressure

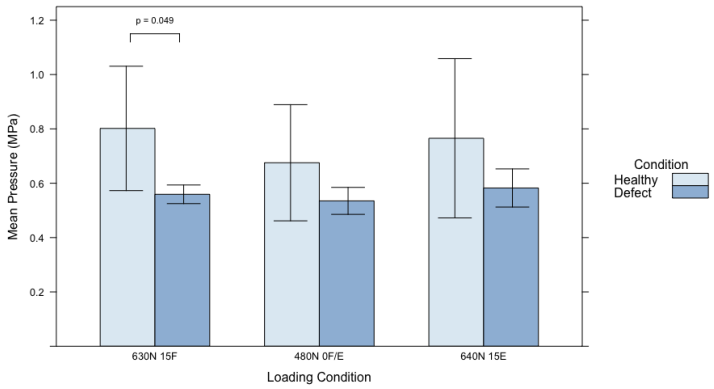

(b) Mean contact pressure

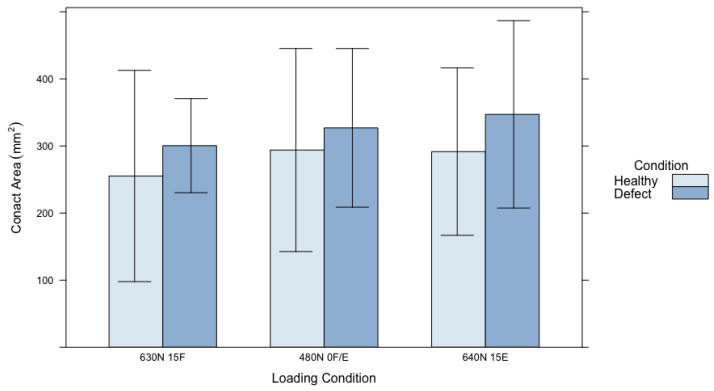

(c) Mean contact area

Figure 4.17: Whole porcine joint contact mechanics data for healthy and defect conditions for simplified gait cycles showing standard deviation bars (n= 5)
(A) Mean max contact pressure represented the mean value of max pressure seen across all 5 samples for each loading condition in MPa, (B) mean pressure measured across the entire sensor in MPa for all 5 samples and (C) mean contact area (mm^2)

Regional Changes

Analysis of changes in contact mechanics across the four regions of the tibiotalar joint showed similar trends to that seen across the whole joint. Results of the regional analysis showed a reduction in the average max pressure across all four regions for each loading condition. However only significant changes in max pressure were seen for the 630 N 15° F ($p < 0.05$; paired t-test, fig. 4.18a).

Regional analysis of average contact area showed that the introduction of a defect caused an increase in the mean contact area across the samples, values are provided in table below 4.3.

Table 4.3: Regional changes in contact area across the porcine talar dome for healthy and defect conditions for the simplified walking gait cycle

Loading condition	**Region**	**Healthy**	**Defect**
		Contact area (mm^2) ± SD	**Contact area (mm^2) ± SD**
630 N 15° F	AM	45.8 ± 49.5	54.5 ± 48.8
	AL	44.6 ± 26.8	45.2 ± 33.7
	PM	103.4 ± 82.9	109.9 ± 78.5
	PL	61.5 ± 38.4	90.9 ± 53.0
480 N 0° F/E	AM	52.5 ± 51.8	52.5 ± 49.7
	AL	47.9 ± 28.8	48.9 ± 35.0
	PM	97.0 ± 77.8	106.3 ± 73.4
	PL	97.0 ± 31.6	119.4 ± 54.9
640 N 15° E	AM	52.4 ± 47.2	58.8 ± 47.0
	AL	45.8 ± 41.1	36.9 ± 35.2
	PM	86.2 ± 54.5	115.6 ± 50.5
	PL	107.1 ± 45.6	135.9 ± 63.2

Although an increase was seen for all regions after the introduction of a defect, the contact area across the anterior regions were similar in both the healthy and defect conditions. Furthermore, the greatest increase in contact area was seen in the posterior lateral region, where the defect was situated (fig. 4.18a).

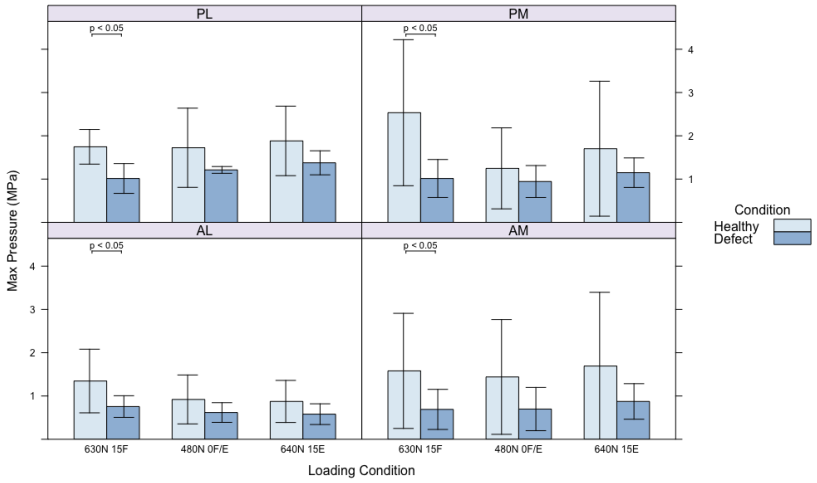

(a) Max regional contact pressure

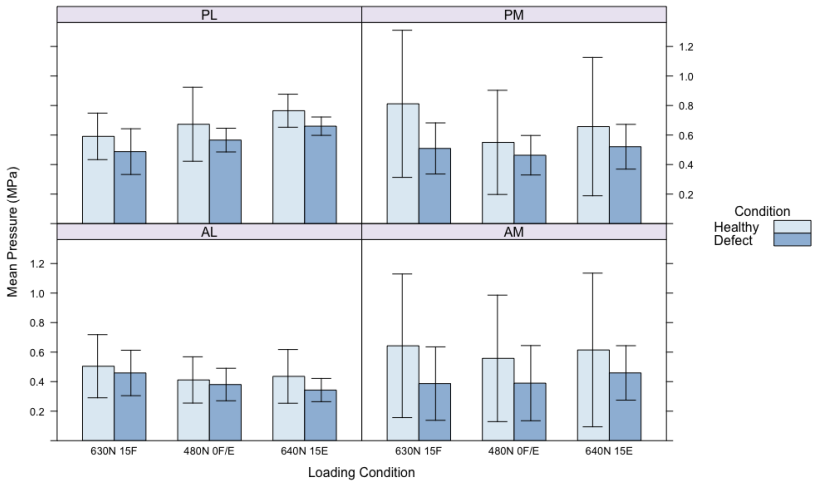

(b) Mean regional contact pressure

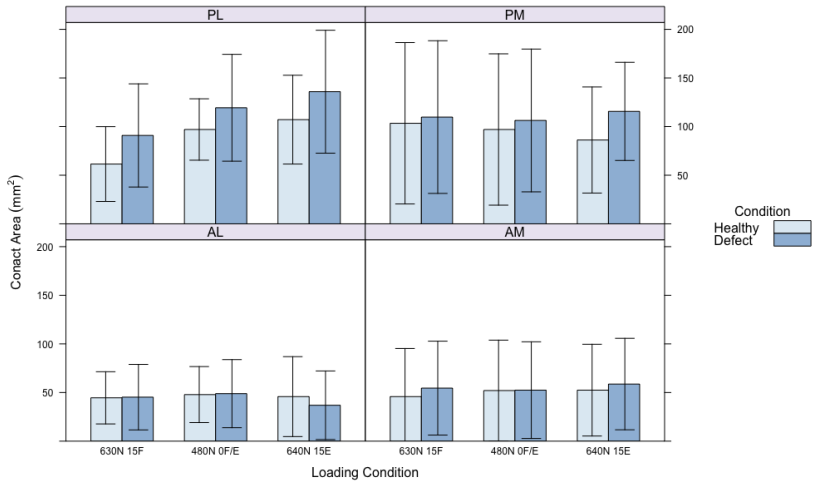

(c) Mean regional contact area

Figure 4.18: Average regional contact mechanics across the four areas of the porcine talar dome before and after the introduction of a OLT in the posterior lateral region of the talar dome for a simplified gait cycle (n= 5) with standard deviation bars. (A) Mean max contact pressure across the different loading condition in MPa, (B) mean pressure measured across the sensor in MPa and (C) mean contact area (mm^2) AL= Anterior Lateral, AM = Anterior Medial, PL= Posterior Lateral and PM = Posterior Medial,

4.4.2 Friction testing

Coefficient of friction was calculated for each condition, healthy and defect, during the 1 hour test and normalised using the pre and post test data. The results of this are shown in figure 4.19a. No significant difference was seen between the mean friction factor for both the healthy and 5 mm defected samples with mean friction factors of 0.153 ± 0.065 Defect = 0.152 ± 0.046, respectively ($p = 0.06$).

During friction testing the coefficient of friction for the healthy sample remained at a constant at 0.151 ± 0.067 for the first 1200 cycles and 0.154 ± 0.064 for cycles 1201 - 3600. However after the introduction of a 5 mm defect the mean friction factor started at a higher value of 0.157 ± 0.046 for cycles 1 - 1200 and then reduced to 0.149 ± 0.046 for cycles 1200 - 3600.

The introduction of a 5 mm defect did not cause consistent changes to the coefficient of friction across all samples. Figure 4.19b show the sample specific mean friction factor during testing for both the healthy and 5 mm defect condition. It can be seen that for 2 samples; specimen 1 and 4, the mean friction factor increased after the introduction of a defect. For specimen 2 and 3 a decrease in the mean friction factor was seen and for specimen 5 the mean friction factor remained the same for both conditions.

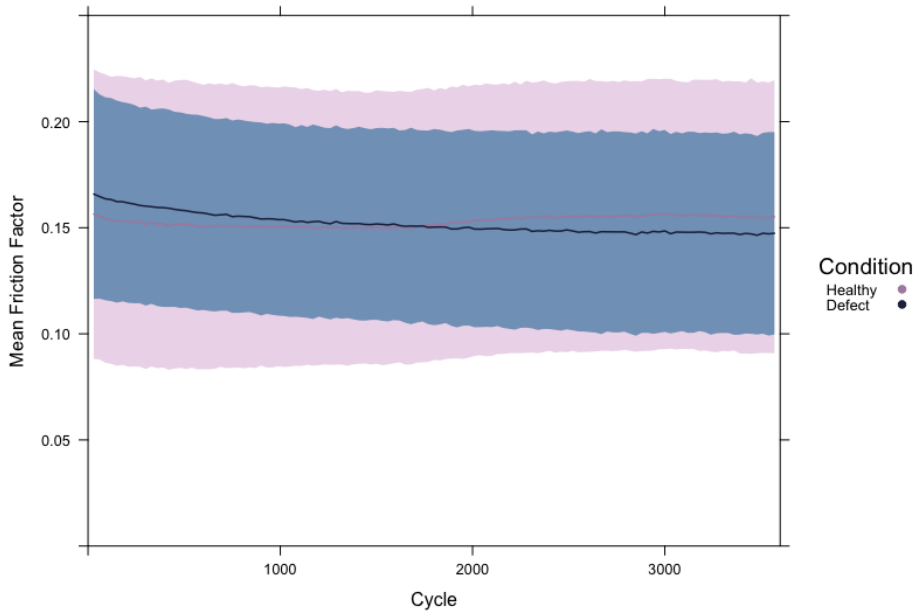

(a) Average friction factor

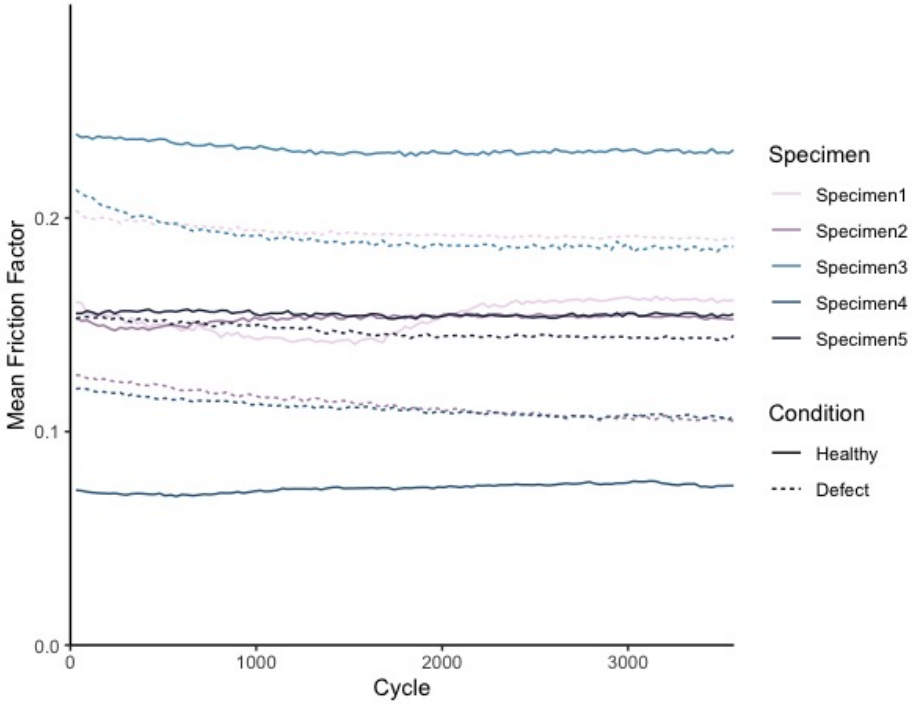

(b) Sample specific friction factor

Figure 4.19: Mean friction factor for healthy and defect natural tibiotalar joint tested on the pendulum friction simulator for 1 hour using a dynamic loading profile.
A shows the mean friction factor ± the standard deviation across the samples for the healthy and defect conditions. Graphs B shows the sample specific mean friction factors for both the healthy and defect complete natural porcine tibiotalar joint (n=5).

4.4.3 Angular velocity sensitivity tests

Natural variation can be seen within the tali specimens tested in this study, including the size and the morphology of the sample, it was important to consider how testing protocols could be adjusted to minimise the effects of this variation on the data generated. As frictional output is dependent on equation 4.1, reducing the arc length and increasing the frequency of the swing should maintain the same friction coefficient. Thus the aim of this study was to assess whether changes to the frequency or the arc effected the calculated friction coefficient for a known sample and to ensure that the machine was able to obtain the desired arc length or motor position.

The results of motor position and the output friction factors are seen in figure 4.20. During the sensitivity tests the machine was able to maintain the desired motor position in both the forward and reverse direction (fig. 4.20a and fig. 4.20b). Furthermore, figure 4.20 shows the motion of the FE rocker and the load during testing. It can be seen that at the higher frequency and with the reduced motion of the FE rocker arm, the loading profile remains the same throughout testing for all conditions.

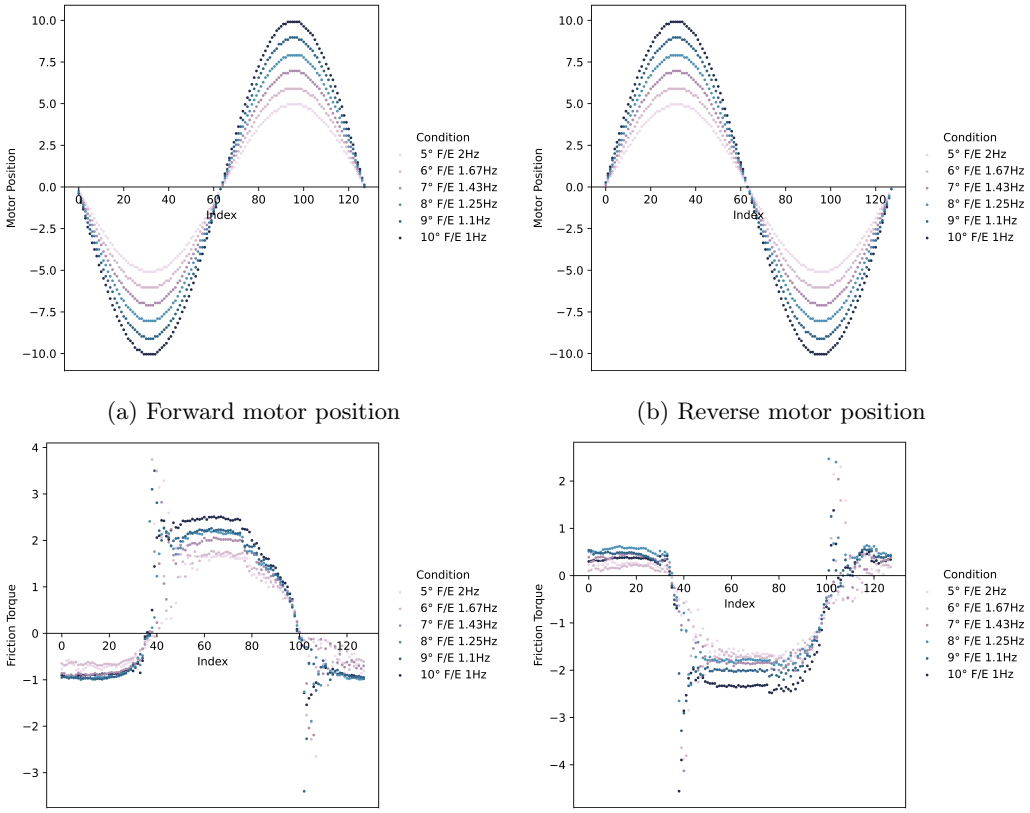

(a) Forward motor position

(b) Reverse motor position

(c) Forward frictional torque

(d) Reverse frictional torque

Figure 4.20: Effects of changes in frequency and range of motion on the forward and reverse coefficients of frictions using the pendulum friction simulator during one cycle.
A and B shows the forward and reverse motor position to show the reduction in arc length or flexion extension angle of the motion of arm of the simulator. C and D show the forward and reverse frictional torque measured by the simulator during a cycle for each condition.

Table 4.4: Flexion and extension and frequency conditions used for sensitivity test

Flexion Extension Angle (°)	**Frequency (Hz)**	**Average Frictional Torque**	**Mean Friction Coefficient**
10	1	2.38	0.084
9	1.1	2.11	0.074
8	1.25	1.98	0.069
7	1.43	1.83	0.064
6	1.67	1.77	0.061
5	2	1.58	0.054

For the metal-on-polyethylene hip implant tested, a 0.076 value for the friction coefficient had previously been obtained for calibration of the simulator. Results of the sensitivity test showed that as the frequency of the swing increased, the obtained coefficient of friction decreased between 1 and 2 Hz (fig. 4.21a). However, variations in the coefficient of friction obtained and the higher coefficient

of friction seen at 1 Hz then expected value of 0.084 could be caused by use of 25% serum as the lubricant, due to batch variation seen in serum. Further analysis of the obtained average coefficient of friction during the test was performed. The acquired coefficient of friction remained constant throughout the test within the frequencies of 1-1.43 Hz (fig. 4.21b). Above which greater variation can be seen during the test for the samples. Thus, it was possible to assume that up to a limit of 1.43 Hz the measured friction is considered representative to ensure consistent measurements are obtained. This range was then carried forward to future studies included here.

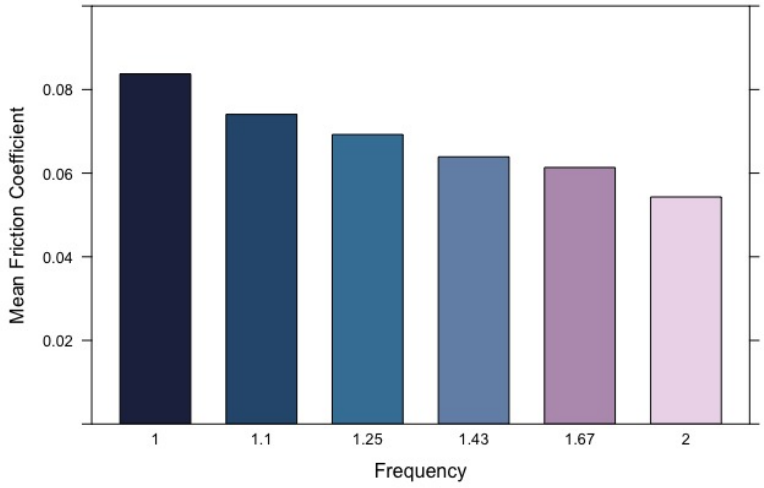

(a) Mean friction coefficient compared to frequency

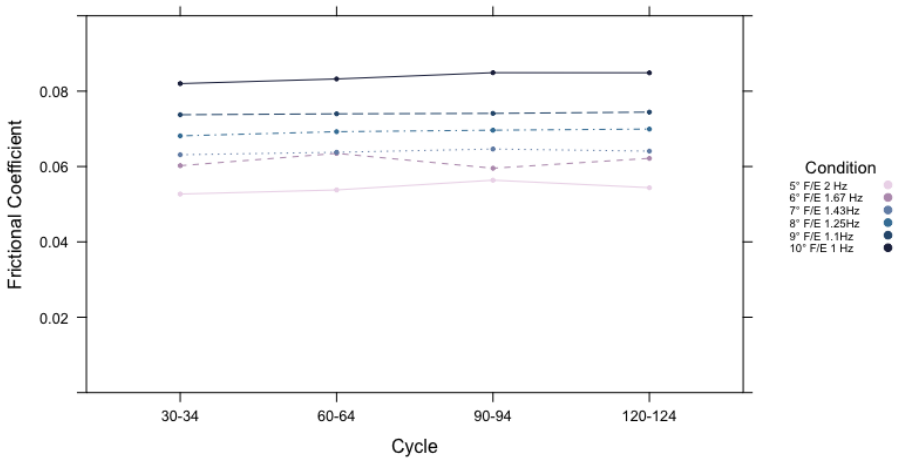

(b) Mean friction coefficient during test

Figure 4.21: Obtained mean coefficient of friction measured at each frequency for both the forward and reverse conditions

4.5 Discussion

The aim of this study was to develop two methodologies to assess the changes in the biomechanical and tribological performance of cartilage as a result of the introduction of an OLT using a porcine talar joint. Both methods investigated here were able to measure local joint biomechanics before and after the introduction of an OLT on the talar dome. Changes to local contact area and pressures were seen after the introduction of a defect. However, no changes were seen in the coefficient of friction after the introduction of a defect. Both methods were able to show differences in contact mechanics and frictional properties between the natural 'healthy' porcine tissue and after the introduction of a simulated defect. The outcomes of these studies were to optimise and develop the methodologies to inform future work on the biomechanical characterisation of OLTs, including the studies presented in Chapter 5 and 6. The results and limitations for both studies are further discussed below.

4.5.1 Selection and challenges of porcine ankle model

The use of animals in foot and ankle research is sparse. Findings related to basic science in small animal models are limited especially as healing process in the foot and ankle are not analogous. Research in the ankle is often translated from work performed in knees, which include vascularity, soft tissues and also differing local factors pertaining to biology of joint. Often rats are a popular model to study the tibiotalar joint but morphologically differ in shape and size (Gadomski et al., 2022).

One of the main challenges associated with the studies presented here was the use of a porcine tibiotalar joint for testing. The main aim of these studies was to develop robust methods to assess changes to the biomechanics of the tibiotalar joint as a result of the presence of an OLT. Natural porcine tissue is a common model that has been adopted for research in the hip and knee (Groves et al., 2017, Liu et al., 2019, Lizhang et al., 2013). The bone density of porcine tissue is similar to that seen within human bone and it is cheap and readily available tissue (Aerssens et al., 1998, Christensen et al., 2018, Mattos e Dinato et al., 2010). Furthermore, the porcine talus is of similar size, morphology and, bone and cartilage properties to that of human tissue, but it is not identical. Current alternative joints available include ovine, caprine, rabbit and rodent. Generally a caprine model would be the best model for assessing a human ankle joint as goats have been seen to have the most translatable or comparable ankle joint complexes to that of humans with regards to the

general joint morphology including the orientation and direction of the joint (Kok et al., 2013, van Bergen et al., 2013). However, tissue availability made this a non viable option for testing.

Previous literature has shown that porcine models can be used as an *ex vivo* model that for human tissue in particular with regards to joint size, bone structure and cartilage structure. Key differences between a human tibiotalar joint a porcine tibiotalar joint can be attributed to the natural porcine gait. Firstly the morphology of the tibiotalar joint is different between humans and pigs. The porcine ankle has a greater degree of curvature and is more conforming than the human ankle joint. This is demonstrated by how the tibial surface curves tightly against the talar dome (fig. 4.5).

This geometry is reflected within the morphology of the porcine trochlea, which shows a greater degree of curvature compared to the human tali. This level of curvature results in the talar dome having a smaller radius compared with the shallower human tali. Further morphological differences can be seen within the depth of the trochlea groove and the resultant widths of both the medial and lateral trochlea. Due to width of each trochlea, a 5 mm defect could only be successfully introduced in the centrolateral region of talar dome. Clinically, incidents of medial defects are more common compared with lateral defects. However the width of the medial ridge on the porcine trochlea was too small to introduce a 5 mm defect on the surface. For future cadaveric studies a medial defect will be used to represent a more clinically relevant model.

Further challenges associated with the geometry of the natural porcine joint included the joint angle and the range of motion (ROM) observed. The natural porcine joint has a neutral sagittal tibiotalar angle (STTA) of around 150 °, whereas the average human STTA is around 112 ° (Mirkiani et al., 2022). This variation in STTA was accounted for by dissecting the neck of the talus and ensuring the natural alignment of the joint was preserved for testing (fig. 4.6b). The ROM during gait cycle for the internal value of the tibiotalar joint in pigs has been show to be within the range of $25.1 \pm 3.1^{\circ}$ during walking gait and $44.5 \pm 2.5^{\circ}$ for running gait This was assessed by studying the internal angle between the tibia and talus using markers to measure changes in the ROM during gait at different speeds (Mirkiani et al., 2022). In addition, porcine ankles display a greater plantarflexion angle compared with the human tibiotalar joint (Mattos e Dinato et al., 2010). The values for dorsi- and plantarflexion selected for this study reflected the range of motion experienced within a human gait rather than that documented for a porcine ankle. The increased range of flexion and extension angles tested within this study may have introduced abnormal loading within the joint. Thus causing additional torque which may have resulted in the higher coefficient of frictions obtained compared

to other whole joint friction studies (Groves et al., 2017, Kuganenderan, 2018). However, there have never been friction studies looking at a complete tibiotalar joint.

4.5.2 Uniaxial compression testing

Uniaxial compression testing of a porcine tibiotalar joint in both healthy and defect conditions showed visible changes in contact area and max pressure across the whole talus. General trends across the ankle showed that the introduction of a 5 mm defect to the talar dome caused a decrease in the max and mean contact pressure seen for all three alignments and an increase in contact area (fig. 4.17). This may be caused by a compensatory mechanism hypothesised within the natural ankle joint as a method to redistribute load across the talar dome after damage (Shepherd and Seedhom, 1999). In which the additional compressive load is redistributed across a wider area therefore decreasing local contact pressures, but increasing in contact area. Although the data trended in this direction the lack of significance differences between the two conditions may be attributed to the compensatory mechanisms and also related to the variation seen between tissues.

Regional analysis of the samples showed similar trends across all the regions of the talar dome; with significant changes in max pressure for all four regions of the talus for the 630 N 15 ° F, which represented heel strike (fig 4.18a). However, even though a decrease in mean and max pressure was seen across all four regions, it was observed that contact area remained similar in the anterior regions of the talar dome between the healthy and defect samples for all loading conditions. For all samples a 5 mm osteochondral defect was created in the flattest region of the talar dome, which tended to be located in the centrolateral or posterior lateral region of the talar dome (fig. 4.16).

For all loading conditions the posterior lateral region (PL) showed the greatest increase in contact area after the introduction of defect; suggesting that the introduction of a defect could cause the contact pressure to disperse into the surrounding tissue without creating a point of increased stress. This behaviour may potentially be attributed to the low incidence levels of early or small OLTs being discovered, as the defect site is not subject to increased contact pressure and therefore, further degradation of tissue does not occur. Minimising the risk of subchondral bone cysts forming. This is attributed to physical discomfort a patient feels in later stage ankle OA as pressure builds in the underlying bone.

A key limitation within the study was the size of the simulated OLT. This may have played a

role in the lack of frictional changes and the absence of significant changes to contact pressure or area after its introduction. Within the literature, small lesions are often asymptomatic, with many patients not showing any clinical presentation of an OLT. For this study the simulated OLT tested had an area of 19.6 mm^2. This is much smaller than that previously tested in the literature of 6 mm diameter (Hunt et al., 2012). The size of defect created within the porcine model was limited due to the curvature of the porcine talus, to ensure that a uniform defect size was created for each sample using the aforementioned technique. Furthermore, Hunt *et al.,* showed that for smaller defects ($>$ 10 mm) there was less of effect on local contact stresses around the rim of the defect. The ability of the talus to produce compensatory loading and the use of a smaller defect for this model may be why significant differences were not observed between the sample for both testing methods. For future cadaveric work defect sizes $\geq$ 10 mm in diameter will be chosen for further testing. Clinically poorer patient reported outcomes have been seen for lesions greater than 10 mm in diameter (Guo et al., 2010, Hannon et al., 2012). Furthermore, the work by Hunt *et al.,* highlights that mechanical changes can be observed within defects greater then 10 mm, therefore would be the appropriate size for further investigation.

4.5.3 Pendulum friction simulator testing

Assessment of friction within the natural ankle joint and OLTs was performed using a pendulum friction simulator. The methodology developed was able to measure differences in the friction coefficient could be seen between the two conditions and changes in the frictional properties over the duration of the test. Although, no significant differences in the coefficient of friction was seen between the two conditions, a p-value of 0.06 indicated that the data may be approaching significance. The lack of significance could be attributed to the small sample size used for the test, thus a bigger sample size may highlight more of a relationship. For both conditions, the values for the coefficient of friction obtained were higher than the range previously reported in the literature for *in vitro* cartilage-on-cartilage tribological studies of 0.003 to 0.08 (Groves et al., 2017).

The higher coefficient of friction, could be attributed to the shape and morphology of the tissue, with the ROM used for the FE rocker being greater than that normally experienced in a porcine talus. This study utilised a simplified human gait cycle and tested the intended methodology on porcine tissue, resulting in a clinically relevant range of motion being tested. However, as previously described, this is a greater ROM that seen in porcine gait (Mirkiani et al., 2022), thus the ankle does

not normally undergo such a degree of flexion and extension. This one axis of motion and constraint of the tissue, does not directly mimic the kinematics normally seen within the ankle joint including medial/lateral rotation. During testing rotation of the joint could be seen within the simulator as it went through an exaggerated gait cycle. This additional rotation caused by the higher ROM tested could have introduced abnormal loading or torque into the system resulting in the increased coefficient of friction seen within the samples.

The biphasic behaviour of cartilage plays crucial role in its ability to bear load and to control friction properties. It has been shown that different lubricants will affect the ability for cartilage to provide effective boundary lubrication. In particular, a study showed that synovial fluid reduced the coefficient of friction for cartilage compared with solutions like Ringer's as it was able to provide effective boundary lubrication (Forster and Fisher, 1996). Previous studies using the PFS have utilised 25% foetal calf serum in saline. PBS was selected as the lubricant for this study as it is common, physiologically relevant lubricant present within laboratory settings that is used to hydrate the tissue, it can be used with cadaveric tissue samples, and shows less variation then serum. It has also been previously used as an alternative lubricant for friction studies. PBS, however, has been shown to increase the coefficient of friction obtained for bovine cartilage samples tested using pin on plate testing, with PBS showing a significant increase in coefficient of friction compared to synovial fluid (Schmidt and Sah, 2007). The higher coefficient of friction seen for both samples may be caused by the use of PBS as a lubricant during testing.

Although PBS has shown to increase the coefficient of friction and is a poorer natural lubricant compared to synovial fluid, it is a more reproducible method which reduces impact of variation in properties seen in serum. PBS will be used as a lubricant for the pendulum friction simulator testing in chapters 5 and 6 as it is better for translation to cadaveric samples as there is reduced risks of contamination and to minimise risks associated with using animal derived lubricants with cadaveric samples. Furthermore, PBS is used to hydrate the tissue for compression testing being performed. To maximise future cadaveric studies, the samples will undergo sequential compression and tribological testing, thus ensuring that the method of lubrication in both tests are the same.

4.5.4 Conclusion

The methods described in these studies were able to measure differences in the biomechanics and biotribology of the natural porcine tibiotalar joint with and without an osteochondral defect. Overall changes to joint contact mechanics were able to be assessed and differences in pressure and contact area could be identified after the introduction of a defect on the talar dome. Although not significant, changes in joint friction were able to be assessed and the values obtained were within that previously observed for cartilage-on-cartilage studies. Furthermore, additional modifications to the flexion-extension arc and the frequency of the proposed methodology can be applied to account for morphological variation seen in tissue. The testing parameters outlines in this study were able to be translated for subsequent testing using cadaveric tissue samples.

Chapter 5

The Effect of Chondral Defects and Current Treatments on Natural Joint Biomechanics

5.1 Introduction

OLTs are a common occurrence and often arise after a traumatic incident, such as an acute ankle sprain, ligament injury or a fracture. Due to the high loads experienced in the ankle and small articulating surface area, OLTs can be unstable and this can cause symptoms within the ankle such as persistent pain, impaired function and also a reduction in activity. Due to the nature of the talus and cartilage being a relatively avascular, aneural tissue, it shows reduced repair and the formation of fibrotic scar tissue within the defect site. A conservative approach is normally successful in younger patients or for lower classification of defects: Berndt and Harty type I and type II defects (table 1.2). However, for more severe pathologies surgical approaches have shown improved outcomes (Hurley et al., 2021, O'loughlin et al., 2010). Nevertheless, a systematic review in 2017 observed that in 52 studies assessing treatments of primary OLTs, no superior treatment was identified between the approaches taken (Dahmen et al., 2018).

One of the main challenges with many of these techniques, is that they have been translated

from other joints, such as the hip and knee, and not directly tested in the ankle joint. However, it has been shown the cartilage properties within the ankle joint vary significantly compared with the hip and knee joint (Athanasiou et al., 1995). As discussed in chapter 1, these differences include the uniformity of cartilage thickness across the surface of the talar dome and the high level of conformity between the tissues on the articulating surfaces (Shepherd and Seedhom, 1999). Furthermore, there is a lack of models available to test treatments within the ankle joint, specifically assessing both contact mechanics and tribological performance of repairs within the ankle joint due to the challenges attributed to joint morphology as discussed in Chapter 4 (Delco et al., 2017).

5.1.1 Study rationale

The work presented in this chapter builds upon the two methods developed and optimised in the previous chapters and translates the techniques developed from porcine to cadaveric tissues. During translation of the methods, the approach was amended to model current clinical practise better and to also allow for a more reproducible methodology. Expert advice was provided by Mr Mark Farndon, a consultant foot and ankle surgeon.

The rationale for modification and adaptions of the previous methodology will be presented below.

Defect selection

For the experimental studies carried out in the subsequent bodies of work, chondral defects were selected as the method to study instead of osteochondral defects. A chondral defect is a defect for which the subchondral bone under the cartilage remains fully intact and is usually indicative of an early lesion (table 1.2). For most matrix based treatments, adequate subchondral bone stock is required when attempting to treat a lesion with AMIC, MACI or microfracture treatments. Acquiring adequate bone stock to be able to successfully fill the lesion for testing is challenging due to the availability of cadaveric material of appropriate quality. Furthermore, as the material developed is aimed as a potential AMIC treatment it would generally be used as a primary treatment for small-mid sized lesions in which adequate subchondral bone is present. Generally, within the literature, studies including talar OCLs encompasses both chondral and osteochondral defects within their reports. This is because clinically OCLs include both early lesions which include only articular cartilage (Hepple

classification stage) and also a cartilage defect with underlying bone damage (Hepple classification stage 2) (table 1.4).

10 mm diameter defects were selected for testing within these studies. A 10 mm defect has a smaller area than that of the critical defect size derived by Choi et al., of 78.5 mm^2 and 150 mm^2, respectively, for which improved healing was seen for treatments like microfracture (Choi et al., 2009). A study by Hunt *et al.,* showed that there is a threshold of 10 mm for the defect size after which, changes to local peak stresses could be seen close to the rim of the defect (Hunt et al., 2012). They hypothesised that poorer success rates and higher clinical failure seen for defects above this size regardless of location may be attributed to these changes in pressure. Therefore, to minimise the impact of this and to accurately assess situations where biomaterials or hydrogels are an appropriate alternative treatment, 10 mm was selected as an appropriate defect size.

Microfracture versus nanofracture and AMIC

Multiple techniques exists in which BMS used in conjunction with AMIC treatments. Generally BMS have been commonly performed as a method to manage OLTs. AMIC is a single surgical approach in which BMS is performed on the debrided tissue and a membrane is placed into the defect. This matrix, usually collagen type I/III, is a used to help retain the clot and the arising bone marrow derived MSCs in the defect site (Migliorini et al., 2022b). This membrane also acts to protect the clot from the articular environment and shear forces that can occur. AMIC is becoming a more interesting technique as it is a one-stage procedure that has been shown to provide improved regeneration of the cartilage due its ability to maintain the recruitment of MSCs to the defect site (Waltenspül et al., 2023). As described previously, it has been shown to have good midterm clinical success in the midterm but revision for AMIC procedures have been reportedly required for up to 58% of cases (Gottschalk et al., 2017, Waltenspül et al., 2023).

Different techniques exist to perform BMS, one of the most common being microfracture. The main limitations with microfracture is the access that the awl requires to the subchondral bone and the damage it causes to the subchondral plate due to compaction of the bone around the defect site (Steadman et al., 1997). This is thought to be what causes the formation of fibrocartilage often seen with this technique (Zedde et al., 2016).

Nanofracture provides a good alternative as it uses a needle/pin that is thinner and shorter than

the awl used for microfracture. These cause less destruction to the bone plate and this hopefully promoting the migration of MSCs in to the defect site (Benthien and Behrens, 2013, Chen et al., 2009). An ovine study has shown that after 6-months nanofracture treatment allowed for improved restoration of the normal subchondral bone architecture compared to microfracture. It also showed improved perforation into the subchondral bone, reduced trabecular fragmentation and compaction compared to microfracture, providing a better and improved treatment (Zedde et al., 2016). Furthermore, a microCT study comparing microfracture, nanofracture and fine wire drilling showed that increased permeation of contrast agent into the surrounding trabecular bone was seen for nanofractured samples, further supporting that nanofracture treatment reduced damage to surrounding trabecular tissue (Warren et al., 2022). Thus, nanofracture, was selected instead of microfracture for use in this study to provide the basis for the AMIC treatment used.

Modifications to friction testing methodology

As previously described, human tibiotalar joints differ in morphology compared to porcine tibiotalar tissue; in particular, the increased congruency and more 'ball and socket' like morphology observed in porcine ankles. Therefore the previously developed methodology needed to be further adapted and optimised to be successfully translated to cadaveric tissue.

Due to constraints relating to tissue availability, the samples tested within this chapter utilised only the tibia and the talar bones. Therefore, it was important to consider joint stability when translating the methodology as all supporting soft tissue and the fibula were not provided and, as discussed in section 1.2.1, these are integral for joint stability during gait. The result of the angular velocity sensitivity tests for the pendulum friction simulator was used to inform the later testing performed in human tissue. Based on the results of the sensitivity tests, it was deemed that the simulator was able to measure the frictional outputs between 1 - 1.43 Hz and a total motion arc of 20°- 14 ° , respectively. This accommodates for variation seen in the different sizes of cadaveric samples tested and the lack of supporting tissue structure including soft tissues and the fibula, minimising the risk of dislocation of the joint during testing. In particular, the lack of the fibula in the tests increased the risk of dislocation or ankle instability as the distal end of the fibula is integral in ensuring the stability of the ankle joint complex especially during inversion and eversion, which could not be constrained during testing (Uchiyama et al., 2006). Thus, the total length of the motion arc would not be greater then 20° within the range of ± 15° of flexion or extension.

In addition, due to simplification of the model and the removal of additional supporting structures, the testing profile was changed to maintain a constant load during testing. The loaded selected was the highest load tested of 640 N as this represents the largest ground force reaction experienced by a 60 kg person during walking gait and thus allowed for the sample to be tested at the greatest loading value.

5.1.2 Study aims

The aims of the studies in this chapter were to investigate the effects of different treatments on the contact area, peak stress, mean stress and friction properties within 10 mm chondral defects. This work further developed the methodologies previously presented in chapter 4 on the porcine talus and translate it to cadaveric tissue. In addition, this study was used to assess the ability of the 4VBC-MA collagen hydrogel to fill in a defect site and compare its behaviour as a treatment for OLT with two current clinical treatments: ChondroGide®, an alternative collagen type I/III scaffold, and an osteochondral allograft plug.

5.2 Materials and Methods

The porcine methodologies presented in the previous chapter were translated to cadaveric samples and following conditions were tested: healthy intact tissue, 10 mm full thickness chondral defect, 4 VBC-MA collagen type I hydrogel, ChondroGide® matrix and Tisseel® glue with nanofracture treatment to the subchondral bone and an osteochondral allograft plug.

5.2.1 Materials

Phosphate buffered saline was selected as the lubricant for all testing and to maintain tissue hydration throughout testing (Oxoid Ltd, Basingstoke, UK). It was chosen as it readily available, a physiological solution and has minimal ethical implications for use with human tissue. PBS solutions were changed after every tests. Contact area measurements were performed using the TekScan pressure mapping sensors as detailed in Section 5.3.1 (TekScan, MA, USA). TekScan sensors were calibrated using the methods described in section 5.3.1. at the start of each test. Friction measurements studies were carried out using the ProSim Pendulum Friction Simulator (Simulator Solutions,

Manchester, UK). Calibration of the simulator was performed as previously described in section 5.3.1. The simulator was calibrated at least once a month during the testing process and controls samples with known friction coefficients were used to ensure consistent outcomes throughout the study.

ChondroGide® membranes (Geistlich Pharma AG, Switzerland)and Tisseel ® Fibrin Sealant (Baxter, USA) were provided by Joint Operations Ltd, UK. Joint Operations Ltd also supplied all cadaveric tissue that was used in the tests described below. Ethical approval for all studies conducted was obtained form the University of Leeds Research Ethics Committee (MEEC 20-031).

5.2.2 Cadaveric assessment of defect and repair models

The following diagram represented the intended testing methodology used for all samples within this chapter. As all testing described here was non-destructive, samples were tested using the experimental testing sequence documented in figure 5.1. As described within the experimental testing sequence for each condition both tribological and compression testing was performed on all samples for each condition.

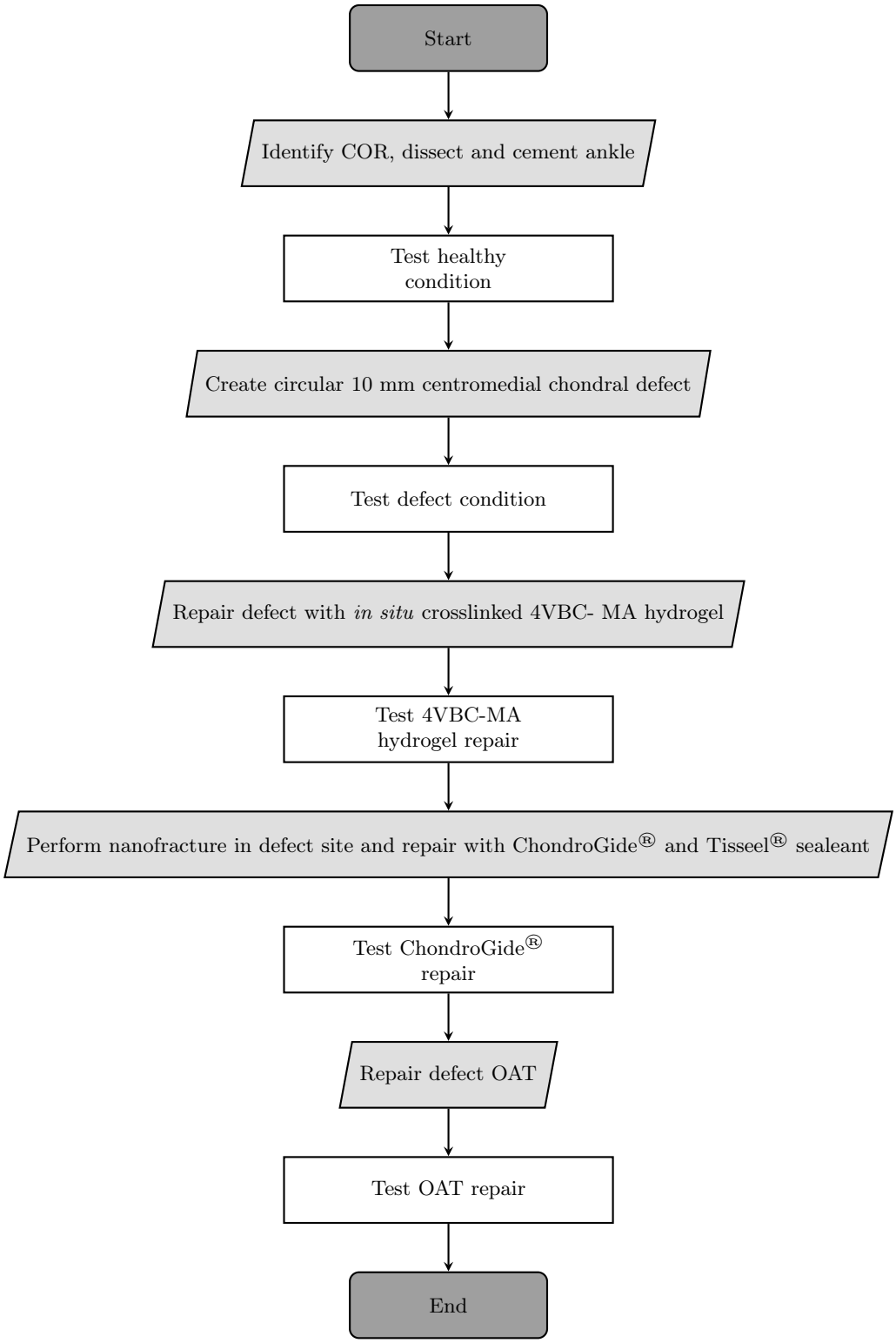

Figure 5.1: Flow chart of experimental testing sequence
Flow chart shows the intended tissue processing and testing methodology used for each sample to through the following test conditions: healthy, 10 mm defect, 4VBC-MA hydrogel, ChondroGide® with Nanofracture and Tisseel®, and osteochondral allograft core (OAT). Centre of rotation (COR) was determined for each sample prior to testing. For all conditions the testing process included compression and tribological testing of samples.

5.2.3 Specimen Preparation

Seven fresh-frozen, paired tibia and tali specimens were used for this study. The typical age range for the specimens was between 19 and 30 years old with the testing group comprising of 5 left ankles and 2 right ankles. Ethical approval for studies were acquired prior to receipt of tissue (MEEC 20-031). Samples were provided by Joint Operations Ltd. (UK). The samples provided were expired allograft material and thus were already preprocessed prior to receipt of the tissue. All soft tissue had been removed and little to no bone marrow was present within the samples. All specimens were thawed to room temperature on receipt of tissue. The packaging media was removed from the tissues and samples were stored in PBS in a -80° C freezer which was Human Tissue Act compliant. Samples were thawed for 24 hours at 4° C and were brought to room temperature prior to testing. All dissecting, cementing and testing was optimised to minimise freeze-thaw cycles for the tissue and to ensure sample integrity and uniformity throughout the testing process. Samples underwent no more then three freeze thaw cycles. All sample preparation was performed within an approved cabinet for human tissue work.

Samples were sequentially tested through uniaxial compression testing and then using the friction simulator for tribological assessment of each condition (as seen in fig 5.1). Thus samples were cemented using the methodology for friction simulator testing to ensure correct alignment (as described in section 4.3.4). Due to the differences in morphology between porcine and human tali, a modified circular template methodology was employed to identify the centre of rotation (COR) of the talus. This methodology has been previously used to determine the COR by defining the talus as circle and identifying the centre of the concentric circle as the centre of rotation and the arc of the talar articulating surface representing the edge of the circle (Veljkovic et al., 2013). Furthermore, it has been shown that the shape of the talar trochlear and the radii of curvature of the talus can be used to inform the dorsiflexion and plantarflexion axes of the talocrural joint (Nozaki et al., 2019). Thus the circle template works as a way to identify the centre of rotation of the joint.

Identification of centre of rotation and cementing of samples

A selection of circular templates were created in 1 mm intervals ranging from 34 mm to 52 mm in diameter. The natural curvature of the talar dome was measured for each sample by aligning the medial edge of the talar dome with the appropriately fitted template (fig. 5.2). The circle was

fit to the talar dome to measure the trochlear talar length. The size of the template was used to determine the diameter of the hypothetical circle that is represented by the convex surface of the talar trochlear. It is assumed that the COR for the tibiotalar joint sat at the centre of this circle.

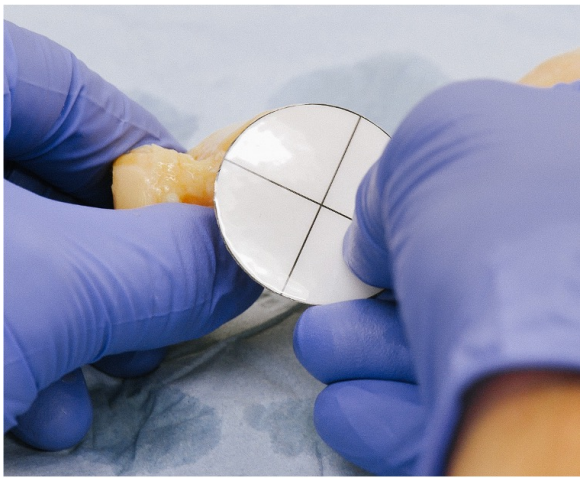

Figure 5.2: Circular template method used to identify the centre of rotation using the talar dome
Image shows a circular template positioned on the medial face of the talus with the edge of the circle aligning with the curvature of the talar dome.

The selected diameter was then used to inform the cementing process to ensure the alignment of COR for the sample and the PFS. A summary of the identified diameters for the specimens is shown in table 5.1.

Table 5.1: Measure diameter of human tali specimens

Specimen	**Diameter of talus (mm)**	**L/R foot**
1	42	L
2	36	L
3	42	L
4	37	L
5	34	L
6	48	R
7	38	R
Mean	39.6	-
SD	4.8	-

Delrin cementing arcs were used to ensure that the COR was set to the correct height for the COR of the joint (fig 5.3). Three cementing arcs of varying lengths (34 mm, 39 mm and 42 mm) were used with slip gauges, allowing for the height to be adjusted in 1 mm increments, to position the centre of rotation of each sample. The cementing arcs allowed for the curvature of the tibial articulating surface to be a set distance away from the known COR of the pendulum friction simulator. An oscillating bone saw was used to reduce the length of the tibial shaft of the sample, allowing it to

sit within the fixture with the cementing arc positioned flush to the inferior articulating surface of the tibia. Key markers on the inferior articular surface were used to aid with the alignment process, including aligning the centre of the cementing arc with the anterior lip of the distal tibia (fig. 5.3). Figure 5.3 shows a 5 mm delrin screw within the tibial shaft. This was required to provide additional support and contact between the PMMA cement and the bone, reducing the risk of the sample fracturing out of the cement and fixture during testing. The positioning and orientation of the tibia was adjusted using three grub screws which held the tibial shaft in position. 30 mL of PMMA cement was added to the tibial fixture pot and the cement was left to set for at least 1 hour. During cementing tissue was kept hydrated with PBS solution.

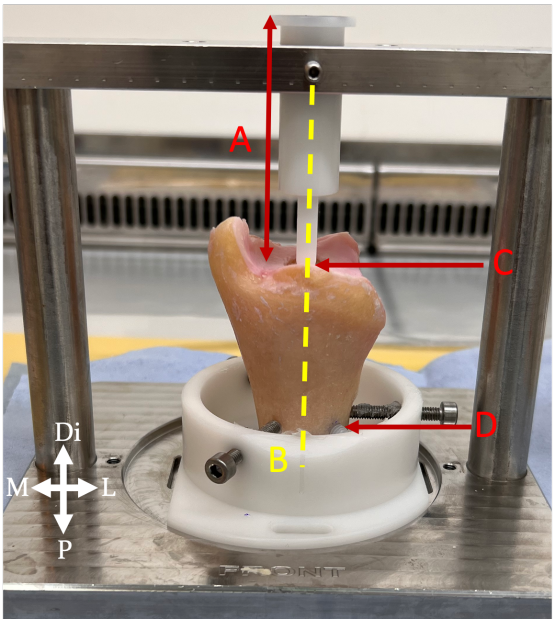

Figure 5.3: Alignment and orientation of tibia for testing
Anterior view of the tibia alignment set up within the tibial pot. Length A is set based on the diameter of the circle obtained from the template. B shows alignment of the cementing arc with the anterior lip (C) of the distal tibia. D shows the delrin screw positioned within the tibial shaft. Di = Distal, P = Proximal, M = Medial and L = Lateral.

The cementing jig was then rearrange so that the tibial pot was attached to the top bar. This allowed for the tibia to inform the positioning of the talus to cement the samples whilst preserving normal joint alignment (fig. 5.4). An oscillating saw was used to dissect the following regions on the talus to ensure that the articulating surface of the talar dome would fit within the talar pot: the head and the neck of the talus, the medial, anterior or posterior facet and the lateral process. This varied depending on the size and morphology of each sample. The removal of these regions ensured that the sample could fit within the constraints of the talar pot. Furthermore it permitted the adjustment of the tissue to ensure the alignment of the two articulating surfaces. All tissue that

was removed from the sample was collected and stored with the test specimens in compliance with the Human Tissue Act.

Three grub screws were used to hold the talus in position and roughly 30 mL of PMMA cement was added to the talar pot. PMMA cement was left to cure for at least 1 hour prior to testing. Tissue hydration was maintained by soaking the tissue in PBS or covering it in a PBS soaked towel.

Input from the specialist Surgeon was provided through the initial cementing process to identify key features to ensure alignment and geometry of joint was conserved as much as possible.

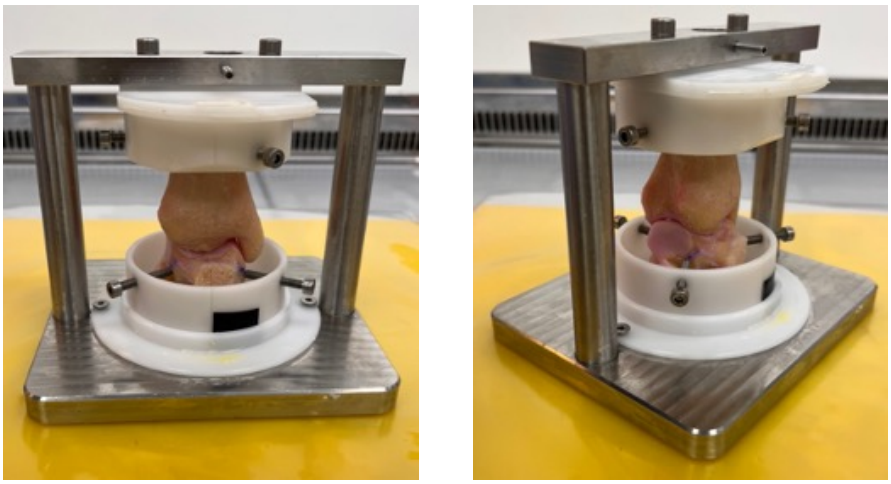

(a) anterior view (b) medial view

Figure 5.4: Alignment and orientation of the tibiotalar joint during cementing
A) shows the anterior view and B) the medial view of the whole joint within the custom ankle cementing rig.

5.2.4 Contact stress testing of cadaveric samples

As Instron (Instron, MA, USA) and TekScan 5033 pressure sensor was prepared and calibrated as described in section 5.3.1 using the same calibration profile. A 5kN load cell was used for all tests described below. The TekScan 5033 pressure sensor was surrounded in polytetrafluoroethylene (PTFE) sheet to reduce the risk of damage to the sensor and minimise the risk of sensel dropout during testing (fig. 5.5a).

All tibiotalar samples (N=7) were tested in an intact healthy state. Tissue hydration was maintained during testing by soaking the sample in PBS soaked towels prior to and after testing. Samples were loaded on an identical set up to that previously in fig 4.11. Figure 5.5 shows the alignment and

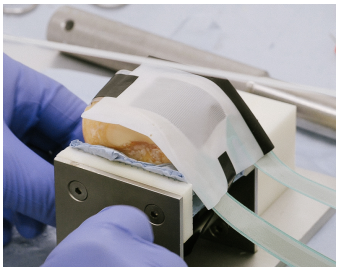

(a) Placement of Sensor on talar dome

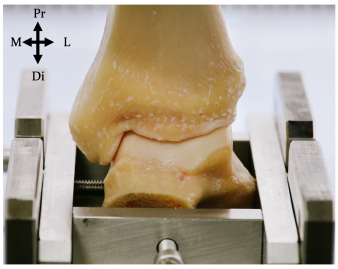

(b) Alignment of tibiotalar joint in fixtures

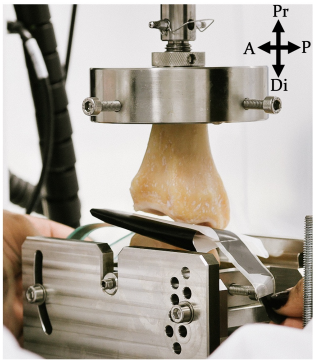

(c) Complete Instron set up for cadaveric samples

Figure 5.5: Set up of natural cadaveric tibiotalar joint for compression testing
A) shows the set up of the TekScan 5033 sensor with PTFE film placed on the surface of the talar dome. B) Shows the final alignment of the tibia talar joint when in contact in the in the neutral (0 °F/E) when placed into the Instron. C) Shows the final set up of TekScan sensor placed within the tibiotalar joint in the Instron. Di = Distal, Pr = Proximal, M = Medial and L = Lateral, A = Anterior, P = Posterior

set up of the cadaveric samples within the custom Instron fixtures. For all samples, adjustments to the positioning of the talar fixtures on the base plate of the Instron were made to ensure the alignment of the tibia and talus in the neutral position (fig. 5.5b). Natural joint shape was used to ensure that the joint was correctly aligned prior to sensor placement between the tibia and talus. The sensor was attached using PTFE tape to the sides of talar fixture table and positioned to ensure that the sensor was in the centre of the talar dome (fig. 5.5a).

For each sample, three testing conditions were selected to simulate a simplified gait cycle with the load and angle selected based on the average ground reaction force seen within the natural ankle joint for a 600 N person (table 5.2) (Anderson et al., 2010). Each sample was loaded in to the Instron as seen in figure 5.5c. A load was applied at a constant strain rate of 2 mm/min until the desired load was reached. Max load was held for 2 minutes and contact pressure was measured at a rate of 64 frames per second. ASCII files were obtained for the whole tests and a single frame was selected from the region where maximum load was applied for analysis. The tibiotalar joint was unloaded and the angle of the talus (and thus the joint angle) were changed using the adjustable table of the talar component of fixture before testing the next condition.

Table 5.2: Loading conditions for uniaxial compression testing relating back to the stage of gait cycle simulated

Stage of Gait Cycle	**Load (N)**	**Flexion-Extension Angles**
Heel strike	630	15°F
Midstance	480	0°F/E
Toe off	640	15°E

Gait cycle conditions were tested sequentially for each sample. Post compression testing samples were left to recover for at least one hour in PBS prior to being tested in the pendulum friction simulator.

5.2.5 Tribological testing of cadaveric samples

Post uniaxial compression testing, tribological testing was performed on the samples for each condition following the testing methodology outlined in fig. 5.1.

Samples were loaded into the friction simulator as seen in figure 5.6. Motion of the motor arm was used to control the flexion-extension angle applied during a cycle and was limited to a range of ± 7°to ± 15°, with a max total motion arc of 20°, at a frequency of 1.43 - 1 Hz, respectively (Table 5.3). A constant peak load was applied to all samples of 640 N during each cycle. This was to minimise additional torque which could be introduced into the system caused by constraining the talus and preventing the slight pronation or supination that would occur as the talocrural joint moved through the range of motion. The applied flexion-extension angle was initially set at the largest range available for the sample where dislocation did not occur during testing and normal movement of the joint could be observed. For each subsequent condition tested (fig. 5.1) the flexion-extension angle and frequency were adjusted if the sample dislocated during testing with the initial condition used. Dislocation of the tibiotalar joint within the simulator did not damage the sample as dislocation usually occurred during the ramping stage and the test was stopped immediately.

Tests were run for 3600 cycles. Friction values were calculated through the piezoelectric sensor which measured the frictional torque between the contacting articulating surfaces of the distal tibia and the talar dome. The hydrostatic bearing eliminated the effects of friction of the machine from the obtained measurements. Pre- and post- testing was performed for all tests. These consisted of 121-cycles tested at a constant load of 640 N with the identified flexion-extension motion and corresponding frequencies (table 5.3).

Table 5.3: Pendulum friction simulator loading profiles for flexion and extension of motion arm and its corresponding frequency

Flexion-Extension Angle (°)	**Frequency (Hz)**
10	1
9	1.1
8	1.25
7	1.43

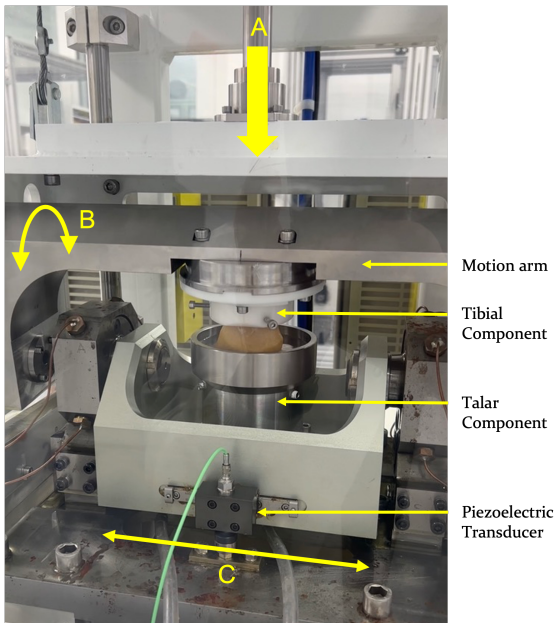

Figure 5.6: Cadaveric natural joint set up in the pendulum friction simulator
Image of the ProSim Pendulum Friction Simulator with the cadaveric tibiotalar joint showing the flexion-extension (FE) motion arm, tibia fixture attached to the FE rocker, talus is sitting within a pot in the talar fixture submerged in a PBS bath. The talar fixture is placed within the friction measuring carriage containing the piezoelectric transducer. A- shows the direction of the load applied, B- direction of movement for the rocker arm, C- Translation direction of the measuring carriage.

Frictional outputs were analysed using the same methods as described in section 5.3.6. Images of the articulating surfaces were taken before and after each test to observe any changes to tissue surface.

Modifications of pendulum friction simulator input profile

Table 5.4 contains the loading conditions that were used for each sample during the friction tests. The introduction of defects on the talar dome sometimes caused a change to the stability of the joint within the simulator and thus the range of motion was adjusted for each sample, as needed, to ensure that the joint alignment was maintained during testing. This minimised the chance of additional friction or torque being introduced into the system. The range of flexion and extension was changed depending on levels of movement or dislocation seen within the ankle during testing. Reductions in the motion arc were compensated with a change in the frequency of the swing to ensure that the same maximum angular velocity was met and that the values were comparable. Flexion - extension of motion arm and frequency of swing were adjusted prior to initial forward and reverse test. Table 5.4 shows the initial PFS inputs used for each sample and any secondary profiles used.

Table 5.4: Pendulum friction simulator sample profiles Initial and secondary flexion and extension input values

Samples	**Flexion (+) -Extension(-)** Initial angles (°)	**Profile** Secondary angles (°)
1	+ 10 - 10	+ 7 - 7
2	+ 5 - 15	No Change
3	+ 5 - 15	No Change
4	+ 5 - 15	+ 4 - 10
5	+ 5 - 15	No Change
6	+ 5 - 15	No Change
7	+ 5 - 15	+ 4 - 10

5.2.6 Creation of 10 mm chondral defect

For all specimens the following surgical procedures were performed after the first set of uniaxial compression and tribological testing for the healthy condition. A 10 mm, full thickness chondral defect was created in the centromedial region of the talus. This was chosen as it is the most common location of an OLT seen on the talar dome (Elias et al., 2009). Methodology for defect creation was supported through advice and training provided by the Specialist Surgeon and is documented below.

A round metallic cutting die was used to mark a 10 mm defect template onto the cartilage in the centromedial region of the talar dome. Figure 5.7a shows examples of the dies used to mark the cartilage surface. This region was then cut to the depth of subchondral bone using a No. 15 blade scalpel (fig. 5.7b). A diamond pattern was then scored across the cartilage within the defect site. An osteotome was used to excise the cartilage to the depth of the subchondral bone by scraping the tissue out of the defect (fig. 5.7c). This produced a full-thickness, 10 mm circular chondral defect on the surface of the talar dome (fig. 5.7d).

The tissue was then allowed recover in PBS for one hour before repeating the testing process described above.

Post-testing with a 10 mm defect, three different treatment methods were tested within the defect going from the most to least conservative as described in fig. 5.1.

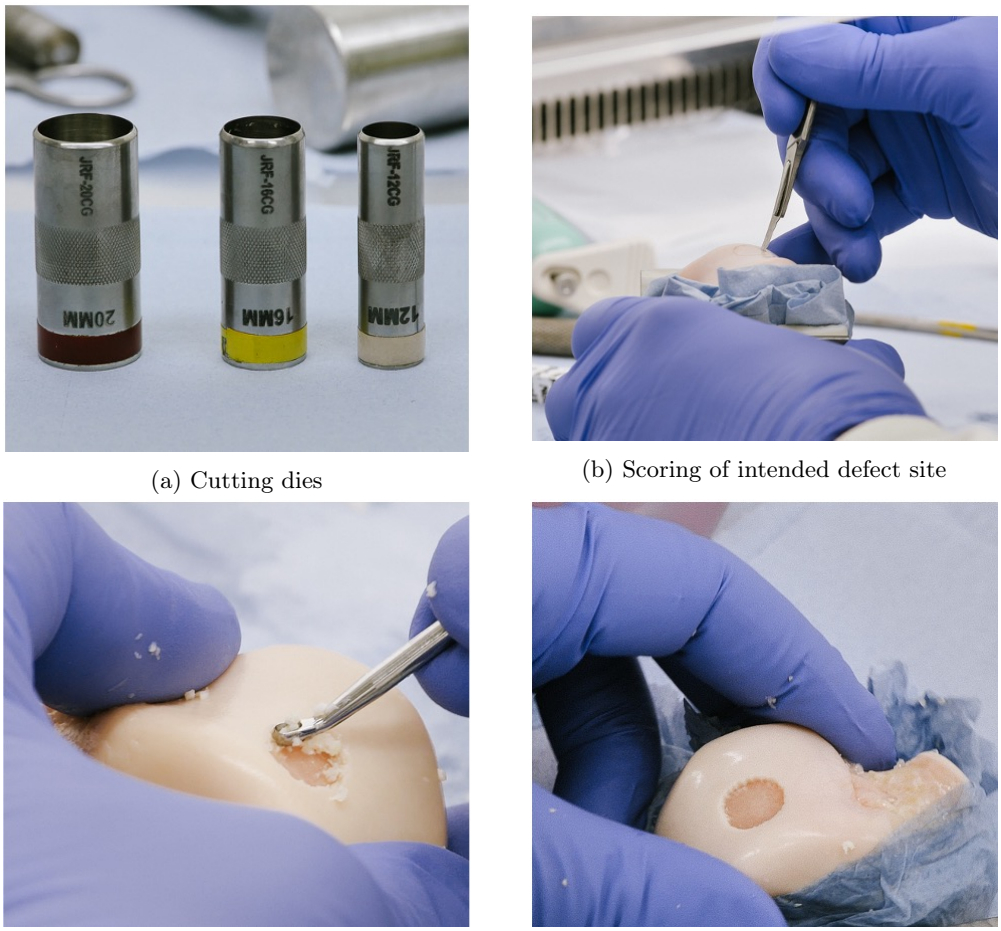

(a) Cutting dies

(b) Scoring of intended defect site

(c) Removal of cartilage using osteotome

(d) Complete chondral defect

Figure 5.7: Full thickness chondral defect creation
Methods used for the creation of chondral defects. A) Osteochondral cores used as cutting dues to mark the defect site. B) Shows the creation of scores on in the cartilage demarking the areas to be removed. C) Osteotome removing the cartilage tissue to the depth of the subchondral bone. D) Completed chondral defect.

5.2.7 Defect repair using 4VBC-MA Collagen Hydrogel

The first treatment method tested was the novel 4VBC-MA collagen hydrogel developed in Chapter 4. The following precursor solutions were prepared in advance as described in Section 4.2.3: a 1.6 wt/% solution of 4VBC- MA collagen precursor in 10 mM HCl, 1% LAP solution in 2X PBS and 1 M NaOH solution. 4VBC-MA collagen precursor solution was neutralised with 1 M NaOH. Equal volumes of neutralised collagen precursor solution and LAP photoinitiator solution were mixed by vortexing. The solution was placed into a 1 mL syringe with a 16 gauge needle. The collagen mix was injected into the defect site. *In situ* crosslinking of the precursor solution was performed under 405 nm light for 5 minutes (fig. 5.8a). Successful and complete crosslinking was observed after 5

minutes, when the defect site was filled with a homogeneous clear gel (fig. 5.8b & 5.8c).

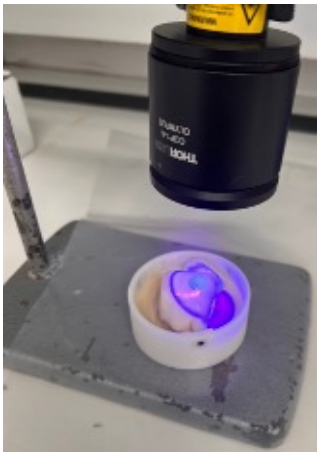

(a) Vis-Light Crosslinking of hydrogel in defect site

(b) Dorsal view of filled defect with hydrogel

(c) Medial view of filled defect with hydrogel

Figure 5.8: 4VBC- MA collagen hydrogel generation within chondral defect
A) Vis-light crosslinking of 4VBC-MA collagen hydrogel in chondral talar defect. B and C) Medial and dorsal views of completely crosslinked hydrogel within the chondral talar defect

5.2.8 Simulated AMIC treatment using nanofracture of defect site and repair with ChondroGide® membrane and Tisseel® fibrin sealant

Tisseel® fibrin glue was brought to room temperature by placing it into a luke-warm water bath at least 30 minutes prior to use to ensure that it is fully defrosted. Nanofracture was performed using the assembled NanoFx® tool. This consisted of the A-Curve NanoFx® handle instrument and PleuriStik™ Guide Wire and thumb tab accessory tool (fig. 5.10) (Arthosurface, Inc. USA). Guidance for AMIC procedure was provided by the Surgeon to ensure that process mimicked clinical practise.

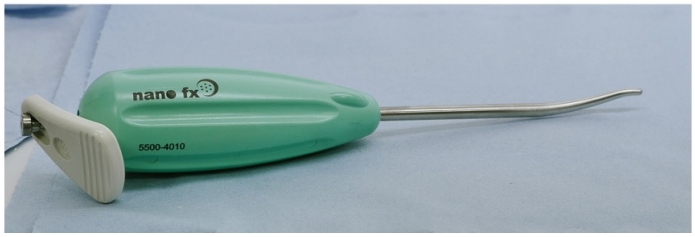

Figure 5.9: NanoFx® system consisting of the assembled A-Curve NanoFx® handle instrument and PleuriStik™ Guide Wire and thumb tab accessory tool

Nanofracture was performed in the defect to simulate AMIC treatment. The NanoFx® handle was placed perpendicular to the subchondral bone and a mallet was used to tap the top of the guide

wire causing the needle to create a small channel in the underlying subchondral bone (fig. 5.10a). Multiple channels were evenly spaced throughout the defect site (fig. 5.10b).

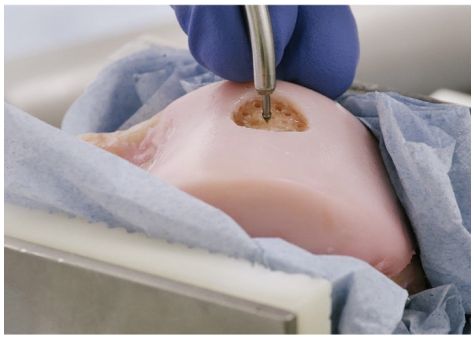

(a) Lateral view of fully dissected tibiotalar joint

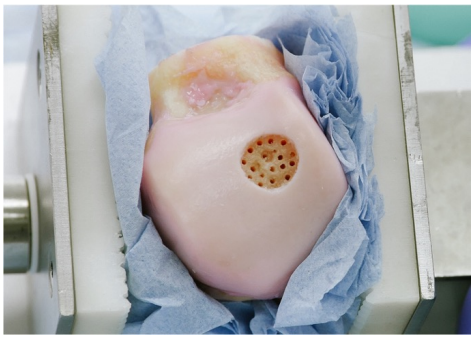

(b) Lateral view of fully dissected tibiotalar joint

Figure 5.10: Nanofracture of chondral defect
A shows the deneration of nanofractured channels in the defect site. B shows the completed nanofracture of the chondral defect displaying the distribution of the trabecular channels within the defect.

A foil template was placed into the defect site and cut to shape (fig. 5.11a). This template was used to cut a circular piece of the collagen type I/II ChondroGide ® membrane (fig. 5.11b). The membrane was hydrated using PBS until fully saturated immediately before use. Tisseel fibrin sealant was injected into defect site and ChondroGide® membrane was placed onto it (fig. 5.11c). Samples were then tested following the uniaxial compression and tribological testing protocols described above.

(a) Foil template cut to size

(b) Prepared ChondroGide® membrane

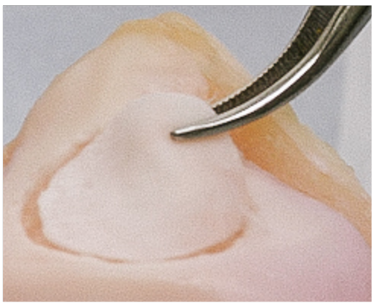

(c) Application of hydrated ChondroGide® membrane

Figure 5.11: Repair of defect with ChondroGide ® membrane
Repair of defect with ChondroGide ® membrane. A shows positioning of foil template within talar defect. B and C shows placement of ChondroGide ® membrane into defect site.

5.2.9 Osteochondral allograft repair of chondral defect

Osteochondral allograft treatment of the defect was performed by Mr Mark Farndon, a foot and ankle clinician. 10 mm osteochondral allograft cores were provided by Joint Operations Ltd. Figure 5.12 shows the process used to repair the defect with an osteochondral cores. All cores were measured for their maximum depth (fig. 5.12a). A 10 mm drill was used to create a hole to depth of 10 mm within the chondral defect site, perpendicular to the articular surface allowing for congruent placement of grafts (fig. 5.12b). An osteotome was used to ensure that a flat surface was present within defect site to ensure the core would sit flush within the defect. A scalpel was used to remove excess bone stock on the allograft plug (fig. 5.12c). The allograft plug was then pressed into the defect site, and a mallet was gently used to ensure that the core was flush with both the exposed trabecular bone and the surface of the talus. Figure 5.12d shows the core placed within a sample. This process was repeated for all samples and samples were tested following the previously described protocols.

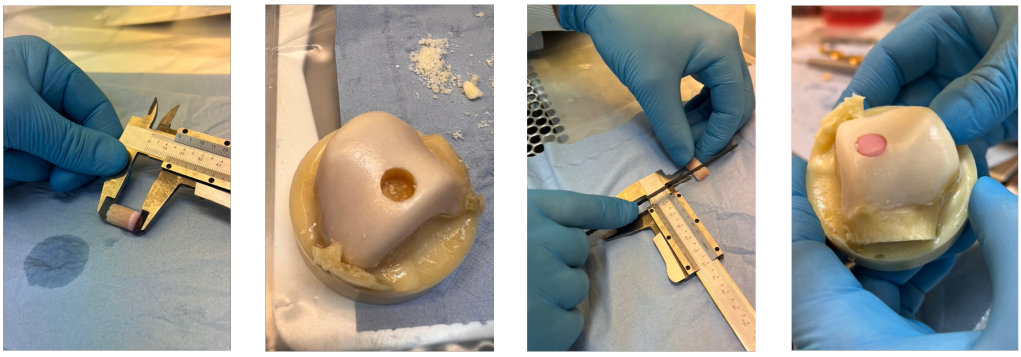

(a) Measurement of the length of allograft core (b) Creation of completed debrided site (c) Removal of excess bone stock (d) Situation of graft within defect site

Figure 5.12: Preparation of osteochondral plug repair of talar defect
(A) measurement of osteochondral core. (B) Creation of implantation site. (C) Removal of excess bone stock from core. (D) Repair of defect site with the plug.

5.2.10 Data and Statistical Analysis

Data analysis was performed as described in Section 5.2 for both the data collected from friction simulator and uniaxial compression testing. The R script was modified to analyse each of the 5 different conditions. Overall summary statistics were calculated studying the means, and standard deviations for all samples.

The human talus was divided into four regions based on the acquired sensor data. For each

condition, samples were split in left and right ankles prior to analysis to ensure that the posterior and anterior regions were correctly assigned. Each region of the sensor consisted of 368 sensels and a grid representing a region of 256 mm^2. Max contact pressure, mean contact pressure and contact area for the four regions were obtained for every sample.

Statistical analysis was performed to assess for normal distribution of results using the Shapiro-Wilks tests and variance of the data was assessed using box plots and Levene test between the groups. Based on the outcomes of these tests, samples showed to be normal or non-normal distribution of data. For non-normal data sets Friedmen test or aligned rank transformation (ART) ANOVA tests were performed, for samples where unequal variance was seen Welch's ANOVA was performed. For samples with equal variance and normal distribution one-way ANOVA was used to analyse the data. T-tests were performed when comparing two samples to assess differences in mean. Statistical significance was demonstrated by $p < 0.05$. Appropriate post-hoc tests were used including Dunn's test with Bonferroni correction, Tukey's HSD and contrast tests where outcomes were significant. Due to the sequential nature of testing, samples were treated as paired samples during statistical analysis.

5.3 Results

5.3.1 4VBC-MA collagen Hydrogel defect repair

Successful *in situ* crosslinking of the hydrogel was seen within the defect site. On observation the hydrogel was able to completely fill the defect site and the gel was able to conform and follow the natural curvature of the talus. Figure 5.13 shows various views of the crosslinked 4VBC-MA collagen hydrogel within a 10 mm chondral defect. The crosslinking hydrogel was homogenous in appearance and did not seem to release from the edge of the defect after photocrosslinking with 405 nm vis-light for all samples.

5.3.2 Uniaxial compression testing of cadaveric tissue

The results described below show the changes to the local joint contact mechanics under the tested conditions healthy, defect, 4VBC- MA collagen I hydrogel, ChondroGide and OAT repair. Pressures

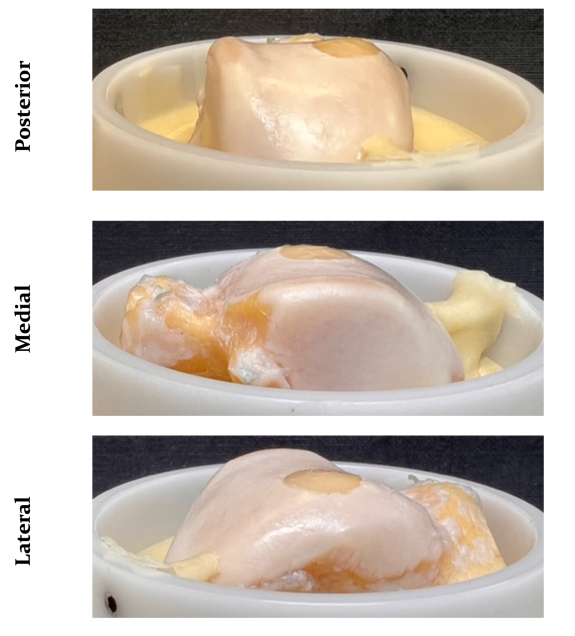

Figure 5.13: 4VBC-MA hydrogel crosslinked within chondral talar defect
Lateral, medial and posterior views of hydrogel filling defect site.

maps were generated for all samples and conditions and can be seen in appendix B.1. An example set of pressure maps are displayed in figure 5.14.

For all 7 samples, heat maps showed visible changes in pressure distribution after the introduction of a 10 mm chondral defect for both 480 N 0° F/E and 640 N 15 ° E, representing neutral and plantarflexion conditions, respectively. For 4 out of 7 of the samples tested, the presence of a chondral defect resulted in the introduction of increased pressure within the posterior lateral region of the talar dome for the 640 N 15° E. No loading was measured through the defect site when repaired with the 4VBC-MA collagen hydrogel for any samples. Partial return of loading could be seen within the defect site when repaired with a ChondroGide ® membrane and Tisseel® fibrin sealant for 3 of the samples tested at 640 N and 15 ° E. No loading was observed through the ChondroGide® repair for the neutral or dorsiflexion loading conditions. OAT treatment was the only treatment that was able to successfully reintroduce loading through the defect site, but did not produce the same pressure distribution as the healthy native samples. OAT repair condition also showed a general trend displaying an increase in max contact pressure seen in the ankle. However, these differences were not significant (One-way ANOVA; $p = 0.83$, $p = 0.98$ and $p = 0.74$ for 630 N & 15° F, 480 N & 0° F/E and 640 N & 15° E, respectively).

Contour plots were generated from the same data location for each sample. Contour maps were

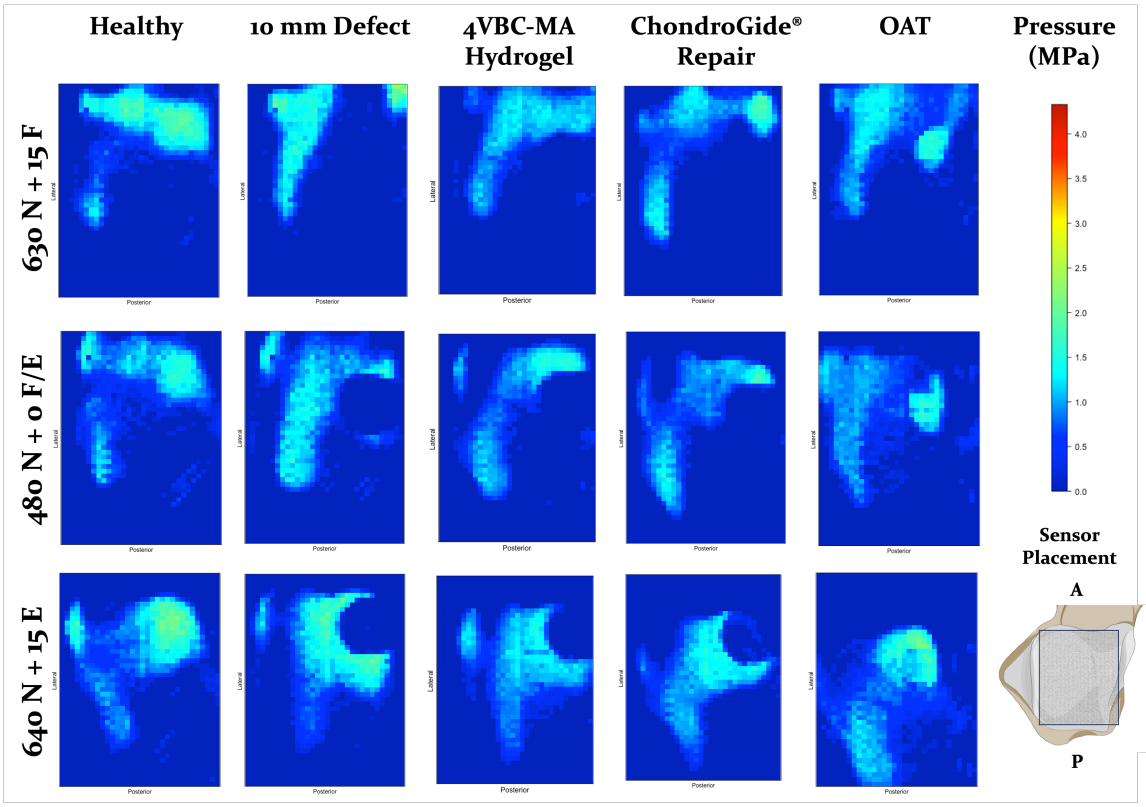

Figure 5.14: Sample pressure maps showing distribution of pressure around the talar dome
Images show a sample of pressure maps for one sample showing pressure distribution across the talar dome for each condition (left to right) healthy, chondral defect, 4VBC-MA hydrogel, ChondroGide ® Repair and OAT treatment. Pressure maps represent a 38.4 x 26.7 mm area on the talar dome. A = Anterior, P = Posterior

used to aid in the visual assessment of changes in the contact area for each loading and testing condition. A sample set of contour maps can be seen in figure 5.15. The results of all contour plots can be seen in appendix section B.2. Although no significant changes in contact area were seen, the introduction of a defect created a loss of contact at the defect site. The dorsiflexion condition, 630 N 15° flexion, shows the least amount of change in contact area due to the presence of a chondral defect or different treatments. For the neutral and plantarflexion conditions, the presence of a chondral defect caused new regions of contact including in the posterior and anterior lateral regions of the talus and the anterior lateral. New points of contact remained for both the 4VBC-MA hydrogel treatment and the ChondroGide® repair. Although pressure maps showed low/ no levels of loading through the ChondroGide® repair, contour plots showed loading through the defect site in 6 out of 7 of the samples. OAT treatments were able to successful redistribute pressure and load through the defect site.

Changes in contact area, max pressure and mean pressure across the tibiotalar joint for each

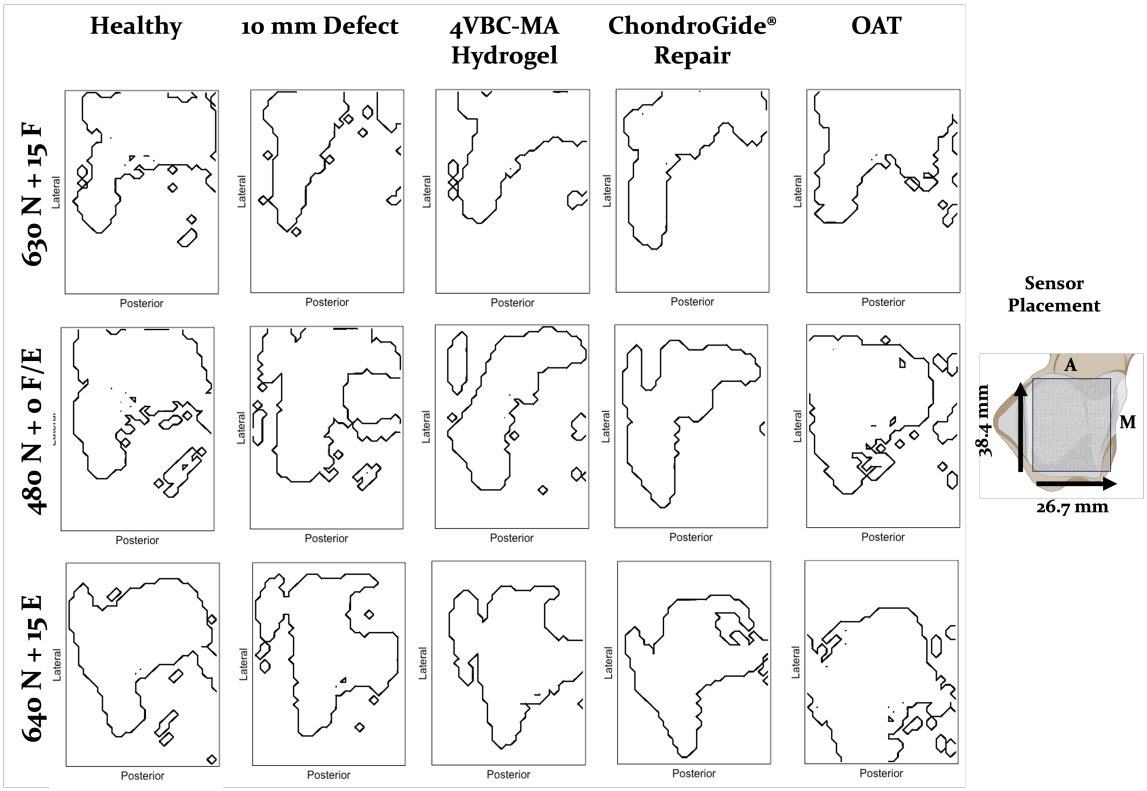

Figure 5.15: Sample contour plots showing contact area across the talar dome.
A sample of contour plots for one sample showing areas of contact across the talar dome for each condition (left to right) healthy, Chondral defect, 4VBC-MA hydrogel, ChondroGide ® repair and OAT treatment. Regions of contact outline with black line. Region mapped represent an area of 38.4 x 26.7 mm on the talar dome. A = Anterior, M = Medial

condition can be seen in figure 5.16. Scatter plots show variation seen for each sample across the different testing condition 5.17. For all conditions the highest pressures were measured for 630 N 15° flexion, which simulated heel strike and also corresponded with the smallest average contact area. Table 5.5 shows the average max pressure across the different loading condition for each testing group. No significant differences were measured between the groups (One way ANOVA or Friedman; $p > 0.05$). Furthermore, no significant differences were seen between the native and chondral defect conditions for all loading conditions (T-test; $p > 0.05$).

A general trend can be seen that the introduction of a defect caused an increase in max pressure across the talar dome. It can be seen that all repair methods reduced the average max contact pressure, with OAT condition returning it to a similar value seen with native sample, but the differences were not significant (fig. 5.16a).

A negative relationship was observed between max contact pressure and contact area, except

when a defect was present. For samples containing a defect, an increase in max contact pressure and contact area can be seen for all conditions (fig. 5.16a & 5.16c). No changes in mean contact pressure can be seen across all conditions, except for the OAT sample at 630 N 15° F, where a decrease in the mean contact pressure can be seen. However, these difference are not significant ($p > 0.05$).

Table 5.6 shows the average contact area for every sample for each loading condition. No significant differences were reported in contact area between treatment or defect condition (One-way ANOVA or Friedman Test; $p > 0.05$). Generally, for all conditions, presence of a defect increased the measured contact area across all samples compared to healthy. This was especially pronounced in the neutral and plantarflexion conditions however, this was not significant. The three repair methods appeared to reduce the average contact area across the samples, except for the ChondroGide® repair at neutral position, as this showed an increase in the average contact area. This corresponds with a lower average max pressure measured (fig. 5.16). At neutral conditions OAT appears to reduce the average contact area to a similar value observed in the healthy sample but performs similarly to the hydrogel and Chondrogide® repair in both plantar and dorsiflexion. In addition, the treatment modalities tended to show a lower contact area compared to the defect and healthy sample in the plantarflexion position compared.

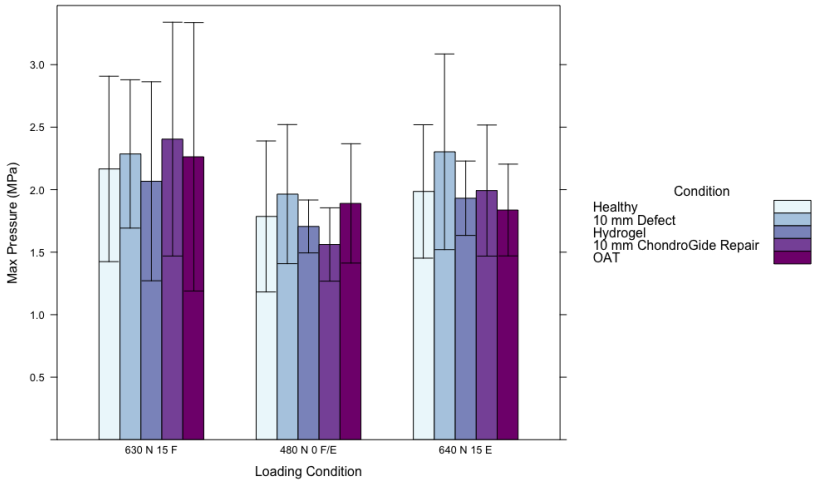

(a) Max contact pressure

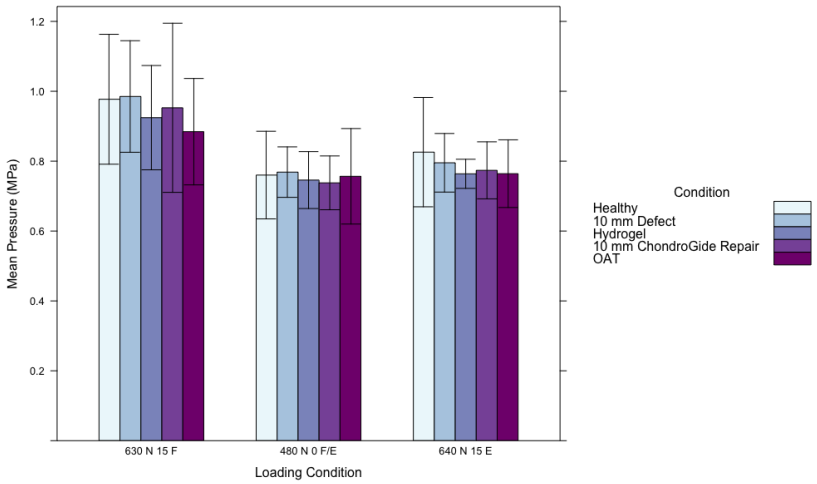

(b) Mean contact pressure

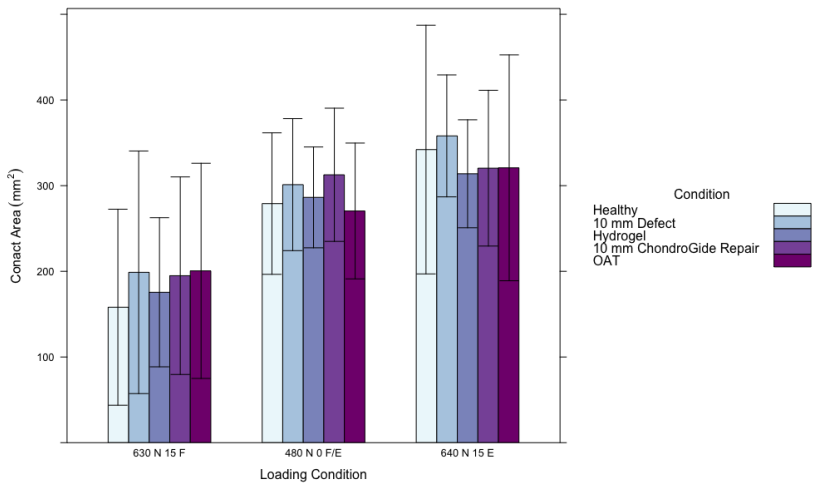

(c) Average total contact area

Figure 5.16: Average contact area and pressure across the whole talar dome showing (N=7) (A) max average contact pressure in MPa, (B) average mean contact pressure in MPa and (B) average contact area (mm^2) with standard deviation bars.

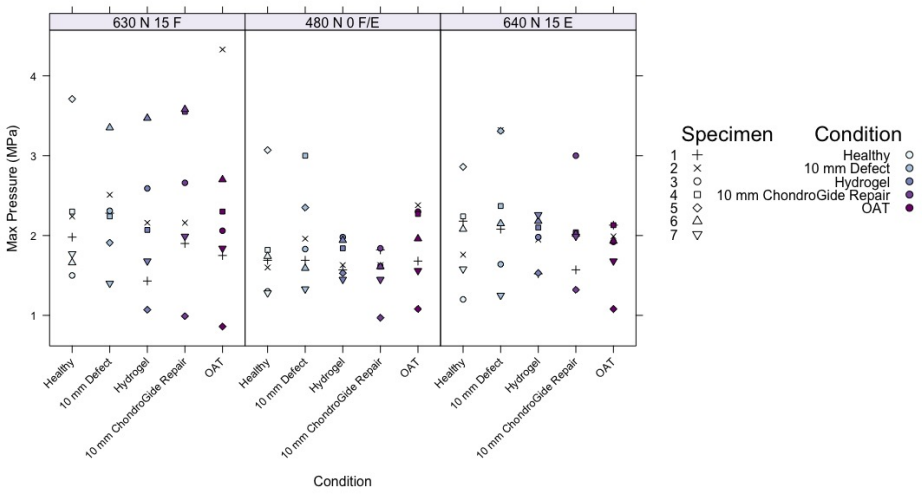

(a) Max contact pressure

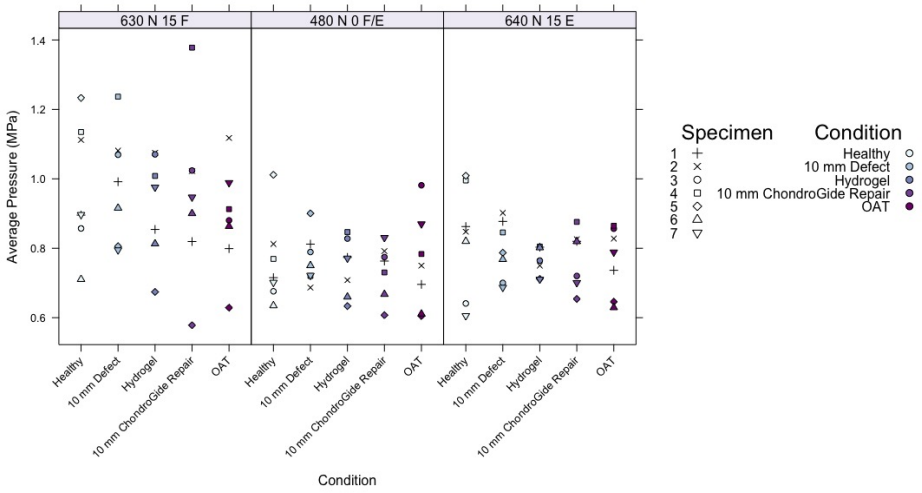

(b) Mean contact pressure

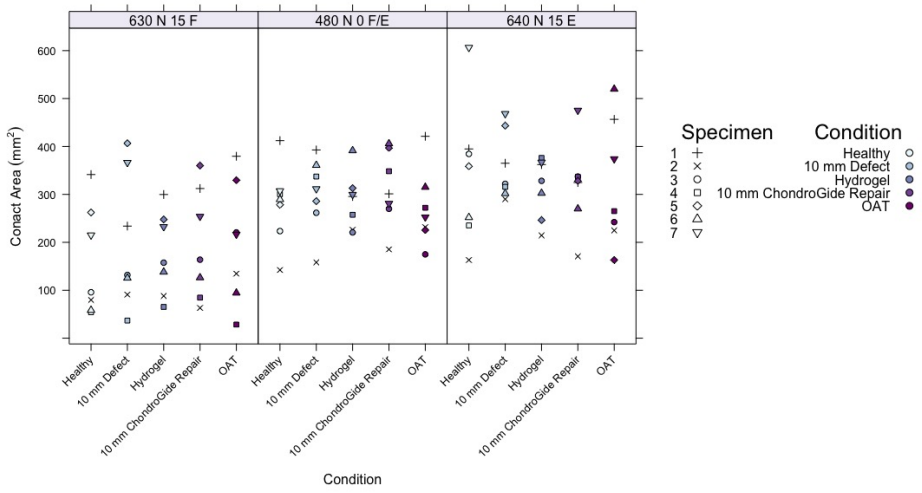

(c) Average total contact area

Figure 5.17: Average contact area and pressure across the whole talar dome showing (N=7) (A) max average contact pressure in MPa, (B) average mean contact pressure in MPa and (B) average contact area (mm^2) for each specimen tested.

Table 5.5: Average max pressure measured for healthy, chondral defect, 4VBC- MA hydrogel, ChondroGide® Repair and OAT treatment with standard deviation

Loading condition	**Average Max Pressure (MPa) ± SD**				
	Healthy	**Defect**	**4VBC-MA Hydrogel**	**ChondroGide® Repair**	**OAT**
630 N 15°F	2.17 ± 0.74	2.29 ± 0.59	2.07 ± 0.80	2.40 ± 0.94	2.26 ± 1.07
480 N 0°F/E	1.79 ± 0.60	1.96 ± 0.55	1.70 ± 0.21	1.56 ± 0.29	1.89 ± 0. 48
640 N 15°E	1.99 ± 0.53	2.30 ± 0.78	1.93 ± 0.30	1.99 ± 0.52	1.84 ± 0.36

Table 5.6: Average contact area measured for healthy, chondral defect, 4VBC- MA hydrogel, ChondroGide® Repair and OAT treatment with standard deviation

Loading condition	**Average Total Contact Area (mm^2) ± SD**				
	Healthy	**Defect**	**4VBC-MA Hydrogel**	**ChondroGide® Repair**	**OAT**
630 N 15°F	158.1 ± 114.4	198.9 ± 141.6	175.6 ± 87.0	194.9 ±115.3	200.6 ± 125.6
480 N 0°F/E	279.1 ± 82.6	301.8 ± 77.0	286. 3 ± 58.8	312.7 ± 77.7	270.4 ±79.2
640 N 15°E	342.1 ± 145.6	358.1 ± 71.2	313.9 ± 63.0	320.4 ± 91.0	320.8 ± 131.8

Regional analysis of joint contact mechanics

Analysis of the four regions of the ankle was performed to study regional changes in contact mechanics and can be seen in figure 5.18 and table 5.7. In the neutral and plantarflexion positions, the introduction of a 10 mm chondral defect caused an increase in the max contact pressure in the posterior lateral region and an increase in the mean pressure (fig. 5.18a & 5.18b). This also corresponded to a pronounced increase in contact area in the posterior lateral region, especially in the plantarflexion condition (fig. 5.18b). Within the AL region of the talus, the presence of a defect caused an increase in contact area for all three loading conditions. For the dorsiflexion and neutral conditions, this corresponded with a reduction in max contact pressure. However, in the plantarflexion condition, an increase in max pressure was seen. Furthermore, all three treatment conditions appeared to reduce max contact pressure, mean contact pressure and contact area in the AL region of the talar dome, with the greatest reduction in pressure and area being seen for the OAT condition.

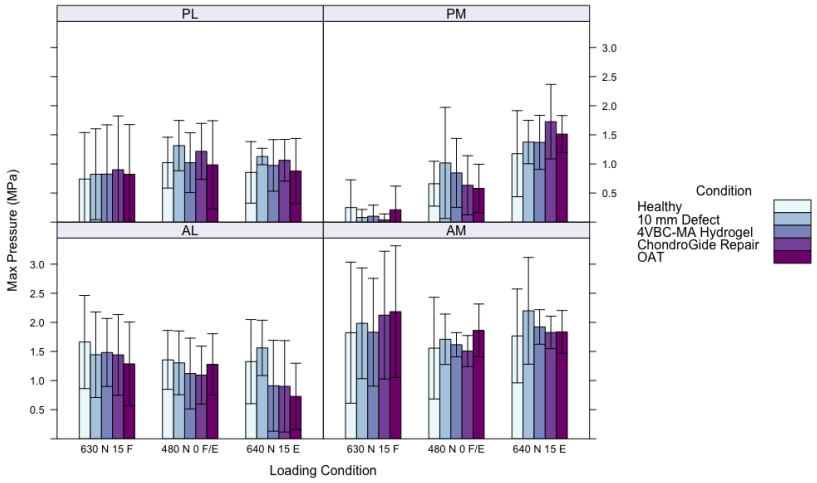

(a) Max regional contact pressure

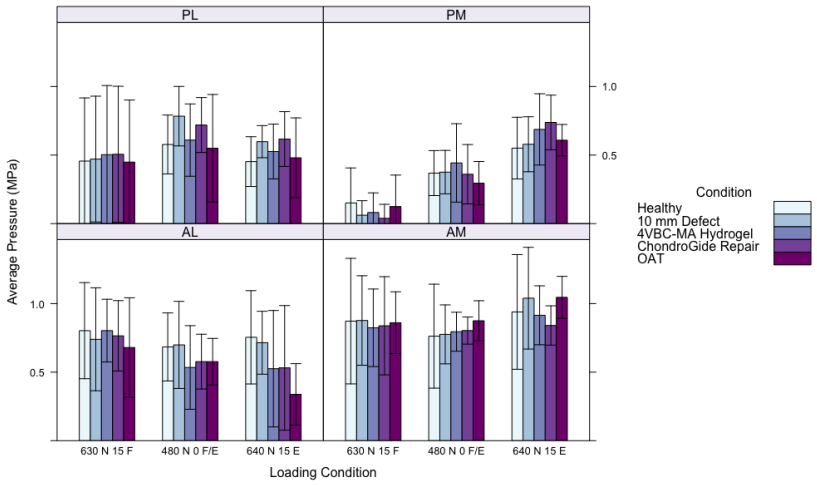

(b) Mean regional contact pressure

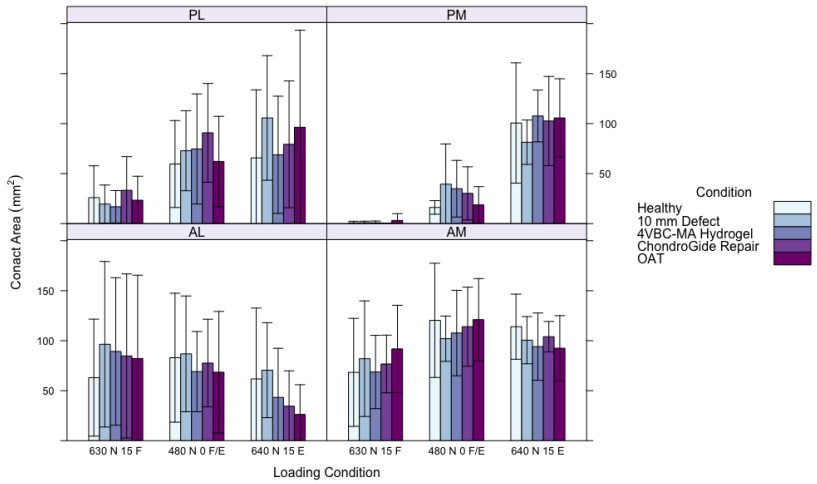

(c) Mean regional contact area

Figure 5.18: Average regional contact mechanics across the four areas of the talar dome (n= 7) with standard deviation bars. 10 mm chondral defect located in the centromedial region of the talar dome (Present in both the PM + AM) (A) Mean max contact pressure across the different loading condition in MPa, (B) mean pressure measured across the sensor in MPa and (C) mean contact area (mm^2) AL= Anterior Lateral, AM = Anterior Medial, PL= Posterior Lateral and PM = Posterior Medial.

Table 5.7: Regional changes in contact area across the talar dome for healthy, chondral defect, 4VBC- MA hydrogel, ChondroGide® Repair and OAT treatment with standard deviation

Loading condition	**Region**	**Average Regional Contact Area (mm^2) ± SD**				
		Healthy	**Defect**	**4VBC-MA Hydrogel**	**ChondroGide® Repair**	**OAT**
630 N 15°F	AM	68.3 ± 54.0	82.0 ± 57.8	68.7 ± 36.7	76.7 ± 28.8	91.8 ± 43.6
	AL	63.1 ± 58.5	96.5 ± 82.8	89.2 ± 73.8	84.8 ± 82.0	82.2 ± 83.3
	PM	0.8 ± 1.6	0.9 ± 1.5	0.8 ± 1.8	0.1 ± 0.3	3.2 ± 6.7
	PL	26.0 ± 31.8	19.5 ± 19.1	16.9 ± 16.2	33.3 ± 33.7	23.4 ± 24. 0
480 N 0°F/E	AM	120.3 ± 57.1	102.0 ± 22.7	107.7 ± 42.7	114.0 ± 39.6	121.0 ± 41.1
	AL	83.0 ± 64.5	86.8 ± 57.9	69.1 ± 40.1	77.6 ± 43.9	68.5 ± 60.8
	PM	16.2 ± 1.6	39.5 ± 40.2	34.9 ± 28.3	30.2 ± 26.6	18.7 ± 18.3
	PL	59.6 ± 43.5	72.9 ± 40.0	74.7 ± 55.1	90.8 ± 49.4	62.2 ± 45.1
640 N 15°E	AM	114.0 ± 32.5	100.5 ± 23.6	94.1 ± 33.6	104.0 ± 15.2	92.5 ± 32.6
	AL	61.8 ± 70.9	70.5 ± 47.5	43.3 ± 49.0	34.5 ± 35.3	26.3 ± 29.7
	PM	100.6 ± 60.2	81.4 ± 22.2	107.7 ± 25.9	102.6 ± 44.6	105.7 ± 39.2
	PL	65.7 ± 68.1	105.7 ± 62.3	68.8 ± 58.6	79.3 ± 63.4	96.4 ± 97.0

5.3.3 Friction measurements

Changes in the coefficient of friction or friction factor against time for the 5 conditions (healthy, 10 mm chondral defect, 4VBC-MA hydrogel repair, ChondrGide® repair and OAT) is shown in figure 5.19 and figure 5.20a. The lowest coefficient of friction was observed for the healthy, native tibiotalar joint with a mean coefficient of friction ± SD of 0.023 ± 0.001. The presence of a 10 mm chondral defect caused an increase in the mean coefficient of friction across the whole test to 0.050 ± 0.002. Significant increase in the mean coefficient of friction was measured between healthy and chondral defect conditions (Wilcoxon signed ranked test with continuity correction $p < 0.001$).

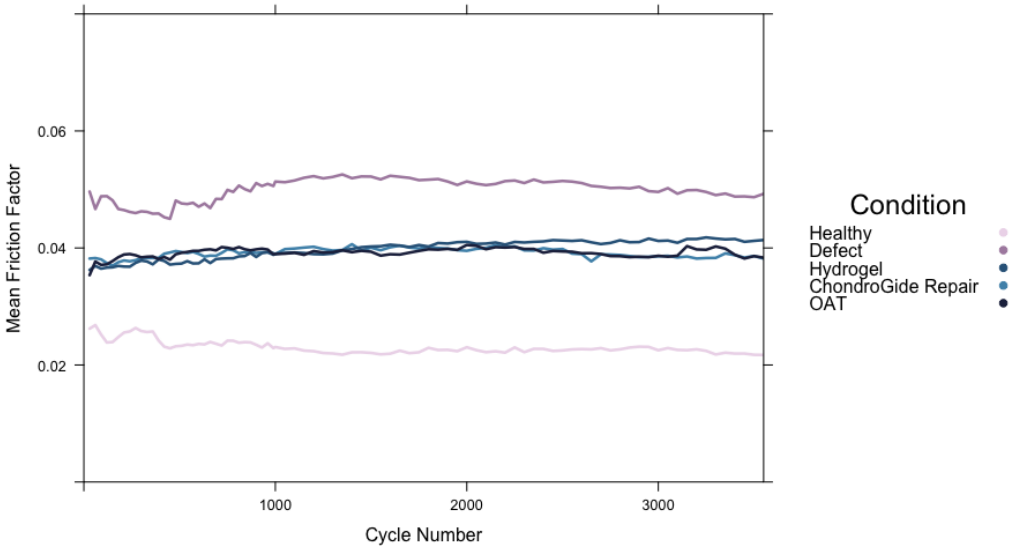

Figure 5.19: Mean friction factor for healthy, defect, 4VBC-MA Hydrogel, ChondroGide® Repair and OAT treatment on the tibiotalar joint during 3600 cycle test on pendulum friction simulator (N=7).

For all three repair methods, the average coefficient of friction measured during the tests were lower than the value obtained for a chondral defect, but higher than the friction coefficient obtained from the native joint. ART-ANOVA showed significant difference between the groups ($p < 0.01$). Post hoc, pairwise contrasts test with Tukey adjustment showed that significant differences can be seen between all conditions ($p < 0.01$) except ChondroGide® repair and the 4VBC-MA hydrogel ($p = 0.11$). 4VBC-MA collagen hydrogel had a coefficient of friction to 0.039 ± 0.0007 which was a similar value to that seen with ChondroGide® membrane and OAT treatment of 0.039 ± 0.002, 0.0039 ± 0.0008, respectively. All three treatments significantly reduced the coefficient of friction compared to the chondral defect ($p < 0.01$).

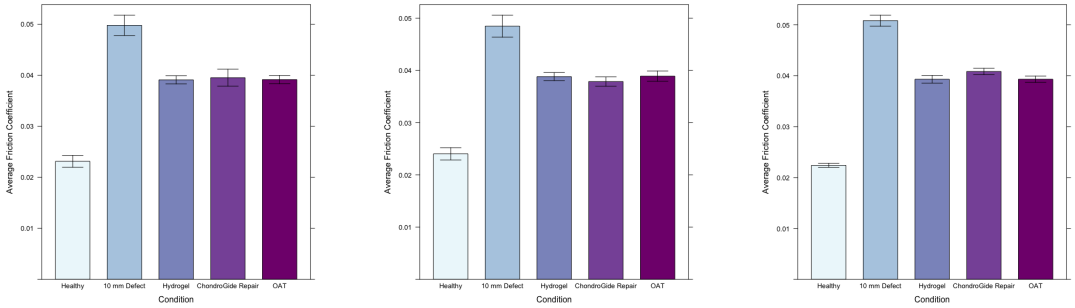

(a) 0 - 3600 cycles (b) 0 - 1200 cycles (c) 1200 - 3600 cycles

Figure 5.20: Mean coefficient of friction during different stages of tribological test with standard deviation. A) Mean coefficient friction during whole test. B) Mean coefficient of friction during the first 1200 cycles. C) Mean coefficient of friction across the final 2400 cycles fo the test.

Figure 5.20 shows the average coefficient of friction during the 3600 cycle test. The coefficient of friction remained constant throughout the test for all of the samples; with no differences seen within the first 1200 cycles and 1201 - 3600 cycles.

Stability of repairs during testing

For all samples, images of the tibia and talar articulating cartilage were taken pre- and post- testing. An example of pre- and post- testing images can be seen in fig. 5.21 and appendix A.3. contains the pre- and post- test images for all samples.

Delamination was seen on the reciprocal tibial tissue for 3 samples after the introduction of a defect (fig. 5.21, fig B.15 & B.17). For most conditions where delamination was seen on the reciprocal tibial cartilage, the tissue appeared to continue showing signs of further damage during testing, even when a treatment was present.

The stability of the 4VBC-MA collagen hydrogel within the defect site did not appear to withstand the testing process as, for most samples, 4VBC- MA collagen hydrogel did not appear intact within the defect site when observed post testing (fig. 5.21). The ChondroGide® membrane remained intact within the defect site for all samples during testing. Some puckering was seen of the membrane around the rim of the defect but the membrane remained stable inside the site (fig B.15). OAT repair stayed within the defect site during testing, with no damage or movement of the core seen in the post testing images. However delamination of the tibial surface was observed after the treatment of OAT (fig. 5.22).

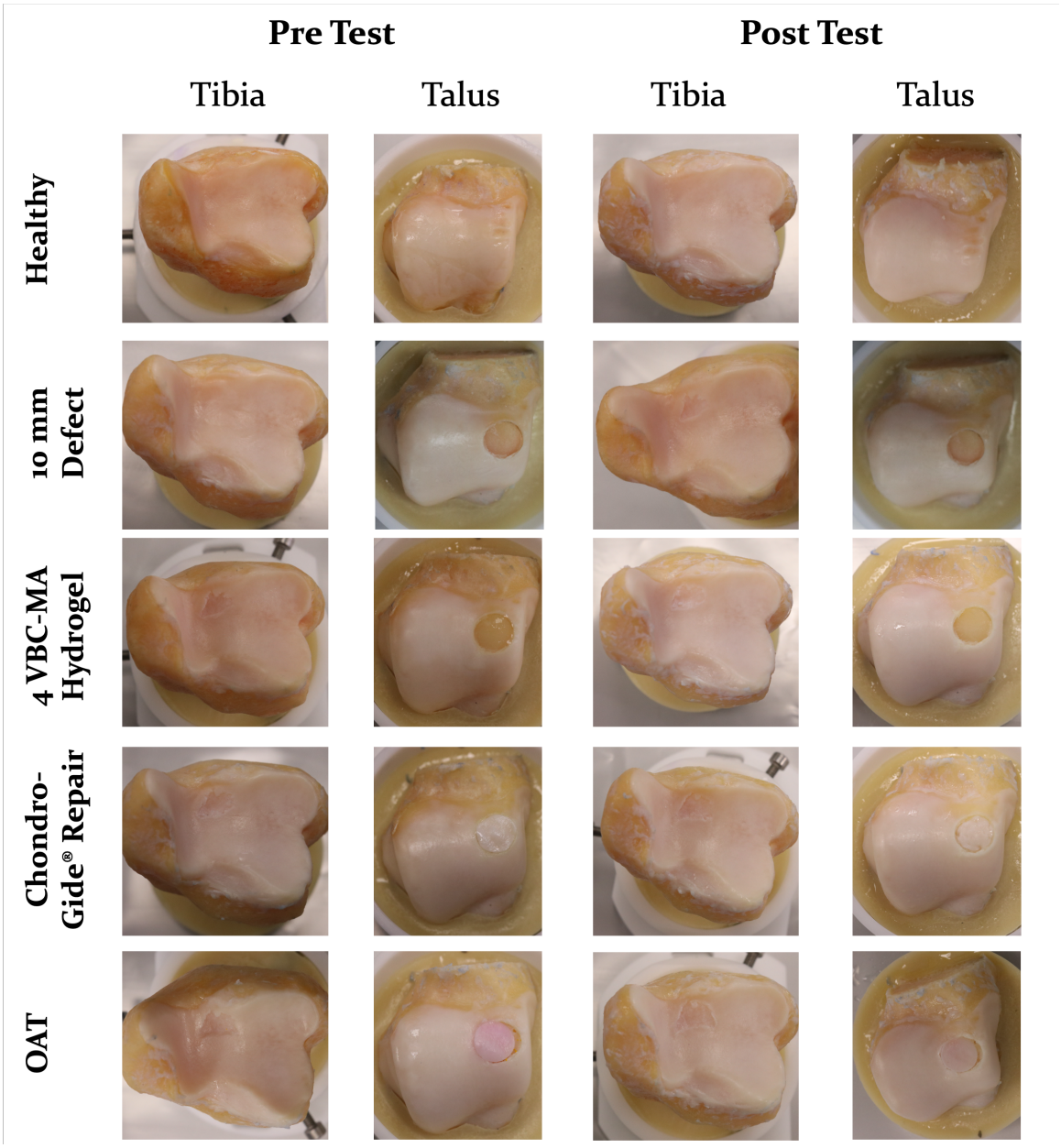

Figure 5.21: Samples of pre and post test photographs of the paired tibia and talar articulating cartilage during tribological testing of conditions. Images show the integrity of the tissues and treatment modalities, documenting damage or changes to the tissue during testing. Damage or delamination of the tissue was can be seen in the tibial cartilage surface after testing with a 10 mm chondral defect.

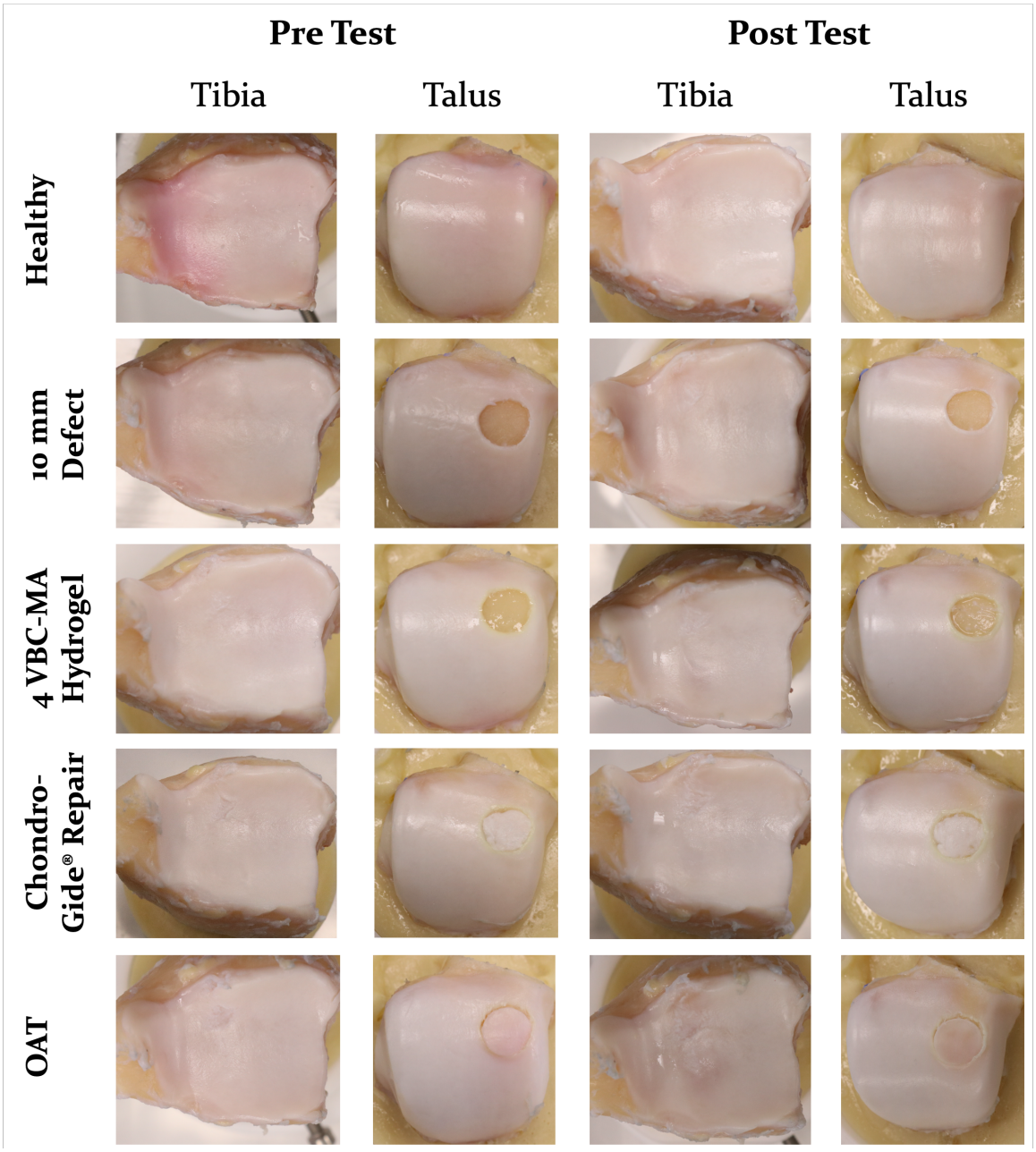

Figure 5.22: Example of pre and post test photographs of a paired tibial and talar articulating cartilage during tribological testing of conditions showing delamination of tibial cartilage caused by OAT repair.

5.4 Discussion

The outcome of the studies presented within this chapter showed that the porcine methodology developed in chapter 5 was successfully translated to cadaveric samples and could show differences between the native tibiotalar joint, chondral defect and the three different treatment modalities

examined.

Analysis of the contact mechanics showed that for all conditions, although variations was observed in peak pressure, mean pressure and contact area, none of the differences were significant for the whole ankle or through regional analysis of the talar dome. This agrees with the previously reported literature which has shown that the introduction of a 10 mm OLT caused no difference in peak stress in the talar joint compared with native tissue (Hunt et al., 2012). However, the same study did see significant difference in contact area of the samples in the 15° plantarflexion condition when loaded with 686 N between the native and defect conditions. They reported peak contact pressures for native tissue and 10 mm osteochondral defect of 2.63 ± 0.23 MPa and 2.59 ± 0.64 MPa, and 2.86 ± 0.67 MPa and 2.69 ± 0.76 MPa for neutral and plantarflexion conditions, respectively (mean ± 95 % confidence interval). Here, lower axial load of 480 N was applied in the neutral position and a peak pressure of 1.79 ± 0.60 MPa and 1.96 ± 0.55 MPa was measured for the healthy and 10 mm chondral defects and for the axial load of 640 N in the plantarflexion condition this study also measured lower peak contact pressures of 1.99 ± 0.53 MPa and 2.30 ± 0.78 MPa.

The study also reported an average contact area of 492 and 368 mm^2 for the native joint in neutral and plantar flexion (Hunt et al., 2012). This is greater then the contact area seen in the current study of 279 and 342 mm^2. The lower contact areas and peak pressures seen within this study compared to that reported in the literature could be attributed to the lower axial load applied. The loads used in this test were selected to represent the load seen through the tibiotalar joint during normal gait, whereas the loads tested by Hunt *et al.*, were selected to represent the body weight of a 70 kg individual. As stress per unit area increases due to increase in axial force, it is expected that the contact area could also increase. Both sets of values for contact area are similar and within the range of those previously reported in the literature of 2.3 - 6.7 cm^2 (Ramsey and Hamilton, 1976).

Increase in mean contact pressure as a result of the introduction of a full thickness chondral defect is supported by the findings of Christensen *et al.,* and Choung *et al.,* (Choung and Christensen, 2002, Christensen et al., 1994). The increase in contact pressure as a result of the introduction of a defect and changes to contact area may initiate an higher amount of strain on the articulating surface that perpetuates the degenerative process leading to further damage and progression into an osteoarthritic disease state.

Lack of significant differences between the samples may be attributed to the redistribution of pressure across the talar dome after the introduction of a 10 mm chondral defect. Due to the congru-

ency of the talar joint and the uniformity of the cartilage, it is believed that biomechanical changes caused by a defect would be redistributed across the talus resulting in the non-significance observed (Shepherd and Seedhom, 1999). Changes to max pressure was not significant when comparing the healthy to defect to treatment (paired t test, p-values = 0.61, 0.77, 0.88). Changes to contact area was not significant when comparing the healthy to defect to condition (paired t test, p-values = 0.86, 0.95, 0.66). This can be seen in changes in loading patterns observed within the pressure maps and contour plots. Introduction of a defect did not cause an increase in the mean max pressure on the tibiotalar joint but caused changes in contact area directly around the defect site, where more contact was seen. A reduction in loading in this region was only achieved when an OAT implant was placed into the defect site. Generally, the effects were pronounced in the plantarflexion as there is increased contact area in this condition compared with the neutral loading condition. Dorsiflexion conditions have the smallest contact area measured and greatest average max pressure observed. This is expected as the load was being applied through a smaller area of contact.

Despite variations in peak pressure being observed between samples, there was no significant differences between groups. The lack of significance could be attributed to the previously discussed compensatory nature of the tibiotalar joint (Shepherd and Seedhom, 1999). With the highly congruent morphology of the joint allowing for redistribution of the load across the talus; indicated by the increase in contact area observed on the talar dome and the similarities in mean pressure across the talar dome. This suggests that the load is displaced, even after the removal of 78.5 mm^2 of tissue.

Although significant differences in contact mechanics could be seen, changes in pressure distribution were observed. These differences were visualised when translated on to contour maps, as seen in figure 5.15 and appendix B.2. As reported, the presence of a chondral defect caused the creation of a new locus of pressure in plantarflexion in the posterior lateral region for some samples (fig. 5.14 & 5.15). This could be related to the ankle appearing to "dislocate" when tested in the pendulum friction simulator resulting in the need for a secondary loading profile. The presence of this region of pressure would introduce force through new area during the flexion stage of the motion arc. This change in loading could affect the normal movement of the joint and the absence of soft tissue or the fibula to stabilise the joint caused the resultant observed dislocation.

Furthermore, it has been previously reported that for patients presenting with chronic lateral ankle instability (CLAI), concomitantly present with chondral or osteochondral lesion of the talus. A systematic review reporting 2145 patients presenting with chronic ankle instability, of the 32.5%

with both CLAI and OLTs, 43% had chondral defects and 68% were located medially (Wijnhoud et al., 2022). Although it is unclear which aetiology initiates the process, CLAI and OLTs are often seen together in patients and this may be attributed to the changes in local contact mechanics causing compensatory load distribution through the supporting structures.

Finally, the new point of pressure was not removed by either the 4VBC-MA collagen hydrogel or ChondroGide® membrane repair but was alleviated by the OAT treatment. Furthermore, regional analysis however, did not show any significant differences between the groups in any of the four regions of the tibiotalar joint, including in either of the medial regions after the introduction of a chondral defect. This could be due to the variability of the pressure distribution seen across samples.

One of the major limitations of past studies assessing changes in contact mechanics associated with treatment methods for OLTs, is the use of pressure sensitive films or transducers to study pressure changes across the cartilage. The uniaxial compression design of the experiments and the fragility of the sensors during articulation prevents the assessment of additional tribological changes. One of the key benefits of the experimental design presented in this study was the concurrent assessment of changes in contact mechanics and tribology of the tibiotalar joint. Thus permitting a greater understanding of the implication OLTs have on joint mechanics.

The outcomes of the tribological study showed that the introduction of a chondral defect caused an elevation in the coefficient of friction and frictional shear stresses experienced by the tibiotalar joint. This resulted in delamination of the reciprocal tibial cartilage in some samples. An increase in the coefficient of friction within the hip or knee joint have been previously attributed to osteoarthritic changes (Jahn et al., 2016). An increase in shear strain in the cartilage can cause disruption to lubrication, which can affect the function and structure of cartilage, and cause upregulation of the secretion of catabolic enzymes that further degrade cartilage via mechanotransduction of stress to the underlying chondrocytes (Blain et al., 2001, Lee et al., 2005, Vincent, 2013). The presence of the 4VBC-MA collagen hydrogel, ChondroGide® membrane or OAT repair significantly reduced the coefficient of friction compared to the defect conditions, but were unable to return frictional properties to that measured in the healthy samples.

Previously, friction coefficients for articular cartilage have been shown to range from 0.002 - 0.5 depending on the loading configuration (Forster and Fisher, 1999, McCutchen, 1962). The low values are thought to be representative of the functional range of frictional coefficient within physiological loading conditions of cartilage-on-cartilage articulation (Caligaris and Ateshian, 2008, Caligaris et al.,

2009). Henak *et al.,* reported that the mean coefficient of friction from talar osteochondral cores ranged between 0.2 and 0.3. However, this measured the coefficient of friction of a cartilage pin sliding against a different counter face, such as sandblasted glass, and also used PBS as the lubricant for the test (Henak et al., 2016). It has been previously reported that PBS, when used as a lubricant, results in an increase in the coefficient of friction for cartilage as it is not able to maintain the biphasic behaviour of cartilage as well as synovial fluid (Schmidt and Sah, 2007). The coefficients of friction obtained in this study ranged from 0.023 and 0.05, these values sit within the range reported for the coefficient of friction obtained for cartilage-on-cartilage articulation. As there are no comparable studies assessing the frictional properties of the natural tibiotalar joint, it is unclear as to whether these values are elevated due to the use of PBS as a lubricant. Additional studies using simulated synovial fluid would permit further investigation into the frictional properties of the tissue.

This is the first study which evaluates whole joint biomechanical testing of cartilage defects and repairs within the tibiotalar joint, instead of solely studying the frictional properties attributed to material-cartilage interactions. A recent study produced by Mahmood *et al.,* in 2020 looked at the coefficient of friction of intact bovine articular cartilage and a 4 mm defect filled wiht a calcium alginate based hydrogel repair. They observed a coefficient of friction of 0.38 for cartilage-on-hydrogel interactions and 0.36 for cartilage-on-cartilage interactions using Ringer's solution at a constant load of 0.06 MPa and 1 Hz (Mahmood et al., 2020). Although the values for the coefficient friction for cartilage-on-cartilage articulation is greater then the value reported in this study of 0.36 compared to 0.002, it is within the expected range for the tissue but is greater than unidirectional pin-on-plate studies (Kuganenderan, 2018). However, the source of the cartilage used within this study is the bovine femur and the mechanical properties of the tissue is not only species dependent but also joint dependent (Delco et al., 2017). Moreover, this study also did not identify any significant differences between the cartilage-on-cartilage or cartilage-on-hydrogel interactions; including measuring the frictional impact of a defect on the cartilage properties.

The methodology presented in this study is preferential compared to pin-on-plate studies as it applies a whole joint approach which allows for anatomical movement of the tissue during testing. Furthermore, due to the biphasic nature of cartilage, damage to surface can affect fluid flow within the tissue. The production of a tissue pin or plate may potentially affect the frictional properties of the tissue and result in the increased observed frictional properties. This may be why a lower coefficient of friction is seen in this study for the healthy cartilage-on-cartilage interaction.

5.4.1 Stability of 4VBC- MA hydrogel within defect

Injectable hydrogel systems provide an attractive approach for cartilage engineering as they are able to be delivered through direct injection or arthroscopically to the defect site. Often injectable hydrogel systems rely on non covalent crosslinking capabilities, in which reversible, non covalent interaction are relied upon to allow for gelation and result in removable sheer-thinning hydrogels (Guvendiren et al., 2012, Vega et al., 2017). The 4VBC-MA hydrogel developed here has a collagen type I backbone with two functional moieties on it. The two functional moieties have both shown to have properties that inhibit the activity of MMP family *in situ* and have resulted in improved healing capabilities for chronic wound treatment (Tronci et al., 2016). They also allow for photopolymerisation of the hydrogel *in situ*. One of the benefits of photopolymerisation is that the crosslinking reaction is unaffected by water because it utilises the generation of free radicals through exposure of a photoinitiator to the vis-light. This reaction is therefore controllable both temporally and spatially, with the physical crosslinking occurring as a rapid process within a couple of minutes. It can be seen that the 4VBC-MA collagen type I hydrogel was able was able to successfully completely fill the defect site and conform to the congruency of the talus (fig. 5.13). Further studies should be performed to assess the interface between the hydrogel and the defect site through histology or SEM imaging to assess the hydrogel-defect interface.

Performance of 4VBC-MA Hydrogel compared with current therapeutics

When comparing the performance of the 4VBC-MA hydrogel with the other two current clinical treatment modalities, ChondroGide® membrane and OAT treatment, the 4VBC-MA hydrogel displayed no loading through the gel, whereas the OAT treatment displayed pressure distribution through the defect site. The contour maps showed that pressure also was measured through the ChondroGide® membrane. However, all three treatments resulted in the similar coefficient of frictions measured consistently throughout the 3600- cycle test (fig. 5.19). All three conditions significantly reduced the coefficient of friction seen for the chondral defect, but not to the level seen in the native tibiotalar joint.

Pre- and post-test imaging showed stability of the ChondroGide® membrane within the defect site but not of the 4VBC-MA hydrogel (fig. 5.21). Although 4VBC-MA collagen hydrogel did not appear to remain within the defect site at the end of the test, the consistency and maintenance of

the frictional coefficient throughout the test, and the absence of an increase in friction to a value similar to that seen in the defect samples, suggests that the hydrogel was able to stay in the defect site during testing and that removal of the lubricant PBS or separation of the tibiotalar joint at the end of the test may have damaged the gel. Clinically, repair of a defect with a hydrogel will be performed in a similar way to microfracture/ChondroGide® in which open surgery would be performed and the joint capsule would be opened to debride the site. Therefore, it is not expected that a second joint distraction would take place. Thus the forces that the gel experience when the joint was separated would not occur. In addition, the amount of fluid present in the tibiotalar joint capsule is not comparable to the volume of liquid used in the simulator to provide lubrication and hydration for the tissue during testing.

This study did not account for additional shear forces introduced into the system. The axial load applied through the tibia was intended to be a more physiologically representative load. This higher load would result in increased shear stresses seen within the defect, at the interface of the hydrogel-defect and the hydrogel-lubricant fluid. The high volume of fluid present in the PBS bath used to lubricate the test is much greater than the volume experienced in the natural ankle joint; with the maximum volume of liquid that the natural, healthy ankle joint has been reported to range between 16- 30 ml (Draeger et al., 2009). The increased amounts of fluid present may have further caused damaged to the hydrogel resulting in the post-testing images seen.

Within this study, the 4VBC-MA hydrogels mechanical properties were assessed as an acellular scaffold. Scaffolds face the challenge of mimicking the anisotropic, non-linear and viscoelastic biomechanical characteristics of native cartilage whilst also providing an environment for cell growth and differentiation (Moutos and Guilak, 2010). Studies have shown cellularisation of a scaffold can cause changes to both stiffness and the coefficient of friction. Friction testing has previously shown that cellularised scaffolds demonstrate an increased coefficient of friction compared to their decellularised counterparts (Accardi et al., 2013). A PCL scaffold showed a non-significant increase in the coefficient of friction from 0.96 $\pm$ 0.11 which to 1.25 $\pm$ 0.09 attributed to the cellularisation of the scaffold. But this also coincided with a significant decrease in the Young's modulus from 162 $\pm$ 33.30 to 139.66 $\pm$ 5.30 ($p < 0.05$). Furthermore, it is believed that tissue engineered articular cartilage does not display the low friction coefficients seen at the initial loading times as that seen with natural tissue as the material presents with only boundary lubrication regimes resulting in a reduction in coefficient of friction over time. However, this may be material dependent as no differences were reported in the friction coefficient of cellularised or acellular alginate hydrogels (Gleghorn

et al., 2007).

This could be attributed to material composition, fibre orientation and many other factors seen within hydrogels. As cells begin to remodel their surrounding pericellular matrix and deposit ECM components the frictional properties may change. Gleghorn *et al.,* showed that lubricin, a key glycoprotein mediator attributed to the friction properties present at the load bearing articulating surface, was secreted by chondrocytes within alginate constructs after 6 weeks but this was shown to not have a significant effect on the friction coefficient (Gleghorn et al., 2007). In addition, the frictional properties may change over time. A fibrinogen sponge hydrogel containing chondrocytes displayed a decrease in the friction coefficient after 7 days of cultivation in the coefficient of friction (Morita et al., 2006). This was greater than that observed for native porcine tissue. This decrease was attributed to the production of chondroitin sulfate which aids as a water attaching component of the ECM. Therefore, permitting the presence of a high water content layer at the top of the material. This could behave like the interstitial fluid present at the boundary of the tissue, thus mimicking the fluid dependent frictional properties of cartilage. Thus creating the hydrophilic layer which improves the frictional properties of the material (Morita et al., 2006). Future work could be performed to study the changes in the frictional properties of cellularised 4VBC-MA hydrogels to assess changes in the tribological performance of the material.

5.4.2 Osteochondral core treatment

For all specimens tested in this study, the osteochondral core was implanted into the defect site by a foot and ankle surgeon. The clinician implanted the core ensuring that it was flush 'to the touch' and thus assumed congruent with the surface of the talar dome. This ensured that implantation process of the core was comparable to clinical practise. The efficacy of osteochondral cores have been presented in multiple studies (Choung and Christensen, 2002, Fansa et al., 2011, Latt et al., 2011). One of the key features reported about osteochondral graft treatments is that it is able to restore the hyaline cartilage surface congruity, and the weight bearing capabilities of the articular talar cartilage (Choung and Christensen, 2002). The results of this study have shown that osteochondral cores were the only treatment tested that were able to successfully return load through the treated defect site. This is in agreement with the previous literature, supporting that both single implantation of osteochondral cores and multiple cores through mosaicplasty approaches are able to successfully allow for contact to return to the talar defect (Choung and Christensen, 2002, Fansa et al., 2011,

Latt et al., 2011).

Within this study, OAT was unable to return the contact mechanics to that seen in the healthy ankle. This was most likely caused by incongruity of the graft causing it to sit proud with the articular surface. Small differences in congruity potentially caused the decrease in contact area compared to the healthy sample, which was more pronounced in the neutral position and the plantarflexion positions where average total contact area reduced from 279.1 ± 82.6 mm^2 to 270.4 ± 79.2 mm^2 and 342.1 ± 145.6 mm^2 to 320.8 ± 131.8 mm^2, respectively. This can also be seen in the contact pressure maps, where the OAT repair allowed for loading within the defect site but the contour maps showed a changed in the area of contact.

When the core was not flush to the surface of the talus, it caused an irregular loading pattern, as seen in fig 5.14 within both neutral and plantarflexion position. This introduced a point of increased contact pressure in the sample, resulting in changes to the loading profile and distribution across the talus. This additional loci of stress may result in further reciprocal damage (seen in fig. 5.21) through abnormal loading. As the 10 mm cores were pre-produced for clinical use in allograft treatment the curvature of the core could not be chosen to compliment the tissue perfectly, as is often done when be harvested from an autograft. The lack of complete congruity could result in new areas of contact, and if the core is elevated, prevents loading in the surrounding area. This potentially creates areas of increased contact pressures. However, partial restoration of contact mechanics has been observed when grafts were placed in the most congruent position. No significant differences were seen with contact mechanics of the ankle joint if the graft was flush, proud or sunken (Fansa et al., 2011). They attributed the differences to variation in structural properties of the donor cartilage (Fansa et al., 2011). Latt *et al,.* performed a cadaveric study which assessed the effect of graft elevation and recession on contact pressure. The saw that recession of the graft causes transfer of pressure to the opposite facets of the talus, as seen within the defect samples in this study. Elevation of graft was reported to cause a significant increase in contact pressure, whereas, recession of graft caused significant decrease in contact pressure (Latt et al., 2011). In addition, the reported impact of OAT height has greater impact on lateral side compared to medial side. Regional analysis of the talus showed that in the plantarflexion condition, changes in contact mechanics were more pronounced on the anterolateral region of the ankle, but these differences were non-significant (fig. 5.18).

Osteochondral allografts are considered to be one of the only current treatments that is able to restore healthy articular cartilage and provide a low friction and wear resistant surface. The

data presented in this study showed that the reduction in coefficient of friction in OAT repair is comparable to coefficient of friction seen with other alternative scaffold based treatments such as ChondroGide®. The lack of complete congruity with the graft and the articulating surface may also result in a higher coefficient of friction being obtained for OAT treatment compared to the intact tissues.

The source of the graft tissue can have implications on the mechanical properties of the repair. Acquisition of autogenic tissue for osteochondral cores often occurs from regions of the femur such as the superomedial and superolateral trochlear groove. Clinicians must select an area of donor tissue that follows the congruity to ensure that contact mechanics of the talar joint are unaffected by the repair. However, the tribological properties of the tissues have been shown to show significantly lower coefficient of friction (Henak et al., 2016). This may result in the tissue having inferior mechanical properties compared to the native tissue and thus reducing the success of the treatment. Additional testing could be performed using the methods presented in this chapter to study the changes in the frictional coefficient using different sources of osteochondral cores to increase our understanding on the implications of the source material.

5.4.3 Limitations

It is evident that the outcomes of both the contact pressure and tribological assessments are able to provide insight into changes in the behaviour of the tibiotalar joint as a result of the presence of a chondral defect and subsequent repair methods.

One of the key challenges associated with the data collected here is the high degree of variability seen in natural tissue. This is visually represented by the differences in the pressure maps generated and the variability of the tissue. The lack of significant differences seen within the contact mechanics for the difference conditions may be attributed to the variations in contact patterns across the different tali; as the methodology has defined plantar- and dorsiflexion values tested rather then scaling the range of motion for each sample. Thus loading occurred at 15° plantarflexion or dorsiflexion. Loading in the dorsiflexion condition resulted in small contact regions, often with no contact being seen in and around the defect region. An alternative is to reduce the level of flexion and extension tested. The natural ankle does show dorsiflexion angles of this range, as the ROM for tribological testing was reduced to ± 20°. Accepted range of motion within human tali is 40 - 50° and 10 -

20 ° for plantarflexion and dorsiflexion, respectively, but this has been reported to be as low as 30° when walking (Brockett and Chapman, 2016, Nordin and Frankel, 2001, Roaas and Andersson, 1982). Furthermore, population and age can have an impact in the ROM measured. Both age and gender have been shown to affect the reported ROM of the ankle in dorsiflexion and plantarflexion (table 5.8)(CDC, 2023). Therefore the range used for contact mechanics was within the values experienced by the natural joint, however, may represent more extreme levels of dorsiflexion. The increased level of dorsiflexion tested also resulted in smaller areas of contact for most samples at 630 N 15° E for most samples.

Table 5.8: Reported range of motions for ankle joint dorsiflexion and plantarflexion separated by sex and age (mean ± 95 % CI) (CDC, 2023)

Age Range	**Motion**	**ROM°**	
		Female	**Male**
9 - 19	Dorsiflexion	17.3 ± 1.7	16.3 ± 1.4
	Plantarflexion	57.3 ± 2.5	52.8 ± 2.0
20 - 44	Dorsiflexion	13.8 ± 0.9	12.7 ± 1.1
	Plantarflexion	62.1 ± 1.5	54.6 ± 1.4
44 - 69	Dorsiflexion	11.6 ± 1.0	11.9 ± 1.0
	Plantarflexion	56.5 ± 1.5	49.4 ± 1.7

Another limitation of this study is the lack of supporting tissue or constraints present to ensure alignment of the natural joint. The fibula is able to to inform the placement of the tibia and the talus, especially in preventing the joint sliding out due to changes in contact pressures as a result of the presence of chondral defects or repairs. The fibula may have reduced the need to change flexion extension motion arc used to test the samples. The increase in the frequency of testing profile may have affected the frictional properties of the tissue, as cartilage frictional properties change during loading due to the viscoelastic nature of the tissue (Wang and Ateshian, 1997). Therefore the increased frequency of the motion arm may put additional stress on the tissue causing an increase in frictional properties. However, misalignment caused by instability introduced by a defect or a repair and the lack of constraints can further cause the ankle to move out of position resulting in the malalignment of the joint surfaces. This may introduce new areas of contact and therefore change the joint tribology. In addition, supporting structures may act as additional dissipation modes for friction and loads therefore resulting the measured values of coefficient of friction for the articular cartilage being elevated compared to the values that actually occur within the intrinsic tibiotalar joint (Jahn et al., 2016).

5.4.4 Clinical implications of study and conclusions

To the authors knowledge, this is one of the only studies which assesses the coefficient of friction directly between the talar dome and the reciprocating articular cartilage, testing repairs and treatments. Most other studies have measured the coefficient of friction of plugs obtained from the cartilage using a multiaxial compression and shear testing (Accardi et al., 2013, Gleghorn et al., 2007, Henak et al., 2016, Mahmood et al., 2020, Wang and Ateshian, 1997). The work presented here represents a pivotal study and methodology for testing future potential replacement biomaterials for articular cartilage. Furthermore this appears to be the only study that assesses the ability of repairs to treat osteochondral defects in the talus and to assess both the biomechanics and tribological performances.

Clinical insight was sought during method development stages and with the implantation of the osteochondral grafts to improve validity of approach and ensure clinical relevance of studies. The findings of this work supports the hypothesis that introduction of a defect in the tibiotalar joint causes increases in coefficient of friction resulting in reciprocal delamination of the tibial tissue. That talar cartilage is able to redistribute load across the talar surface when a lesion is present acting as method of protecting the tissue and preventing new peak stresses. Within the literature, it has been shown that OLTs often do not progress into symptomatic ankle OA (O'loughlin et al., 2010). This could be due to the lack of focal points of excessive contact stresses surrounding the defect or on the talar dome. This redistribution of load could be the preventative, compensatory mechanism present in the ankle resulting in the primary cause of ankle OA being a product of traumatic injury rather then a progressive degeneration of the joint, as seen in the hip and knee (Herrera-Pérez et al., 2021).

Differences in energy dissipation, changes to the shear modulus and changes to the coefficient of friction will have implications on the success and longevity of treatment (Henak et al., 2016). Osteochondral grafts are the only treatment that was able to immediately provide full thickness hyaline cartilage, allow for loading to occur through the defect site and also reduce the friction coefficient. However, the ability to place the graft to ensure congruency with the surrounding cartilage tissue is imperative for the success of such treatments. If the tissues surfaces are malaligned it can cause further reciprocal damage to the inferior tibial articulating surfaces. The novel 4VBC-MA hydrogel performed as well as the AMIC treatment using a ChondroGide® membrane and Tisseel® sealant. Both materials were unable to provide reloading through the repaired defect site but were able to reduce the coefficient of friction for the tibiotalar joint compared to the defect

and to a similar value seen for the OAT repair. This indicates that the 4VBC-MA collagen type I hydrogel performed comparably to the AMIC treatment.

Finally, this is the first study to have to tested a complete true ankle joint to measure its frictional properties. It has been shown that the composition of talar cartilage is different to that seen in the knee and hip, therefore, understanding differences in the biotribological properties of these joints is crucial in translating treatments throughout the body; in particular to the ankle joint. The combined insight presented in this study will allow for a better understanding of how a single traumatic event and the presence of an OLT can change the biomechanical and tribological behaviour of the ankle joint, causing progressive damage through changes in loading and frictional properties. Thus resulting degeneration of the joint and progression to an osteoarthritic state. It also provides a platform for future work to assess both the tribological and biomechanical properties of OLT treatments for more targeted treatments.

Chapter 6

Exploring the Effect of Clinical Factors of Defect Size and Location

6.1 Introduction

The talar dome has a high incidence of osteochondral lesions with a range of locations and sizes having been previously reported (Götze et al., 2021, Hurley et al., 2021, O'loughlin et al., 2010). Traditional treatment of symptomatic OLTs have included reparative treatments or replacement based procedures. Management of OLTs is not currently standardised, with much of the literature defining treatment choices based on the size or location of lesion (Hurley et al., 2021). Smaller lesions ($<$ 10 mm) favour minimally invasive treatments such as microfracture, medium lesions (10-20 mm) have shown positive results for OAT, PRP and scaffold based treatments and large lesions strategies ($>$ 20 mm) include requiring treatment such as bulk tissue transplantation and talar resurfacing (Hurley et al., 2021). Prognostic factors that can affect the repair methods seen for OLTs include lesion size, location and type; with all three of these factors affecting the choice of treatment and the success rates discussed clinically. In most cases short- and medium-term results have been reported with a noticeable lack of basic science understanding of treatments and outcomes of long term studies (Gianakos et al., 2017, Murawski and Kennedy, 2013). Reported clinical success for different treatment modalities vary within the literature with mid-term results reporting good to excellent outcomes for 46 % - 100 % of patients (Hannon et al., 2014).

AMIC is scaffold based treatment that has many benefits over other treatments presented within the ankle joint. This is because it does not require a harvest or donor site, cell expansion and can be performed in single surgical session. Furthermore, it exploits the regenerative potential of bone marrow stimulation whilst covering the lesion with a resorbable membrane or matrix that can stabilise the clot to promote regeneration and repair of the tissue (Götze et al., 2021, Migliorini et al., 2021). AMIC has shown favourable outcomes as a treatment and is becoming more commonly used in clinical practise.

Through developing the work previously described with a clinician, Mr Mark Farndon, further application of the techniques were identified to help progress clinical understanding of treatments for less commonly studied lesions seen within the body and to inform current clinical practise. Through these discussions some key areas of interest were identified involving lesion size, lesion location and AMIC treatments. These included studying larger lesions assessing whether a circular or square shaped debridement and AMIC repair is preferential and assessing lesions where AMIC treatment is less favourable as an approach.

Outcomes of previous studies have shown that lesion size can affect the contact mechanics within the ankle joint with increasing lesion size showing a reduction in contact area, shift in the loci of peak stress and a change in joint stability (Hunt et al., 2012, Li et al., 2022). Both studies tested lesions of a maximum diameter/width of 12 mm and observed the highest contact stresses for this condition. However, clinically, mid size lesions may be up to 20 mm. Therefore there is a paucity in understanding mechanical characteristics in larger lesions and how the underlying frictional properties of the tibiotalar joint might change as a result of these large defects.

Two types of lesions less commonly discussed in OLT management studies include shoulder lesions and kissing lesions. Current literature suggests that shoulder lesions display poorer clinical outcomes when treated with BMS or microfracture. AMIC treatments is a key surgical intervention used for the treatment of shoulder lesions, with small cohort studies showing positive outcomes in the midterm (Götze et al., 2021, Migliorini et al., 2021).

The tibiotalar joint contains two key articulating surfaces. The first of which is the talar dome and second tissue is the tibial plafond. Kissing lesions is a term used to described coexisting lesions present on both the articular cartilage of the talus and the tibial plafond; which match each other or come into contact during normal joint movement. The presence of a kissing lesion in many studies results in that patient data being excluded (Butler et al., 2021, Jantzen et al., 2022). Studies that

have assessed the clinical outcomes of kissing lesions have shown poorer outcomes for microfracture (Hurley et al., 2021, Ross et al., 2014).

6.1.1 Study Aims

The aim of this study was to further translate the methods developed through Chapters 4 and 5 for the assessment the biomechanical changes associated with different clinically relevant defects commonly identified within the literature to inform clinical practise. Changes in contact stress, pressure and friction caused by a defect or its subsequent repair may lead to direct surface degradation or negatively affect the mechanical properties of the joint. Therefore, developing an understanding of the mechanical forces at play and the impact and stability of a repair within a defect could be used to inform decisions for surgical interventions using pre-clinical findings to support clinical literature and practise.

The aims of this investigation were achieved through the following objectives:-

1. Assessment of the biomechanical and tribological changes of the natural tibiotalar joint under a simplified walking gait using the following conditions:
   (a) Large circular defect
   (b) Large square defect/debridement shape
   (c) Shoulder lesion
   (d) Kissing lesion
2. Evaluate the ability of AMIC treatment to repair the defects.

The experimental values obtained for the natural tibiotalar joint for a healthy condition obtained in Chapter 5 will be used as a negative control for the discussion of these studies, where appropriate.

6.2 Methods

6.2.1 Specimen preparation and defect generation

Different sizes, shapes and location of defects were assessed within this study. These included:

1. 16 mm large circular defects
2. 16 mm square defects
3. 16 mm shoulder defects
4. 10 mm kissing lesions

Sequential testing was used to test both the large circular defect and the large square defect. Figure 6.1 shows the testing process for these samples.

All tissue used for this study were provided by Joint Operations Ltd. (UK) and work was conducted following local ethics (MEEC20-031). Cadaveric tissue had an age range of 19-30 years old. Defects were generated by the surgeon prior to cementing of the samples following modifications of the techniques described previously section 5.2.6. Modifications of the techniques are described below in the relevant sections. Centre of rotation and cementing of each sample was performed using the technique described in chapter 5.2.3.

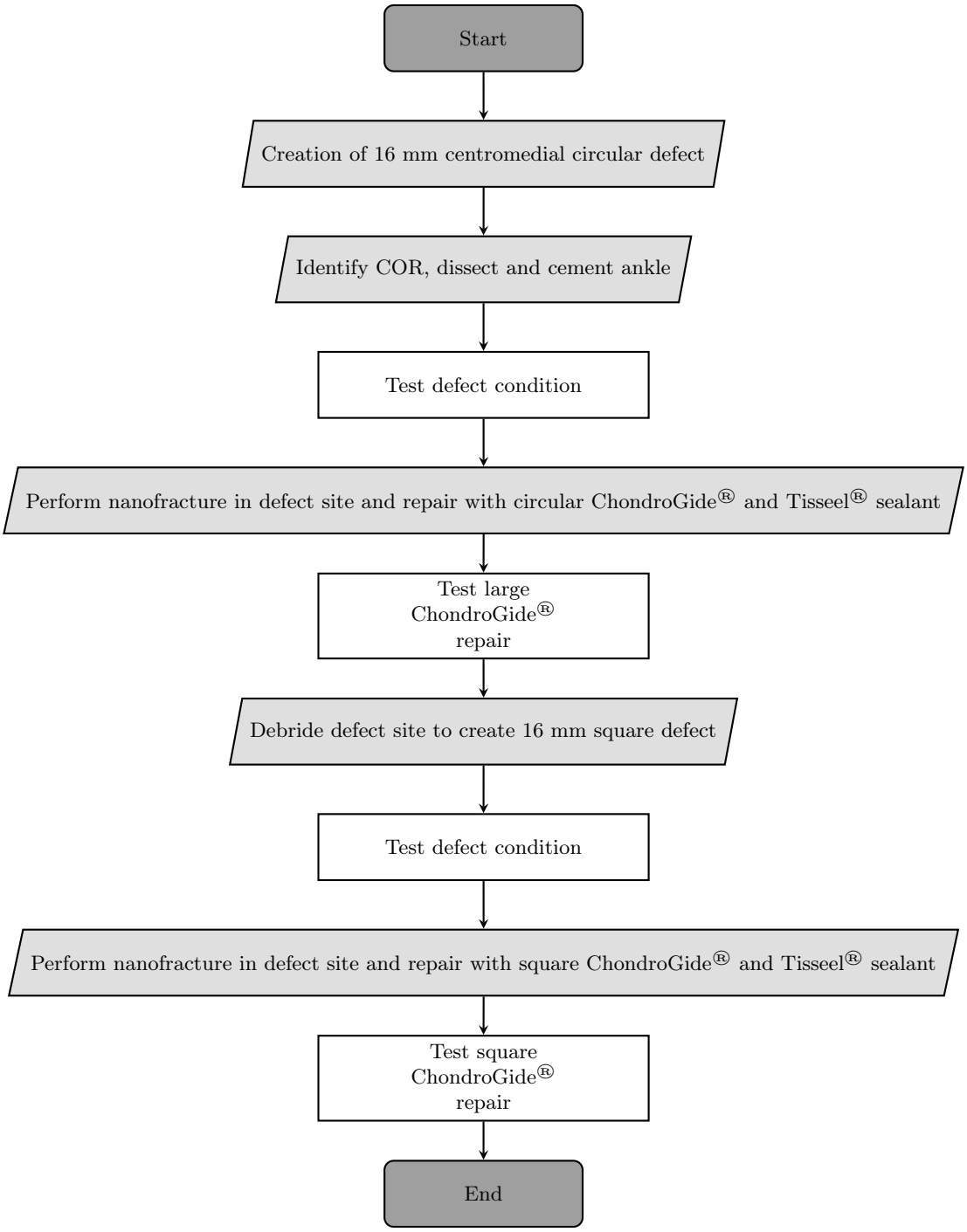

Figure 6.1: Flow chart of experimental testing sequence used for the larger circular defects and large square defects.
Flow chart shows the intended tissue processing and testing methodology used for each sample to test through the following test conditions: large circular defect, large square defect and the ChondroGide® with Nanofracture and Tisseel® of both defect sizes and shapes. The centre of rotation (COR) was determined for each sample prior to testing but after initial defect generation. For all conditions the testing process included both uniaxial compression and friction testing of samples.

6.2.2 Large circular and square defects

Seven healthy cadaveric tibiotalar samples were taken and an initial 16 mm circular defect was made as previously described in section 5.2.6. A 16 mm circular dye was used to mark the centre of talar dome and cartilage was excised. Samples were tested using the friction and compression methods described in section 5.2.4 and 5.2.5. Loading profiles for the samples can be seen in table 6.1. These were determined experimentally by identifying flexion and extension angles within the ProSim Pendulum Friction Simulator (Simulator Solutions, Manchester UK) that the joint was able to articulate completely through the motion arc without dislocating. Due to the size and location of the defect, the extension of the swing was favoured to as it maintained natural joint motion and stability throughout the test. Nanofracture was performed on the defect site and the site was repaired with a circular ChondroGide repair using the same method described in 5.2.8. This was then tested using the same uniaxial compression and friction testing process. ChondroGide® repair was then removed and residual Tisseel® was cleared from the defect site. Additional cartilage was excised from the edge of the defect to create a square defect. The diameter of the circular defect was used to guide max width and length of a defect to create a 16 mm $\times$ 16 mm square defect in the site. The square defect was then tested using the same methods as previously described and then repaired with Nanofracture, Tisseel® and ChondroGide® and tested again using the same testing profiles.

Table 6.1: Pendulum friction simulator sample profiles for large defect studies
Initial and secondary flexion and extension input values

Samples	Flexion(°)	Extension(°)	Frequency of Swing (Hz)
1	10	10	1.0
2	10	10	1.0
3	5	15	1.0
4	15	5	1.0
5	5	15	1.0
6	5	15	1.0
7	10	10	1.0

6.2.3 Lateral shoulder lesion

For n=7 cadaveric tibia and talar samples, a square shoulder lesion was created on the medial edge of the talar dome extending onto the articulating surface of the medial malleolus. The total dimensions of the defect was 16 mm x 16 mm. Lesions were generated following a similar method as described in

section 5.2.6. Samples were tested using the friction and compression methods described in section 5.2.4 and 5.2.5. Loading profiles were determined as described in section 5.2.5 for the samples and can be seen in table 6.2. Nanofracture was performed on the defect site on both the talar dome and the medial malleolus. AMIC repair was performed on the defect site using a hydrated square ChondroGide® membrane and Tisseel® using the method described in 5.2.8. This was then tested using the same uniaxial compression and friction testing process.

Table 6.2: Pendulum friction simulator sample profiles for shoulder lesion studies
Initial and secondary flexion and extension input values

Samples	**Flexion(°)**	**Extension(°)**	**Frequency of Swing (Hz)**
1	10	10	1.0
2	4	10	1.43
3	5	15	1.0
4	5	15	1.0
5	7	7	1.43
6	7	7	1.43
7	10	10	1.0

6.2.4 Kissing Lesions

Kissing lesions were created in a two step procedure. Initially a defect was created onto the centromedial region of the talar dome as described in section 6.2.6. A reciprocal imprinting technique was used to mark the tibial cartilage with a circle based on the location of the talar defect. Ink was placed around the rim of the talar defect and the tibia and talus were manually aligned in a neutral position. The ink was transferred on to the tibial cartilage. This mark was used to inform the location of the 10 mm cutting dye to create the template for the chondral defect on the tibial plafond. Chondral defects were prepared as described previously and nanofracture was performed on the samples post defect creation. Samples were tested using both the friction and compression methods (section 5.2.4 and 5.2.5). Flexion and extension arc and frequency of swing for the friction simulator for each sample can be seen in table 6.3. AMIC repair was performed on both the tibial defect and the talar defect using a hydrated 10 mm circular ChondroGide® membrane and Tisseel® fibrin glue following the method described in 5.2.8. Samples were then tested using the same uniaxial compression and friction testing process.

Table 6.3: Pendulum friction simulator sample profiles for kissing lesion tests
Initial and secondary flexion and extension input values

Samples	**Flexion(°)**	**Extension(°)**	**Frequency of Swing (Hz)**
1	7	7	1.43
2	10	10	1.0
3	10	10	1.0
4	10	10	1.0
5	5	15	1.0
6	10	10	1.0
7	4	10	1.43

6.2.5 Data and Statistical Analysis

Data analysis was performed as described in Section 4.2 for both the data collected from friction simulator and uniaxial compression testing. Overall summary statistics were calculated studying the means and standard deviations for all samples.

Statistical analysis was performed to assess for normality data using the Shapiro-Wilks tests and variance of the tests were assessed using box plots and Levene test between the groups. Based on the outcomes of these tests, samples were shown to be normal or non-normal distribution of data. For the studies involving more than two groups, ANOVA and its variants were selected to analyse the data. One-way ANOVA, Friedman tests or ART ANOVA were selected to perform statistical analysis of the data depending on the normality. Paired T-tests were performed when comparing two samples to assess differences in mean. Statistical significance was demonstrated by $p < 0.05$. Tukey's HSD *post hoc* test and contrast tests were performed where the outcomes were significant.

6.3 Results

6.3.1 Large circular and large square defects and their repairs

Uniaxial compression testing was performed on samples (n=7) for large circular and square defects and their subsequent repairs. The defect area for the large circular defect was 201 mm^2 and 256 mm^2 for the square defect. Heatmaps were generated for each testing and loading condition. A sample of the compression profiles generated from the pressure sensor can be seen in figure 6.2 and in appendix C (figs C.1 - C.7). Changes in contact area was visibly assessed using the generation of a contour map showing where contact was measured on the pressure sensor (sensels value > 0). Samples of contour maps can be seen figure 6.3 and appendix C (fig. C.8 - C.14).

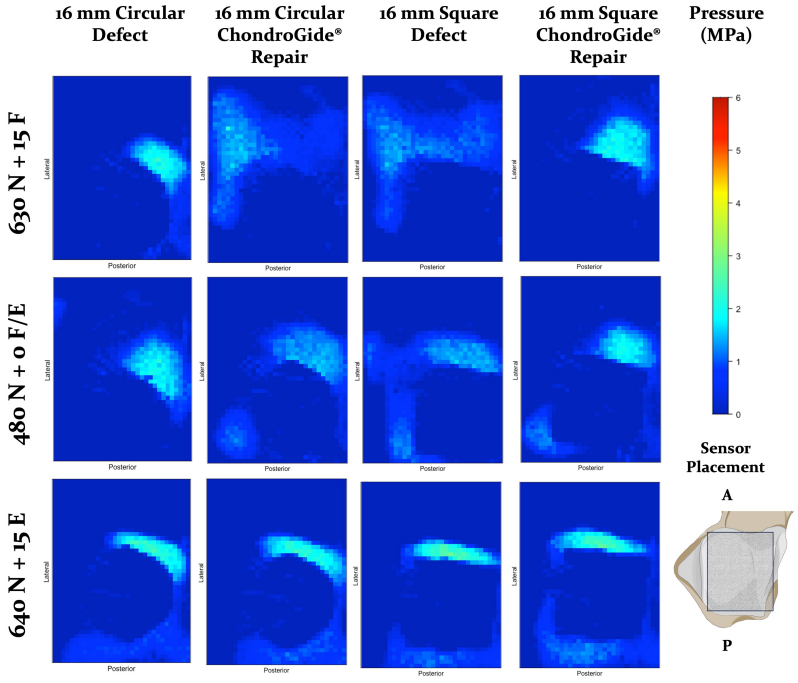

Figure 6.2: Sample of pressure maps showing contact area and distribution pressure for each loading condition for across the talar dome. Image show sample of pressure maps for one sample looking at pressure distribution across the talar dome for each condition (left to right) 16 mm circular defect, 16 mm Circular ChondroGide® repair, 16 mm square defect and 16 mm Square ChondroGide® repair. A = Anterior, P = Posterior.

For most samples, loading can be seen around the edge or rim of the large circular defect, with changes in loading pattern visible between the circular and square defects. Loading patterns differed between the samples and the different testing conditions, however, no visible trends were observed with no new regions of contact visible consistently between samples. Only one sample appeared to

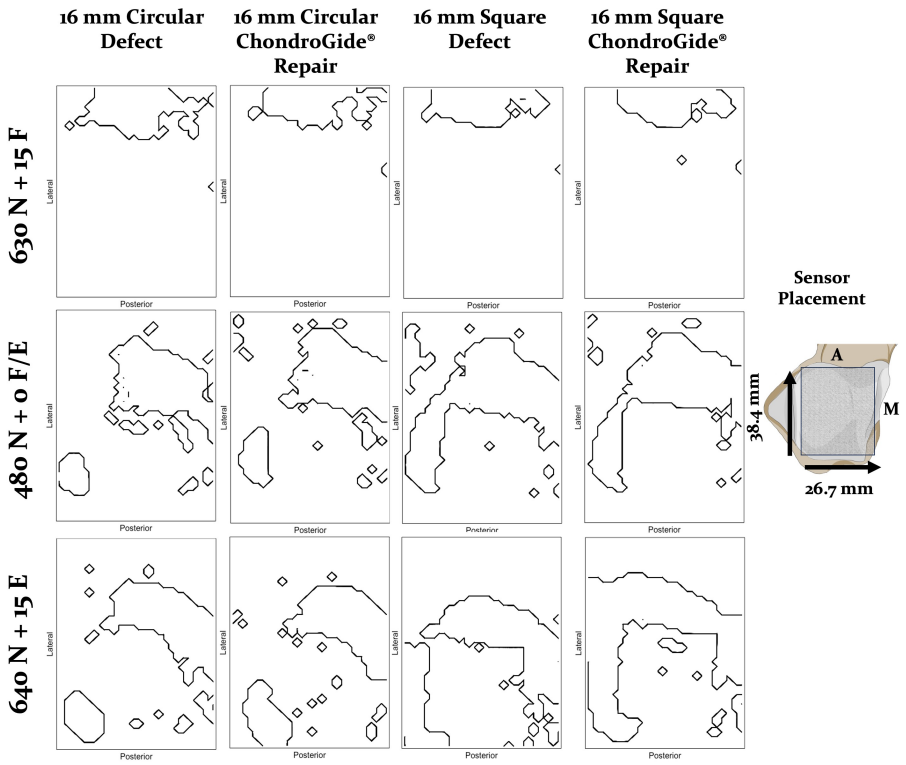

Figure 6.3: Sample of contour plots showing contact area across the talar dome for each condition. Samples of contour plots generated from one specimen showing areas of contact on the talar dome for each condition (left to right) 16 mm circular defect, 16 mm Circular ChondroGide ® repair, 16 mm square defect and 16 mm Square ChondroGide ® repair. Region mapped represent a 38.4 x 26.7 mm area on the talar dome. A = Anterior, M = Medial.

show loading through the square ChondroGide® membrane repair at neutral and 15° plantarflexion conditions (fig. C.6). Two samples showed an increase in contact pressures as a results of treatment of the circular defect with a circular ChondroGide® membrane (fig. C.4 & C.6). Contour plots generated showed that shape of the defect and how the AMIC repair altered the contact distribution across all conditions but no visible trends were observed between samples.

Quantifiable changes to contact pressure and area were measured using a pressure sensor. The highest pressure was seen for the large circular ChondroGide® repair with a maximum observed pressure of 2.42 ± 1.10 MPa, 2.90 ± 1.45 MPa and 2.95 ± 1.33 MPa for 15° dorsiflexion, 0° neutral and 15° plantarflexion loading conditions, respectively (table 6.4). This was coupled with the largest inter-sample variation was seen within the circular ChondroGide® repair group (fig. 6.5). Max contact pressures for all other testing conditions were similar (fig. 6.5a). No significant differences were seen for max contact pressure for 15° dorsiflexion and 0° neutral conditions (Friedman, $p = 0.63$ and $p = 0.18$, respectively). Significant differences were seen in max pressure at 15° plantarflexion

(One-way ANOVA $p = 0.04$) where post-hoc Tukey's HSD showed that a significant differences were measured between the circular defect and circular repair.

Significant changes were measured in the mean contact pressure at 640 N 15° E between the circular ChondroGide® repair and the square ChondroGide® repair (One-way ANOVA with Tukey's Post Hoc test, $p = 0.02$). Highest mean contact pressure was observed for the circular ChondroGide® repair (table 6.5). Mean contact pressure across the other three samples were similar with lowest pressures seen for the square ChondroGide® repair (fig. 6.4b). This also corresponds with the largest measured contact area for 15 ° dorsi- and plantarflexions of 255.8 ± 73.3 mm^2 and 292.0 ± 92.0 mm^2, respectively (fig. 6.4c and table 6.6). However, no significant differences were measured for contact area (One- way ANOVA; $p = 0.60$, $p = 0.94$, $p = 0.14$; 630 N 15° F, 480 N 0° F/E, 640 N 15° E, respectively).

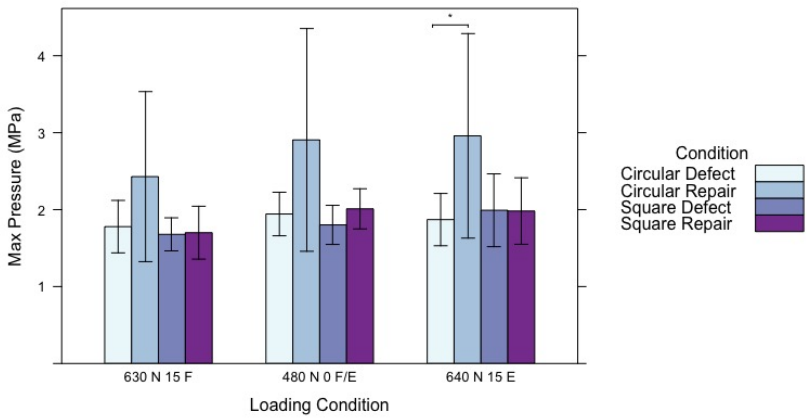

(a) Max contact pressure

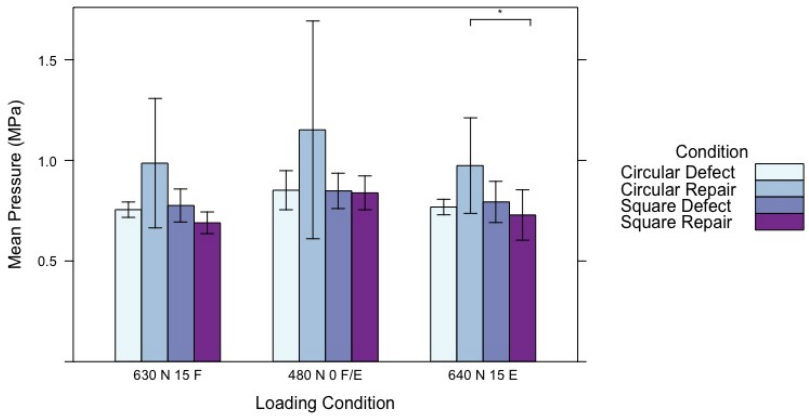

(b) Mean contact pressure

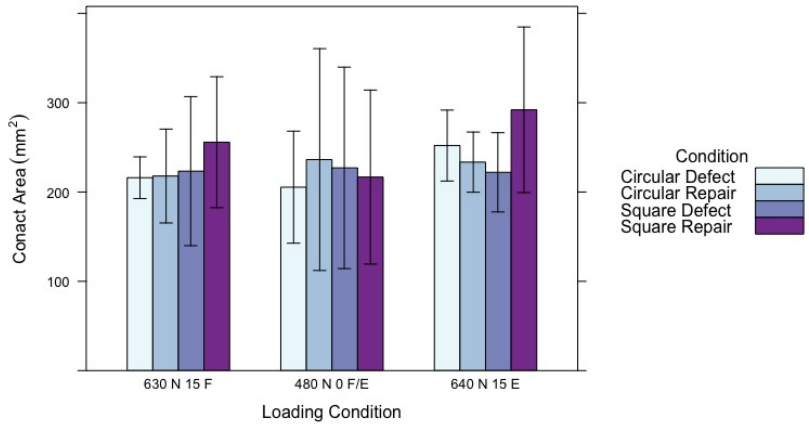

(c) Average total contact area

Figure 6.4: Average contact area and pressures across the whole talar dome (N=7) for all conditions and loading profiles. (A) max average contact pressure in MPa, (B) average mean contact pressure in MPa and (B) average contact area (mm^2) with standard deviation bars. Statistical analysis using One-way ANOVA or Friedman test. * $p < 0.05$.

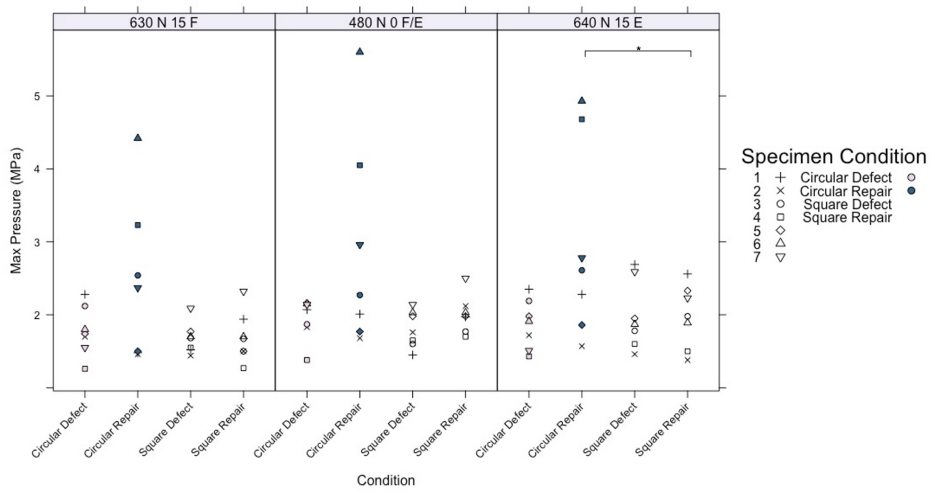

(a) Max contact pressure

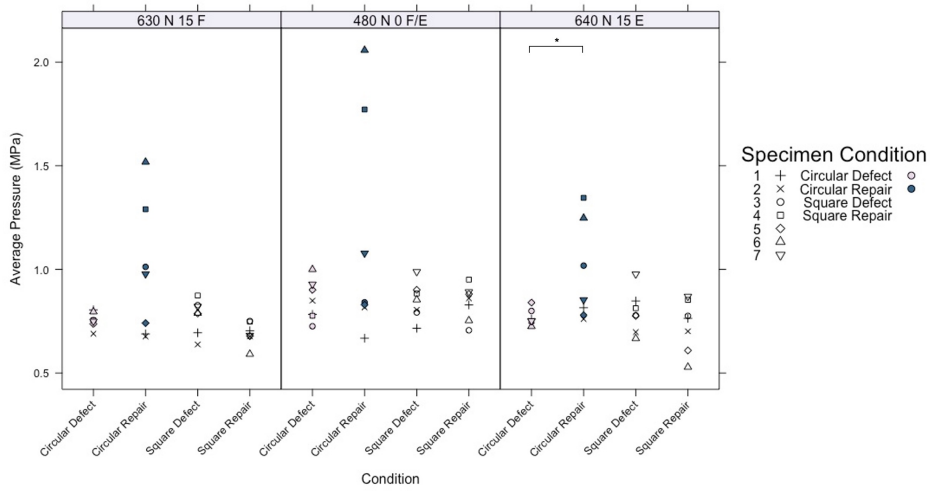

(b) Mean contact pressure

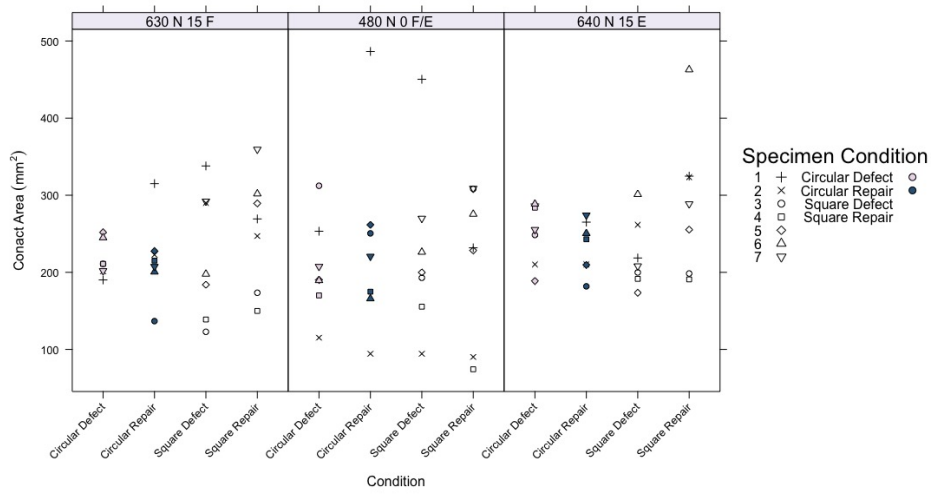

(c) Average total contact area

Figure 6.5: Average contact area and pressure across the whole talar dome showing (N=7). (A) max average contact pressure in MPa, (B) average mean contact pressure in MPa and (B) average contact area (mm^2) for each specimen tested. Statistical analysis using One-way ANOVA or Friedman test. * $p < 0.05$.

Table 6.4: Results of average max pressure measured for the natural ankle with different defect shapes and treatment shapes during loading with a simplified gait cycle (mean ± standard deviation).

Loading condition	**Max Pressure (MPa) ± SD**			
	16 mm Circular Defect	**Circular ChondroGide® Repair**	**16 mm Square Defect**	**Square ChondroGide® Repair**
630 N 15° F	1.79 ± 0.34	2.42 ± 1.10	1.68 ± 0.21	1.70 ± 0.34
480 N 0° F/E	1.94 ± 0.28	2.90 ± 1.45	1.80 ± 0.25	2.01 ± 0.26
640 N 15° E	1.87 ± 0.34	2.95 ± 1.33	1.99 ± 0.47	1.98 ± 0.43

Table 6.5: Results of average mean pressure measured for the natural ankle with different defect shapes and treatment shapes during loading with a simplified gait cycle (mean ± standard deviation).

Loading condition	**Mean Pressure (MPa) ± SD**			
	16 mm Circular Defect	**Circular ChondroGide® Repair Repair**	**16 mm Square Defect**	**Square ChondroGide® Repair**
630 N 15° F	0.75 ± 0.04	0.99 ± 0.32	0.77 ± 0.08	0.69 ± 0.05
480 N 0° F/E	0.85 ± 0.09	1.15 ± 0.54	0.84 ± 0.08	0.84 ± 0.08
640 N 15° E	0.76 ± 0.04	0.97 ± 0.24	0.79 ± 0.10	0.72 ± 0.12

Table 6.6: Results of average contact area measured for the natural ankle using a pressure sensor with different defect shapes and treatment shapes during loading with a simplified gait cycle (mean ± standard deviation).

Loading condition	**Average Total Contact Area (mm^2) ± SD**			
	16 mm Circular Defect	**Circular ChondroGide® Repair**	**16 mm Square Defect**	**Square ChondroGide® Repair**
630 N 15° F	216.0 ± 23.3	217.9 ± 52.5	223.3 ± 83.4	255.8 ± 73.3
480 N 0° F/E	205.4 ± 62.7	236.3 ± 124.2	227. 0 ± 112.8	216.7 ± 97.4
640 N 15° E	252.0 ± 39.7	233.5 ± 33.7	222.1 ± 44.3	292.0 ± 92.0

6.3.2 Frictional changes with circular and square repairs

Changes in the coefficient of friction or the mean friction factor against time was measured for all conditions (fig. 6.6). The highest coefficient of friction was measured for 16 mm circular defect with a value of 0.066 ± 0.001 (Mean ± SD). Lower coefficient of friction was measured for all other conditions of 0.043 ± 0.002, 0.049 ± 0.001 and 0.047 ± 0.001 for circular ChondroGide® repair, square defect and square ChondroGide® repair, respectively. Significant differences in measured mean friction factor were observed for all conditions (ART ANOVA with post-hoc contrast test, $p < 0.001$; table 6.7).

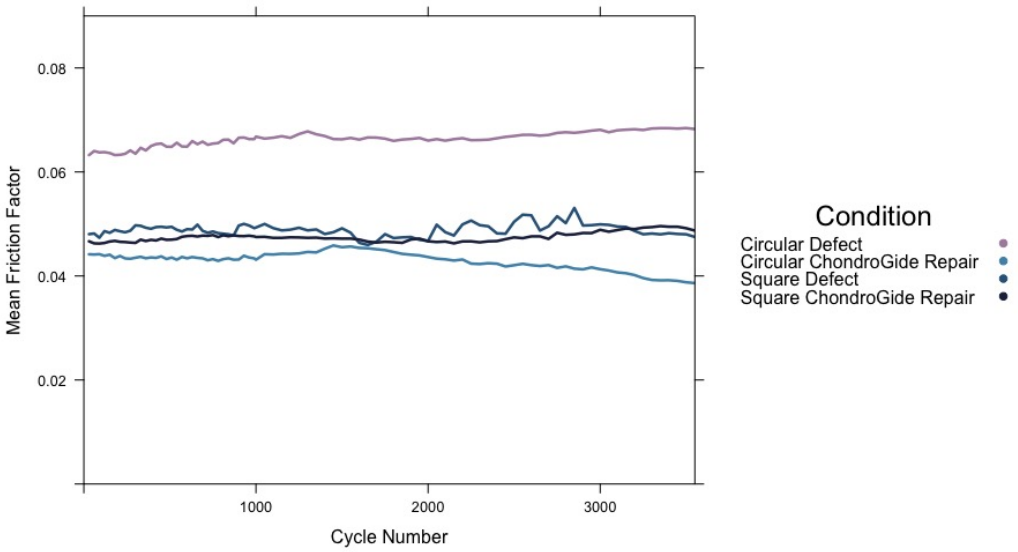

Figure 6.6: Mean friction factor obtained during 3600 cycle test for 16 mm circular defect, circular ChondroGide® repair, square defect and square ChondroGide® repair using pendulum friction simulator (N=7).

Table 6.7: Results of Statistical analysis for post hoc contrast test for comparison between the testing conditions

Condition A	Condition B	p - value
16 mm Circular Defect	**16 mm Circular Defect**	$p < 0.01$
16 mm Circular Defect	**Circular ChondroGide®**	$p < 0.01$
16 mm Circular Defect	**Square ChondroGide®**	$p = 0.61$
Circular ChondroGide®	**Square ChondroGide®**	$p < 0.01$
16 mm Square Defect	**Square ChondroGide®**	$p < 0.01$

For the 16 mm circular defect the coefficient of friction increased over the duration of the test with an initial coefficient of friction of 0.066 ± 0.001 for the first 1200 cycles and 0.067 ± 0.001 for 1201 - 3600 cycles. 16 mm circular ChondroGide® repair had the lowest coefficient of friction. The

coefficient of friction remained constant for the first 1200 cycles at 0.043 ± 0.0004 and increased to 0.044 ± 0.001 for 1201- 2400 cycles and then decreased to 0.039 ± 0.001 for the final 2401-3600 cycles. Measured coefficients of friction for both the square defect and square ChondroGide repair remained constant throughout the test with measured values of 0.049 ± 0.0006 and 0.047 ± 0.0005 for cycles 0-1200 and, 0.049 ± 0.001 and 0.047 ± 0.001 for cycles 1201-3600, respectively. Increased variability of the coefficient of friction in the square defect could be seen over the duration of test compared with the other three conditions (fig. 6.6).

Stability of repairs and damage to reciprocal tibial tissue

For all samples, pre- and post- testing images were taken of the cartilage surfaces (Appendix C3 fig. C.15 - C.21). Pre- and post- testing images of the talar domes are presented in figure 6.7. Assessment of reciprocal tissue damage caused during the test and to assess the stability of the repairs within the defect site was performed post testing by comparing the two images. Post-testing, 5 out of 7 of the circular ChondroGide® membranes remained completely within the defect site, with one partially removed from site and one remained within the site but was no longer flush with the focal edges of the defect. Low levels of puckering was observed in the membrane of 5 samples that remained fully in the defect, with minimal changes in appearance seen between the samples pre and post test. Whereas, for the square shaped ChondroGide® membrane repairs, 3 of the 7 remained intact and flush with the surface of the defect after testing. Two samples was no longer fully within the defect site, and 2 of the samples showed puckering and dislocation of the membrane resulting in it no longer sitting flush with the rim of the defect.

No delamination was observed on the reciprocal tibial tissue after the introduction of a 16 mm circular medial defect. Delamination of the reciprocal tibial cartilage was only seen for one sample after testing with a circular ChondroGide® membrane repair (fig. C.20). The presence of a square defect caused delamination to 4 out of 7 of the tibial cartilage after testing for 3600 cycles (fig.C.15, C.17, C.19 & C.20), with further damage to the tissue being seen with the square ChondroGide® repair for all 4 cases. For all these samples, the membrane did not remain in the defect site after subsequent testing in the sample. Figure C.16 showed some damage to the tibial tissue post testing and this corresponded with partial dislocation of the membrane in the anterior medial corner of the sample 6.7.

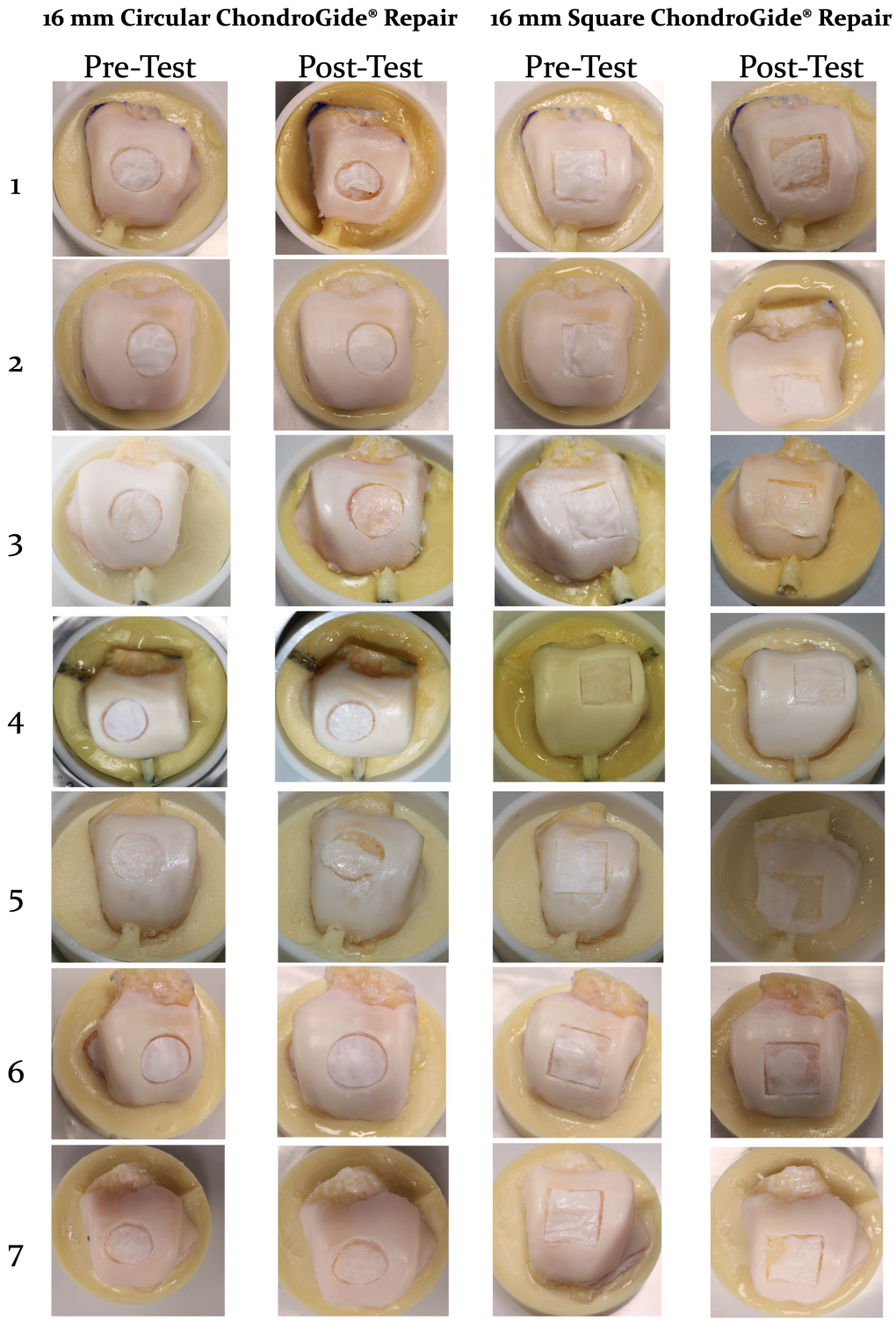

Figure 6.7: Pre and post friction testing images of the talus containing the circular and square 16 mm ChondroGide® repairs for all samples.

6.3.3 Biomechanical changes attributed to shoulder lesions and their repair

Contact mechanics including contact pressure and area were assessed for samples (n = 7) containing a medial shoulder lesion before and after repair with nanofracture, ChondroGide® membrane and Tisseel®. Pressure maps were generated for all samples (Appendix C fig. C.22 - C.28) and an example set of maps are presented in figure 6.8a.

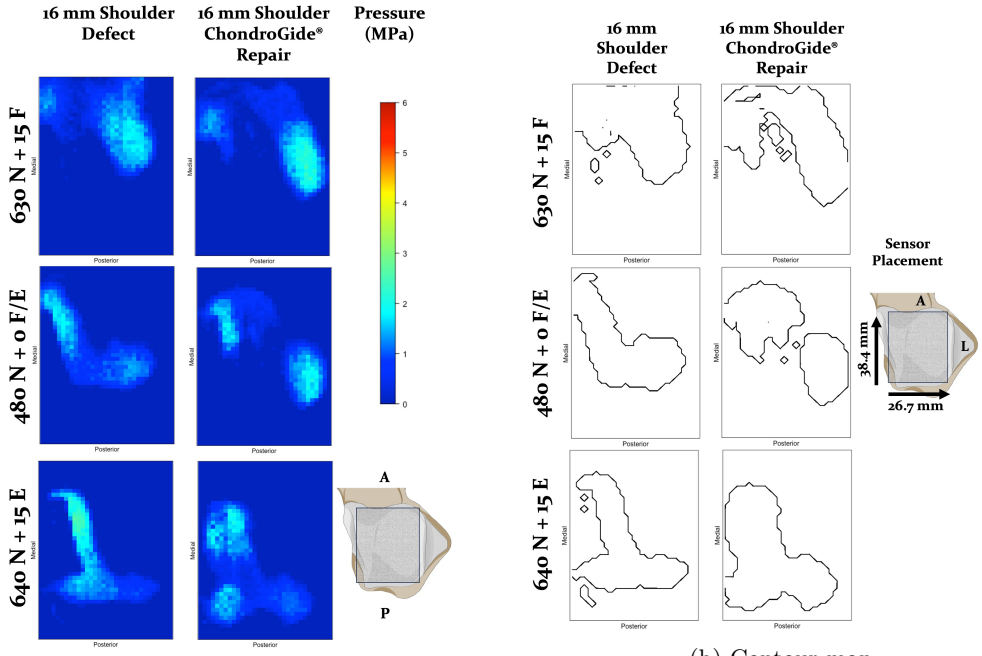

(a) Contact Pressure Map

(b) Contour map

Figure 6.8: Sample of pressure maps and contour maps showing contact area and pressure distribution profile for each loading condition for across the talar dome with a shoulder lesion and the ChondroGide® repair for each loading condition of a simplified gait cycle. Region mapped represents a 38.4 x 26.7 mm area on the talar dome. A = Anterior, P = Posterior and L = Lateral.

For shoulder lesion samples, the maximum contact pressure measured ranged from 2.23 ± 1.13 MPa to 3.28 ± 2.86 MPa. The highest contact pressure was measured for the shoulder lesion at 480 N 0° F/E or neutral position. The lowest peak contact pressure was seen in 630 N 15° dorsiflexion. For both the 630 N 15° dorsiflexion and 480 N 0° F/E, a non-significant decrease in max contact pressure was seen after repair of shoulder lesion with ChondroGide® membrane (fig. 6.9a; T-test, $p = 0.50$ and$p = 0.13$, respectively). This also corresponded with a reduction in mean pressure for these conditions (fig. 6.9b; paired T-test, $p = 0.26$ and $p = 0.16$, respectively). However, for 640 N 15° plantarflexion, an increase in both contact pressure and contact area was observed after the repair of the defect with a ChondroGide® membrane (fig. 6.9). This difference was not significant

(p = 0.96 and 0.578 for max pressure and mean pressure, respectively). Figure 6.10 shows the inter sample variation seen between the conditions.

Visible changes in contact pressures can be seen in the pressure maps after the repair of the shoulder defect with a ChondroGide® membrane compared with just the defect. Visible differences in the mapped contact area could be seen for most samples (fig. 6.8b & Appendix C fig. C.29 - C.35). A reduction in mean contact area was observed after defect repair at neutral and plantarflexion conditions of 245 ± 111 mm^2 and 275 ± 63 mm^2 to 230 ± 103 and 235 ± 114 mm^2, respectively (p = 0.24 and p =0.32, respectively). Repair of the defect caused a non-significant increase in contact area in the dorsiflexion condition (fig. 6.9c).

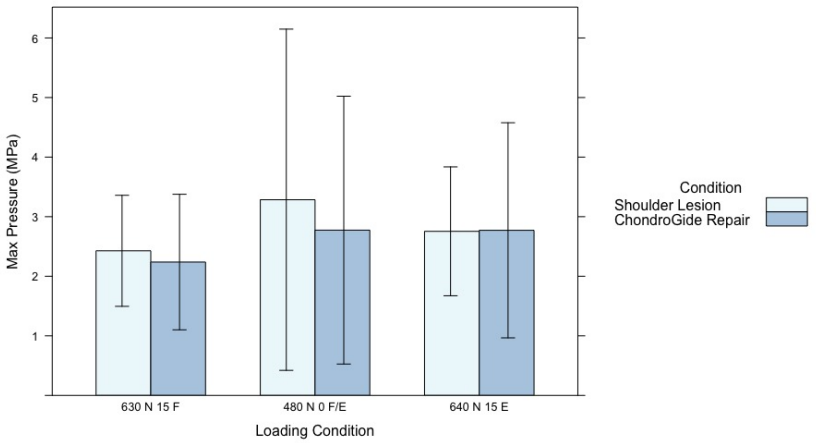

(a) Max contact pressure

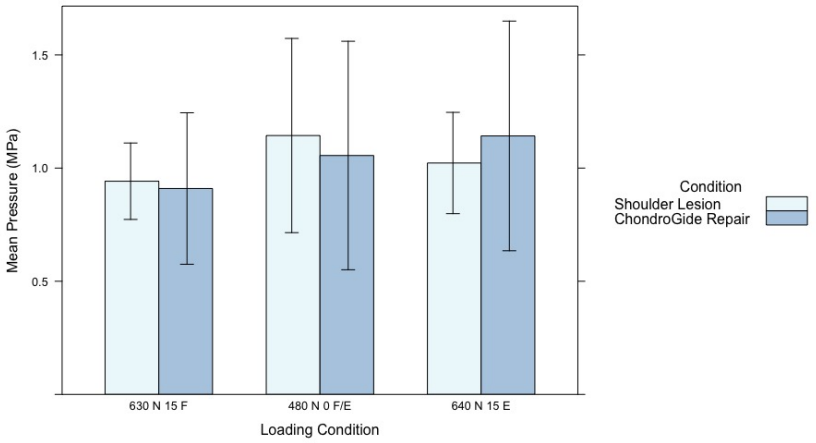

(b) Mean contact pressure

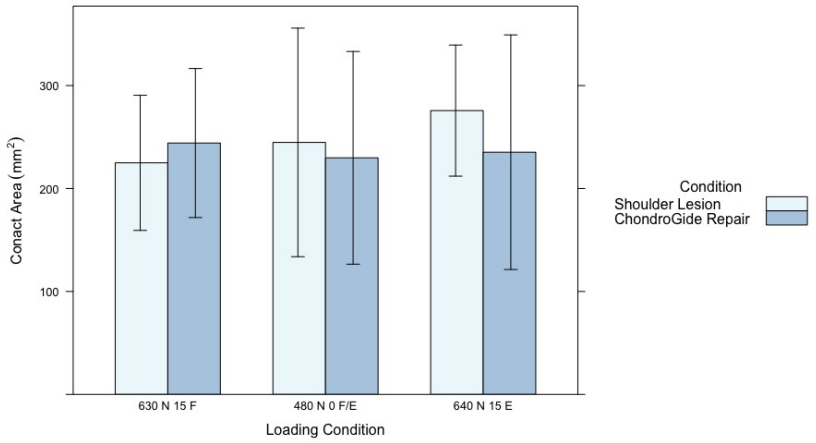

(c) Average total contact area

Figure 6.9: Average contact area and pressures across the whole talar dome (N=7) for all conditions and loading profiles for shoulder lesions and ChondroGide® repair. (A) max average contact pressure in MPa, (B) average mean contact pressure in MPa and (B) average contact area (mm^2) with standard deviation bars. Statistical analysis using paired T-test. * $p < 0.05$.

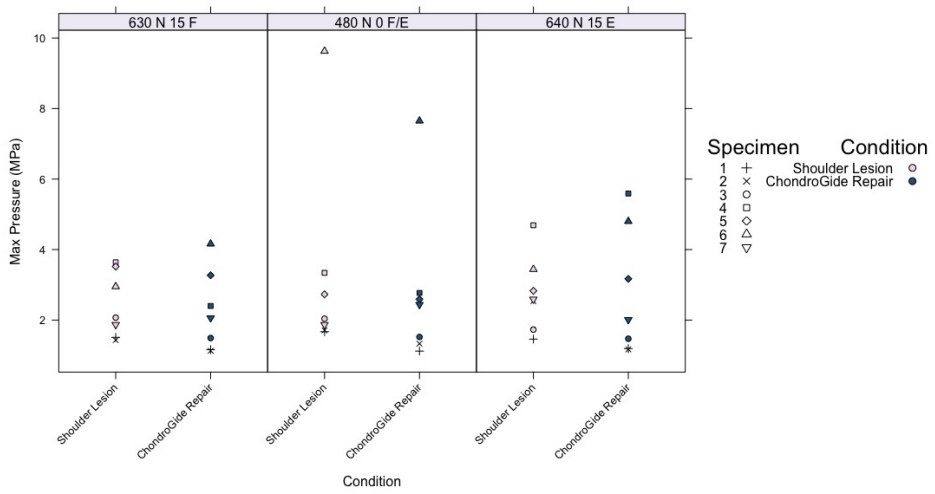

(a) Max contact pressure

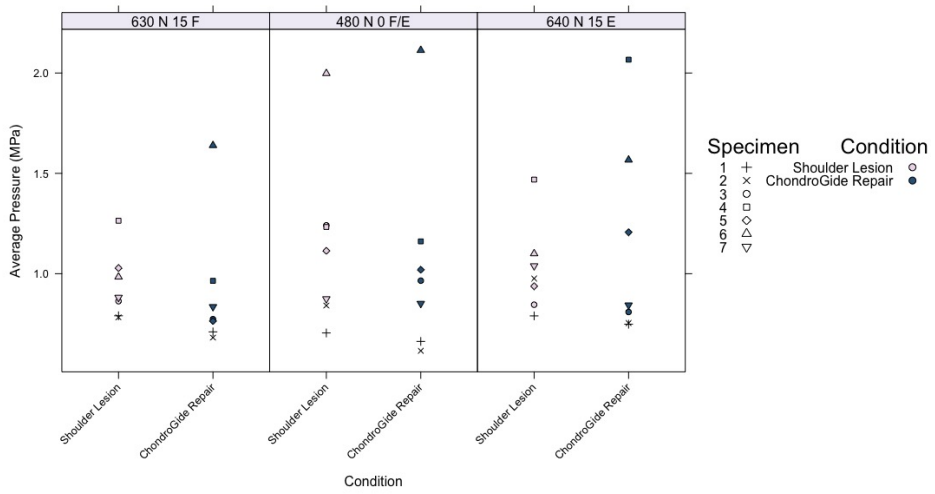

(b) Mean contact pressure

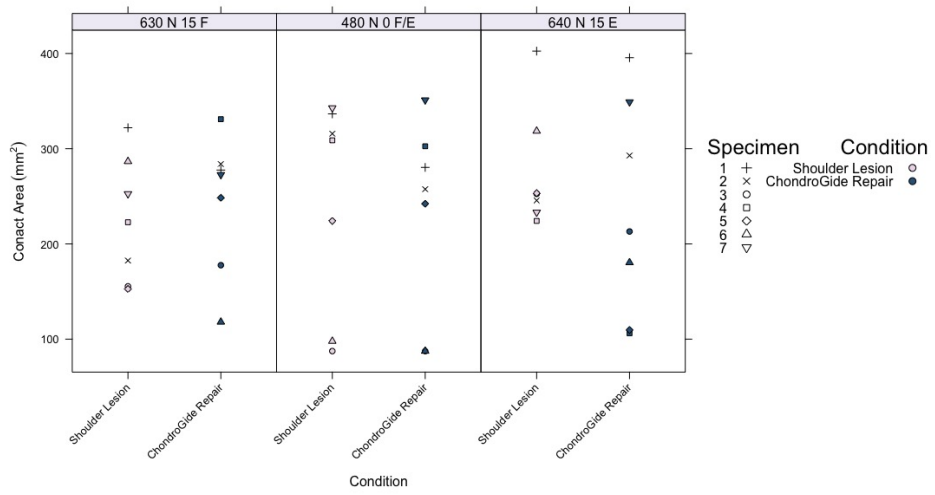

(c) Average total contact area

Figure 6.10: Average contact area and pressure across the whole talar dome showing (N=7) (A) max average contact pressure in MPa, (B) average mean contact pressure in MPa and (B) average contact area (mm^2) for each specimen tested. Statistical analysis using paired T-test. * $p < 0.05$.

Frictional changes attributed to repair of shoulder lesion using AMIC treatment

Friction was assessed pre and post repair of the shoulder defect with a ChondroGide® membrane. The results obtained for the coefficient of friction was measured over the course of 3600 cycles and can be seen in figure 6.11.

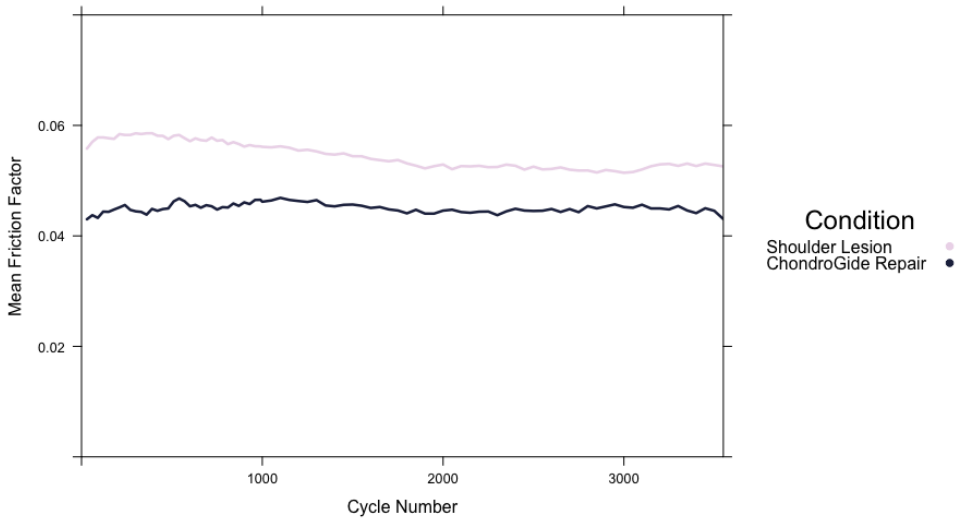

Figure 6.11: Mean friction factor obtained during 3600 cycle test for 16 mm Shoulder Lesion and AMIC repair.

Repair of the defect with ChondroGide® caused a significant reduction in the overall coefficient of friction from 0.055 ± 0.002 to 0.045 ± 0.001 (Wilcoxon-Signed Rank Test; $p = 0.005$). Over the duration of the test, the coefficient of friction for both samples stayed constant, with a slight increase within the first 1000 cycles observed for both conditions. The average coefficient of friction for the first 1200 cycles was 0.057 ± 0.0009 and 0.045 ± 0.0009 and 0.052 ± 0.001 and 0.044 ± 0.0006 for the shoulder lesion and ChondroGide® repair samples, respectively.

Visualisation of the cartilage surface and the stability of the lesion was assessed pre- and post-testing. Images of the cartilage surface can be seen in appendix C5 (fig. C.36 - C.42). Figure 6.12 shows the stability of ChondroGide® membrane in the defect site pre and post testing with the pendulum friction simulator. Three of the membranes remained fully in the defect site. Four of the membranes showed partial puckering, deformation and movement within the defect site after testing. Two samples showed damage to the reciprocal tibial surface (fig. C.41 & C.42), with both displaying signs of cartilage delamination post introduction of the defect and continued damage seen after the repair of the tissue.

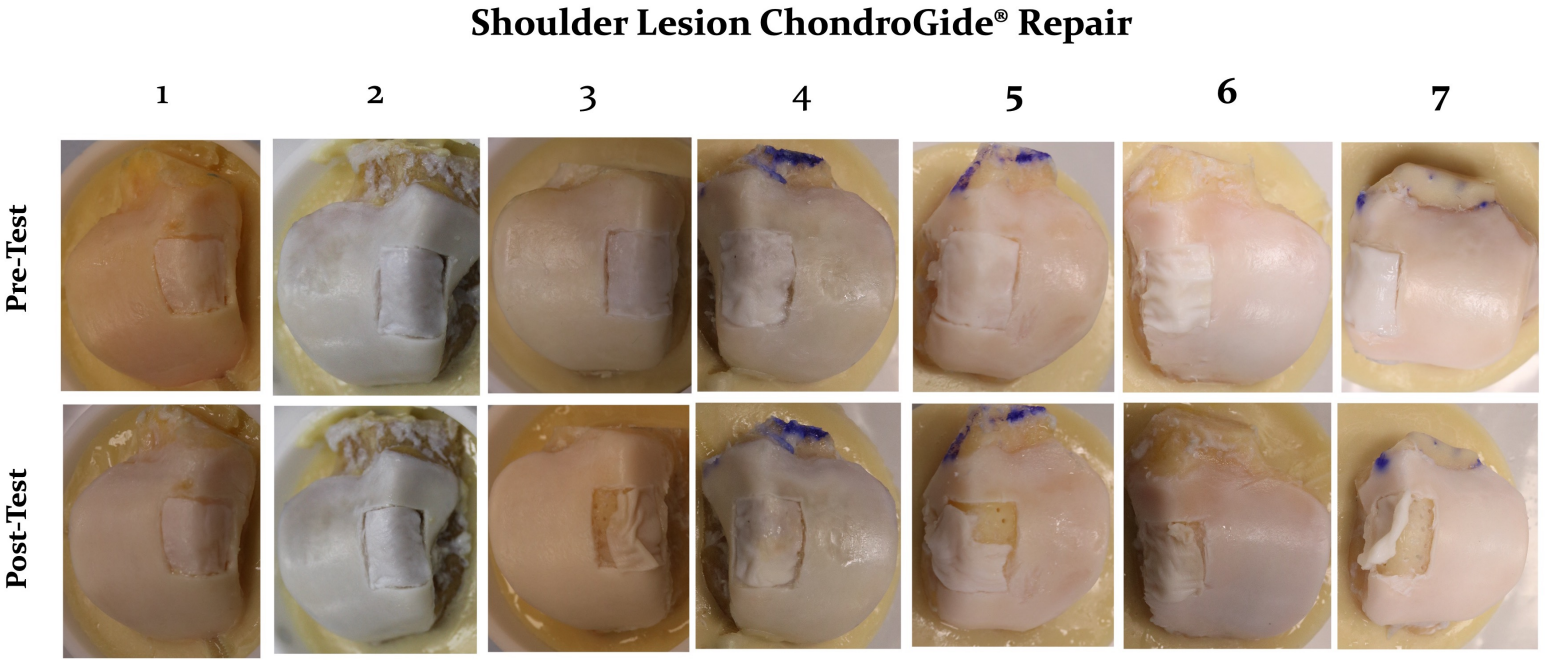

Figure 6.12: Stability of AMIC repair in chondral shoulder lesions pre- and post- friction testing
Images of each talus containing AMIC repair of focal talar shoulder lesion pre and post friction testing using a pendulum friction simulator.

6.3.4 Biomechanical changes caused by AMIC treatment of tibiotalar kissing lesions

10 mm circular, full-thickness chondral lesions were created on the talar dome and the reciprocal tibial cartilage, to simulate a kissing lesion within the tibiotalar joint. Changes in contact mechanics was assessed. Pressure maps and contour maps were generated for every sample to visually assess changes in contact pressure and contact area with a kissing lesion and its subsequent repair using nano-Fx, Tisseel® and ChondroGide® membrane. A sample of which can be seen in figure 6.13 and also in appendix C (fig. C.43 - C.56).

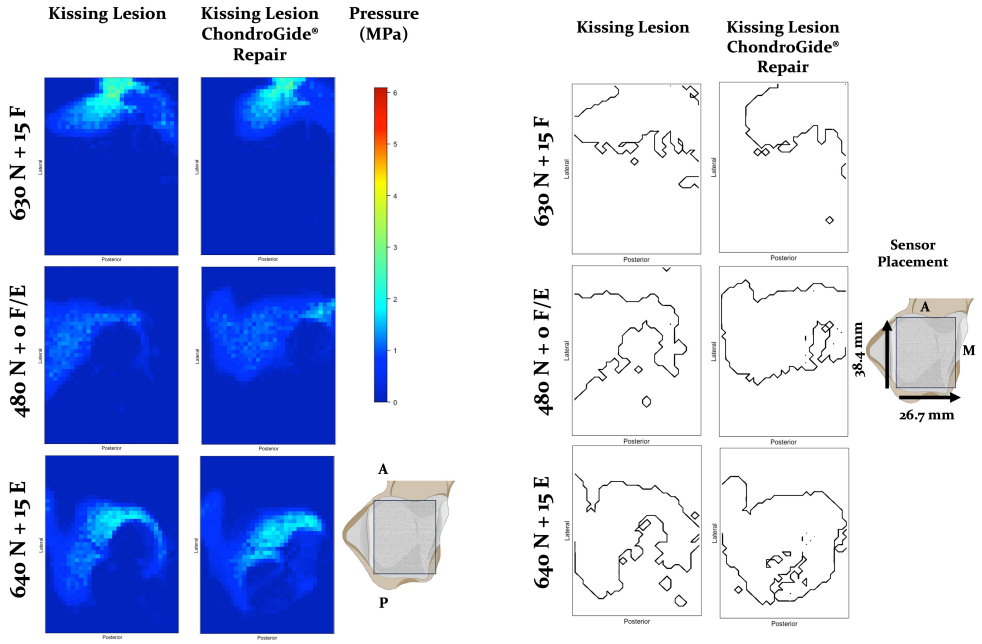

(a) Contact Pressure Map

(b) Contour Map

Figure 6.13: Sample of pressure maps and contour maps showing contact area and pressure distribution profile for each loading condition for across the talar dome with a 10 mm kissing lesion and the ChondroGide® repair for each loading condition of a simplified gait cycle. Region mapped represents a 38.4 x 26.7 mm area on the talar dome. A = Anterior, P = Posterior and M = Medial.

Changes in contact area and pressure were measured using the pressure sensor. For all loading conditions, it can be seen that the repair of the kissing lesion with the ChondroGide® membrane provided a non-significant reduction in both the maximum pressure and mean pressure measured on the talar dome (Paired T-test, $p > 0.05$) (fig. 6.14). For all three loading conditions, the ChondroGide® repair showed an increase in contact area. The largest observed contact area was seen in 630 N 15° dorsiflexion for the AMIC treated kissing lesion of 312 ± 58 mm^2 and this corresponded with lowest observed max pressure of 2.12 ± 0.54 MPa. For 630 N 15° dorsiflexion

and 480 N 0° F/E this change was not significant ($p = 0.32$ & $p = 0.90$, respectively). At 640 N 15° plantarflexion a significant increase in contact area was seen from 222 ± 122 mm^2 to 260 ± 115 mm^2 (fig. 6.14c; $p = 0.02$). Presence of the ChondroGide® membrane visually changed the contact area profiles of the samples and introduce loading within the defect site for 3 specimens in the plantarflexion condition (appendix C fig. C.44, C.52 & C.54). Figure 6.15 shows the inter sample variation seen between the conditions.

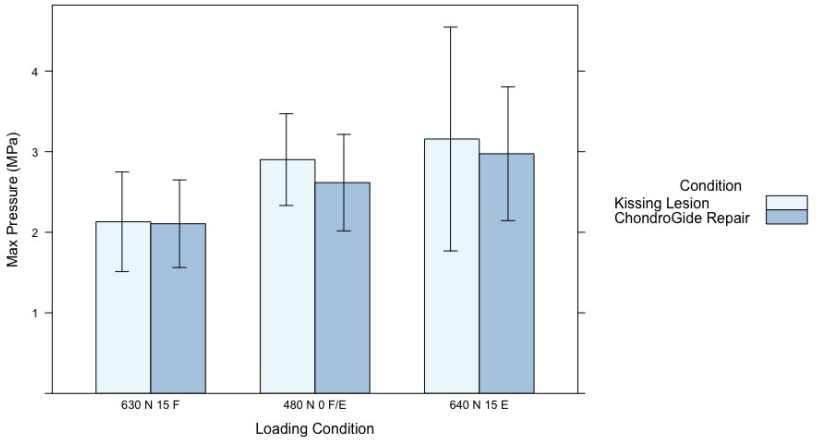

(a) Max contact pressure

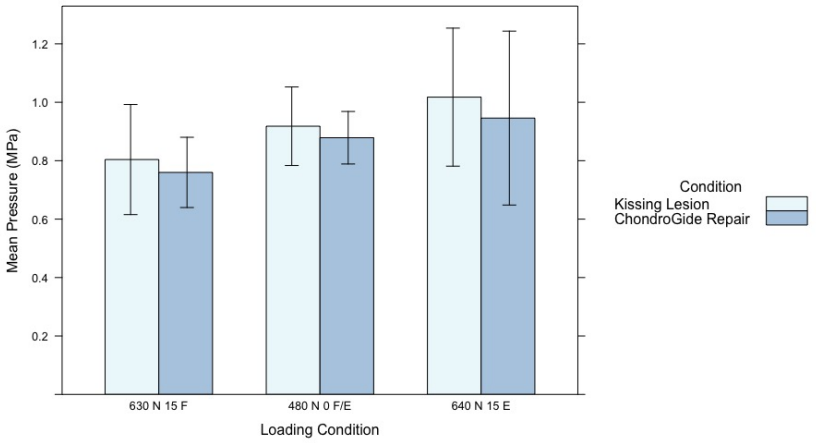

(b) Mean contact pressure

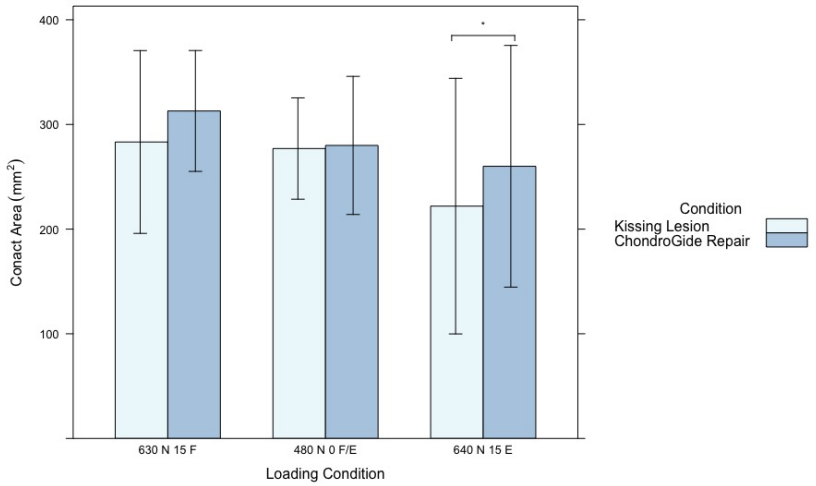

(c) Average total contact area

Figure 6.14: Average contact area and pressure across the whole talar dome showing (N=7). A) max average contact pressure in MPa, (B) average mean contact pressure in MPa and (B) average contact area (mm^2) with standard deviation bars. Statistical analysis using paired T-test. * $p < 0.05$.

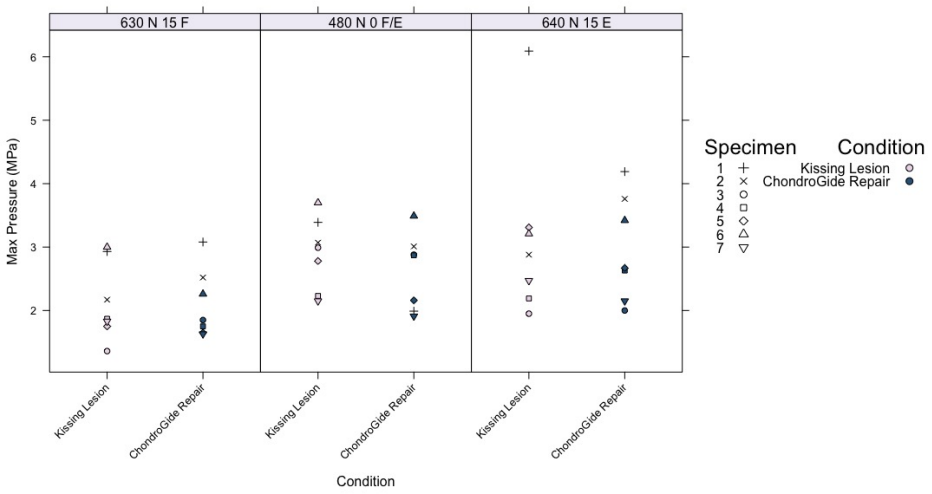

(a) Max contact pressure

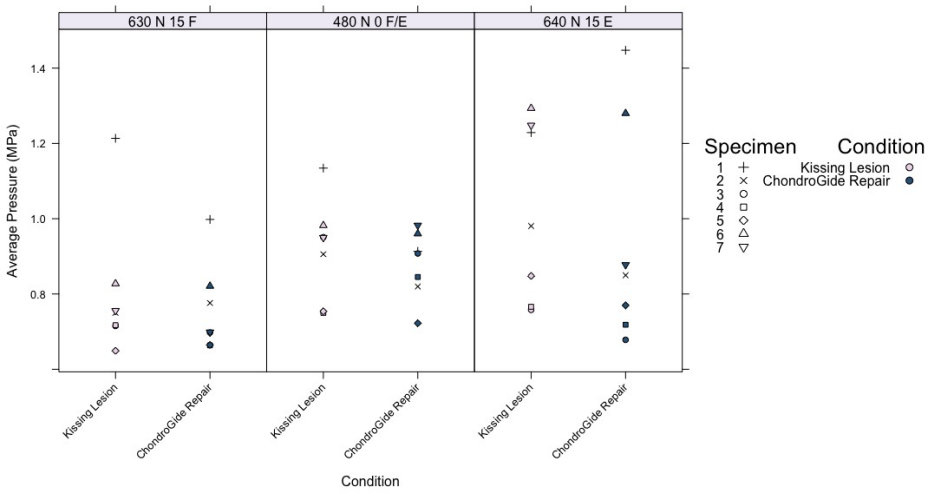

(b) Mean contact pressure

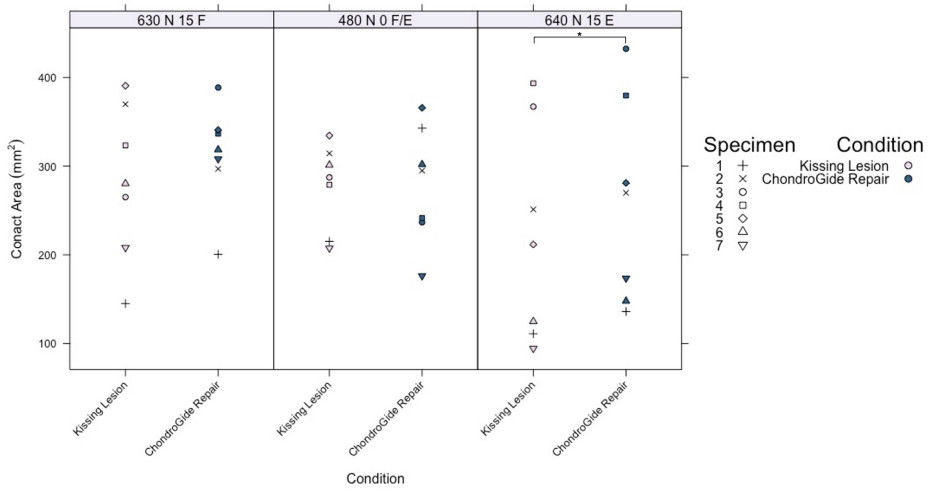

(c) Average total contact area

Figure 6.15: Average contact area and pressure across the whole talar dome showing (N=7). (A) max average contact pressure in MPa, (B) average mean contact pressure in MPa and (B) average contact area (mm^2) for each specimen tested. Statistical analysis using paired T-test. * $p < 0.05$.

Frictional changes

Frictional changes were assessed pre- and post-repair of the 10 mm kissing lesion with a ChondroGide® membrane and normalised using the pre- and post- test data. The coefficient of friction for the whole joint (n=7) was calculated for the duration of a 3600 cycle test and can be seen in figure 6.16. Repair of the defect site caused a significant increase in the overall coefficient of friction from 0.035 ± 0.002 to 0.037 ± 0.002 for the samples (Wilcoxon-Signed Rank Test; $p = 0.009$). In addition, over the duration of the test the coefficient of friction for both samples decreased but at different rates. During the initial stages of the test the friction coefficient for the first 1200 cycles was 0.035 ± 0.002 and 0.039 ± 0.0009 for the kissing lesion and the ChondroGide® repair samples, respectively. Between 1201 - 3600 cycles coefficient of friction reduced to 0.034 ± 0.0014 and 0.036 ± 0.001 for kissing lesion and the ChondroGide repair sample, respectively.

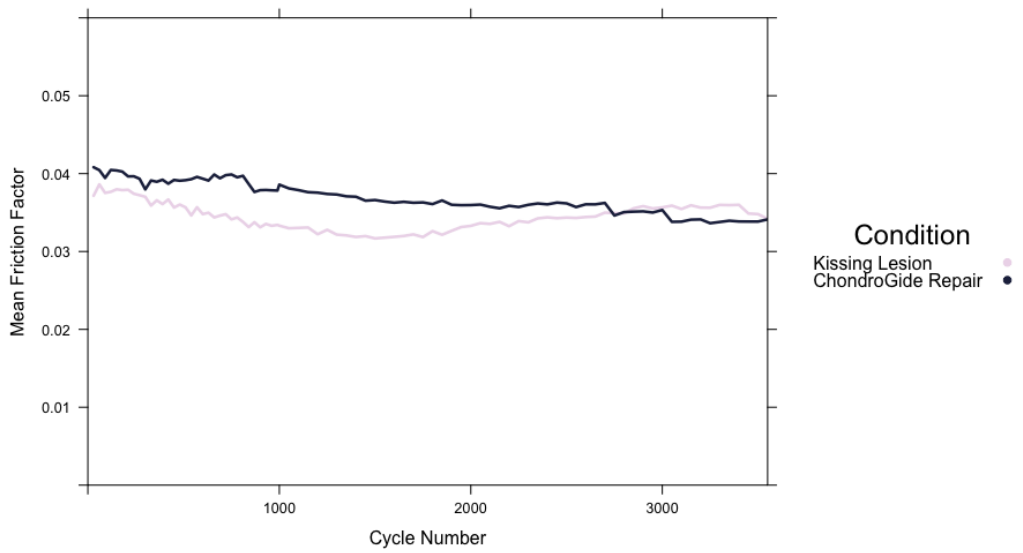

Figure 6.16: Mean friction factor obtained during 3600 cycle test for tibiotalar kissing lesion and subsequent AMIC repair (N=7).

Visualisation of the stability of the lesion was assessed pre- and post- testing. Images of the cartilage surface pre- and post-friction testing tissue for both the defect only and AMIC repair are shown in appendix C5 (fig. C.57 - C.63). No visible damage was seen on the talar cartilage as a result of the introduction of a tibial defect, but damage was seen in 4 of the tibial samples post testing with a kissing lesion, where delamination of the cartilage in the anterior region of the tibial plafond was observed.

Figure 6.17 shows the stability of ChondroGide® membrane in the tibial and talar defect sites for each sample, pre-and post-friction testing in the PFS. It can be seen that the membrane was more stable within the defect site on the tibial defect compared with the talar defect. Only one sample showed showed partial dislocation of the membrane from the defect site and some puckering was seen across the samples (fig. 6.17). Whereas, on the talar dome, one sample displayed complete removal of the membrane from the defect site during testing and for two other samples the membrane was partially removed from the defect.

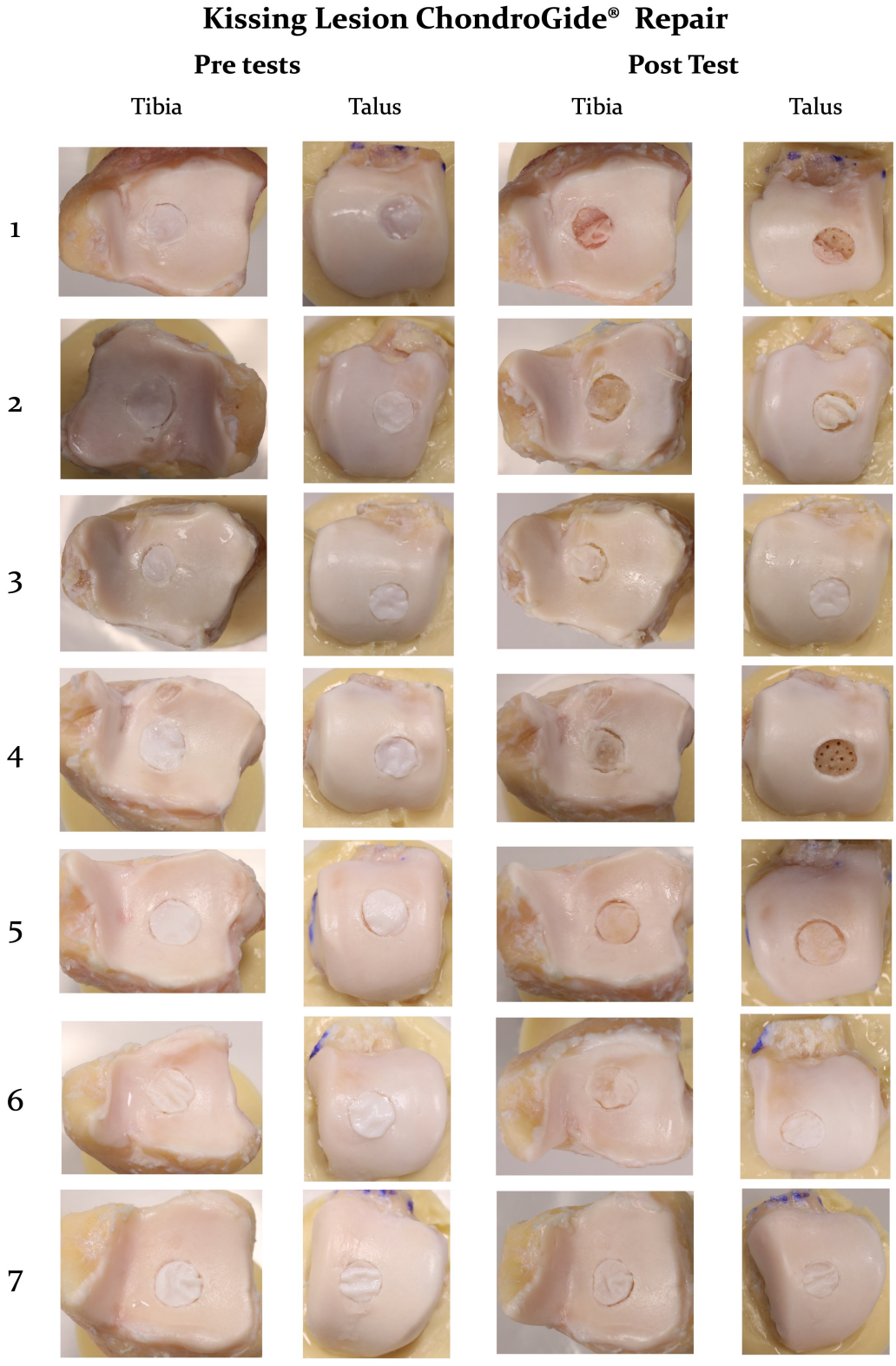

Figure 6.17: Stability of AMIC repair in chondral kissing lesions pre and post friction testing in both the tibial plafond and the talar dome

Images of paired tibia and tali containing 10 mm chondral defects with AMIC repairs pre- and post- friction testing using a pendulum friction simulator.

6.3.5 Impact of lesion size and location on biomechanical properties of the tibiotalar joint

Comparisons between contact pressure, area and coefficients of friction were assessed to inform about the impact different lesion locations and sizes had on the joint contact mechanics. The healthy or intact ankle measurements (n=7) produced in chapter 5 were used as a reference condition and compared to the different defects sizes and locations.

Although no significant differences were seen in max contact pressure measured in the samples, higher peak pressures were observed in both the shoulder lesion and the kissing lesion talar domes (dorsiflexion: $p = 0.351$ & 0.06 , neutral: $p = 0.157$ & 0.313, plantarflexion: $p = 0.127$ & 0.079, respectively). This also corresponds with a higher mean pressure observed across the whole talar dome for the shoulder lesion, which was significant increase in neutral position ($p = 0.04$) and but was non-significant in dorsi- and plantarflexion ($p = 0.373$ and 0.084, respectively).

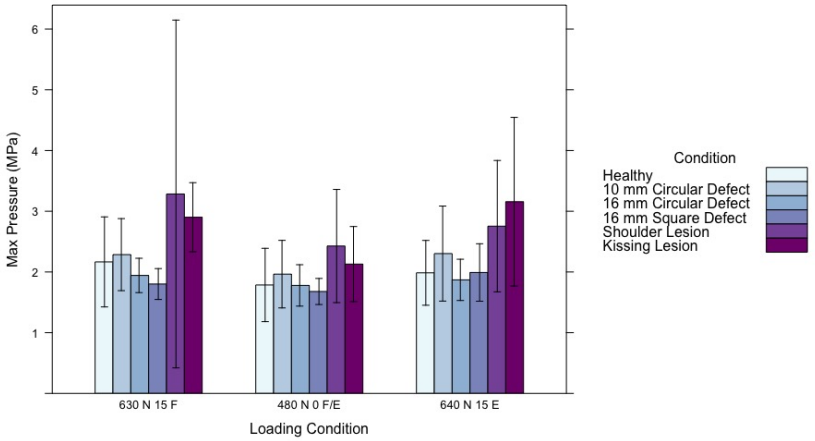

(a) Max contact pressure

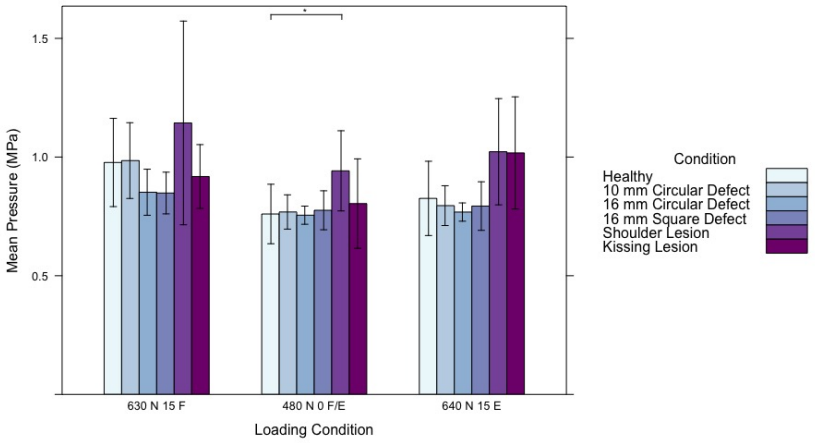

(b) Mean contact pressure

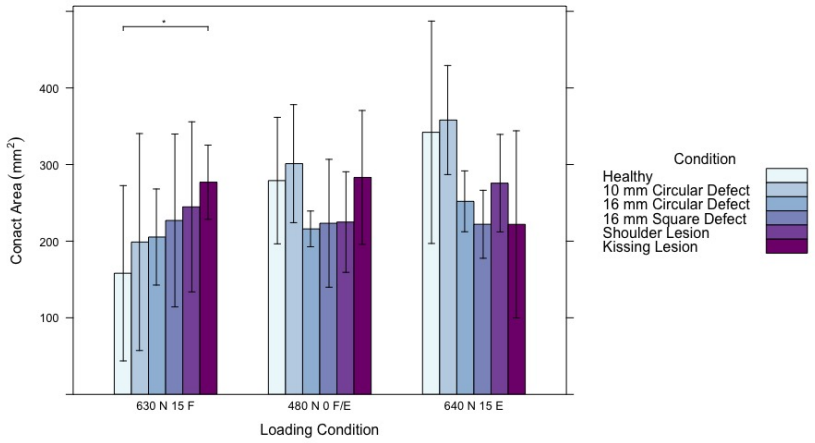

(c) Average total contact area

Figure 6.18: Average contact area and pressures across the whole talar dome for the intact, healthy condition compared to defects of different sizes and location (n=7) . (A) max average contact pressure in MPa, (B) average mean contact pressure in MPa and (B) average contact area (mm^2) with standard deviation bars. Paired T-tests compared healthy to 10 mm chondral defect and T-test was used to to compare 16 mm circular defect, 16 mm square defect, shoulder defect and kissing lesion to healthy samples. * $p < 0.05$

Additional comparisons between the coefficient of friction obtained for each defect condition and the healthy intact tibiotalar joint were made. It can be see that for all conditions, a significant increase in the coefficient of friction was seen between the intact/ healthy condition and the full thickness chondral defects ($p > 0.005$).

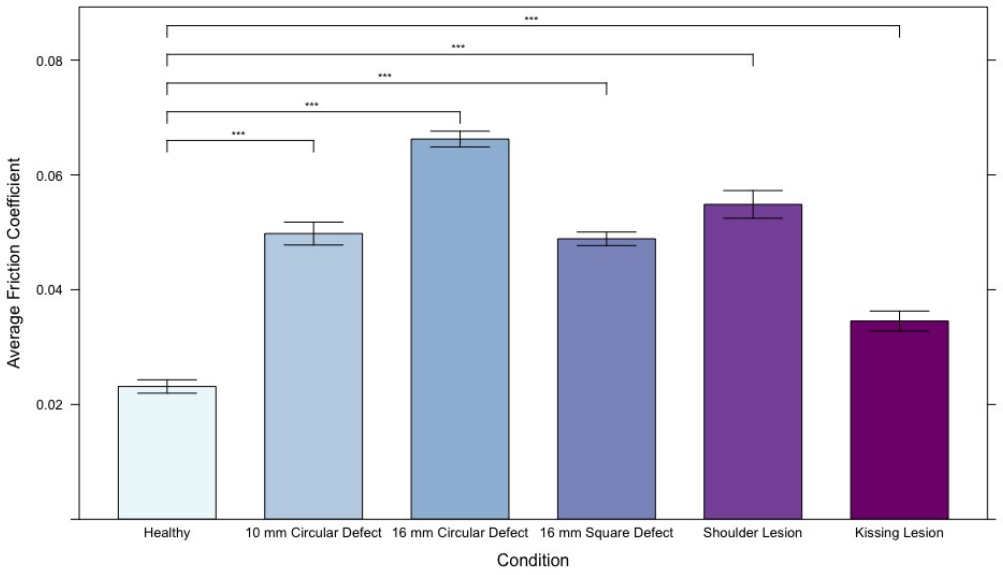

Figure 6.19: Mean friction factor obtained during 3600 cycle test comparing healthy intact tibiotalar joint compared with the tibiotalar containing different sizes and locations of chondral defects (n=7). Paired T-tests compared healthy to 10 mm chondral defect and T- test was used to to compare 16 mm circular defect, 16 mm square defect, shoulder defect and kissing lesion to healthy samples. *** $p < 0.005$

6.4 Discussion

The results of these studies demonstrate that functional properties such as contact mechanics and tribology can be altered due to the presence of different lesions and their repair with AMIC treatments. Analysis of the different defect locations and sizes are discussed below focusing on the clinical implications of the studies relating to current practise. Generally AMIC procedures have been seen to significantly improve patient-related outcomes and are used to treat medium sized lesions on the talus (< 20 mm) and also shoulder lesions (Irwin et al., 2018, Jantzen et al., 2022), however they are less commonly used for treatments of coexisting tibial and talar lesions.

6.4.1 Debridement shape affects the frictional properties of the tibiotalar joint

Debridement of OLTs is a widely implemented strategy, popularised in the nineties, as a treatment alongside BMS and has been shown to have a high level of clinical success as reparative techniques for both short and mid term studies, with positive patient reported outcomes being the measurement of success (Fermín et al., 2021, Valderrabano et al., 2013). Current literature does not often discuss the shape of defect debridement. Limited literature suggests that lesions should be debrided into to a circular or oval shape to facilitate the tight fit of the graft (Seo et al., 2011). Yet little to no guidance is present beyond this relating to the shape of debridement. Anecdotal evidence suggests that surgeons may choose to debride a defect into a square shape, as it allows for easier implantation of a membrane, with more controllable sizes and edges.

In this study, no significant differences were seen between the circle and square debridement shapes for observed max pressure or mean pressure. Generally, generated heat maps showed differences in the loading profiles between the circle and square defects. This indicates that although the mean contact pressures across the talar dome remained the same, the loading distribution differs. No identifiable *ex vivo* studies have looked at lesions as large as 16 mm in diameter, therefore no data is available for comparison. No significant differences were also observed in contact area between the two conditions. However, compared to the previously obtained healthy samples, the average measured contact area is higher for both the circle and square defect at 630 N 15° dorsiflexion but lower in neutral condition and plantarflexion. This could indicate that some compensatory loading is occurring in dorsiflexion to minimise point loading in the tissue and to spread the load when the lesions are greater as this was not seen for the 10 mm centromedial lesions. Where changes in the pressure distribution were observed, increases in pressure were in the anterior region of the talar dome on both the lateral (3/7) and medial sides (2/7).

Frictional assessment of the tibiotalar joint showed that the circular defect had a higher friction factor of 0.066 ± 0.001 compared to 0.049 ± 0.001 observed for the square defect. This is higher than the values obtained for the healthy tissue in the same conditions of 0.023 ± 0.001, previously reported in section 5.3.3. Both these values sit within the range previously reported for cartilage on cartilage studies (Groves et al., 2017). However, the inter-test variability seen for the square defect and the higher number of samples with delamination on the tibial surface could suggests that although the coefficient of friction observed is lower, the reduction is attributed to damage and wear

of the cartilage surface. This may be caused by changes in cartilage properties as the tissue is unable to articulate efficiently and instead experiences higher shear forces. This increase in shear causes damage to tissue and results in the delamination at the interface of the tissue. This subsurface fatigue may result in the decrease of friction seen as it is no longer articulating against one another but by damaging the tissue and exposing the subsurface tissue which has different properties. Thus, resulting in the higher amount of delamination was observed on the tibial tissue with a square debridement (appendix C fig. C.57 - C.63).

The outcomes of this study suggests that following current clinical practise of debriding a defect to a circular or oval shape is more favourable to reduced risk of additional damage caused by abnormal biomechanical properties.

6.4.2 Stability of AMIC treatment is improved using a circular template compared with a square template

Building upon the previous work focusing on debridement/defect shape, the chosen debrided shape will thus affect the shape of membrane or matrix used for AMIC treatment. This study showed that although no loading was seen through the repair material for both the large square and circle AMIC repairs, changes in pressure distribution was observed after the repair of defect. Circular AMIC treatment showed a significant increase in the max contact pressure ($p < 0.05$) compared with the circular defect. Significant differences were seen between the mean pressure for the circular and square ChondroGide® repairs ($p < 0.05$). It can be seen that in dorsi- and plantarflexion, the contact area is greater for the square ChondroGide® repair compared to the circular ChondroGide® membrane and this corresponds to a lower mean pressure across the talar dome (fig. 6.4). Visually, the contour plots showed increased areas of loading around the rim of the square defect after AMIC treatment. Pressure maps for the circular ChondroGide® membrane displayed reduced loading around the rim of the defect and increased contact pressure in 4 out of 7 of the specimens and increased contact area in 2 samples (Appendix C. figs. C.1- C.28).

Furthermore, circular ChondroGide® repair showed significantly lower coefficient of friction compared to the square membrane ($p < 0.001$). For both conditions the coefficient of friction obtained is greater then value obtained previously for healthy tissue but still within the range reported for healthy tissues of 0.003 - 0.08 (Groves et al., 2017).

Circular AMIC repairs appeared to display greater success at remaining intact within the defect site during tests (fig. 6.7). This could be because the circular edge of the membrane is less susceptible to fluid pressure changes and edge effects compared to the square defect, permitting it to sit and maintain a tight fit of the graft to the edge of the defect site. Increased wrinkling and deformation can also be seen in the square membrane treatments. This suggest that current clinical practise favouring a circular or oval debridement followed by the appropriate templated matrix provides improved retention and stability of membrane to the defect site.

6.4.3 Biomechanical changes of AMIC treatment of shoulder lesions

Focal shoulder chondral lesions of the talus are relatively common with poorer outcomes reported for microfracture based treatments, thus shoulder lesions are often treated using cartilage replacement biomaterials (Steele et al., 2018). AMIC treatment for shoulder lesions from 2.2 - 2.8 cm^2 have been shown to have improved outcomes within patient based reporting of AOFAS scores (Götze et al., 2021, Migliorini et al., 2021). However, compared to microfracture no differences in MOCART scores were observed after 5 years (Götze et al., 2021).

To the authors knowledge, only one reported study looked at the biomechanical changes attributed to shoulder lesions within the talar joint. They showed that larger shoulder OLTs ($<$16 mm) resulted in increase in mean peak pressure and a decrease in contact area when compressed in a neutral position using 800 N of load (Lawson et al., 2019). They attributed these changes in contact mechanics as explanation for risks of secondary injuries for treatment failures associated with OLTs. The maladaptive cartilage tissue present on the talar dome results in a change in pressure distribution laterally along the talar dome introducing instability. This instability and changes in loading could result in re-injury and additional damage to the tissue.

In this study it can be seen that the measured mean peak pressure for the shoulder lesion was higher than the values obtained for the healthy conditions for each loading conditions (fig. 5.16a & 6.9a). Increased contact area is observed in the dorsiflexion condition but decreases in contact area are seen in neutral or plantarflexion conditions when compared with the healthy samples. This difference in contact area can also be seen in changes to the pressure and contour maps for the shoulder lesion in which loading appears to be distributed more across the talar surface (fig. C.22- C.28 & fig. C.29- C.35). The presence of a shoulder lesion appear to increase the loading

in the anterior region of the talar dome compared to the pressure distribution maps generated for the healthy samples. These findings agree with that previously reported for a neutral condition (Lawson et al., 2019). Although visible changes in the pressure distribution were not seen between the shoulder lesion and AMIC repair, non-significant reduction in mean peak pressure and contact area were observed for the samples. Repair of a shoulder lesion using AMIC treatment allowed for loading through the defect in the neutral condition, but introduce a new point of peak pressure in plantarflexion (fig. C.25). In plantarflexion, 3 of the samples showed reduction in contact area and an increase in peak pressure after repair with the ChondroGide® membrane. Overall, a reduction in peak pressure could be attributed to the reported success of AMIC treatment of focal shoulder lesion previously reported (Götze et al., 2021, Migliorini et al., 2021). As this would allow for less abnormal loading seen on the talar dome and improved joint stability.

The coefficient of friction attained for the shoulder lesion was higher than that previously reported for healthy, native tibiotalar joint. Treatment of the shoulder lesion using AMIC reduced the coefficient of friction from 0.055 ± 0.002 to 0.045 ± 0.001, which is still greater than 0.023 ± 0.001 for the shoulder defect, AMIC repair and healthy samples. This reduction in the coefficient of friction for the repaired tibiotalar joint could provide a biomechanical explanation of the success of AMIC for mid-sized shoulders lesions of the talar dome. Reduction in the coefficient of friction of the joint would reduce the shear forces experienced by the cartilage and thus minimise further degradation of the tissue, reduce the risk of delamination and also allow for increased stability of the AMIC repair; permitting improved clinical outcomes.

6.4.4 AMIC repair of kissing lesion changes the mechanical properties within the tibiotalar joint

Limited studies have been performed to assess the aetiology of kissing lesions within the tibiotalar joint. It is believed that they are the result of an acute injury which causes the talus to impinge on the tibial cartilage at the point injury. As lesions of the tibial plafond are often seen directly opposite a talar lesion, it likely that it is a direct result of the impaction of the talar bone on the opposite tibial tissue (Sijbrandij et al., 2000). Furthermore, it is believed that the concave nature of the tibial surface allows it to dissipate loads better compared with the convex surface of the talus which converges forces into a central point (the centre of the talus). This results in higher amounts of damage observed on the talar dome than the tibial tissue after injury (Camasta et al., 1994,

Sijbrandij et al., 2000).

The occurrence of kissing lesions vary within the literature with one study reporting that 11% of the 146 patients assessed had kissing lesions, which was higher than the 5% previously reported but lower than the incidences reported by Elias *et al.,* and Cuttica *et al.,* of 30% and 15% (Camasta et al., 1994, Cuttica et al., 2012, Elias et al., 2009, Irwin et al., 2018, Sijbrandij et al., 2000). However, many of these studies do not take into account patients with asymptomatic talar OCLs, and have relatively small sample size (Irwin et al., 2018). Patients with lateral talar OCL were reported to show increased incidents of coexisting tibial OCLs (Irwin et al., 2018). This may be attributed to trauma or ankle instability, for which the initial insult and subsequent damage to the soft tissue and ligaments may cause subluxation of the talus and changes to the ankle mortise. This will result in variations in loading and wear damage on the lateral side of the talar dome resulting eventually causing additional cartilage degradation and the concurrent damage to the tibial tissue.

These coexisting lesions have been negatively correlated with lower clinical outcomes (Irwin et al., 2018). Nevertheless, the literature relating to current treatment of kissing lesion is limited, but treatment approaches for osteochondral lesions of the tibial plafond (OLTPs) are the same as those used in OLTs. These include AMIC, BMS and osteochondral transplants. However, it has been identified that the low incidence numbers, paucity of studies and small sample sizes make it challenging to identify and established an appropriate protocol for OLTP treatments (Nery et al., 2021). This adds to the lack of knowledge pertaining to treatments of coexistent lesions, as many studies include this as an exclusion criteria for a patient.

Unlike other AMIC repairs, the coefficient of friction increased for the natural tissues samples after repair with the ChondroGide® membrane on both the tibial and talar tissues. The manufacturer does not recommend that ChondroGide® membrane is used on two opposite articulating surfaces as it hypothesised that it could cause an increase in coefficient of friction and this would have a negative effect on the membrane and also the tissues (Schüttler and Andjelkov, 2012). This was observed within this study. Furthermore, it is believed that the higher friction coefficient may affect the membrane stability within both sites, thus also increasing friction, membrane delamination and failure of the treatment. Our study reveals membrane stability for the kissing lesion was lower than that seen for only a 10 mm talar defect but higher than that observed for larger lesions in the same location (16 mm circular defects). Suggesting that AMIC repair of smaller lesions is a viable treatment modality when using the same membrane to repair both sides of the defect.

More damage is observed on the tibial surface compared to the talar surface after testing within the friction simulator. Tibial cartilage is known to be stiffer resulting in fewer incidences of tibial lesions being reported (Athanasiou et al., 1995). However, the stiffer cartilage may be more susceptible to damage as it cannot absorb changes in loading as well as that seen in the talus. Therefore changes in contact pressures could resulting in the increased damage seen on the tibial tissue. Thus the occurrence of tibial lesions may be a secondary pathology to an initial OLT as continued improper loading of the joints causes additional damage to the corresponding tibial tissue, resulting in an older patient demographic compared to OLTs (Irwin et al., 2018).

6.4.5 Limitations

Currently, for all defects and repair strategies tested, there is a lack of experimental literature to understand the biomechanical and tribological changes involved with different defect locations and size. This is one of the first studies to assess the biomechanical changes associated with kissing lesions and shoulder lesions (Lawson et al., 2019). Furthermore, it is the only study to assess the tribological response of the tibiotalar joint to the presence of different defects. The lack of long term clinical studies for AMIC treatment of defects, with mid-term clinical success being reported but primarily through patient reported outcomes, results in a absence of comparisons to the clinical success or failure of the AMIC treatment, especially when discussing the inherent stability of the repair or of any concomitant tibial damage (Götze et al., 2021).

It was not feasible, in the time allotted, to perform tests on all samples in the healthy or intact state. Instead the values obtained for the healthy tissue in chapter 5 are used as a control group. The absence of testing in a healthy state could impact the studies in a multitude of ways. Firstly, changes in loading for each sample after the introduction of a defect could not be identified. This means that changes in the pressure distribution and contact area attributed to the presence of the defect was not observed. This reduces the clinical discussion available on the impact of the defect but focuses the study onto the repair/treatment modality tested. Furthermore, dislocation or instability introduced by the defect could also not be accounted for as the testing conditions applied to joint during friction testing were chosen after the defect had been made. This means that if the defect did introduce instability to the joint through abnormal loading it would not be identified due to changes in the motion/ flexion or extension that the joint could experience without dislocation.

Another limitation of the friction studies, previously discussed, is the higher amount of fluid present within the tissue bath compared to that normally seen within the joint capsule. This could create increased pressures which could have affected the stability of the AMIC repair within the defects. Literature has suggested that AMIC treatments do fail due to puckering or instability of the membrane within the defect (Jantzen et al., 2022, Migliorini et al., 2022b). The higher pressures attributed to the increased amount of fluid may have increased the likelihood of the AMIC membrane moving within the defect site during testing.

6.4.6 Conclusions

Mechanical characterisations of a range of lesion sizes, locations and the effectiveness of AMIC treatments were presented in this chapter. Changes in pressure distribution, contact area and coefficient of friction will all have implications on the clinical success and longevity of a treatment (Henak et al., 2016). Results of these studies showed that debridement of a lesion into a square shape and treatment using a square AMIC membrane is less favourable then a circular debridement or membrane shape. For both lesion shapes (diameter = 16 mm) the AMIC treatments were unable to return load through the defect site, but did improve the frictional properties compared to the square or circular defect alone. However, increased stability was seen for the circular AMIC membrane in the defect compared to the square defect. Indicating that it is a more favourable shape due to lack of edge loading and thus agrees with current clinical practise.

Treatment of shoulder lesions of the talus are challenging, yet successful outcomes have been reported for AMIC repair of shoulder OLTs (Götze et al., 2021). The outcomes of this study showed that AMIC repair was unable to redistribute pressure though the defect site, but was able to significantly reduce the coefficient of friction observed for the samples. This partial reduction in friction may result in the short/mid-term clinical success attributed to AMIC treatment of shoulder defects. As increasing lesion size has been reported to result in the redistribution of pressure laterally across the talar dome, further studies could be done to assess the stability of the joint relating to the introduction of a shoulder lesion on the talar dome (Lawson et al., 2019).

Kissing lesions present a unique and challenging pathology to treat. The presence of a 10 mm kissing lesion resulted in the lowest observed coefficient of friction of the defects types tested. The use of AMIC to repair kissing lesions showed increase the overall friction coefficient in the joint

compared to the defects alone, the inverse of that observed for other defects tested. Thus, reducing the stability of the repair within the talar defect site compared to a 10 mm OLT alone. Nonetheless, the ChondroGide® membrane repair of the kissing lesion was more stable than the large defects indicating that it may be acceptable treatment for smaller lesions.

Investigations into the biomechanical changes attributed to different lesions and their repairs have scarcely been reported (Hunt et al., 2012, Latt et al., 2011, Lawson et al., 2019). The work presented in this chapter represents a key study assessing the biomechanical changes associated with different lesions and the capabilities of AMIC treatment to repair them. Although AMIC treatment is advised for the repair of mid-sized lesions ($<$ 20 mm), it can be seen that it is unable to return contact mechanics to the defect site for all lesions tested in this chapter (Hurley et al., 2021). Thus indicating that it may be a preferential treatment for lesions smaller than the critical defect size 150 mm^2. Future studies may be performed looking at a larger range of defect sizes between 10 and 16 mm as a well as alternative treatments may help to elucidate the clinical 'gold standard' for OLT treatments.

Chapter 7

Discussion

7.1 Introduction

The aim of the research presented in this thesis was to understand the changes in the biomechanics of the ankle joint due to the presence of osteochondral defects in the talar dome and to assess whether an injectable collagen based hydrogel could be an appropriate intervention. A biomechanical approach was taken for identifying the appropriateness of hydrogel as a treatment for OLTs. This included the development of a natural tissue, whole joint based approach to understanding and characterising the biomechanical changes, contact mechanics and frictional properties seen within the tibiotalar joint as a result of a full thickness chondral lesion. Here, biomechanical *ex vivo* studies and cellular characterisation of both the human ankle joint and the material were used to assess the changes caused by OLTs and to study the affect of current and novel treatments on the tibiotalar biomechanics.

In chapter 1 an assessment of current literature showed that the clinical presentation of osteoarthritis appears often in younger patients, with early arthritis symptoms present in a low number of patients. This can be attributed to the conformity and behaviour of the ankle joint. Interestingly, this provides more clinical challenges compared to osteoarthritis in joints in the leg. This is because of the asymptotic nature of early OA in the ankle, and that it is seen normally as a product of acute injury. In patients where low levels of arthritic changes are seen, minimal interventions are available until the disease has progressed to a point where surgical interventions are deemed appropriate such

as bone marrow stimulation (BMS), AMIC or osteochondral allograft treatment. For OTLs size of the defect often informs the therapeutic strategy adopted by the surgeon. Surgical interventions or non-conservative approaches are favoured for lesions greater than 10mm but there is a lack of literature to support the long term efficacy of current treatment methods (Hurley et al., 2021). Furthermore, in most cases treatments are supported by pre-clinical animal studies in other joints such as the knee and hip and translated clinically into the ankle without a fully understanding of the differences in tissue properties or mechanical loading (Choi et al., 2009). Only a few experimental studies look at the impact of OLTs on the biomechanics of the ankle joint, with two studies looking at the capabilities of treatments to repair contact mechanics. None of the studies presented looked at frictional or tribological changes.

Biomaterials, especially AMIC based treatments, provide a promising technique that can be harnessed to treat OLTs within the ankle, with relatively high success rates seen in smaller lesions for short term studies. Due to the pathological changes associated with OLTs within the ankle joint, there is an opportunity to enhance biomaterials to further promote tissue regeneration for novel OA treatments; which can interact with the biological changes seen within the joint space and enhance the regenerative capacity of the tissue.

Chapter 3 presented the development of a collagen type I hydrogel for injection into a defect site for *in situ* crosslinking of the gel. To allow for *in situ* crosslinking of the gel within the defect site using visible light, the collagen type I gel systems manufacturing had to be modified in a number of ways. The active component of the gel that allowed for MMP inhibitory activity was the functionalisation of 4VBC to the collagen backbone. MA was added to increase solubility closer to neutral pH to allow for the use of LAP photoinitiator to initiate crosslinking after exposure to visible light. The studies presented in this chapter include preliminary morphological characterisation of the hydrogel through SEM and swelling ratios but also studied the viability of immortalised chondrocytes and MSCs within the scaffold. This will provide a platform to study the behaviour and activity of the cells within the scaffold to later look at MMP inhibition or phenotypic changes of cells within the scaffold.

The studies presented in chapter 4 show the development of *ex vivo* porcine models to characterise changes in the natural biomechanics within the tibiotalar joint: focusing on changes in contact mechanics and frictional properties. A few previous cadaveric tissue methods exist for characterising biomechanical changes within the ankle joint using a pressure sensor (Anderson et al., 2007, Choung

and Christensen, 2002, Fansa et al., 2011, Hunt et al., 2012). Furthermore, to this author's knowledge no models exist studying the frictional behaviour of the natural ankle joint. A previous study has been conducted performing pin-on-plate friction testing of the ankle cartilage, without including geometry (Kuganenderan, 2018). In this chapter we present successful porcine methodologies, that were able to measure changes in biomechanics and friction within the ankle joint. Contact pressure and area changes were assessed using a pressure sensor placed between the articulating surfaces of the tibiotalar joint and a friction simulator was used to measure changes in frictional properties. Significant differences were seen between the mean and max contact pressure measured in dorsiflexion conditions between the healthy and 5 mm defects ($p < 0.05$; paired T-test). No significant differences were seen in contact area or in the coefficient of friction between the two conditions. The methodologies successfully measured changes in the joint biomechanics. However, due to the differences in the morphology of the porcine tibiotalar joint and the human ankle, it was not deemed a clinically relevant model to study further and thus the methodologies were translated to human tissue.

Chapter 5 presented the translation of the porcine model to cadaveric tissue to study the changes in tibiotalar joint biomechanics as a result of the present of midsize (10 mm) OLTs and to assess the effect of different treatments on joint biomechanics including the 4VBC-MA collagen type I hydrogel developed in Chapter 4. It was hypothesised that the hydrogel would perform as well as a current membrane based AMIC treatment, ChondroGide®. For some samples, the presence of a defect introduced a new contact point in the posterior lateral region of the talar dome, which could be related to increased joint instability often seen with OLTs (Lee et al., 2015). The 4VBC-MA hydrogel was able to be injection loaded into the defect site and cured to produce a homogenous gel that filled the defect site completely. It performed comparatively to ChondroGide®, with them both showing similar loading profiles for contact area and pressure. The only repair that was able to allow for loading through the defect site was the OAT which was expected as it was an allograft treatment and was assumed to match the mechanical properties of the natural tissue. The presence of a defect was shown to significantly increase the coefficient of friction compared to the healthy tissue. Interestingly, all three repairs tested were able to reduce the coefficient of friction to a similar value compared to the defect alone, but still be significantly higher than the healthy tissue. As expected mechanically, OAT provides the best treatment for OLTs, but the novel hydrogel system developed in this study was able to perform comparatively to current clinical treatments.

Additional clinically driven investigations were performed to utilize the cadaveric mechanical

characterisations to study a range of lesion sizes, locations and the effectiveness of AMIC treatments in those lesions. These studies were developed through discussion with clinicians to identify lesions that clinically provide treatment challenges for surgeons. Outcomes of these studies showed that debridement of a lesion into a square shape and treatment using a square AMIC membrane is less favourable and could negatively impact the joint mechanics resulting in increased damage seen on the tibial tissue as well as decreased stability in the defect site. AMIC treatment in shoulder lesions is a common treatment currently used to treat OLTs (Götze et al., 2021). AMIC treatment of a 16 mm shoulder defect did not significantly change the contact mechanics within the tibiotalar joint compared to the 16 mm circular defect. It did however cause a significant reduction in the overall coefficient of friction to 0.0045 ± 0.001 ($p = 0.005$). The use of AMIC to repair kissing lesions was shown to increase the overall friction coefficient in the joint compared to the defects alone, reducing the stability of the repair within the talar defect site.

In this chapter the challenges raised during material and method development, the outcomes of the mechanical testing of the natural joint with different treatments will be discussed with additional commentary of the clinical implications of the findings.

7.1.1 Material performance of the Hydrogel compared to other AMIC repairs for OLTs

The development of minimally invasive approaches to treat osteochondral lesions is a widely growing field with improvements occurring due to the development of injectable systems and the tuneable properties of hydrogels (Singh et al., 2018). The materials presented in this study were able to be injected into a defect site and crosslinked *in situ*, potentially interacting with the biological environment (Liang et al., 2018a, Singh et al., 2018). The 4VBC-MA hydrogel presented within this work meets many of the design considerations defined by Singh *et al.,*; including its ability to support cells within the scaffold, provide some porosity within the scaffold and its biocompatibility and biodegradability. However, challenges associated with the variability of porosity, lack of the gradient architecture and zonal organisation means that further work and refinement must be performed on the material.

Further studies should be performed to assess the biological properties of the 4VBC-MA scaffold to assess its ability to promote regeneration of tissue and its affect on the phenotype of the damaged

joint through inhibition of MMP activity. Nevertheless, the 4VBC-MA gel presents a promising opportunity for further development for OA treatments.

It is believed that the new material described within this thesis would sit within the realms of AMIC as a treatment and potentially be used in conjunction with BMS, similar to that seen with ChondroGide® or CARGEL® (formerly BST-CarGel, Smith & Nephew, USA). CARGEL ® is an injectable chitosan based hydrogel that is implanted over the defect site and is believed to stabilise blood clots, preventing their retraction and allowing for the maintenance of critical factors, such as MSCs,above the defect site (Shive et al., 2015). This is currently undergoing clinical trials to assess its success treating OCLs of the knee. Mid term results from clinical trials showed a significant improvement in T2 relaxation times and patient reported outcomes were seen using the CARGEL and microfracture compared to just microfracture alone (Shive et al., 2015). However *in vivo* assessments of the material showed that although improved healing was seen compared to BMS alone with increased collagen type II deposition, formation of hyaline cartilage did not occur; histomorphometric results were indicative of fibrocartilage formation (Hede et al., 2020). This highlights the potential associated with the development of materials for OCL treatments to use in conjunction with micro- or nanofracture to enable stabilisation of the blood clot and provide improved healing for the tissue. Comparisons made between the 4VBC-MA hydrogel and ChondroGide® showed that mechanically both materials behaved in a similar way. Both treatment strategies were able to reduce the coefficient of friction of the joint, and although the ChondroGide® treatment did show a non-significant increase in contact area compared to the hydrogel, neither of them presented with loading through the defect site.

7.1.2 Capabilities and limitations of developed methodologies

The limitations for the studies presented within this thesis are discussed in the respective sections. Overarching limitations within the project will be highlighted below and discussed.

The studies presented in this thesis build upon methods previously utilised for assessing contact mechanics within the ankle and also other natural tissues to assess frictional properties (Anderson et al., 2007, Calhoun et al., 1994, Choung and Christensen, 2002, Fansa et al., 2011, Groves et al., 2017, Hunt et al., 2012, Latt et al., 2011). The work presented here is the first time both changes to contact mechanics and friction have been assessed for the same conditions. This allows for a

greater understanding of the "forces at play" within the ankle joint and allows for an improved understanding regarding the biomechanical changes occurring only in the true natural ankle joint caused by lesions and their subsequent repair. Furthermore, this is the first whole joint model testing a hydrogels ability to repair a cartilage based defect, going beyond the work of Mahmood *et al.,* assessing pin-on-plate repair of cartilage defects to provide a more clinically relevant model for testing frictional properties, tribological changes and also stability of treatments.

One of the major limitations of the methodologies presented here is the lack of supporting structures and soft structures. Within these studies, only the talus and tibia were included in the model. Previous contact mechanics work has used the whole ankle joint including the supporting substructures such as the fibula and many of the ligamentous structures (Brockett and Chapman, 2016). The simplicity of the model however, allowed for basic understanding of the interactions between the tibial plafond and the talar dome to be assessed. However, not only could removal of such tissues allow for increases in loads to be transmitted through the tibiotalar joint, there is a loss of stabilisation provided by the tibiofibular syndesmosis and the medial collateral ligaments. This could have resulted in increased inversion or eversion or additional torque due to the lack of constraints in the model, resulting in the 'dislocation' that was sometimes seen after defects were created resulting in the need to alter the friction simulator profile. The presence of soft tissue constraints may play a role in stabilising this reaction thus preventing the dislocation that was seen. Future work could be performed to include the fibula or soft tissues to develop a greater understanding of the interactions of the whole joint.

Sample size is a key challenge associated with any cadaveric work. In all tests using cadaveric tissue a sample size of 7 was used for each condition and for the porcine testing an n=5 was used. The low sample size and high amount of variation between individual samples meant that although statistical analyses were performed, meaningful outcomes or inferences may have been lost due to the high variation seen between the samples. Thus preventing the identification of trends associated with statistically significant outcomes but instead requiring discussion of qualitative changes and general patterns.

7.1.3 Contact pressure within the natural ankle joint, rim stresses and chronic ankle instability

Previously identified by Hunt *et al.,* changes in rim stress could be seen in samples as a result of the introduction of an osteochondral defect greater then 10 mm, increasing the defect size caused a decrease in the distance of the peak stress from the rim. This suggested that there is a threshold for which increasing the lesion results in greater rim stresses without changes in the magnitude of peak stress. Furthermore, they also showed that changes in contact area were more apparent in plantarflexion compared to neutral position (Hunt et al., 2012).

Within this study, the pressure maps presented in figure 5.14 and appendix B figure B.1 - B.7 were scaled for all specimens and conditions to allow for the data to be visually comparable. This results in challenges in identifying changes in peak pressure around the rim of the defect. To study rim stress attributed to the presence of a defect, changes in the pressure measured by each sensel were calculated by taking the pressure measured for the 10 mm defect containing specimen and deducting the value obtained for the same sensel for healthy condition. This calculates any changes in pressure measured by this sensel. Figure 7.1 shows the differences between the 10 mm defect and healthy samples for each condition with the red colours indicating an increase in pressure after the introduction of a defect and a blue colour indicating a decrease in the measured pressure for a defect.

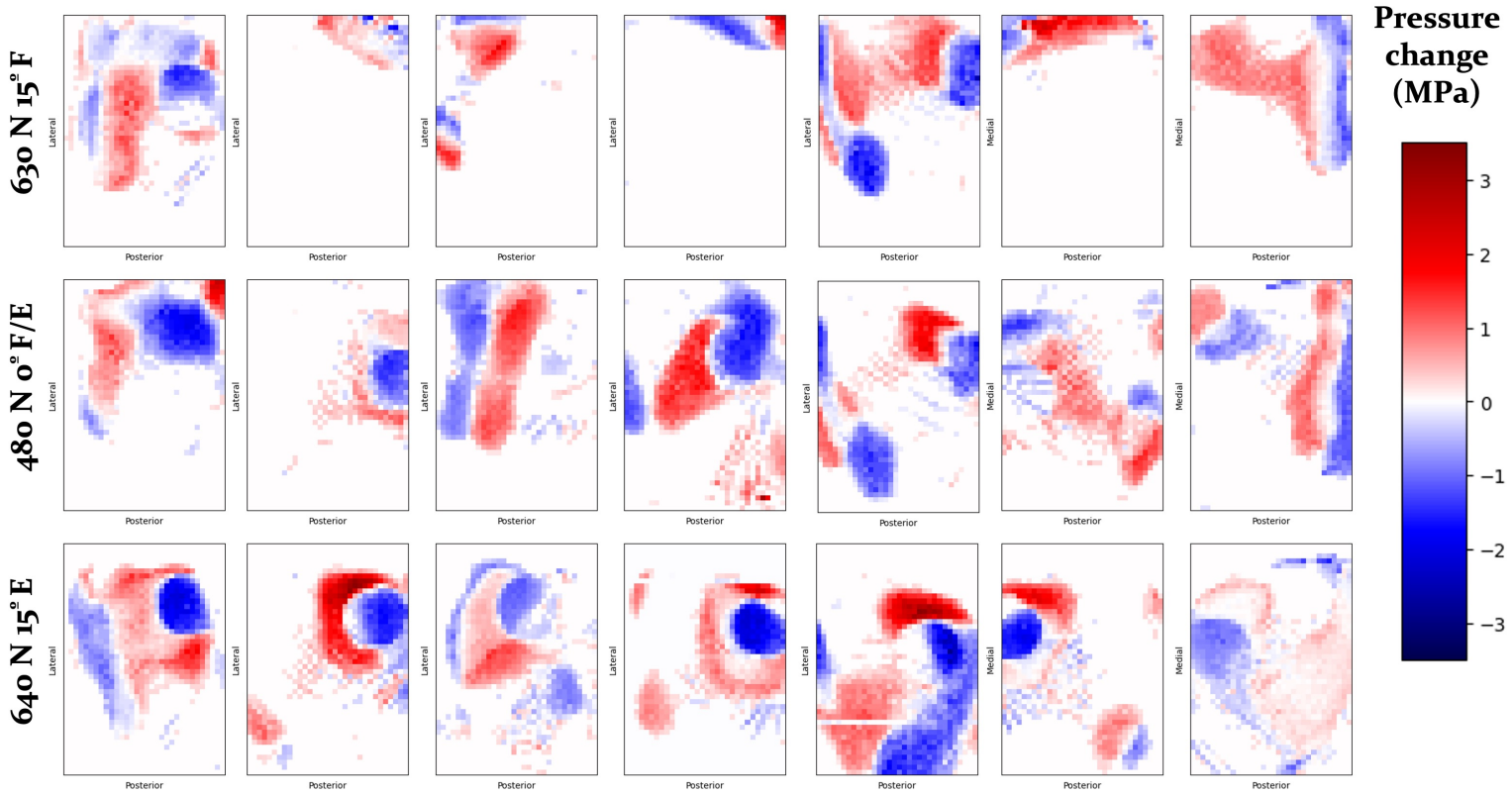

Figure 7.1: Specimen (n =7) specific heat maps showing changes in local talar contact pressure caused by the introduction of a 10 mm chondral centromedial lesion in dorsiflexion/ 15° Flexion (F), neutral condition and plantarflexion 15° Extension (E).

For most samples, an increase in pressure can be seen directly around the defect site in plantarflexion or at 15° E. Furthermore for three specimens in plantarflexion, an increase in pressure was observed in the posterior lateral region of the talar dome. Maximum increase in peak pressure was seen at the rim of the defect in plantarflexion and this is likely the effect observed by Hunt *al.,* (2012). Although this effect did not translate into significant changes in contact pressure or area across the talar dome, it is likely that the changes in pressure distribution are a contributing factor to the significant increase in the friction coefficient observed after the creation of a chondral defect.

The change in friction seen could be attributed to the increase loci of high pressure introduced around the defect rim, that if tested for a longer duration of time would cause more damage to the tissue or reciprocal tibial tissue. Tibial delamination was noted in one sample, but longer testing durations could show increased damage across the samples. In addition, these continued changes in joint biomechanics and elevated localised contact stresses introduced through incongruity of the joint caused by a defect or an acute injury may result in the further cartilage degradation and the eventual development of PTOA. Finite element modelling of the natural ankle joint identified similar changes to contact stresses after a tibial plafond fracture. They showed that post-fracture, there was an increase in areas experiencing high contact stress and concordance with the development of OA within 2 years of injury, most likely caused by abnormal biomechanical loading resulting in changes to the contact pressure (Anderson et al., 2011, Kern and Anderson, 2015).

Kempsen *et al.,* studied age related degeneration of cartilage and saw that talar cartilage behaves differently to that seen in the knee and the hip potentially resulting in the low incidence of OA in the ankle without a traumatic injury (Kempson, 1991). Therefore, it may be more resistant to "wear and tear" during normal function as it is able to distribute load across the whole talar dome. It is less resistant to the changes in contact mechanics attributed to traumatic injury, resulting in the high incidence of PTOA in the ankle.

Furthermore, mechanical abnormalities associated with changes in articular cartilage and joint degeneration and dysfunction have been linked to instability, injury or deformity (Buckwalter and Brown, 2004, McKinley et al., 2008). 10 mm defect creates a new area of contact for some samples in the posterior lateral regions (fig. 7.1). There is concomitant/co-morbidity of OLTs with chronic lateral ankle instability. It is unknown if one caused another, however, they are often found together.

During the study, two key findings elucidate that there are biomechanical changes occurring in the joint as a result of defects as small as 10 mm or 73 mm^2. The first being the introduction

of loading within the plantarflexion position. For 3 samples, a new point of loading was seen in the lateral posterior region of the ankle joint (fig. 7.2, B.2, B.3 & B.6). The second being the requirement to alter the testing profile of friction simulator due to the joint 'dislocating' during testing using the same conditions that the ankle was able to previously able to run in without a defect present. This meant that as load was applied during the ramping stage of the experimental procedure the tibia and talus separated and came out of alignment (fig. 7.2). This suggest that the 10 mm defect was able to change the testing profile of the sample in plantarflexion. For 3 samples a secondary loading profile was adopted to ensure that the test was able to be completed for the full duration of 3600 cycles. Due to simplifications of the methodology presented here, the model used here does not contain any soft tissue constraints or the fibula present. The absence of these soft tissue constraints may result in the dislocation that is seen and therefore, this may not be observed clinically. Removal of the soft tissue, however, has allowed this effect to observed *ex vivo*, and could suggest that although dislocation is not observed clinically, increased stress may be being loaded through the soft tissues due to the presence of an OLT. Thus, this may be relevant in elucidating some of the complex relationship between CLAI and OLTs.

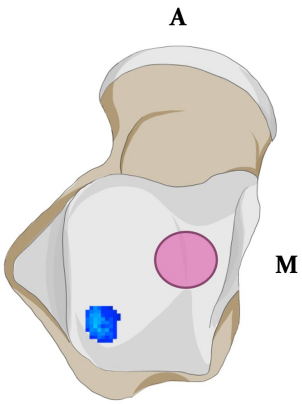

Figure 7.2: Schematic of the superior view of talus showing estimated location of new region of contact on the talar dome after creation of a 10 mm defect. A = Anterior and M = medial

7.1.4 Impact of lesion size and location on tibiotalar mechanical properties

Previous works looking at OLTs within the ankle joint have primarily focused on smaller lesions $\leq$ 12 mm in diameter (Hunt et al., 2012, Li et al., 2022). Within this body of work, lesions of a greater range of sizes and locations were examined. Figure 7.3 shows examples of the different defects tested.

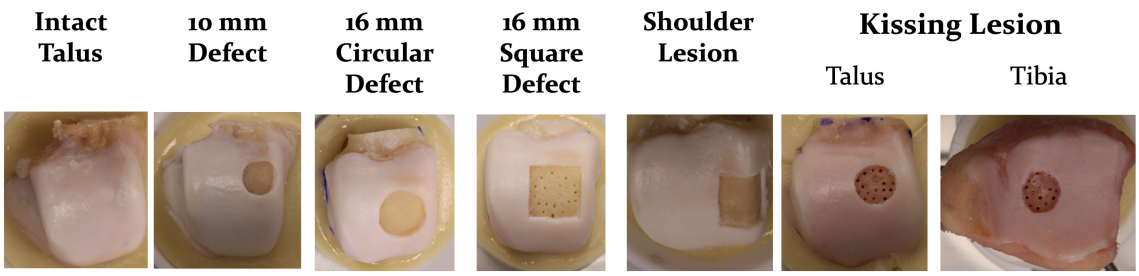

Figure 7.3: Samples of intact talus and the defect sizes and locations tested.

As discussed in chapter 6, differences in the contact mechanics and frictional properties of the joint were observed with each lesion compared to the healthy, intact reference group. For all conditions no significant changes in max contact pressure were observed. In dorsiflexion, the presence of a lesion caused an increase in contact area across the talar dome for all samples, with a significant increase seen in the kissing lesion ($p = 0.03$). Presence of a 10 mm lesion caused an increase in contact area after the introduction of a defect in neutral and plantarflexion conditions. Whereas mean contact area non-significantly decreased for the 16 mm circle and square defect in neutral and plantarflexion conditions. Interestingly, the kissing lesions showed similar contact pressures on the talar dome to that of the healthy and 10 mm talar defect condition. This could be attributed to the size of kissing lesion as it was the same size as the smallest defect tested. Thus it is expected that the contact area on the talar dome would be similar as in neutral position as the coexisting lesion would sit above each other therefore producing a similar contact area between the unaffected tissue ($p = 0.928$). The changes seen in dorsi- and plantarflexion are most likely attributed to the misalignment of the coexisting lesions, resulting in new distributions of contact pressure compared to that see with the 10 mm talar defect alone.

For all studies, full thickness defects had significantly higher friction than then healthy ankle. The increase in coefficient of friction seen is expected as higher friction coefficients have been related to increases in OA severity in the joint (Neu et al., 2010). The lower comparable coefficients of friction seen for both the 16 mm square defect and the kissing lesions compared to the 16 mm circular defect and the 10 mm square defect, respectively, could be attributed to damage to or the lack of the opposite articulating surface causing changes to the superficial zone of the tissue (fig. 6.19). In some cases visible delamination of the reciprocal tissue was seen, indicating damage and may have resulted in the lower friction properties caused by flattening of the cartilage or changes to the creep characteristics of the tissue. Furthermore, increases in contact area can result in a lower

coefficient of friction as the same load is being distributed across a greater area, resulting in the reduction seen for the kissing lesion samples.

The data presented here may contribute to the overall discussion of a critical defect size for OLT of 150 mm^2 or roughly 14 mm in diameter (Choi et al., 2009). The results demonstrate that the patterns of biomechanical changes are not mirrored between the 10 mm circular defect and the 16 mm circular defect, with the 16 mm circular defect displaying reduced contact area and pressures compared to the 10 mm defect and the healthy tissue. This could suggest that there is a threshold at which compensatory loading mechanisms present in the talus are no longer able to counteract the impact of the lesion, thus causing poor prognoses and clinical outcomes for patients.

One of the major limitations of the comparisons made is the variability seen within natural tissue. Although these observations are discussed above, it is important to note that the pressure maps and large sample variation of measurements indicated through the standard deviations for each sample highlight the variability seen in the tissue and the loading profiles produced. To have greater understanding of the actual biomechanical changes for the groups presented in chapter 6, intact measurements of the natural tibiotalar joints should have been made. Due to time constraints it was not feasible to test all these samples as intact condition, thus the intact values obtained in chapter 5 were used to inform the discussion. Having a healthy reference for each sample would have permitted more comparisons to be made to identify patterns in changes of loading as seen in section 7.1.3.

7.1.5 Clinical translation for the repair for OLTs

Lesion size plays a prognostic factor in OLT treatment and is used to inform operative planning: identifying the chosen strategies and also applying a cut off at which a treatment is not viable a (Choi et al., 2009, Jantzen et al., 2022). Guo *et al.,* showed strong correlation between the size of lesion and the successful outcome (Guo et al., 2010). Currently, although widely debated, OLT treatments are believed to be more successful for defects which are lower than 150 mm^2. AMIC treatment has shown success in patients whose lesions are greater then 150 mm^2 (Yontar et al., 2022). For larger lesions a range of treatments are suggested to work including OATs and AMIC but none appear to be superior to one or the other. Hunt *et al.,* and Hannon *et al,.* suggests that outcomes change a lot more beyond the 10 mm. Mid-term studies of primary OLTs have reported

a success rate of 95.3% with an average lesion size of 193.8 mm^2 with a failure rate as low as 4.8%, with higher failure rates being reported for revision treatments of OLT % (Lenz et al., 2020, Yontar et al., 2022). Failure of AMIC for smaller lesions (< 150 mm^2) has been attributed to concomitant pathologies rather than performance of the graft within mid-term studies (median 32 month follow up period) similar to the challenges associated with microfracture (Waltenspül et al., 2023).

This is the first ankle study to assess the biomechanical changes associated with AMIC treatment of lesions in the ankle and one of the first to report on the use of AMIC for kissing lesions. This study has shown that the presence of defects greater than 10 mm in diameter cause biomechanical changes to the joint. As defect size increases and the biomechanics of the joint changes, the redistribution in load may make the ankle more sensitive to load alterations and this could be why lower clinical success is seen (Guo et al., 2010, Hunt et al., 2012, Ramos et al., 2021). Surgical intervention is required to treat OLTs of < 10 mm in diameter size, as the joint biomechanics has been altered to compensate for the presence of the defect and the progressive degeneration of the joint may have begun.

Treatment of OLTs are often informed by clinicians preference or size/location of defect, as there is no gold standard of treatment (Gerards et al., 2015). The outcomes of the biomechanical studies presented in this thesis suggests that for an grade 1 OLT, the only treatment that is able to return joint biomechanics and provide full thickness hyaline cartilage is OAT repair; which is further supported by the literature (Choung and Christensen, 2002, Fansa et al., 2011, Latt et al., 2011). For BMS and AMIC based treatments the outcomes chapter 6 suggests that circular templates for defect debridement and membrane application are favourable for both their stability and to reduce the risk of reciprocal damage encountered on the tibial surface. Furthermore, of the treatments presented here OAT is the only treatment that is able to repair any subchondral bone loss, often seen in later stage OLTs. It can be inferred from the findings of this thesis that inherent stability provided by the morphology of the bone can be lost as a result of an cartilage only OLT. These changes in the natural joint geometry can result in the surrounding soft tissue or ligaments receiving additional loading thus risking CLAI and further damage to the talar dome. An ideal treatment for OLTs needs to minimise or recover biomechanical changes within the tibiotalar joint to prevent further instability and progression into OA.

7.2 Conclusions

The two key functions of articular cartilage are to absorb load and reduced friction for improved motion of the joint. Thus understanding and analysing changes seen in both the biomechanical (contact pressures and area) and tribological changes attributed to osteochondral lesions of the tibiotalar joint provides a more holistic understanding of the implications of OLTs to the general behaviour of the joint. These methodologies can be used to develop and contribute to the current understanding relating to the impacts of OLTs but also provides the platform for improved pre-clinical testing of treatments. Furthermore, understanding the biomechanical changes associated with OLTs will help improve early interventions and provided greater insight for the selection of appropriate treatment based on the lesion size and location. Although several studies exist looking at the clinical success associated with current treatment modalities for OLTs, including OAT, AMIC and BMS, very few studies asses the biomechanical changes attributed to these treatments.

In this thesis, two methods were developed and applied to study the behaviour of full thickness chondral lesions of the talus to understand the biomechanical implications of such changes, relating these to the disease progression seen in OA and also used these method to validate the development of treatments aimed for minimally invasive treatment of OLTs.

Mechanical characterisation of the tibiotalar joint with a 10 mm OLT showed visible changes in contact pressure and contact area on the talar dome. Overall no significant differences were measured for either condition highlighting the potential compensatory behaviour of the tibiotalar joint to redistribute load and pressure across the talar dome as a result of injury. New points of contact introduced through the presence of a small OLT could infer a deepening connection between OLTs and CLAI associated with changes in biomechanical loading during plantarflexion within the tibiotalar joint. Frictional changes showed that presence of a defect caused a significant increase in the coefficient of friction measured within the joint.

A collagen based hydrogel was developed for injectable delivery and *in situ* crosslinking using vis-light within this thesis. The 4VBC-MA hydrogel system was successfully adapted for the intended application for directly delivery and crosslinking in the talus. Cell viability of MSCs and chondrocytes encapsulated within the scaffold suggest biocompatibility of the scaffold and provides a platform to further study the cell-scaffold interaction, including the ability of the scaffold to promote tissue regeneration through the inhibition of MMP enzymes upregulated in an OA environ-

ment. However, further work needs to be performed on the 4VBC-MA hydrogels to understands it biological interactions. This includes further biological characterisation and development to control the pore size, understand the mechanical properties of the acellular and cellularised scaffolds and to study the MMP inhibitory activity of the scaffolds directly relating to OLT environment.

The novel 4VBC-MA collagen hydrogel developed in chapter 4 was successfully tested within cadaveric tissue to assess its ability to mechanically repair the tibiotalar joint. Preclinical testing of the 4VBC-MA hydrogel showed that it was able to provide similar levels of biomechanical recovery to the tibiotalar joint as current AMIC treatment such as ChondroGide®. Furthermore, the preclinical testing of current and novel treatment showed that osteochondral allograft treatment was the only treatment to successfully reintroduce loading through the defect site. However, all three treatments produced similar mean frictional coefficients which were still greater then the values in native healthy tissues. This suggests that mechanically the 4VBC-MA hydrogel performs as well as an equivalent current clinical treatment such as AMIC.

Translation of the developed methodologies was used to assess the biomechanical changes for larger defects, shoulder lesions and kissing lesions and their subsequent AMIC repair. The larger 16 mm circular defects can be attributed to a different pattern of mechanical changes within the tibiotalar joint compared with the 10 mm circular defects. Debridement of a defect into a square shape or AMIC repair using a square template produced poorer mechanical properties and stability compared with their circular counterparts and should be a less favoured shape for treatment. Further studies should be performed to look at repair of shoulder lesions using a circular or oval based defect to study stability of the membrane within the defect site. Additionally, further friction studies should be performed looking material-material interactions for use in kissing lesions to enhance their repair and treatment.

In summary the findings presented within this thesis contribute to our understanding of the biomechanical changes associated with OLTs and provide a platform for future study to support and develop the understanding of the pathology of OLTs and the importance biomechanics plays in disease progression.

7.3 Future work

7.3.1 Material Development

The findings of these studies present multiple possibilities for future work, with the idealistic long term aim of the study translating the 4VBC-MA collagen hydrogel into a viable treatment for OLT treatments.

To achieve this more work needs to performed to characterise the material and understand the properties and behaviour of the hydrogel. Initially characterisation of the mechanical properties of both the cell free and cell laden scaffolds need to be understood. This is because it has been previously reported that scaffolds containing cells show different mechanical properties (Elisseeff et al., 2000). Furthermore, the scaffold system modified for this study has been previously applied to the treatment of bone regeneration but further work must be performed to assess its ability to promote chondrocyte remodelling and cartilage regeneration, as well as understand its ability to interact with the OA micro-environment present in the joint space (Liang et al., 2022). Chapter 4 provides the platform to perform more studies to assess the behaviour of cells within the scaffolds through the development of an encapsulation methodology. These tests would highlight the bioactive component of the material and also show its ability to promote the regeneration of cartilage. If the scaffold does not support the differentiation of chondrocytes or the remodelling, an alternative application could be as an injectable system bone regeneration, which would still be a beneficial outcome.

7.3.2 Biomechanical testing of the tibiotalar joint

The success of the methods developed in chapter 5 and translated through chapter 6 and 7 to cadaveric testing, provide an exciting opportunity to increase our understanding of treatment for OA in the tibiotalar joint. Further research is required to fill the paucity in knowledge relating to biomechanical changes caused by OLTs and the impact these changes have on the critical defect size seen in literature. In this study we aimed to assess clinically relevant defects whose size were greater than or smaller than 150 mm^2. An incremental size approach has been done previously to study biomechanical changes in the talus to a maximum of 12 mm in diameter in cadaveric testing (Hunt et al., 2012, Ramos et al., 2021). Computational testing has assessed the contact mechanics

changes up to 20 mm but these have not been validated against cadaveric samples, but instead simulated using a 3D printed *in vitro* methodology (Ramos et al., 2021). Future studies, looking at both biomechanical and tribological changes around the critical defect size, should be performed to understand if there is a threshold after which compensatory mechanisms hypothesised in the talus are no longer able to overcome the biomechanical changes, thus the resulting in the poor clinical outcome attributed to larger lesions.

Bibliography

M. A. Accardi, S. D. McCullen, A. Callanan, S. Chung, P. M. Cann, M. M. Stevens, and D. Dini. Effects of fiber orientation on the frictional properties and damage of regenerative articular cartilage surfaces. *Tissue Engineering Part A*, 19(19-20):2300–2310, 2013.

S. B. Adams, L. A. Setton, R. D. Bell, M. E. Easley, J. L. Huebner, T. Stabler, V. B. Kraus, E. M. Leimer, S. A. Olson, and D. L. Nettles. Inflammatory cytokines and matrix metalloproteinases in the synovial fluid after intra-articular ankle fracture. *Foot & ankle international*, 36(11):1264–1271, 2015.

S. B. Adams Jr, D. L. Nettles, L. C. Jones, S. D. Miller, G. P. Guyton, and L. C. Schon. Inflammatory cytokines and cellular metabolites as synovial fluid biomarkers of posttraumatic ankle arthritis. *Foot & Ankle International*, 35(12):1241–1249, 2014.

J. Aerssens, S. Boonen, G. Lowet, and J. Dequeker. Interspecies differences in bone composition, density, and quality: potential implications for in vivo bone research. *Endocrinology*, 139(2): 663–670, 1998.

S. Akizuki, V. C. Mow, F. Müller, J. C. Pita, D. S. Howell, and D. H. Manicourt. Tensile properties of human knee joint cartilage: I. influence of ionic conditions, weight bearing, and fibrillation on the tensile modulus. *Journal of Orthopaedic Research*, 4(4):379–392, 1986. ISSN 0736-0266.

D. D. Anderson, J. K. Goldsworthy, W. Li, M. J. Rudert, Y. Tochigi, and T. D. Brown. Physical validation of a patient-specific contact finite element model of the ankle. *Journal of biomechanics*, 40(8):1662–1669, 2007.

D. D. Anderson, Y. Tochigi, M. J. Rudert, T. Vaseenon, T. D. Brown, and A. Amendola. Effect of implantation accuracy on ankle contact mechanics with a metallic focal resurfacing implant. *The Journal of Bone and Joint Surgery. American volume.*, 92(6):1490, 2010.

D. D. Anderson, J. L. Marsh, and T. D. Brown. The pathomechanical etiology of post-traumatic osteoarthritis following intraarticular fractures. *The Iowa orthopaedic journal*, 31:1, 2011.

J. G. Anderson, J. C. Coetzee, and S. T. Hansen. Revision ankle fusion using internal compression arthrodesis with screw fixation. *Foot & ankle international*, 18(5):300–309, 1997.

R. Andrade, S. Vasta, R. Pereira, H. Pereira, R. Papalia, M. Karahan, J. M. Oliveira, R. L. Reis, and J. Espregueira-Mendes. Knee donor-site morbidity after mosaicplasty–a systematic review. *Journal of experimental Orthopaedics*, 3:1–17, 2016.

E. Anitua, M. Sánchez, A. Nurden, M. Zalduendo, M. De La Fuente, J. Azofra, and I. Andia. Platelet-released growth factors enhance the secretion of hyaluronic acid and induce hepatocyte growth factor production by synovial fibroblasts from arthritic patients. *Rheumatology*, 46(12): 1769–1772, 2007. ISSN 1462-0332.

D. Armstrong. *DAMisc: Dave Armstrong's Miscellaneous Functions*, 2022. URL `https://CRAN.R-project.org/package=DAMisc`. R package version 1.7.2.

G. A. Ateshian. The role of interstitial fluid pressurization in articular cartilage lubrication. *Journal of biomechanics*, 42(9):1163–1176, 2009. ISSN 0021-9290.

K. Athanasiou, M. Rosenwasser, J. Buckwalter, T. Malinin, and V. Mow. Interspecies comparisons of in situ intrinsic mechanical properties of distal femoral cartilage. *Journal of Orthopaedic Research*, 9(3):330–340, 1991. ISSN 0736-0266.

K. Athanasiou, A. Agarwal, and F. Dzida. Comparative study of the intrinsic mechanical properties of the human acetabular and femoral head cartilage. *Journal of Orthopaedic Research*, 12(3): 340–349, 1994. ISSN 0736-0266.

K. Athanasiou, G. Niederauer, and R. Schenck. Biomechanical topography of human ankle cartilage. *Annals of biomedical engineering*, 23:697–704, 1995.

K. A. Athanasiou, E. M. Darling, and J. C. Hu. Articular cartilage tissue engineering. *Synthesis Lectures on Tissue Engineering*, 1(1):1–182, 2009.

B. Auguie. *gridExtra: Miscellaneous Functions for "Grid" Graphics*, 2017. URL `https://CRAN.R-project.org/package=gridExtra`. R package version 2.3.

C. S. Bahney, C.-W. Hsu, J. U. Yoo, J. L. West, and B. Johnstone. A bioresponsive hydrogel tuned to chondrogenesis of human mesenchymal stem cells. *The FASEB Journal*, 25(5):1486, 2011.

I. M. Basalo, D. Raj, R. Krishnan, F. H. Chen, C. T. Hung, and G. A. Ateshian. Effects of enzymatic degradation on the frictional response of articular cartilage in stress relaxation. *Journal of biomechanics*, 38(6):1343–1349, 2005. ISSN 0021-9290.

D. Bates, M. Maechler, and M. Jagan. *Matrix: Sparse and Dense Matrix Classes and Methods*, 2022. URL `https://CRAN.R-project.org/package=Matrix`. R package version 1.5-1.

R. Bazaz and R. D. Ferkel. Treatment of osteochondral lesions of the talus with autologous chondrocyte implantation. *Techniques in Foot & Ankle Surgery*, 3(1):45–52, 2004. ISSN 1536-0644.

H. Bengtsson. *matrixStats: Functions that Apply to Rows and Columns of Matrices (and to Vectors)*, 2022. URL `https://CRAN.R-project.org/package=matrixStats`. R package version 0.62.0.

M. Benjamin and E. Evans. Fibrocartilage. *Journal of anatomy*, 171:1, 1990.

J. Benthien and P. Behrens. Autologous matrix-induced chondrogenesis (amic) combining microfracturing and a collagen i/iii matrix for articular cartilage resurfacing. *Cartilage*, 1(1):65–68, 2010. ISSN 1947-6035.

J. P. Benthien and P. Behrens. Reviewing subchondral cartilage surgery: considerations for standardised and outcome predictable cartilage remodelling: a technical note. *International orthopaedics*, 37:2139–2145, 2013.

A. L. Berndt and M. Harty. Transchondral fractures (osteochondritis dissecans) of the talus. *J Bone Joint Surg Am*, 41(6):988–1020, 1959.

M. A. Bidmos, M. R. Dayal, and O. A. Adegboye. Measurements of the talus in the assessment of population affinity. *Forensic science international*, 287:221. e1–221. e7, 2018. ISSN 0379-0738.

R. C. Billinghurst, L. Dahlberg, M. Ionescu, A. Reiner, R. Bourne, C. Rorabeck, P. Mitchell, J. Hambor, O. Diekmann, and H. Tschesche. Enhanced cleavage of type ii collagen by collagenases in osteoarthritic articular cartilage. *The Journal of clinical investigation*, 99(7):1534–1545, 1997. ISSN 0021-9738.

E. J. Blain, S. J. Gilbert, R. J. Wardale, S. Capper, D. J. Mason, and V. C. Duance. Up-regulation of matrix metalloproteinase expression and activation following cyclical compressive loading of articular cartilage in vitro. *Archives of biochemistry and biophysics*, 396(1):49–55, 2001.

J. M. Brimacombe, D. R. Wilson, A. J. Hodgson, K. C. Ho, and C. Anglin. Effect of calibration method on tekscan sensor accuracy. *Journal of Biomechanical Engineering*, 2009. doi: 10.1115/1.3005165.

M. Brittberg, A. Lindahl, A. Nilsson, C. Ohlsson, O. Isaksson, and L. Peterson. Treatment of deep cartilage defects in the knee with autologous chondrocyte transplantation. *New england journal of medicine*, 331(14):889–895, 1994. ISSN 0028-4793.

C. L. Brockett and G. J. Chapman. Biomechanics of the ankle. *Orthopaedics and trauma*, 30(3): 232–238, 2016. ISSN 1877-1327.

C. Brooker and G. Tronci. Effect of mammalian tissue source on the molecular and macroscopic characteristics of uv-cured type i collagen hydrogel networks. *Prosthesis*, 4(1):1–14, 2022.

J. Buckwalter and H. Mankin. Articular cartilage: tissue design and chondrocyte-matrix interactions. *Instructional course lectures*, 47:477–486, 1998. ISSN 0065-6895.

J. A. Buckwalter and T. D. Brown. Joint injury, repair, and remodeling: roles in post-traumatic osteoarthritis. *Clinical Orthopaedics and Related Research®*, 423:7–16, 2004.

R. Buda, F. Vannini, F. Castagnini, M. Cavallo, A. Ruffilli, L. Ramponi, G. Pagliazzi, and S. Giannini. Regenerative treatment in osteochondral lesions of the talus: autologous chondrocyte implantation versus one-step bone marrow derived cells transplantation. *International Orthopaedics*, 39(5):893–900, 2015. ISSN 0341-2695. doi: 10.1007/s00264-015-2685-y.

E. Budiman-Mak, K. J. Conrad, and K. E. Roach. The foot function index: a measure of foot pain and disability. *Journal of clinical epidemiology*, 44(6):561–570, 1991. ISSN 0895-4356.

R. Burdett. Forces predicted at the ankle during running. *Medicine and Science in Sports and Exercise*, 14(4):308–316, 1982.

P. S. Burrage, J. T. Huntington, M. B. Sporn, and C. E. Brinckerhoff. Regulation of matrix metalloproteinase gene expression by a retinoid x receptor–specific ligand. *Arthritis & Rheumatism*, 56 (3):892–904, 2007. ISSN 0004-3591.

J. J. Butler, N. P. Mercer, E. T. Hurley, Y. Shimozono, and J. G. Kennedy. Osteochondral lesions of the tibial plafond: A systematic review. *Orthopaedic Journal of Sports Medicine*, 9(11): 23259671211029208, 2021.

J. H. Calhoun, F. Li, B. R. Ledbetter, and S. F. Viegas. A comprehensive study of pressure distribution in the ankle joint with inversion and eversion. *Foot & ankle international*, 15(3): 125–133, 1994. ISSN 1071-1007.

M. Caligaris and G. A. Ateshian. Effects of sustained interstitial fluid pressurization under migrating contact area, and boundary lubrication by synovial fluid, on cartilage friction. *Osteoarthritis and Cartilage*, 16(10):1220–1227, 2008.

M. Caligaris, C. E. Canal, C. S. Ahmad, T. R. Gardner, and G. A. Ateshian. Investigation of the frictional response of osteoarthritic human tibiofemoral joints and the potential beneficial tribological effect of healthy synovial fluid. *Osteoarthritis and Cartilage*, 17(10):1327–1332, 2009.

J. J. Callaghan. *The adult knee*, volume 1. Lippincott Williams & Wilkins, 2003. ISBN 0781732476.

C. Camasta, T. Pitts, and S. Corey. Bilateral osteochondritis dissecans of the first metatarsophalangeal joint. *Journal of the American Podiatric Medical Association*, 84(6):297–310, 1994.

M. Casper, J. Fitzsimmons, J. Stone, A. Meza, Y. Huang, T. Ruesink, S. O'Driscoll, and G. Reinholz. Tissue engineering of cartilage using poly caprolactone nanofiber scaffolds seeded in vivo with periosteal cells. *Osteoarthritis and cartilage*, 18(7):981–991, 2010. ISSN 1063-4584.

CDC, 2023, Apr 2023. URL \url{https://www.cdc.gov/ncbddd/jointrom/}.

C. K. Chan, G. S. Gulati, R. Sinha, J. V. Tompkins, M. Lopez, A. C. Carter, R. C. Ransom, A. Reinisch, T. Wearda, and M. Murphy. Identification of the human skeletal stem cell. *Cell*, 175 (1):43–56. e21, 2018a. ISSN 0092-8674.

K. W. Chan, R. D. Ferkel, B. Kern, S. S. Chan, and G. R. Applegate. Correlation of mri appearance of autologous chondrocyte implantation in the ankle with clinical outcome. *Cartilage*, 9(1):21–29, 2018b. ISSN 1947-6035.

S. H. Chang, T. Yasui, S. Taketomi, T. Matsumoto, J. Kim-Kaneyama, T. Omiya, Y. Hosaka, H. Inui, Y. Omata, R. Yamagami, et al. Comparison of mouse and human ankles and establishment of mouse ankle osteoarthritis models by surgically-induced instability. *Osteoarthritis and cartilage*, 24(4):688–697, 2016.

H. Chen, J. Sun, C. D. Hoemann, V. Lascau-Coman, W. Ouyang, M. D. McKee, M. S. Shive, and M. D. Buschmann. Drilling and microfracture lead to different bone structure and necrosis during

bone-marrow stimulation for cartilage repair. *Journal of Orthopaedic Research*, 27(11):1432–1438, 2009.

Y. Chen, J. Sui, Q. Wang, Y. Yin, J. Liu, Q. Wang, X. Han, Y. Sun, Y. Fan, and X. Zhang. Injectable self-crosslinking ha-sh/col i blend hydrogels for in vitro construction of engineered cartilage. *Carbohydrate polymers*, 190:57–66, 2018.

W. J. Choi, K. K. Park, B. S. Kim, and J. W. Lee. Osteochondral lesion of the talus: is there a critical defect size for poor outcome? *The American journal of sports medicine*, 37(10):1974–1980, 2009. ISSN 0363-5465.

Y. S. Choi, H. G. Potter, and T. J. Chun. Mr imaging of cartilage repair in the knee and ankle. *Radiographics*, 28(4):1043–1059, 2008. ISSN 0271-5333.

D. Choung and J. C. Christensen. Mosaicplasty of the talus: a joint contact analysis in a cadaver model. *The Journal of foot and ankle surgery*, 41(2):65–75, 2002. ISSN 1067-2516.

J. Christensen, H. Driscoll, and A. Tencer. 1994 william j. stickel gold award. contact characteristics of the ankle joint. part 2. the effects of talar dome cartilage defects. *Journal of the American Podiatric Medical Association*, 84(11):537–547, 1994.

J. Christensen, B. Fischer, M. Nute, and R. Rizza. Fixation strength of polyetheretherketone sheath-and-bullet device for soft tissue repair in the foot and ankle. *The Journal of Foot and Ankle Surgery*, 57(1):60–64, 2018.

B. Chuckpaiwong, E. M. Berkson, and G. H. Theodore. Microfracture for osteochondral lesions of the ankle: outcome analysis and outcome predictors of 105 cases. *Arthroscopy*, 24(1):106–112, 2008. ISSN 0749-8063.

D. Correa and S. A. Lietman. Articular cartilage repair: current needs, methods and research directions. In *Seminars in cell & developmental biology*, volume 62, pages 67–77. Elsevier, 2017.

D. J. Cuttica, W. B. Smith, C. F. Hyer, T. M. Philbin, and G. C. Berlet. Arthroscopic treatment of osteochondral lesions of the tibial plafond. *Foot & Ankle International*, 33(8):662–668, 2012.

J. Dahmen, K. T. A. Lambers, M. L. Reilingh, C. J. A. van Bergen, S. A. S. Stufkens, and G. M. M. J. Kerkhoffs. No superior treatment for primary osteochondral defects of the talus. *Knee Surgery, Sports Traumatology, Arthroscopy*, 26(7):2142–2157, 2018. ISSN 0942-2056. doi: 10.1007/s00167-017-4616-5.

E. N. B. Davidson, D. F. Remst, E. L. Vitters, H. M. van Beuningen, A. B. Blom, M.-J. Goumans, W. B. van den Berg, and P. M. van der Kraan. Increase in alk1/alk5 ratio as a cause for elevated mmp-13 expression in osteoarthritis in humans and mice. *The Journal of Immunology*, 182(12): 7937–7945, 2009.

A. S. de Boer, R. J. Tjioe, F. Van der Sijde, D. E. Meuffels, P. T. den Hoed, C. H. Van der Vlies, W. E. Tuinebreijer, M. H. Verhofstad, and E. M. Van Lieshout. The american orthopaedic foot and ankle society ankle-hindfoot scale; translation and validation of the dutch language version for ankle fractures. *BMJ open*, 7(8):e017040, 2017. ISSN 2044-6055.

H. De Rosario-Martinez. *phia: Post-Hoc Interaction Analysis*, 2015. URL `https://CRAN.R-project.org/package=phia`. R package version 0.2-1.

M. L. Delco, J. G. Kennedy, L. J. Bonassar, and L. A. Fortier. Post-traumatic osteoarthritis of the ankle: a distinct clinical entity requiring new research approaches. *Journal of Orthopaedic Research*, 35(3):440–453, 2017.

A. Dinno. *dunn.test: Dunn's Test of Multiple Comparisons Using Rank Sums*, 2017. URL `https://CRAN.R-project.org/package=dunn.test`. R package version 1.3.5.

R. W. Draeger, B. Singh, and S. G. Parekh. Quantifying normal ankle joint volume: an anatomic study. *Indian journal of orthopaedics*, 43(1):72, 2009.

S. Dunn, J. Soul, S. Anand, J.-M. Schwartz, R. Boot-Handford, and T. Hardingham. Gene expression changes in damaged osteoarthritic cartilage identify a signature of non-chondrogenic and mechanical responses. *Osteoarthritis and cartilage*, 24(8):1431–1440, 2016. ISSN 1063-4584.

C. Egloff, T. Hügle, and V. Valderrabano. Biomechanics and pathomechanisms of osteoarthritis. *Swiss medical weekly*, 142(2930), 2012.

J. J. El-Jawhari, C. L. Brockett, I. Ktistakis, E. Jones, and P. V. Giannoudis. The regenerative therapies of the ankle degeneration: a focus on multipotential mesenchymal stromal cells. *Regenerative medicine*, 13(2):175–188, 2018. ISSN 1746-0751.

I. Elias, S. M. Raikin, M. E. Schweitzer, M. P. Besser, W. B. Morrison, and A. C. Zoga. Osteochondral lesions of the distal tibial plafond: localization and morphologic characteristics with an anatomical grid. *Foot & Ankle International*, 2009. ISSN 1071-1007.

J. Elisseeff, W. McIntosh, K. Anseth, S. Riley, P. Ragan, and R. Langer. Photoencapsulation of chondrocytes in poly (ethylene oxide)-based semi-interpenetrating networks. *Journal of Biomedical Materials Research: An Official Journal of The Society for Biomaterials, The Japanese Society for Biomaterials, and The Australian Society for Biomaterials and the Korean Society for Biomaterials*, 51(2):164–171, 2000.

L. A. Elkin, M. Kay, J. J. Higgins, and J. O. Wobbrock. An aligned rank transform procedure for multifactor contrast tests, 2021.

L. Engebretsen, K. Steffen, J. Alsousou, E. Anitua, N. Bachl, R. Devilee, P. Everts, B. Hamilton, J. Huard, and P. Jenoure. Ioc consensus paper on the use of platelet-rich plasma in sports medicine. *British Journal of Sports Medicine*, 44(15):1072–1081, 2010. ISSN 0306-3674.

A. M. Fansa, C. D. Murawski, C. W. Imhauser, J. T. Nguyen, and J. G. Kennedy. Autologous osteochondral transplantation of the talus partially restores contact mechanics of the ankle joint. *The American journal of sports medicine*, 39(11):2457–2465, 2011. ISSN 0363-5465.

R. D. Ferkel, R. M. Zanotti, G. A. Komenda, N. A. Sgaglione, M. S. Cheng, G. R. Applegate, and R. M. Dopirak. Arthroscopic treatment of chronic osteochondral lesions of the talus: long-term results. *The American journal of sports medicine*, 36(9):1750–1762, 2008. ISSN 0363-5465.

T. M. Fermín, J. M. Hovsepian, P. D'Hooghe, and E. T. Papakostas. Arthroscopic debridement of osteochondral lesions of the talus: a systematic review. *The Foot*, 49:101852, 2021.

C. R. Flannery, C. E. Hughes, B. L. Schumacher, D. Tudor, M. B. Aydelotte, K. E. Kuettner, and B. Caterson. Articular cartilage superficial zone protein (szp) is homologous to megakaryocyte stimulating factor precursor and is a multifunctional proteoglycan with potential growth-promoting, cytoprotective, and lubricating properties in cartilage metabolism. *Biochemical and biophysical research communications*, 254(3):535–541, 1999. ISSN 0006-291X.

A. Flick and N. Gould. Osteochondritis dissecans of the talus (transchondral fractures of the talus): review of the literature and new surgical approach for medial dome lesions. *Foot & ankle*, 5(4): 165–185, 1985. ISSN 0198-0211.

H. Forster and J. Fisher. The influence of loading time and lubricant on the friction of articular cartilage. *Proceedings of the Institution of Mechanical Engineers, Part H: Journal of Engineering in Medicine*, 210(2):109–119, 1996.

H. Forster and J. Fisher. The influence of continuous sliding and subsequent surface wear on the friction of articular cartilage. *Proceedings of the Institution of Mechanical Engineers, Part H: Journal of Engineering in Medicine*, 213(4):329–345, 1999.

J. Fox and S. Weisberg. *An R Companion to Applied Regression*. Sage, Thousand Oaks CA, third edition, 2019. URL `https://socialsciences.mcmaster.ca/jfox/Books/Companion/`.

J. Fox, S. Weisberg, and B. Price. *carData: Companion to Applied Regression Data Sets*, 2022. URL `https://CRAN.R-project.org/package=carData`. R package version 3.0-5.

E. J. Fraser, M. C. Harris, M. P. Prado, and J. G. Kennedy. Autologous osteochondral transplantation for osteochondral lesions of the talus in an athletic population. *Knee Surgery, Sports Traumatology, Arthroscopy*, 24(4):1272–1279, 2016. ISSN 0942-2056. doi: 10.1007/s00167-015-3606-8.

A. Funayama, Y. Niki, H. Matsumoto, S. Maeno, T. Yatabe, H. Morioka, S. Yanagimoto, T. Taguchi, J. Tanaka, and Y. Toyama. Repair of full-thickness articular cartilage defects using injectable type ii collagen gel embedded with cultured chondrocytes in a rabbit model. *Journal of orthopaedic science*, 13:225–232, 2008.

B. C. Gadomski, K. M. Labus, H. L. Stewart, K. T. Bisazza, B. B. Nelson, C. M. Puttlitz, K. C. McGilvray, D. P. Regan, and J. T. Easley. A large animal model for orthopedic foot and ankle research. *Frontiers in Veterinary Science*, 9:816529, 2022.

A. Galarza Torre, J. E. Shaw, A. Wood, H. T. Gilbert, O. Dobre, P. Genever, K. Brennan, S. M. Richardson, and J. Swift. An immortalised mesenchymal stem cell line maintains mechano-responsive behaviour and can be used as a reporter of substrate stiffness. *Scientific reports*, 8 (1):8981, 2018.

M. Galla, I. Duensing, T. L. Kahn, and A. Barg. Open reconstruction with autologous spongiosa grafts and matrix-induced chondrogenesis for osteochondral lesions of the talus can be performed without medial malleolar osteotomy. *Knee Surgery, Sports Traumatology, Arthroscopy*, pages 1–7, 2018. ISSN 0942-2056. doi: 10.1007/s00167-018-5063-7.

Y. Gao, W. Kong, B. Li, Y. Ni, T. Yuan, L. Guo, H. Lin, H. Fan, Y. Fan, and X. Zhang. Fabrication and characterization of collagen-based injectable and self-crosslinkable hydrogels for cell encapsulation. *Colloids and Surfaces B: Biointerfaces*, 167:448–456, 2018.

R. M. Gerards, K. T. Opdam, C. J. van Bergen, and C. N. van Dijk. Diagnostic imaging modalities for osteochondral defects of the talus. *Fuß & Sprunggelenk*, 13(2):78–84, 2015. ISSN 1619-9987.

A. L. Gianakos, Y. Yasui, C. P. Hannon, and J. G. Kennedy. Current management of talar osteochondral lesions. *World journal of orthopedics*, 8(1):12, 2017.

S. Giannini, R. Buda, F. Vannini, F. Di Caprio, and B. Grigolo. Arthroscopic autologous chondrocyte implantation in osteochondral lesions of the talus: Surgical technique and results. *The American Journal of Sports Medicine*, 36(5):873–880, 2008. ISSN 0363-5465. doi: 10.1177/0363546507312644.

S. Giannini, M. Battaglia, R. Buda, M. Cavallo, A. Ruffilli, and F. Vannini. Surgical treatment of osteochondral lesions of the talus by open-field autologuous chondrocyte implantation: a 10-year follow-up clinical and magnetic resonance imaging t2-mapping evaluation. *The American journal of sports medicine*, 37(1):112–118, 2009a. ISSN 0363-5465.

S. Giannini, R. Buda, F. Vannini, M. Cavallo, and B. Grigolo. One-step bone marrow-derived cell transplantation in talar osteochondral lesions. *CLINICAL ORTHOPAEDICS AND RELATED RESEARCH*, 467(12):3307–3320, 2009b. ISSN 0009-921X. doi: 10.1007/s11999-009-0885-8.

S. Giannini, R. Buda, M. Battaglia, M. Cavallo, A. Ruffilli, L. Ramponi, G. Pagliazzi, and F. Vannini. One-step repair in talar osteochondral lesions: 4-year clinical results and t2-mapping capability in outcome prediction. *The American Journal of Sports Medicine*, 41(3):511–518, 2013. ISSN 0363-5465. doi: 10.1177/0363546512467622.

S. Giannini, R. Buda, A. Ruffilli, M. Cavallo, G. Pagliazzi, M. C. Bulzamini, G. Desando, D. Luciani, and F. Vannini. Arthroscopic autologous chondrocyte implantation in the ankle joint. *Knee Surgery, Sports Traumatology, Arthroscopy*, 22(6):1311–1319, 2014. ISSN 0942-2056.

M. Glazebrook, T. Daniels, A. Younger, C. Foote, M. Penner, K. Wing, J. Lau, R. Leighton, and M. Dunbar. Comparison of health-related quality of life between patients with end-stage ankle and hip arthrosis. *JBJS*, 90(3):499–505, 2008.

J. Gleghorn, A. Jones, C. Flannery, and L. Bonassar. Boundary mode frictional properties of engineered cartilaginous tissues. *Eur Cell Mater*, 14(20):2007–24, 2007.

O. Gottschalk, S. Altenberger, S. Baumbach, S. Kriegelstein, F. Dreyer, A. Mehlhorn, H. Hörterer, A. Töpfer, A. Röser, and M. Walther. Functional medium-term results after autologous matrix-induced chondrogenesis for osteochondral lesions of the talus: a 5-year prospective cohort study. *The Journal of Foot and Ankle Surgery*, 56(5):930–936, 2017. ISSN 1067-2516.

C. Götze, C. Nieder, H. Felder, C. D. Peterlein, and F. Migliorini. Amic for traumatic focal osteochondral defect of the talar shoulder: a 5 years follow-up prospective cohort study. *BMC Musculoskeletal Disorders*, 22:1–8, 2021.

D. Groves, J. Fisher, and S. Williams. An in vitro simulation method for the tribological assessment of complete natural hip joints. *PloS one*, 12(9):e0184226, 2017.

F. Guilak, W. R. Jones, H. P. Ting-Beall, and G. M. Lee. The deformation behavior and mechanical properties of chondrocytes in articular cartilage. *Osteoarthritis and Cartilage*, 7(1):59–70, 1999. ISSN 1063-4584.

Q.-w. Guo, Y.-l. Hu, C. Jiao, C.-l. Yu, and Y.-f. Ao. Arthroscopic treatment for osteochondral lesions of the talus: analysis of outcome predictors. *Chinese medical journal*, 123(03):296–300, 2010.

M. Guvendiren, H. D. Lu, and J. A. Burdick. Shear-thinning hydrogels for biomedical applications. *Soft matter*, 8(2):260–272, 2012.

C. Hannon, N. Smyth, C. Murawski, I. Savage-Elliott, T. Deyer, J. Calder, and J. Kennedy. Osteochondral lesions of the talus: aspects of current management. *Bone Joint J*, 96(2):164–171, 2014. ISSN 2049-4394.

C. P. Hannon, C. D. Murawski, N. A. Smyth, and J. G. Kennedy. Critical defect size for osteochondral lesions of the talus. *The American Journal of Sports Medicine*, 40(9):NP23–NP24, 2012.

W. Hayes and L. Mockros. Viscoelastic properties of human articular cartilage. *Journal of applied physiology*, 31(4):562–568, 1971. ISSN 8750-7587.

K. Hede, B. Christensen, M. Olesen, J. Thomsen, C. Foldager, and M. Lind. Cargel bioscaffold improves cartilage repair tissue after bone marrow stimulation in a minipig model. *Journal of Experimental Orthopaedics*, 7(1):1–11, 2020.

C. R. Henak, K. A. Ross, E. D. Bonnevie, L. A. Fortier, I. Cohen, J. G. Kennedy, and L. J. Bonassar. Human talar and femoral cartilage have distinct mechanical properties near the articular surface. *Journal of biomechanics*, 49(14):3320–3327, 2016.

S. Hepple, I. G. Winson, and D. Glew. Osteochondral lesions of the talus: a revised classification. *Foot & ankle international*, 20(12):789–793, 1999. ISSN 1071-1007.

M. Herrera-Pérez, D. González-Martín, M. Vallejo-Márquez, A. L. Godoy-Santos, V. Valderrabano, and S. Tejero. Ankle osteoarthritis aetiology. *Journal of Clinical Medicine*, 10(19):4489, 2021.

B. Hintermann and V. Valderrabano. Total ankle replacement. *Foot and ankle clinics*, 8(2):375–405, 2003. ISSN 1083-7515.

M. Hlaváček. Squeeze-film lubrication of the human ankle joint with synovial fluid filtrated by articular cartilage with the superficial zone worn out. *Journal of biomechanics*, 33(11):1415–1422, 2000.

M. Horisberger, V. Valderrabano, and B. Hintermann. Posttraumatic ankle osteoarthritis after ankle-related fractures. *Journal of orthopaedic trauma*, 23(1):60–67, 2009. ISSN 0890-5339.

J.-M. Howes, D. Bihan, D. A. Slatter, S. W. Hamaia, L. C. Packman, V. Knauper, R. Visse, and R. W. Farndale. The recognition of collagen and triple-helical toolkit peptides by mmp-13: sequence specificity for binding and cleavage. *Journal of Biological Chemistry*, 289(35):24091–24101, 2014.

Q. Hu and M. Ecker. Overview of mmp-13 as a promising target for the treatment of osteoarthritis. *International Journal of Molecular Sciences*, 22(4):1742, 2021.

K. J. Hunt, A. T. Lee, D. P. Lindsey, W. Slikker, and L. B. Chou. effect of defect size and plantarflexion angle on ankle joint stresses: osteochondral lesions of the talus. *American Journal of Sports Medicine*, 40(4):895–901, 2012.

E. B. Hunziker, M. Michel, and D. Studer. Ultrastructure of adult human articular cartilage matrix after cryotechnical processing. *Microscopy research and technique*, 37(4):271–284, 1997. ISSN 1059-910X.

E. T. Hurley, S. K. Stewart, J. G. Kennedy, E. J. Strauss, J. Calder, and A. Ramasamy. Current management strategies for osteochondral lesions of the talus. *The Bone & Joint Journal*, 103(2): 207–212, 2021.

A. Iordan, A. Duperray, A. Gérard, A. Grichine, and C. Verdier. Breakdown of cell-collagen networks through collagen remodeling. *Biorheology*, 47(5-6):277–295, 2010.

R. M. Irwin, Y. Shimozono, Y. Yasui, R. Megill, T. W. Deyer, and J. G. Kennedy. Incidence of coexisting talar and tibial osteochondral lesions correlates with patient age and lesion location. *Orthopaedic Journal of Sports Medicine*, 6(8):2325967118790965, 2018.

L. J. Plotrix: a package in the red light district of r. *R-News*, 6(4):8–12, 2006.

S. Jahn, J. Seror, and J. Klein. Lubrication of articular cartilage. *Annual review of biomedical engineering*, 18:235–258, 2016.

C. Jantzen, L. B. Ebskov, and J. K. Johansen. Amic procedure for treatment of osteochondral lesions of talus—a systematic review of the current literature. *The Journal of Foot and Ankle Surgery*, 61(4):888–895, 2022.

R. Jin, L. M. Teixeira, A. Krouwels, P. J. Dijkstra, C. Van Blitterswijk, M. Karperien, and J. Feijen. Synthesis and characterization of hyaluronic acid–poly (ethylene glycol) hydrogels via michael addition: An injectable biomaterial for cartilage repair. *Acta biomaterialia*, 6(6):1968–1977, 2010.

A. Kassambara. *ggpubr: 'ggplot2' Based Publication Ready Plots*, 2023a. URL `https://CRAN.R-project.org/package=ggpubr`. R package version 0.6.0.

A. Kassambara. *rstatix: Pipe-Friendly Framework for Basic Statistical Tests*, 2023b. URL `https://CRAN.R-project.org/package=rstatix`. R package version 0.7.2.

J. Kaupp. *nord: Arctic Ice Studio's Nord and Group of Seven Inspired Colour Palettes for 'ggplot2'*, 2019. URL `https://CRAN.R-project.org/package=nord`. R package version 1.0.0.

S. Kawabata, T. Nakasa, Y. Ikuta, J. Sumii, A. Nekomoto, and N. Adachi. High incidence of osteoarthritic changes in patients with osteochondral lesions of the talus without chronic lateral ankle instability. *Journal of Orthopaedic Science*, 2022.

M. Kay, L. A. Elkin, J. J. Higgins, and J. O. Wobbrock. *ARTool: Aligned Rank Transform for Nonparametric Factorial ANOVAs*, 2021. URL `https://github.com/mjskay/ARTool`. R package version 0.11.1.

T. J. Kean, Z. Ge, Y. Li, R. Chen, and J. E. Dennis. Transcriptome-wide analysis of human chondrocyte expansion on synoviocyte matrix. *Cells*, 8(2):85, 2019. ISSN 2073-4409. URL `http://www.mdpi.com/2073-4409/8/2/85`.

T. Keitt. *colorRamps: Builds Color Tables*, 2022. URL `https://CRAN.R-project.org/package=colorRamps`. R package version 2.3.1.

G. Kempson, M. Freeman, and S. Swanson. Tensile properties of articular cartilage. *Nature*, 220 (5172):1127–1128, 1968. ISSN 0028-0836.

G. E. Kempson. Age-related changes in the tensile properties of human articular cartilage: a comparative study between the femoral head of the hip joint and the talus of the ankle joint. *Biochimica et Biophysica Acta (BBA)-General Subjects*, 1075(3):223–230, 1991.

A. M. Kern and D. D. Anderson. Expedited patient-specific assessment of contact stress exposure in the ankle joint following definitive articular fracture reduction. *Journal of biomechanics*, 48(12): 3427–3432, 2015.

J.-H. Kim, G. Lee, Y. Won, M. Lee, J.-S. Kwak, C.-H. Chun, and J.-S. Chun. Matrix cross-linking–mediated mechanotransduction promotes posttraumatic osteoarthritis. *Proceedings of the National Academy of Sciences*, 112(30):9424–9429, 2015. ISSN 0027-8424.

A. C. Kok, G. J. Tuijthof, S. den Dunnen, J. van Tiel, M. Siebelt, V. Everts, C. N. van Dijk, and G. M. Kerkhoffs. No effect of hole geometry in microfracture for talar osteochondral defects. *Clinical Orthopaedics and Related Research®*, 471(11):3653–3662, 2013.

L.-S. Kontturi, E. Järvinen, V. Muhonen, E. C. Collin, A. S. Pandit, I. Kiviranta, M. Yliperttula, and A. Urtti. An injectable, in situ forming type ii collagen/hyaluronic acid hydrogel vehicle for chondrocyte delivery in cartilage tissue engineering. *Drug delivery and translational research*, 4: 149–158, 2014.

D. Koulalis, W. Schultz, and M. Heyden. Autologous chondrocyte transplantation for osteochondritis dissecans of the talus. *Clinical Orthopaedics and Related Research®*, 395:186–192, 2002. ISSN 0009-921X.

M. J. Kraeutler, J. Chahla, C. S. Dean, J. J. Mitchell, M. G. Santini-Araujo, S. J. Pinney, and C. Pascual-Garrido. Current concepts review update: osteochondral lesions of the talus. *Foot & ankle international*, 38(3):331–342, 2017. ISSN 1071-1007.

V. B. Kraus, T. V. Stabler, S. Kong, G. Varju, and G. McDaniel. Measurement of synovial fluid volume using urea. *Osteoarthritis and cartilage*, 15(10):1217–1220, 2007.

F. Krause and H. Anwander. Osteochondral lesion of the talus: still a problem? *EFORT open reviews*, 7(6):337, 2022.

P. C. M. D. P. Kreuz, R. H. c. D. m. Kalkreuth, P. M. D. P. Niemeyer, M. M. D. P. Uhl, and C. M. D. P. Erggelet. Treatment of a focal articular cartilage defect of the talus with polymer-based autologous chondrocyte implantation: A 12-year follow-up period. *Journal of Foot and Ankle Surgery, The*, 56(4):862–864, 2017. ISSN 1067-2516. doi: 10.1053/j.jfas.2017.03.001.

R. Krishnan, M. Kopacz, and G. A. Ateshian. Experimental verification of the role of interstitial fluid pressurization in cartilage lubrication. *Journal of orthopaedic research*, 22(3):565–570, 2004.

N. Kuganenderan. *Biotribology of the Natural Ankle Joint*. PhD thesis, University of Leeds, 2018.

S. K. Kwak, B. S. Kern, R. D. Ferkel, K. W. Chan, S. Kasraeian, and G. R. Applegate. Autologous chondrocyte implantation of the ankle: 2-to 10-year results. *The American journal of sports medicine*, 42(9):2156–2164, 2014. ISSN 0363-5465.

A. Kwanyuang. *Biomechanical Evaluation of Total Ankle Replacements*. PhD thesis, University of Leeds, 2016.

K. Y. Lam and H. M. Siow. Conservative treatment for juvenile osteochondritis dissecans of the talus. *Journal of Orthopaedic Surgery*, 20(2):176–180, 2012. ISSN 2309-4990.

R. Lane Smith, M. Trindade, T. Ikenoue, M. Mohtai, P. Das, D. Carter, S. Goodman, and D. Schurman. Effects of shear stress on articular chondrocyte metabolism. *Biorheology*, 37(1, 2):95–107, 2000. ISSN 0006-355X.

L. D. Latt, R. R. Glisson, H. E. Montijo, F. G. Usuelli, and M. E. Easley. Effect of graft height mismatch on contact pressures with osteochondral grafting of the talus. *The American journal of sports medicine*, 39(12):2662–2669, 2011.

L. Laver, N. Marom, L. Dnyanesh, O. Mei-Dan, J. Espregueira-Mendes, and A. Gobbi. Prp for degenerative cartilage disease: A systematic review of clinical studies. *Cartilage*, 8(4):341–364, 2017. ISSN 1947-6035. doi: 10.1177/1947603516670709.

P. Lawson, P. Kumparatana, T. Baldini, S. Challa, D. Moon, and K. Hunt. Osteochondral lesions of the talus–a biomechanical explanation for larger olt shoulder lesions leading to increased patient risk. *Foot & Ankle Orthopaedics*, 4(4):2473011419S00046, 2019.

J. H. Lee, J. B. Fitzgerald, M. A. DiMicco, and A. J. Grodzinsky. Mechanical injury of cartilage explants causes specific time-dependent changes in chondrocyte gene expression. *Arthritis & Rheumatism: Official Journal of the American College of Rheumatology*, 52(8):2386–2395, 2005.

M. Lee, J. W. Kwon, W. J. Choi, and J. W. Lee. Comparison of outcomes for osteochondral lesions of the talus with and without chronic lateral ankle instability. *Foot & Ankle International*, 36(9): 1050–1057, 2015. ISSN 1071-1007. doi: 10.1177/1071100715581477.

S.-Y. Lee and G. Tae. Formulation and in vitro characterization of an in situ gelable, photopolymerizable pluronic hydrogel suitable for injection. *Journal of controlled release*, 119(3):313–319, 2007.

R. V. Lenth. *emmeans: Estimated Marginal Means, aka Least-Squares Means*, 2023. URL `https://CRAN.R-project.org/package=emmeans`. R package version 1.8.8.

C. G. Lenz, S. Tan, A. L. Carey, K. Ang, and T. Schneider. Matrix-induced autologous chondrocyte implantation (maci) grafting for osteochondral lesions of the talus. *Foot & ankle international*, 41 (9):1099–1105, 2020.

H. Li, D. Wang, Y. Yuan, and J. Min. New insights on the mmp-13 regulatory network in the pathogenesis of early osteoarthritis. *Arthritis research & therapy*, 19(1):248, 2017. ISSN 1478-6362.

J. Li, Y. Wang, Y. Wei, D. Kong, Y. Lin, D. Wang, S. Cheng, P. Yin, and M. Wei. The effect of talus osteochondral defects of different area size on ankle joint stability: a finite element analysis. *BMC Musculoskeletal Disorders*, 23(1):500, 2022.

N.-G. Li, Z.-H. Shi, Y.-P. Tang, Z.-J. Wang, S.-L. Song, L.-H. Qian, D.-W. Qian, and J.-A. Duan. New hope for the treatment of osteoarthritis through selective inhibition of mmp-13. *Current medicinal chemistry*, 18(7):977–1001, 2011. ISSN 0929-8673.

H. Liang, S. J. Russell, D. J. Wood, and G. Tronci. A hydroxamic acid–methacrylated collagen conjugate for the modulation of inflammation-related mmp upregulation. *Journal of Materials Chemistry B*, 6(22):3703–3715, 2018a.

H. Liang, S. J. Russell, D. J. Wood, and G. Tronci. Monomer-induced customization of uv-cured atelocollagen hydrogel networks. *Frontiers in chemistry*, 6, 2018b.

H. Liang, J. Yin, K. Man, X. B. Yang, E. Calciolari, N. Donos, S. J. Russell, D. J. Wood, and G. Tronci. A long-lasting guided bone regeneration membrane from sequentially functionalised photoactive atelocollagen. *Acta Biomaterialia*, 140:190–205, 2022.

A. Liu, E. Ingham, J. Fisher, and L. M. Jennings. Development of a pre-clinical experimental simulation model of the natural porcine knee with appropriate ligamentous constraints. *PloS one*, 14(5):e0216872, 2019.

C. Liu, T. Li, Z. Yang, D. Liu, Y. Li, Z. Zhou, and Q. Zhang. Kartogenin enhanced chondrogenesis in cocultures of chondrocytes and bone mesenchymal stem cells. *Tissue Engineering Part A*, 24 (11-12):990–1000, 2018.

M. Liu, X. Zeng, C. Ma, H. Yi, Z. Ali, X. Mou, S. Li, Y. Deng, and N. He. Injectable hydrogels for cartilage and bone tissue engineering. *Bone research*, 5:17014, 2017.

J. Lizhang, S. D. Taylor, Z. Jin, J. Fisher, and S. Williams. Effect of clearance on cartilage tribology in hip hemi-arthroplasty. *Proceedings of the Institution of Mechanical Engineers, Part H: Journal of Engineering in Medicine*, 227(12):1284–1291, 2013.

C. A. Looze, J. Capo, M. K. Ryan, J. P. Begly, C. Chapman, D. Swanson, B. C. Singh, and E. J. Strauss. Evaluation and management of osteochondral lesions of the talus. *Cartilage*, 8(1):19–30, 2017. ISSN 1947-6035.

H. Mahmood, D. Eckold, I. Stead, D. E. Shepherd, D. M. Espino, and K. D. Dearn. A method for the assessment of the coefficient of friction of articular cartilage and a replacement biomaterial. *Journal of the Mechanical Behavior of Biomedical Materials*, 103:103580, 2020.

A. Mak. The apparent viscoelastic behavior of articular cartilage—the contributions from the intrinsic matrix viscoelasticity and interstitial fluid flows. *Journal of biomechanical engineering*, 108 (2):123–130, 1986. ISSN 0148-0731.

H. J. Mankin and L. Lippiello. The turnover of adult rabbit articular cartilage. *JBJS*, 51(8): 1591–1596, 1969. ISSN 0021-9355.

J. M. Mansour and V. C. Mow. The permeability of articular cartilage under compressive strain and at high pressures. *The Journal of bone and joint surgery. American volume*, 58(4):509–516, 1976. ISSN 0021-9355.

T. Marasović, M. Cecić, and V. Zanchi. Analysis and interpretation of ground reaction forces in normal gait. *WSEAS transactions on systems*, 8(9):1105–14, 2009.

S. Marlovits, P. Singer, P. Zeller, I. Mandl, J. Haller, and S. Trattnig. Magnetic resonance observation of cartilage repair tissue (mocart) for the evaluation of autologous chondrocyte transplantation: determination of interobserver variability and correlation to clinical outcome after 2 years. *European journal of radiology*, 57(1):16–23, 2006. ISSN 0720-048X.

A. Maroudas, P. Bullough, S. Swanson, and M. Freeman. The permeability of articular cartilage. *The Journal of bone and joint surgery. British volume*, 50(1):166–177, 1968. ISSN 0301-620X.

A. Maroudas, H. Muir, and J. Wingham. The correlation of fixed negative charge with glycosaminoglycan content of human articular cartilage. *Biochimica et Biophysica Acta (BBA)-General Subjects*, 177(3):492–500, 1969. ISSN 0304-4165.

B. Marquass, J. Somerson, P. Hepp, T. Aigner, S. Schwan, A. Bader, C. Josten, M. Zscharnack, and R. Schulz. A novel msc-seeded triphasic construct for the repair of osteochondral defects. *Journal of Orthopaedic Research*, 28(12):1586–1599, 2010.

M. C. Mattos e Dinato, M. de Faria Freitas, and A. S. Iutaka. A porcine model for arthroscopy. *Foot & Ankle International*, 31(2):179–181, 2010.

L. McCann, I. Udofia, S. Graindorge, E. Ingham, Z. Jin, and J. Fisher. Tribological testing of articular cartilage of the medial compartment of the knee using a friction simulator. *Tribology International*, 41(11):1126–1133, 2008.

C. W. McCutchen. The frictional properties of animal joints. *Wear*, 5(1):1–17, 1962.

N. McGoldrick, E. Murphy, and S. Kearns. Osteochondral lesions of the ankle: The current evidence supporting scaffold-based techniques and biological adjuncts. *Foot and Ankle Surgery*, 2017. ISSN 1268-7731.

T. O. McKinley, Y. Tochigi, M. J. Rudert, and T. D. Brown. Instability-associated changes in contact stress and contact stress rates near a step-off incongruity. *JBJS*, 90(2):375–383, 2008.

J. Medley, D. Dowson, and V. Wright. Transient elastohydrodynamic lubrication models for the human ankle joint. *Engineering in medicine*, 13(3):137–151, 1984.

O. Mei-Dan, M. R. Carmont, L. Laver, G. Mann, N. Maffulli, and M. Nyska. Platelet-rich plasma or hyaluronate in the management of osteochondral lesions of the talus. *The American journal of sports medicine*, 40(3):534–541, 2012. ISSN 0363-5465.

Y. Melenevsky, R. A. Mackey, R. B. Abrahams, and N. B. Thomson III. Talar fractures and dislocations: a radiologist's guide to timely diagnosis and classification. *Radiographics*, 35(3): 765–779, 2015. ISSN 0271-5333.

J. M. Michael, A. Golshani, S. Gargac, and T. Goswami. Biomechanics of the ankle joint and clinical outcomes of total ankle replacement. *Journal of the mechanical behavior of biomedical materials*, 1(4):276–294, 2008.

F. Migliorini, N. Maffulli, A. Baroncini, M. Knobe, M. Tingart, and J. Eschweiler. Matrix-induced autologous chondrocyte implantation versus autologous matrix-induced chondrogenesis for chondral defects of the talus: a systematic review. *British medical bulletin*, 2021.

F. Migliorini, J. Eschweiler, C. Goetze, T. Pastor, R. Giorgino, F. Hildebrand, and N. Maffulli. Cell therapies for chondral defects of the talus: a systematic review. *Journal of Orthopaedic Surgery and Research*, 17(1):1–9, 2022a.

F. Migliorini, N. Maffulli, A. Bell, F. Hildebrand, C. D. Weber, and P. Lichte. Autologous matrix-induced chondrogenesis (amic) for osteochondral defects of the talus: A systematic review. *Life*, 12(11):1738, 2022b.

S. Mirkiani, D. A. Roszko, C. L. O'Sullivan, P. Faridi, D. S. Hu, D. Fang, D. G. Everaert, A. Toossi, P. E. Konrad, K. Robinson, et al. Overground gait kinematics and muscle activation patterns in the yucatan mini pig. *Journal of Neural Engineering*, 19(2):026009, 2022.

Y. Morita, N. Tomita, H. Aoki, M. Sonobe, S. Wakitani, Y. Tamada, T. Suguro, and K. Ikeuchi. Frictional properties of regenerated cartilage in vitro. *Journal of biomechanics*, 39(1):103–109, 2006.

F. T. Moutos and F. Guilak. Functional properties of cell-seeded three-dimensionally woven poly (ε-caprolactone) scaffolds for cartilage tissue engineering. *Tissue Engineering Part A*, 16(4):1291–1301, 2010.

V. C. Mow and R. Huiskes. *Basic orthopaedic biomechanics & mechano-biology*. Lippincott Williams & Wilkins, 2005. ISBN 0781739330.

V. C. Mow, S. Kuei, W. M. Lai, and C. G. Armstrong. Biphasic creep and stress relaxation of articular cartilage in compression: theory and experiments. *Journal of biomechanical engineering*, 102(1):73–84, 1980. ISSN 0148-0731.

V. C. Mow, M. H. Holmes, and W. M. Lai. Fluid transport and mechanical properties of articular cartilage: a review. *Journal of biomechanics*, 17(5):377–394, 1984. ISSN 0021-9290.

C. Muehleman, A. Berzins, H. Koepp, W. Eger, A. Cole, K. Kuettner, and D. Sumner. Bone density of the human talus does not increase with the cartilage degeneration score. *The Anatomical Record: An Official Publication of the American Association of Anatomists*, 266(2):81–86, 2002.

H. Muir, P. Bullough, and A. Maroudas. The distribution of collagen in human articular cartilage with some of its physiological implications. *The Journal of bone and joint surgery. British volume*, 52(3):554–563, 1970. ISSN 0301-620X.

C. D. Murawski and J. G. Kennedy. Operative treatment of osteochondral lesions of the talus. *JBJS*, 95(11):1045–1054, 2013.

E. P. Murphy, N. P. McGoldrick, M. Curtin, and S. R. Kearns. A prospective evaluation of bone marrow aspirate concentrate and microfracture in the treatment of osteochondral lesions of the talus. *Foot and ankle surgery : official journal of the European Society of Foot and Ankle Surgeons*, 2018. ISSN 1268-7731. doi: 10.1016/j.fas.2018.02.011.

E. K. Nam, R. D. Ferkel, and G. R. Applegate. Autologous chondrocyte implantation of the ankle: a 2-to 5-year follow-up. *The American journal of sports medicine*, 37(2):274–284, 2009. ISSN 0363-5465.

A. T. Neffe, B. F. Pierce, G. Tronci, N. Ma, E. Pittermann, T. Gebauer, O. Frank, M. Schossig, X. Xu, B. M. Willie, M. Forner, A. Ellinghaus, J. Lienau, G. N. Duda, and A. Lendlein. One step creation of multifunctional 3d architectured hydrogels inducing bone regeneration. *Advanced Materials*, 27(10):1738–1744, 2015. ISSN 0935-9648. doi: 10.1002/adma.201404787.

C. Nery, M. Prado, G. Brauer, and A. V. Lemos. Retrograde autologous osteochondral transplantation in treating osteochondral lesion of distal tibial plafond: A case report and technical tips. *Foot & Ankle International*, 42(8):1081–1092, 2021.

C. Neu, A. Reddi, K. Komvopoulos, T. Schmid, and P. Di Cesare. Increased friction coefficient and superficial zone protein expression in patients with advanced osteoarthritis. *Arthritis & Rheumatism*, 62(9):2680–2687, 2010.

E. Neuwirth. *RColorBrewer: ColorBrewer Palettes*, 2022. URL `https://CRAN.R-project.org/package=RColorBrewer`. R package version 1.1-3.

NICE. Overview | joint distraction for ankle osteoarthritis | guidance | nice, 2015. URL `https://www.nice.org.uk/guidance/ipg538`.

NICE, 2019. URL \url{https://www.nice.org.uk/guidance/ipg637/chapter/1-Recommendations}.

P. Niemeyer, G. Salzmann, H. Schmal, H. Mayr, and N. P. Südkamp. Autologous chondrocyte implantation for the treatment of chondral and osteochondral defects of the talus: a meta-analysis of available evidence. *Knee Surgery, Sports Traumatology, Arthroscopy*, 20(9):1696–1703, 2012. ISSN 0942-2056.

M. Nordin and V. H. Frankel. *Basic biomechanics of the musculoskeletal system*. Lippincott Williams & Wilkins, 2001.

E. Nott, L. M. Matheny, T. O. Clanton, C. Lockard, B. W. Douglass, K. K. Tanghe, N. Matta, and A. W. Brady. Accessibility and thickness of medial and lateral talar body cartilage for treatment of ankle and foot osteochondral lesions. *Foot & Ankle International*, 42(10):1330–1339, 2021.

S. Nozaki, K. Watanabe, T. Kato, T. Miyakawa, T. Kamiya, and M. Katayose. Radius of curvature at the talocrural joint surface: inference of subject-specific kinematics. *Surgical and Radiologic Anatomy*, 41(1):53–64, 2019.

D. H. Ogle, J. C. Doll, A. P. Wheeler, and A. Dinno. *FSA: Simple Fisheries Stock Assessment Methods*, 2023. URL `https://CRAN.R-project.org/package=FSA`. R package version 0.9.4.

P. F. O'loughlin, B. E. Heyworth, and J. G. Kennedy. Current concepts in the diagnosis and treatment of osteochondral lesions of the ankle. *The American journal of sports medicine*, 38(2): 392–404, 2010. ISSN 0363-5465.

N. Olov, S. Bagheri-Khoulenjani, and H. Mirzadeh. Injectable hydrogels for bone and cartilage tissue engineering: a review. *Progress in Biomaterials*, 11(2):113–135, 2022.

T. Pap and A. Korb-Pap. Cartilage damage in osteoarthritis and rheumatoid arthritis—two unequal siblings. *Nature Reviews Rheumatology*, 11(10):606, 2015. ISSN 1759-4804.

H. Park, B. Choi, J. Hu, and M. Lee. Injectable chitosan hyaluronic acid hydrogels for cartilage tissue engineering. *Acta biomaterialia*, 9(1):4779–4786, 2013.

Y. Park, M. P. Lutolf, J. A. Hubbell, E. B. Hunziker, and M. Wong. Bovine primary chondrocyte culture in synthetic matrix metalloproteinase-sensitive poly (ethylene glycol)-based hydrogels as a scaffold for cartilage repair. *Tissue engineering*, 10(3-4):515–522, 2004.

J. Pelletier, J. Martel-Pelletier, and S. B. Abramson. Osteoarthritis, an inflammatory disease: potential implication for the selection of new therapeutic targets. *Arthritis & Rheumatism: Official Journal of the American College of Rheumatology*, 44(6):1237–1247, 2001. ISSN 0004-3591.

J. W. Peters, S. G. Trevino, and P. A. Renstrom. Chronic lateral ankle instability. *Foot & ankle*, 12(3):182–191, 1991. ISSN 0198-0211.

R. J. Petrella and M. Petrella. A prospective, randomized, double-blind, placebo controlled study to evaluate the efficacy of intraarticular hyaluronic acid for osteoarthritis of the knee. *The Journal of rheumatology*, 33(5):951–956, 2006. ISSN 0315-162X.

J. Peyron. The epidemiology of osteoarthritis. *Osteoarthritis. Diagnosis and treatment.*, pages 9–27, 1984.

T. M. Pham, L. H. Frich, K. L. Lambertsen, S. Overgaard, H. Schmal, et al. Elevation of inflammatory cytokines and proteins after intra-articular ankle fracture: a cross-sectional study of 47 ankle fracture patients. *Mediators of Inflammation*, 2021, 2021.

G. Polat, A. Erşen, M. E. Erdil, T. Kızılkurt, Ö. Kılıçoğlu, and M. Aşık. Long-term results of microfracture in the treatment of talus osteochondral lesions. *Knee Surgery, Sports Traumatology, Arthroscopy*, 24:1299–1303, 2016.

B. Poulet, R. de Souza, A. Kent, L. Saxon, O. Barker, A. Wilson, Y.-M. Chang, M. Cake, and A. Pitsillides. Intermittent applied mechanical loading induces subchondral bone thickening that may be intensified locally by contiguous articular cartilage lesions. *Osteoarthritis and cartilage*, 23(6):940–948, 2015.

R Core Team. *R: A Language and Environment for Statistical Computing*. R Foundation for Statistical Computing, Vienna, Austria, 2022. URL `https://www.R-project.org/`.

M. M. Rahman, J. A. Kopec, J. Cibere, C. H. Goldsmith, and A. H. Anis. The relationship between osteoarthritis and cardiovascular disease in a population health survey: a cross-sectional study. *BMJ open*, 3(5):e002624, 2013.

S. M. Raikin, I. Elias, A. C. Zoga, W. B. Morrison, M. P. Besser, and M. E. Schweitzer. Osteochondral lesions of the talus: localization and morphologic data from 424 patients using a novel anatomical grid scheme. *Foot & ankle international*, 28(2):154–161, 2007. ISSN 1071-1007.

A. Ramos, C. Rocha, and M. Mesnard. The effect of osteochondral lesion size and ankle joint position on cartilage behavior-numerical and in vitro experimental results. *Medical Engineering & Physics*, 98:73–82, 2021.

L. Ramponi, Y. Yasui, C. D. Murawski, R. D. Ferkel, C. W. DiGiovanni, G. M. Kerkhoffs, J. D. Calder, M. Takao, F. Vannini, and W. J. Choi. Lesion size is a predictor of clinical outcomes after bone marrow stimulation for osteochondral lesions of the talus: a systematic review. *The American journal of sports medicine*, 45(7):1698–1705, 2017. ISSN 0363-5465.

P. L. Ramsey and W. Hamilton. Changes in tibiotalar area of contact caused by lateral talar shift. *JBJS*, 58(3):356–357, 1976.

I. Redler, V. C. Mow, M. L. Zimny, and J. Mansell. The ultrastructure and biomechanical significance of the tidemark of articular cartilage. *Clinical orthopaedics and related research*, 112(1):357–362, 1975. ISSN 0009-921X. URL `http://europepmc.org/abstract/MED/1192647`.

M. Reilingh, C. van Bergen, L. Blankevoort, R. Gerards, I. van Eekeren, G. Kerkhoffs, and C. van Dijk. Computed tomography analysis of osteochondral defects of the talus after arthroscopic debridement and microfracture. *Knee Surgery, Sports Traumatology, Arthroscopy*, 24(4):1286–1292, 2016. ISSN 0942-2056.

M. Richter and S. Zech. Matrix-associated stem cell transplantation (mast) in chondral defects of foot and ankle is effective. *Foot and Ankle Surgery*, 19(2):84–90, 2013. ISSN 1268-7731.

M. Richter, S. Zech, J. Geerling, M. Frink, K. Knobloch, and C. Krettek. A new foot and ankle outcome score: questionnaire based, subjective, visual-analogue-scale, validated and computerized. *Foot and Ankle Surgery*, 12(4):191–199, 2006. ISSN 1268-7731.

C. L. Riegger. Anatomy of the ankle and foot. *Physical therapy*, 68(12):1802–1814, 1988. ISSN 0031-9023.

A. Roaas and G. B. Andersson. Normal range of motion of the hip, knee and ankle joints in male subjects, 30–40 years of age. *Acta Orthopaedica Scandinavica*, 53(2):205–208, 1982.

D. Robinson, I. Winson, W. Harries, and A. Kelly. Arthroscopic treatment of osteochondral lesions of the talus. *The Journal of bone and joint surgery. British volume*, 85(7):989–993, 2003. ISSN 0301-620X.

A. A. Romeo, B. J. Cole, A. D. Mazzocca, J. A. Fox, K. B. Freeman, and E. Joy. Autologous chondrocyte repair of an articular defect in the humeral head. *Arthroscopy The Journal of Arthroscopic & Related Surgery*, 18(8):925–929, 2002. ISSN 0749-8063.

K. A. Ross, C. P. Hannon, T. W. Deyer, N. A. Smyth, M. Hogan, H. T. Do, and J. G. Kennedy. Functional and mri outcomes after arthroscopic microfracture for treatment of osteochondral lesions of the distal tibial plafond. *JBJS*, 96(20):1708–1715, 2014.

B. B. Rothrauff, C. D. Murawski, C. Angthong, C. Becher, S. Nehrer, P. Niemeyer, M. Sullivan, V. Valderrabano, M. Walther, and R. D. Ferkel. Scaffold-based therapies: Proceedings of the international consensus meeting on cartilage repair of the ankle. *Foot & Ankle International*, 39 (1):41S–47S, 2018. ISSN 1071-1007.

P. J. Roughley and E. R. Lee. Cartilage proteoglycans: structure and potential functions. *Microscopy research and technique*, 28(5):385–397, 1994. ISSN 1059-910X.

A. D. Rowan, G. J. Litherland, W. Hui, and J. M. Milner. Metalloproteases as potential therapeutic targets in arthritis treatment. *Expert opinion on therapeutic targets*, 12(1):1–18, 2008.

R. S. Salk, T. J. Chang, W. F. D'costa, D. J. Soomekh, and K. A. Grogan. Sodium hyaluronate in the treatment of osteoarthritis of the ankle: a controlled, randomized, double-blind pilot study. *JBJS*, 88(2):295–302, 2006. ISSN 0021-9355.

A. L. G. Santos, M. K. Demange, M. P. Prado, T. D. Fernandes, P. N. Giglio, and B. Hintermann. Cartilage lesions and ankle osteoarthrosis: review of the literature and treatment algorithm. *Revista brasileira de ortopedia*, 49(6):565–572, 2014. ISSN 0102-3616.

D. Sarkar. *Lattice: Multivariate Data Visualization with R*. Springer, New York, 2008. URL `http://lmdvr.r-forge.r-project.org`. ISBN 978-0-387-75968-5.

D. Sarkar and F. Andrews. *latticeExtra: Extra Graphical Utilities Based on Lattice*, 2022. URL `https://CRAN.R-project.org/package=latticeExtra`. R package version 0.6-30.

A. Saxena and C. Eakin. Articular talar injuries in athletes: Results of microfracture and autogenous bone graft. *The American Journal of Sports Medicine*, 35(10):1680–1687, 2007. ISSN 0363-5465. doi: 10.1177/0363546507303561.

H. Schmal, A. Mehlhorn, F. Stoffel, W. Köstler, N. P. Südkamp, and P. Niemeyer. In vivo quantification of intraarticular cytokines in knees during natural and surgically induced cartilage repair. *Cytotherapy*, 11(8):1065–1075, 2009. ISSN 1465-3249.

H. Schmal, G. M. Salzmann, E. R. Langenmair, R. Henkelmann, N. P. Südkamp, and P. Niemeyer. Biochemical characterization of early osteoarthritis in the ankle. *The Scientific World Journal*, 2014, 2014. ISSN 2356-6140.

H. Schmal, R. Henkelmann, A. T. Mehlhorn, K. Reising, G. Bode, N. P. Südkamp, and P. Niemeyer. Synovial cytokine expression in ankle osteoarthritis depends on age and stage. *Knee Surgery, Sports Traumatology, Arthroscopy*, 23(5):1359–1367, 2015. ISSN 0942-2056.

T. Schmidt and R. Sah. Effect of synovial fluid on boundary lubrication of articular cartilage. *OsteoArthritis and cartilage*, 15(1):35–47, 2007.

S. Schüttler and N. Andjelkov. Periosteal transplantation combined with the autologous matrix-induced chondrogenesis (amic) technique in isolated patellofemoral osteoarthritis: a case report. *Cartilage*, 3(2):194–198, 2012.

S.-S. Seo, C.-W. Kim, D.-W. Jung, et al. Management of focal chondral lesion in the knee joint. *Knee Surgery and Related Research*, 23(4):185–196, 2011.

C. Sermer, B. Devitt, J. Chahal, R. Kandel, and J. Theodoropoulos. The addition of platelet-rich plasma to scaffolds used for cartilage repair: a review of human and animal studies. *Arthroscopy The Journal of Arthroscopic & Related Surgery*, 31(8):1607–1625, 2015. ISSN 0749-8063.

C. Shearer, R. Loomer, and D. Clement. Nonoperatively managed stage 5 osteochondral talar lesions. *Foot & ankle international*, 23(7):651–654, 2002. ISSN 1071-1007.

D. Shepherd and B. Seedhom. Thickness of human articular cartilage in joints of the lower limb. *Annals of the rheumatic diseases*, 58(1):27–34, 1999. ISSN 0003-4967.

M. S. Shive, W. D. Stanish, R. McCormack, F. Forriol, N. Mohtadi, S. Pelet, J. Desnoyers, S. Méthot, K. Vehik, and A. Restrepo. Bst-cargel® treatment maintains cartilage repair superiority over microfracture at 5 years in a multicenter randomized controlled trial. *Cartilage*, 6(2):62–72, 2015.

A. Signorell. *DescTools: Tools for Descriptive Statistics*, 2023. URL `https://CRAN.R-project.org/package=DescTools`. R package version 0.99.48.

E. S. Sijbrandij, A. P. van Gils, J. W. K. Louwerens, and E. E. de Lange. Posttraumatic subchondral bone contusions and fractures of the talotibial joint: occurrence of "kissing" lesions. *American Journal of Roentgenology*, 175(6):1707–1710, 2000. ISSN 0361-803X.

W. H. Simon, S. Friedenberg, and S. Richardson. Joint congruence: a correlation of joint congruence and thickness of articular cartilage in dogs. *JBJS*, 55(8):1614–1620, 1973.

P. Singh, K. B. Marcu, M. B. Goldring, and M. Otero. Phenotypic instability of chondrocytes in osteoarthritis: on a path to hypertrophy. *Annals of the New York Academy of Sciences*, 2018.

A. J. Sophia Fox, A. Bedi, and S. A. Rodeo. The basic science of articular cartilage: structure, composition, and function. *Sports Health*, 1(6):461–8, 2009. ISSN 1941-7381 (Print) 1941-0921. doi: 10.1177/1941738109350438.

S. Standring. *Gray's anatomy e-book: the anatomical basis of clinical practice*. Elsevier Health Sciences, 2015. ISBN 0702068519.

J. R. Steadman, W. G. Rodkey, S. B. Singleton, and K. K. Briggs. Microfracture technique forfull-thickness chondral defects: Technique and clinical results. *Operative techniques in orthopaedics*, 7(4):300–304, 1997.

J. R. Steele, T. J. Dekker, A. E. Federer, J. L. Liles, S. B. Adams, and M. E. Easley. Osteochondral lesions of the talus: current concepts in diagnosis and treatment. *Foot & Ankle Orthopaedics*, 3 (3):2473011418779559, 2018.

J. Steinhagen, O. Niggemeyer, and J. Bruns. Ätiologie und pathogenese der osteochondrosis dissecans talietiology and pathogenesis of osteochondritis dissecans of the talus. *Der Orthopäde*, 30(1):20–27, 2001. ISSN 0085-4530.

M. Sánchez, E. Anitua, J. Azofra, J. Aguirre, and I. Andia. Intra-articular injection of an autologous preparation rich in growth factors for the treatment of knee oa: a retrospective cohort study. *Clin Exp Rheumatol*, 26(5):910–913, 2008.

J. S. Temenoff and A. G. Mikos. Tissue engineering for regeneration of articular cartilage. *Biomaterials*, 21(5):431–440, 2000. ISSN 0142-9612.

J. Tol, P. Struijs, P. Bossuyt, R. Verhagen, and C. Van Dijk. Treatment strategies in osteochondral defects of the talar dome: a systematic review. *Foot & ankle international*, 21(2):119–126, 2000. ISSN 1071-1007.

S. Treppo, H. Koepp, E. C. Quan, A. A. Cole, K. E. Kuettner, and A. J. Grodzinsky. Comparison of biomechanical and biochemical properties of cartilage from human knee and ankle pairs. *Journal of Orthopaedic Research*, 18(5):739–748, 2000. ISSN 0736-0266.

G. Tronci, J. Yin, R. A. Holmes, H. Liang, S. J. Russell, and D. J. Wood. Protease-sensitive atelocollagen hydrogels promote healing in a diabetic wound model. *Journal of Materials Chemistry B*, 4(45):7249–7258, 2016.

E. Uchiyama, D. Suzuki, H. Kura, T. Yamashita, and G. Murakami. Distal fibular length needed for ankle stability. *Foot & ankle international*, 27(3):185–189, 2006.

V. Valderrabano, B. M. Nigg, V. von Tscharner, D. J. Stefanyshyn, B. Goepfert, and B. Hintermann. Gait analysis in ankle osteoarthritis and total ankle replacement. *Clinical Biomechanics*, 22(8): 894–904, 2007. ISSN 0268-0033.

V. Valderrabano, M. Horisberger, I. Russell, H. Dougall, and B. Hintermann. Etiology of ankle osteoarthritis. *Clinical Orthopaedics and Related Research®*, 467(7):1800, 2009. ISSN 0009-921X.

V. Valderrabano, M. Miska, A. Leumann, and M. Wiewiorski. Reconstruction of osteochondral lesions of the talus with autologous spongiosa grafts and autologous matrix-induced chondrogenesis. *The American Journal of Sports Medicine*, 41(3):519–527, 2013. ISSN 0363-5465. doi: 10.1177/0363546513476671.

V. Valderrabano, A. Barg, A. Alattar, and M. Wiewiorski. Osteochondral lesions of the ankle joint in professional soccer players: Treatment with autologous matrix-induced chondrogenesis. *Foot & Ankle Specialist*, 7(6):522–528, 2014. ISSN 1938-6400. doi: 10.1177/1938640014539811.

C. J. van Bergen, G. M. Kerkhoffs, N. Marsidi, C. M. Korstjens, V. Everts, L. J. van Ruijven, C. N. van Dijk, and L. Blankevoort. Osteochondral defects of the talus: a novel animal model in the goat. *Tissue Engineering Part C: Methods*, 19(6):449–457, 2013.

C. J. van Bergen, I. C. van Eekeren, M. L. Reilingh, R. M. Gerards, and C. N. van Dijk. The use of hemicap for the treatment of osteochondral lesions. *Operative Techniques in Orthopaedics*, 24(3): 190–194, 2014. ISSN 1048-6666.

P. Van der Kraan and W. Van den Berg. Chondrocyte hypertrophy and osteoarthritis: role in initiation and progression of cartilage degeneration? *Osteoarthritis and cartilage*, 20(3):223–232, 2012.

P. R. van Diepen, J. Dahmen, J. N. Altink, S. A. Stufkens, and G. M. Kerkhoffs. Location distribution of 2,087 osteochondral lesions of the talus. *Cartilage*, 13(1_suppl):1344S–1353S, 2021.

C. N. Van Dijk, M. L. Reilingh, M. Zengerink, and C. J. Van Bergen. Osteochondral defects in the ankle: why painful? *Knee Surgery, Sports Traumatology, Arthroscopy*, 18(5):570–580, 2010. ISSN 0942-2056.

F. Vannini, G. Filardo, E. Kon, A. Roffi, M. Marcacci, and S. Giannini. Scaffolds for cartilage repair of the ankle joint: The impact on surgical practice. *Foot Ankle Surg*, 19(1):2–8, 2013. ISSN 1268-7731. doi: 10.1016/j.fas.2012.07.001.

F. Vannini, G. G. Costa, S. Caravelli, G. Pagliazzi, and M. Mosca. Treatment of osteochondral lesions of the talus in athletes: what is the evidence? *Joints*, 4(2):111, 2016.

S. L. Vega, M. Y. Kwon, and J. A. Burdick. Recent advances in hydrogels for cartilage tissue engineering. *European cells & materials*, 33:59, 2017.

A. Veljkovic, A. Norton, P. Salat, C. Saltzman, J. Femino, P. Phisitkul, and A. Amendola. Lateral talar station: a clinically reproducible measure of sagittal talar position. *Foot & ankle international*, 34(12):1669–1676, 2013.

R. Verhagen, P. Struijs, and P. Bossuyt. Systematic review of treatment strategies for osteochondral defects of the talar dome. *Foot and ankle clinics*, 8(2):233–42, viii–ix, 2003. ISSN 1083-7515.

F. Veronesi, M. Maglio, S. Brogini, A. Mazzotti, E. Artioli, and G. Giavaresi. A systematic review of the retrograde drilling approach for osteochondral lesion of the talus: Questioning surgical approaches, outcome evaluation and gender-related differences. *Journal of Clinical Medicine*, 12 (13):4523, 2023.

T. L. Vincent. Targeting mechanotransduction pathways in osteoarthritis: a focus on the pericellular matrix. *Current opinion in pharmacology*, 13(3):449–454, 2013.

T. L. Vincent and J. Saklatvala. Is the response of cartilage to injury relevant to osteoarthritis? *ARTHRITIS AND RHEUMATISM*, 58(5):1207–1210, 2008. ISSN 0004-3591. doi: 10.1002/art.23443.

M. Waltenspül, C. Suter, J. Ackermann, N. Kühne, and S. F. Fucentese. Autologous matrix-induced chondrogenesis (amic) for isolated retropatellar cartilage lesions: outcome after a follow-up of minimum 2 years. *Cartilage*, 13(1_suppl):1280S–1290S, 2021.

M. Waltenspül, M. Meisterhans, J. Ackermann, and S. Wirth. Typical complications after cartilage repair of the ankle using autologous matrix-induced chondrogenesis (amic). *Foot & Ankle Orthopaedics*, 8(1):24730114231164150, 2023.

L. Wan, R. De Asla, H. Rubash, and G. Li. Determination of in-vivo articular cartilage contact areas of human talocrural joint under weightbearing conditions. *Osteoarthritis and cartilage*, 14 (12):1294–1301, 2006. ISSN 1063-4584.

H. Wang and G. A. Ateshian. The normal stress effect and equilibrium friction coefficient of articular cartilage under steady frictional shear. *Journal of biomechanics*, 30(8):771–776, 1997.

X. Wang, P. A. Manner, A. Horner, L. Shum, R. S. Tuan, and G. H. Nuckolls. Regulation of mmp-13 expression by runx2 and fgf2 in osteoarthritic cartilage. *Osteoarthritis and Cartilage*, 12(12): 963–973, 2004. ISSN 1063-4584.

G. R. Warnes, B. Bolker, L. Bonebakker, R. Gentleman, W. Huber, A. Liaw, T. Lumley, M. Maechler, A. Magnusson, S. Moeller, M. Schwartz, and B. Venables. *gplots: Various R Programming Tools for Plotting Data*, 2022. URL `https://CRAN.R-project.org/package=gplots`. R package version 3.1.3.

J. Warren, C. Brockett, A. Canden, and M. A. Farndon. How does surgical technique affect fluid permeability? a laboratory study comparing nanofracture, microfracture and fine wire drilling approaches. *Foot & Ankle Orthopaedics*, 7(4):2473011421S00995, 2022.

J.-P. Whittaker, G. Smith, N. Makwana, S. Roberts, P. Harrison, P. Laing, and J. Richardson. Early results of autologous chondrocyte implantation in the talus. *The Journal of bone and joint surgery. British volume*, 87(2):179–183, 2005. ISSN 0301-620X.

H. Wickham. Reshaping data with the reshape package. *Journal of Statistical Software*, 21(12), 2007a. URL `https://www.jstatsoft.org/v21/i12/`.

H. Wickham. Reshaping data with the reshape package. *Journal of Statistical Software*, 21(12): 1–20, 2007b. URL `http://www.jstatsoft.org/v21/i12/`.

H. Wickham. The split-apply-combine strategy for data analysis. *Journal of Statistical Software*, 40 (1):1–29, 2011. URL `https://www.jstatsoft.org/v40/i01/`.

H. Wickham, M. Averick, J. Bryan, W. Chang, L. D. McGowan, R. François, G. Grolemund, A. Hayes, L. Henry, J. Hester, M. Kuhn, T. L. Pedersen, E. Miller, S. M. Bache, K. Müller, J. Ooms, D. Robinson, D. P. Seidel, V. Spinu, K. Takahashi, D. Vaughan, C. Wilke, K. Woo, and H. Yutani. Welcome to the tidyverse. *Journal of Open Source Software*, 4(43):1686, 2019. doi: 10.21105/joss.01686.

H. Wickham, J. Bryan, and M. Barrett. *usethis: Automate Package and Project Setup*, 2022a. URL `https://CRAN.R-project.org/package=usethis`. R package version 2.1.6.

H. Wickham, J. Hester, W. Chang, and J. Bryan. *devtools: Tools to Make Developing R Packages Easier*, 2022b. URL `https://CRAN.R-project.org/package=devtools`. R package version 2.4.4.

M. Wiewiorski, A. Barg, and V. Valderrabano. Autologous matrix-induced chondrogenesis in osteochondral lesions of the talus. *Foot and Ankle Clinics*, 18(1):151–158, 2013. ISSN 1083-7515. doi: 10.1016/j.fcl.2012.12.009. URL `\url{https://doi.org/10.1016/j.fcl.2012.12.009}`.

M. Wiewiorski, L. Werner, J. Paul, A. E. Anderson, A. Barg, and V. Valderrabano. Sports activity after reconstruction of osteochondral lesions of the talus with autologous spongiosa grafts and autologous matrix-induced chondrogenesis. *The American Journal of Sports Medicine*, 44(10): 2651–2658, 2016. ISSN 0363-5465. doi: 10.1177/0363546516659643.

E. J. Wijnhoud, Q. G. Rikken, J. Dahmen, I. N. Sierevelt, S. A. Stufkens, and G. M. Kerkhoffs. One in three patients with chronic lateral ankle instability has a cartilage lesion. *The American Journal of Sports Medicine*, page 03635465221084365, 2022.

J. O. Wobbrock, L. Findlater, D. Gergle, and J. J. Higgins. The aligned rank transform for nonparametric factorial analyses using only anova procedures. In *Proceedings of the ACM Conference on Human Factors in Computing Systems (CHI '11)*, pages 143–146, New York, 2011. ACM Press. doi: 10.1145/1978942.1978963. URL `https://depts.washington.edu/acelab/proj/art/`.

R. Wodicka, E. Ferkel, and R. Ferkel. Osteochondral lesions of the ankle. *Foot & ankle international*, 37(9):1023–1034, 2016.

B. L. Wong, W. C. Bae, K. R. Gratz, and R. L. Sah. Shear deformation kinematics during cartilage articulation: effect of lubrication, degeneration, and stress relaxation. *Molecular & cellular biomechanics: MCB*, 5(3):197, 2008.

J. E. Woodell-May and S. D. Sommerfeld. Role of inflammation and the immune system in the progression of osteoarthritis. *Journal of Orthopaedic Research®*, 38(2):253–257, 2020.

V. Wright and D. Dowson. Lubrication and cartilage. *Journal of anatomy*, 121(Pt 1):107, 1976.

J. Wu, W. Herzog, and M. Epstein. Joint contact mechanics in the early stages of osteoarthritis. *Medical engineering & physics*, 22(1):1–12, 2000. ISSN 1350-4533.

J. P. Wu, T. B. Kirk, and M. H. Zheng. Study of the collagen structure in the superficial zone and physiological state of articular cartilage using a 3d confocal imaging technique. *Journal of orthopaedic surgery and research*, 3(1):29, 2008. ISSN 1749-799X.

J. Yang, Y. S. Zhang, K. Yue, and A. Khademhosseini. Cell-laden hydrogels for osteochondral and cartilage tissue engineering. *Acta biomaterialia*, 57:1–25, 2017. ISSN 1742-7061.

Y. Yang, J. Zhang, Z. Liu, Q. Lin, X. Liu, C. Bao, Y. Wang, and L. Zhu. Tissue-integratable and biocompatible photogelation by the imine crosslinking reaction. *Advanced Materials*, 28(14): 2724–2730, 2016.

N. S. Yontar, L. Aslan, and T. Öğüt. Functional outcomes of autologous matrix-related chondrogenesis to treat large osteochondral lesions of the talus. *Foot & Ankle International*, 43(6):783–789, 2022.

L. Yuan, B. Li, J. Yang, Y. Ni, Y. Teng, L. Guo, H. Fan, Y. Fan, and X. Zhang. Effects of composition and mechanical property of injectable collagen i/ii composite hydrogels on chondrocyte behaviors. *Tissue Engineering Part A*, 22(11-12):899–906, 2016.

T. Yuan, L. Zhang, K. Li, H. Fan, Y. Fan, J. Liang, and X. Zhang. Collagen hydrogel as an immunomodulatory scaffold in cartilage tissue engineering. *Journal of Biomedical Materials Research Part B: Applied Biomaterials*, 102(2):337–344, 2014.

P. Zedde, S. Cudoni, G. Giachetti, M. L. Manunta, G. Masala, A. Brunetti, and A. F. Manunta. Subchondral bone remodeling: comparing nanofracture with microfracture. an ovine in vivo study. *Joints*, 4(02):087–093, 2016.

M. Zengerink, P. A. Struijs, J. L. Tol, and C. N. Van Dijk. Treatment of osteochondral lesions of the talus: a systematic review. *Knee Surgery, Sports Traumatology, Arthroscopy*, 18(2):238–246, 2010. ISSN 0942-2056.

L. Zhou, P. Guo, M. D'Este, W. Tong, J. Xu, H. Yao, M. J. Stoddart, G. J. van Osch, K. K.-W. Ho, Z. Li, et al. Functionalized hydrogels for articular cartilage tissue engineering. *Engineering*, 2022.

Appendix A

A.1 Pendulum Friction Simulator Fixtures and Assembly

A.1.1 Tibial Fixture Assembly Drawing

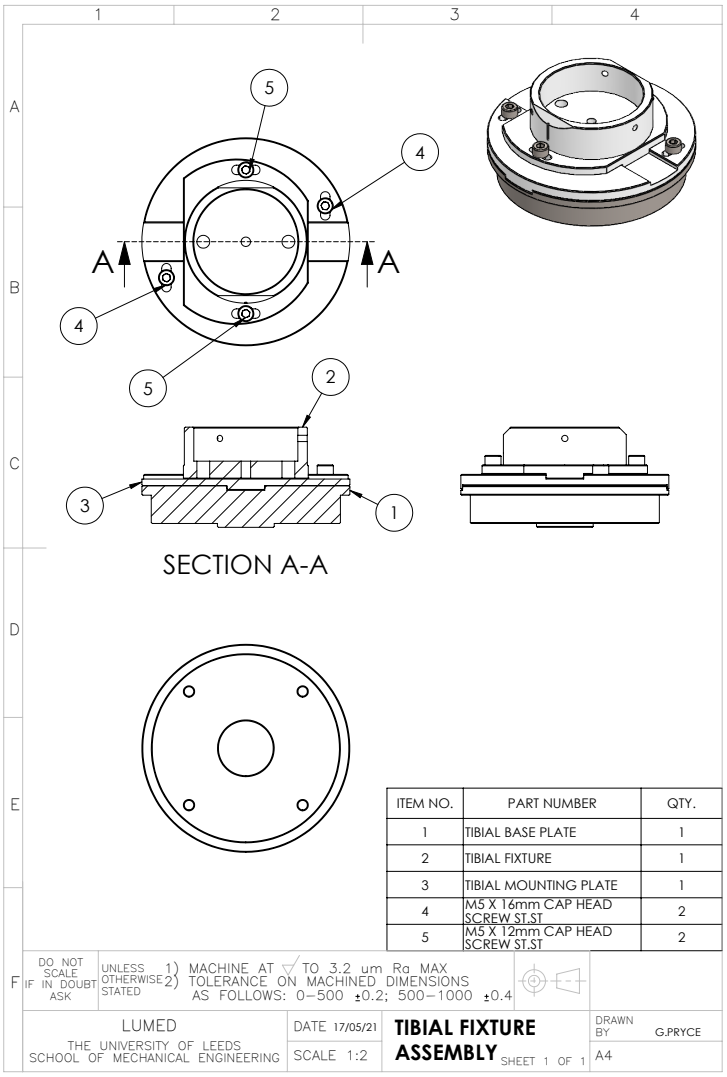

ITEM NO.	PART NUMBER	QTY.
1	TIBIAL BASE PLATE	1
2	TIBIAL FIXTURE	1
3	TIBIAL MOUNTING PLATE	1
4	M5 X 16mm CAP HEAD SCREW ST.ST	2
5	M5 X 12mm CAP HEAD SCREW ST.ST	2

DO NOT SCALE IF IN DOUBT ASK

UNLESS OTHERWISE STATED 1) MACHINE AT $\sqrt{}$ TO 3.2 um Ra MAX 2) TOLERANCE ON MACHINED DIMENSIONS AS FOLLOWS: 0–500 ±0.2; 500–1000 ±0.4

LUMED
THE UNIVERSITY OF LEEDS
SCHOOL OF MECHANICAL ENGINEERING

DATE 17/05/21
SCALE 1:2

TIBIAL FIXTURE ASSEMBLY SHEET 1 OF 1

DRAWN BY G.PRYCE
A4

A.1.2 Tibia Pot Drawing

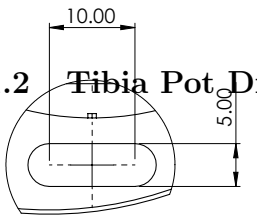

DETAIL C
SCALE 2 : 1

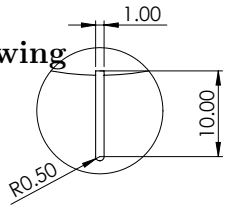

DETAIL D
SCALE 2 : 1

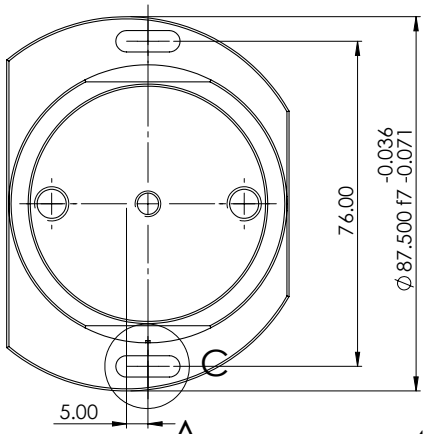

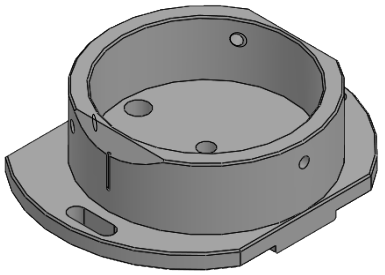

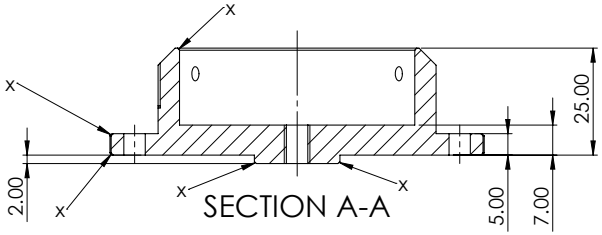

SECTION A-A

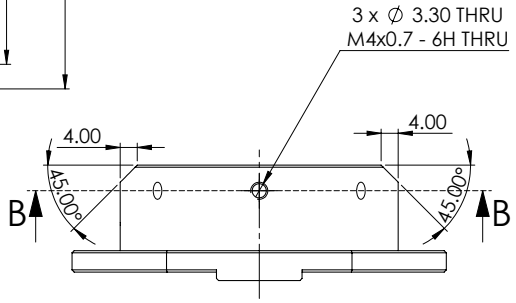

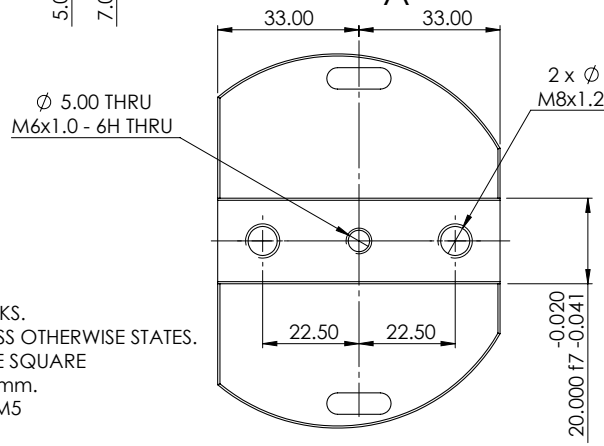

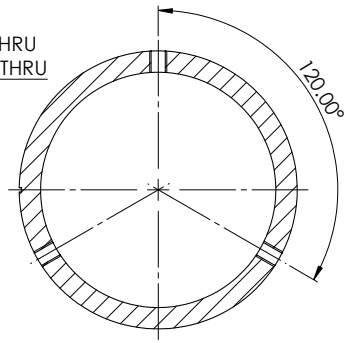

SECTION B-B

CHAMFER: X = 0.5 X 45°

MATERIAL: DELRIN

NOTES:
1. REMOVE ALL SHARP EDGES AND CUTTING MARKS.
2. ALL HOLES TO BE MACHINED AT ±0.1 mm UNLESS OTHERWISE STATES.
3. FEATURE SHOWN IN DETAIL D IS REQUIRED TO BE SQUARE PROFILE AND MACHINED TO THE DEPTH OF 0.5 mm.
4. M8 THREADS ARE REQUIRED TO BE FITTED WITH M5 STAINLESS STEEL INSERTS.

DO NOT SCALE IF IN DOUBT ASK	UNLESS OTHERWISE STATED 1) MACHINE AT ▽ TO 3.2 um Ra MAX 2) TOLERANCE ON MACHINED DIMENSIONS AS FOLLOWS: 0–500 ±0.2; 500–1000 ±0.4	LUMED THE UNIVERSITY OF LEEDS SCHOOL OF MECHANICAL ENGINEERING	DATE 10/05/21 SCALE 1:1	**TIBIA FIXTURE** SHEET 1 OF 1	DRAWN BY G.PRYCE A3

A.1.3 Tibial Mounting Plate Drawing

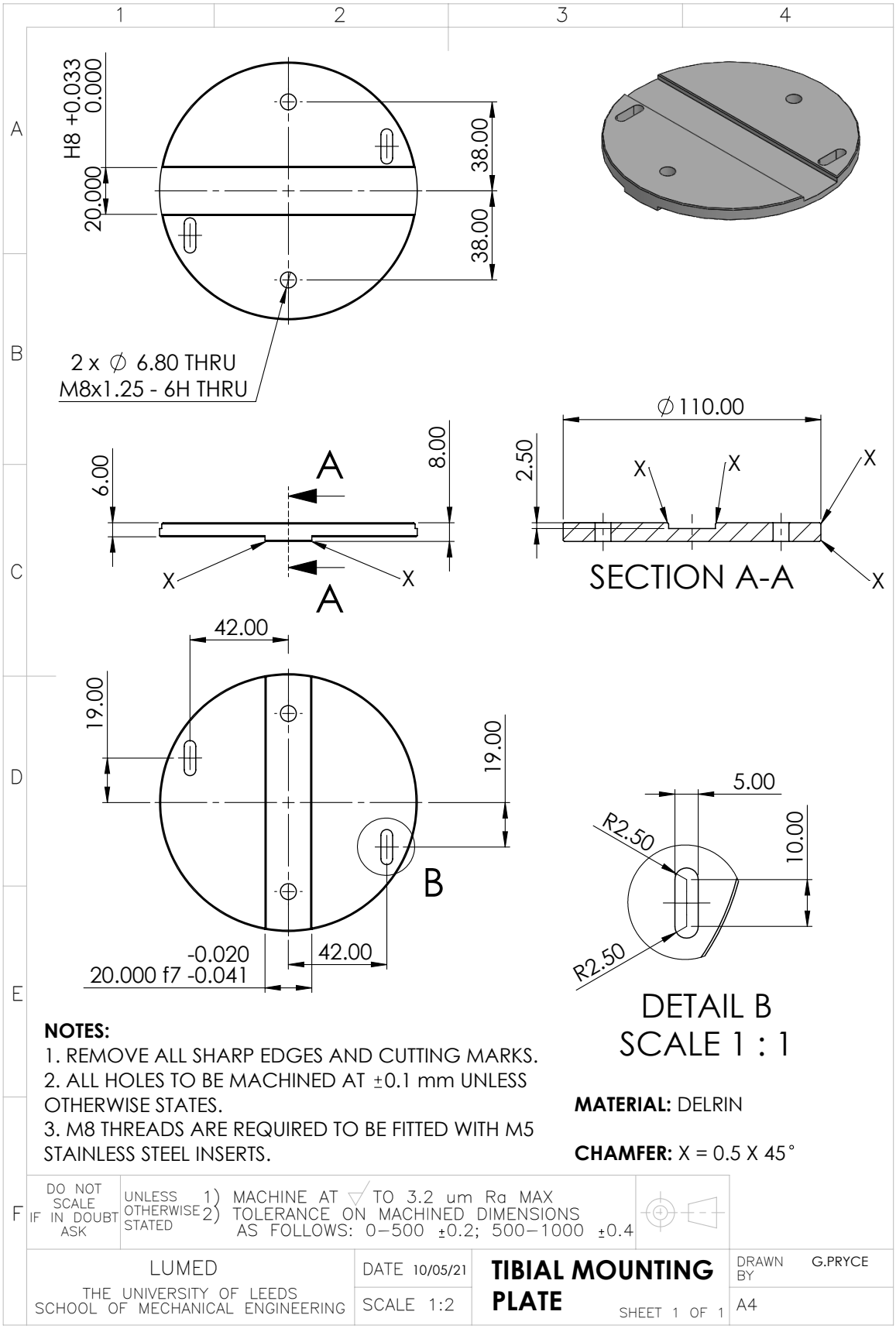

A.1.4 Tibial Base Plate Drawing

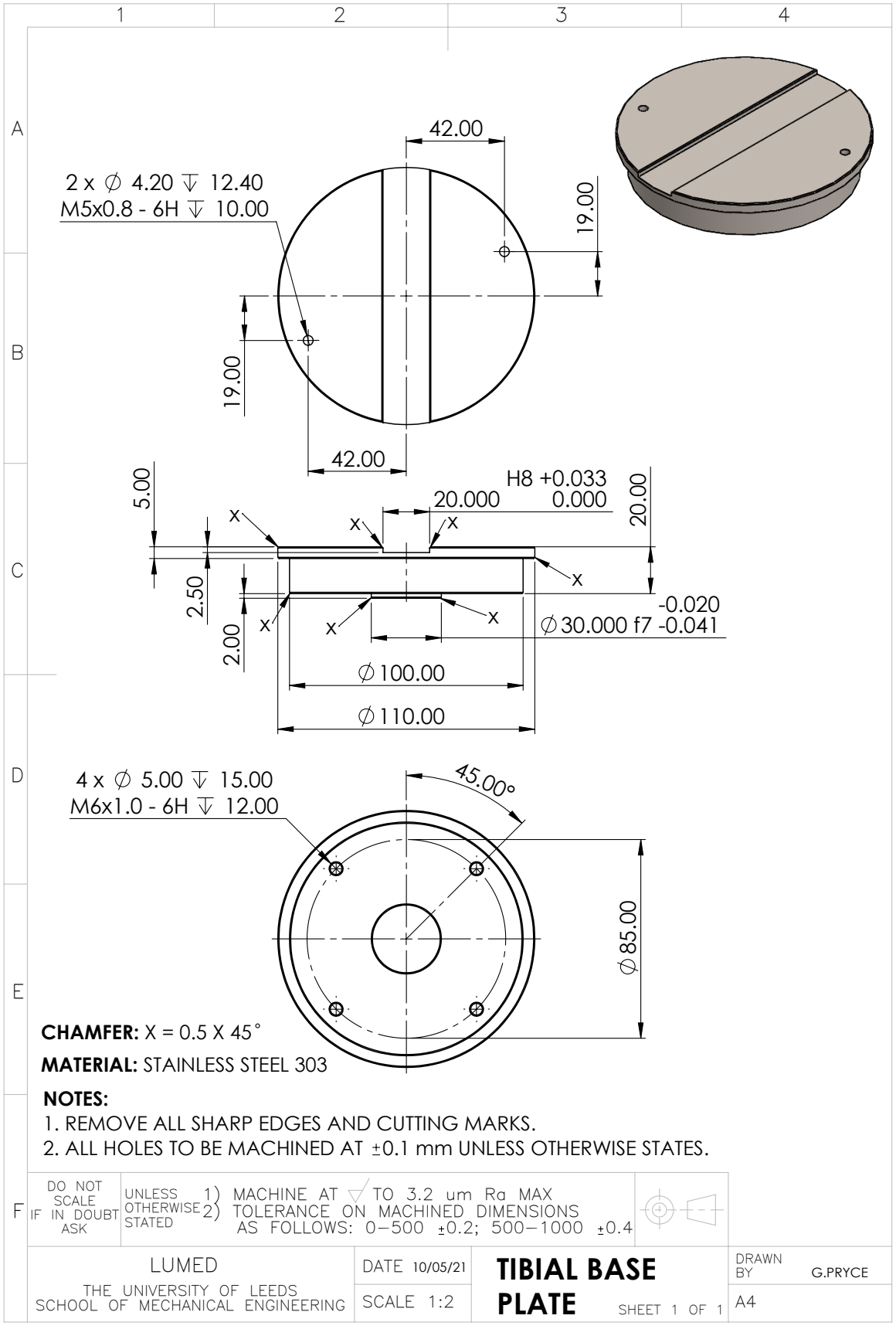

A.1.5 Talar Fixture Assembly Drawing

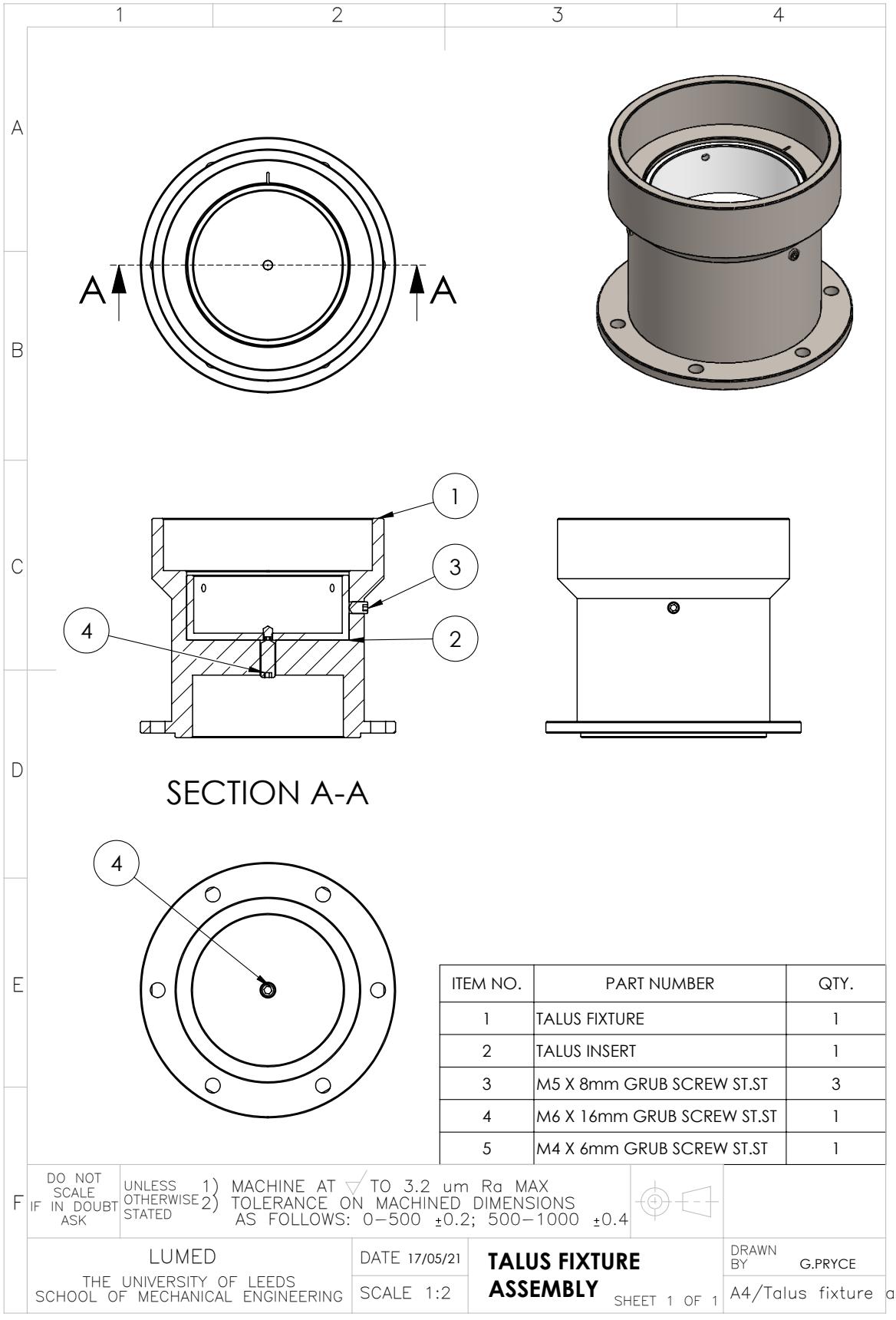

ITEM NO.	PART NUMBER	QTY.
1	TALUS FIXTURE	1
2	TALUS INSERT	1
3	M5 X 8mm GRUB SCREW ST.ST	3
4	M6 X 16mm GRUB SCREW ST.ST	1
5	M4 X 6mm GRUB SCREW ST.ST	1

DO NOT SCALE IF IN DOUBT ASK

UNLESS OTHERWISE STATED 1) MACHINE AT ▽ TO 3.2 um Ra MAX
2) TOLERANCE ON MACHINED DIMENSIONS AS FOLLOWS: 0–500 ±0.2; 500–1000 ±0.4

LUMED
THE UNIVERSITY OF LEEDS
SCHOOL OF MECHANICAL ENGINEERING

DATE 17/05/21
SCALE 1:2

TALUS FIXTURE ASSEMBLY
SHEET 1 OF 1

DRAWN BY G.PRYCE
A4/Talus fixture assen

A.1.6 Talar Fixture Drawing

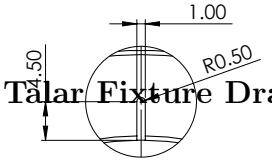

DETAIL C
SCALE 2 : 1

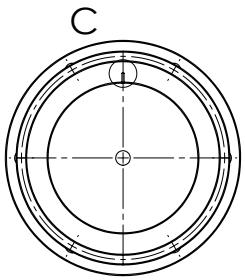

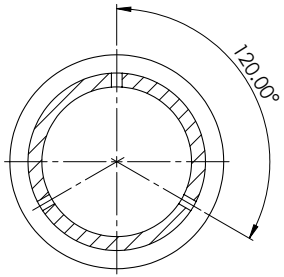

SECTION B-B

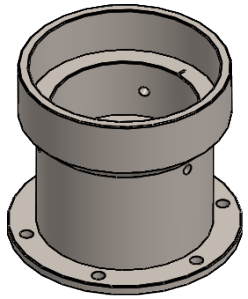

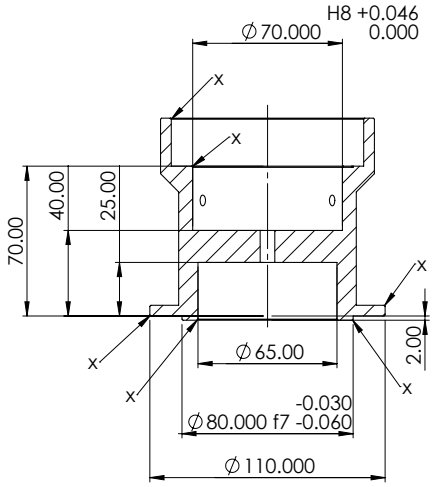

SECTION A-A

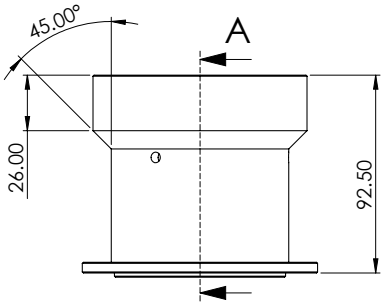

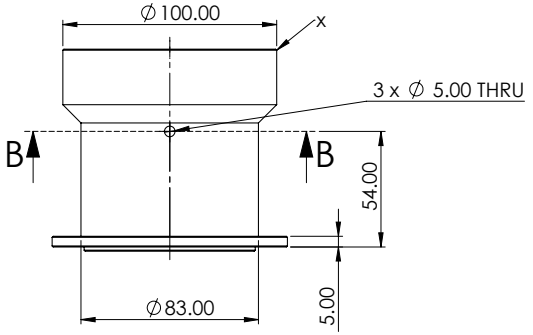

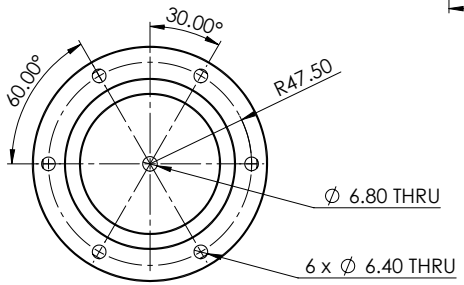

NOTES:
1. REMOVE ALL SHARP EDGES AND CUTTING MARKS.
2. ALL HOLES TO BE MACHINED AT ±0.1 mm UNLESS OTHERWISE STATES.
3. FEATURE SHOWN IN DETAIL 'C' IS REQUIRED TO BE SQUARE PROFILE AND MACHINED TO THE DEPTH OF 0.5 mm.

MATERIAL: STAINLESS STEEL 303 **CHAMFER:** X = 0.5 X 45°

DO NOT SCALE IF IN DOUBT ASK	UNLESS OTHERWISE STATED 1) MACHINE AT ▽ TO 3.2 um Ra MAX 2) TOLERANCE ON MACHINED DIMENSIONS AS FOLLOWS: 0–500 ±0.2; 500–1000 ±0.4	LUMED THE UNIVERSITY OF LEEDS SCHOOL OF MECHANICAL ENGINEERING	DATE 10/05/21 SCALE 1:2	**TALUS FIXTURE** SHEET 1 OF 1	DRAWN BY G.PRYCE A3

A.1.7 Talar Pot Insert Drawing

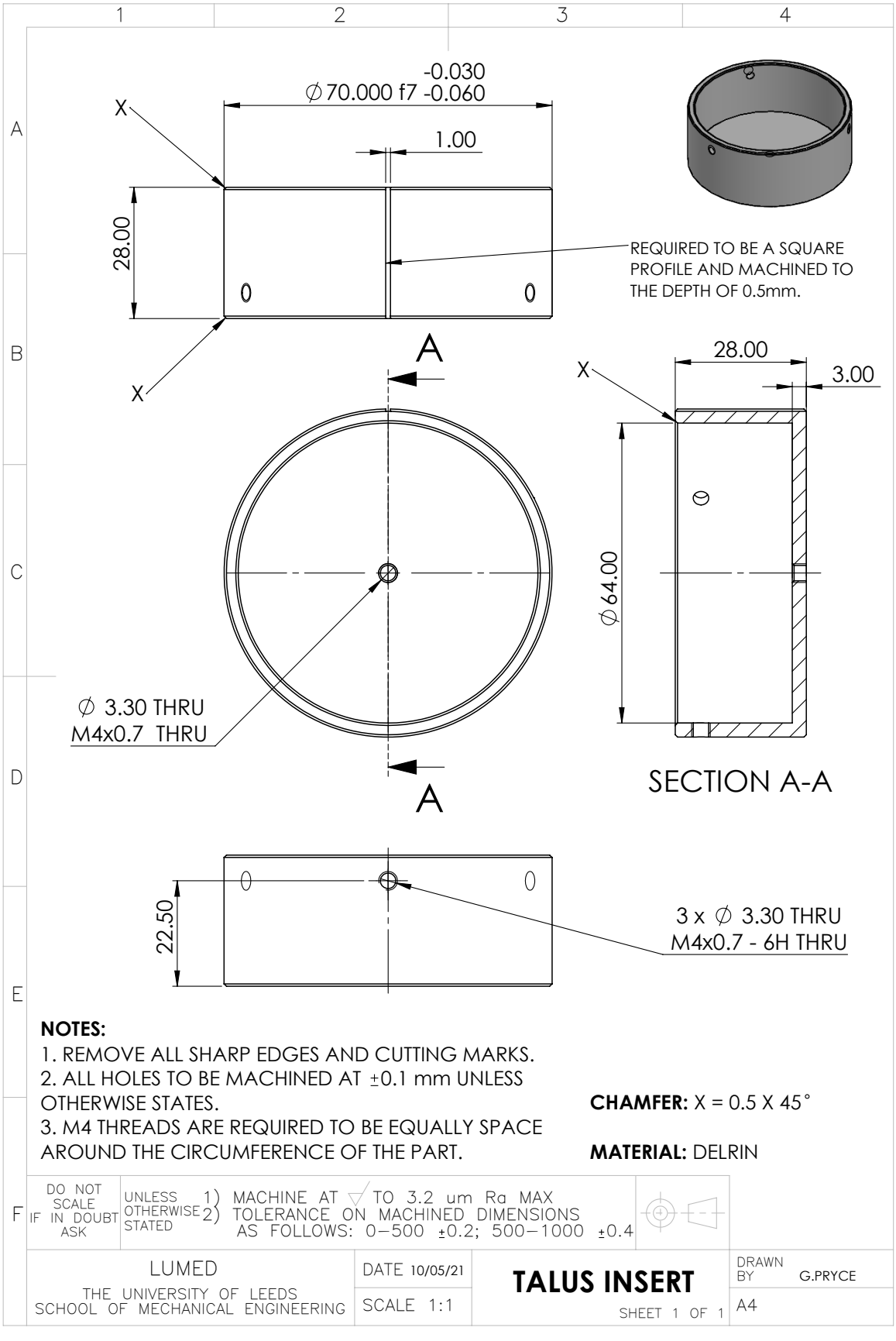

A.1.8 Cementing Base Drawing

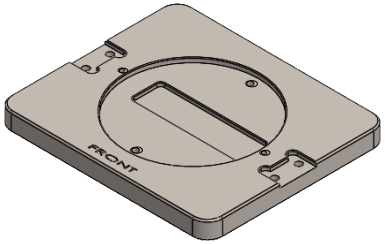

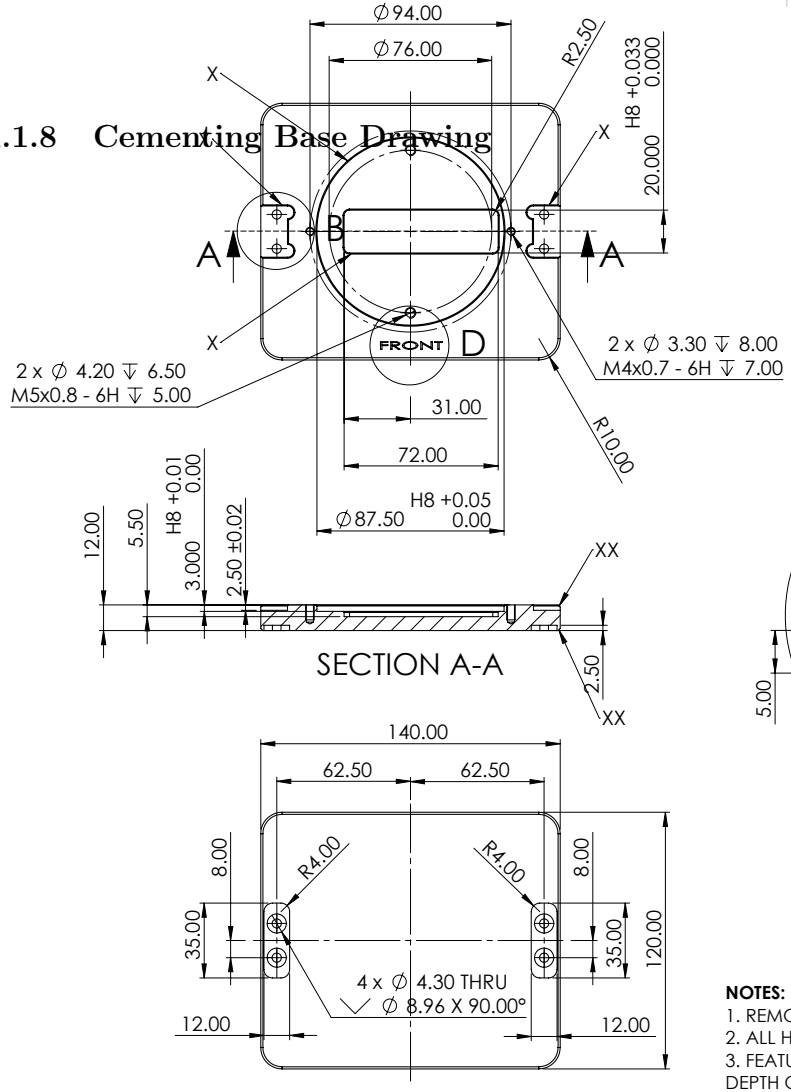

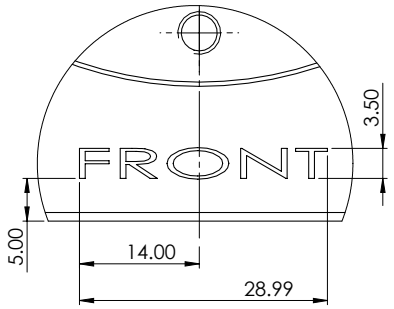

DETAIL D
SCALE 2 : 1

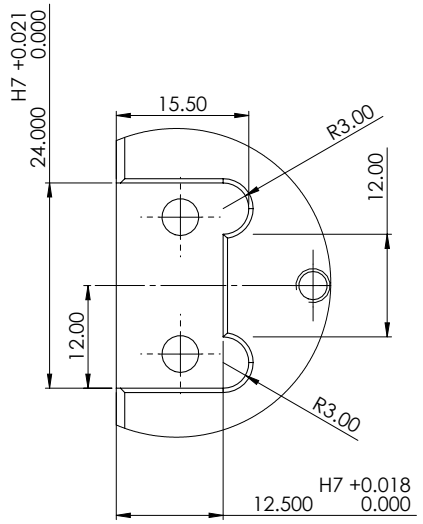

DETAIL B
SCALE 2 : 1

NOTES:
1. REMOVE ALL SHARP EDGES AND CUTTING MARKS.
2. ALL HOLES TO BE MACHINED AT ±0.1 mm UNLESS OTHERWISE STATES.
3. FEATURE SHOWN IN DETAIL 'D' IS REQUIRED TO BE MACHINED TO THE DEPTH OF 0.5 mm.

MATERIAL: STAINLESS STEEL 303

CHAMFER: X = 0.5 X 45°
XX = 1.0 X 45°

DO NOT SCALE IF IN DOUBT ASK	UNLESS OTHERWISE STATED 1) MACHINE AT ▽ TO 3.2 um Ra MAX 2) TOLERANCE ON MACHINED DIMENSIONS AS FOLLOWS: 0–500 ±0.2; 500–1000 ±0.4	LUMED THE UNIVERSITY OF LEEDS SCHOOL OF MECHANICAL ENGINEERING	DATE 17/05/21 SCALE 1:2	**Cementing Base** SHEET 1 OF 1	DRAWN BY G.PRYCE A3

A.1.9 Cementing Uprights Drawing

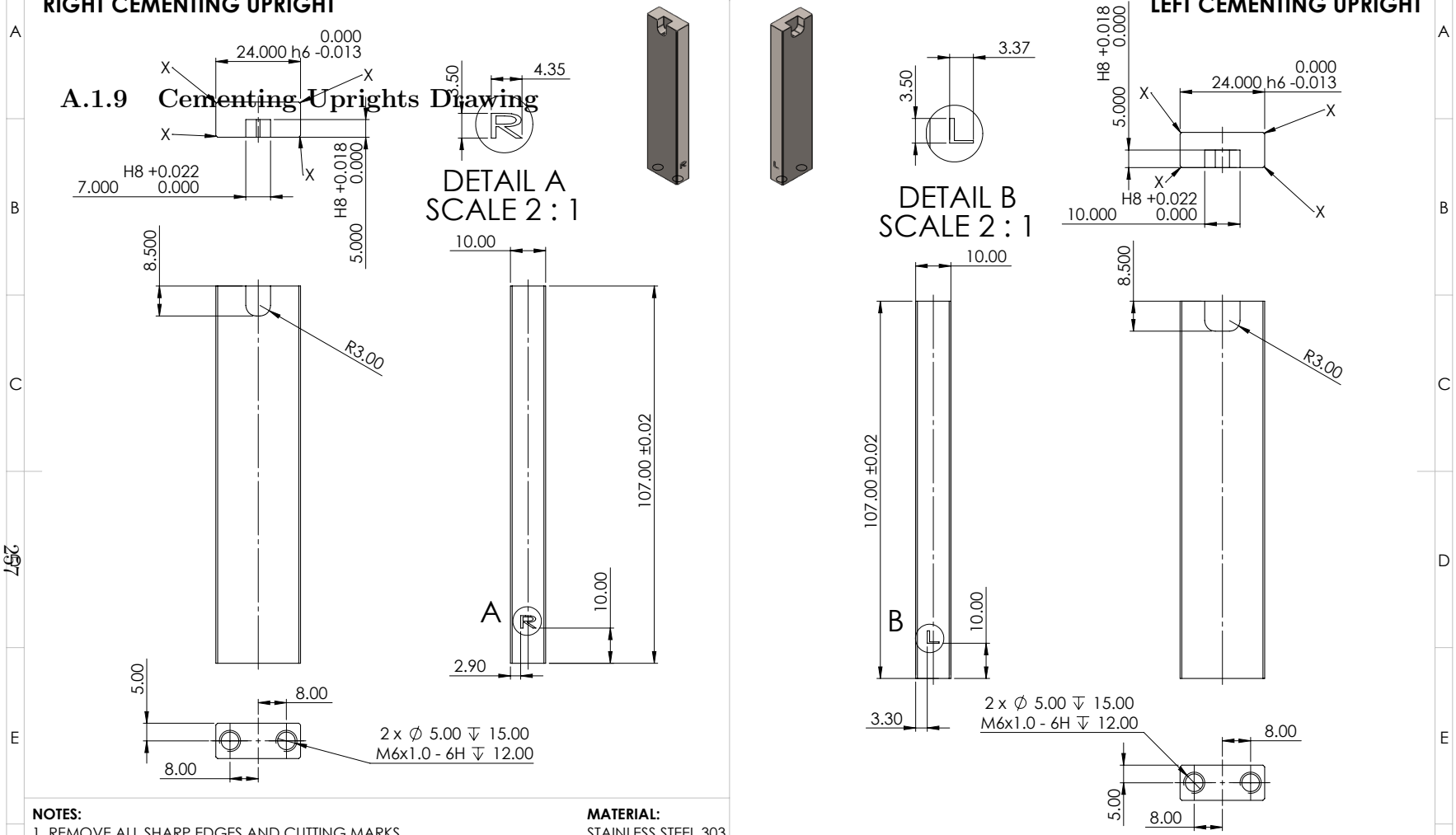

NOTES:
1. REMOVE ALL SHARP EDGES AND CUTTING MARKS.
2. ALL HOLES TO BE MACHINED AT ±0.1 mm UNLESS OTHERWISE STATES.
3. FEATURE SHOWN IN DETAILS 'A' AND 'B' IS REQUIRED TO BE MACHINED TO THE DEPTH OF 0.5 mm.

MATERIAL:
STAINLESS STEEL 303

CHAMFER:
X = 0.5 X 45°

DO NOT SCALE IF IN DOUBT ASK	UNLESS OTHERWISE STATED 1) MACHINE AT ▽ TO 3.2 um Ra MAX 2) TOLERANCE ON MACHINED DIMENSIONS AS FOLLOWS: 0–500 ±0.2; 500–1000 ±0.4	LUMED THE UNIVERSITY OF LEEDS SCHOOL OF MECHANICAL ENGINEERING	DATE 04/05/21 SCALE 1:1	**CEMENTING UPRIGHTS** SHEET 1 OF 1	DRAWN BY G.PRYCE A3

A.1.10 Cementing Top Beam Drawing

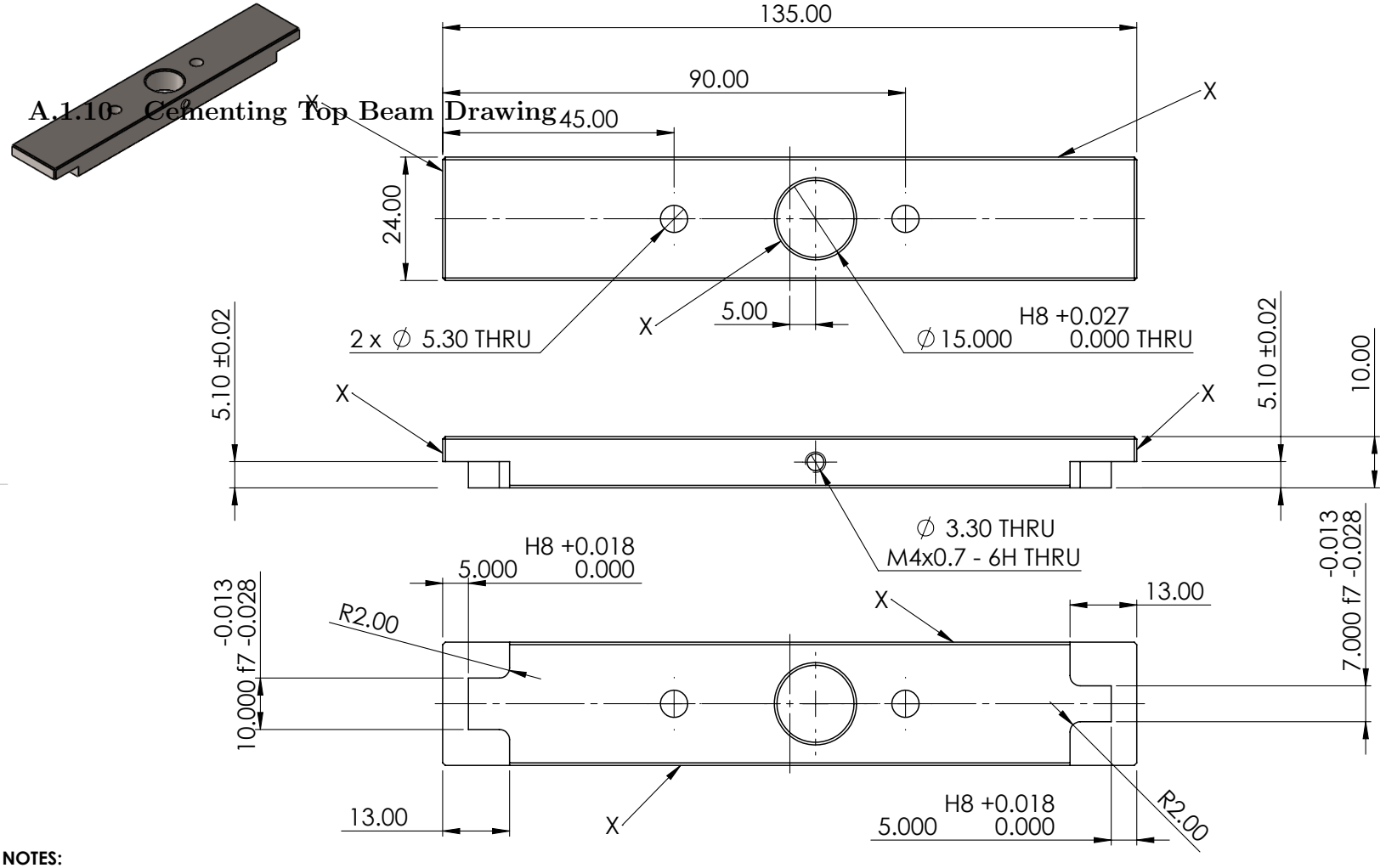

NOTES:

1. REMOVE ALL SHARP EDGES AND CUTTING MARKS.
2. ALL HOLES TO BE MACHINED AT ±0.1 mm UNLESS OTHERWISE STATES.

CHAMFER: X = 0.5 X 45°

MATERIAL: STAINLESS STEEL 303

DO NOT SCALE IF IN DOUBT ASK	UNLESS OTHERWISE STATED 1) MACHINE AT ▽ TO 3.2 um Ra MAX 2) TOLERANCE ON MACHINED DIMENSIONS AS FOLLOWS: 0–500 ±0.2; 500–1000 ±0.4	LUMED THE UNIVERSITY OF LEEDS SCHOOL OF MECHANICAL ENGINEERING	DATE 10/05/21 SCALE 1:1	TITLE **CEMENTING TOPBEAM**	DRAWN BY G.PRYCE DRG No	

A.1.11 Tibia Cementing Arcs

34mm CEMENTING ARC

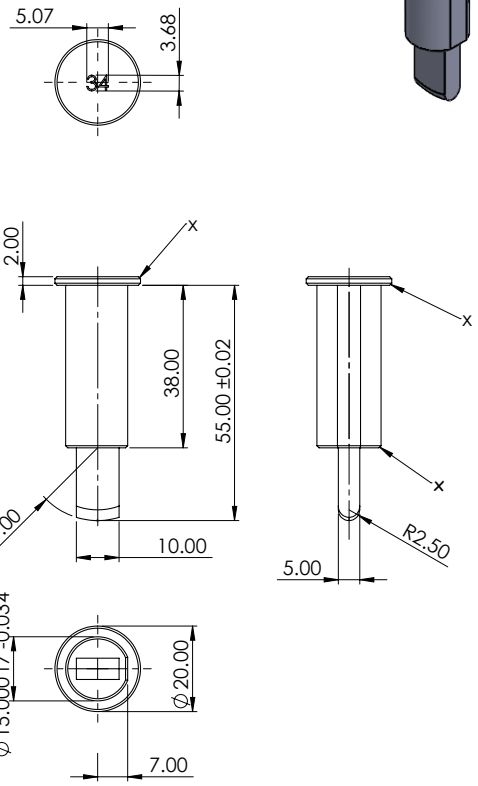

39mm CEMENTING ARC

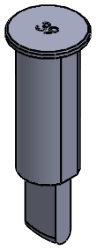

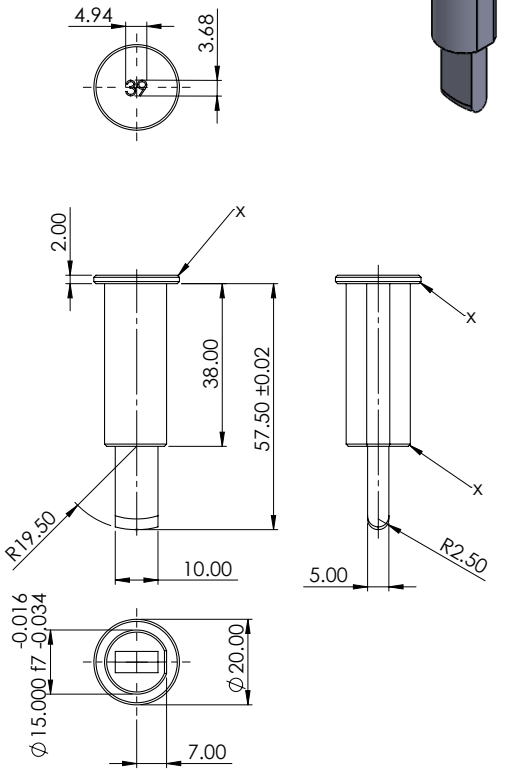

47mm CEMENTING ARC

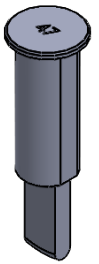

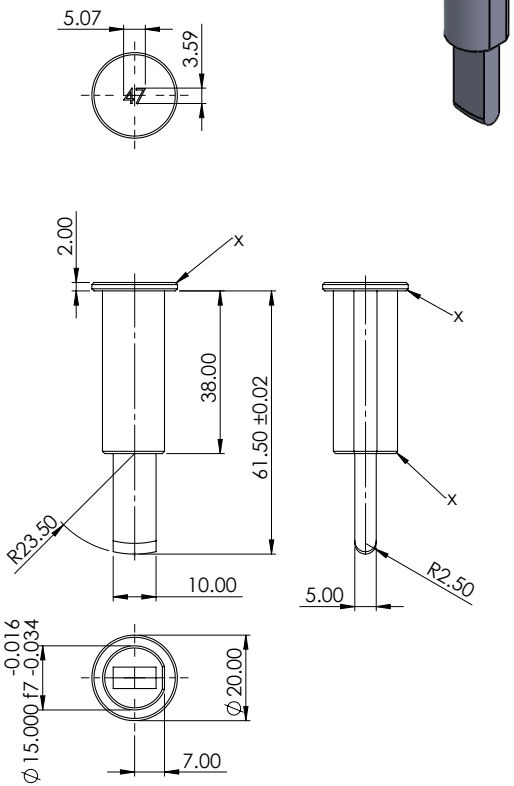

NOTES:
1. REMOVE ALL SHARP EDGES AND CUTTING MARKS.
2. ALL HOLES TO BE MACHINED AT ±0.1 mm UNLESS OTHERWISE STATES.
3. TEXT ON THE TOP OF PARTS IS REQUIRED TO BE MACHINED TO THE DEPTH OF 0.5mm.

MATERIAL: DELRIIN

CHAMFER: X = 0.5 X 45°

DO NOT SCALE IF IN DOUBT ASK

UNLESS OTHERWISE STATED 1) MACHINE AT ▽ TO 3.2 um Ra MAX 2) TOLERANCE ON MACHINED DIMENSIONS AS FOLLOWS: 0–500 ±0.2; 500–1000 ±0.4

LUMED
THE UNIVERSITY OF LEEDS
SCHOOL OF MECHANICAL ENGINEERING

DATE 04/05/21
SCALE 1:1

CEMENTING ARCS

SHEET 1 OF 1

DRAWN BY G.PRYCE
A3

A.1.12 Tibial Cementing Assembly Drawing

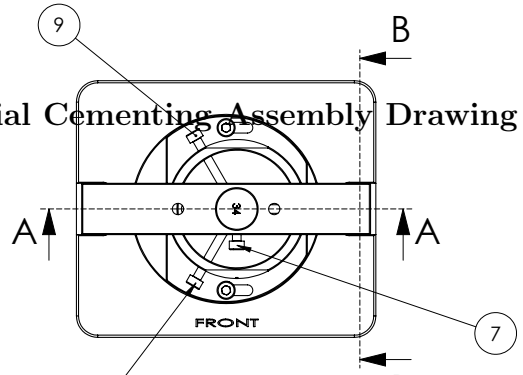

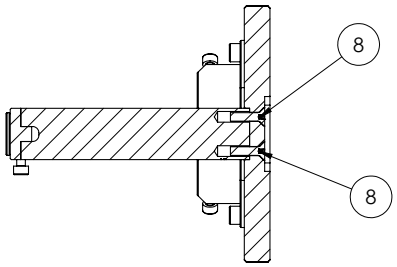

SECTION B-B

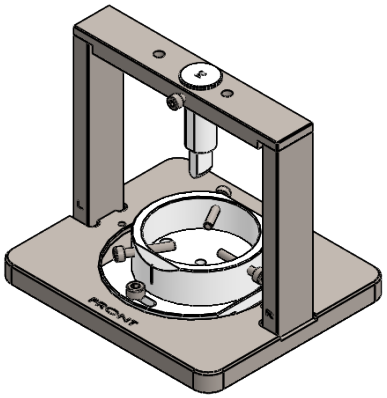

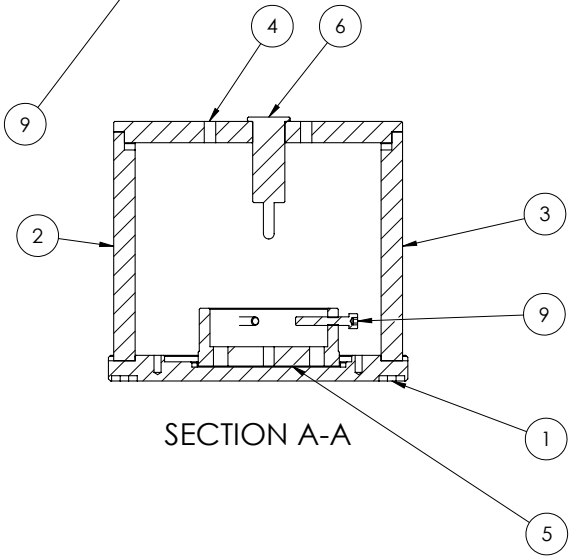

SECTION A-A

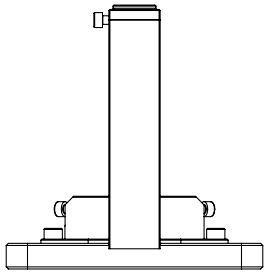

ITEM NO.	PART NUMBER	QTY.
1	CEMENTING BASE	1
2	CEMENTING UPRIGHT LEFT	1
3	CEMENTING UPRIGHT RIGHT	1
4	CEMENTING TOPBEAM	1
5	TIBIA FIXTURE	1
6	CEMENTING 34mm ARC	1
7	M4 X 8mm CAP HEAD SCREW ST.ST	1
8	M4 x 16mm COUNTERSUNK SCREW ST.ST	4
9	M4 X 25mm CAP HEAD SCREW ST.ST	3
10	M5 x 10mm CAP HEAD SCREW ST.ST	2

DO NOT SCALE IF IN DOUBT ASK

UNLESS OTHERWISE STATED 1) MACHINE AT ▽ TO 3.2 um Ra MAX
2) TOLERANCE ON MACHINED DIMENSIONS AS FOLLOWS: 0–500 ±0.2; 500–1000 ±0.4

LUMED
THE UNIVERSITY OF LEEDS
SCHOOL OF MECHANICAL ENGINEERING

DATE 17/05/21
SCALE 1:2

TIBIA CEMENTING ASSEMBLY
SHEET 1 OF 1

DRAWN BY G.PRYCE
A3

A.1.13 Talar Cementing Base Adaptor

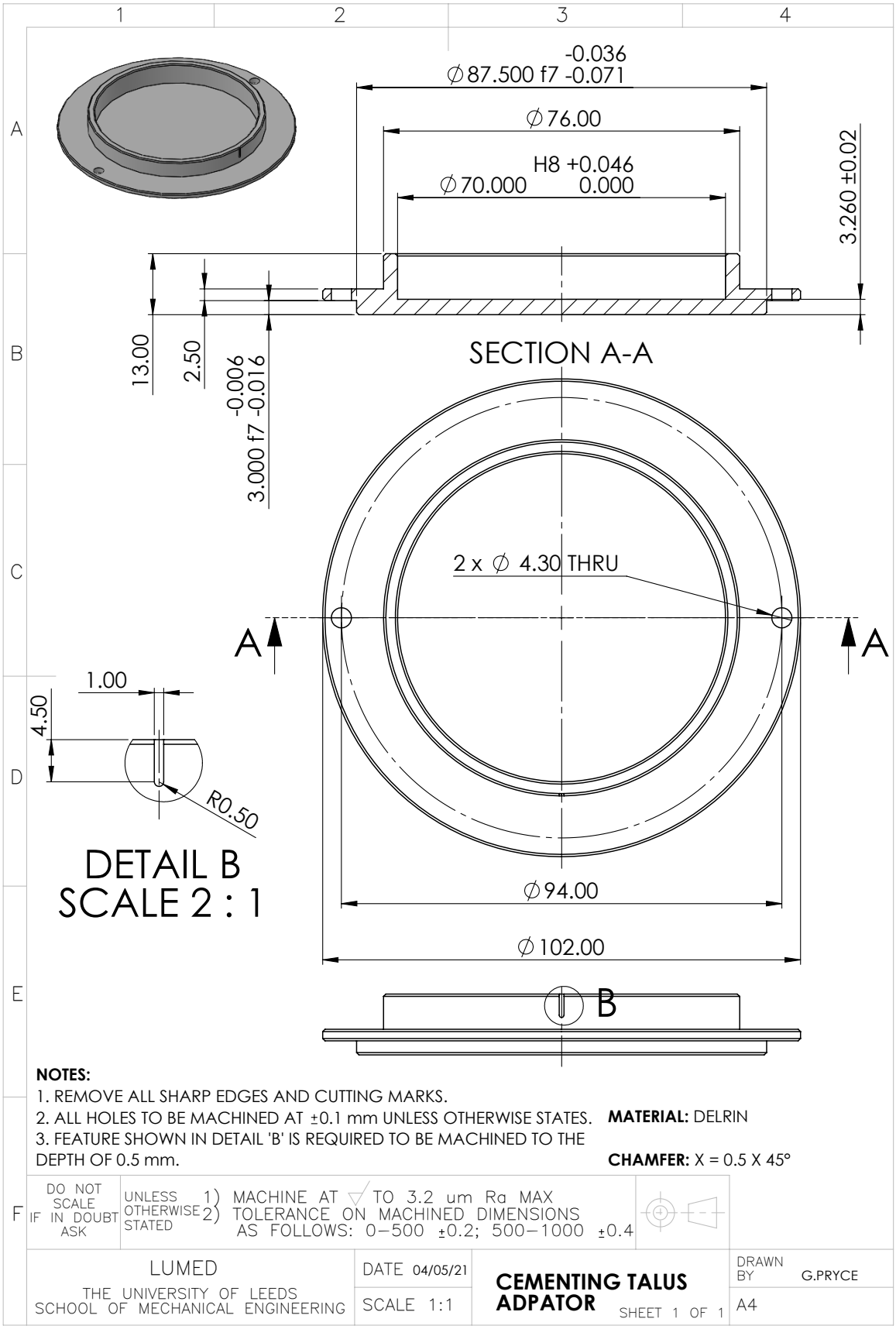

A.1.14 Talar Cementing Assembly Drawing

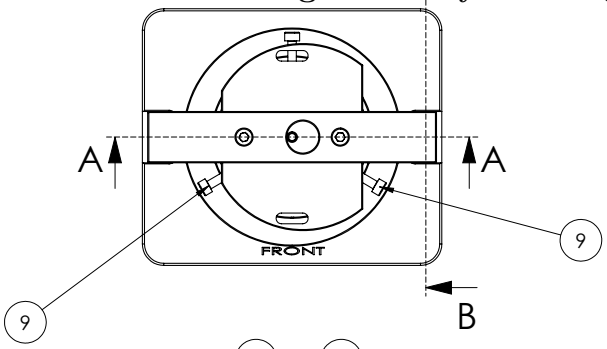

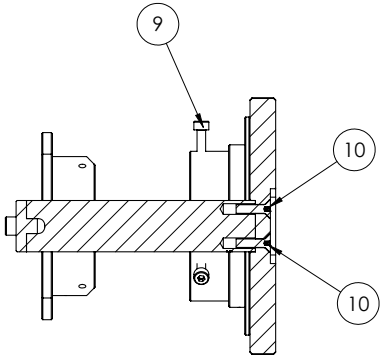

SECTION B-B

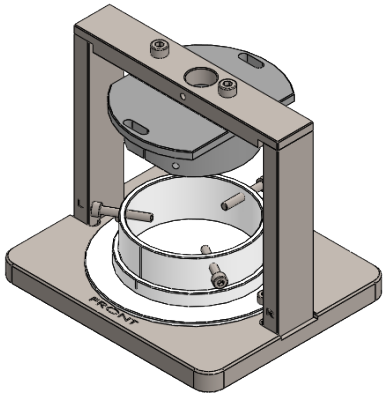

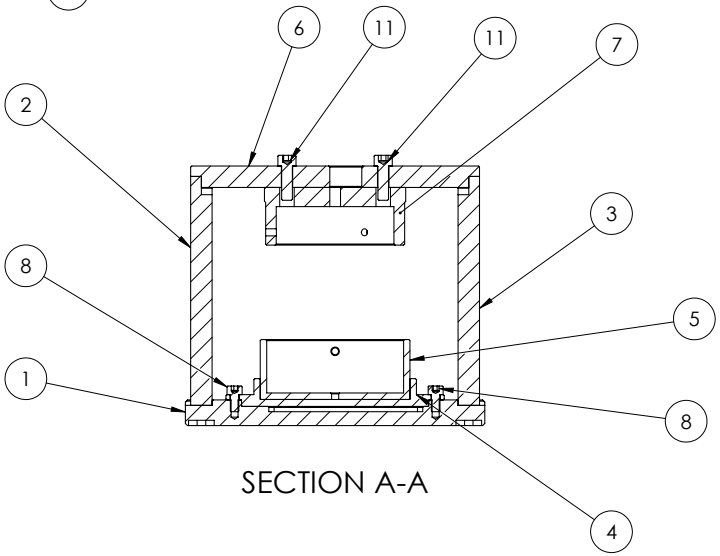

SECTION A-A

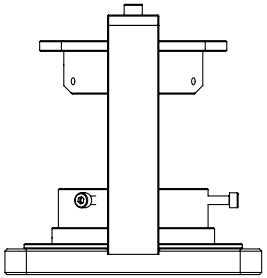

ITEM NO.	PART NUMBER	QTY.
1	CEMENTING BASE	1
2	CEMENTING UPRIGHT LEFT	1
3	CEMENTING UPRIGHT RIGHT	1
4	CEMENTING TALUS ADPATOR	1
5	TALUS INSERT	1
6	CEMENTING TOPBEAM	1
7	TIBIA FIXTURE	1
8	M4 X 8 mm CAP HEAD SCREW ST.ST	2
9	M4 X 25 mm CAP HEAD SCREW ST.ST	3
10	M4 X 16mm COUNTERSUNK SCREW ST.ST	4
11	M5 X 16mm CAP HEAD SCREW ST.ST	2

DO NOT SCALE IF IN DOUBT ASK

UNLESS OTHERWISE STATED 1) MACHINE AT ▽ TO 3.2 um Ra MAX
2) TOLERANCE ON MACHINED DIMENSIONS AS FOLLOWS: 0–500 ±0.2; 500–1000 ±0.4

LUMED
THE UNIVERSITY OF LEEDS
SCHOOL OF MECHANICAL ENGINEERING

DATE 17/05/21
SCALE 1:2

TALUS CEMENTING ASSEMBLY
SHEET 1 OF 1

DRAWN BY G.PRYCE
A3

Appendix B

B.1 Chapter 6

B.1.1 Contact pressure maps

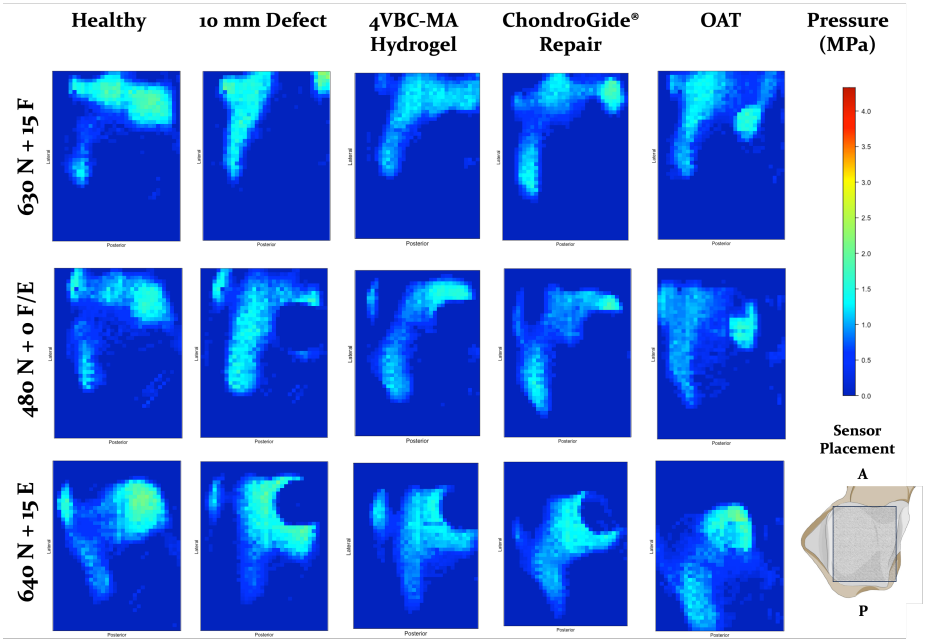

Figure B.1: Pressure maps for sample 1 showing distribution of pressure around the talar dome. Images show a sample of pressure maps for one sample showing pressure distribution across the talar dome for each condition (left to right) healthy, chondral defect, 4VBC-MA hydrogel, ChondroGide ® Repair and OAT treatment. Pressure maps represent a 38.4 x 26.7 mm area on the talar dome. A = Anterior, P = Posterior

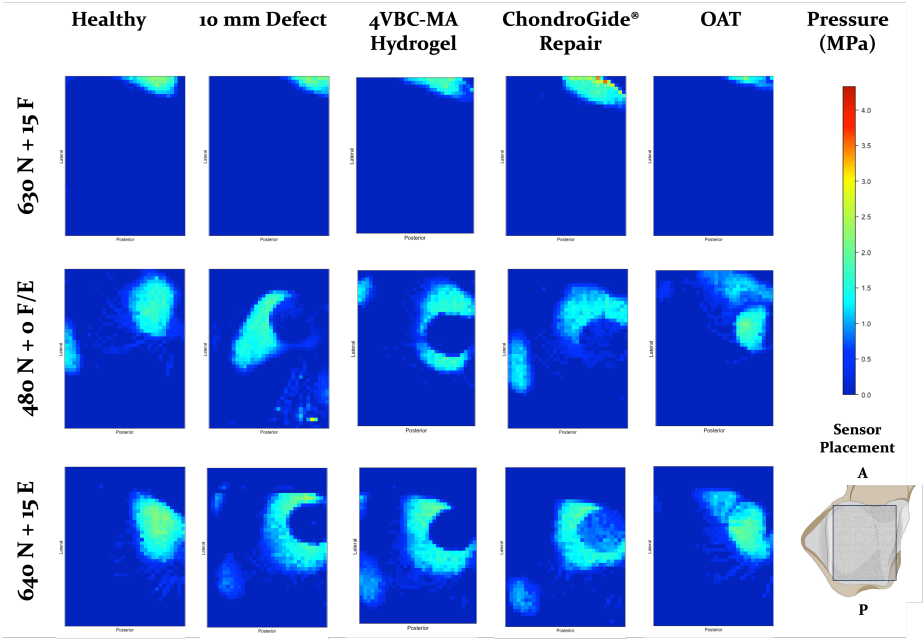

Figure B.2: Pressure maps for sample 2 showing distribution of pressure around the talar dome. Images show a sample of pressure maps for one sample showing pressure distribution across the talar dome for each condition (left to right) healthy, chondral defect, 4VBC-MA hydrogel, ChondroGide ® Repair and OAT treatment. Pressure maps represent a 38.4 x 26.7 mm area on the talar dome. A = Anterior, P = Posterior

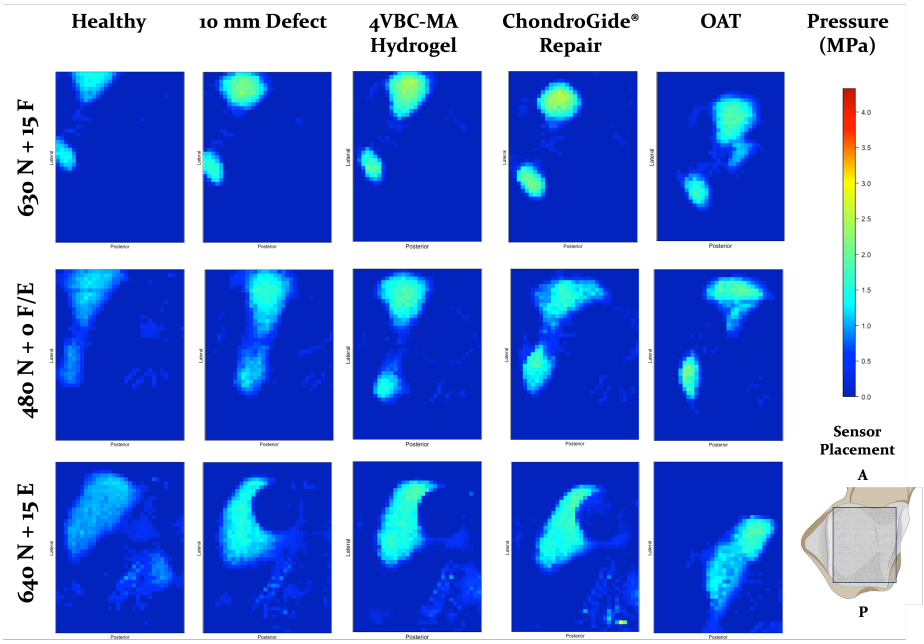

Figure B.3: Pressure maps for sample 3 showing distribution of pressure around the talar dome. Images show a sample of pressure maps for one sample showing pressure distribution across the talar dome for each condition (left to right) healthy, chondral defect, 4VBC-MA hydrogel, ChondroGide ® Repair and OAT treatment. Pressure maps represent a 38.4 x 26.7 mm area on the talar dome. A = Anterior, P = Posterior

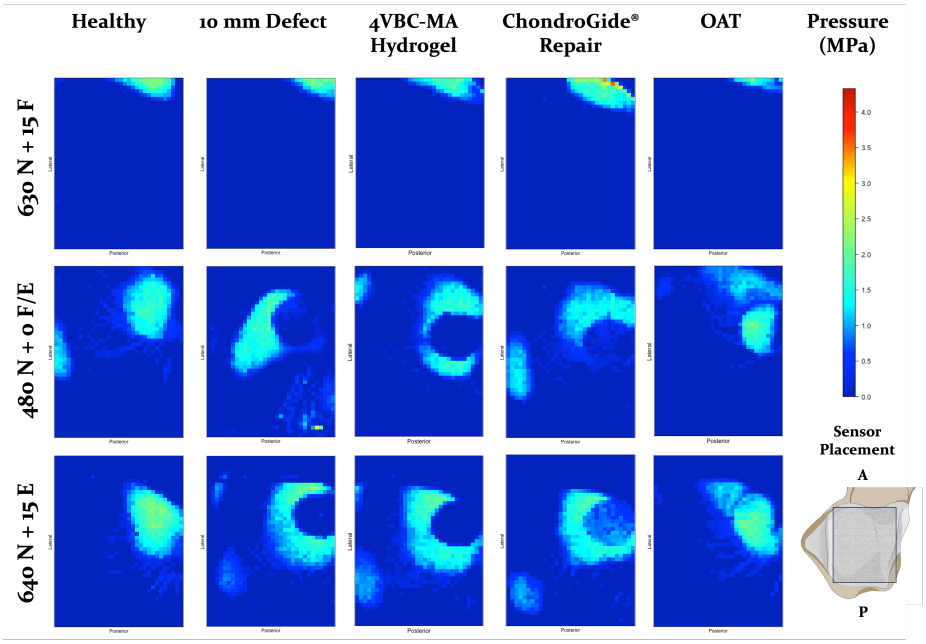

Figure B.4: Pressure maps for sample 4 showing distribution of pressure around the talar dome. Images show a sample of pressure maps for one sample showing pressure distribution across the talar dome for each condition (left to right) healthy, chondral defect, 4VBC-MA hydrogel, ChondroGide ® Repair and OAT treatment. Pressure maps represent a 38.4 x 26.7 mm area on the talar dome. A = Anterior, P = Posterior

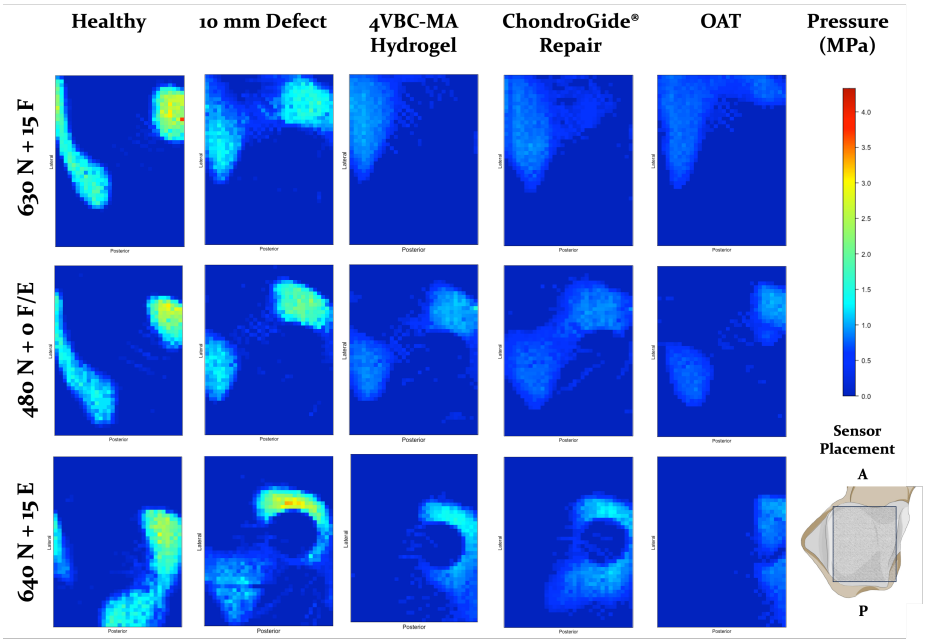

Figure B.5: Pressure maps for sample 5 showing distribution of pressure around the talar dome. Images show a sample of pressure maps for one sample showing pressure distribution across the talar dome for each condition (left to right) healthy, chondral defect, 4VBC-MA hydrogel, ChondroGide ® Repair and OAT treatment. Pressure maps represent a 38.4 x 26.7 mm area on the talar dome. A = Anterior, P = Posterior

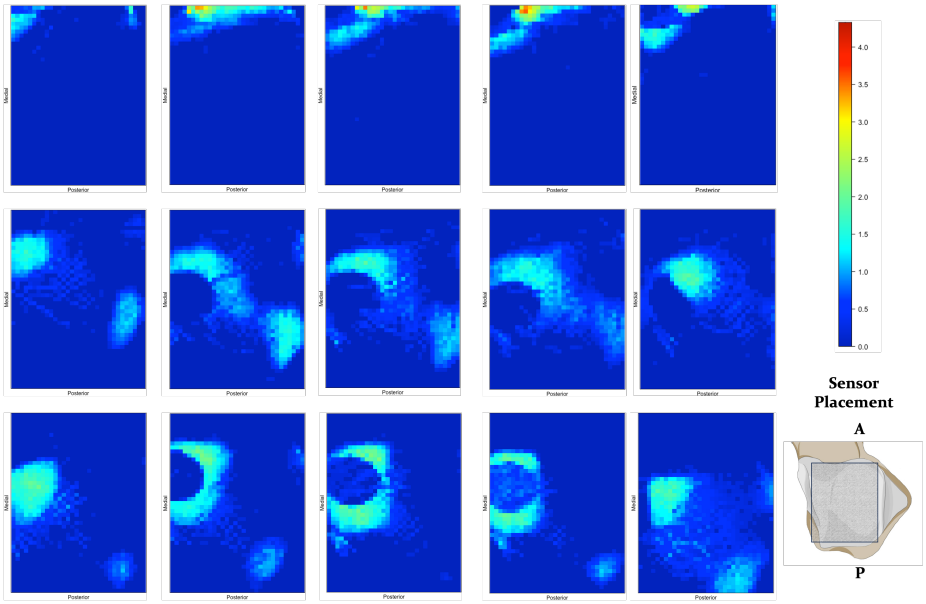

Figure B.6: Pressure maps for sample 6 showing distribution of pressure around the talar dome. Images show a sample of pressure maps for one sample showing pressure distribution across the talar dome for each condition (left to right) healthy, chondral defect, 4VBC-MA hydrogel, ChondroGide ® Repair and OAT treatment. Pressure maps represent a 38.4 x 26.7 mm area on the talar dome. A = Anterior, P = Posterior

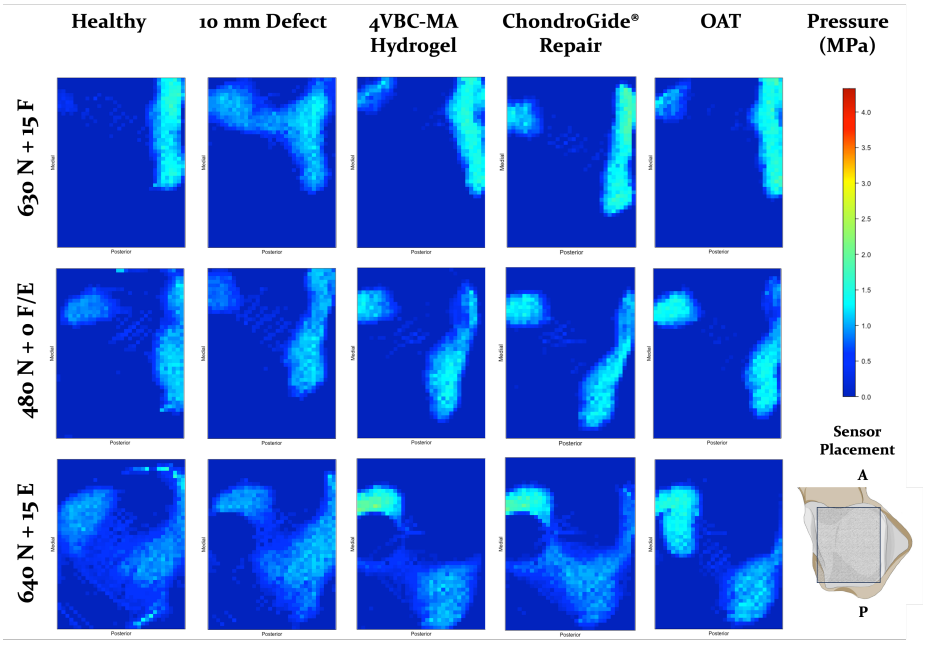

Figure B.7: Pressure maps for sample 7 showing distribution of pressure around the talar dome. Images show a sample of pressure maps for one sample showing pressure distribution across the talar dome for each condition (left to right) healthy, chondral defect, 4VBC-MA hydrogel, ChondroGide ® Repair and OAT treatment. Pressure maps represent a 38.4 x 26.7 mm area on the talar dome. A = Anterior, P = Posterior

B.1.2 Chapter 6 Contour maps

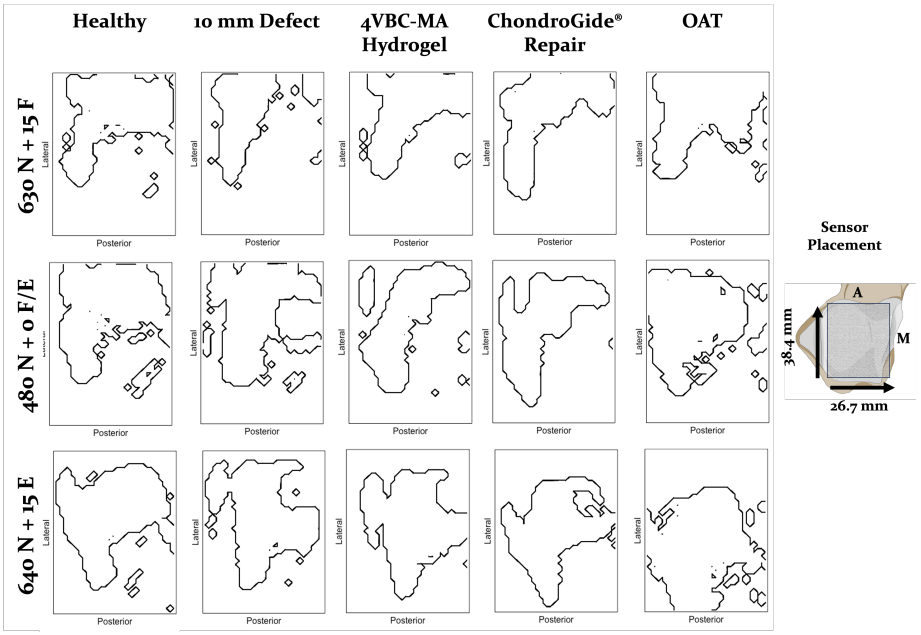

Figure B.8: Contour plot for sample 1 showing contact area across the talar dome.
A sample of contour plots for one sample showing areas of contact across the talar dome for each condition (left to right) healthy, Chondral defect, 4VBC-MA hydrogel, ChondroGide ® repair and OAT treatment. Regions of contact outline with black line. Region mapped represent an area of 38.4 x 26.7 mm on the talar dome. A = Anterior, M = Medial

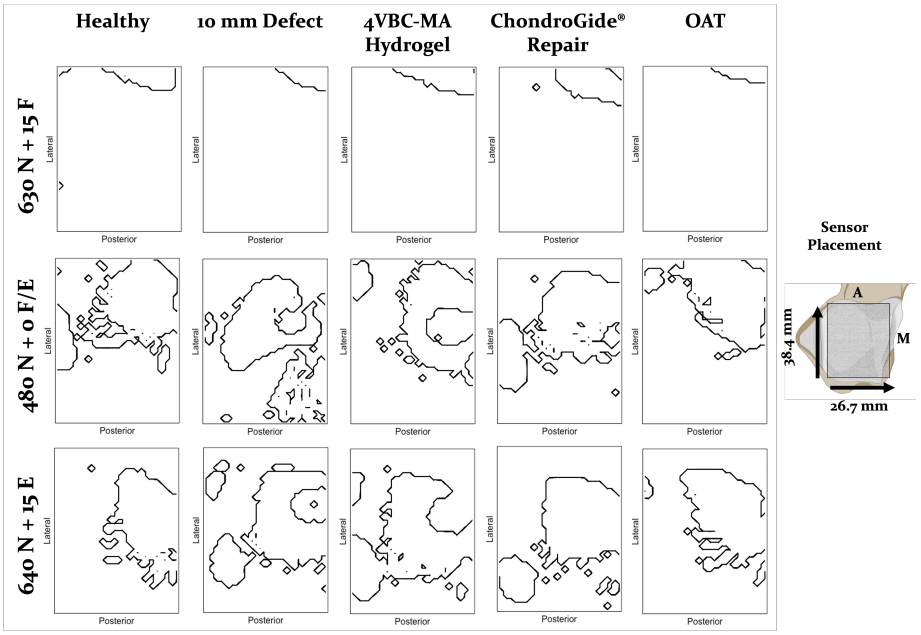

Figure B.9: Contour plot for sample 2 showing contact area across the talar dome.
A sample of contour plots for one sample showing areas of contact across the talar dome for each condition (left to right) healthy, Chondral defect, 4VBC-MA hydrogel, ChondroGide ® repair and OAT treatment. Regions of contact outline with black line. Region mapped represent an area of 38.4 x 26.7 mm on the talar dome. A = Anterior, M = Medial

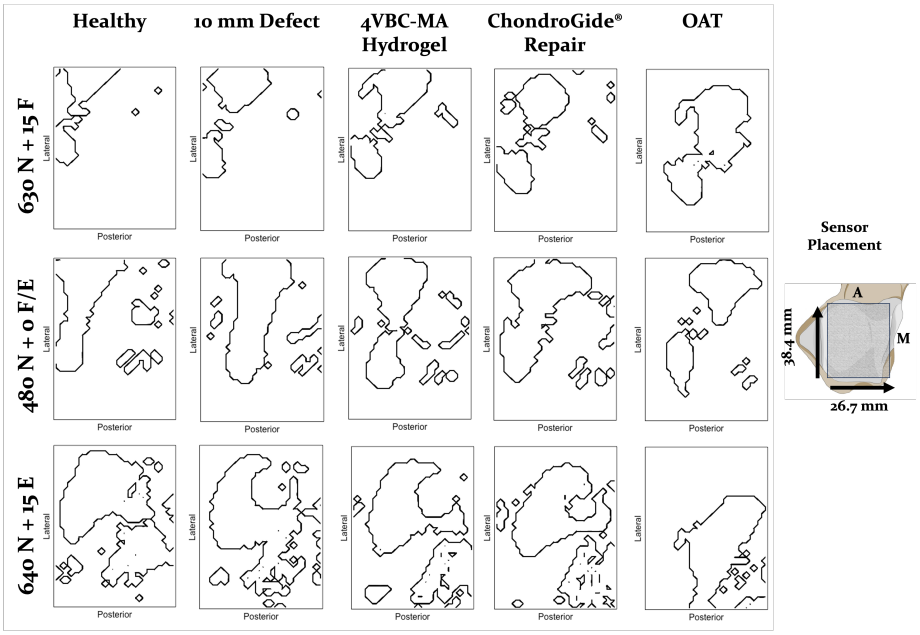

Figure B.10: Contour plot for sample 3 showing contact area across the talar dome.
A sample of contour plots for one sample showing areas of contact across the talar dome for each condition (left to right) healthy, Chondral defect, 4VBC-MA hydrogel, ChondroGide ® repair and OAT treatment. Regions of contact outline with black line. Region mapped represent an area of 38.4 x 26.7 mm on the talar dome. A = Anterior, M = Medial

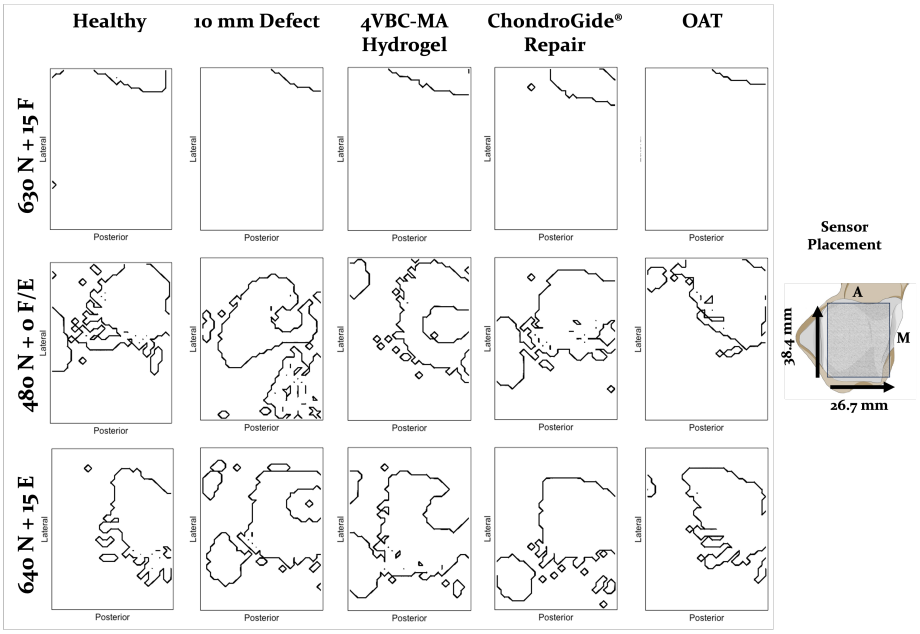

Figure B.11: Contour plot for sample 4 showing contact area across the talar dome.
A sample of contour plots for one sample showing areas of contact across the talar dome for each condition (left to right) healthy, Chondral defect, 4VBC-MA hydrogel, ChondroGide ® repair and OAT treatment. Regions of contact outline with black line. Region mapped represent an area of 38.4 x 26.7 mm on the talar dome. A = Anterior, M = Medial

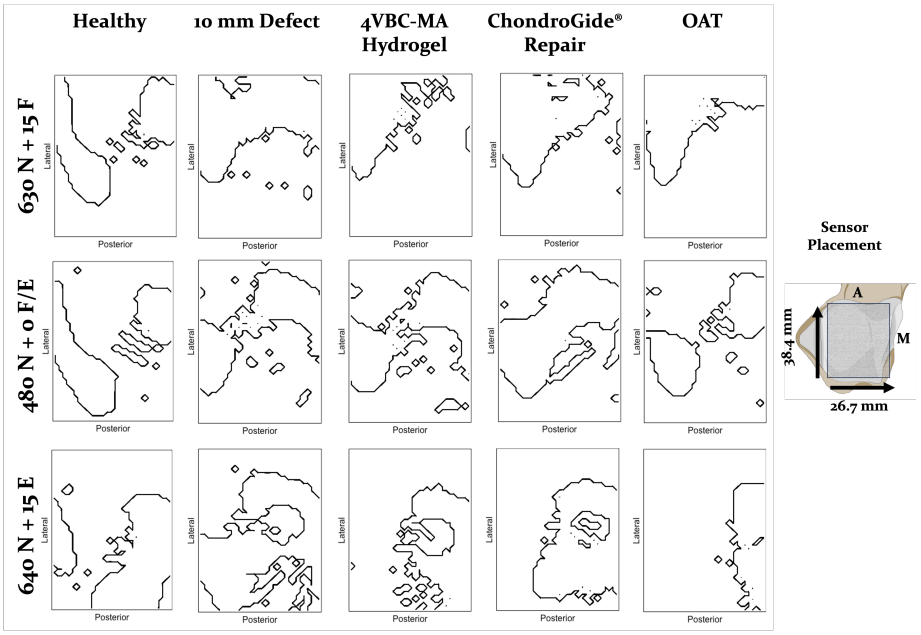

Figure B.12: Contour plot for sample 5 showing contact area across the talar dome.
A sample of contour plots for one sample showing areas of contact across the talar dome for each condition (left to right) healthy, Chondral defect, 4VBC-MA hydrogel, ChondroGide ® repair and OAT treatment. Regions of contact outline with black line. Region mapped represent an area of 38.4 x 26.7 mm on the talar dome. A = Anterior, M = Medial

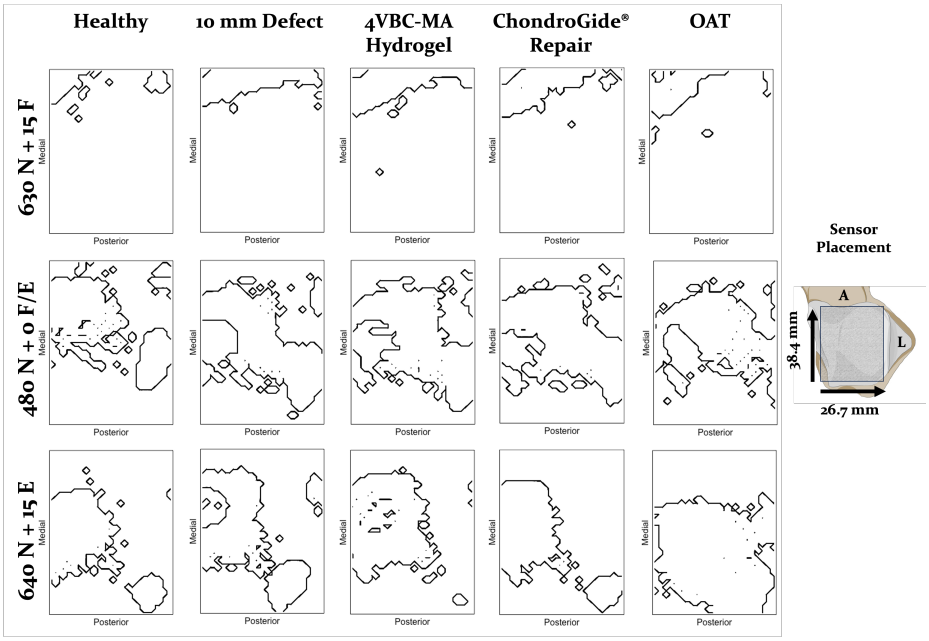

Figure B.13: Contour plot for sample 6 showing contact area across the talar dome.
A sample of contour plots for one sample showing areas of contact across the talar dome for each condition (left to right) healthy, Chondral defect, 4VBC-MA hydrogel, ChondroGide ® repair and OAT treatment. Regions of contact outline with black line. Region mapped represent an area of 38.4 x 26.7 mm on the talar dome. A = Anterior, L = Lateral

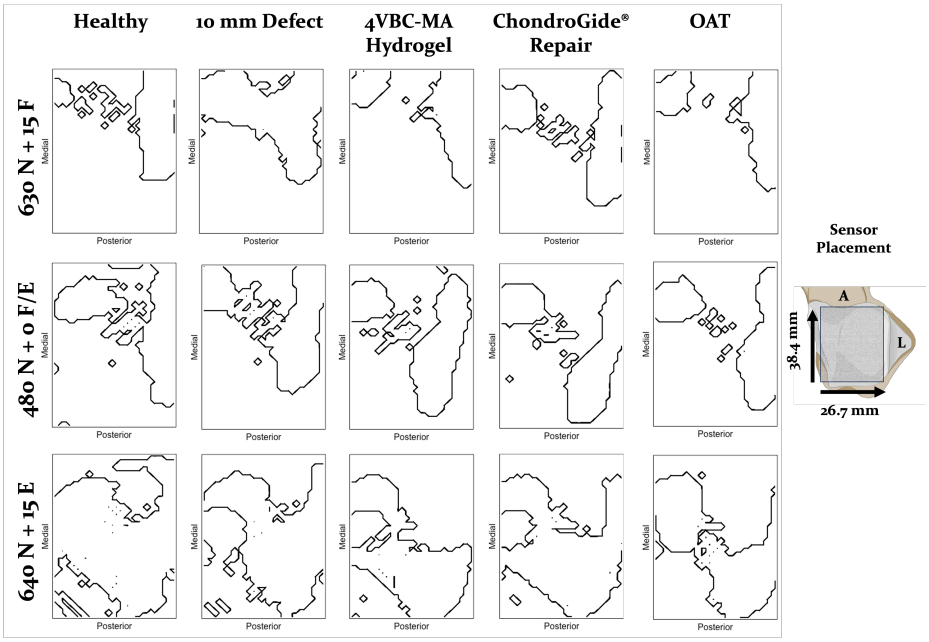

Figure B.14: Contour plot for sample 7 showing contact area across the talar dome.
A sample of contour plots for one sample showing areas of contact across the talar dome for each condition (left to right) healthy, Chondral defect, 4VBC-MA hydrogel, ChondroGide ® repair and OAT treatment. Regions of contact outline with black line. Region mapped represent an area of 38.4 x 26.7 mm on the talar dome. A = Anterior, L = Lateral

B.1.3 Pre and post testing membrane stability images

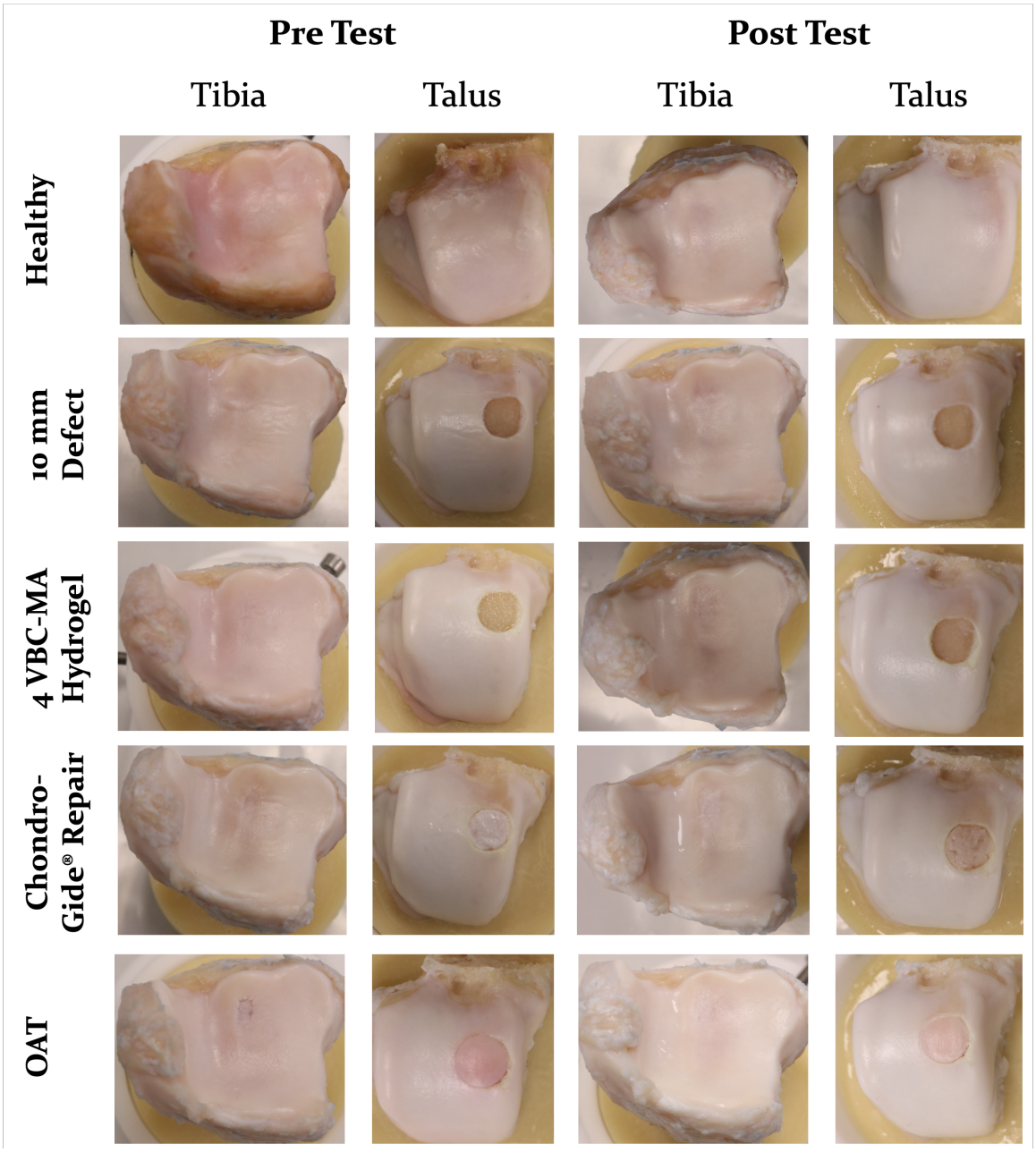

Figure B.15: Pre and post test photographs of sample 1 paired tibia and talar articulating cartilage during tribological testing of conditions

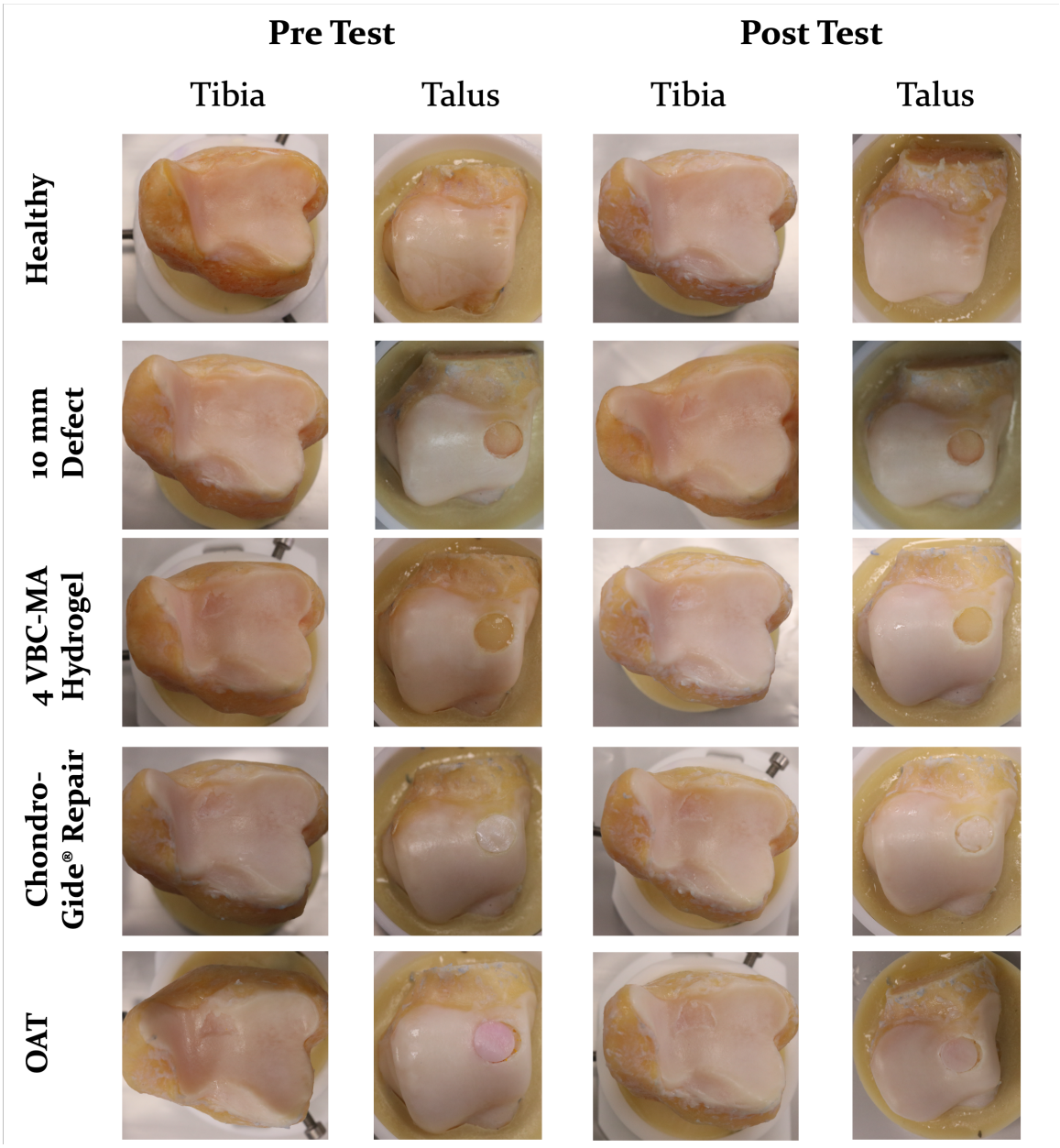

Figure B.16: Pre and post test photographs of sample 2 paired tibia and talar articulating cartilage during tribological testing of conditions

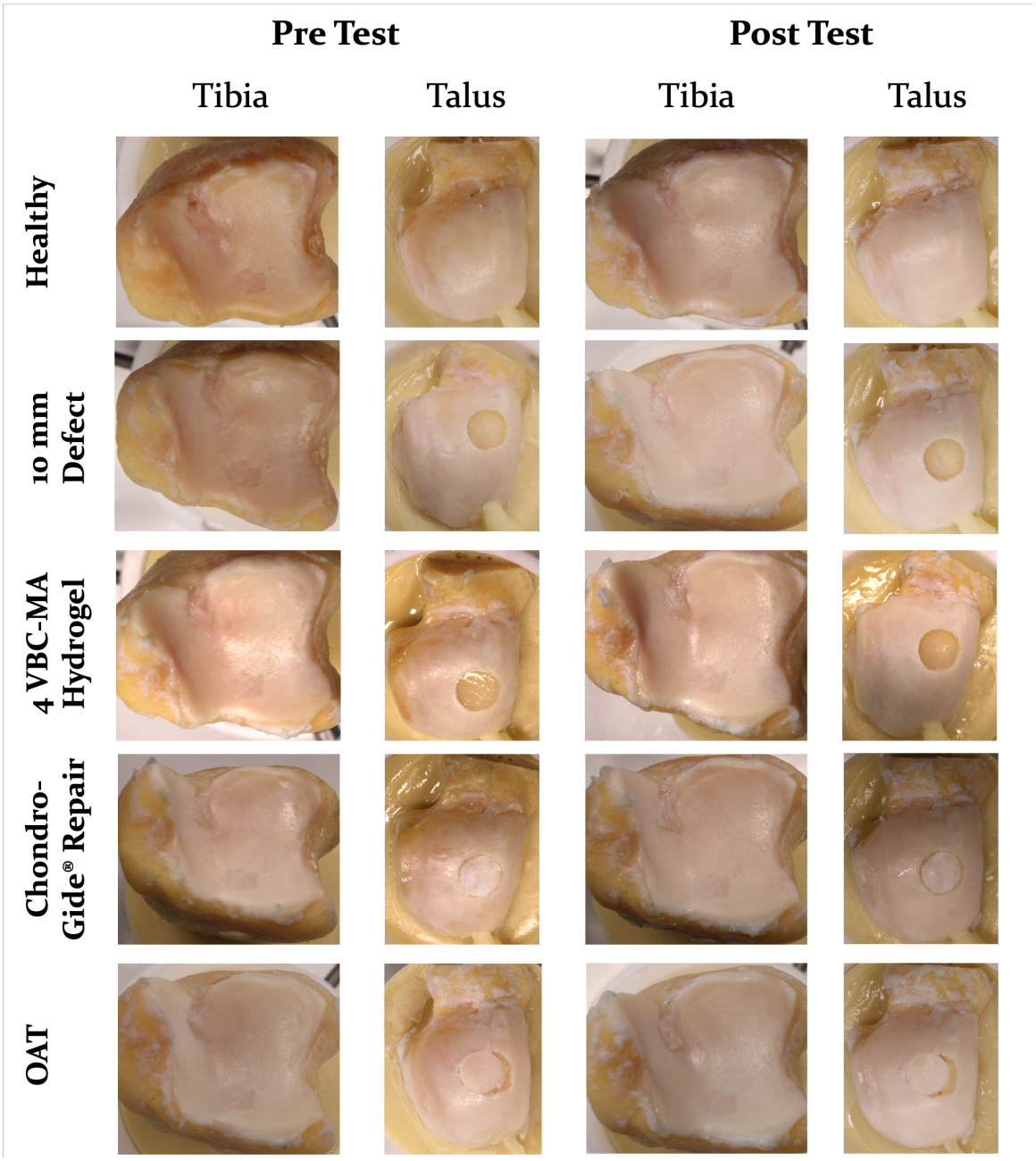

Figure B.17: Pre and post test photographs of sample 3 paired tibia and talar articulating cartilage during tribological testing of conditions

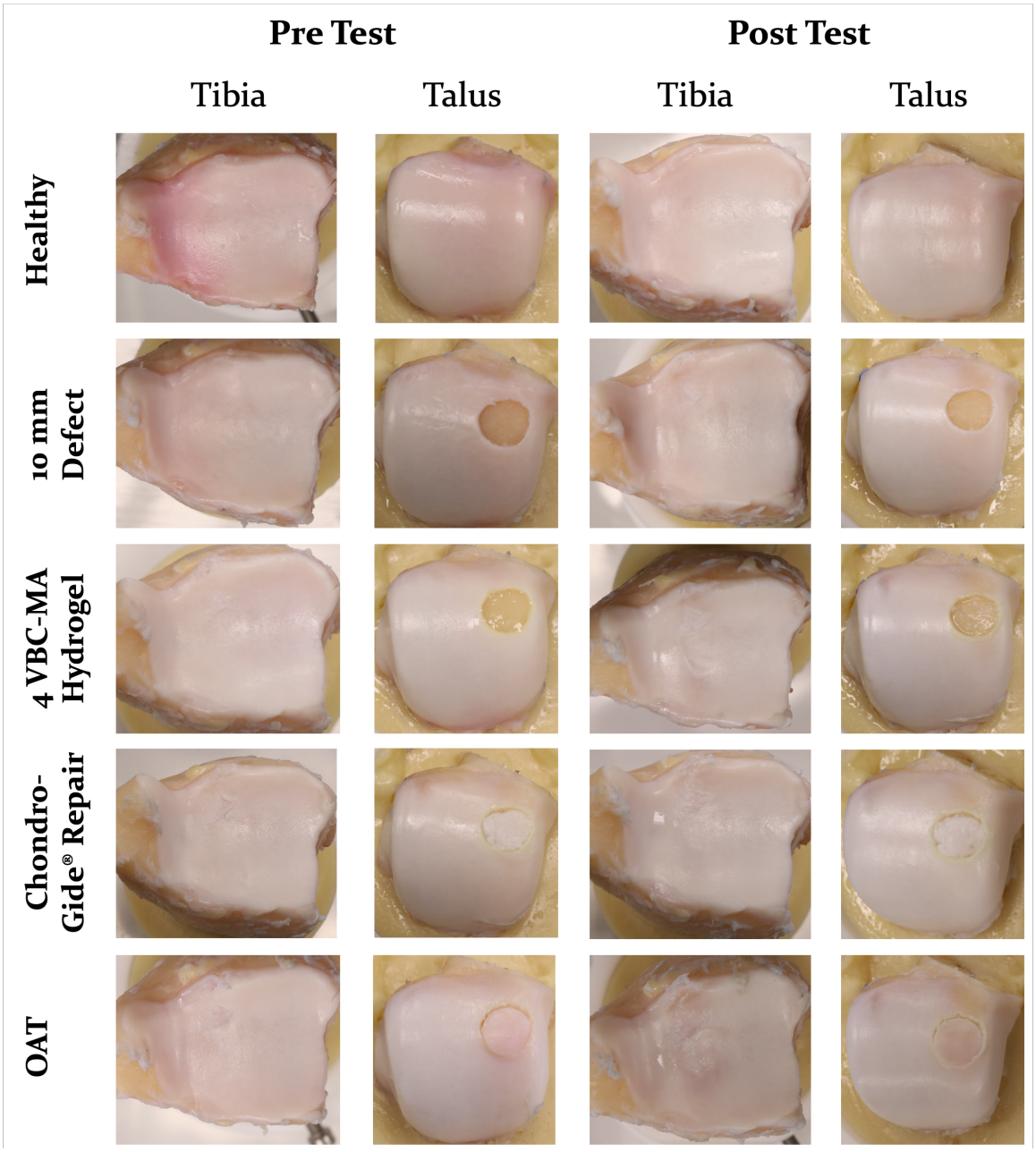

Figure B.18: Pre and post test photographs of sample 4 paired tibia and talar articulating cartilage during tribological testing of conditions

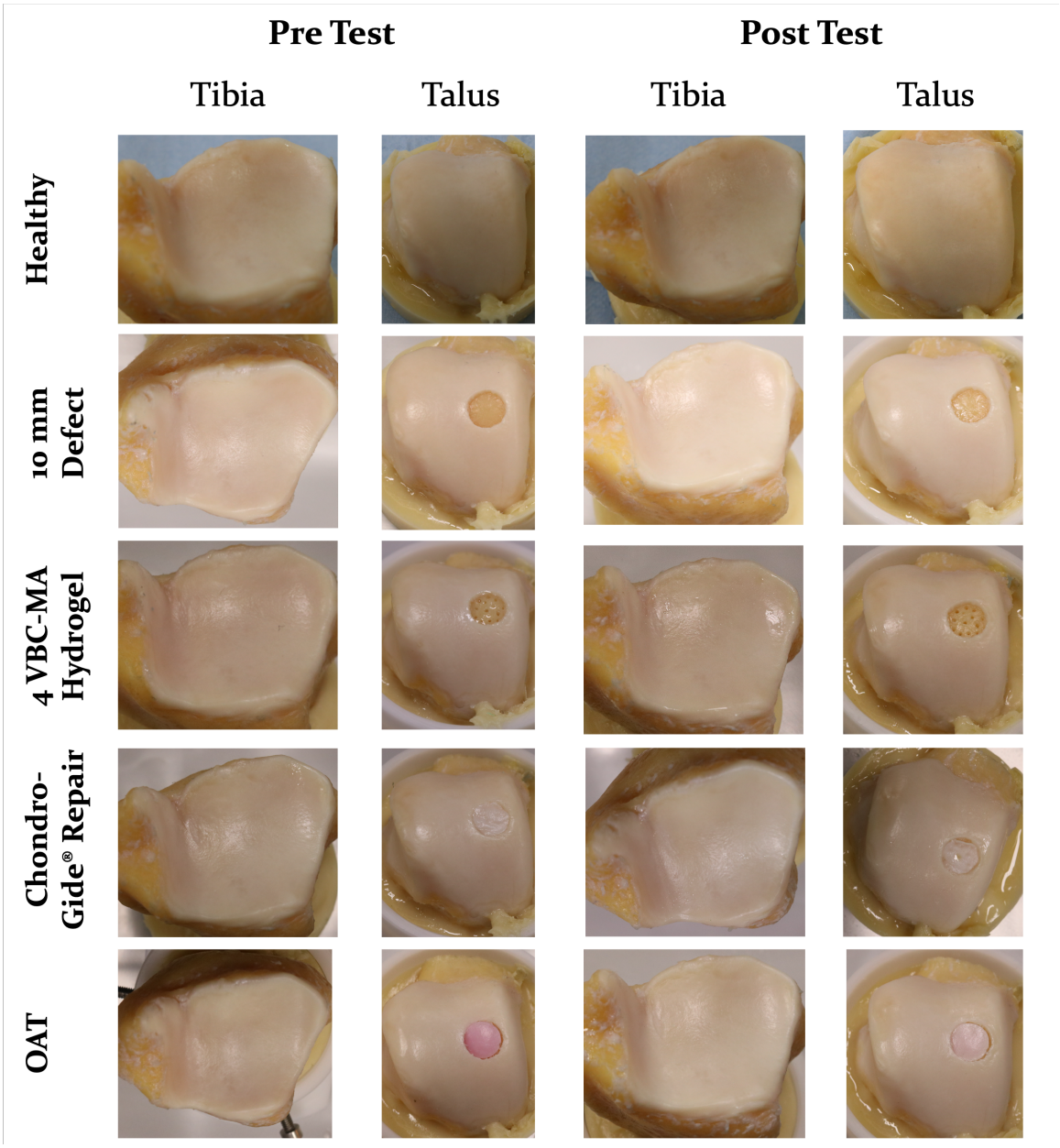

Figure B.19: Pre and post test photographs of sample 5 paired tibia and talar articulating cartilage during tribological testing of conditions

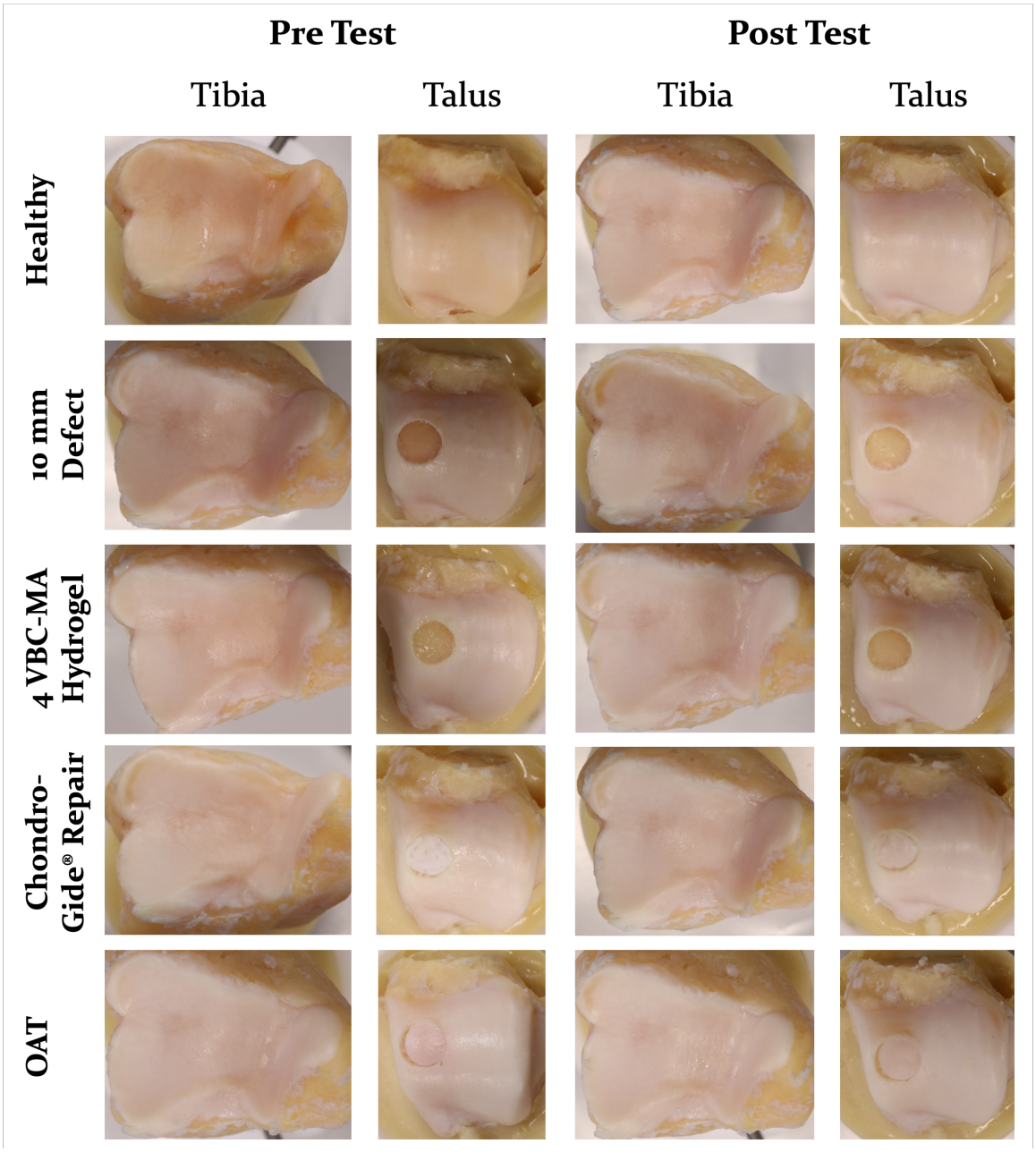

Figure B.20: Pre and post test photographs of sample 6 paired tibia and talar articulating cartilage during tribological testing of conditions

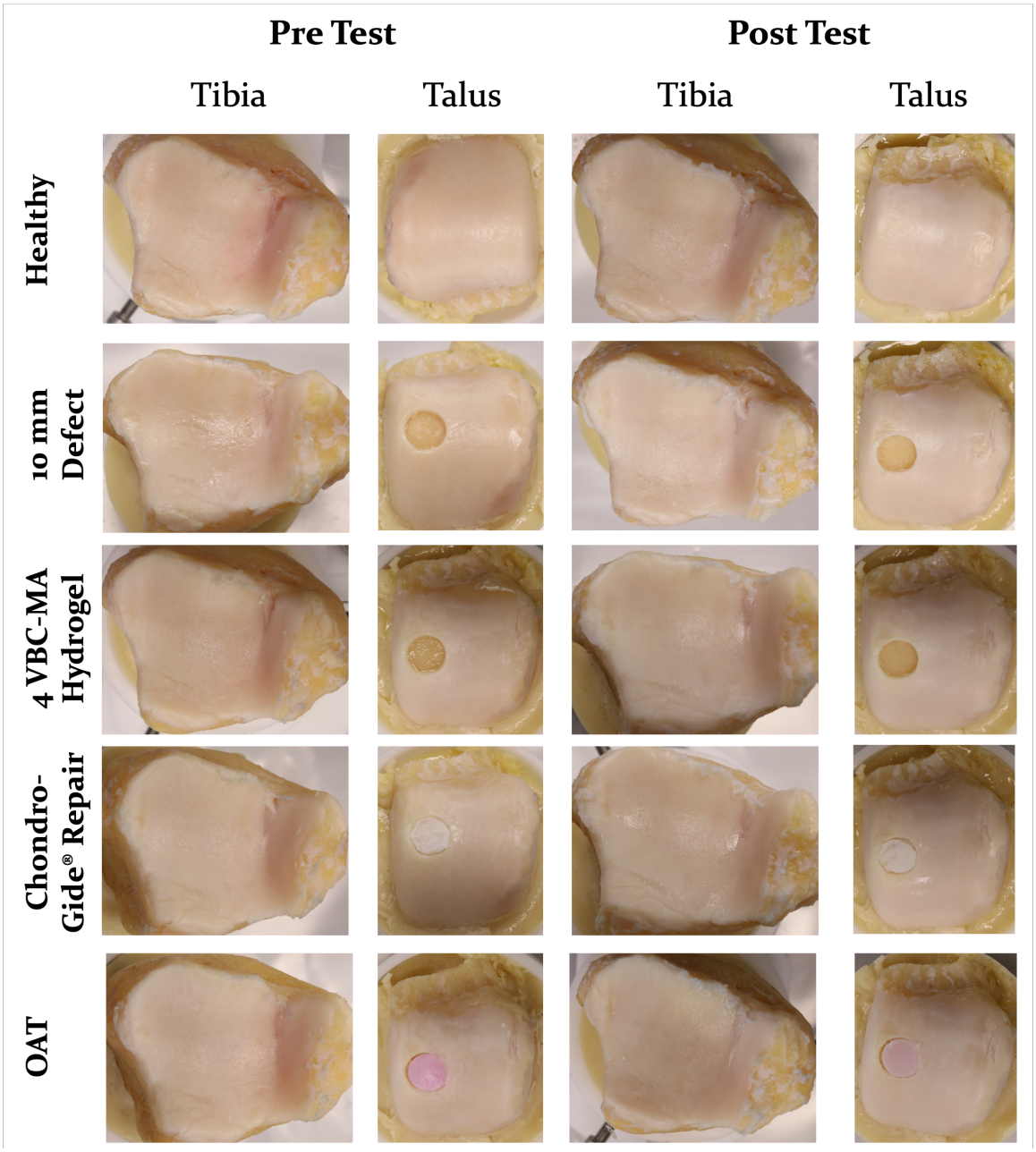

Figure B.21: Pre and post test photographs of sample 7 paired tibia and talar articulating cartilage during tribological testing of conditions

Appendix C

C.1 Chapter 7 - Large Circle Vs Large Square

C.1.1 Contact pressure maps

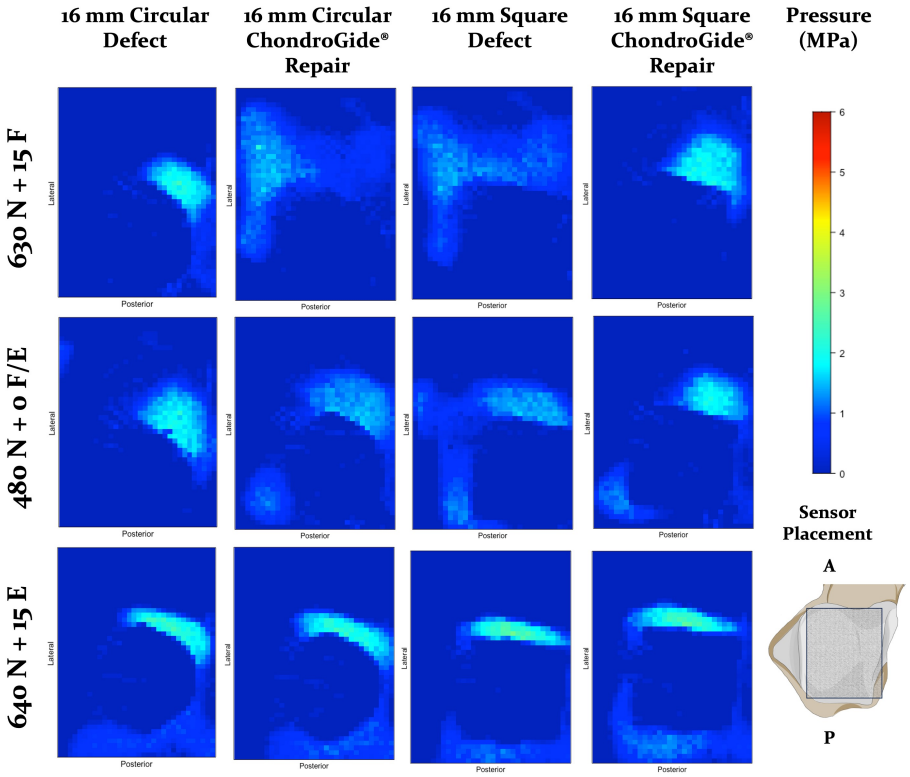

Figure C.1: Pressure maps showing contact area and distribution pressure for each loading condition for across the talar dome for sample 1. Image show sample of pressure maps for one sample looking at pressure distribution across the talar dome for each condition (left to right) 16 mm circular defect, 16 mm Circular ChondroGide® repair, 16 mm square defect and 16 mm Square ChondroGide® repair. A = Anterior, P = Posterior.

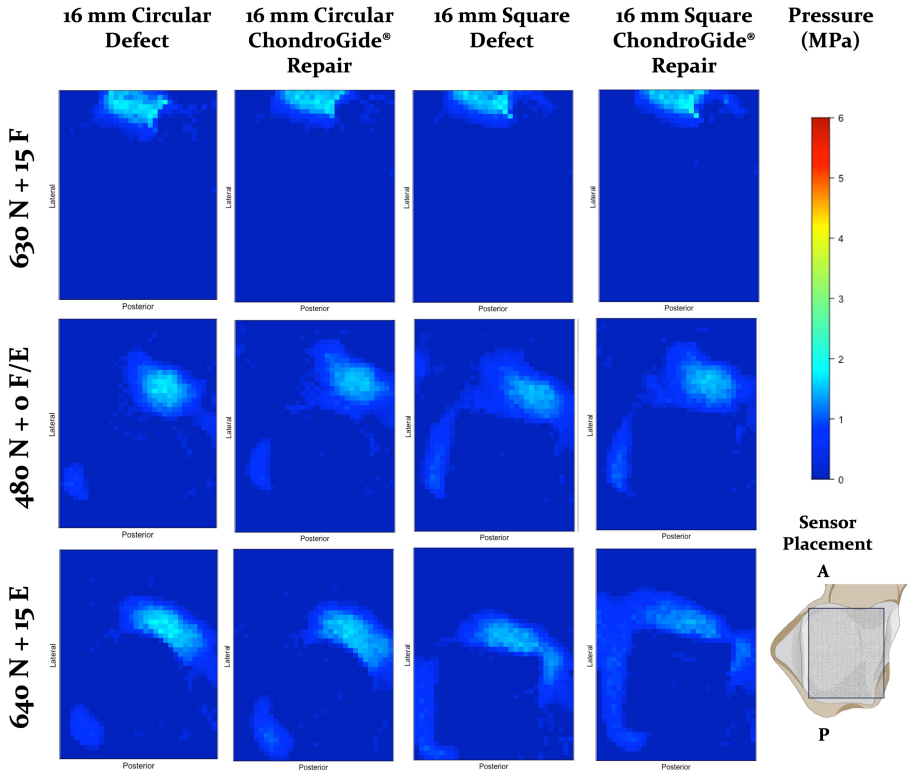

Figure C.2: Pressure maps showing contact area and distribution pressure for each loading condition for across the talar dome for sample 2. Image show sample of pressure maps for one sample looking at pressure distribution across the talar dome for each condition (left to right) 16 mm circular defect, 16 mm Circular ChondroGide® repair, 16 mm square defect and 16 mm Square ChondroGide® repair. A = Anterior, P = Posterior.

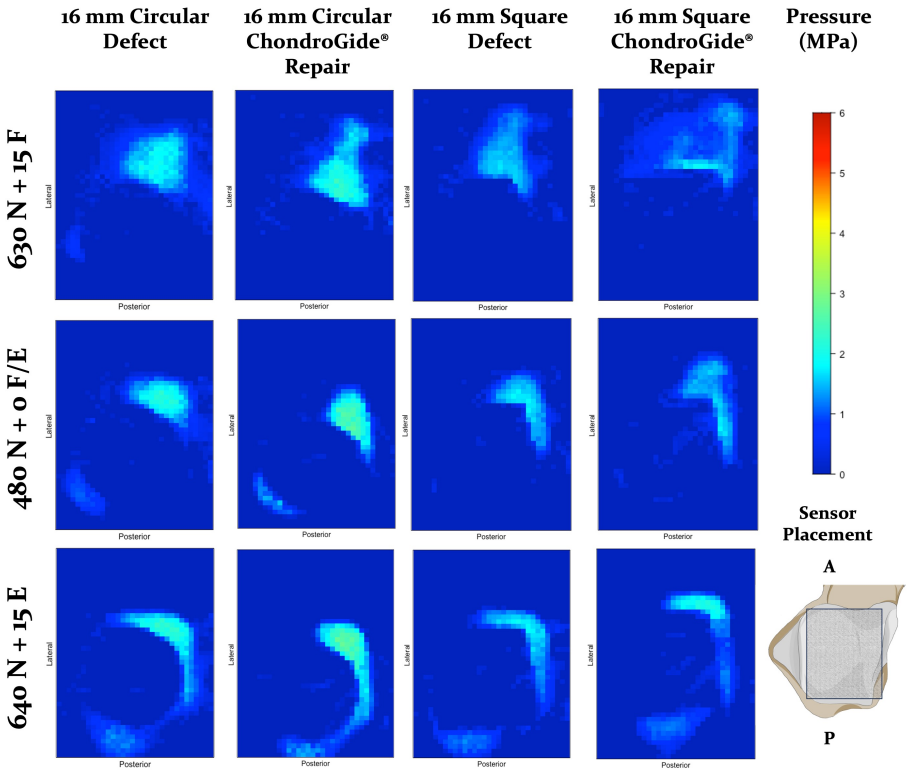

Figure C.3: Pressure maps showing contact area and distribution pressure for each loading condition for across the talar dome for sample 3. Image show sample of pressure maps for one sample looking at pressure distribution across the talar dome for each condition (left to right) 16 mm circular defect, 16 mm Circular ChondroGide® repair, 16 mm square defect and 16 mm Square ChondroGide® repair. A = Anterior, P = Posterior.

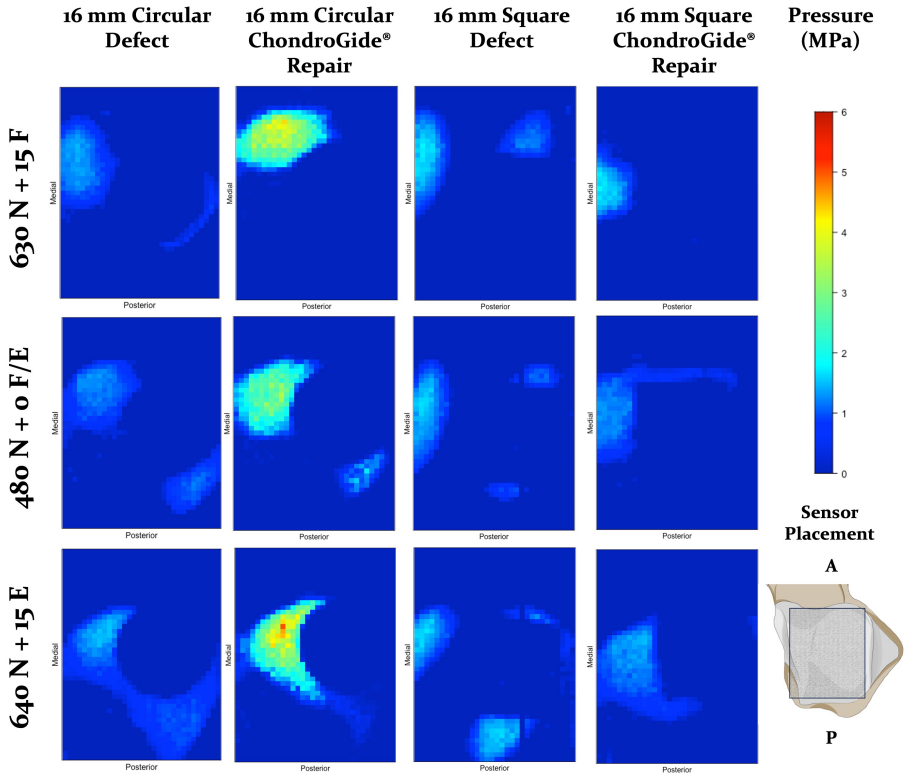

Figure C.4: Pressure maps showing contact area and distribution pressure for each loading condition for across the talar dome for sample 4. Image show sample of pressure maps for one sample looking at pressure distribution across the talar dome for each condition (left to right) 16 mm circular defect, 16 mm Circular ChondroGide® repair, 16 mm square defect and 16 mm Square ChondroGide® repair. A = Anterior, P = Posterior.

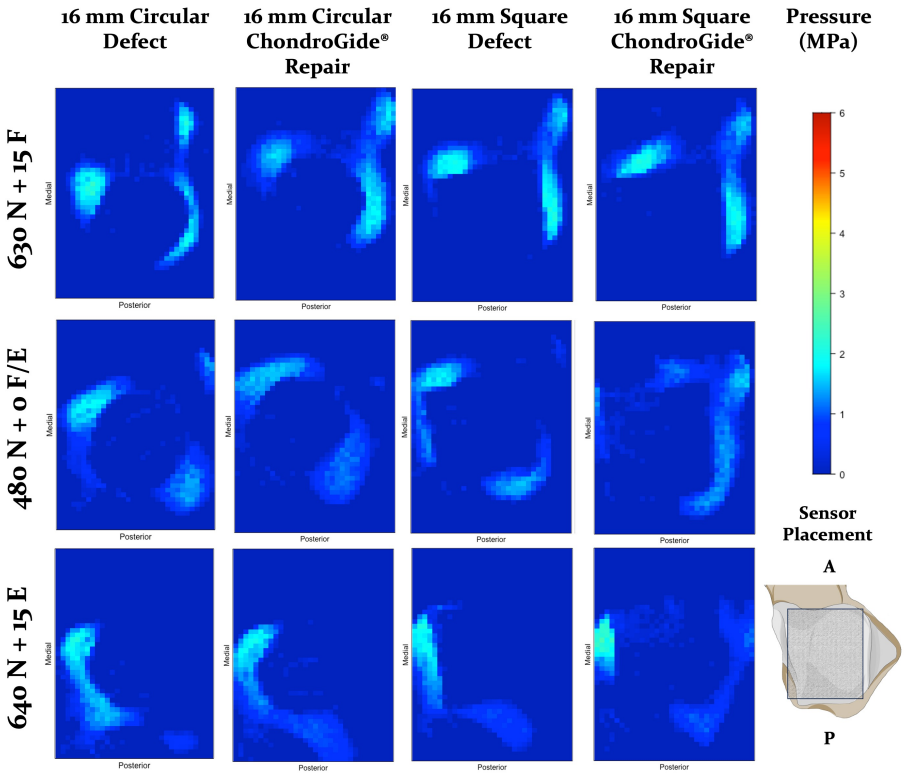

Figure C.5: Pressure maps showing contact area and distribution pressure for each loading condition for across the talar dome for sample 5. Image show sample of pressure maps for one sample looking at pressure distribution across the talar dome for each condition (left to right) 16 mm circular defect, 16 mm Circular ChondroGide® repair, 16 mm square defect and 16 mm Square ChondroGide® repair. A = Anterior, P = Posterior.

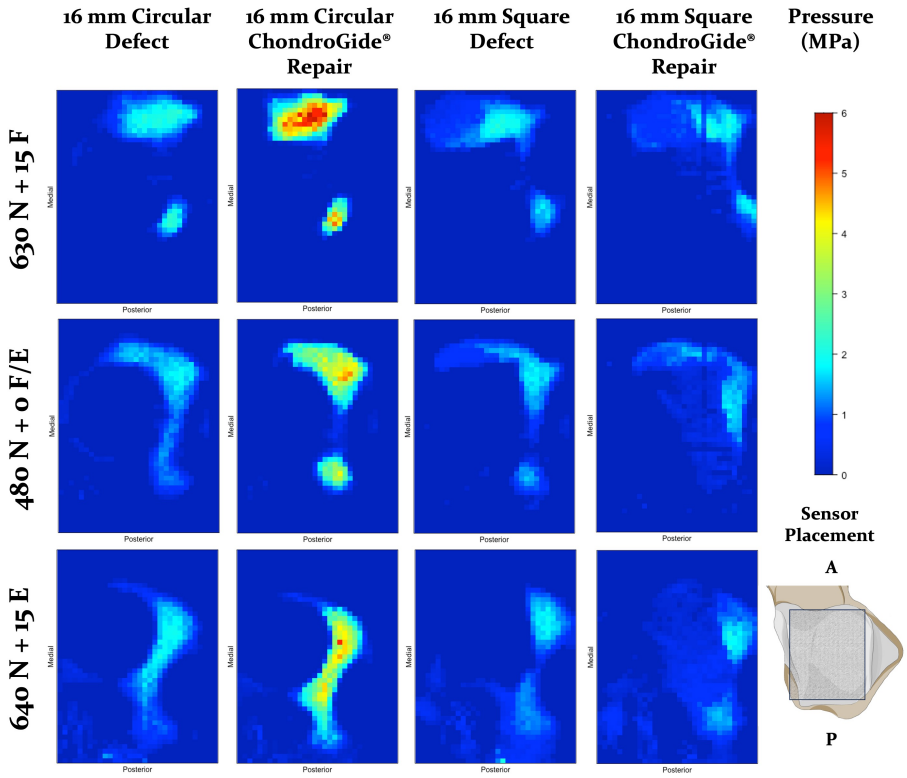

Figure C.6: Pressure maps showing contact area and distribution pressure for each loading condition for across the talar dome for sample 6. Image show sample of pressure maps for one sample looking at pressure distribution across the talar dome for each condition (left to right) 16 mm circular defect, 16 mm Circular ChondroGide® repair, 16 mm square defect and 16 mm Square ChondroGide® repair. A = Anterior, P = Posterior.

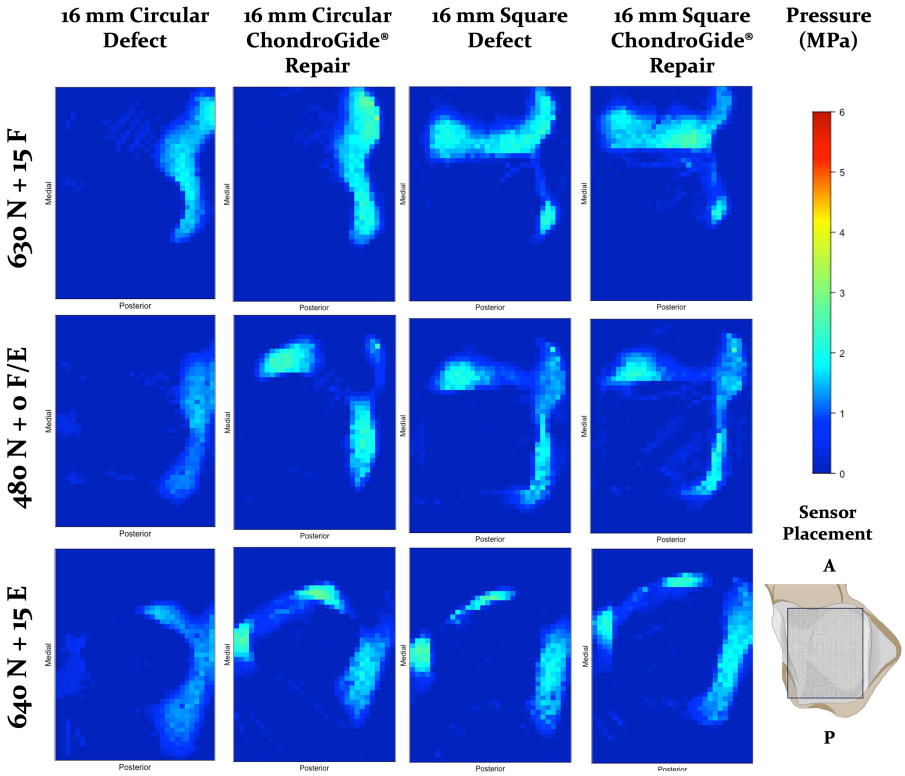

Figure C.7: Pressure maps showing contact area and distribution pressure for each loading condition for across the talar dome for sample 7. Image show sample of pressure maps for one sample looking at pressure distribution across the talar dome for each condition (left to right) 16 mm circular defect, 16 mm Circular ChondroGide® repair, 16 mm square defect and 16 mm Square ChondroGide® repair. A = Anterior, P = Posterior.

C.1.2 Contour maps

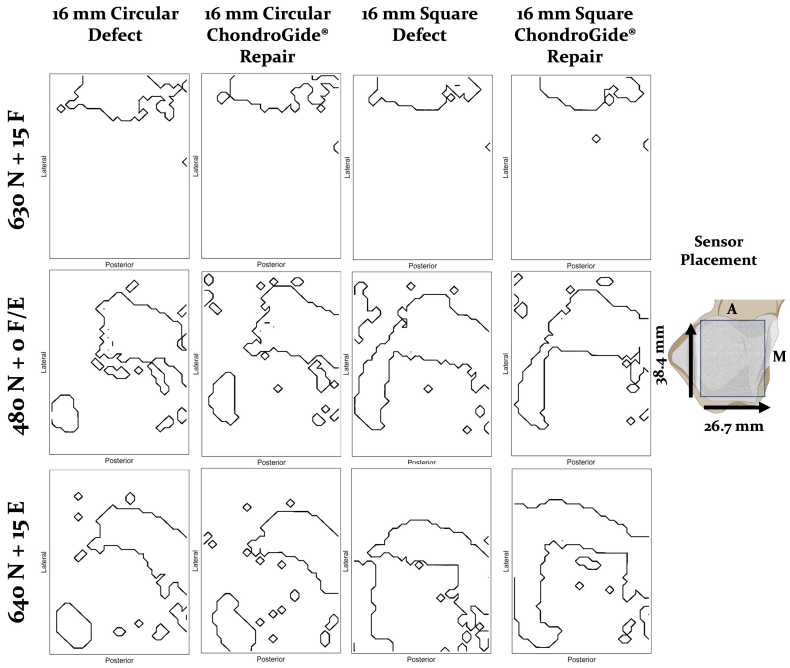

Figure C.8: Contour plots for sample 1 showing contact area across the talar dome for each condition. Samples of contour plots showing areas of contact on the talar dome for each condition (left to right) 16 mm circular defect, 16 mm Circular ChondroGide ® repair, 16 mm square defect and 16 mm Square ChondroGide ® repair. Maps represent a 38.4 x 26.7 mm area on the talar dome. A = Anterior, M = Medial.

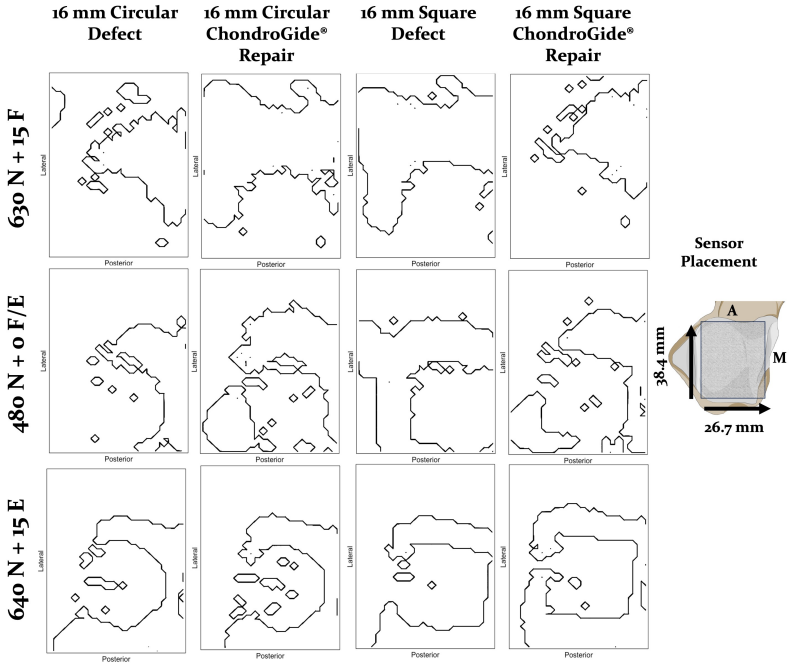

Figure C.9: Contour plots for sample 2 showing contact area across the talar dome for each condition. Samples of contour plots generated showing areas of contact on the talar dome for each condition (left to right) 16 mm circular defect, 16 mm Circular ChondroGide ® repair, 16 mm square defect and 16 mm Square ChondroGide ® repair. Maps represent a 38.4 x 26.7 mm area on the talar dome. A = Anterior, M = Medial.

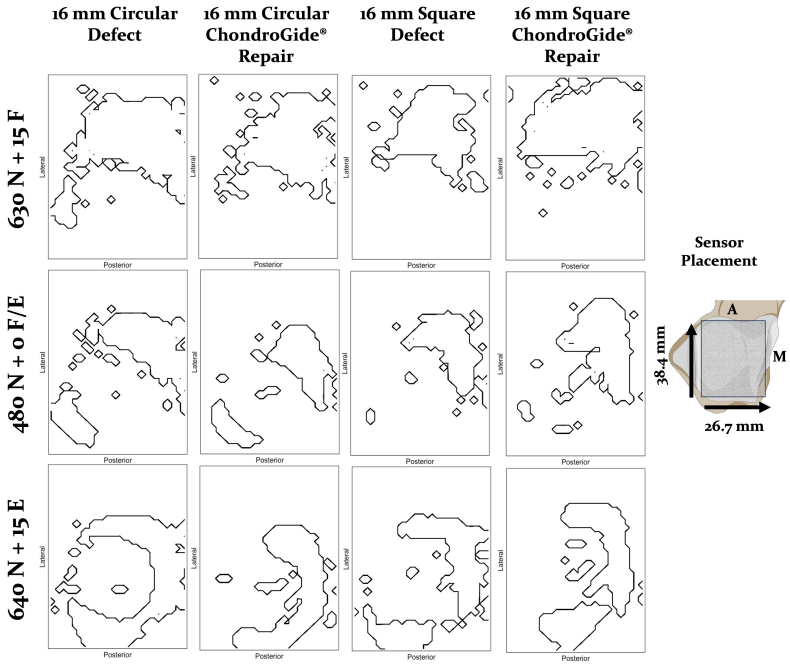

Figure C.10: Contour plots for sample 3 showing contact area across the talar dome for each condition. Samples of contour plots generated showing areas of contact on the talar dome for each condition (left to right) 16 mm circular defect, 16 mm Circular ChondroGide ® repair, 16 mm square defect and 16 mm Square ChondroGide ® repair. Maps represent a 38.4 x 26.7 mm area on the talar dome. A = Anterior, M = Medial.

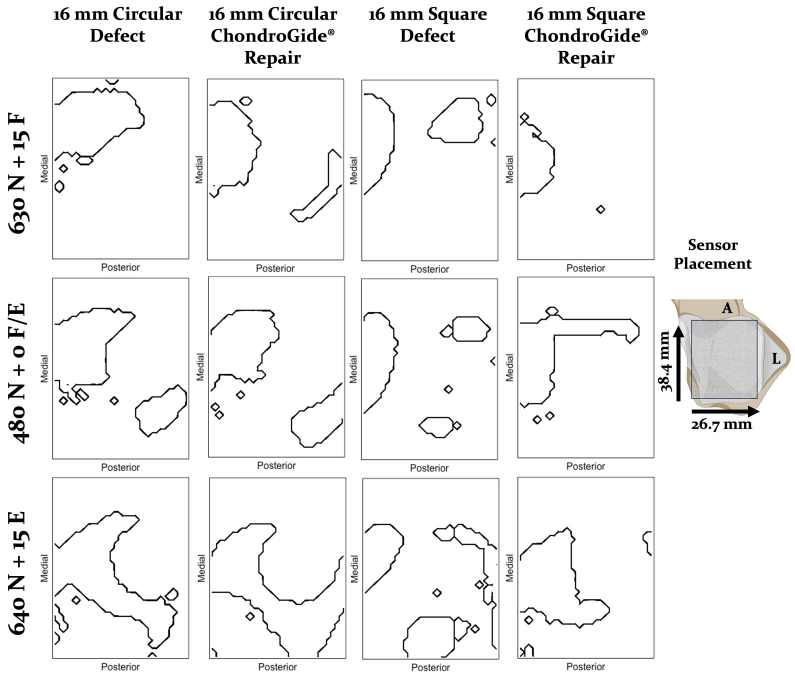

Figure C.11: Contour plots for sample 4 showing contact area across the talar dome for each condition. Samples of contour plots showing areas of contact on the talar dome for each condition (left to right) 16 mm circular defect, 16 mm Circular ChondroGide ® repair, 16 mm square defect and 16 mm Square ChondroGide ® repair. Maps represent a 38.4 x 26.7 mm area on the talar dome. A = Anterior, L = Lateral.

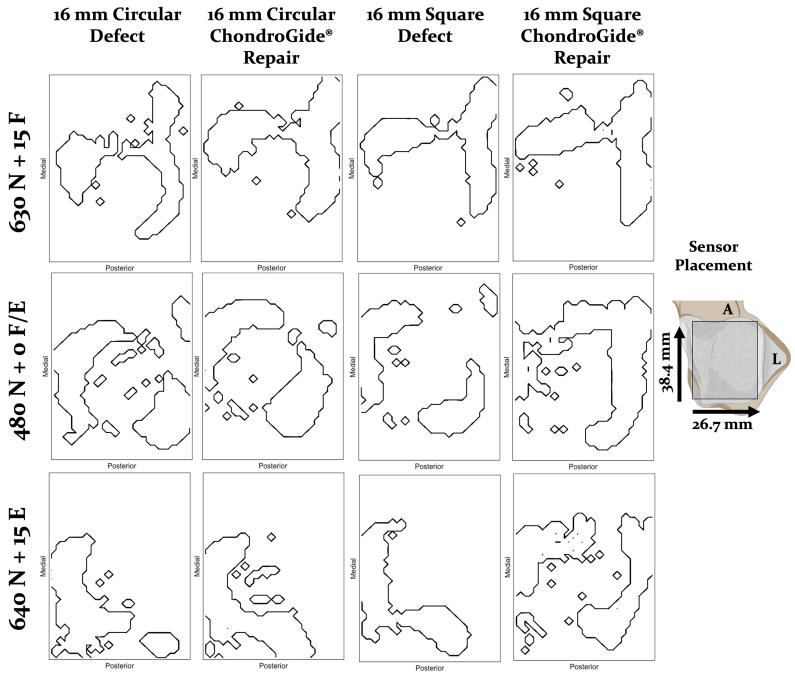

Figure C.12: Contour plots for sample 5 showing contact area across the talar dome for each condition. Samples of contour plots showing areas of contact on the talar dome for each condition (left to right) 16 mm circular defect, 16 mm Circular ChondroGide ® repair, 16 mm square defect and 16 mm Square ChondroGide ® repair. Maps represent a 38.4 x 26.7 mm area on the talar dome. A = Anterior, L = Lateral.

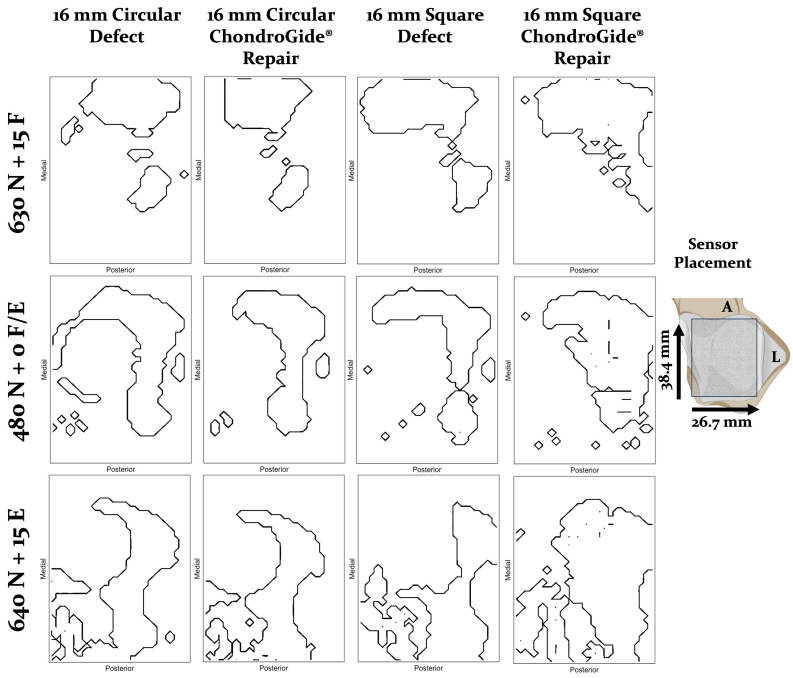

Figure C.13: Contour plots for sample 6 showing contact area across the talar dome for each condition. Samples of contour plots showing areas of contact on the talar dome for each condition (left to right) 16 mm circular defect, 16 mm Circular ChondroGide ® repair, 16 mm square defect and 16 mm Square ChondroGide ® repair. Maps represent a 38.4 x 26.7 mm area on the talar dome. A = Anterior, L = Lateral.

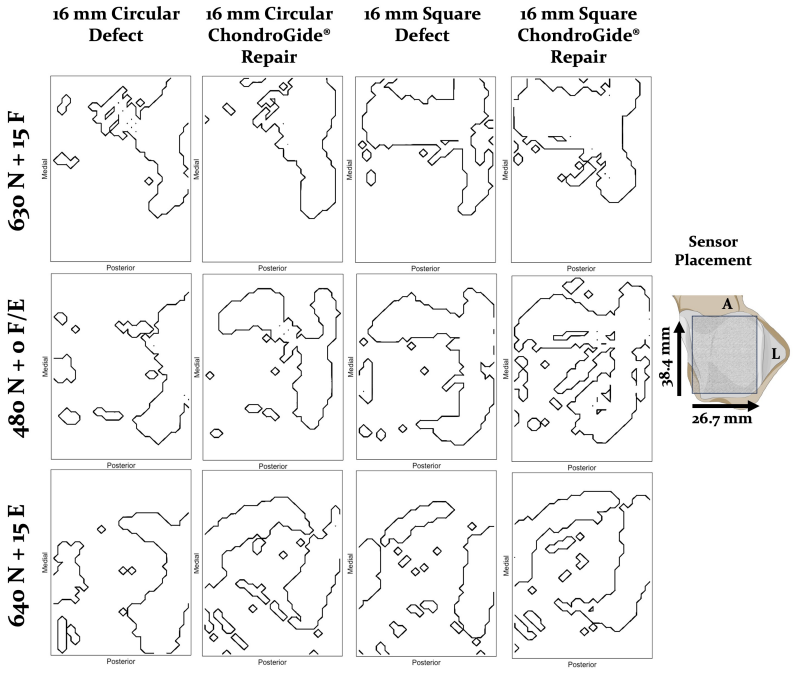

Figure C.14: Contour plots for sample 7 showing contact area across the talar dome for each condition. Samples of contour plots showing areas of contact on the talar dome for each condition (left to right) 16 mm circular defect, 16 mm Circular ChondroGide ® repair, 16 mm square defect and 16 mm Square ChondroGide ® repair. Maps represent a 38.4 x 26.7 mm area on the talar dome. A = Anterior, L = Lateral.

C.1.3 Pre and post testing membrane stability images

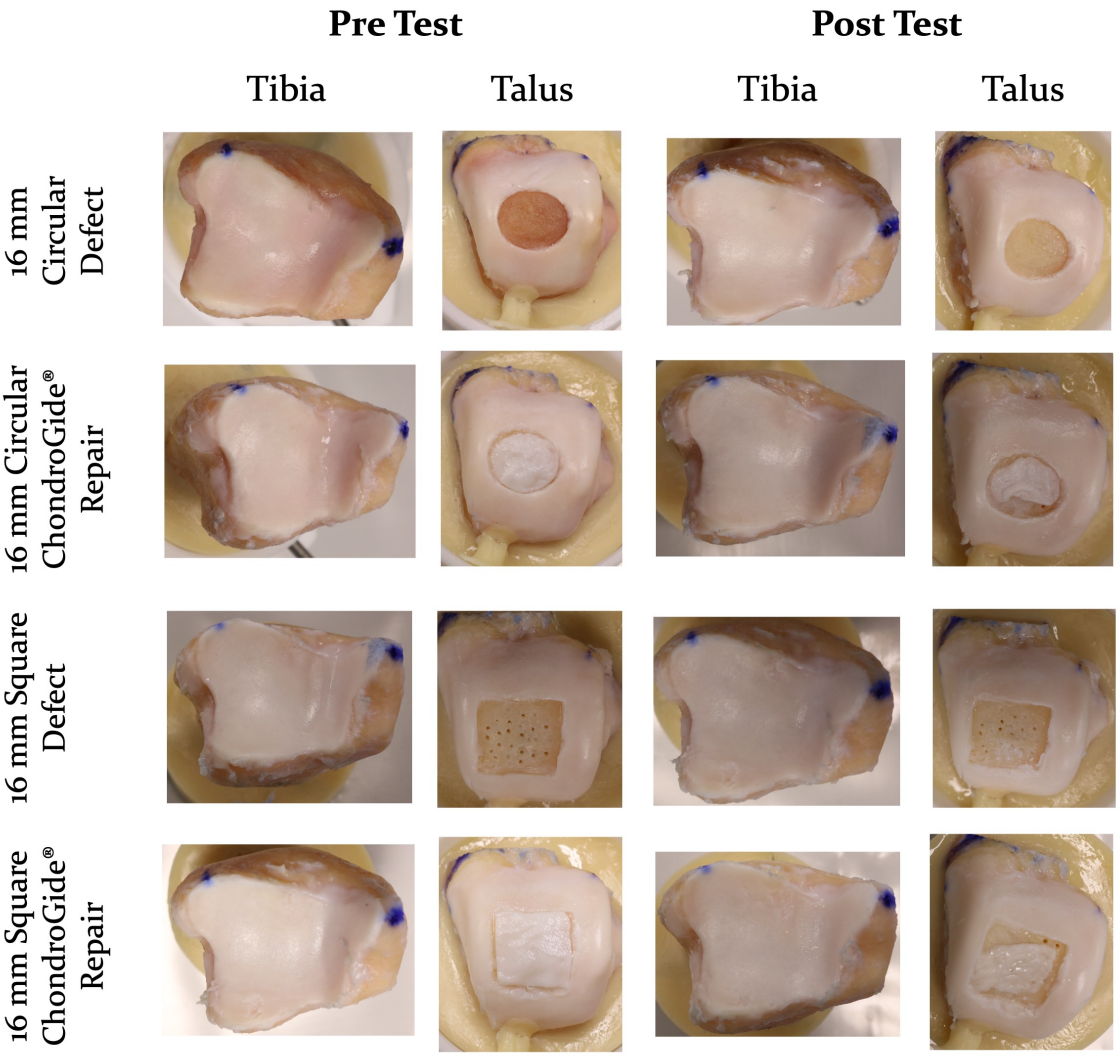

Figure C.15: Pre and post test photographs of sample 1 paired tibia and talar articulating cartilage during tribological testing of conditions

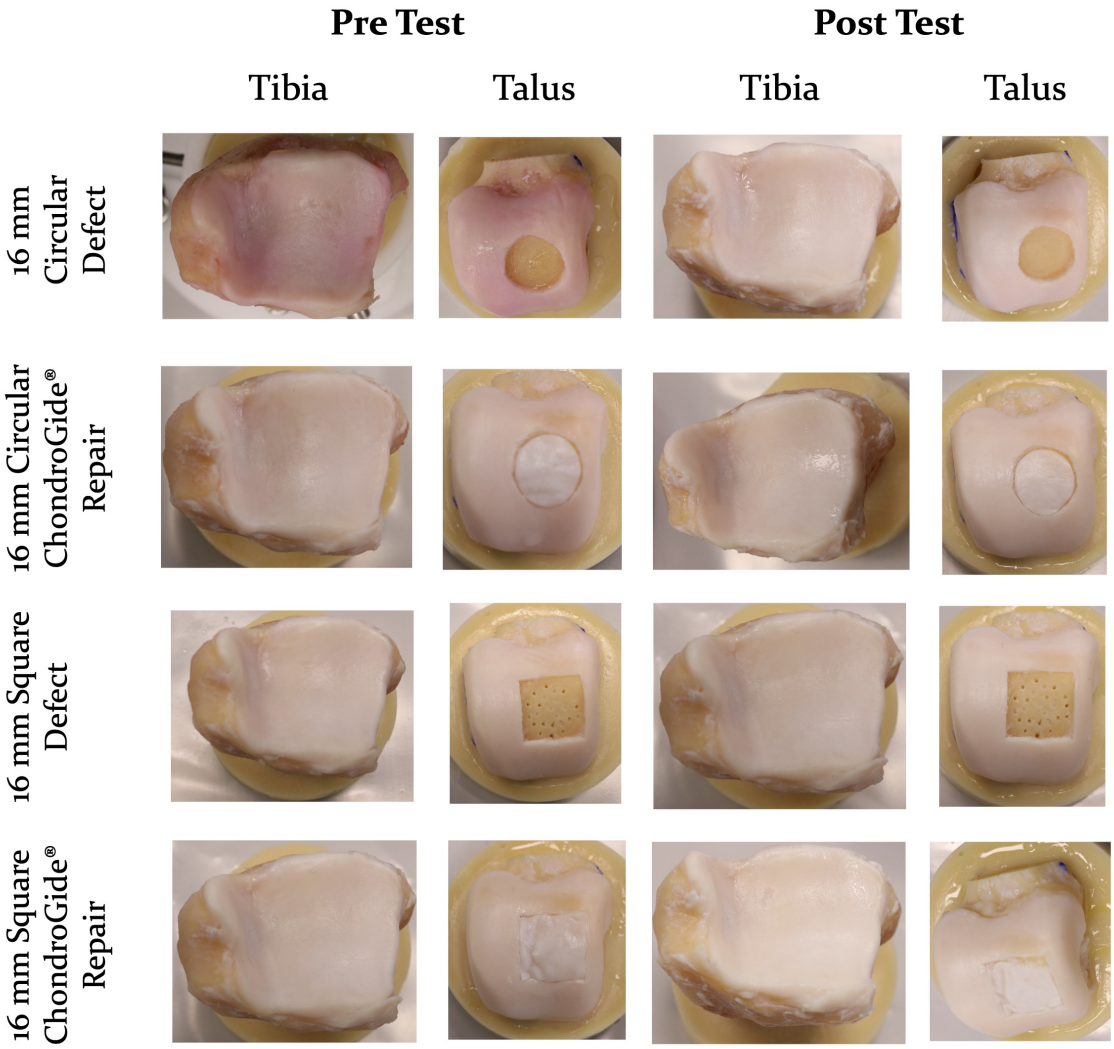

Figure C.16: Pre and post test photographs of sample 2 paired tibia and talar articulating cartilage during tribological testing of conditions

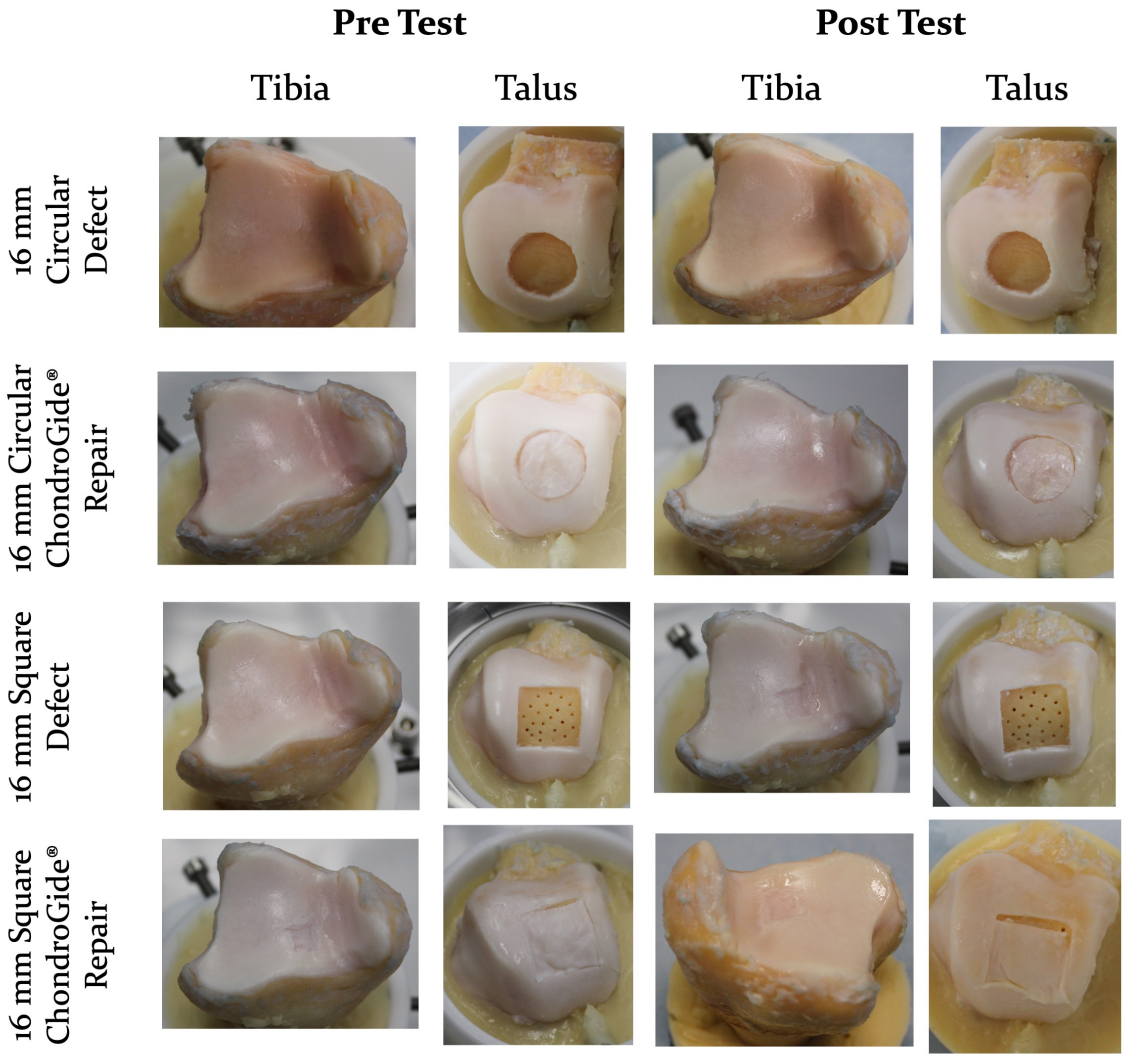

Figure C.17: Pre and post test photographs of sample 3 paired tibia and talar articulating cartilage during tribological testing of conditions

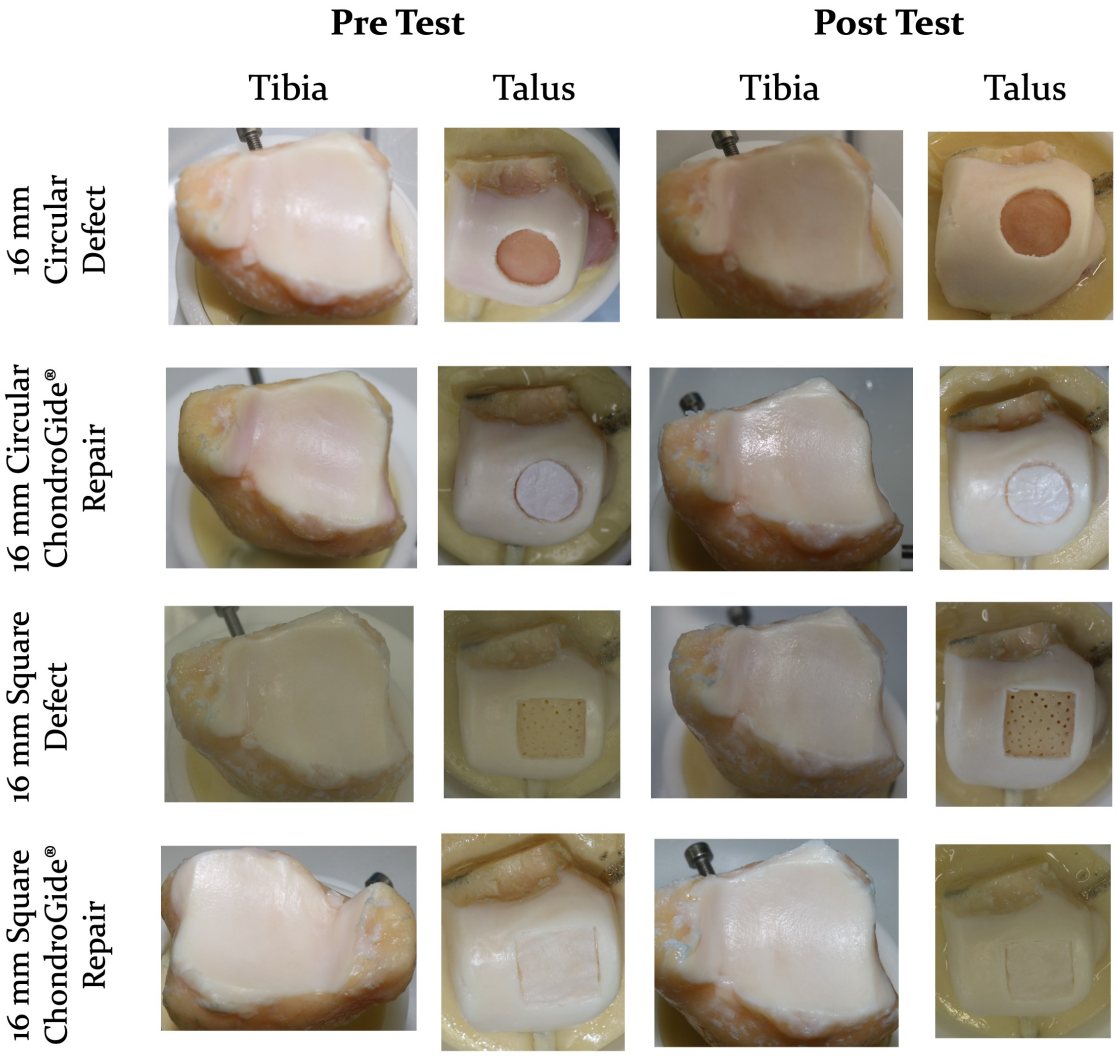

Figure C.18: Pre and post test photographs of sample 4 paired tibia and talar articulating cartilage during tribological testing of conditions

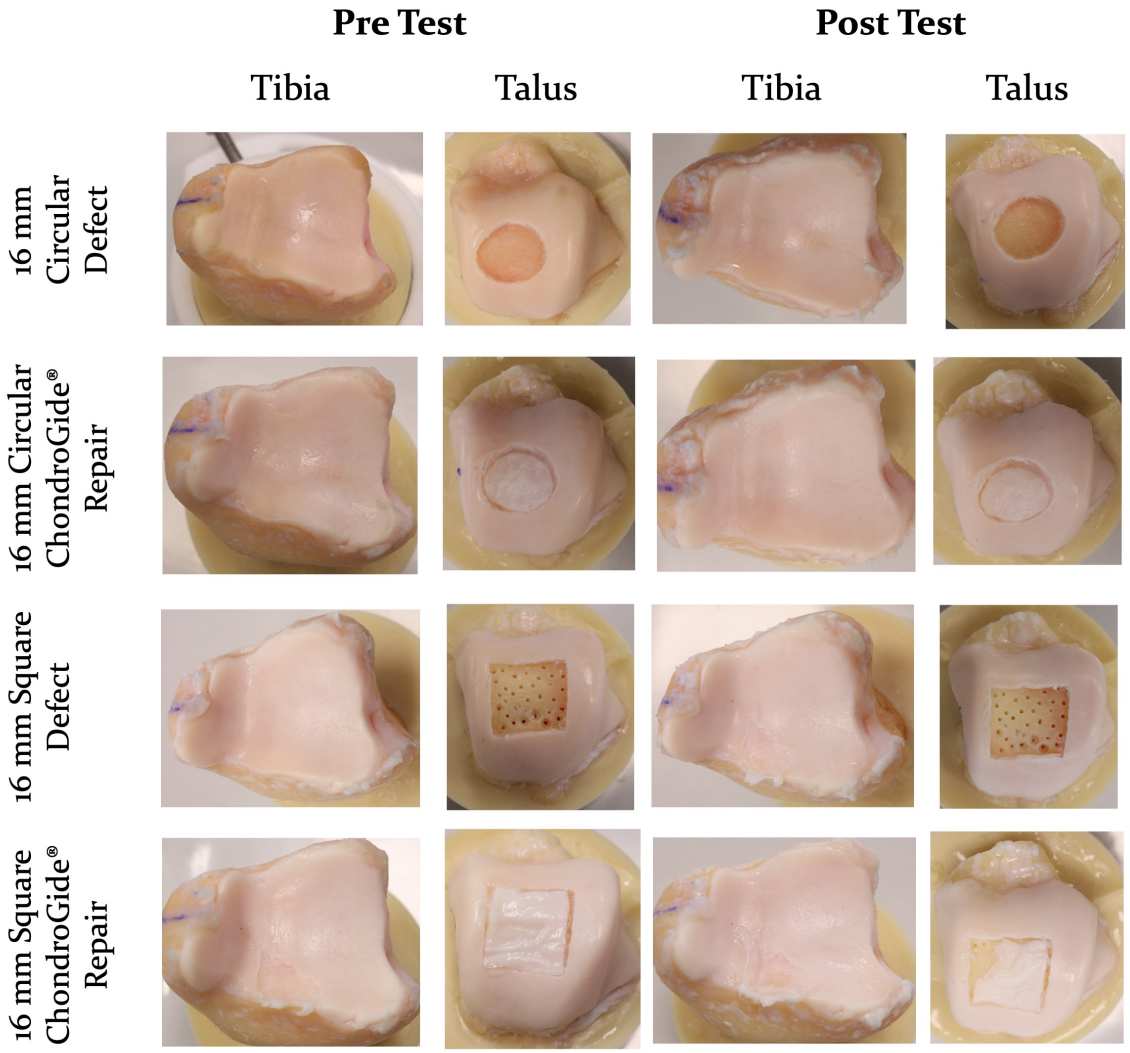

Figure C.19: Pre and post test photographs of sample 5 paired tibia and talar articulating cartilage during tribological testing of conditions

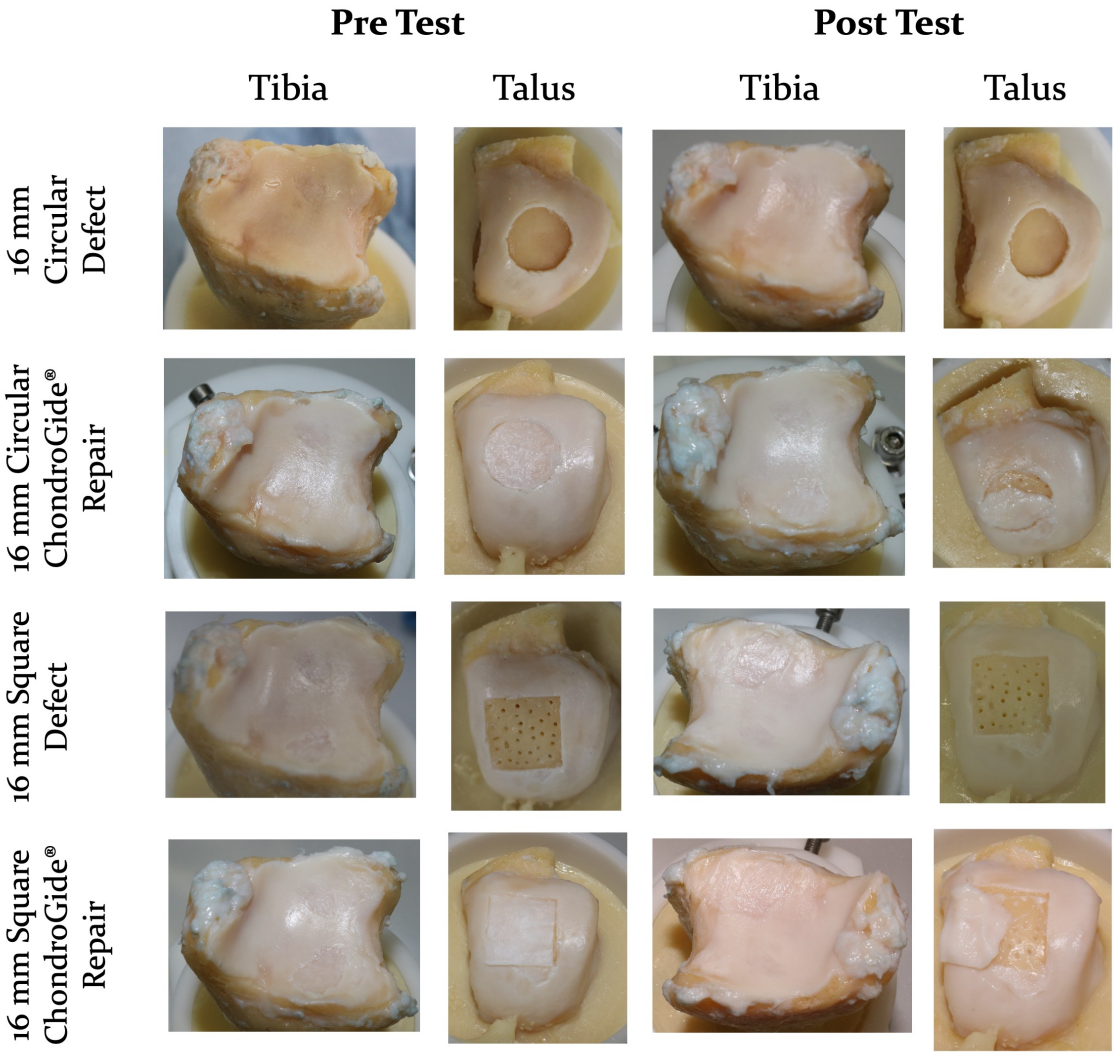

Figure C.20: Pre and post test photographs of sample 6 paired tibia and talar articulating cartilage during tribological testing of conditions

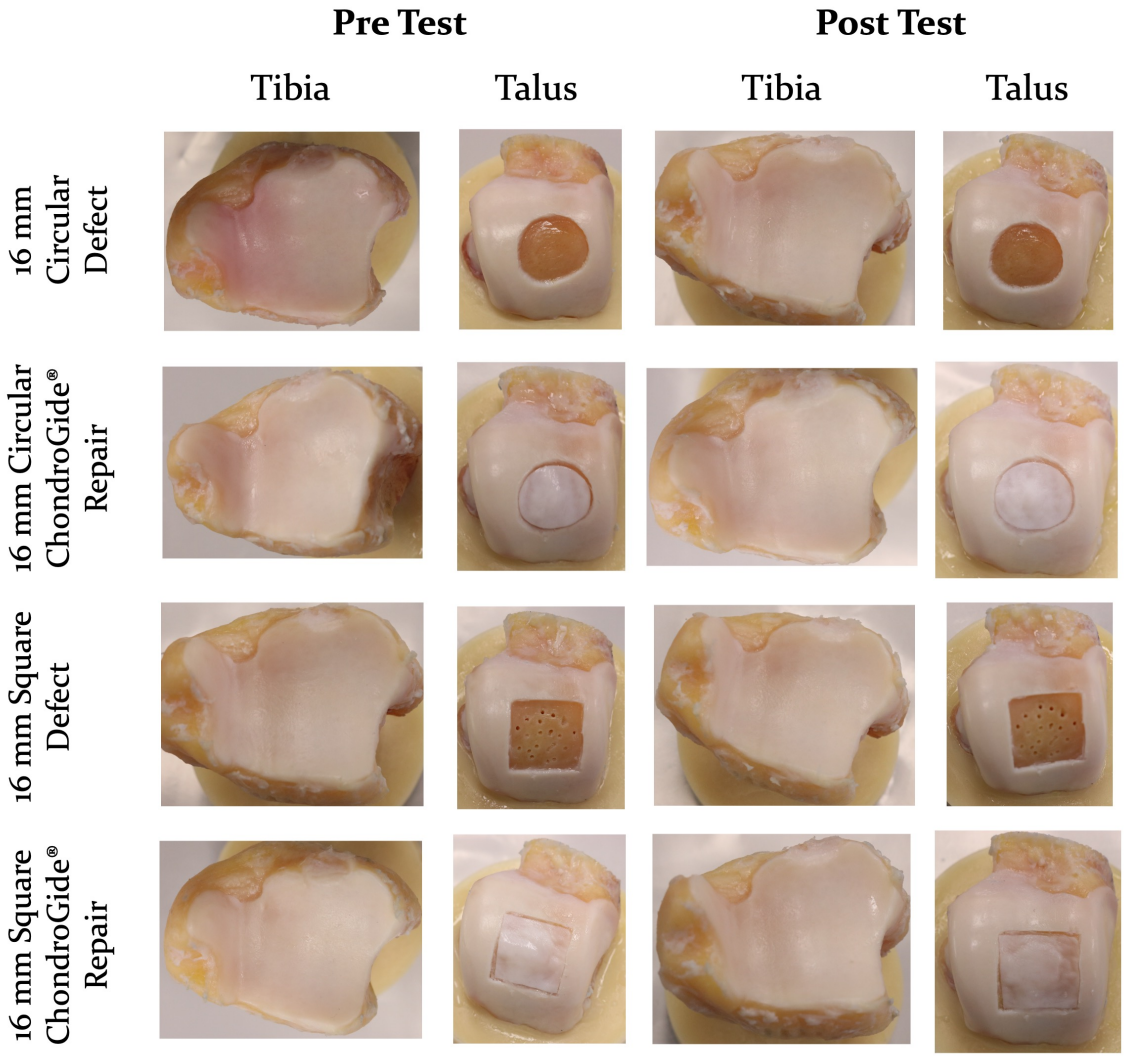

Figure C.21: Pre and post test photographs of sample 7 paired tibia and talar articulating cartilage during tribological testing of conditions

C.2 Chapter 7 - Shoulder Lesions

C.2.1 Contact pressure and contour maps

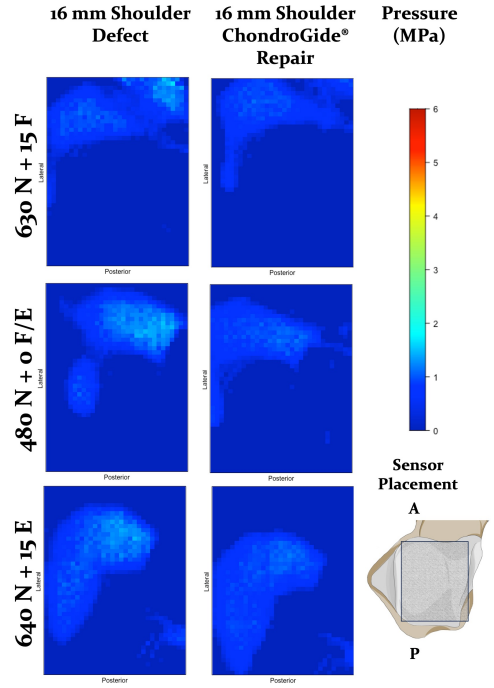

Figure C.22: Sample 1
Pressure maps showing contact area and distribution pressure for each loading condition for across the talar dome for shoulder defect and ChondroGide® repair. A = Anterior, P = Posterior.

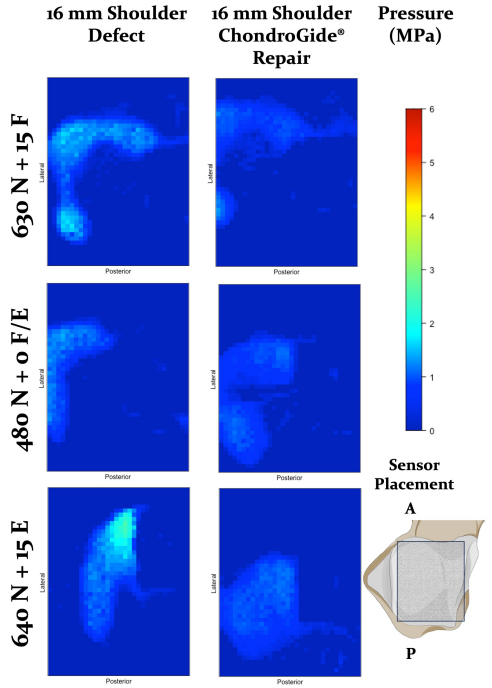

Figure C.23: Sample 2
Pressure maps showing contact area and distribution pressure for each loading condition for across the talar dome for shoulder defect and ChondroGide® repair. A = Anterior, P = Posterior.

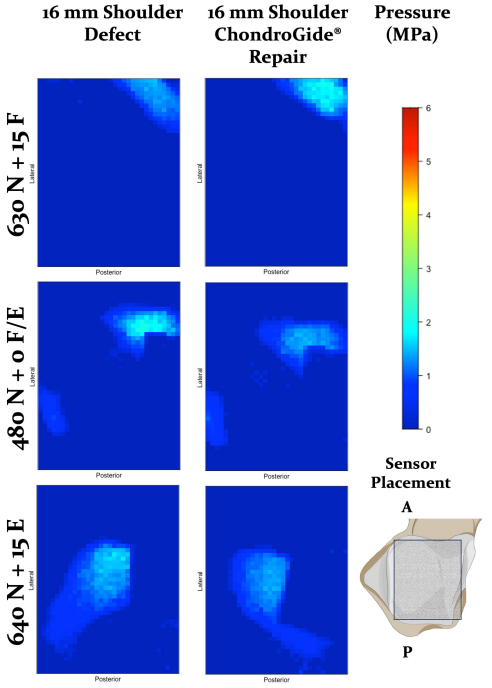

Figure C.24: Sample 3
Pressure maps showing contact area and distribution pressure for each loading condition for across the talar dome for shoulder defect and ChondroGide® repair. A = Anterior, P = Posterior.

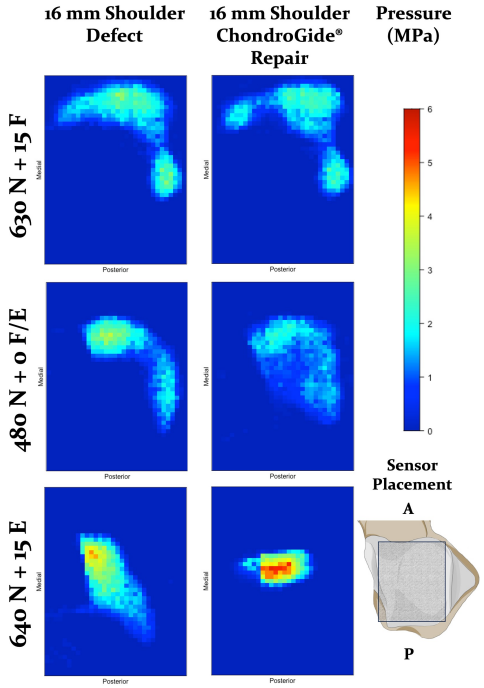

Figure C.25: Sample 4
Pressure maps showing contact area and distribution pressure for each loading condition for across the talar dome for shoulder defect and ChondroGide® repair. A = Anterior, P = Posterior.

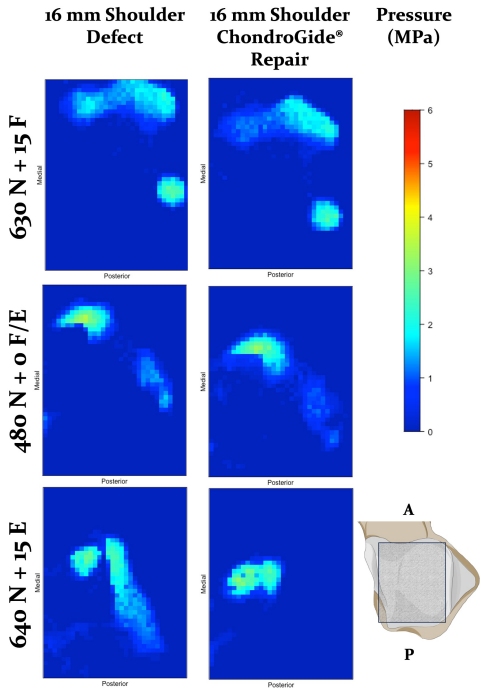

Figure C.26: Sample 5
Pressure maps showing contact area and distribution pressure for each loading condition for across the talar dome for shoulder defect and ChondroGide® repair. A = Anterior, P = Posterior.

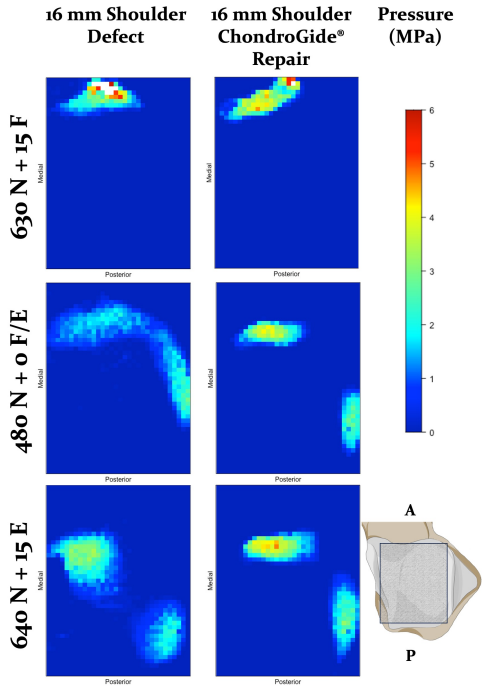

Figure C.27: Sample 6
Pressure maps showing contact area and distribution pressure for each loading condition for across the talar dome for shoulder defect and ChondroGide® repair. A = Anterior, P = Posterior.

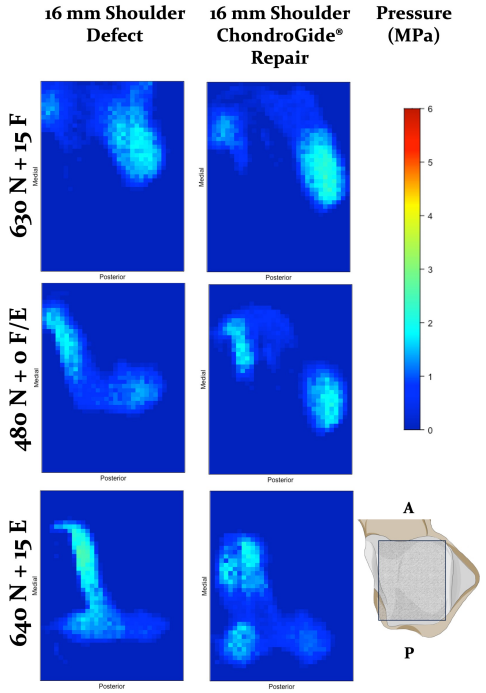

Figure C.28: Sample 7
Pressure maps showing contact area and distribution pressure for each loading condition for across the talar dome for shoulder defect and ChondroGide® repair. A = Anterior, P = Posterior.

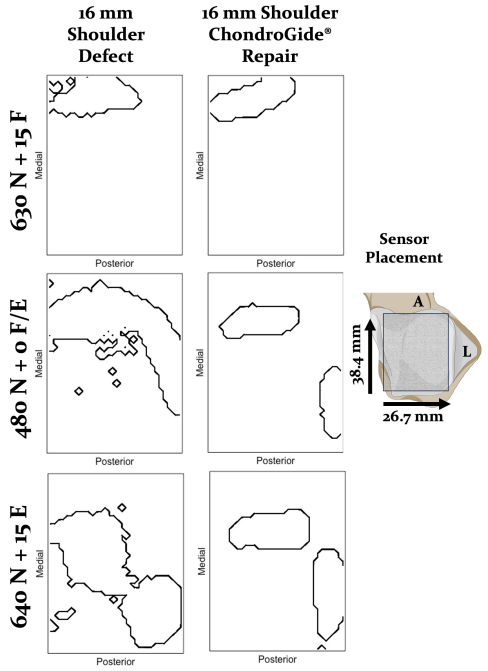

Figure C.29: Sample 1
Contour plots showing contact area across the talar dome for each condition. Region represent a 38.4 x 26.7 mm area on the talar dome. A = Anterior, L = Lateral

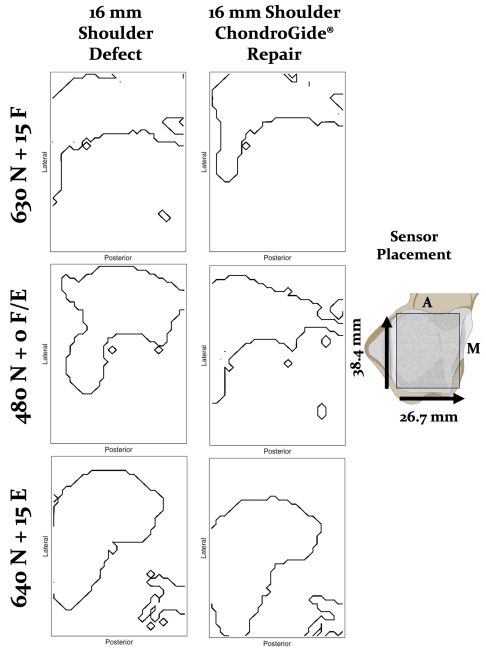

Figure C.30: Sample 2
Contour plots showing contact area across the talar dome for each condition. Region represent a 38.4 x 26.7 mm area on the talar dome. A = Anterior, M = Medial

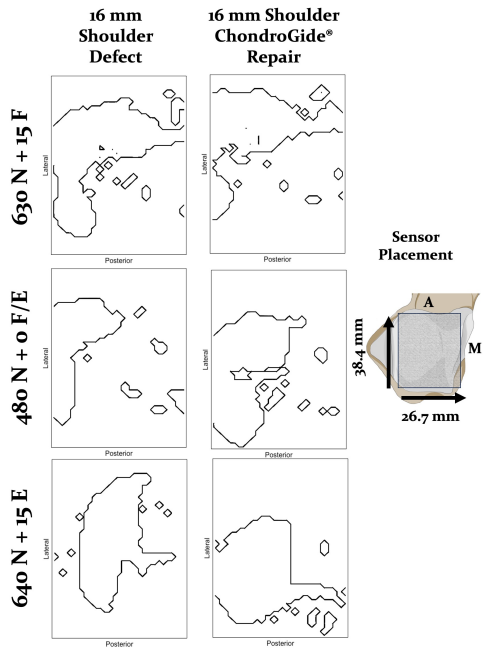

Figure C.31: Sample 3
Contour plots showing contact area across the talar dome for each condition. Region represent a 38.4 x 26.7 mm area on the talar dome. A = Anterior, M = Medial

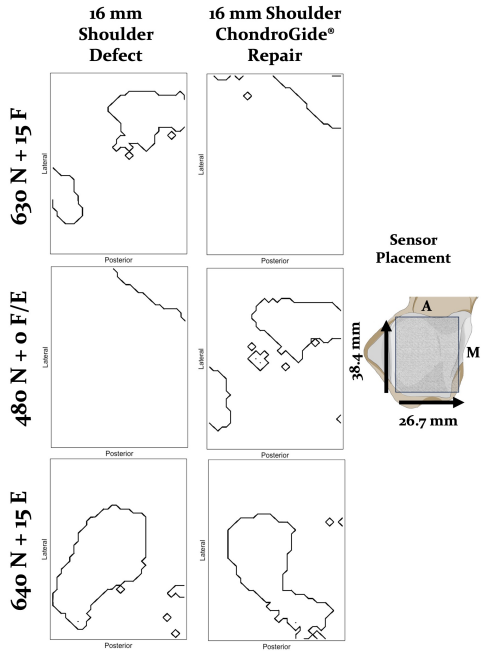

Figure C.32: Sample 4
Contour plots showing contact area across the talar dome for each condition. Region represent a 38.4 x 26.7 mm area on the talar dome. A = Anterior, M = Medial

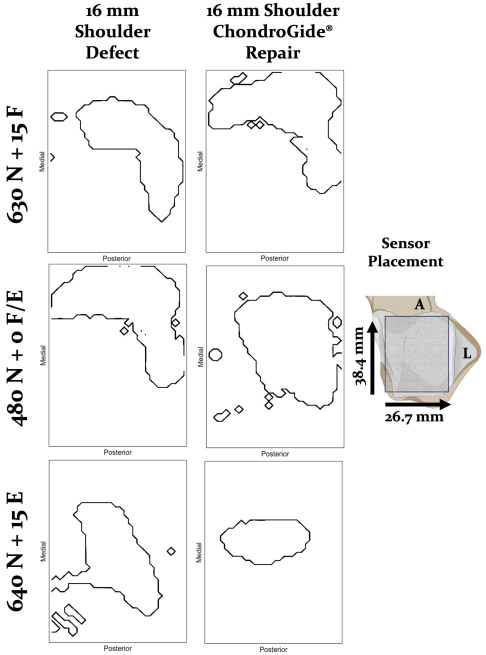

Figure C.33: Sample 5
Contour plots showing contact area across the talar dome for each condition. Region represent a 38.4 x 26.7 mm area on the talar dome. A = Anterior, L = Lateral

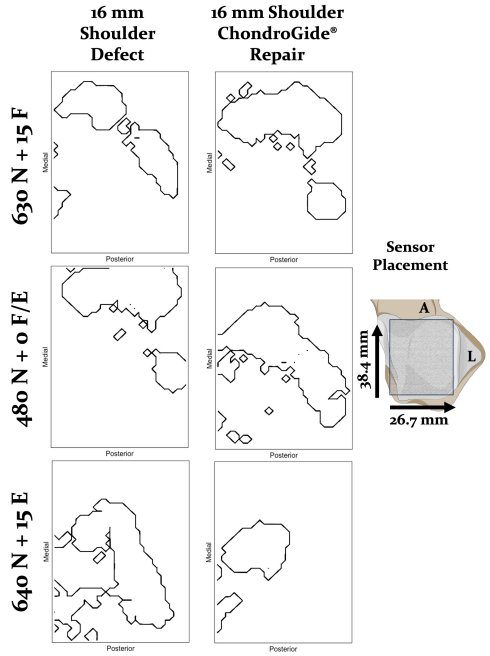

Figure C.34: Sample 6
Contour plots showing contact area across the talar dome for each condition. Region represent a 38.4 x 26.7 mm area on the talar dome. A = Anterior, L = Lateral

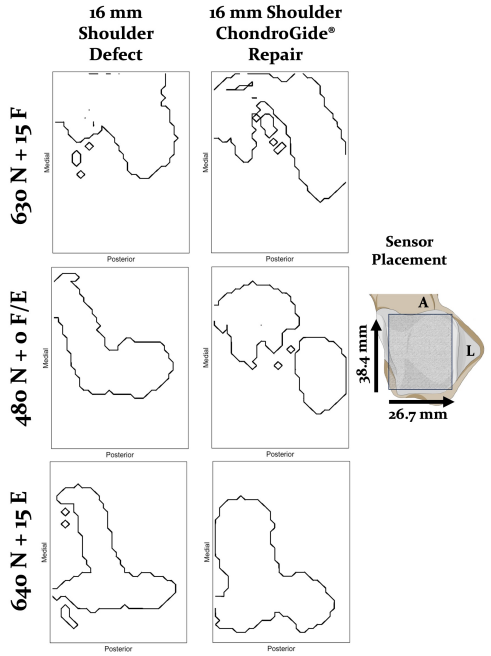

Figure C.35: Sample 7
Contour plots showing contact area across the talar dome for each condition. Region represent a 38.4 x 26.7 mm area on the talar dome. A = Anterior, L = Lateral

C.3 Pre and post testing membrane stability images

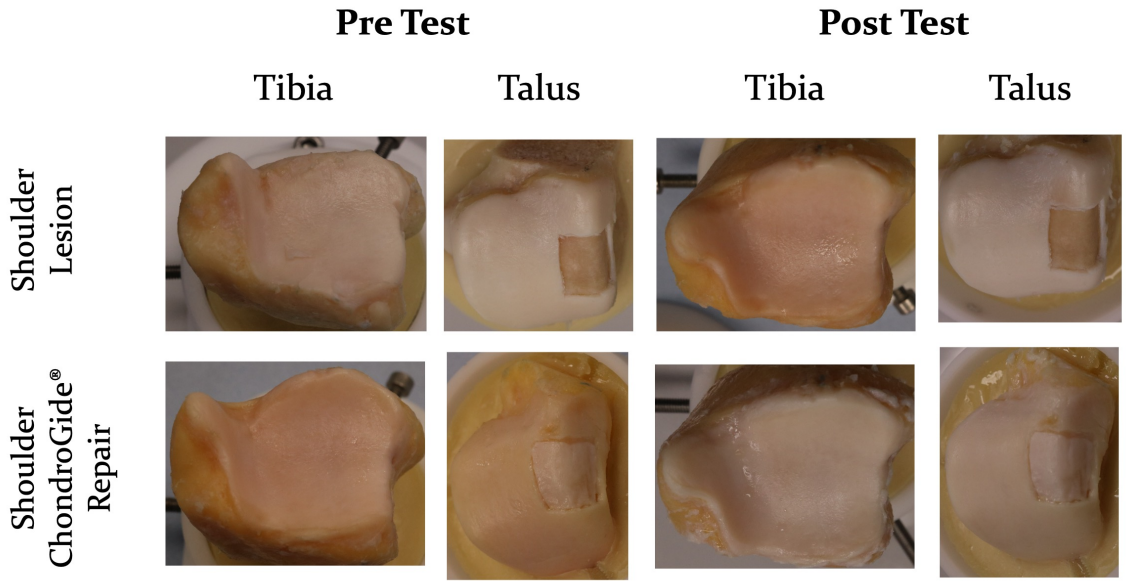

Figure C.36: Pre and post test photographs of sample 1 paired tibia and talar articulating cartilage during tribological testing of conditions

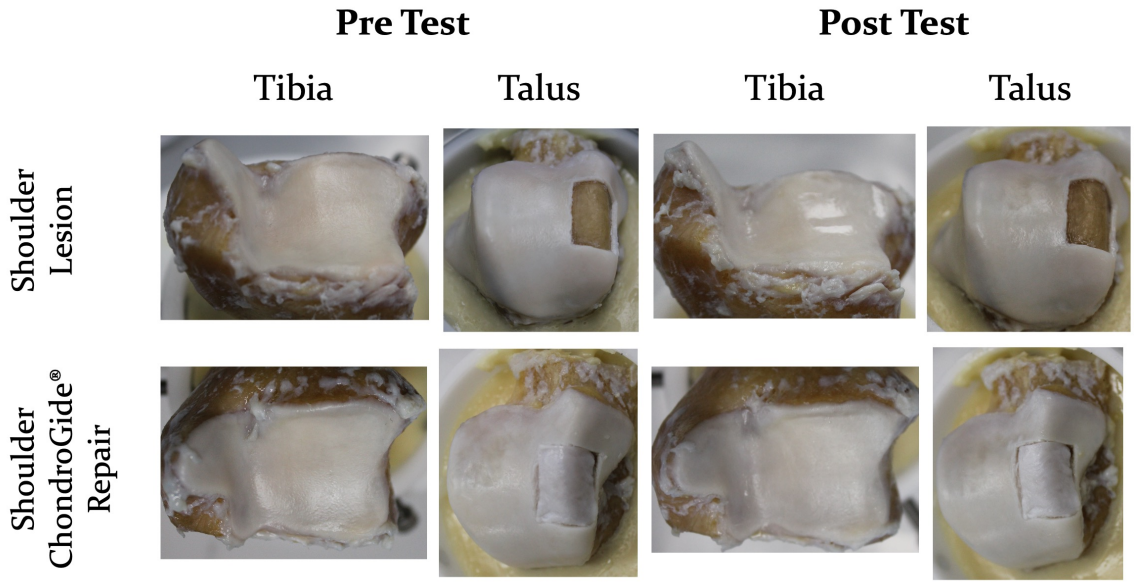

Figure C.37: Pre and post test photographs of sample 2 paired tibia and talar articulating cartilage during tribological testing of conditions

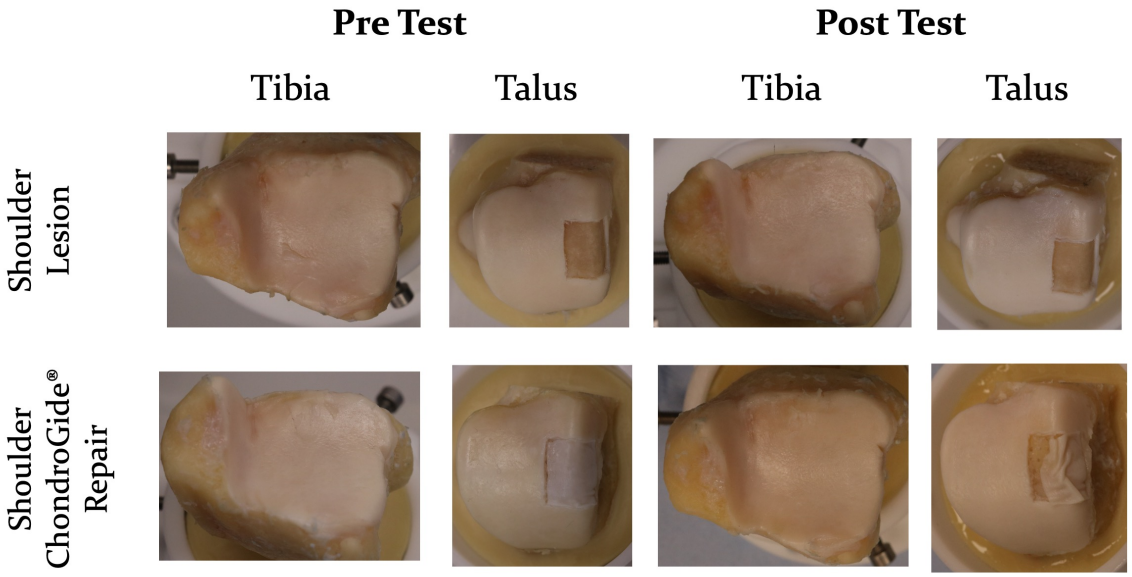

Figure C.38: Pre and post test photographs of sample 3 paired tibia and talar articulating cartilage during tribological testing of conditions

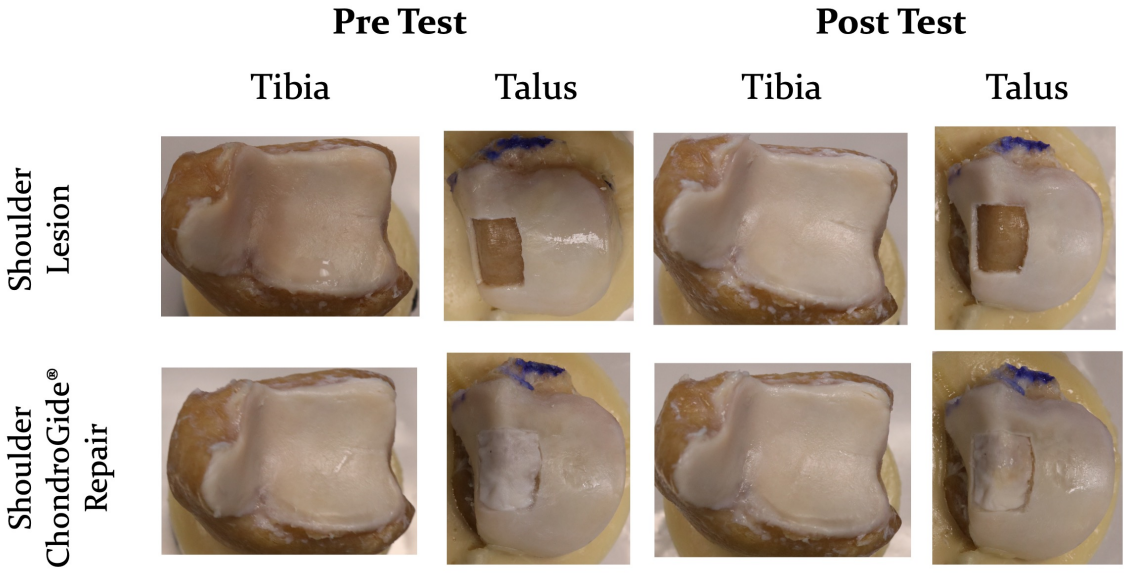

Figure C.39: Pre and post test photographs of sample 4 paired tibia and talar articulating cartilage during tribological testing of conditions

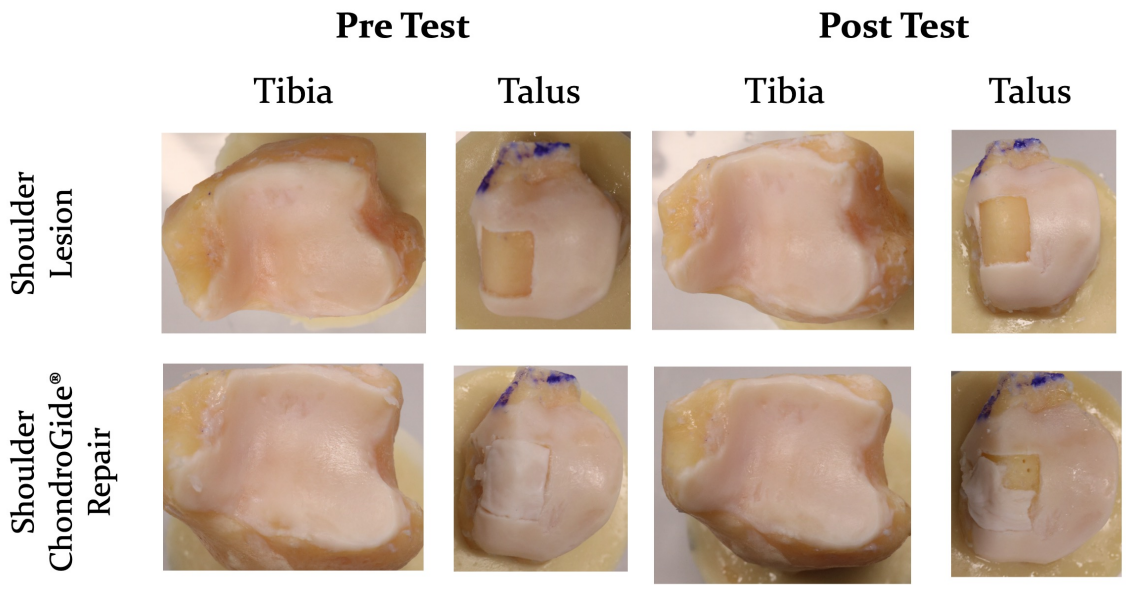

Figure C.40: Pre and post test photographs of sample 5 paired tibia and talar articulating cartilage during tribological testing of conditions

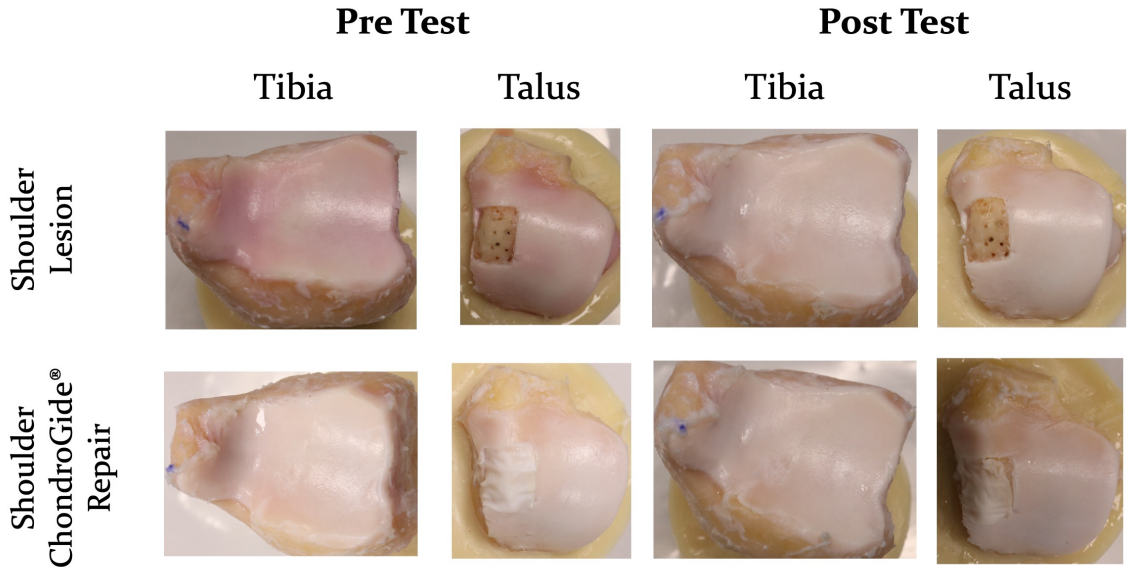

Figure C.41: Pre and post test photographs of sample 6 paired tibia and talar articulating cartilage during tribological testing of conditions

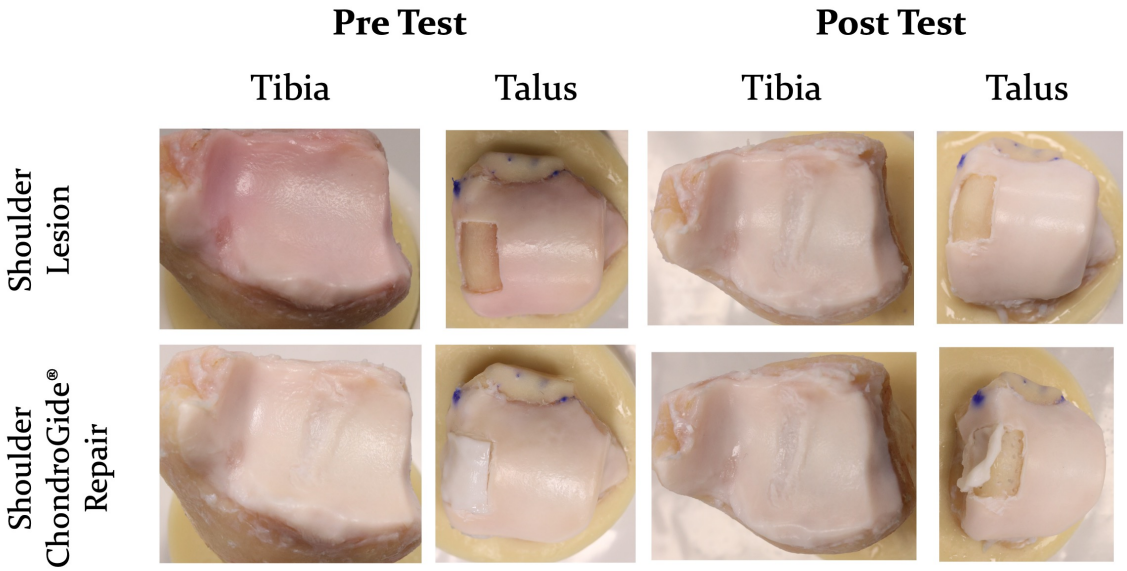

Figure C.42: Pre and post test photographs of sample 7 paired tibia and talar articulating cartilage during tribological testing of conditions

C.4 Chapter 7 - Kissing Lesions

C.4.1 Chapter 7 Contact pressure and contour maps

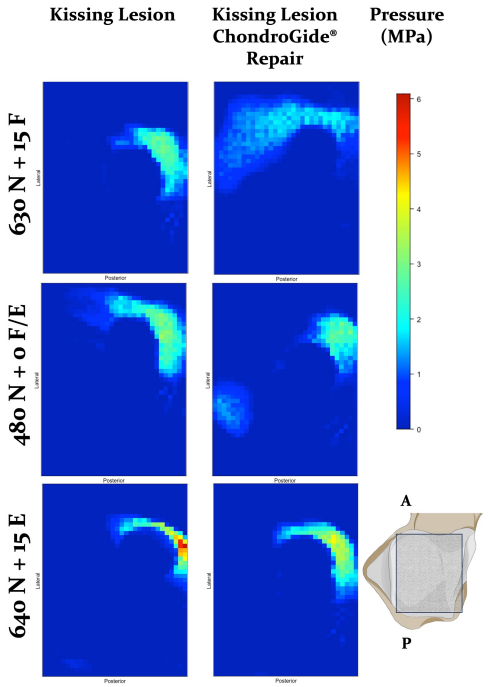

Figure C.43: Sample 1
Pressure maps showing contact area and distribution pressure for each loading condition for across the talar dome for 10 mm kissing lesion and ChondroGide® repair. A = Anterior, P = Posterior.

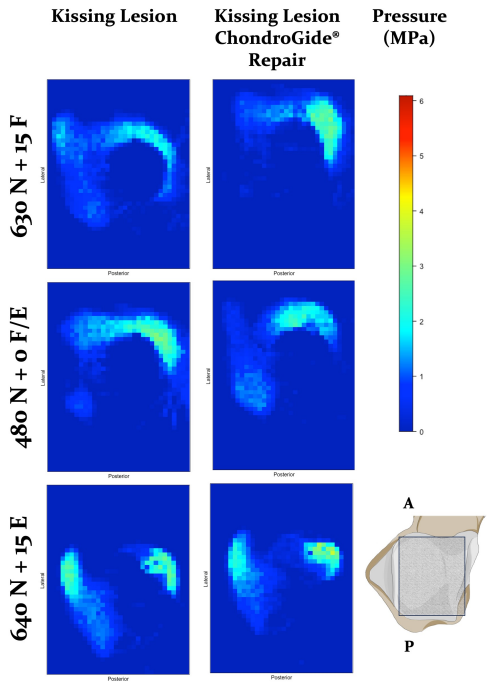

Figure C.44: Sample 2
Pressure maps showing contact area and distribution pressure for each loading condition for across the talar dome for 10 mm kissing lesion and ChondroGide® repair. A = Anterior, P = Posterior.

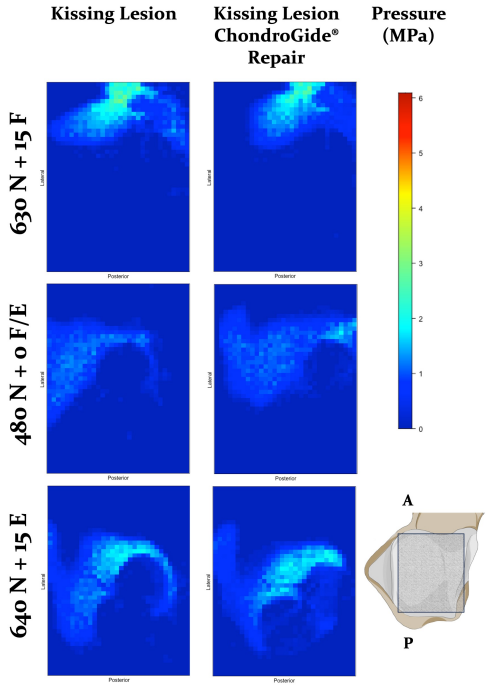

Figure C.45: Sample 3
Pressure maps showing contact area and distribution pressure for each loading condition for across the talar dome for 10 mm kissing lesion and ChondroGide® repair. A = Anterior, P = Posterior.

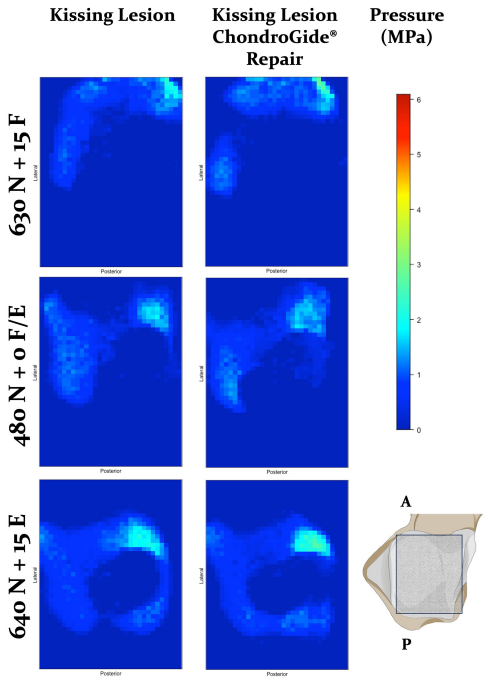

Figure C.46: Sample 4
Pressure maps showing contact area and distribution pressure for each loading condition for across the talar dome for 10 mm kissing lesion and ChondroGide® repair. A = Anterior, P = Posterior.

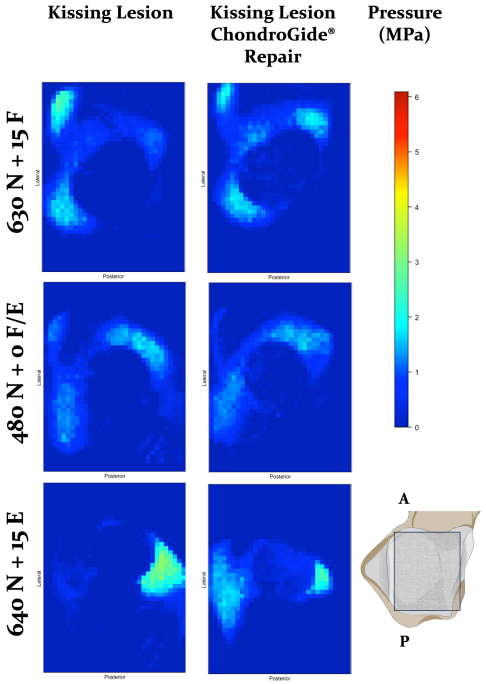

Figure C.47: Sample 5
Pressure maps showing contact area and distribution pressure for each loading condition for across the talar dome for 10 mm kissing lesion and ChondroGide® repair. A = Anterior, P = Posterior.

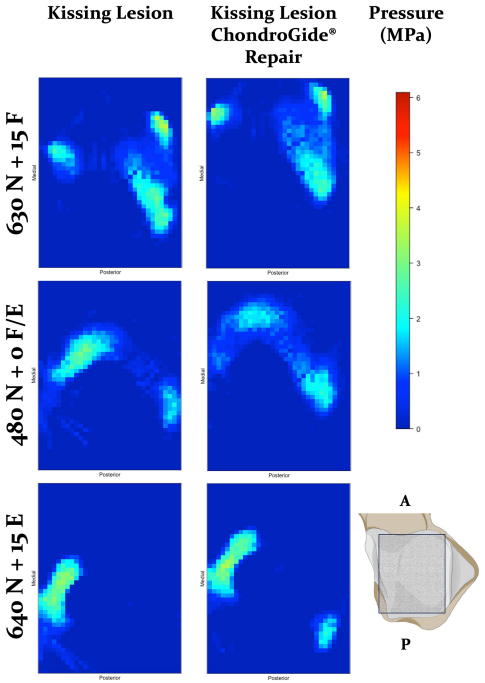

Figure C.48: Sample 6
Pressure maps showing contact area and distribution pressure for each loading condition for across the talar dome for 10 mm kissing lesion and ChondroGide® repair. A = Anterior, P = Posterior.

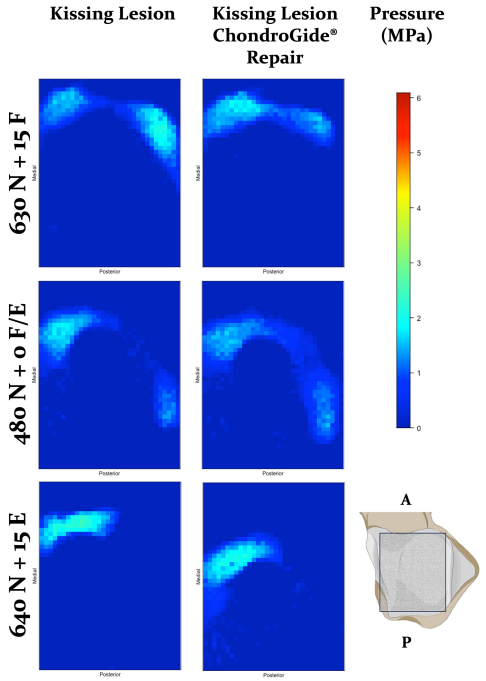

Figure C.49: Sample 7
Pressure maps showing contact area and distribution pressure for each loading condition for across the talar dome for 10 mm kissing lesion and ChondroGide® repair. A = Anterior, P = Posterior.

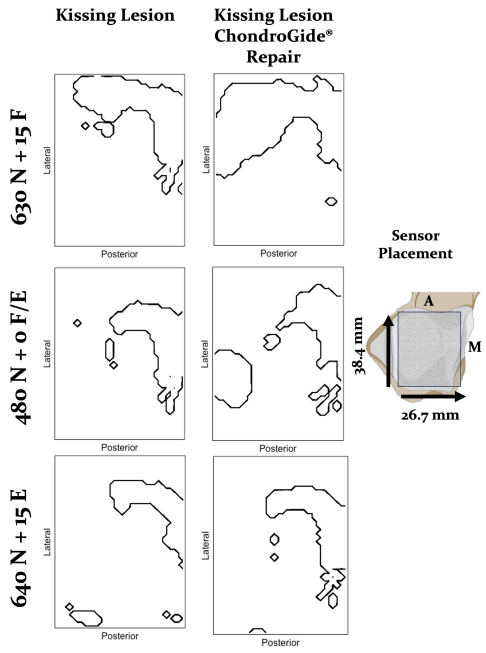

Figure C.50: Sample 1
Contour plots showing contact area across the talar dome for with a kissing lesion and its AMIC repair. Region represent a 38.4 x 26.7 mm area on the talar dome. A = Anterior, M = Medial.

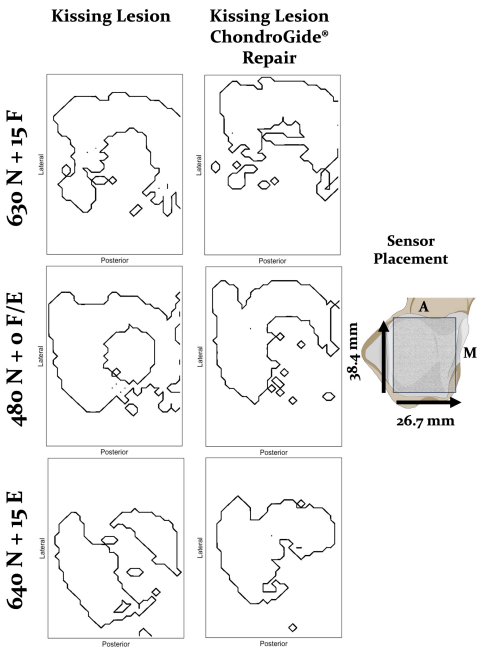

Figure C.51: Sample 2
Contour plots showing contact area across the talar dome for with a kissing lesion and its AMIC repair. Region represent a 38.4 x 26.7 mm area on the talar dome. A = Anterior, M = Medial.

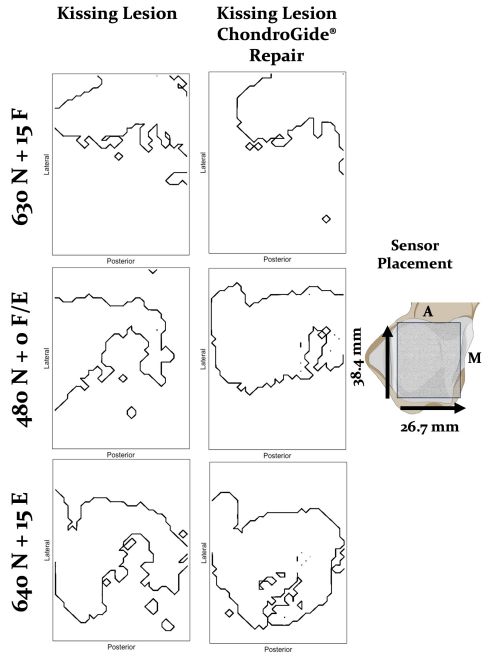

Figure C.52: Sample 3
Contour plots showing contact area across the talar dome for with a kissing lesion and its AMIC repair. Region represent a 38.4 x 26.7 mm area on the talar dome. A = Anterior, M = Medial.

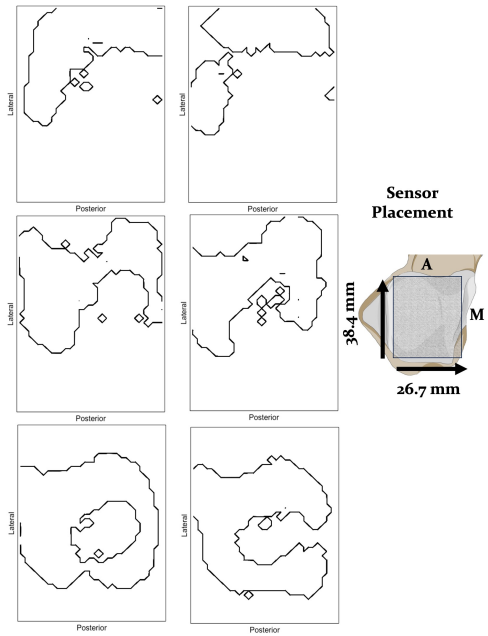

Figure C.53: Sample 4
Contour plots showing contact area across the talar dome for with a kissing lesion and its AMIC repair. Region represent a 38.4 x 26.7 mm area on the talar dome. A = Anterior, M = Medial.

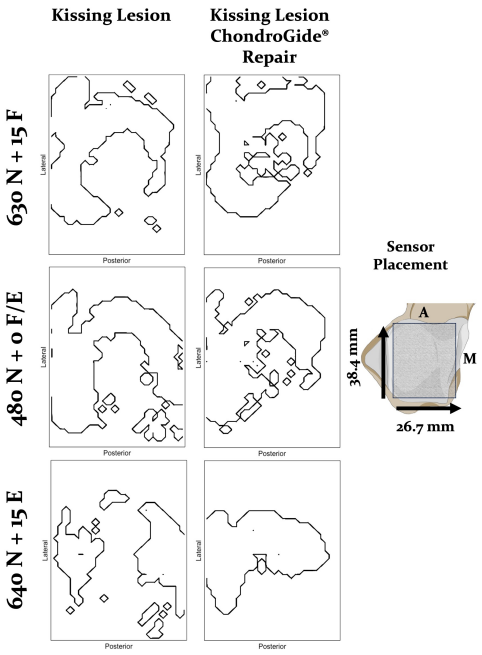

Figure C.54: Sample 5
Contour plots showing contact area across the talar dome for with a kissing lesion and its AMIC repair. Region represent a 38.4 x 26.7 mm area on the talar dome. A = Anterior, L = Lateral.

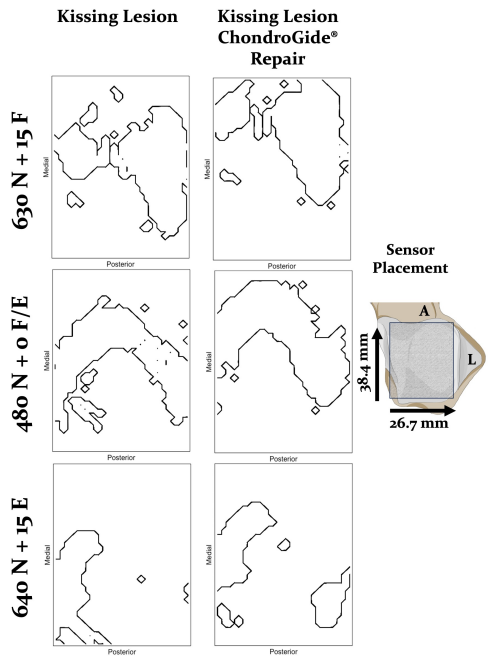

Figure C.55: Sample 6
Contour plots showing contact area across the talar dome for with a kissing lesion and its AMIC repair. Region represent a 38.4 x 26.7 mm area on the talar dome. A = Anterior, L = Lateral.

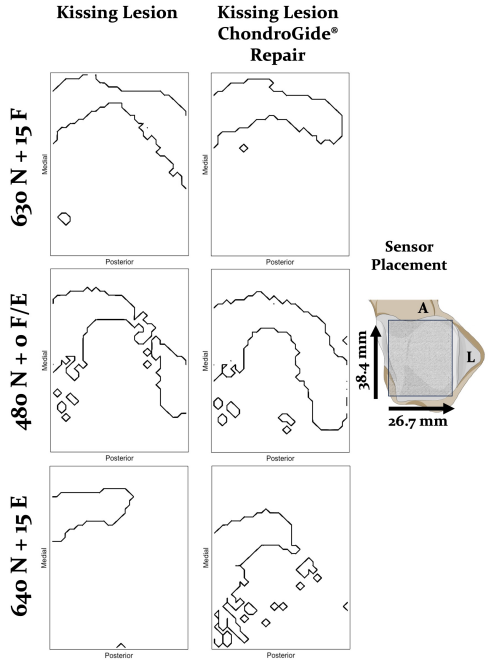

Figure C.56: Sample 1
Contour plots showing contact area across the talar dome for with a kissing lesion and its AMIC repair. Region represent a 38.4 x 26.7 mm area on the talar dome. A = Anterior, L = Lateral.

C.5 Pre and post testing membrane stability images

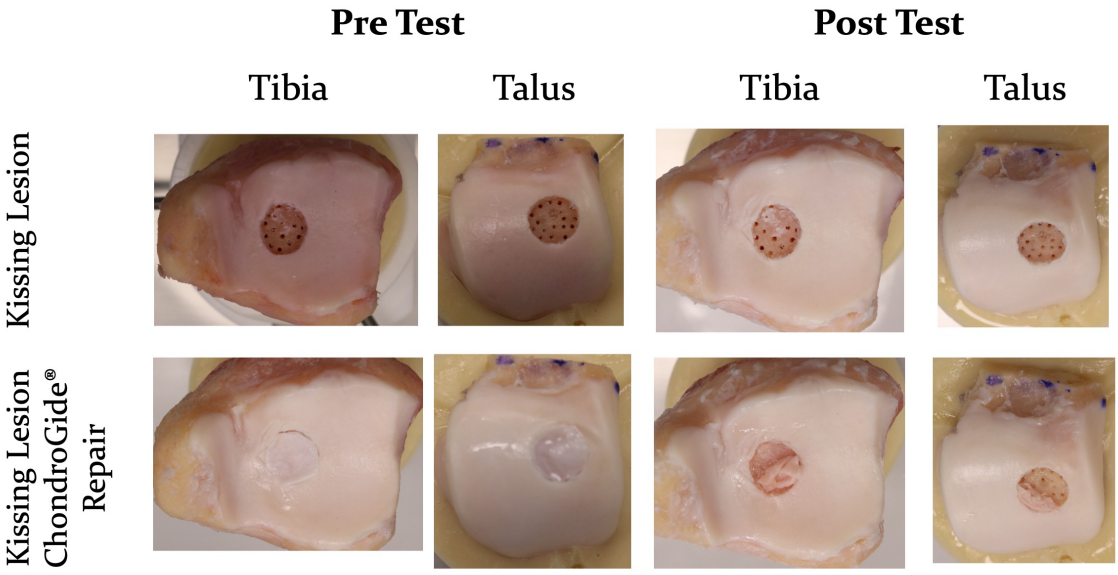

Figure C.57: Pre and post test photographs of sample 1 paired tibia and talar articulating cartilage during tribological testing of conditions

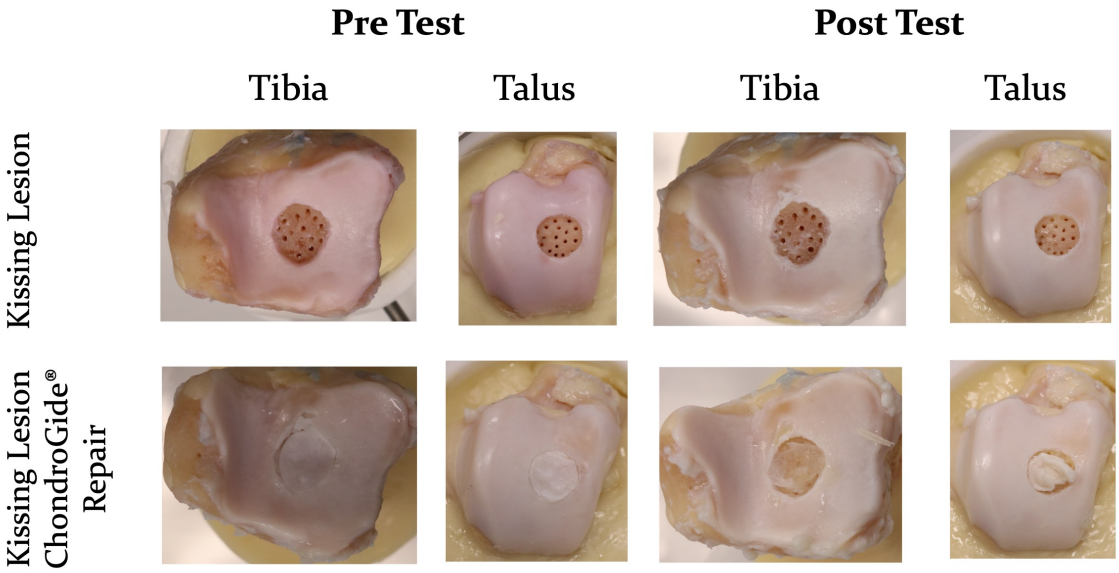

Figure C.58: Pre and post test photographs of sample 2 paired tibia and talar articulating cartilage during tribological testing of conditions

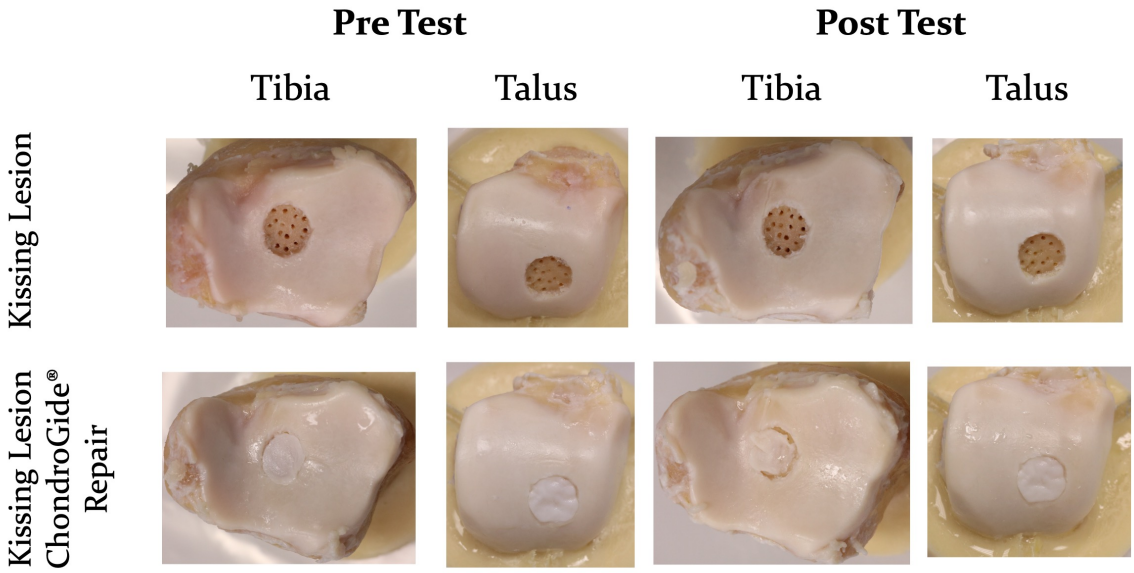

Figure C.59: Pre and post test photographs of sample 3 paired tibia and talar articulating cartilage during tribological testing of conditions

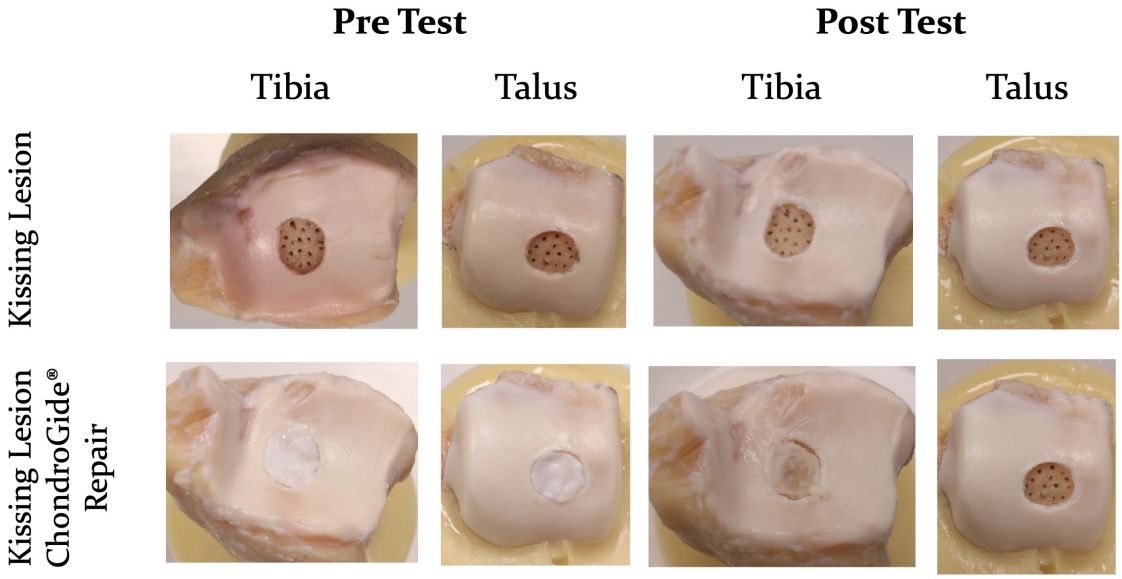

Figure C.60: Pre and post test photographs of sample 4 paired tibia and talar articulating cartilage during tribological testing of conditions

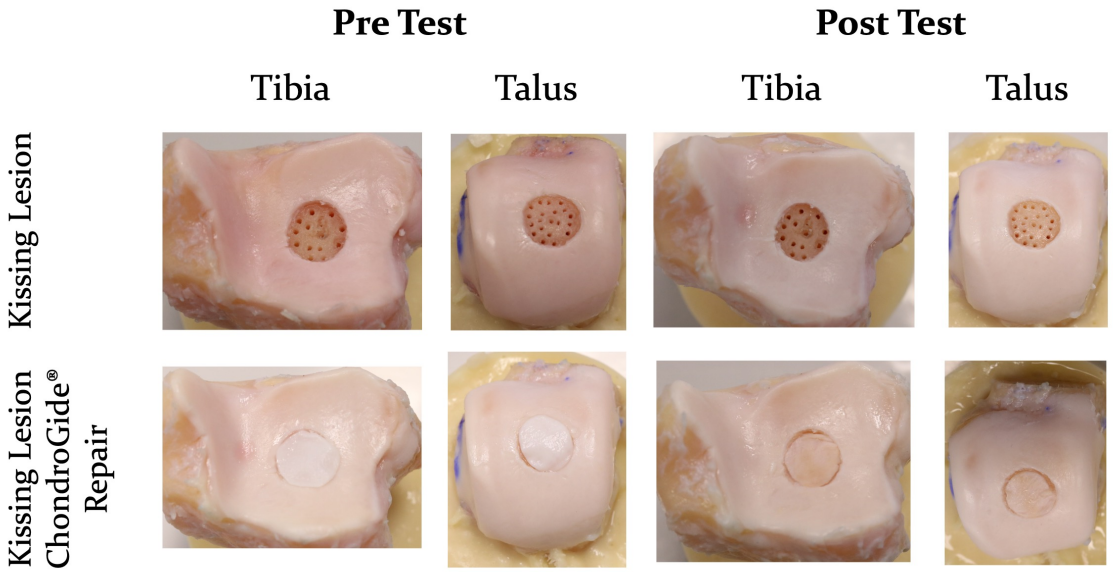

Figure C.61: Pre and post test photographs of sample 5 paired tibia and talar articulating cartilage during tribological testing of conditions

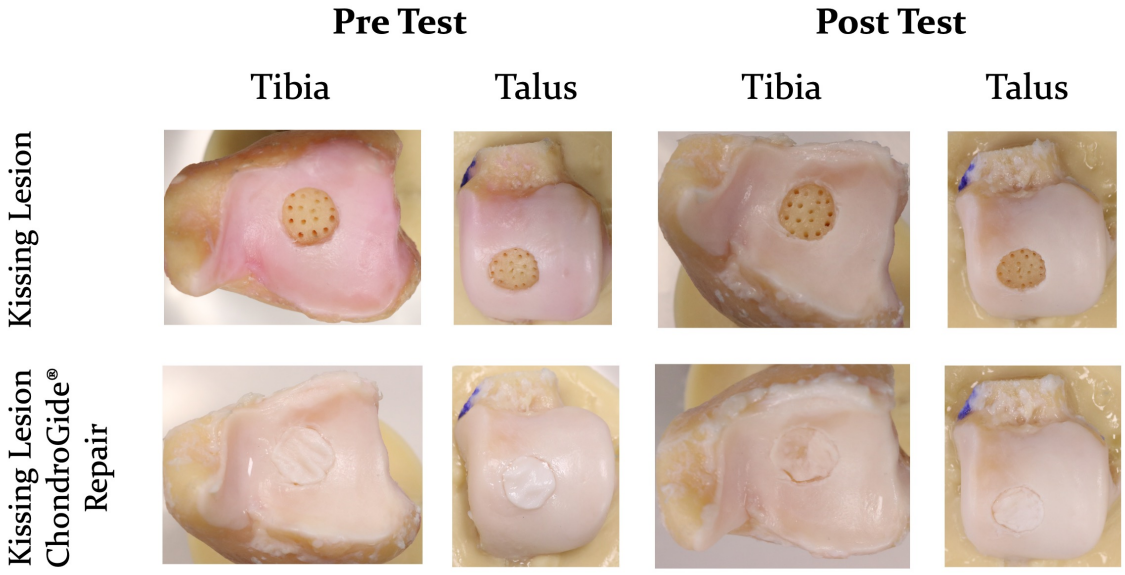

Figure C.62: Pre and post test photographs of sample 6 paired tibia and talar articulating cartilage during tribological testing of conditions

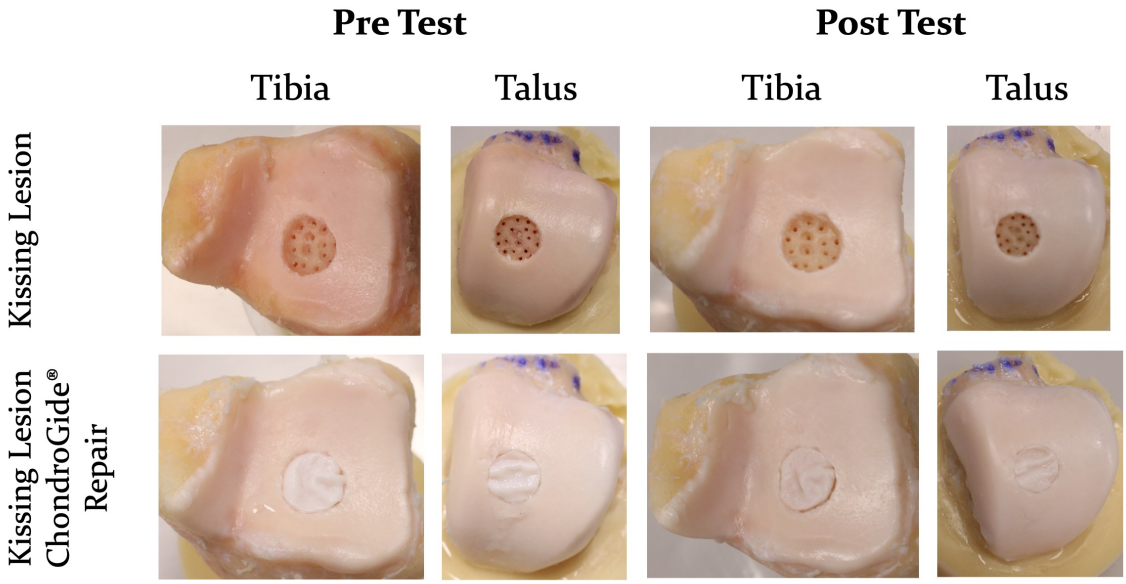

Figure C.63: Pre and post test photographs of sample 7 paired tibia and talar articulating cartilage during tribological testing of conditions

Appendix D

D.1 R Packages

A complete list of R packages used for data analysis is presented here.

M. Kay, L. A. Elkin, J. J. Higgins, and J. O. Wobbrock. *ARTool: Aligned Rank Transform for Nonparametric Factorial ANOVAs*, 2021. URL `https://github.com/mjskay/ARTool`. R package version 0.11.1

J. O. Wobbrock, L. Findlater, D. Gergle, and J. J. Higgins. The aligned rank transform for nonparametric factorial analyses using only anova procedures. In *Proceedings of the ACM Conference on Human Factors in Computing Systems (CHI '11)*, pages 143–146, New York, 2011. ACM Press. doi: 10.1145/1978942.1978963. URL `https://depts.washington.edu/acelab/proj/art/`

L. A. Elkin, M. Kay, J. J. Higgins, and J. O. Wobbrock. An aligned rank transform procedure for multifactor contrast tests, 2021

R Core Team. *R: A Language and Environment for Statistical Computing*. R Foundation for Statistical Computing, Vienna, Austria, 2022. URL `https://www.R-project.org/`

J. Fox and S. Weisberg. *An R Companion to Applied Regression*. Sage, Thousand Oaks CA, third edition, 2019. URL `https://socialsciences.mcmaster.ca/jfox/Books/Companion/`

J. Fox, S. Weisberg, and B. Price. *carData: Companion to Applied Regression Data Sets*, 2022. URL `https://CRAN.R-project.org/package=carData`. R package version 3.0-5

T. Keitt. *colorRamps: Builds Color Tables*, 2022. URL https://CRAN.R-project.org/package=colorRamps. R package version 2.3.1

D. Armstrong. *DAMisc: Dave Armstrong's Miscellaneous Functions*, 2022. URL https://CRAN.R-project.org/package=DAMisc. R package version 1.7.2

A. Signorell. *DescTools: Tools for Descriptive Statistics*, 2023. URL https://CRAN.R-project.org/package=DescTools. R package version 0.99.48

H. Wickham, J. Hester, W. Chang, and J. Bryan. *devtools: Tools to Make Developing R Packages Easier*, 2022b. URL https://CRAN.R-project.org/package=devtools. R package version 2.4.4

A. Dinno. *dunn.test: Dunn's Test of Multiple Comparisons Using Rank Sums*, 2017. URL https://CRAN.R-project.org/package=dunn.test. R package version 1.3.5

R. V. Lenth. *emmeans: Estimated Marginal Means, aka Least-Squares Means*, 2023. URL https://CRAN.R-project.org/package=emmeans. R package version 1.8.8

D. H. Ogle, J. C. Doll, A. P. Wheeler, and A. Dinno. *FSA: Simple Fisheries Stock Assessment Methods*, 2023. URL https://CRAN.R-project.org/package=FSA. R package version 0.9.4

A. Kassambara. *ggpubr: 'ggplot2' Based Publication Ready Plots*, 2023a. URL https://CRAN.R-project.org/package=ggpubr. R package version 0.6.0

G. R. Warnes, B. Bolker, L. Bonebakker, R. Gentleman, W. Huber, A. Liaw, T. Lumley, M. Maechler, A. Magnusson, S. Moeller, M. Schwartz, and B. Venables. *gplots: Various R Programming Tools for Plotting Data*, 2022. URL https://CRAN.R-project.org/package=gplots. R package version 3.1.3

B. Auguie. *gridExtra: Miscellaneous Functions for "Grid" Graphics*, 2017. URL https://CRAN.R-project.org/package=gridExtra. R package version 2.3

D. Sarkar. *Lattice: Multivariate Data Visualization with R*. Springer, New York, 2008. URL http://lmdvr.r-forge.r-project.org. ISBN 978-0-387-75968-5

D. Sarkar and F. Andrews. *latticeExtra: Extra Graphical Utilities Based on Lattice*, 2022. URL https://CRAN.R-project.org/package=latticeExtra. R package version 0.6-30

D. Bates, M. Maechler, and M. Jagan. *Matrix: Sparse and Dense Matrix Classes and Methods*, 2022. URL https://CRAN.R-project.org/package=Matrix. R package version 1.5-1

H. Bengtsson. *matrixStats: Functions that Apply to Rows and Columns of Matrices (and to Vectors)*, 2022. URL https://CRAN.R-project.org/package=matrixStats. R package version 0.62.0

J. Kaupp. *nord: Arctic Ice Studio's Nord and Group of Seven Inspired Colour Palettes for 'ggplot2'*, 2019. URL https://CRAN.R-project.org/package=nord. R package version 1.0.0

H. De Rosario-Martinez. *phia: Post-Hoc Interaction Analysis*, 2015. URL https://CRAN.R-project.org/package=phia. R package version 0.2-1

L. J. Plotrix: a package in the red light district of r. *R-News*, 6(4):8–12, 2006

H. Wickham. The split-apply-combine strategy for data analysis. *Journal of Statistical Software*, 40(1):1–29, 2011. URL https://www.jstatsoft.org/v40/i01/

E. Neuwirth. *RColorBrewer: ColorBrewer Palettes*, 2022. URL https://CRAN.R-project.org/package=RColorBrewer. R package version 1.1-3

H. Wickham. Reshaping data with the reshape package. *Journal of Statistical Software*, 21(12), 2007a. URL https://www.jstatsoft.org/v21/i12/

H. Wickham. Reshaping data with the reshape package. *Journal of Statistical Software*, 21(12): 1–20, 2007b. URL http://www.jstatsoft.org/v21/i12/

A. Kassambara. *rstatix: Pipe-Friendly Framework for Basic Statistical Tests*, 2023b. URL https://CRAN.R-project.org/package=rstatix. R package version 0.7.2

H. Wickham, J. Bryan, and M. Barrett. *usethis: Automate Package and Project Setup*, 2022a. URL https://CRAN.R-project.org/package=usethis. R package version 2.1.6

H. Wickham, M. Averick, J. Bryan, W. Chang, L. D. McGowan, R. François, G. Grolemund, A. Hayes, L. Henry, J. Hester, M. Kuhn, T. L. Pedersen, E. Miller, S. M. Bache, K. Müller, J. Ooms, D. Robinson, D. P. Seidel, V. Spinu, K. Takahashi, D. Vaughan, C. Wilke, K. Woo, and H. Yutani. Welcome to the tidyverse. *Journal of Open Source Software*, 4(43):1686, 2019. doi: 10.21105/joss.01686